ABSTRACT

Title of Document: GRAPHITE OXIDATION AND DAMAGE UNDER IRRADIATION AT HIGH TEMPERATURES IN AN IMPURE HELIUM ENVIRONMENT

Cameron S. Goodwin,

Doctor of Philosophy, 2012

Directed By: Professor Mohamad Al-Sheikhly, Department of Materials Science and Engineering

The High Temperature Gas-Cooled Reactor (HTGR) is a Generation IV reactor concept that uses a graphite-moderated nuclear reactor with a once-through uranium fuel cycle. In order to investigate the mechanism for corrosion of graphite in HTGRs, the graphite was placed in a similar environment in order to evaluate its resistance to corrosion and oxidation. While the effects of radiation on graphite have been studied in the past, the properties of graphite are largely dependent on the coke used in manufacturing the graphite. There are no longer any of the previously studied graphite types available for use in the HTGR. There are various types of graphite being considered for different uses in the HTGR and all of these graphite types need to be analyzed to determine how radiation will affect them. Extensive characterization of samples of five different types of graphite was conducted. The irradiated samples were analyzed with electron paramagnetic resonance spectroscopy, Raman spectroscopy, x-ray diffraction, x-ray photoelectron spectroscopy and

gas chromatography. The results prove a knowledge base for considering the graphite types best suited for use in HTGRs.

In my dissertation work graphite samples were gamma irradiated and also irradiated in a mixed field, in order to study the effects of neutron as well as gamma irradiation. Thermal effects on the graphite were also investigated by irradiating the samples at room temperature and at 1000 °C. From the analysi of the samples in this study there is no evidence of substantial damage to the grades of graphite analyzed. This is significant in approving the use of these graphites in nuclear reactors. Should significant damage had occurred to the samples, the use of these grades of graphite would need to be reconsidered. This information can be used to further characterize other grades of nuclear graphite as they become available.

GRAPHITE OXIDATION AND DAMAGE UNDER IRRADIATION AT HIGH TEMPERATURES IN AN IMPURE HELIUM ENVIRONMENT

By

Cameron S. Goodwin

Dissertation submitted to the Faculty of the Graduate School of the
University of Maryland, College Park, in partial fulfillment
of the requirements for the degree of
Doctor of Philosophy,
2012

Advisory Committee:
Professor Mohamad Al-Sheikhly, Chair
Professor Aaron Barkatt
Professor Michael Coplan, Dean's Representative
Professor Lourdes Salamanca-Riba
Associate Professor Gary Pertmer

Acknowledgements

Many people have contributed to the completion of this dissertation. I would like to sincerely thank everyone who has offered advice, an attentive ear or their precious time to me during my Ph.D.

I would like to thank Dr. Al-Sheikhly for all of his support and advice and for allowing me to work in his group. Dr. Barkatt served as an integral mentor and provided hours of discussion, without which I would not have been able to complete my dissertation. Mr. Vince Adams provided me all of the help and encouragement I needed to construct my experimental set-up and solve technical problems. Without his help, I might still be building shielding.

I would like to thank the U.S. Nuclear Regulatory Commission and my division director, Mr. Michael Mayfield, for allowing me to come to the University of Maryland and complete research to increase our knowledge base at the NRC and also complete a life-long dream of earning a Ph.D.

This would not have been possible without the love and support of my family. My parents always encouraged me to go for my dreams and to never give up. My husband, Jared, provided the support I needed to complete this process and was especially understanding of the last minute late evening meetings. None of this would be possible without your unwavering support and the outlet you provided me to vent my frustrations. Finally, I would like to thank my children, Madeleine and Harrison, for hanging out at the reactor and helping Mommy. Those days were the best part of this and I will always look back and cherish those memories.

Table of Contents

Acknowledgements i
Table of Contents iii
List of Tables vi
List of Figures viii
Chapter 1 Introduction 1
1.1 Helium contaminants 1
1.2 Objectives 4
1.3 Structure of Graphite 6
Chapter 2 Nuclear Graphite Use and Its Production 14
2.1 Importance of Nuclear Graphite 14
2.2 Previous Use of Graphite in Nuclear Power Plants 16
2.3 How Nuclear Graphite is Manufactured 16
Chapter 3 Irradiation Induced Damage in Graphite 18
3.1 Background 18
3.2 Energy Transfer 19
3.3 Irradiation Induced Defects 22
3.4 Irradiation Induced Dimensional Changes 27
Chapter 4 Graphite Oxidation 30
4.1 Oxidation Reactions of Graphite 30
4.1.1 Reaction with Oxygen 31
4.1.2 Reaction with Carbon Dioxide 32
4.1.3 Reaction with Water 33
4.1.4 Reactivity Differences in Carbon 34
4.1.5 Radiolytic Oxidation 39
4.2 Temperature Regimes of Oxidation 42
4.2.1 Region 1 43
4.2.2 Region 2 45

4.2.3 Region 3 46
Chapter 5 Sample Description and Preparation 48
5.1 Sample Description 48
5.2 Sample Preparation 50
Chapter 6 Gamma Irradiation 55
6.1 Gamma Irradiation Background 55
6.2 Gamma Source Description 57
6.3 Dosimetry 60
6.3.1 Far West Films 60
6.3.2 Fricke Dosimetry 62
6.4 Gamma Irradiation of Graphite Samples 63
Chapter 7 Nuclear Irradiation 64
7.1 Neutron Irradiation at Armed Forces Radiobiology Research Institute 64
7.2 Neutron Irradiation Facilities at UMD 67
7.2.1 Pneumatic Transfer System 68
7.2.2 East Beam Port 71
Chapter 8 Experimental Design 75
8.1 Shielding 75
8.1.1 Shutter 75
8.1.2 Walls 79
8.1.3 Collar for the Face of the Reactor 80
8.1.4 Cave 82
8.1.5 Dose Mapping 85
8.2 East Beam Port Experimental Set-up 89
8.2.1 Sample Flow Path 89
8.2.2 GC 94
8.2.3 Heater 96
8.3 Analytical Techniques 98
8.3.1 Graphite Oxidation Techniques 98
8.3.2 Magnetic Properties 114

Chapter 9 Results and Discussion....120
9.1 Oxidation Results....120
9.1.1 Characterizing the oxidation of graphite using GC.... 120
9.1.2 Characterizing the irradiation induced changes in graphite using Raman spectroscopy.... 124
9.1.3 Determining the oxygen content of graphite using XPS.... 138
9.1.4 Determining structural changes in graphite using XRD.... 175
9.2 Magnetic Properties....201
9.2.1 Invesitgating the mechanism causing changes to the unpaired electrons in graphite using EPR spectroscopy.... 201
9.2.2 Investigation of the radiation-induced changes diamagnetic properties of PCEA using the SQUID magnetometer.... 219
Chapter 10 Conclusions and Future Work....228
10.1 Conclusions....228
10.2 Future Work....232
10.3 Contribution to Science....234
Appendix A. The Manufacturing of Graphite....236
Appendix B. Raman Spectroscopy Results....245
Appendix C. XRD Results....311
Appendix D. Special Experimental Proposals Approved by the Reactor Safety Committee335
References....363

List of Tables

Table 1-1: The above table lists G values for the radiolysis of water at pHs between 3 and 11 [Takamoto and Chance, 2006]. 4
Table 1-2: Ionization potential for carbon electrons [Pierson, 1993]. 7
Table 1-3: This table lists impurities present in the samples of PCEA, PPEA and PCIB. These results are from Glow Discharge Mass Spectrometry elemental analysis performed by UCAR Carbon Co. Inc. 13
Table 3-1: Atomic Displacements in Graphite Produced by Various Energetic Particles [Simmons, 1965]. 23
Table 4-1: G Values for various irradiating particles in CO_2 [Marsh, 1989]. 40
Table 5-1: This table shows the 5 types of graphite used in the experiments. It lists their manufacturer, coke type, forming method, maximum particle size and density [NRC, 2010]. 49
Table 5-2: This table shows the lettering system for the laser etching of the samples. 54
Table 6-1: Radioactive isotopes commonly used for γ radiation sources. This table shows the isotope, half-life and type and energy of the radiation released (Woods and Pikaev, 1994). 56
Table 6-2: This table shows the irradiation time, total dose and uncertainty for the three set of samples irradiated in the UMD Co-60 gamma source. 63
Table 7-1: Irradiation data for the first set of samples irradiated at the AFRRI reactor. 67
Table 7-2: Irradiation data for the second set of samples irradiated at the AFRRI reactor. .. 67
Table 7-3: Radiation rates for the pneumatic transfer system [MUTR, 2000]. 69
Table 7-4: Graphite irradiations in the pneumatic tube heated to 300 ºC. Each run was approximately 6-hours long. 71
Table 7-5: Accumulated fluence for the room temperature irradiated samples. 74
Table 7-6: Accumulated fluence for the 1000 °C irradiated samples. 74
Table 8-1: Dose rate measurements taken in the vicinity of the east beam port with the beam shutter OPEN. The drawing above the table denotes the areas where measurements were taken. This table shows the gamma dose rate in mR/hr and the neutron dose rate in cpm at 250 kW. 88

Table 8-2: This table lists several properties of the Alumina used to make the sample chamber. 93
Table 9-1: G-value for carbon monoxide calculated from GC data. 124
Table 9-2: Summary of Raman peaks (cm^{-}) for all experiments. 127
Table 9-3: I_D/I_G and I_{2D}/I_G including 95 % confidence levels for each experimental condition. Also shown are the calculated L_a values. 132
Table 9-4: This table shows the 5 types of graphite used in the experiments. It lists their forming method and maximum particle size [NRC, 2010]. 133
Table 9-5: XPS results for the gamma irradiated graphite samples. 141
Table 9-6: XPS results for the mixed field irradiated graphite samples. 156
Table 9-7: EPR data collection parameters. 201
Table 9-8: Standard sample deviation and 95% confidence limits for PCEA AG EPR samples. 204
Table A-1: Typical Properties of Room-Temperature Graphite (Nightingale, 1962). 243
Table C-1: XRD data results for all samples. 334

List of Figures

Figure 1-1: Products of the radiolysis of water. The following radicals and molecular products are produced: $\dot{e}_{aq}^{-}$, $\dot{H}$, $\dot{O}H$, H_2O_2, H_2 and H^+ [Takamoto and Chance, 2006].... 3
Figure 1-2: Single-crystal structure of hexagonal graphite [Pierson, 1993]. 8
Figure 1-3: Single crystal structure of rhombohedral graphite [Pierson, 1993]..... 9
Figure 1-4: The above image shows the sp^3 hybridized bonding structure of diamond. The crystal structure is equivalent to a face-centered cubic lattice [Pierson, 1993]..... 13
Figure 2-1: Pebble-bed reactor [IAEA, 1996]. This drawing depicts the typical design for a pebble bed HTGR. This design is being considered for commercial use in China. 15
Figure 2-2: Manufacturing process for nuclear graphite [Nightingale, 1962]. The entire process takes 6 to 9 months to complete. 17
Figure 3-1: The image above shows increasing LET for certain particles [Woods and Pikaev, 1994]. 20
Figure 3-2: This image shows a Frenkel pair in the graphite lattice [Tellig and Heggie, 2007]. 24
Figure 3-3: Common defects in graphite [absoluteastronomy.com]. This image shows a vacancy, an interstitial, substitution by both larger and smaller atoms and a Frenkel pair (where a vacancy and interstitial are formed together). 24
Figure 3-4: Growth of new basal plane in graphite (left); collapse of basal plane due to vacancies (right) [Delhaes, 2001]..... 26
Figure 3-5: Intercalation of graphite with potassium [Dresselhaus and Dresselhaus, 2002]. 27
Figure 4-1: Boudouard equilibrium [Bioenergylist.org]. This graph shows that at lower temperatures the equilibrium is on the exothermic carbon dioxide side and on higher temperatures the endothermic formation of carbon monoxide is the dominant reaction. The equilibrium shifts to the right with increasing pressure. 33
Figure 4-2: a. edge atoms arranged in an arm-chair configuration; b. edge atoms arranged in a zig-zag configuration [Delhaès, 2001]. 35
Figure 4-3: Representation of events in molecular (a) and atomic (b) oxygen adsorption.... 36
Figure 4-4: The three regime oxidation of graphite showing the concentration of gas within the gas and graphite. The top diagram represents the change in rate of the carbon

gasification reaction with temperature. The lower diagram shows how the concentration of reactant gas in the graphite varies with the rate controlling zone [Marsh, 1989]. 43
Figure 5-1: This image shows a single graphite sample after cutting. The size is 10 mm by 2 mm by 2 mm. 50
Figure 5-2 REGe detector configuration [Canberra, 2003]. 52
Figure 5-3 Results of the REGe analysis on the cut irradiated graphite sample. 53
Figure 6-1: Decay scheme for Co-60. Co-60 decays predominantly by the emission of a β-particle (0.313 MeV) to give an excited state of nickel-60 (Ni-60). The Ni-60 further decays by emitting two photons with energies of 1.17 MeV and 1.33 MeV (Woods and Pikaev, 1994). 57
Figure 6-2: Top down vies of the UMD Co-60 gamma source. 58
Figure 6-3: Close-up image of the Co-60 pencils in the UMD gamma source. 58
Figure 6-4: Top hat of the Co-60 source at UMD. 60
Figure 7-1: Image of the nuclear reactor at AFRRI [AFRRI, 2004]. 65
Figure 7-2: Overhead layout of the reactor core at UMD. Block C4 is where the pneumatic transfer system is located [MUTR, 2000]. 69
Figure 7-3: The image above shows the heater assembly used to irradiated the PCEA, PPEA and PCIB samples in the pneumatic transfer system. 70
Figure 7-4: Drawing of beam port from the MUTR Safety Analysis Report. This drawing shows the stepped tube of the beam port [MUTR, 2000]. 72
Figure 7-5: Looking down into the reactor pool. The east beam port is the short tube on the left side of the core and is labeled East Beam Port. This port was used for the graphite experiments. 73
Figure 7-6: Outside of East Beam Port with the normal plugs installed. 73
Figure 8-1: a. The head-on view of the modified beam port plugs. b. The length-wise view of the modified beam plugs, which were inserted into East Beam Port. There are two modified beam plugs. They are 31 inches long Al-clad and concrete-filled. They have a 2 inch hole in the center to allow radiation to stream out from the core. 76
Figure 8-2: Initial design for the East Beam Port shutter. The arm is 7 feet long, allowing for operation of the shutter without entering the high radiation area near the open port. The shutter can slide back and forth and can be used for either the beam port or through tube, should the need arise in the future. 77

Figure 8-3: The shutter system installed in front of the East Beam Port. The shutter is attached to the concrete of the reactor and is able to provide a shutter for either the beam port or the through tube. 78
Figure 8-4: Close-up view of shutter system. This view shows how the shutter may be used for both the beam port and the through tube. 78
Figure 8-5: U-shaped concrete walls built along east wall of reactor building. The walls are 24 inches thick and 7 feet high. 79
Figure 8-6: Drawing of borated polyethylene brick. The bricks are 2 inches by 4 inches by 8 inches. 80
Figure 8-7: Filling of the collar. The collar was filled with paraffin wax and boron carbide powder. 81
Figure 8-8: Fitting of the collar onto the face of the reactor. 81
Figure 8-9: Image of the collar installed on the reactor face. Its design still allows for movement of the shutter. 82
Figure 8-10: This figure shows the design of the cave. On one side are fans to draw air through the box to ensure adequate cooling and on the other side is a filter to ensure particulates are not activated in the flux from the reactor. 83
Figure 8-11: View of the interior of the cave. This photograph shows the random arrangement of the borated polyethylene blocks inside the cave, as well as the fans and filter on either side of the cave. 84
Figure 8-12: This image shows the south filtered side of the cave in place against the reactor face. 84
Figure 8-13: This image shows the north side of the cave installed against the reactor face. 85
Figure 8-14: Locations of the dose measurements in Table 8-1. 87
Figure 8-15: This image shows the regulator system used to deliver the research grade He to the samples and to the GC, as the carrier gas. 89
Figure 8-16: Image of water bubbler used for east beam port experiments. 90
Figure 8-17: Image of the HX86A used to measure the temperature and humidity of the gas entering the samples chamber. 91
Figure 8-18: Close-up image of the HX86A probe, used to measure the temperature and humidity of the gas entering the sample chamber. 91
Figure 8-19: Design for the sample chamber. 92

Figure 8-20: Photo of sample chamber used for east beam port experiments. 93
Figure 8-21: Parker Hannifin Corporation filter used to remove water vapor from the sample gas after leaving the sample chamber before it is injected into the GC. 94
Figure 8-22: Gow-Mac 400 GC used for east beam port experiments. 95
Figure 8-23: Installed columns in the Gow-Mac 400. 95
Figure 8-24: Gas connections on the back of the GC. In the center is the carrier gas connection (He). The upper connections on the left and right are for operating the pneumatically actuated sample valves. Below those are the sample inlets. 96
Figure 8-25: MHI robust radiator™ used for east beam port experiments. 97
Figure 8-26: MHI robust radiator™ connected to the control system with DACS software system open. 98
Figure 8-27: A typical GC. The carrier gas flows continually through the injection port, the column and the detector. The sample is injected into the heated injection port and travels through the column. It then enters the detector and the results are recorded [McNair and Miller, 2009]. 100
Figure 8-28: The three scattering frequencies generated by oscillating dipoles [Sibilia, 1996]. 101
Figure 8-29: A typical Raman spectrometer. The laser is shined onto sample through a microscope. The returning light goes through a focusing lens and a notch filter (to remove the Rayleigh scattered light) before going to the spectrometer [Ferraro and Nakamoto, 2003]. 102
Figure 8-30: Constant energy surfaces for the two lowest conduction and two highest valence bands of 2-D graphite. On the right, shows an image of the constant energy contours of the cones near the K point in the BZ. The extreme left shows the density of electronic states versus the energy for the highest two valence bands and lowest two conduction bands [Dresselhaus, 2012]. 103
Figure 8-31: (a) This graph shows the calculated phonon dispersion relations of two dimensional graphite. (b) This graph shows phonon density of states for 2D graphite [Dresselhaus *et al.*, 2005]. 104
Figure 8-32: Raman spectra of PPEA AG control sample taken with a 532 nm laser. The labeled peaks correspond to the description in the text. 106

Figure 8-33: (a) First order Raman process. (b) One phonon second order processes. (c) Two-phonon second order Raman process. The top line represents incident photon resonance while the bottom line indicates scattered photon resonance conditions. For one phonon second order processes one of the scattering events is elastic and is represented by dashed lines. Resonance points are represented by solid circles [Dresselhaus *et al*., 2005]. 108
Figure 8-34: This image shows the photoelectric effect [Sibilia, 1996]. 110
Figure 8-35: Photoelectric and Auger electron production [Chorkendorff and Niemantsverdriet, 2007]. 110
Figure 8-36: This image shows a typical set-up for XPS. The basic elements are: a source of fixed-energy radiation (an x-ray source), an electron energy analyzer (which can disperse the emitted electrons according to their kinetic energy, and thereby measure the flux of emitted electrons of a particular energy), and an ultra high vacuum environment to prevent surface contamination [Sibilia, 1996]. 111
Figure 8-37: This image shows the method for calculating the sampling depth for XPS [Sibilia, 1996]. 112
Figure 8-38: Cross-section of a typical x-ray tube [U.S. Geological Survey, 2001]. 112
Figure 8-39: Illustration of Bragg's law [Suryanarayana and Norton, 1998]. 113
Figure 8-40: This image shows the energy splitting of electron spin states as a function of the magnetic field [Eaton *et al*, 2010]. 115
Figure 8-41: The image above depicts the thin-film SQUID device which acts as a sensitive current-to-voltage converter [McElfresh, 1994]..... 118
Figure 9-1: Comparison of 1000 °C irradiated samples with the carbon dioxide calibration data. 121
Figure 9-2: This graph shows the comparison between the carbon monoxide calibration data and the 1000 °C irradiated samples. 122
Figure 9-3: Comparison of PPEA samples in the room temperature and 1000 °C experiments to the CO calibration. 123
Figure 9-4: Three stage model of the variation of the Raman G position and the D to G intensity ratio, I_D/I_G, with increasing disorder [Ferrari and Robertson, 2001]. 128
Figure 9-5: Comparison of the shift in the G peak compared to the gamma irradiation dose. 129

Figure 9-6: I_D/I_G ratio compared to the gamma irradiation dose of the samples. Error bars represent 95 % confidence levels. 134
Figure 9-7: I_D/I_G ratio compared to the AFRRI mixed field irradiation doses. Error bars represent calculated 95 % confidence levels. 135
Figure 9-8: I_D/I_G ratio compared to the room temperature and 1000 °C mixed field irradiations conducted at the east beam port of the MUTR. Error bars represent 95 % confidence levels. 136
Figure 9-9: XPS wide-range spectrum for the gamma irradiated graphite samples of PCEA AG. 144
Figure 9-10: XPS wide-range spectrum for the gamma irradiated graphite samples of PCEA WG. 145
Figure 9-11: XPS wide-range spectrum for the gamma irradiated graphite samples of PPEA AG. 146
Figure 9-12: XPS wide-range spectrum for the gamma irradiated graphite samples of PPEA WG. 147
Figure 9-13: XPS wide-range spectrum for the gamma irradiated graphite samples of PCIB AG. 148
Figure 9-14: XPS wide-range spectrum for the gamma irradiated graphite samples of PCIB WG. 149
Figure 9-15: XPS wide-range spectrum for the gamma irradiated graphite samples of 2020 AG. 150
Figure 9-16: XPS wide-range spectrum for the gamma irradiated graphite samples of 2020 WG. 151
Figure 9-17: XPS wide-range spectrum for the gamma irradiated graphite samples of IG-110 AG. 152
Figure 9-18: XPS wide-range spectrum for the gamma irradiated graphite samples of IG-110 WG. 153
Figure 9-19: XPS spectra for PCEA AG control, AFRRI irradiated and 300 °C rabbit irradiated samples. 158
Figure 9-20: The graph above shows the results for the AFRRI irradiations and pneumatic system irradiation for PCEA WG. 159

Figure 9-21: XPS spectra for PPEA AG control, AFRRI irradiated and 300 °C rabbit irradiated samples. 160
Figure 9-22: XPS spectra for PPEA WG control, AFRRI irradiated and 300 °C rabbit irradiated samples. 161
Figure 9-23: XPS spectra for PCIB AG control, AFRRI irradiated and 300 °C rabbit irradiated samples. 162
Figure 9-24: XPS spectra for PCIB AG control, AFRRI irradiated and 300 °C rabbit irradiated samples. 163
Figure 9-25: XPS spectra for PCEA AG east beam port experiments. 164
Figure 9-26: XPS spectra for PCEA WG east beam port experiments. 165
Figure 9-27: XPS spectra for PPEA AG east beam port experiments. 166
Figure 9-28: XPS spectra for PPEA WG east beam port experiments. 167
Figure 9-29: XPS spectra for PCIB AG east beam port experiments. 168
Figure 9-30: XPS spectra for PCIB WG east beam port experiments. 169
Figure 9-31: XPS spectra for 2020 AG east beam port experiments. 170
Figure 9-32: XPS spectra for 2020 WG east beam port experiments. 171
Figure 9-33: XPS spectra for IG-110 AG east beam port experiments. 172
Figure 9-34: XPS spectra for IG-110 WG east beam port experiments. 173
Figure 9-35: XPS results for 2020 AG. These results show the increase in oxygen between the 1000 °C unirradiated and irradiated samples. 174
Figure 9-36: PPEA WG 1000 °C unirradiated east beam port sample. 175
Figure 9-37: XRD spectrum of PPEA WG 1000 °C unirradiated east beam port sample. The Miller indices associated with each Bragg peak are labeled. 176
Figure 9-38: XRD results for PCEA AG. The graph shows the gamma irradiation results as well as the mixed field irradiation results. 178
Figure 9-39: XRD results for PCEA WG. The graph shows the gamma irradiation results as well as the mixed field irradiation results. 179
Figure 9-40: XRD results for PPEA AG. The graph shows the gamma irradiation results as well as the mixed field irradiation results. 180
Figure 9-41: XRD results for PPEA WG. The graph shows the gamma irradiation results as well as the mixed field irradiation results. 181

Figure 9-42: XRD results for PCIB AG. The graph shows the gamma irradiation results as well as the mixed field irradiation results. 182
Figure 9-43: XRD results for PCIB WG. The graph shows the gamma irradiation results as well as the mixed field irradiation results. 183
Figure 9-44: XRD results for 2020 AG. The graph shows the gamma irradiation results as well as the mixed field irradiation results. 184
Figure 9-45: XRD results for 2020 WG. The graph shows the gamma irradiation results as well as the mixed field irradiation results. 185
Figure 9-46: XRD results for IG-110 AG. The graph shows the gamma irradiation results as well as the mixed field irradiation results. 186
Figure 9-47: XRD results for IG-110 WG. The graph shows the gamma irradiation results as well as the mixed field irradiation results. 187
Figure 9-48: PCEA AG 002 peak. 189
Figure 9-49: PCEA WG 002 peak. Broad peak between 10 and 20 indicates an amorphous area. 190
Figure 9-50: PPEA AG 002 peak. Broad peak between 10 and 20 indicates an amorphous area. 191
Figure 9-51: PPEA WG 002 peak. Broad peak between 10 and 20 indicates an amorphous area. 192
Figure 9-52: PCIB AG 002 peak. Broad peak between 10 and 20 indicates an amorphous area. 193
Figure 9-53: PCIB WG 002 peak. Broad peak between 10 and 20 indicates an amorphous area. 194
Figure 9-54: 2020 AG 002 peak. Broad peak between 10 and 20 indicates an amorphous area. 195
Figure 9-55: 2020 WG 002 peak. Broad peak between 10 and 20 indicates an amorphous area. 196
Figure 9-56: IG-110 AG 002 peak. Broad peak between 10 and 20 indicates an amorphous area. 197
Figure 9-57: IG-110 WG 002 peak. Broad peak between 10 and 20 indicates an amorphous area. 198

Figure 9-58: XRD results for the two uncleaned and one cleaned (nitric acid and hydrochloric acid) samples..... 199
Figure 9-59: IG-110 WG (004) peak. No significant broadening is noted, indicating that there is little to no change in the interlayer spacing of the samples. 200
Figure 9-60: Typical hyperfine for PCEA AG..... 205
Figure 9-61: Typical hyperfine for PCEA WG..... 206
Figure 9-62: Typical hyperfine for PPEA AG. 207
Figure 9-63: Typical hyperfine for PPEA WG. 208
Figure 9-64: Typical hyperfine for PCIB AG. 209
Figure 9-65: Typical hyperfine for PCIB WG. 210
Figure 9-66: Typical hyperfine for 2020 AG. 211
Figure 9-67: Typical hyperfine for 2020 WG. 212
Figure 9-68: Typical hyperfine for IG-110 AG. This sample was irradiated with mixed field irradiation at 1000 °C. 213
Figure 9-69: Typical hyperfine for IG-110 WG. 214
Figure 9-70: The graph above illustrates the change in spins per gram versus the gamma irradiation dose for all graphite grades. The three doses represented are 15 MGy, 45 MGy and 87 MGy. 215
Figure 9-71: Bar graphs representing the 1000 °C irradiated and unirradiated samples..... 216
Figure 9-72: Bar graphs representing the room temperature irradiated and unirradiated samples. Graph a. represents PCEA AG, b. PCEA WG, c. PPEA AG, d. PPEA WG, e. PCIB AG, f. PCIB WG, g. 2020 AG, and h. 2020 WG. 219
Figure 9-73: Diamagnetic anisotropy of PGCCL samples: X, pristine; •, neutron-irradiated (26C sample); 0, neutron irradiated (28C sample) [Maaroufi, et al., 1982]. 222
Figure 9-74: SQUID measurement for PCEA AG control and mixed field irradiated rabbit sample. These results show a slight decrease in the diamagnetism with mixed field irradiation. 223
Figure 9-75: SQUID measurement for PCEA WG control and mixed field irradiated rabbit sample. These results show a decrease in the diamagnetism with mixed field irradiation. 224
Figure 9-76: Image of natural Kish graphite [Delhaès, 2001].: 225

Figure 9-77: SQUID measurement for PCEA AG samples. These results show an increase in the diamagnetism with gamma irradiation. 226
Figure 9-78: SQUID measurement for PCEA WG samples. These results show an increase in the diamagnetism with gamma irradiation. 227
Figure A-1: Manufacturing process for nuclear graphite (Hassel and Mark, 1924). The entire process takes 6 to 9 months to complete. 236
Figure B-1: PCEA AG control and gamma Raman spectra. 246
Figure B-2: Image of PCEA AG control sample prior to Raman spectra collection. 246
Figure B-3: Image of PCEA AG 15 MGy gamma irradiated sample prior to Raman spectra collection. 247
Figure B-4: Image of PCEA AG 45 MGy gamma irradiated sample prior to Raman spectra collection. 247
Figure B-5: Image of PCEA AG 87 MGy gamma irradiated sample prior to Raman spectra collection. 247
Figure B-6: PCEA AG control, AFRRI and rabbit heater (300 °C) samples Raman spectra. 248
Figure B-7: Image of PCEA AG AFRRI 1 sample prior to Raman spectra collection..... 248
Figure B-8: Image of PCEA AG AFRRI 2 sample prior to Raman spectra collection..... 249
Figure B-9: Image of PCEA AG 300 °C rabbit irradiated sample prior to Raman spectra collection. 249
Figure B-10: Raman spectra of PCEA AG room temperature irradiated and unirradiated samples. 250
Figure B-11: Image of PCEA AG room temperature unirradiated sample prior to Raman spectra collection. 250
Figure B-12: Image of PCEA AG room temperature irradiated east beam port sample prior to Raman spectra collection..... 251
Figure B-13: Raman spectra of PCEA AG 1000 °C irradiated and unirradiated samples. .. 251
Figure B-14: Image of PCEA AG unirradiated 1000 °C sample prior to Raman spectra collection. 252
Figure B-15: Image of PCEA AG irradiated 1000 °C sample prior to Raman spectra collection. 252
Figure B-16: Raman spectra of PCEA WG control and gamma irradiated samples. 253

Figure B-17: Image of PCEA WG control sample prior to Raman spectra collection. 253
Figure B-18: Image of PCEA WG 15 MGy gamma irradiated sample prior to Raman spectra collection. 254
Figure B-19: Image of PCEA WG 45 MGy gamma irradiated sample prior to Raman spectra collection. 254
Figure B-20: Image of PCEA WG 87 MGy gamma irradiated sample prior to Raman spectra collection. 254
Figure B-21: Raman spectra of PCEA WG control, AFRRI irradiated and 300 °C rabbit irradiated samples. 255
Figure B-22: Image of PCEA WG AFRRI 1 sample prior to Raman spectra collection. 255
Figure B-23: Image of PCEA WG AFRRI 2 sample prior to Raman spectra collection. 256
Figure B-24: Image of PCEA WG 300 °C rabbit irradiated sample prior to Raman spectra collection. 256
Figure B-25: Raman spectra of PCEA WG room temperature irradiated and unirradiated samples. 257
Figure B-26: Image of PCEA WG room temperature unirradiated sample prior to Raman spectra collection. 257
Figure B-27: Image of PCEA WG room temperature east beam port irradiated sample prior to Raman spectra collection. 258
Figure B-28: Image of PCEA WG 1000 °C unirradiated sample prior to Raman spectra collection. 259
Figure B-29: Image of PCEA WG 1000 °C irradiated sample prior to Raman spectra collection. 259
Figure B-30: Raman spectra of PPEA AG control and gamma irradiated samples. 260
Figure B-31: Image of PPEA AG control sample prior to Raman spectra collection. 260
Figure B-32: Image of PPEA AG 15 MGy gamma irradiated sample prior to Raman spectra collection. 261
Figure B-33: Image of PPEA AG 45 MGy gamma irradiated sample prior to Raman spectra collection. 261
Figure B-34: Image of PPEA AG 87 MGy gamma irradiated sample prior to Raman spectra collection. 261

Figure B-35: Raman spectra of PPEA WG control, AFRRI irradiated and rabbit irradiated samples. 262
Figure B-36: Image of PPEA AG AFRRI 1 sample prior to Raman spectra collection. 262
Figure B-37: Image of PPEA AG AFRRI 2 sample prior to Raman spectra collection. 263
Figure B-38: Image of PPEA AG 300 °C rabbit irradiated sample prior to Raman spectra collection. 263
Figure B-39: Raman spectra of PPEA AG room temperature irradiated and unirradiated samples. 264
Figure B-40: Image of PPEA AG room temperature unirradiated sample prior to Raman spectra collection. 264
Figure B-41: Image of PPEA AG room temperature east beam port irradiated sample prior to Raman spectra collection..... 265
Figure B-42: Raman spectra of PPEA AG 1000 °C irradiated and unirradiated samples. .. 265
Figure B-43: Image of PPEA AG 1000 °C unirradiated east beam port sample prior to Raman spectra collection..... 266
Figure B-44: Image of PPEA AG 1000 °C irradiated east beam port sample prior to Raman spectra collection. 266
Figure B-45: Raman spectra of PPEA WG control and gamma irradiated samples. 267
Figure B-46: Image of PPEA WG control sample prior to Raman spectra collection..... 267
Figure B-47: Image of PPEA WG 15 MGy gamma irradiated sample prior to Raman spectra collection. 268
Figure B-48: Image of PPEA WG 45 MGy gamma irradiated sample prior to Raman spectra collection. 268
Figure B-49: Image of PPEA WG 87 MGy gamma irradiated sample prior to Raman spectra collection. 268
Figure B-50: Raman spectra of PPEA WG control, AFRRI irradiated and 300 °C rabbit irradiated samples..... 269
Figure B-51: Image of PPEA WG AFRRI 1 sample prior to Raman spectra collection. 269
Figure B-52: Image of PPEA WG AFRRI 2 sample prior to Raman spectra collection. 270
Figure B-53: Image of PPEA WG 300 °C rabbit irradiated sample prior to Raman spectra collection. 270

Figure B-54: Raman spectra of PPEA WG room temperature irradiated and unirradiated samples. 271
Figure B-55: Image of PPEA WG room temperature unirradiated east beam port sample prior to Raman spectra collection. 271
Figure B-56: Image of PPEA WG room temperature east beam port irradiated sample prior to Raman spectra collection. 272
Figure B-57: Raman spectra of PPEA WG 1000 °C irradiated and unirradiated samples... 272
Figure B-58: Image of PPEA WG 1000 °C unirradiated east beam port sample prior to Raman spectra collection. 273
Figure B-59: Image of PPEA WG 1000 °C irradiated east beam port sample prior to Raman spectra collection. 273
Figure B-60: Raman spectra for PCIB AG control and gamma irradiated samples. 274
Figure B-61: Image of PCIB AG control sample prior to Raman spectra collection. 274
Figure B-62: Image of PCIB AG 15 MGy gamma irradiated sample prior to Raman spectra collection. 275
Figure B-63: Image of PCIB AG 45 MGy gamma irradiated sample prior to Raman spectra collection. 275
Figure B-64: Image of PCIB AG 87 MGy gamma irradiated sample prior to Raman spectra collection. 275
Figure B-65: Raman spectra for PCIB AG control, AFRRI irradiated and 300 °C rabbit irradiated samples. 276
Figure B-66: Image of PCIB AG AFRRI 1 sample prior to Raman spectra collection. 276
Figure B-67: Image of PCIB AG AFRRI 2 sample prior to Raman spectra collection. 277
Figure B-68: Image of PCIB AG 300 °C rabbit irradiated sample prior to Raman spectra collection. 277
Figure B-69: Raman spectra for PCIB AG room temperature irradiated and unirradiated samples. 278
Figure B-70: Image of PCIB AG room temperature unirradiated east beam port sample prior to Raman spectra collection. 278
Figure B-71: Image of room temperature irradiated east beam port sample prior to Raman spectra collection. 279
Figure B-72: Raman spectra for PCIB AG 1000 °C irradiated and unirradiated samples. .. 279

Figure B-73: Image of PCIB AG 1000 °C unirradiated east beam port sample prior to Raman spectra collection. 280
Figure B-74: Image of PCIB AG 1000 °C irradiated east beam port sample prior to Raman spectra collection. 280
Figure B-75: Raman spectra for PCIB WG control and gamma irradiated samples. 281
Figure B-76: Image of PCIB WG control sample prior to Raman spectra collection. 281
Figure B-77: Image of PCIB WG 15 MGy gamma irradiated sample prior to Raman spectra collection, ... 282
Figure B-78: Image of PCIB WG 45 MGy gamma irradiated sample prior to Raman spectra collection. 282
Figure B-79: Image of PCIB WG 87 MGy gamma irradiated sample prior to Raman spectra collection. 282
Figure B-80: Raman spectra for PCIB WG control, AFRRI irradiated and 300 °C rabbit irradiated samples. 283
Figure B-81: Image of PCIB WG AFRRI 1 irradiated sample prior to Raman spectra collection. 283
Figure B-82: Image of PCIB WG AFRRI 2 sample prior to Raman spectra collection. 284
Figure B-83: Image of PCIB WG 300 °C rabbit irradiated sample prior to Raman spectra collection. 284
Figure B-84: Raman spectra for PCIB WG room temperature irradiated and unirradiated samples. 285
Figure B-85: Image of PCIB WG room temperature unirradiated east beam port sample prior to Raman spectra collection. 285
Figure B-86: Image of PCIB WG room temperature irradiated east beam port sample prior to Raman spectra collection. 286
Figure B-87: Raman spectra for PCIB WG 1000 °C irradiated and unirradiated samples. . 286
Figure B-88: Image of PCIB WG 1000 °C unirradiated east beam port sample prior to Raman spectra collection. 287
Figure B-89: Image of PCIB WG 1000 °C irradiated east beam port sample prior to Raman spectra collection. 287
Figure B-90: Raman spectra for 2020 AG control and gamma irradiated samples. 288
Figure B-91: Image of 202 AG control sample prior to Raman spectra collection. 288

Figure B-92: Image of 2020 AG 15 MGy gamma irradiated sample prior to Raman spectra collection. 289
Figure B-93: Image of 2020 AG 45 MGy gamma irradiated sample prior to Raman spectra collection. 289
Figure B-94: Image of 2020 AG 87 MGy gamma irradiated sample prior to Raman spectra collection. 289
Figure B-95: Raman spectra for 2020 AG room temperature irradiated and unirradiated samples. 290
Figure B-96: Image of 2020 AG room temperature east beam port unirradiated sample prior to Raman spectra collection. 290
Figure B-97: Image of 2020 AG room temperature east beam port irradiated sample prior to Raman spectra collection..... 291
Figure B-98: Raman spectra for 2020 AG 1000 °C irradiated and unirradiated samples.... 291
Figure B-99: Image of 2020 AG 1000 °C unirradiated east beam port sample prior to Raman spectra collection. 292
Figure B-100: Image of 2020 AG 1000 °C irradiated east beam port sample prior to Raman spectra collection. 292
Figure B-101: Raman spectra for 2020 WG control and gamma irradiated samples. 293
Figure B-102: Image of 2020 WG control sample prior to Raman sample collection. 293
Figure B-103: Image of 2020 WG 15 MGy gamma irradiated sample prior to Raman spectra collection. 294
Figure B-104: Image of 2020 WG 45 MGy gamma irradiated sample prior to Raman spectra collection. 294
Figure B-105: Image of 2020 WG 87MGy gamma irradiated sample prior to Raman spectra collection. 294
Figure B-106: Raman spectra for 2020 WG room temperature irradiated and unirradiated samples. 295
Figure B-107: Image of 2020 WG room temperature east beam port unirradiated sample prior to Raman spectra collection. 295
Figure B-108: Image of 2020 WG room temperature east beam port irradiated sample prior to Raman spectra correction. 296
Figure B-109: Raman spectra for 2020 WG 1000 °C irradiated and unirradiated samples. 296

Figure B-110: Image of 2020 WG 1000 °C unirradiated east beam port sample prior to Raman spectra collection..... 297
Figure B-111: Image of 2020 WG 1000 °C unirradiated east beam port sample prior to Raman spectra collection..... 297
Figure B-112: Raman spectra for IG-110 AG control and gamma irradiated samples..... 298
Figure B-113: Image of IG-110 AG control sample prior to Raman spectra collection..... 298
Figure B-114: Image of IG-110 AG 15 MGy gamma irradiated sample prior to Raman spectra collection..... 299
Figure B-115: Image of IG-110 AG 45 MGy gamma irradiated sample prior to Raman spectra collection..... 299
Figure B-116: Image of IG-110 AG 87 MGy gamma irradiated sample prior to Raman spectra collection..... 299
Figure B-117: Raman spectra for IG-110 AG room temperature irradiated and unirradiated samples..... 300
Figure B-118: Image of IG-110 AG room temperature east beam port unirradiated sample prior to Raman spectra collection..... 300
Figure B-119: Image of IG-110 AG room temperature east beam port irradiated sample prior to Raman spectra collection. 301
Figure B-120: Raman spectra for IG-110 AG 1000 °C irradiated and unirradiated samples. 301
Figure B-121: Image of IG-110 AG 1000 °C unirradiated east beam port sample prior to Raman spectra collection..... 302
Figure B-122: Image of IG-110 AG 1000 °C irradiated east beam port sample prior to Raman spectra collection..... 302
Figure B-123: Raman spectra for IG-110 WG control and gamma irradiated samples..... 303
Figure B-124: Image of IG-110 WG control sample prior to Raman spectra collection..... 303
Figure B-125: Image of IG-110 WG 15 MGy gamma irradiated sample prior to Raman spectra collection..... 304
Figure B-126: Image of IG-110 WG 45 MGy gamma irradiated sample prior to Raman spectra collection..... 304
Figure B-127: Image of IG-110 WG 87 MGy gamma irradiated sample prior to Raman spectra collection..... 304

Figure B-128: Raman spectra for IG-110 WG room temperature irradiated and unirradiated samples. 305
Figure B-129: Image of IG-110 WG room temperature east beam port unirradiated sample prior to Raman spectra collection. 305
Figure B-130: Image of IG-110 WG room temperature east beam port irradiated sample prior to Raman spectra collection. 306
Figure B-131: Raman spectra for IG-110 WG 1000 °C irradiated and unirradiated samples. 306
Figure B-132: Image of IG-110 WG 1000 °C unirradiated east beam port sample prior to Raman spectra collection 307
Figure B-133: Image of IG-110 WG 1000 °C irradiated east beam port sample prior to Raman spectra collection 307
Figure B-134: I_D/I_G versus irradiation temperature for all graphite types. Error bars represent 95 % confidence limits. 308
Figure B-135: I_D/I_G versus gamma irradiation dose for all graphite types. Error bars represent 95 % confidence limits. 309
Figure B-136: I_D/I_G versus mixed field irradiation dose for the AFRRI irradiated graphite types. Error bars represent 95 % confidence limits. 310

Chapter 1 Introduction

The High Temperature Gas-Cooled Reactor (HTGR) is a Generation IV reactor concept that uses a graphite-moderated nuclear reactor with a once-through uranium fuel cycle [Nuclear Regulatory Commission (NRC), 2010]. This reactor uses helium (He) as the coolant and a closed-cycle gas turbine for power generation. The He from the reactor is used directly or indirectly by heating air or nitrogen to drive the turbine [NRC, 2010].

The deployment of advanced reactors requires an understanding of materials in the reactor degradation in extreme environments. Although some work has been done on degradation in impure helium environments at high temperatures, full understanding of the degradation processes and satisfactory prediction of the extent of these processes requires further studies.

1.1 Helium contaminants

The He in the reactor is expected to have trace amounts of contaminants, such as water (H_2O) and oxygen (O_2), due to degassing from air ejectors and water leaks from the secondary system [NRC, 2010]. Other components of the gaseous environment may include nitrogen (N_2) and hydrogen (H_2) from contamination of the He coolant. The water molecules from the contaminants will undergo radiolysis in the radiation environment, leading to the production of several species that can take part in corrosion processes. These products and their G-values can be seen in the following figure. The G value is defined as the number of species produced per 100 eV of energy deposited [Marsh, 1989]. The most important product of the radiolysis process is hydrogen peroxide (H_2O_2), one of the strongest oxidizers. In the presence of a transition metal such as iron or copper (that may be present as impurities in the graphite), hydrogen peroxide reacts much more vigorously and aggressively than without the

metal (acting as a catalyst). The reaction of iron-catalyzed hydrogen peroxide oxidation is called a "Fenton's Reagent" after its discoverer H.J.H. Fenton in 1894. This increase in oxidation power is attributed to the production of hydroxyl radicals (•OH). The iron cycles between the iron(II) and iron(III) oxidation states, yielding the hydroxyl radical and other by-products, as seen in the following equation: [Suthersan, 2002]

$$Fe^{2+} + H_2O_2 \rightarrow OH^{\bullet} + OH^{-} + Fe^{3+}$$

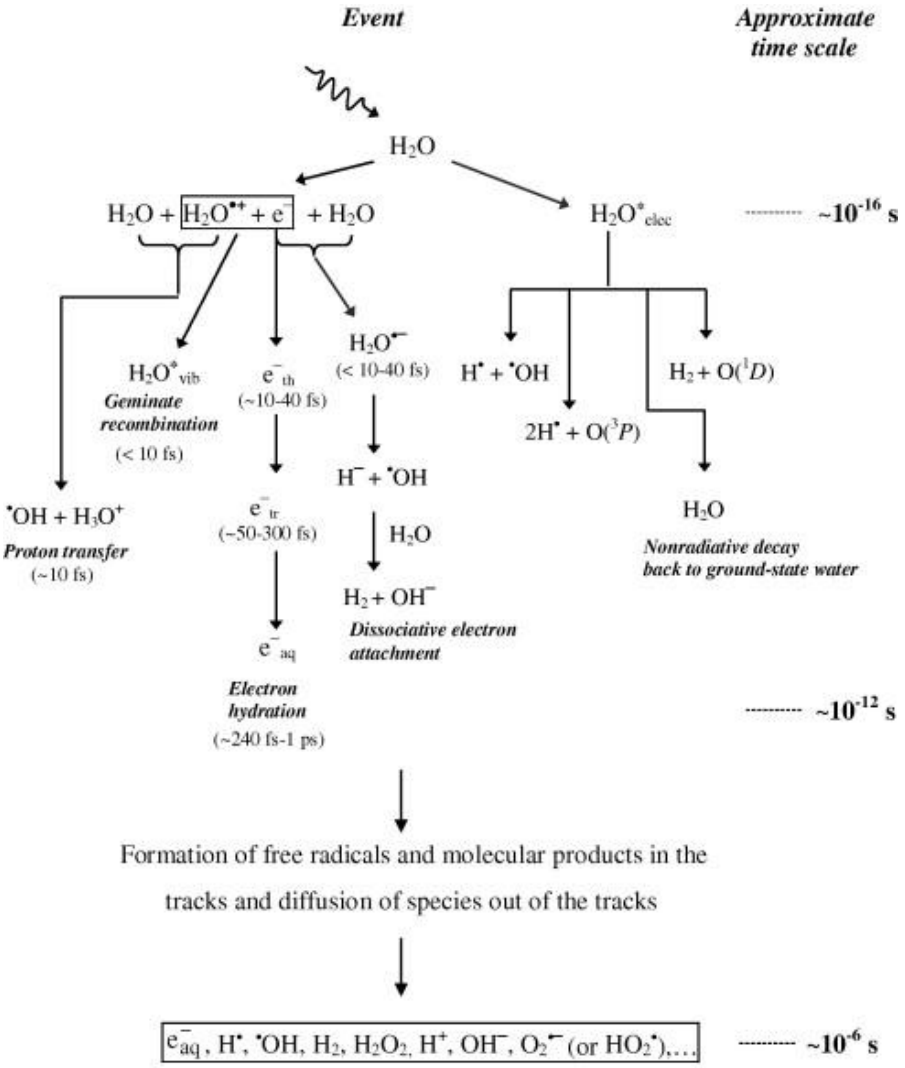

Figure 1-1: Products of the radiolysis of water. The following radicals and molecular products are produced: e_{aq}^-, H, OH, H_2O_2, H_2 and H^+ [Takamoto and Chance, 2006].

$G(-H_2O)$	4.08
$G(H_2)$	0.45
$G(H_2O_2)$	0.68
$G(e_{aq}^-)$	2.63
$G(H)$	0.55
$G(OH)$	2.72

$G(HO_2)$	0.026

Table 1-1: The above table lists G values for the radiolysis of water at pHs between 3 and 11 [Takamoto and Chance, 2006].

The corrosion of the reactor structural materials at high temperatures (operating temperatures for HTGRs are 700 °C to 900 °C) may be due to oxidation, carburization or decarburization, etc. For instance, oxidation of graphite produces carbon monoxide (CO), carbon dioxide (CO_2), and methane (CH_4). Therefore, there is a need to evaluate the materials' resistance to corrosion in this environment.

For this research graphite was gamma irradiated in the University of Maryland (UMD) gamma source. Samples were also irradiated in the Maryland University Training Reactor (MUTR) and the Armed Forces Radiobiology Research Institute (AFRRI), in order to study the effects of neutrons as well as gamma irradiation. The techniques used to analyze the irradiated samples were electron paramagnetic resonance (EPR) spectroscopy, Raman spectroscopy, x-ray diffraction (XRD), x-ray photoelectron spectroscopy (XPS) and gas chromatography (GC).

1.2 Objectives

The objective of this research is to elucidate the mechanisms of gamma and neutron radiation degradation at elevated temperature for the following nuclear grade graphites:

- PCEA, manufactured by GrafTech International,
- PPEA, manufactured by GrafTech International,
- PCIB, manufactured by GrafTech International,
- Grade 2020, manufactured by Mersen, and

- IG-110, manufactured by Toyo Tanso.

The mechanisms are elucidated by examining chemical and physical changes of the graphites. The chemical changes are examined by looking at the oxidation of the graphite through gas chromatography, x-ray photoelectron spectroscopy and Raman spectroscopy. These changes are also interpretted in forms of the rupturing of the sp^3-hybridized bonds in the graphite. This rupturing is examined with electron paramagnetic resonance spectroscopy and by magnetic susceptibility measurements utilizing a superconducting quantum interference device. The physical changes are examined by changes in crystallinity utilizing x-ray diffraction. Elucidation of these mechanisms will lead to a new strategy for design and manufacturing nuclear grade graphites in the future, that have much higher resistance to both gamma and neutron radiation. This research also develops a method for screening and prequalifying future nuclear graphite grades. If new nuclear grade graphites show degradation under the conditions of these experiments, then reconsideration should be given to their use in nuclear reactors.

Graphite is a good alternative to water as a moderator because it efficiently thermalizes neutrons and has a low neutron absorption cross-section so that they can fission $_{92}U^{235}$. The absorbance cross-section for graphite is 0.0034 barns (b), compared to 0.664 b for water. Graphite is not so good a reflector as water. The scattering cross-section for water is 103 b and 4.75 b for graphite [Nightingale, 1962]. For the best performance, the graphite should have the highest density and the greatest degree of purity. Other important graphite properties are mechanical strength, machinability, thermal conductivity and thermal expansion.

Graphite shows high radiation resistance. Upon irradiation, many of the mechanical properties of graphite, including mechanical strength and hardness, improve [Nightingale, 1962]. The major concern is chemical reactivity at high temperatures, that can only be kept within acceptable limits by controlling the amount of impurities present in the He coolant.

The aquired knowledge from these experiments is especially important in determining the types of graphite best suited for use in the HTGRs and for what purpose. PCEA graphite is being considered for use in the prismatic design in replaceable blocks and in the pebble-bed design as a reflector and in insulation blocks [NRC, 2010]. IG-110 is being discussed for use as a replaceable reflector and in core support pedestals [NRC, 2010]. Reactor core design parts such as the replaceable reflector do not need to be highly resistant to radiation because they will be replaced approximately every six years during refueling. On the other hand, core support pedestals must last for the lifetime of the reactor. These parts must be able to withstand radiation damage over the lifetime of the core, approximately 40 years [NRC, 2010]. By examining the mechanism of radiation effects on different types of graphite, a determination can be made about the grades best suited for lifetime use in the HTGR.

1.3 Structure of Graphite

The electron configuration of carbon (C) is described as: $1s^2 2s^2 2p^2$. Several carbon isotopes exist, namely C^{11}, C^{12}, C^{13} and C^{14}. Most natural samples are 98.9 % C^{12} and 1.1 % C^{13}. Natural samples also contain trace amount of the radioactive carbon isotope C^{14}. Carbon-14 is produced by thermal neutrons from cosmic radiation in the upper atmosphere, and is transported down to earth to be absorbed by living biological material. The half-life of C^{14} is 5700 years, which is why it is used in radiometric dating. Carbon-11 is a radioactive

isotope of carbon. It decays by positron emission to boron-11 (B^{11}), with a half-life of 20.38 minutes. The decay of C^{11} can be seen in the following equation [Pierson, 1993].

$$^{11}C \rightarrow {}^{11}B + e^{+}$$

The carbon valence electrons can be removed from the carbon atom by applying an electric potential, which accelerates the valence electron to a level of kinetic energy which is enough to offset the binding energy of this electron to the atom [Pierson, 1993]. When this happens, the carbon atom becomes ionized forming a cation. The measure of this binding energy is the ionization potential. The first ionization potential is the amount of energy necessary to remove the first valence electron. For carbon the first ionization potential is 11.26 eV [Pierson, 1993]. The ionization potentials for carbon are shown in Table 1.1 below.

Ionization Number	Shell	Orbital	Potential (eV)
1	L	2p	11.26
2	L	2p	24.38
3	L	2s	47.89
4	L	2s	64.49
5	K	1s	392.08
6	K	1s	489.98

Table 1-2: Ionization potential for carbon electrons [Pierson, 1993].

At ordinary temperatures and pressures, graphite is the most stable form of carbon. It is possible to transform the graphite to metastable diamond at high temperatures and pressures with the use of catalysts. A molten form also exists at very high temperatures and pressures. The triple point is above 3900 K and 100 atmospheres [Pierson, 1993]. These are not the only forms of carbon, many other forms also exist (e.g., amorphous, C_{60}, C_{70}, etc.).

In its purest form, graphite has a planar morphology and has a silvery surface. In its polycrystalline form it is dark grey. It is also fairly porous and soft and may be distinguished from ungraphitised carbons by its ability to mark paper. Figure 1-2 shows the single crystal graphite structure. Graphite is made up of layered graphene planes with a typical ABAB, hexagonal form, repeat stacking. Strong, stiff covalent bonds exist in-plane with weak bonds of attraction between graphene planes [Pierson, 1993].

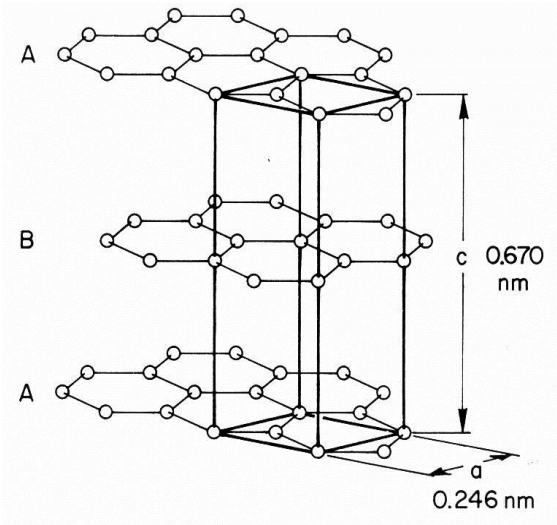

Figure 1-2: Single-crystal structure of hexagonal graphite [Pierson, 1993].

This structure was first proposed by Hull in 1917 and confirmed by Hassel and Mark in 1924 using x-ray diffraction. In natural graphite, a small portion, less than 10 %, exists in the rhombohedral form, ABCABC. This form can be seen in Figure 1-3. This form is not present in synthetic graphite because it is irreversibly converted to the hexagonal form around 2400 ºC.

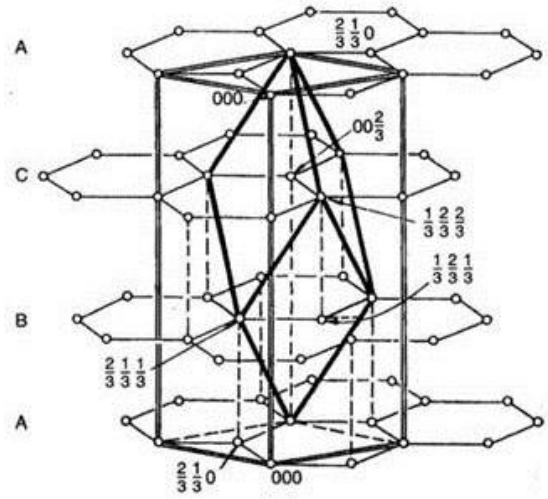

Figure 1-3: Single crystal structure of rhombohedral graphite [Pierson, 1993].

In the hexagonal graphite structure, each carbon (C) atom is sp^2 hybridized and is covalently bonded to three other C atoms giving a trigonal geometry. The sp^2 electrons overlap with those on adjacent C atoms to form tight localized sp^2 sigma bonds. The C-C sigma bond energy is 348 kJ/mol with an average bond length of 1.42 angstoms (Aº) [Pierson, 1993].

The C bonds form planar hexagonal rings which form flat parallel layers. These form parallel layers. The fourth electron is located in the p_z orbital which is perpendicular to the sp^2 plane. The fourth electron is delocalized and is free to move about the structure of the graphite. These free electrons give graphite its conductive properties. These free electrons also create an induced dipole on the atoms which gives rise to van der Waals forces between the layers. These forces are weak and allow the layers to slide over each other [Pierson, 1993]. At the surface of the graphite, the p_z electrons also exist as free electrons.

Nuclear grade graphite, as well as all other commercial graphites, contains impurities. The table below lists impurities and their concentrations present in the PCEA,

PPEA and PCIB graphites. These impurities may lead to the formation of sp^3 hybridized bonds within the graphite. Interstitial carbon atoms produced by irradiation damage can also lead to the formation of sp^3 bonds. As interstitials are added between the planes, sp^2 bonds are broken and new sp^3 bonds can be formed [Bonal and Wu, 1996]. As graphite is exposed to fast neutrons, basal planes begin to degrade and form interstitial loops. In some cases, the carbons can then bond with one another and form sp^3 hybridized bonds. Following high temperature annealing, the carbon atoms then break away from this less favorable state and return to the sp^2 hybridization that is characteristic of in-plane hexagonal unit formation. However, it is also possible for the damage to be so great that annealing is no longer possible [Bonal and Wu, 1996]. Sp^3 hybridized bonds are tetragonal. Each C atom is bonded to another C atom at angles of 109.5º. This bonding is seen in diamond (see image below).

Element	PCEA (ppm)	PPEA (ppm)	PCIB (ppm)
Li	< 0.01	< 0.01	< 0.01
Be	< 0.01	< 0.01	< 0.01
B	0.76	0.58	0.07
N	-	-	-
O	-	-	-
F	< 5	< 5	< 5
Na	0.07	0.08	< 0.05
Mg	< 0.5	< 0.5	< 0.5
Al	< 0.05	< 0.05	< 0.05
Si	2.1	4.5	2.3
P	0.25	0.76	0.19
S	6.7	17	1.1
Cl	0.26	0.47	0.21
K	< 0.1	< 0.1	< 0.1

Element	PCEA (ppm)	PPEA (ppm)	PCIB (ppm)
Ca	< 0.5	< 0.5	< 0.5
Sc	< 0.1	< 0.1	< 0.1
Ti	0.02	0.06	0.04
V	0.73	1.3	0.38
Cr	< 0.5	< 0.5	< 0.5
Mn	< 0.05	< 0.05	< 0.05
Fe	0.29	0.11	0.46
Co	< 0.05	< 0.05	< 0.05
Ni	3.3	1.9	0.91
Cu	< 0.5	< 0.5	< 0.5
Zn	< 0.5	< 0.5	< 0.5
Ga	< 0.1	< 0.1	< 0.1
Ge	< 0.1	< 0.1	< 0.1
As	< 0.1	< 0.1	< 0.1
Se	< 0.1	< 0.1	< 0.1
Br	< 0.1	< 0.1	< 0.1
Rb	< 0.05	< 0.05	< 0.05
Sr	< 0.05	< 0.05	< 0.05
Y	< 0.05	< 0.05	< 0.05
Zr	< 0.05	< 0.05	0.08
Nb	< 0.1	< 0.1	< 0.1
Mo	< 0.05	< 0.05	< 0.05
Ru	< 0.1	< 0.1	< 0.1
Rh	< 0.1	< 0.1	< 0.1
Pd	< 0.1	< 0.1	< 0.1
Ag	< 0.1	< 0.1	< 0.1
Cd	< 0.1	< 0.1	< 0.1
In	< 0.1	< 0.1	< 0.1
Sn	< 0.5	< 0.5	< 0.5
Sb	< 0.5	< 0.5	< 0.5

Element	PCEA (ppm)	PPEA (ppm)	PCIB (ppm)
Te	< 0.1	< 0.1	< 0.1
I	< 0.5	< 0.5	< 0.5
Cs	< 0.5	< 0.5	< 0.5
Ba	< 0.01	< 0.01	< 0.01
La	< 0.5	< 0.5	< 0.5
Ce	< 0.05	< 0.05	< 0.05
Pr	< 0.05	< 0.05	< 0.05
Nd	< 0.05	< 0.05	< 0.05
Sm	< 0.05	< 0.05	< 0.05
Eu	< 0.05	< 0.05	< 0.05
Gd	< 0.05	< 0.05	< 0.05
Tb	< 0.05	< 0.05	< 0.05
Dy	< 0.05	< 0.05	< 0.05
Ho	< 0.05	< 0.05	< 0.05
Er	< 0.05	< 0.05	< 0.05
Tm	< 0.05	< 0.05	< 0.05
Yb	< 0.05	< 0.05	< 0.05
Lu	< 0.05	< 0.05	< 0.05
Hf	< 0.05	< 0.05	< 0.05
Ta	< 100	< 100	< 100
W	< 0.05	< 0.05	< 0.05
Re	< 0.05	< 0.05	< 0.05
Os	< 0.05	< 0.05	< 0.05
Ir	< 0.05	< 0.05	< 0.05
Pt	< 0.05	< 0.05	< 0.05
Au	< 0.1	< 0.1	< 0.1
Hg	< 0.1	< 0.1	< 0.1
Tl	< 0.1	< 0.1	< 0.1
Pb	< 0.5	< 0.5	< 0.5
Bi	< 0.1	< 0.1	< 0.1

Element	PCEA (ppm)	PPEA (ppm)	PCIB (ppm)
Th	< 0.1	< 0.1	< 0.1
U	< 0.1	< 0.1	< 0.1

Table 1-3: This table lists impurities present in the samples of PCEA, PPEA and PCIB. These results are from Glow Discharge Mass Spectrometry elemental analysis performed by UCAR Carbon Co. Inc.

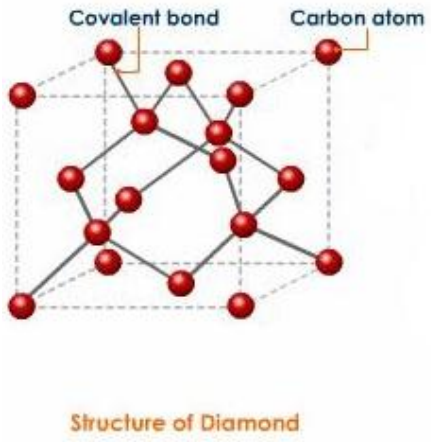

Figure 1-4: The above image shows the sp^3 hybridized bonding structure of diamond. The crystal structure is equivalent to a face-centered cubic lattice [Pierson, 1993].

Chapter 2 Nuclear Graphite Use and Its Production

2.1 Importance of Nuclear Graphite

In 2005, the Energy Policy Act mandated that the Department of Energy (DOE) develop a prototype Next Generation Nuclear Plant (NGNP) [NRC, 2010]. The NGNP project is developing a high temperature gas-cooled reactor (HTGR) to produce energy that is able to run both primary and secondary industrial applications. The heat generated by the high temperature reactor can be used to run more efficient turbines in order to produce electricity for homes and industrial facilities, the residual steam from that process can be used to manufacture plastic components from raw materials or generate ammonia for fertilizer, and it can also be used to produce hydrogen. Numerous industrial applications and energy distribution methods may be integrated into the operation of the NGNP.

The NGNP, using gas-cooled reactor technology, will provide the blueprint industry to manage the heat from the next generation of advanced nuclear plants for energy production and industrial processing. The HTGR can provide heat for industrial processes at temperatures from 700 ºC to 950 °C [IAEA, 1996]. This reactor is expected to open the door for a wider range of commercial applications than possible with the current light water reactor technology that operates near 300 °C [IAEA, 1996]. The design of the HTGR reactors provides for passive heat transfer, where the heat stored in the structures and the decay heat generated is transferred to the outside of the reactor vessel during a loss of coolant flow. Therefore the safety of the reactor is not dependent on the presence of the He coolant. The accident response times for HTGRs are also very slow allowing the operators days as opposed to seconds to handle an accident [NRC, 2010]. The HTGR will meet and exceed

current nuclear standards in reliability, proliferation resistance, waste management and security capabilities.

There are two different HTGR designs that NGNP is investigating [IAEA, 1996]. These designs are pebble-bed and prismatic (Figure 2-1). Nuclear graphite is used extensively in these designs. Different types of graphite are being considered for the moderating material, structural material, reflector material and fuel element matrix material. Some of these graphite grades will be expected to remain in the core for the life of the reactor (30 - 40 years) [IAEA, 1996]. For this reason it is important that there is a full understanding of how the different grades of graphite will handle high doses of radiation.

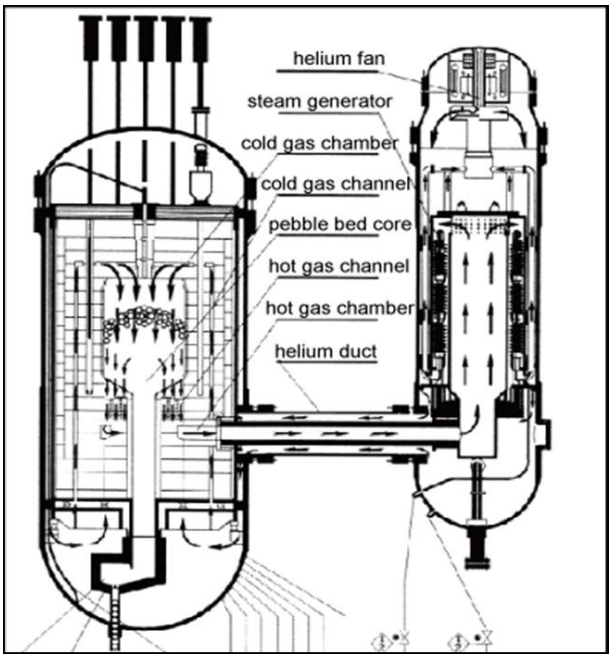

Figure 2-1: Pebble-bed reactor [IAEA, 1996]. This drawing depicts the typical design for a pebble bed HTGR. This design is being considered for commercial use in China.

2.2 Previous Use of Graphite in Nuclear Power Plants

There have been several versions of helium gas-cooled reactors in operation in the past and several in operation today in various parts of the world. In the United States (US) two have been in operation. One of these was Peach Bottom 1, which was in operation from 1966 to 1974 [IAEA, 1996]. It was a prismatic type reactor that generated 40 megawatts electric (MWe). Peach Bottom 1 had an average availability of 85 % and had very low operator doses (less than 10 man-rem/year) [NRC, 2010]. Post examination of materials was performed, and it led to improvements in fuel element and coated particle design. Fort St. Vrain was in operation from 1976 until 1989 [IAEA, 1996]. The plant was capable of producing 330 MWe and also demonstrated very low occupational doses for workers [NRC, 2010]. Fort St. Vrain had several water ingress accidents that have been used as a baseline for evaluating water ingress accidents [IAEA, 1996].

Recently two new gas-cooled reactors have come into operation. One is the High Temperature Engineering Test Reactor (HTTR) in Japan and the other is the High Temperature Reactor (HTR) – 10 in China [NRC, 2010]. The HTTR is a prismatic block reactor which first reached its maximum power of 30 MW on April 19, 2004 [NRC, 2010]. The HTR-10 reached its full power of 10 MW in January of 2003 [NRC, 2010]. Both are test reactors that are being used to certify future designs for the two countries.

2.3 How Nuclear Graphite is Manufactured

In medieval times, a large amount of pure graphite was discovered in Borrowdale, Cumberland, England. It was originally used for marking sheep and it eventually gave rise to the pencil industry. Those deposits have long since run out. Other large deposits of natural graphite have also been found in Madagascar, Korea and the United States. Today, most graphite is made synthetically. Figure 2-2 shows a typical manufacturing process for nuclear

graphite. The process typically takes 6 to 9 months to perform. The final product is largely determined by the starting materials. A detailed description of the manufacturing process can be found in Appendix A.

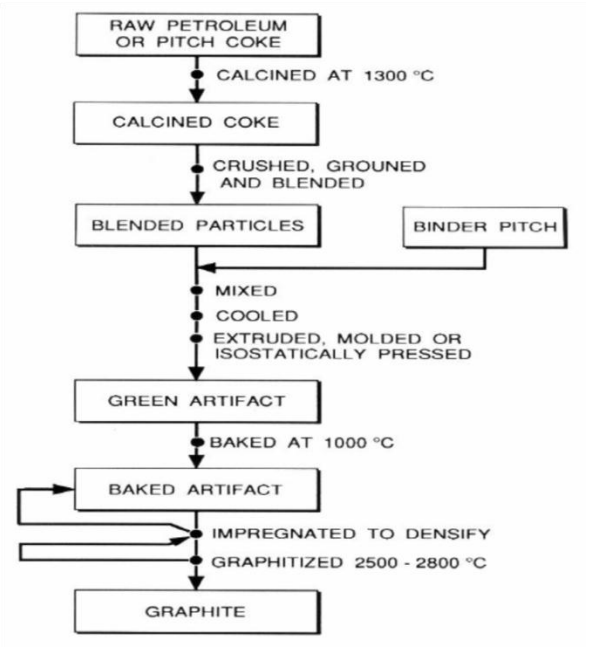

Figure 2-2: Manufacturing process for nuclear graphite [Nightingale, 1962]. The entire process takes 6 to 9 months to complete.

Chapter 3 Irradiation Induced Damage in Graphite

3.1 Background

Studies [Burchell, 2001; Bonal and Wu, 1996; Tanabe, 1996] have been conducted to study the effects on graphite in various types of radiation fields. Most of these studies have been conducted in mixed field fields, that include gamma, beta and neutron irradiation, the environment that nuclear graphite will encounter. Some studies have also been conducted using electron beam irradiation but most of these studies focus on graphene layers. There have been relatively few studies of gamma irradiation alone as it was thought that gamma irradiation alone would have no effect on the properties of the graphite.

Irradiation damage can be defined as the change in the structure (bonds, crystal lattice, etc.) of a material produced by interaction with a flux of either atomic or sub-atomic particles [Kelly, 1981] which leads to changes in the physical properties of the material (tensile strength, density, etc.). In metals and narrow band gap semiconductors electronic excitations decay instantaneously, leaving collisions with nuclei as the sole mechanism responsible for the creation of defects in graphite and related carbon materials [Yazyev et al, 2007]. Graphite has been studied in this regard due to its application as a moderator in nuclear reactors. For nuclear design, dimensional changes due to the bombardment with neutrons are very important. The irradiation damage is dependent on the degree of structural crystallinity. In nuclear graphite, crystallites in the polycrystalline material can grow anisotropically at different rates and directions, resulting in an increase in the internal stresses at the crystallite boundaries. This is discussed further in Section 3.4.

3.2 Energy Transfer

Irradiation may affect materials by exciting electrons from their orbitals, by ionizing atoms, or by displacing atoms [Kelly, 1981]. Excited electrons will eventually lose their excess energy and return to their ground state. The extent of these phenomena depends on the linear energy transfer (LET) of the radiation. LET is defined as the distance over which a particle loses energy [Woods and Pikaev, 1994]. This is generally reported in units of keV/μm. Electromagnetic radiation and β-particles interact with matter, losing only little energy per interaction and therefore have low LETs. In contrast, heavy particles (α-particles, neutrons, and protons) have high LETs losing energy rapidly, producing many ionizations over short distances. The values of LETs range from about 0.2 keV/μm for low-LET radiations (γ radiation and electrons) to 40 - 50 keV/μm for high-LET radiations (neutrons, fission fragments and other heavy positive ions) [Woods and Pikaev, 1994]. The rate of energy loss by a particle changes as it slows down, so the LET will have different values at different points along the particle track. The penetration depth of electron and other charged-particle radiations in matter is inversely related to their LET. This means that the particles with lower-LETs penetrate to greater depths than those with higher-LETs [Woods and Pikaev, 1994]. The figure below illustrates the increasing LET of certain particles.

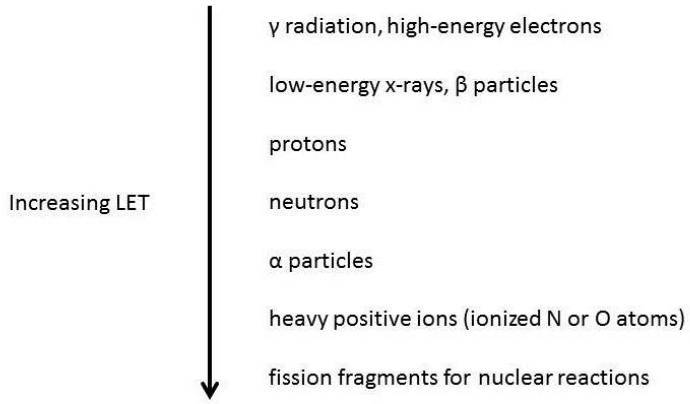

Figure 3-1: The image above shows increasing LET for certain particles [Woods and Pikaev, 1994].

The basic mechanism for the slowing down of a moving charged particle is through coulombic interactions between the particle and electrons in the medium. Heavy charged particles, such as fission fragments, lose energy primarily through the ionization and excitation of atoms. The moving charged particle exerts electromagnetic forces on atomic electrons and imparts energy to them. The energy transferred may be sufficient to knock an electron out of an atom ionizing it or may leave the atom in an excited state [Turner, 1995].

Light charged particles, such as electrons, deposit energy through two mechanisms: collisions and radiative losses. In collisional losses the electrons lose energy via interactions with orbital electrons in the medium. This leads to excitation or ionization of the atom. The second mechanism is possible because of the small mass of the light charged particle. As the charged particle undergoes a change in velocity, it emits electromagnetic radiation known as bremsstrahlung. For electrons, the bremsstrahlung photons have a continuous energy distribution that ranges from the kinetic energy of the incoming electron downward [Turner, 1995].

Neutron irradiation has an immediate effect on the graphite by causing carbon atom displacements. These displacements cause vacancies and interstitials to form within the graphite lattice and result in dimensional and physical property changes [Tanabe, 1996].

The Wigner effect can be used to describe how neutron irradiation causes carbon atom displacement in graphite [Simmons, 1965]. As a neutron passes through the graphite structure it comes in contact with carbon atoms and causes a displacement. The energy required to move an atom from its position in the lattice is termed displacement energy. For most solids, including graphite, this energy is approximately 25 eV [Simmons, 1965]. The displacement energy varies slightly depending on the recoil direction. Since the direction of the recoil is determined from the collision event, which is a random process, the recoil direction is also random [Was, 2007]. The single value of 25 eV represents a spherical average of the potential barrier surrounding the equilibrium lattice site [Was, 2007]. An accurate determination of the displacement energy can be made if the interaction potential between the lattice atoms is known. To do this, the atom is moved in a given direction and the interaction energies between the moving atom and all other nearest neighbors along the trajectory are summed. When the total potential energy reaches a maximum, the difference between this and the equilibrium energy represents the displacement threshold for a given direction [Was, 2007]. This displaced carbon atom moves through the graphite lattice with considerable energy. The displaced atom loses energy by exciting electrons from their normal orbitals, exciting lattice waves or by displacing more atoms. The additional displaced carbon atoms can continue to displace more atoms creating a cascade effect. The cascade continues to grow until the energy is shared between so many atoms that none of them have enough energy to cause any more displacements. Further movement continues, *e.g.*, in a vibrational mode, *etc.*, until thermal equilibrium is reached [Chiang *et al.*, 1997].

There are two factors that determine the amount of damage produced in graphite during neutron irradiation. These factors are the energy of the primary knock-on atoms and the number of primary knock-on atoms [Pierson, 1993]. As the energy of the primary knock-on atom increases, more interactions will occur during the slowing down of this atom. Therefore it will cause more displaced atoms than primary knock-on atoms of lower energy. Also, as the number of primary knock-on atoms increases the likelihood of other atoms being displaced by the primary knock-on atom, increases with more damage to the graphite. Based on a number of models, Dehalas determined that a fission neutron with an average energy of 2 MeV will cause about 22,000 displacements in graphite during its path to thermalization.

3.3 Irradiation Induced Defects

The simplest defects that occur are vacant lattice sites and interstitial atoms. The equilibrium position for an interstitial atom is determined by the minimum energy for the atom. This normally means that the maximum spacing will exist between the interstitial and the surrounding atoms. In graphite, this position is not halfway between adjoining planes but close to the center of a hexagon in the adjoining plane (see Figure 3-2). Displacement groups may be created by interaction with the primary knock-on atom, resulting in a group of vacancies surrounded by interstitial atoms. In order for these defects to exist as point defects, the distance between them must be sufficiently large. Heating of the graphite may cause defects to move through the crystal and aggregate with other defects and it could also have annealing effects on the graphite. Large groups of interstitials and vacancies can be seen with the electron microscope [Bonal and Wu, 1996].

Simmons put together a table (Table 3-1) showing the displacement effect of various particles based on a displacement energy of 25 eV. The primary defects caused by irradiation are interstitials and vacancies but the distribution of these is dependent on the type of particle.

Simple vacancies and interstitials have well-defined energies of formation. By measuring the stored energy in irradiated samples, the number of defects can be determined.

Particle	Energy (MeV)	Displacement Cross-Section (cm^2)	Mean Number of Displacements/Collision
Electrons	1	14.5×10^{-24}	1.6
	2	15.0×10^{-24}	1.9
	3	15.5×10^{-24}	2.3
	4	16.0×10^{-24}	2.5
Protons	1	7.8×10^{-21}	4 – 6
	5	1.56×10^{-21}	4 – 6
	10	0.78×10^{-21}	4 – 6
	20	0.39×10^{-21}	4 – 6
Deuterons	1	1.56×10^{-20}	4 – 6
	5	0.31×10^{-20}	4 – 6
	10	0.15×10^{-20}	4 – 6
	20	0.08×10^{-20}	4 – 6
α Particles	1	1.25×10^{-19}	4 – 6
	5	0.25×10^{-19}	4 – 6
	10	0.12×10^{-19}	4 – 6
	20	0.06×10^{-19}	4 – 6

Table 3-1: Atomic Displacements in Graphite Produced by Various Energetic Particles [Simmons, 1965].

A common defect that occurs as a result of irradiation is the Frenkel defect [Chiang *et al.*, 1997]. A Frenkel defect occurs when an atom is moved from a position in a layer plane and placed interstitially between layers. This defect results in a vacancy and an interstitial in

the lattice (see Figure 3-2). Substitution by impurities present in the graphite can also occur and lead to defects in the lattice structure.

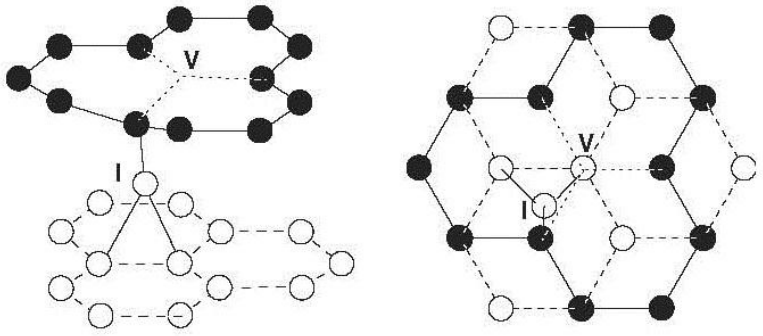

Figure 3-2: This image shows a Frenkel pair in the graphite lattice [Tellig and Heggie, 2007].

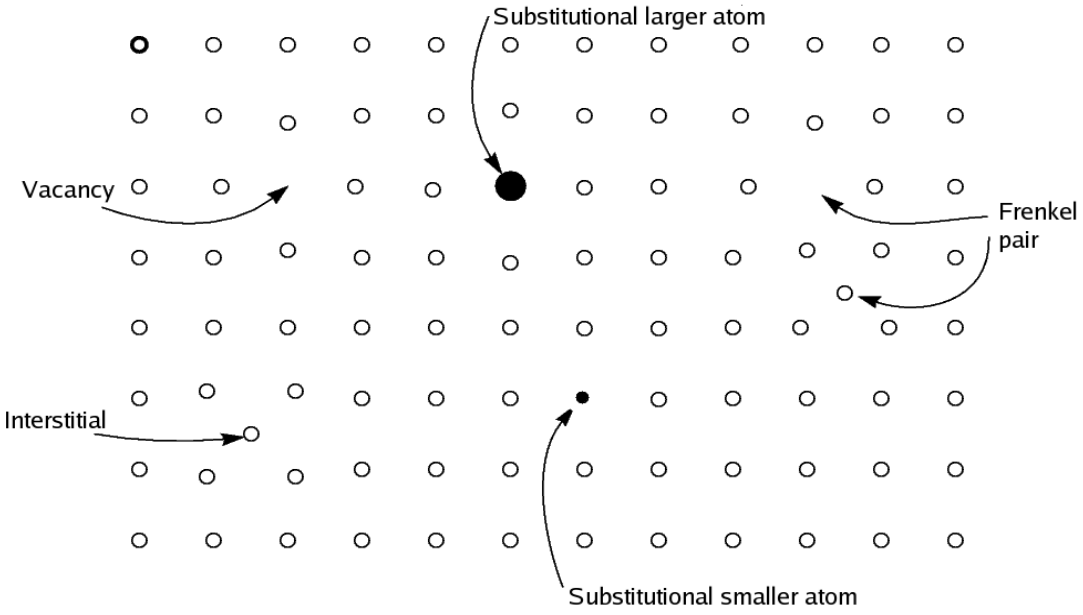

Figure 3-3: Common defects in graphite [absoluteastronomy.com]. This image shows a vacancy, an interstitial, substitution by both larger and smaller atoms and a Frenkel pair (where a vacancy and interstitial are formed together).

Interstitials and vacancies can be either sessile or mobile. This fact leads to two different scenarios. The first is mixed-field irradiation at low temperatures where neither

defect is mobile. The second is mixed-field irradiation at temperatures where one or both defects is mobile. The first to formulate a damage model at low temperatures were Hennig and Hove in 1956. Reynolds and Goggin and others carried on a number of other experiments. A summary of the mobility of interstitials and vacancies is presented below.

As the groups of interstitial atoms become larger, their mobility decreases. Interstitial atoms have a migration energy of approximately 1 eV and are mobile at room temperature. Above 200 ºC, these interstitials can form into clusters of 2 to 4 atoms. As the temperature increases above 300 ºC, more interstitial atoms form together and begin to grow new basal planes (Figure 3-4). This new growth continues to temperatures up to 1400 ºC, where recombination with vacancies is more likely [Burchell, 2001]. As irradiation continues, the number of interstitial groups continues to increase. At a certain point, the likelihood of a newly formed interstitial combining with a mobile group will be less than the likelihood of combining with a sessile group. At this point the number of immobile groups continues to increase but the total number of interstitial groups remains the same.

The migration energy for a mono-vacancy is approximately 1.7 eV. Below 300º C, vacancies tend to be immobile but their mobility increases with increasing temperature. Between 300 ºC and 400 ºC, clusters of 2 to 4 vacancies diffuse through the basal plane. These vacancies begin to form loops above 650 ºC. The dislocation loops are formed by the additional removal of a partial plane. As temperatures increase above 900 ºC, these vacancy loops give rise to collapsing vacancy lines [Burchell, 2001].

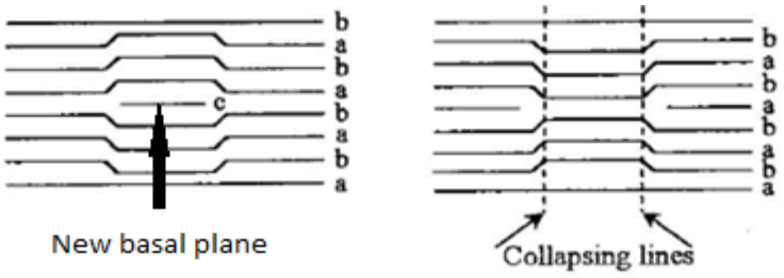

Figure 3-4: Growth of new basal plane in graphite (left); collapse of basal plane due to vacancies (right) [Delhaes, 2001]

Large amounts of interstitials of a single element between two layers of graphite could lead to intercalation of the graphite in some areas. Graphite intercalation compounds are formed by the insertion of atomic or molecular layers of a different chemical species called the intercalant between layers in a graphite host material [Dresselhaus and Dresselhaus, 2002]. The intercalation compounds occur in highly anisotropic layered structures where the intraplanar binding forces are large in comparison with the interplanar binding forces. Intercalation provides a means for controlled variation of many physical properties of the host material. The free carrier concentration of the graphite host is very low (approximately 10^{-4} free carriers/atom at room temperature), therefore intercalation with different chemical species and concentrations permits wide variation of the free carrier concentration and thus of the electrical, thermal and magnetic properties of the host material [Dresselhaus and Dresselhaus, 2002]. The image below depicts graphite intercalated with potassium.

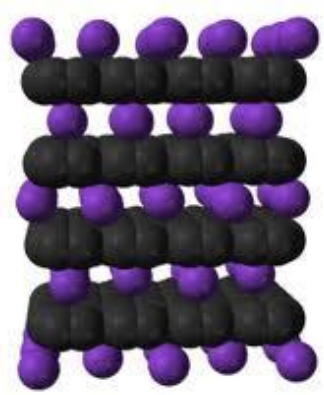

Figure 3-5: Intercalation of graphite with potassium [Dresselhaus and Dresselhaus, 2002].

3.4 Irradiation Induced Dimensional Changes

For highly oriented pyrolytic graphite (HOPG), crystal growth during irradiation occurs parallel to the hexagonal axis and contraction occurs parallel to the basal planes [Tanabe, 1996]. These dimensional changes coincide with changes in the crystal lattice parameters, namely the interatomic spacing in the *a*-axis and the *c*-axis (see Figure 1-2). The dimensional changes in polycrystalline graphite, which is what nuclear grade graphite is, are more difficult to characterize. The changes there represent an average of the behavior of the components which make-up the graphite.

Brown, Kelly and Mayer [1969] showed that Boron (B) doping of Ticonderoga (natural graphite) increased the loop density (the amount of loops in a given volume) causing changes in the nuclei density. Boron was used as a doping agent because B is a common impurity in graphite that is extremely difficult to remove. The cause of the density change was determined to be due to the attractive force between B in substitutional positions and diffusing interstitials. The presence of the B impurities slowed the migration of interstitials. This allows more time for other carbon atoms to form interstitials in the same area creating

interstitial loops. Near the interstitial loops, vacancy loops also exist. These loops lead to the formation and collapse of basal planes. The formation of the interstitial loops leads to growth in the *c*-axis of crystal creating interlayer spacing changes. On the other hand, vacancy loops cause contraction along the *c*-axis. The degree of contraction is linked to the size of the vacancy loop. Large vacancy loops can cause complete collapse of the basal plane causing a larger contraction than small vacancies.

For extruded graphite at temperatures below 300 ºC, the nuclear graphite normally grows in the direction perpendicular to the extrusion and shrinks in the parallel direction. Reports from Bonal and Wu [1996] show that in carbon fiber composites, dimensional changes increased with increasing irradiation temperature from 600 – 1000 °C. However, it is not simply the increase in interstitial space that leads to such drastic growth perpendicular to the basal plane. It has been reported that dislocation loops leads to a maximum expansion of 10 % [Bonal and Wu, 1996]. Therefore, another mechanism must explain the large increase in size, occasionally up to 200 % [Kelly, 1981]. It is speculated that high levels of carbon displacement in the basal planes along with increased presence of carbon atoms within the interstitial space can lead to breaking of hexagonal units and formation of sp^3 hybridization within carbon atoms. The change in hybridization, along with deformation of the normally flat in-plane hexagonal units can be attributed to this large physical swelling [Simmons, 1965]. Voids are created within the basal planes and space gaps form in the interstitial layers as a result of neutron damage and deformation of the graphite crystal lattice becomes more prominent. When this occurs, there is more space for metallic fission products and fission product gases to become trapped within the graphite. Temperature changes lead to expansion and contraction of these gases and can cause increased strain on the lattice. Impurities can also interact with carbon atoms and influence their hybridization.

It is possible for graphite to be metamictized by alpha-particles [Dorbrzhinetskaya, et al., 2011]. Metamictization is a natural process resulting in the gradual destruction of a mineral's crystal structure, resulting in an amorphous material. This was shown by implanting zircon (an alpha-particle emitter) into the graphite. However, in a reactor the graphite will not be exposed to large amount of alpha radiation because these particles are shielded by the fuel.

Chapter 4 Graphite Oxidation

4.1 Oxidation Reactions of Graphite

While the HTGR design is helium cooled, air and steam oxidation is still expected to occur due to the impurities in the helium and gas that may enter the system through air ejectors in the system, leaks, etc. All ejectors operate on a common principle. They entrain air or other fluids in a high velocity jet of air, steam, water or other fluid. They use the kinetic energy of the high velocity stream to push back the atmosphere from the discharge of the ejector. In the HTTR, operating in Japan, the following impurities are present: $O_2 < 0.04$ ppm, $H_2O < 0.2$ ppm, $CO_2 < 0.6$ ppm, $N_2 < 0.2$ ppm, $H_2 < 3$ ppm [NRC, 2010]. These impurities can lead to several different oxidation reactions.

In general, the reactions of carbon with oxidizing gases are controlled by the following processes:

1. Diffusion of gaseous reactants from the bulk gas phase to the carbon surface,
2. Adsorption of reactants on the surface,
3. Formation of carbon-oxygen bonds,
4. Formation of carbon-hydrogen bonds,
5. Breaking of carbon-carbon bonds,
6. Desorption of products, and
7. Transport of the gaseous products away from the carbon surface [Kelly, 1981; Marsh, 1989].

The kinetics of the reactions is governed by the rate determining step, which can basically be described at the slowest step. The rate determining step can be dependent on process parameters and carbon properties. Some of the controlling factors are:

1. The rate at which the oxidant is supplied to the surface,
2. The partial pressure of the oxidant,
3. The surface area available to the oxidant,
4. The catalytic impurities in the graphite,
5. The temperature,
6. The rate at which reaction products are removed,
7. Neutron damage to the graphite, and
8. The quantity of in-pore deposits.

4.1.1 Reaction with Oxygen

$$\frac{1}{2}\,O_2\ (gas) + C\ (solid) = CO\ (gas) \quad (1)$$

$$\Delta H = -110.5\frac{kJ}{mol}$$

$$C\ (solid) + O_2\ (gas) \rightarrow CO_2\ (gas) \quad (2)$$

$$\Delta H = -393.4\frac{kJ}{mol}$$

where ΔH is the standard enthalpy of formation at 298 ºC [Kelly, 1981].

Reaction (1) maximizes the amount of carbon removed by oxygen as carbon monoxide. Reaction (2) maximizes the amount of heat produced by oxidizing carbon to carbon dioxide. Reaction (2) can also be regarded as occurring in stages. By using Hess's law, which states if a reaction takes place in several steps then its standard reaction enthalpy is the sum of the standard enthalpies of the intermediate reactions into which the overall reaction may be divided at the same temperature [Wickham, 1998], reaction (3) is derived.

$$\frac{1}{2}\,O_2\,(gas) + CO(gas) = CO_2\,(gas) \quad (3)$$

$$\Delta H = -282.9\frac{kJ}{mol} \quad [Marsh, 1989]$$

All of these reactions are exothermic, but nuclear grade graphite does not readily react with air at room temperature. Kinetic factors determine reaction rates.

4.1.2 Reaction with Carbon Dioxide

$$CO_2\,(gas) + C\,(solid) \rightarrow 2\,CO\,(gas) \quad (4)$$

$$\Delta H = 172.4\frac{kJ}{mol} \quad [Marsh, 1989]$$

This reaction is also referred to as the Boudouard reaction. The Boudouard reaction is the redox reaction of a chemical equilibrium mixture of carbon monoxide and carbon dioxide at a given temperature. This equilibrium was first investigated by O.L. Boudouard, a French chemist, in 1905 [Marsh, 1989]. It is the disproportionation of carbon monoxide into carbon dioxide and graphite or its reverse (see equation 5 below).

$$2\,CO \leftrightarrow CO_2 + C \quad (5)$$

While the formation enthalpy of CO_2 is more negative than that of CO, the formation entropy of CO_2 is much lower. The Boudouard reaction implies that at lower temperatures the equilibrium is on the exothermic carbon dioxide side and on higher temperatures the endothermic formation of carbon monoxide is the dominant reaction (Figure 4-1). At 400 ºC, it lies almost completely on the side of carbon dioxide, while at 1000 ºC, it is entirely on the side of carbon monoxide at 1 atm. The equilibrium shifts to higher temperatures as the pressure is increased.

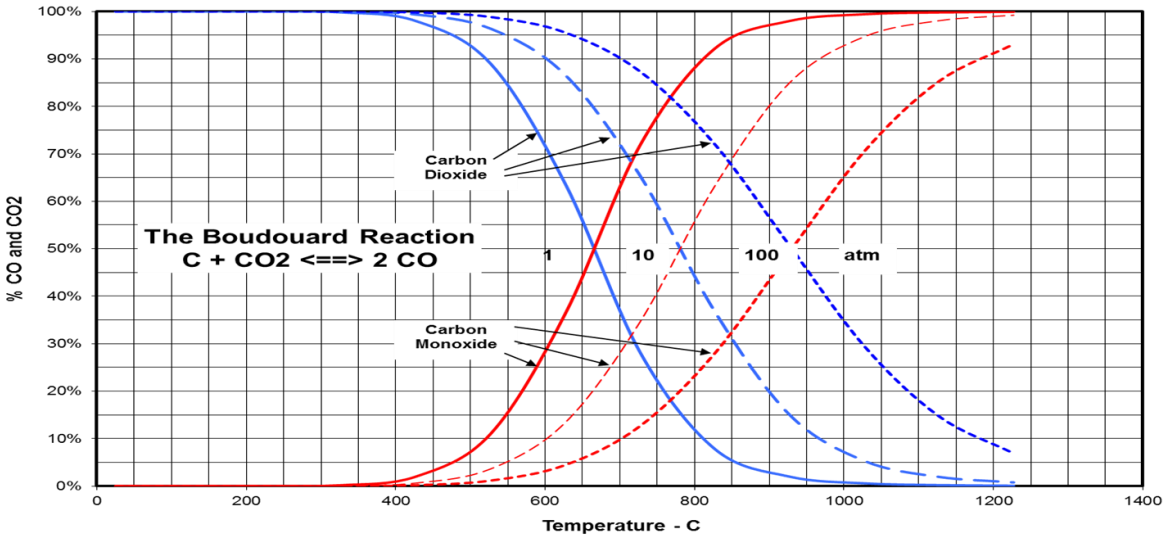

Figure 4-1: Boudouard equilibrium [Bioenergylist.org]. This graph shows that at lower temperatures the equilibrium is on the exothermic carbon dioxide side and on higher temperatures the endothermic formation of carbon monoxide is the dominant reaction. The equilibrium shifts to the right with increasing pressure.

4.1.3 Reaction with Water

$$C\ (solid) + H_2O\ (gas) \rightarrow CO\ (gas) + H_2\ (gas) \quad (6)$$

$$\Delta H = 130.3 \frac{kJ}{mol} \quad [\text{Marsh}, 1989]$$

$$C\ (solid) + 2\ H_2O\ (gas) \rightarrow CO_2(gas) + 2\ H_2(gas) \quad (7)$$

$$\Delta H = -82.4 \frac{kJ}{mol} \quad [\text{Marsh}, 1989]$$

The hydrogen produced in reactions 6 and 7 can react with the carbon in the following reaction.

$$C\ (solid) + 2\ H_2\ (gas) \rightarrow CH_4\ (gas) \quad (8)$$

$$\Delta H = -74.8 \frac{kJ}{mol} \quad [Marsh, 1989]$$

Subtracting equation 6 from equation 7 results in the following equation:

$$CO\ (gas) + H_2O(gas) \rightarrow CO_2(gas) + H_2\ (gas) \quad (9)$$

$$\Delta H = -213.7 \frac{kJ}{mol} \quad [Marsh, 1989]$$

This equation is sometimes referred to as the gas shift reaction. The entire reaction takes place in the gas phase.

Products of the above reactions are normally free to escape so that thermodynamic equilibrium is not reached. The enthalpy changes are still important in measuring the heat produced in exothermic reactions.

4.1.4 Reactivity Differences in Carbon

The differences in the amount and type of gas produced are dependent on the following parameters: the degree of graphitization, the impurity levels, oxygen supply, temperature of reaction, and the irradiation dose level. Different types of carbons react differently to oxidizing gases. Typically the reactivities of carbons, both graphitizing and non-graphitizing, decrease with heat treatment. Heat treatment results in thermal annealing of the graphite which reduces the structural defects present in the carbon thereby reducing the reactivity.

Gasification occurs mainly at preferred sites. These sites are located primarily at prismatic edges of the carbon layers and at defects in the basal plane. Stein and Brown [1985] showed that carbon atoms on the edge of a plane were more reactive than those in the basal plane. They also determined that the presence of impurities increased the reactivity. The edge atoms in the graphene planes have unpaired sp^2 electrons, whereas the basal plane

carbon atoms are use the π-electrons to form bonds between the basal planes. The unpaired electrons of the edge carbon atoms make them more reactive with oxygen atoms. Stein and Brown also examined the different structures of the carbon edge atoms. The edge atoms can be either zig-zag or arm-chair (see figure 4-2). They used structure resonance theory to determine that the zig-zag carbon edges are more reactive than the arm-chair. Overall the rate of gasification at the prismatic edges is 100 to 1000 times faster than on the basal plane.

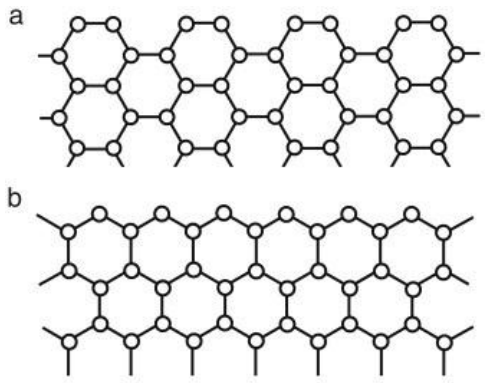

Figure 4-2: a. edge atoms arranged in an arm-chair configuration; b. edge atoms arranged in a zig-zag configuration [Delhaès, 2001].

As discussed above, reactions occur at active or favored sites. These active sites might be edge atoms, defects or impurities. In the reaction the gas molecule is adsorbed, reacts to form an intermediate and desorbs to produce gaseous products and a free site. Figure 4-3 shows a schematic of this mechanism with molecular and atomic oxygen. Both adsorption and desorption can occur via a single site or a dual site mechanism. As their names imply, the single site mechanism requires one free carbon site while the dual site mechanism requires two free carbon sites.

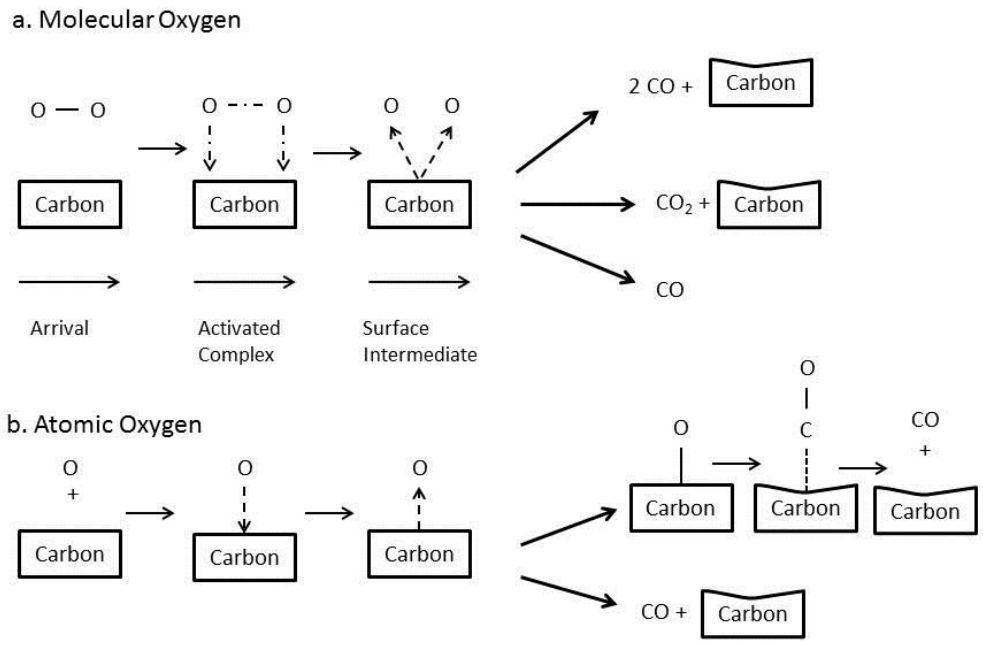

Figure 4-3: Representation of events in molecular (a) and atomic (b) oxygen adsorption.

The single site mechanism can be seen in the following equations.

$$CO_2 + C_f \rightarrow C(O) + CO$$

$$O + C_f \rightarrow C(O)$$

where C(O) denotes a carbon site with a chemisorbed atomic oxygen and C_f denotes a free carbon site. The dual site mechanism requires two free active sites and is represented by the reactions below.

$$O_2 + 2C_f \rightarrow 2C'(O)$$

The C´(O) may migrate to a new site to form a more stable, immobile surface intermediate, C(O). The surface intermediates may then undergo either single or dual site desorption (see below).

$$C(O) \rightarrow CO + C_f$$

$$C'(O) + C'(O) \rightarrow CO_2 + C_f$$

Langmuir-Hinshelwood kinetics can be used to describe the carbon-gas reaction in terms of a chemical adsorption mechanism [Marsh, 1989]. This mechanism is based on the following assumptions:

1. Localized adsorption occurs via collisions with active sites,
2. One molecule or atom is adsorbed per active site,
3. The surface is homogenous with a uniform distribution of active sites over the entire surface,
4. No interactions occur between adsorbed species,
5. The adsorption rate per site is not dependent on the adsorbed species, and
6. There is either no surface migration or it occurs very rapidly so that only adsorption and desorption are rate controlling.

The Langmuir-Hinshelwood kinetics [Marsh, 1989] imply that both the activation energy for adsorption (E_A) and desorption (E_D) remain constant from site to site and over time. Assuming steady state and isothermal conditions,

$$R_a = R_d$$

where R_a is the intrinsic rate of adsorptions and R_d is the intrinsic rate of desorption. If the intrinsic reactivity (R_i) is controlled by either the rate of adsorption or desorption, then the following equations are true using Langmuir-Hinshelwood kinetics:

$$R_i = R_a = R_d$$

$$R_a = k_a P \left(1 - \frac{aP}{1 + aP}\right)$$

$$R_d = k_d \left(\frac{aP}{1 + aP}\right)$$

where k_a is the rate constant for adsorption, k_d is the rate constant for desorption, a is a temperature dependent constant and P is the partial pressure of the reactant gas (Marsh, 1989).

For non-homogenous surfaces, the kinetics can be modified assuming that most active sites react first. As nearby sites are filled, repulsive forces are created inhibiting adsorption and promoting desorption. That means that E_A increases and E_D decreases as the surface coverage increases. The following expression expresses the intrinsic reactivity for a heterogeneous carbon surface, taking into account the active sites:

$$R_i = k_i \, [C_t] W \, P^m$$

where R_i is the intrinsic reactivity, k_i is the intrinsic rate coefficient, $[C_t]$ is the active site concentration, W is the mass of the carbon atom, P is the partial pressure of the reactant gas and m is the reaction order.

Assuming an isothermal sample, the overall reactivity (R) can be expressed as:

$$R = k_i \eta A_g [C_t] W (P_s)^m$$

where k_i is the intrinsic rate coefficient, η is the degree of gaseous penetration, A_g is the total internal surface area, $[C_t]$ is the active site concentration, W is the mass of the carbon atom, P_s is the partial pressure of gas at the surface and m is the reaction order. This equation implies that the carbon reactivity is proportional to the active surface area [Marsh, 1989].

Laine, Vastola and Walker Jr. [1965] verified this conclusion by directly measuring the active surface area on graphitized carbon black. They chemisorbed oxygen onto a clean carbon surface at 300 ºC for 24 hours. The resultant surface oxygen complex was desorbed as carbon monoxide and carbon dioxide at higher temperatures. The amount of oxygen complex formed is a measure of active surface area assuming one oxygen atom reacts with one carbon atom. The active surface area is a measured of the unbound edge carbon atoms. Laine, *et al*. [1965] showed that these surface complexes formed during the reaction can be broadly categorized into two types: a fleeting oxygen complex which readily desorbs to form either CO or CO_2 or a stable surface oxide which does not readily form the reaction products.

4.1.5 Radiolytic Oxidation

Radiolytic oxidation also occurs in the reactor environment leading to the presence of additional oxidizing species. Gaseous carbon dioxide (CO_2) appears stable under radiolysis, except at very high dose rates. While the CO_2 appears stable, there is decomposition and recombination taking place. The ionizing radiation forms ion pairs in the CO_2 which interact and reform stable CO_2. This process occurs when carbon dioxide is decomposed by fast neutron and gamma irradiation to form carbon monoxide and an oxygen free radical. The rate of formation of different species under radiolysis is determined by the G value. The G value is defined as the number of species produced per 100 eV of energy deposited [Marsh, 1989]. The G values can vary depending on the nature of the radiation. This is caused by

differences in the density of the ionization produced. Table 4.1 shows G values for various ionizing particles.

Particle		G Value
Electrons	18 keV	3.05
	67 keV	3.04
Protons	1.83 MeV	2.91
Alpha particles	Po^{210}	2.94
Recoil Ions	Th C 117 keV	0.98
	Th C 168 keV	1.01
	C^{13} 1.64 – 2.92 MeV	2.38
	O^{16} and C^{12} 0.1 – 1.5 MeV	1.47 – 2.56
	O^{16} 30 keV	1.45
	O^{16} 40 keV	1.52
	O^{16} 50 keV	1.58

Table 4-1: G Values for various irradiating particles in CO_2 [Marsh, 1989].

This oxidation occurs primarily within the graphite pores, which initially makeup 20 % of the graphite volume. In order to estimate the number of active species produced, it is necessary to estimate the rate of energy deposition in the pores of the graphite. This means that using calorimetry to estimate the rate of energy deposition may not give appropriate results with the graphite pores. A calorimeter is an experimental apparatus the measures the energy of particles. The particles enter the calorimeter. The particle's energy is deposited in the calorimeter, collected and measured. Most of the radiation yield is caused by secondary particles. If the volume of the pore is small enough to allow some of the secondary particles to leave the pore unstopped, the G value will be altered. Linacre, Taylor and Thomas [1965] determined that taking the dose rate determined by calorimetry and using a G value of 3 the

radiolysis of CO_2 in graphite pores is accurately described [Stein and Brown, 1985]. The mechanism for this can be seen below [Linacre *et al*, 1965].

Gas Phase

$$CO_2 \rightarrow radiation \rightarrow CO + O^*$$

$$CO + O^* \rightarrow CO_2$$

Graphite Pore Surface

$$O^* + C \rightarrow CO$$

In this mechanism, carbon dioxide in a radiation field is broken down into carbon monoxide and atomic oxygen. The atomic oxygen reacts both with the carbon monoxide to reform carbon dioxide and with the carbon on the graphite pore surface to form more carbon monoxide. For a fixed set of conditions the oxidation rate constant will vary in different types of graphite due to differences in porosity. Although there are variations, the accepted G value for CO_2 is 2.35 [Linacre, *et al*, 1965]. The variations in the G value for CO_2 are caused by the presence of CO in the gas composition. The CO inhibits the radiolytic oxidation by reacting with the atomic oxygen and reforming CO_2 before the atomic oxygen is able to react with the graphite. The following equation shows how a small amount of CO can drastically affect the G value for CO_2. A CO presence of one percent can reduce the G value for CO_2 by a factor of two [Linacre, *et al*, 1965].

$$G\ Value = 1.05 + \frac{1.32}{1 + 8.5\ [CO]}$$

The presences of methane will also reduce the G value of carbon dioxide. Experiments have shown that the effectiveness of methane is 10 times greater than that of an

equal amount of carbon monoxide [Marsh, 1989]. This method of oxidation inhibition has been used in the Advance Gas-Cooled reactors (AGRs) in the United Kingdom. AGRs use CO_2 as coolant. The radiolysis of CO_2 produces CO, water and H. In order to inhibit the graphite-CO_2 reaction, an excess amount of CO_2 is maintained in the coolant system to promote the reaction of CO with H to produce methane [Sykes, *et al.*, 1993]. This reaction is shown below. Holes for the methane gas are drilled into the graphite blocks to ensure the methane will be distributed throughout the block.

$$2CO + 2H_2 \leftrightarrow CH_4 + CO_2$$

The rate of radiolytic oxidation of graphite is affected by three things: the number of active species in the gas phase, the number of species reacting with the graphite surface, and the effects of surface protective measures [Marsh, 1989]. Almost all of the products produced in the bulk gas are deactivated before they reach the surface of the graphite. Most of the radiolytic oxidation occurring in the graphite occurs in the pores because the distance traveled by the oxidizing species is small. Therefore the small amount that reaches the graphite pores will remain there and continue the oxidation reaction. The porosity of the graphite is therefore important in the determination of the oxidation rate. Radiolytic oxidation is important because the resultant weight loss may affect reactor economic performance by reducing moderating power and increasing permeability, and it can cause significant changes in graphite properties and loss of strength.

4.2 Temperature Regimes of Oxidation

In the presence of air, graphite temperatures have to be at least 350 ºC before any appreciable reaction will take place. The oxidation of graphite can be broken down into three

regions based on temperature. Figures of these three regions can be seen below [Marsh, 1989].

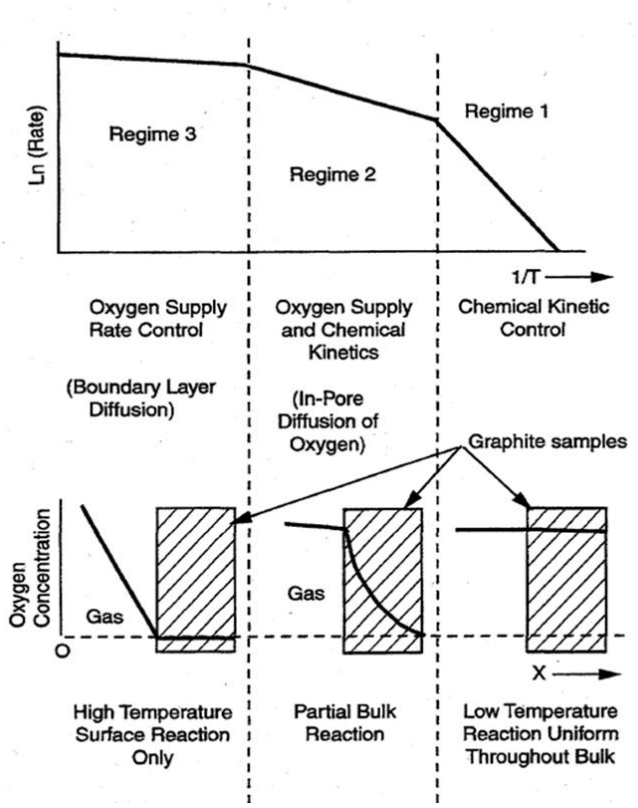

Figure 4-4: The three regime oxidation of graphite showing the concentration of gas within the gas and graphite. The top diagram represents the change in rate of the carbon gasification reaction with temperature. The lower diagram shows how the concentration of reactant gas in the graphite varies with the rate controlling zone [Marsh, 1989].

4.2.1 Region 1

Region 1 is controlled by kinetics and corresponds to temperatures less than 700 ºC. In this regime there are low oxidation rates due to the lower temperatures. The reactant gas concentration is uniform throughout the bulk of the carbon sample and is equal to the concentration in the gas phase. This is also known as the "chemical" regime because the reaction rate is largely determined by the intrinsic reactivity of the graphite. Different parts

of the graphite may react at different rates. Typically the binder and the edge atoms are more reactive than the basal plane atoms. Gas composition may also vary in the pores because the concentration of a given gas can vary with pore shape.

The reaction rate with air only becomes significant as temperatures approach 400 ºC. At this temperature the rate of reaction is $3 – 8 \times 10^{-10}$ kg/kg s. The units for the oxidation rate imply the following equation:

$$\frac{dm}{dt} = km$$

Where m is the graphite mass (kg), t is the time (s) and k is the rate constant (s^{-1}) [Marsh, 1989].

For solid bodies, the rate law is modified to the forms below [Marsh, 1989]:

$$Slabs \quad \frac{dm}{dt} = k$$

$$Cylinders \quad \frac{dm}{dt} = km^{1/2}$$

$$Spheres \quad \frac{dm}{dt} = km^{2/3}$$

The reaction is taking place at the surface of the pores in the graphite. Because of the time dependence of graphite burn-off, the rate law is only superficially similar to a homogenous first-order gas phase expression.

The measured activation energy of this region is the true chemical activation energy of the reaction and can be calculated using the Arrhenius equation, shown below:

$$k = Ae^{-E/RT}$$

where k is the rate constant (s^{-1}), T is the absolute temperature (K), E is the activation energy (J/mol), A is the pre-factor (s^{-1}) and R is the gas constant (J/mol K). The typical activation energy is 170 kJ/mol [Marsh, 1989].

Kinetics in the chemical regime can be further complicated by impurities in the graphite. The impurities act as catalysts that can increase the reaction rate by offering alternate pathways for the reaction. This may lead to a lowering of the activation energy. A simple model of this reaction can be seen below.

$$\frac{1}{2}O_2 + M \rightarrow MO$$

$$MO + C \rightarrow CO + M$$

The model above involves the oxidation of a metal atom (M) by oxygen, followed by the reduction of the oxide by carbon [Chiang et al., 1997].

4.2.2 Region 2

The temperature range for this region is between 700 ºC and 1200 ºC [Marsh, 1989]. In this region the reaction rate becomes high enough for the access of the gas to the in-pore structure to be limited by diffusion and is dependent on the transport of the oxidant to the graphite surface as well as transport of the reaction product from the graphite surface.

The diffusion in the pores can be expressed using Knudsen's diffusion rate for pores. Knudsen diffusion is a means of diffusion that occurs in a long pore with a narrow diameter (2 - 50 nm) because molecules frequently collide with the pore wall. The equation for the Knudsen diffusion is:

$$D_{KA} = \frac{d_{pore}}{3} v = \frac{d_{pore}}{3} \sqrt{\frac{8RT}{\pi M_A}} = 48.5\, d_{pore} \sqrt{\frac{T}{M_A}}$$

where D_{KA} is the diffusion rate, ν is the average molecular velocity (m/s), d_{pore} is the diameter of the pore (m), T is the temperature (K) and M_A is the atomic mass (g/mol) [Pabby, *et al.*, 2009].

Knudsen diffusivity is thus dependent on the pore diameter, the molecular weight of the material and temperature. The gaseous reactant concentration falls gradually to zero at some point within the pore system [Marsh, 1989].

The reaction of graphite with water is important in this region because this region includes normal operating temperatures for HTGRs. Small in-leakage from the steam side can enter into the gas side where it can react with the hot graphite. The partial pressure of the water vapor is variable in the system. The rate equation can be presented in the following form:

$$r = AP^n$$

Where r is the reaction rate (kg/kg s), A is the rate constant (s^{-1} $(Nm^{-2})^{-1}$). Over the temperature range of 1000 – 1200 ºC, n is typically equal to 0.5 [Marsh, 1989].

4.2.3 Region 3

Region 3 is for temperatures above 1200 ºC [Marsh, 1989]. This region is also referred to as the mass transfer region. Here the reaction rate is only controlled by the diffusion of the gas to the external carbon surface. This is true because the reaction at the surface of the graphite is so high that most of the oxidant is consumed there. The oxidation

attack here causes geometry changes of the graphite body without damaging the depth of the materials.

Chapter 5 Sample Description and Preparation

5.1 Sample Description

The graphite grades selected for this study were chosen based on their potential use in Generation IV HTGRs [NRC, 2010]. Five different types of graphite were irradiated in the experiments described below. Information on the different types of graphite is in Table 5-1. For PPEA and PCEA, both with-grain and against-grain samples were irradiated and analyzed. The other three types are isostatically molded and therefore have no grain boundary directions.

The reactor type (pebble bed or prismatic block) has a major influence on the selection of graphite. The core blocks (central and outer reflector) of a pebble bed reactor are core lifetime components, ideally with a life of > 50 years. The pebble bed-facing central and outer reflector blocks receive a high neutron dose, and will require replacement before the end of reactor life. Replacement will be required when the pebble bed-facing graphite component's irradiation-induced dimensional changes become excessive (rapid expansion after volume turnaround), after approximately 15–20 full-power years of operation [NRC, 2010]. The PBMR design uses graphite with good dimensional stability and a long irradiation lifetime (i.e., near-isotropic graphite).

On the other hand, prismatic block reactors discharge fuel blocks and replaceable reflector blocks before they accumulate excessive neutron damage. Therefore, irradiation lifetime is less of a concern than in the pebble bed reactor. The strength of the graphite is a major consideration given the small dimensions of the fuel/coolant channel webs. The use of fine-grained graphite places constraints on the sizes of the graphite block that can be produced because the smaller grain sizes yield a lower strength graphite. Therefore, the

permanent core structure must be a different grade (typically with a larger grain size) than the fuel element graphite.

Graphite Type	Manufacturer	Coke Type	Forming Method	Max Particle Size (μm)	Density (g/cm^3)
PPEA	GrafTech	Pitch	Extruded	760	1.7
PCEA	GrafTech	Petroleum	Extruded	800	1.81
PCIB	GrafTech	Petroleum	Isomolded	<1000	1.7
2020	Mersen	Petroleum	Isomolded	15	1.78
IG-110	Toyo-Tanso	Petroleum	Isomolded	10 (mean)	1.77

Table 5-1: This table shows the 5 types of graphite used in the experiments. It lists their manufacturer, coke type, forming method, maximum particle size and density [NRC, 2010].

Each sample was cut to 10 mm by 2 mm by 2 mm (see Figure 5-1). The PCEA and PPEA samples were cut in both the with-grain (WG) and against-grain (AG) directions. The PCIB, 2020 and IG-110 graphite are all isomolded and do not have any noticeable grain directions. These samples were also cut from two different directions to determine whether there is a preferential direction. These directions will also be referred to as WG and AG, for simplicity. The size of the samples was chosen based on the analytical techniques. For the EPR measurements, the restriction was based on the size of the tube used as a sample holder. The size was also large enough to provide useful data from XPS and XRD measurements.

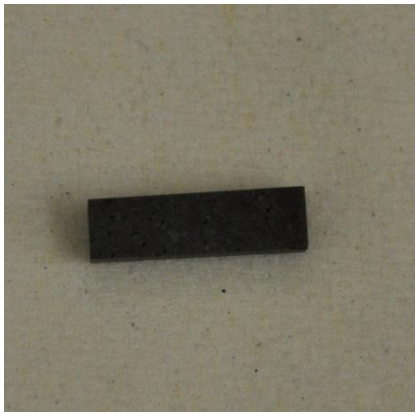

Figure 5-1: This image shows a single graphite sample after cutting. The size is 10 mm by 2 mm by 2 mm.

5.2 Sample Preparation

The graphite samples were cut using a Robofil 300 wire electrical discharge machining (EDM) apparatus manufactured by Charmilles Technologies. This method is an electro-thermal production process in which a thin single-strand metal wire in conjunction with de-ionized water (used to conduct electricity) allows the wire to cut through metal by the use of heat from electrical discharge from the wire. The water is also used to flush debris away from the cutting surface.

The wire used had a copper core with a copper-zinc coating and was 0.25 mm, resulting in a cutting path of 0.335 mm. The spool of wire is held between upper and lower diamond guides. The overcutting is due to sparking from the wire causing erosion of the material. This over-cut is predictable and is accounted for in the cutting process.

Prior to cutting the samples, a small section of wire and cut piece of graphite were irradiated in the pneumatic system (rabbit) in the reactor (see Chapter 7 for description of the pneumatic system). The graphite was first cleaned with methanol before being inserted into the rabbit. The sample was irradiated for 5 minutes and then counted on a high purity

germanium detector (HPGe). In this detector, radiation is measured by the number of charge carriers produced in the depleted volume of the detector. These charge carriers migrate to the positive and negative electrodes through the magnetic field. The charge created is converted into a voltage pulse by a pre-amplifier and is proportional to the energy deposited by the incoming photon.

It is important to keep HPGe detectors cooled to reduce the thermal generation of charge carriers to an acceptable level. The detector is mounted in a vacuum chamber attached to a liquid nitrogen dewar. Liquid nitrogen is used to cool the detector prior to use. The detector takes around 4 hours to properly cool before use.

The particular detector used was a reverse-electrode Germanium (REGe) detector. REGe detectors are opposite from conventional detectors because the p-type electrode is on the outside and the n-type is on the inside (see Figure 5-2). This difference leads to better radiation damage resistance because the hole trapping caused by the radiation damage is collected on the outside electrode rather than the inside electrode. Holes, therefore, have a shorter distance to travel and are less likely to be trapped in any radiation damaged material present [Canberra, 2003].

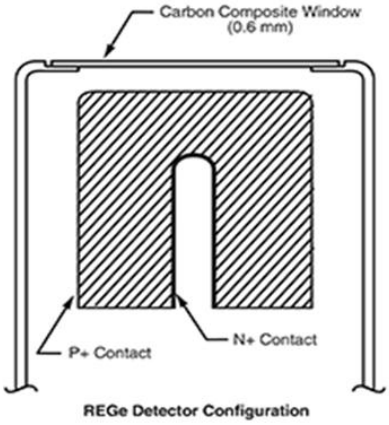

Figure 5-2 REGe detector configuration [Canberra, 2003].

The image below shows the results of the REGe measurement. While Co and other impurities are present in the sample, no Cu or Zn is present from the cutting of the sample.

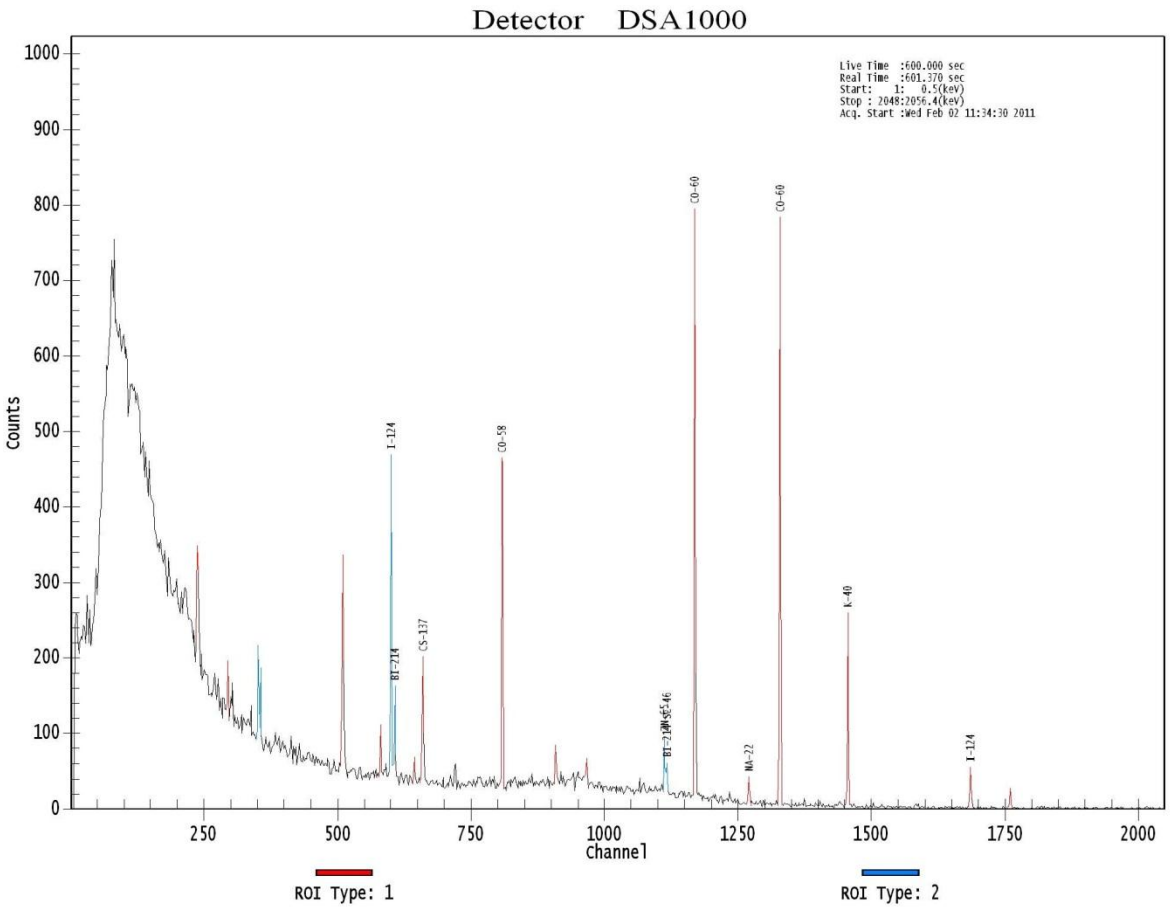

Figure 5-3 Results of the REGe analysis on the cut irradiated graphite sample.

The samples were then laser etched at Wilke Enginuity Inc. located in Hanover, PA. The samples were laser etched with a letter and number according to the graphite type and cut. The table below shows the lettering scheme.

Graphite Type	Grain Direction	Letter
PCEA	Against Grain	A
	With Grain	B
PPEA	Against Grain	C
	With Grain	D
PCIB	Against Grain	E
	With Grain	F
2020	Against Grain	G
	With Grain	H
IG-110	Against Grain	I
	With Grain	J

Table 5-2: This table shows the lettering system for the laser etching of the samples.

Once the samples were laser etched, they were individually bagged. The individual bags were labeled and stored in a desiccator under vacuum. All samples were stored similarly when not being actively irradiated or analyzed. The desiccator used was manufactured by Fisher Scientific. It allows for the removal of air by means of a pump powered by an AC adaptor and is capable of achieving a vacuum of 200 inches of water (7.23 psi). In this case the vacuum was kept at 2 inches of water (0.07 psi).

Chapter 6 Gamma Irradiation

6.1 Gamma Irradiation Background

A photon is an elementary particle which exhibits wave-particle duality. A photon has a rest mass of zero and a charge of zero. The modern concept of the photon was developed gradually by Albert Einstein to explain experimental observations that did not fit the classical wave model of light. In particular, the photon model accounted for the frequency dependence of light's energy, and explained the ability of matter and radiation to be in thermal equilibrium. All photons travel at the speed of light ($c = 2.9979 \times 10^{10}$ cm/sec) in a vacuum [Lamarsh, 1983]. Photons generated by nuclear transitions are also known as gamma rays (γ-rays).

Two artificial radioisotopes are widely used as γ-radiation sources. These are cobalt-60 (Co-60) and cesium-137 (Cs-137). Co-60 is produced by irradiating the stable form of cobalt (Co-59) in a nuclear reactor, while Cs-137 can be separated from spent reactor fuel. Both are relatively inexpensive. Co-60 gives higher-energy, more penetrating γ radiation but Cs-137 has a longer half-life, requiring less frequent source replacement. Co-60 is usually irradiated in the shape of pellets or thin disks in order to give a uniformly active material. Once activated, the disks or pellets are placed into containers that are assembled into radioactive sources. The walls of the metal containers eliminate the β radiation emitted by the Co-60 [Woods and Pikaev, 1994]. Over 80 % of the world's supply of Co-60 is produced in Canada by Ontario Hydro under contract to Nordion International, Inc. [Woods and Pikaev, 1994]. UMD purchased its most recent Co-60 source from REVISS®, a world leader in the manufacture and supply of sealed radiation sources, radioisotope technologies and services.

Co-60 emits electrons (β) as well as two γ-rays. The energies of these particles and those emitted by Cs-137 are given in the table below.

Isotope	Half-life	Type and Energy (MeV) of Radiation Emitted
Co-60	5.272 years	β, 0.313
		γ, 1.332
		γ, 1.173
Cs-137	30.17 years	β, 1.18 (5 %)
		β, 0.51 (95 %)
		γ, 0.662

Table 6-1: Radioactive isotopes commonly used for γ radiation sources. This table shows the isotope, half-life and type and energy of the radiation released (Woods and Pikaev, 1994).

The activity of all radioactive sources decays over time. This can be seen in the following equation,

$$C_t = C_0 e^{-\lambda t}$$

where C_t is the activity after a period of time (t), C_0 is the original activity and λ is the decay constant. The decay constant is determined by the following equation:

$$\lambda = \frac{0.6931}{\text{half-life}}$$

Co-60 decays predominantly by the emission of a β-particle (0.313 MeV) to give an excited state of nickel-60 (Ni-60). The Ni-60 further decays by emitting two photons with energies of 1.17 MeV and 1.33 MeV (Woods and Pikaev, 1994). The decay scheme for Co-60 can be seen in Figure 6-1.

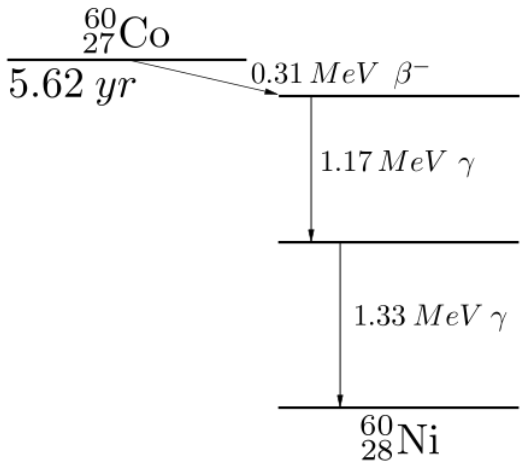

Figure 6-1: Decay scheme for Co-60. Co-60 decays predominantly by the emission of a β-particle (0.313 MeV) to give an excited state of nickel-60 (Ni-60). The Ni-60 further decays by emitting two photons with energies of 1.17 MeV and 1.33 MeV (Woods and Pikaev, 1994).

6.2 Gamma Source Description

A Co-60 gamma source at UMD was used for these experiments. The Co-60 source consists of ten uniformly loaded source pencils, each approximately one half inch in diameter and 14 inches long, normally arranged to form an annulus (see Figure 6-2). The annular source may be arranged on the source platform to provide an internal irradiation volume with a high uniform dose rate. Targets may also be located outside of the source annulus to receive lower dose rates that vary inversely with the square of the distance from the source. The source pencils may also be arrayed on the source platform so as to present a plaque-like configuration for the irradiation of products placed external to the source (see Figure 6-3).

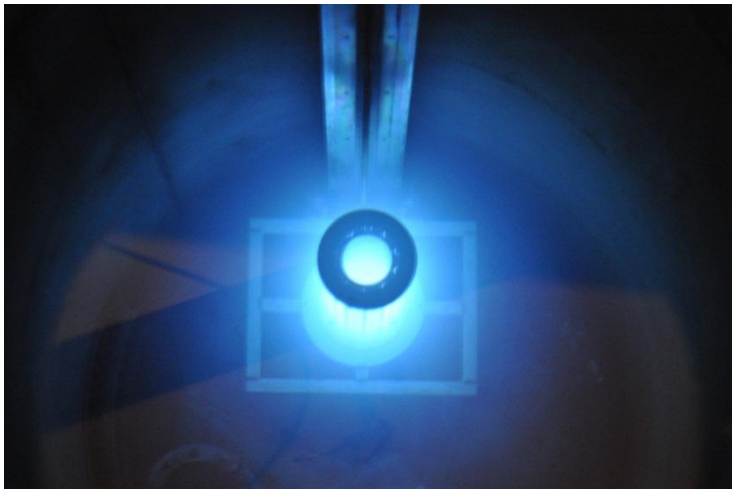

Figure 6-2: Top down vies of the UMD Co-60 gamma source.

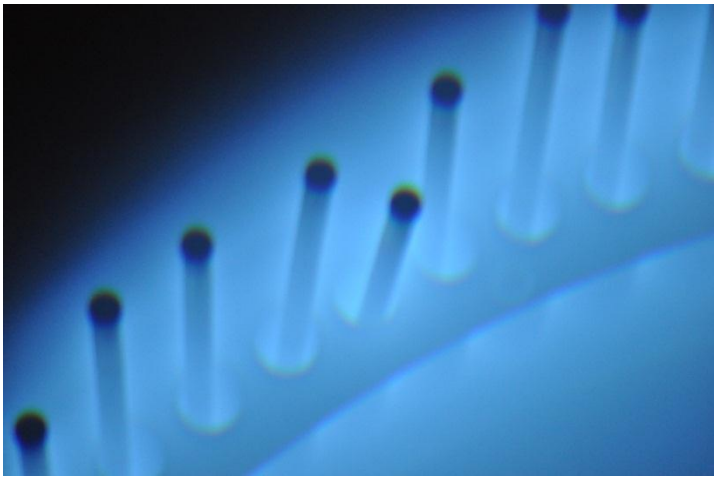

Figure 6-3: Close-up image of the Co-60 pencils in the UMD gamma source.

Two gamma sources are present at UMD. The two radiation sources have activities of 1,343 (7/9/09) Curies and 99,874 (7/9/09) Curies of Co-60 and each of them is in the form of doubly encapsulated mini-pellets located in ten source pencils. The mini-pellets are sealed within welded stainless steel tubes of 0.025" wall thickness. The tubes are sealed within another welded stainless steel tube. The smaller activity source pencils, one half inch in diameter with an active length of 12 inches, are arranged in a ring 3.25 inches in diameter.

The larger activity source pencils, one half inch in diameter with an active length of 17 inches, are lined in a 12 inch planar arrangement. The large source was used for these experiments. This source yields a maximum dose rate of 80.5 kGy/hr at the centerline.

When not in use, the sources are stored at the bottom of a pool of water contained in a stainless steel tank 4 feet in diameter by 14 feet deep. During operation, one source is raised from the pool to 30 inches above floor level, while the other remains in storage at the bottom of the pool.

The source may be rearranged to provide an annular array of up to 10 inches diameter. Other configurations, e.g. a plaque arrangement, can also be assembled while the source is at the bottom of the pool through the use of remote handling tools. The source drive mechanism is housed in a cabinet located along the wall outside the cell. It drives the source elevator by means of a stainless steel chain and sprocket system. Various interlocks are provided to permit safe operation of the system.

An aluminum lid is mounted at the top of the pool tank, and the source rises through a hole in the lid during operation. A sample holder fitted to the tank lid acts as a cover for the source. In general, a 3-inch internal diameter sample well is used. When a source configuration of a different diameter is needed, the normal sample holder is replaced with one of the required dimensions.

Figure 6-4: Top hat of the Co-60 source at UMD.

6.3 Dosimetry

6.3.1 Far West Films

Radiochromic dye film dosimeters are widely used for absorbed dose measurements in radiation processing. They are equally useful for routine measurements at gamma and electron radiation facilities, and the small thickness of the dosimeter films makes them well-suited for dose mapping, measurements with low-energy electrons, or for situations where dose gradients prevail, such as near interfaces of different materials or at product surfaces [McLaughlin et al, 1985; Miller and Batsberg, 1981, Miller 1987]. The versatility of this dosimeter type is also shown by its use as a reference dosimeter [Humphreys and McLaughlin, 1981], where the stability of the response and lack of sensitivity to changes in the absorbed dose rate are important.

When radiochromic film is exposed to ionizing radiation, coloration occurs. This coloration is due to an attenuation of some of the visible light coming through the developed film. The reduction in light passing through the film is a measure of its absorbance. A pivotal

assumption in film dosimetry is that the dose to the film is reflected in the resulting optical density of that film. This relationship can be expressed as follows:

$$A = log_{10}\left(\frac{I}{I_t}\right)$$

where I is the light intensity with no film present, I_t is the light intensity after passing through the film. This relationship is linear with dose.

Radiochromic dyes that are typically used in liquid-phase dosimeters have been incorporated into films to yield solid-state dosimeters that are color sensitive upon exposure to ionizing radiation. Radiochromic films manufactured by Far West Technology (FWT) Inc. were used to measure the dose in the centerline of the gamma source. These 42.5 μm thin colorless radiochromic films are derivatives of the family of aminotriphenyl-methane dyes that turn to a deeply colored state with the intensity of the color being a function of absorbed dose. Specifically, these dosimeters use a hexa(hydroxyethyl) aminotriphenylacetonitrile (HHEVC) dye. Their absorbed radiation dose range is 0.5 to 200 kGy and they are measured by observing the color change at 510 nm or 605 nm with a UV-visible spectrophotometer. The thickness of the Far West films is measured with a digital thickness gauge. The absorbance is measured before and after irradiation, and then divided by thickness, as shown below:

$$FWT\ film\ response = \frac{A_{irradiated,605\ or\ 510\ nm} - A_{initial,605\ or\ 510\ nm}}{thickness\ (mm)} \quad (1)$$

The wavelengths 605 nm and 510 nm are used for different absorbed dose ranges, 0.5 – 20 kGy and 20 kGy – 200 kGy, respectively. At 605 nm, the value calculated from equation 1 is compared to a calibration chart to find the absorbed dose. Dosimetry for

irradiations above 20 kGy uses films measured at 510 nm and the calculated value is input into the formula in equation 2 derived from a calibration:

$$\frac{\Delta A}{mm} = 0.0973\ (Absorbed\ dose, kGy) + 1.6539 \quad (2)$$

6.3.2 Fricke Dosimetry

Chemical dosimeters measure the absorbed dose determined by a chemical change in the dosimeter solution that occurs during irradiation. They are based upon the principle that any changes the chemical dosimeter undergoes upon exposure to ionizing radiation result in changes in optical properties of the dosimeter that are easily and accurately measured using a UV-visible spectrophotometer after irradiation.

The Fricke dosimetry system has been used since the 1920s. The standard solution used consisted of air-saturated 10^{-3} M solution of ferrous sulfate in 0.4 M sulphuric acid. This dosimeter is sensitive to trace quantities of impurities, that can lead to a higher G[Fe^{+3}] values and erroneously low absorbed doses. To counter this, a 10^{-3} M sodium chloride solution was added to inhibit the oxidation of ferrous (Fe^{+2}) ions by organic impurities [Spinks and Woods 1990; Woods and Pikaev 1994]. The addition of chloride reduces the effect of the organic compounds by reacting with $^{\bullet}OH$ to form a radical that prefers to react with the ferrous ions rather than with organic compounds [Swallow 1973].

The yield of Fe^{+3} from the oxidation of Fe^{+2} is given by the following equation [Farahataziz and Rodgers, 1987]:

$$G[Fe^{+3}] = 2G[H_2O_2] + 3G[H^{\bullet}] + G[^{\bullet}OH]$$

The number of Fe^{+3} ions formed during irradiation were determined by UV-visible spectrophotometric measurement of the change in absorbance of the solution at 304 nm. The

change in absorbance represents the oxidation of the ferrous ions to ferric ions and is proportional to the molar concentration of the Fe^{+3} ions. The highest dose that an air-saturated solution can accurately measure is about 500 Gy. Beyond this dose the dissolved oxygen become depleted [Spinks and Woods, 1990]. As a result, great care was taken not to exceed a 500 Gy total absorbed dose to the Fricke dosimeter solution.

6.4 Gamma Irradiation of Graphite Samples

Three different sets of samples were irradiated in the UMD Co-60 source at three different irradiation doses. The samples were placed in 50 mL Pyrex® beaker and covered with aluminum foil. A piece of copper wire was wrapped around the beaker in order to suspend the beaker at the centerline of the source. The samples were irradiated for 190.2 hours, 546.1 hours and 1081.4 hours respectively, in an 80.5 kGy/hr field. This resulted in total exposures of 15.3 MGy, 45.4 MGy and 87.1 MGy. The times, doses, and uncertainty can be seen in Table 6-1. The uncertainty is based on the uncertainty of the absorbed dose in water from NIST standards and is calculated as 2.2 % with a 95 % confidence level.

Sample Group	Time Irradiated (hrs)	Total Dose (MGy)	Uncertainty (MGy)
1	190.2	15.3	0.3
2	564.1	45.4	1.0
3	1081.4	87.1	1.9

Table 6-2: This table shows the irradiation time, total dose and uncertainty for the three set of samples irradiated in the UMD Co-60 gamma source.

The gamma irradiated samples were irradiated in air. The temperatures of the samples were monitored during the irradiation, as well. The temperatures ranged from 107 – 112 ºC. The elevated temperature is due to the irradiation of the samples and not to the use of a heating device.

Chapter 7 Nuclear Irradiation

7.1 Neutron Irradiation at Armed Forces Radiobiology Research Institute

The Armed Forces Radiobiology Research Institute (AFRRI) is located on the grounds of the National Naval Medical Center (NNMC), Bethesda, Maryland. AFRRI operates a Mark F TRIGA reactor. The AFRRI-TRIGA Mark-F reactor was originally developed and installed by the General Atomics Division of the General Dynamics Corporation. The reactor is an open pool-type light water reactor which can operate in either the steady-state mode up to 1 megawatt (MW) (thermal) or in pulse mode with a step reactivity insertion of up to 2.8 % reactivity ($\Delta k/k$) and utilizes standard design General Atomics fuel elements. The AFRRI-TRIGA Mark-F reactor has the unique capability of having a horizontally movable core. There are three principal and one optional experimental facilities associated with the AFRRI-TRIGA reactor. These are Exposure Room #1, Exposure Room #2, the removable in-core experiment tube (CET), and the Pneumatic-Transfer System. Experiments can also be placed either in the reactor tank or in the reactor core between the fuel elements, but these facilities are not normally used [AFRRI, 2004]. A photograph of the AFRRI reactor can be seen below.

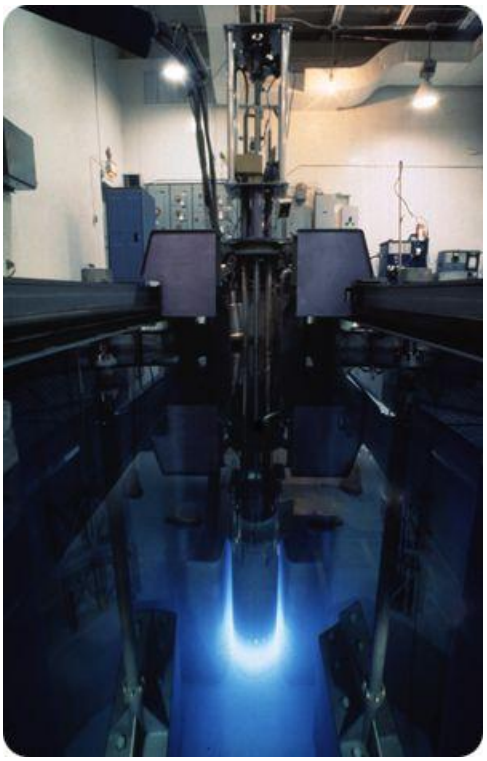

Figure 7-1: Image of the nuclear reactor at AFRRI [AFRRI, 2004].

The graphite experiments were conducted in the CET. The CET provides users with an exposure facility with a characteristic high thermal neutron flux level. The CET is primarily used for the production of radioisotopes and the activation of samples for subsequent analysis. The CET is an air-filled guide tube of aluminum with a 1-5/16 inch inner diameter, into which sealed containers, called "rabbits," are lowered. The guide tube is formed from aluminum tubing with a nipple sealed to the lower end, which fits into the lower grid plate in a core fuel element location. The tube extends upward through the upper grid plate at the same grid array position and terminates at the core carriage. The CET may be positioned in any core fuel element location to achieve the desired flux characteristics [AFRRI, 2004].

The AFRRI-TRIGA Mark-F reactor utilizes standard TRIGA stainless steel clad, cylindrical- fuel elements in which the zirconium hydride moderator is homogeneously mixed with the enriched uranium fuel. The TRIGA fuel was designed by General Atomics. Low-enriched, long-lifetime uranium zirconium hydride (UZrH) fuel is the fundamental feature of the TRIGA family of reactors that accounts for its widely recognized safety, rugged, dependable performance, economy of operation, and its worldwide acceptance. The large prompt negative temperature coefficient of reactivity characteristic of UZrH fuel results in safety margins far above those achieved by any other research reactor fuel. Inadvertent reactivity insertions have been demonstrated to produce no fuel damage in TRIGA cores. The TRIGA design was the work of Frederic de Hoffmann who was looking for a design that would be safe for students to use.

Two sets of experiments were run at the AFRRI reactor. During the first irradiation, ten samples of PCEA AG, PCEA WG, PPEA AG, PPEA WG, PCIB AG and PCIB WG were irradiated for 1000 minutes resulting in an overall accumulated fast fluence of 2.70E17 n/cm^2 and a thermal fluence of 5.40E17 n/cm^2 (Table 7-1). The 2020 and IG-110 samples were not run in these experiments because these samples were not yet available. Five of the samples of each cut of graphite were kept for analysis while the rest were returned to the AFRRI reactor for an additional dose. The overall accumulated fluence for the second set of samples was 5.40E17 n/cm^2 fast fluence and 1.08E18 n/cm^2 thermal fluence.

#1 Graphite irradiations at AFRRI (Ai#1)	Atmosphere:	Ambient/Air	Run date:	Power level (kW):	Run time (min):	Fluence (thermal)	Fluence (fast) (n/cm^2)
	Temperature:	Room					
	Experimental facility:	CET	9-Mar-10	900	540	2.92E+17	1.46E+17
	Flux (thermal) n/cm^2-sec-kW:	1.00E+10	11-Mar-10	900	460	2.48E+17	1.24E+17
	Flux (fast) n/cm^2-sec-kW:	5.00E+09	accumulated time (min):		1000		
				accumulated Fluence (thermal) (n/cm^2):		5.40E+17	
				accumulated Fluence (fast) (n/cm^2) [E>100keV]:			**2.70E+17**

Table 7-1: Irradiation data for the first set of samples irradiated at the AFRRI reactor.

#2 Graphite irradiations at AFRRI (Ai#2)	Atmosphere:	Ambient/Air	Run date:	Power level (kW):	Run time (min):	Fluence (thermal)	Fluence (fast) (n/cm^2)
	Temperature:	Room					
	Experimental facility:	CET	13-May-10	900	540	2.92E+17	1.46E+17
	Flux (thermal) n/cm^2-sec-kW:	1.00E+10	17-May-10	900	460	2.48E+17	1.24E+17
	Flux (fast) n/cm^2-sec-kW:	5.00E+09	accumulated time (min):		1000		
				accumulated Fluence (thermal) (n/cm^2):		1.08E+18	
				accumulated Fluence (fast) (n/cm^2) [E>100keV]:			**5.40E+17**

Table 7-2: Irradiation data for the second set of samples irradiated at the AFRRI reactor.

7.2 Neutron Irradiation Facilities at UMD

The MUTR is an open pool type reactor with a maximum licensed, steady state, thermal power of 250 kW. There is no pulsing capability. The reactor is fueled with 24 modified TRIGA fuel clusters. The reactor core consists of a total of 93 fuel rods (20 fuel clusters each contain four fuel rods, one fuel cluster contains three fuel rods and an instrumented fuel rod, the remaining three assemblies each contain three fuel rods and a control rod guide tube). The fuel-moderator rods are enriched to less than 20 weight-percent (w/o) of U-235, and each of the fuel rods contains top and bottom slugs of graphite that act as reflectors. Additionally, two graphite reflector elements are positioned in the assembled core, adjacent to two of the outer fuel assemblies [MUTR, 2000].

The reactor is primarily a training tool, but it can be used as a source of neutrons for activation studies and a source of neutrons and gamma rays for studies of radiation effects on materials.

The experimental facilities are designed to bring neutron and gamma beams out of the reactor core and to permit small sample irradiations in the core. The reactor contains five experimental facilities. A graphite filled thermal column provides an ex-core beam of thermal neutrons for experiments. Large samples, up to approximately 13.3 cm (5.25 inches) in diameter, can be placed adjacent to the core in either the beam tubes or the through tube. The beam and through tubes can also provide ex-core gamma and neutron beams. Finally, in-core irradiations of small samples (maximum size of approximately 2.5 cm (1 inch) diameter by 5 cm (2 inches) in length) can be done using the pneumatic transfer system [MUTR, 2000]. The pneumatic transfer system and east beam port were utilized for these experiments.

7.2.1 Pneumatic Transfer System

A pneumatic transfer system (rabbit) provides a rapid and convenient means of transferring small samples between the hot room located on the west balcony and the reactor core. The control system for the pneumatic transfer system is located in the control room and is operated under the supervision of the reactor operator when the reactor is critical. The driving force for this system is available pressurized CO_2. The transfer system consists of a pneumatic mechanism located in an exhaust hood on the west balcony, polyethylene tubing for transferring samples between the laboratory and core, and a terminus located in core position C-4 (Figure 7-2). The controls for the rabbit are located on the control room auxiliary panel. The system can be operated in either manual or automatic timing mode

[MUTR, 2000]. Experimental flux data for the pneumatic transfer system are shown in Table 7.3.

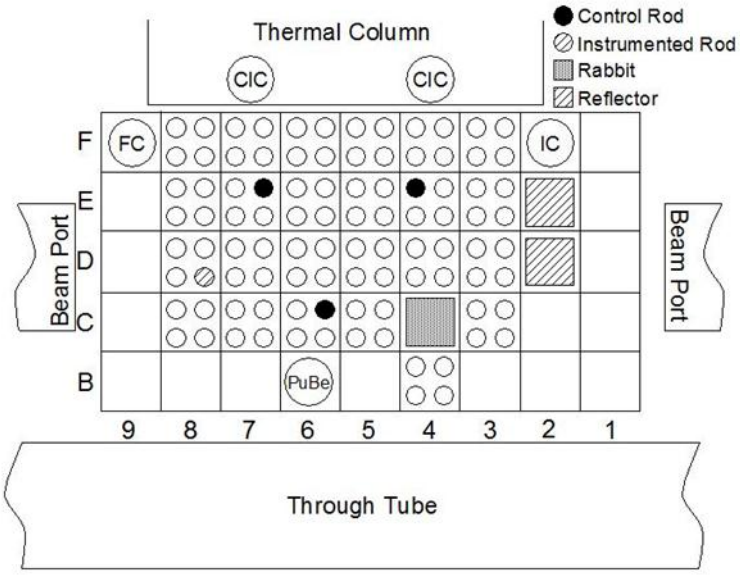

Figure 7-2: Overhead layout of the reactor core at UMD. Block C4 is where the pneumatic transfer system is located [MUTR, 2000].

Radiation Type	Units	Radiation Amount
Flux (thermal)	(n/cm^2 sec kW)	1.60E+10
Flux (epithermal)	(n/cm^2 sec kW)	3.00E+08
Flux (fast)	(n/cm^2 sec kW)	8.00E+09
Flux (1MeV Eq. Si)	(n/cm^2 sec kW)	6.90E+09
Dose Rate (gamma)	(rad/sec kW)	1.90E+01

Table 7-3: Radiation rates for the pneumatic transfer system [MUTR, 2000].

Ten samples of PCEA AG, PCEA WG, PPEA AG, PPEA WG, PCIB AG and PCIB WG were irradiated in the pneumatic system at the MUTR at 300 ºC. The heater that was placed in the sample holder is an aluminum cylinder (Al) (Type 6061). The cylinder also

contained trace amount of other elements, mainly chromium (0.04 – 0.35 %), copper (0.15 – 0.4 %), iron (0 – 0.7 %), magnesium (0.8 – 1.2 %) and manganese (maximum of 0.15 %). The heater components are contained in the aluminum housing. These include the heater element itself, a sample chamber for the graphite and a thermocouple. The heater is attached to the control unit on the reactor bridge by a wiring harness that includes the two wires for the heater, the thermocouple leads and two 0.25 in outer diameter polyethylene tubes, that were intended to be used to flow an inert gas over the graphite sample. The assembly can be seen in the figure below. The accumulated fluence for the samples over multiple reactor runs is given in Table 7-4.

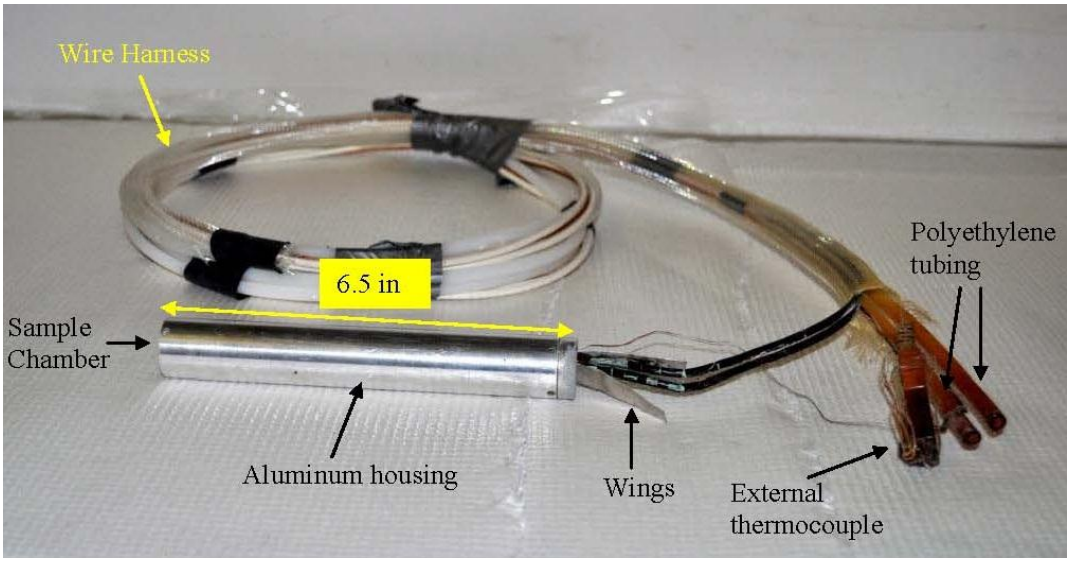

Figure 7-3: The image above shows the heater assembly used to irradiated the PCEA, PPEA and PCIB samples in the pneumatic transfer system.

Graphite irradiations with heater at MUTR	Atmosphere:	Ambient/Air	Run #:	Power level (kW):	Run time (min):	Fluence (thermal)	Fluence (fast) (n/cm^2)
	Temperature:	~300 *C					
	Experimental facility:	Rabbit	4045	250	360	8.64E+16	4.32E+16
	Flux (thermal) n/cm^2-sec-kW:	1.60E+10	4046	250	360	8.64E+16	4.32E+16
	Flux (fast) n/cm^2-sec-kW:	8.00E+09	4047	250	360	8.64E+16	4.32E+16
			4050	250	390	9.36E+16	4.68E+16
			4051	250	301	7.22E+16	3.61E+16
			4052	250	390	9.36E+16	4.68E+16
			4053	250	90	2.16E+16	1.08E+16
			accumulated time (min):		2251		
			accumulated Fluence (thermal) (n/cm^2):			5.40E+17	
			accumulated Fluence (fast) (n/cm^2) [E>100keV]:				**2.70E+17**

Table 7-4: Graphite irradiations in the pneumatic tube heated to 300 °C. Each run was approximately 6-hours long.

7.2.2 East Beam Port

There are two beam ports on the MUTR. A 15.24 cm (6 in) double-stepped beam tube faces the center of each side of the core. The portion of each beam tube extending into the tank is made of aluminum. A bolted gasket seal is used between this sleeve and the pool-tank flange. A steel backup ring prevents warping of the aluminum. The outer portion of the beam-tube assembly is stepped twice to accommodate the two 0.787 m (31 in) shield plugs. These plugs are aluminum-clad concrete machined to fit within the outer end of the beam tubes. The inner plug has a 0.635 cm (0.25 in) boral sheet on the core-facing end. The steps prevent neutron and gamma radiation streaming [MUTR, 2000].

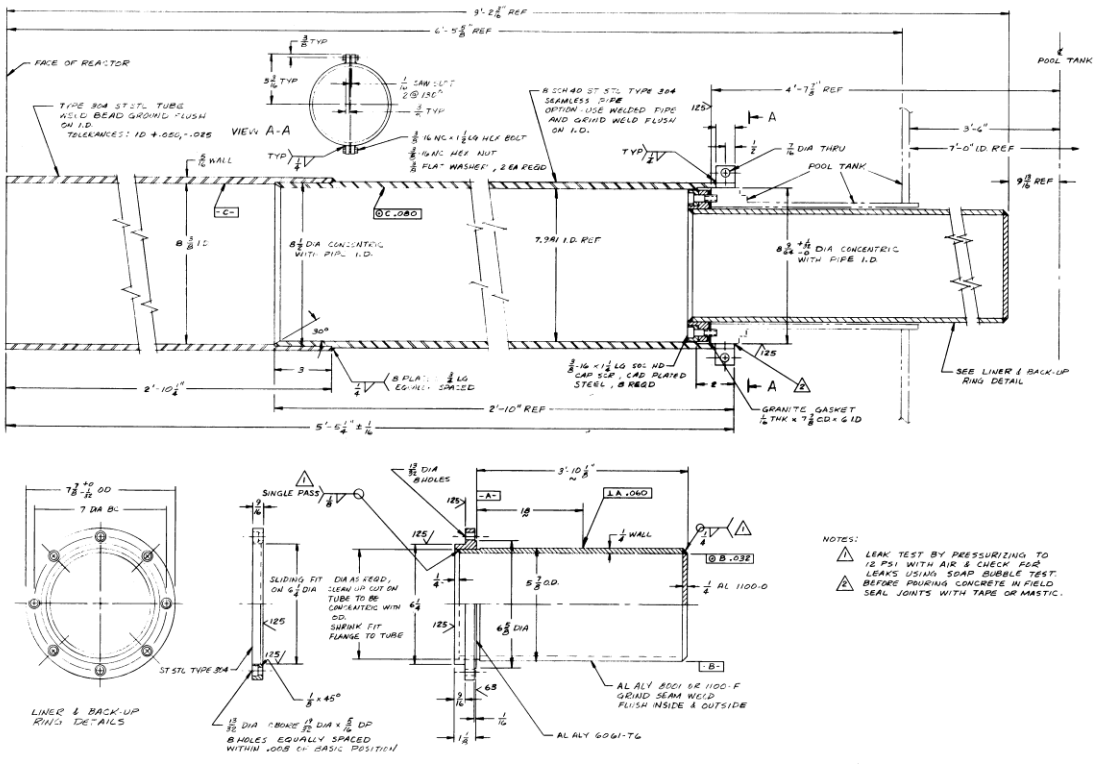

Figure 7-4: Drawing of beam port from the MUTR Safety Analysis Report. This drawing shows the stepped tube of the beam port [MUTR, 2000].

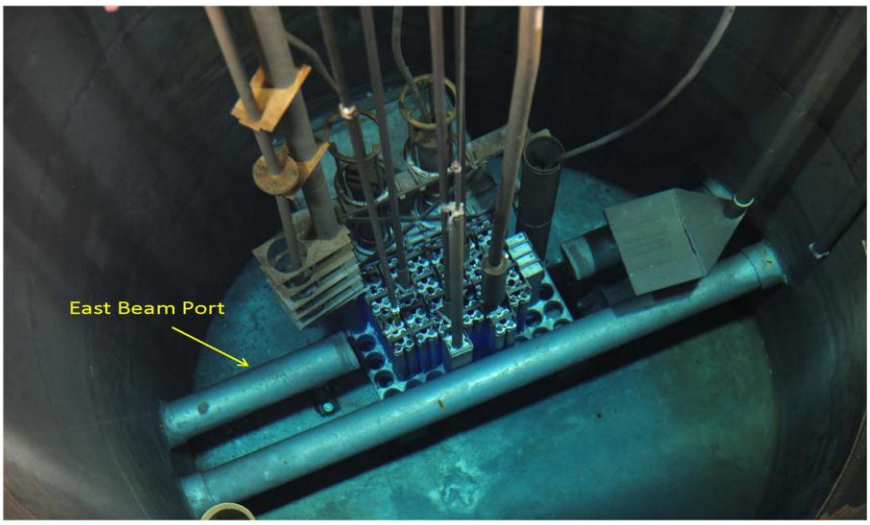

Figure 7-5: Looking down into the reactor pool. The east beam port is the short tube on the left side of the core and is labeled East Beam Port. This port was used for the graphite experiments.

Figure 7-6: Outside of East Beam Port with the normal plugs installed.

The modified tubes were placed in the East Beam Port for the graphite experiments. Dose rates were determined with the modified tubes installed. This information will be discussed in Chapter 8 - Experimental Design.

The east beam port irradiations were conducted at room temperature and 1000 ºC. Each set of samples was irradiated for 960 minutes and received a total thermal and fast fluence of 1.3E11 n/cm^2 and 8.8E11 n/cm^2, respectively. Tables 7-5 and 7-6 give the accumulated fluence levels for the samples.

Room Temperature Irradiated Samples	Atmosphere:	He/H_2O	**Run Numbers:**	**level (kW):**	**Run time (min):**	**Dose Rate (gamma) (kGy)**	**Fluence (thermal) (n/cm^2)**	**Fluence (fast) (n/cm^2)**
	Temperature:	Room						
	Experimental facility:	East Beam Port	4137 -	250	480	2.4E-03	4.4E+11	6.6E+10
	Flux (thermal) n/cm^2-sec-kW:	6.1E+04	4148	250	480	2.4E-03	4.4E+11	6.6E+10
	Flux (fast) n/cm^2-sec-kW:	9.2E+03						
	Gamma (rad/sec-kW)	3.4E-05						
	Average Humidity (%)	55 % +/- 1%	accumulated time (min):		960			
					accumulated Gamma (kGy):	4.9E-03		
					accumulated Fluence (thermal) (n/cm^2):		1.3E+11	
					accumulated Fluence (fast) (n/cm^2) [E>100keV]:			**8.8E+11**

Table 7-5: Accumulated fluence for the room temperature irradiated samples.

High Temperature Irradiated Samples	Atmosphere:	He/H_2O	**Run Numbers:**	**level (kW):**	**Run time (min):**	**Dose Rate (gamma) (kGy)**	**Fluence (thermal) (n/cm^2)**	**Fluence (fast) (n/cm^2)**
	Temperature:	1000 °C						
	Experimental facility:	East Beam Port	4149 -	250	480	2.4E-03	4.4E+11	6.6E+10
	Flux (thermal) n/cm^2-sec-kW:	6.1E+04	4158	250	480	2.4E-03	4.4E+11	6.6E+10
	Flux (fast) n/cm^2-sec-kW:	9.2E+03						
	Gamma (rad/sec-kW)	3.4E-05						
	Average Humidity (%)	53 % +/- 1 %	accumulated time (min):		960			
					accumulated Gamma (kGy):	4.9E-03		
					accumulated Fluence (thermal) (n/cm^2):		1.3E+11	
					accumulated Fluence (fast) (n/cm^2) [E>100keV]:			**8.8E+11**

Table 7-6: Accumulated fluence for the 1000 °C irradiated samples.

Chapter 8 Experimental Design

8.1 Shielding

Before any experiments could be conducted, shielding had to be designed and installed. The MUTR's beam ports face the east and west walls of the confinement. The west wall is an exterior wall of the building but the east wall is not. The east wall is the back wall of a graduate student laboratory. This area is not a radiation area so it was imperative that the limits of Title 10 of the Code of Federal Regulations Part 20 (10 CFR 20), "Standards for Protection Against Radiation," were met. These limits are found in 10 CFR 20.1301 and they state that the dose in any unrestricted area shall not exceed 2 mrem in any one hour [NRC, 2012].

8.1.1 Shutter

The first shielding that was designed was a shutter to cover the modified plug that was installed in the beam port for the experiments. The modified plugs are made of concrete with a thin aluminum covering. The outer diameter of the plugs is 6.5 inches and each is 31 inches long. There are two modified plugs that are inserted when the access plugs are removed. The concrete acts as a radiation shield and therefore radiation is only present in the 2 inch hole through the center of the modified plugs. Images of the modified plugs before installation are shown in Figure 8-1.

a.

b.

Figure 8-1: a. The head-on view of the modified beam port plugs. b. The length-wise view of the modified beam plugs, which were inserted into East Beam Port. There are two modified beam plugs. They are 31 inches long Al-clad and concrete-filled. They have a 2 inch hole in the center to allow radiation to stream out from the core.

The shutter was designed using 80/20 Inc. material (see figure below for initial design). The 80/20 Inc. design utilizes aluminum. The nuclear properties of aluminum make it a good material to use in radiation fields. Aluminum-27 (Al-27) has a low cross-section for absorption of thermal neutrons (0.21 barns). The half-life of Al-28, produced for nuclear irradiation, is short (2.3 minutes) [Lamarsh, 1983]. This ensures that the material will not remain activated for a significant amount of time. It consists of a seven foot long arm to allow for manipulation of the shutter without entering the high radiation area near the

modified plug opening. The dimensions of the rails also allows for the shutter to be used for the beam port or the through tube (should that be needed in a future experiment). The shutter is manually operated and is connected to a sensor. When the sensor is not depressed, a light above the area is illuminated to indicate that the beam port is open.

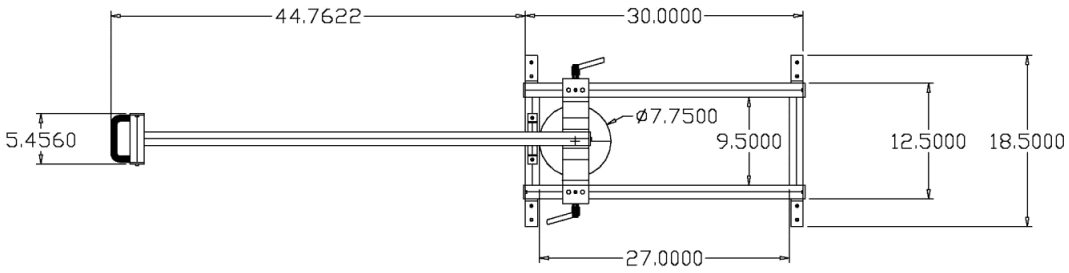

Figure 8-2: Initial design for the East Beam Port shutter. The arm is 7 feet long, allowing for operation of the shutter without entering the high radiation area near the open port. The shutter can slide back and forth and can be used for either the beam port or through tube, should the need arise in the future.

Modifications were made to the original design. The first change was to move the arm from the left to the right side of the shutter system. The shutter material was also changed. At first the shutter was a solid round piece of lead that was 7.75 inches in diameter and 2 inches thick. Due to the high flux present at the opening of the beam port, the lead caused a significant amount of neutron radiation to be scattered at its surface. To counter this effect, the lead was replaced by borated poly bricks two inches thick, cut to make an 8 inch by 8 inch square.

Figure 8-3: The shutter system installed in front of the East Beam Port. The shutter is attached to the concrete of the reactor and is able to provide a shutter for either the beam port or the through tube.

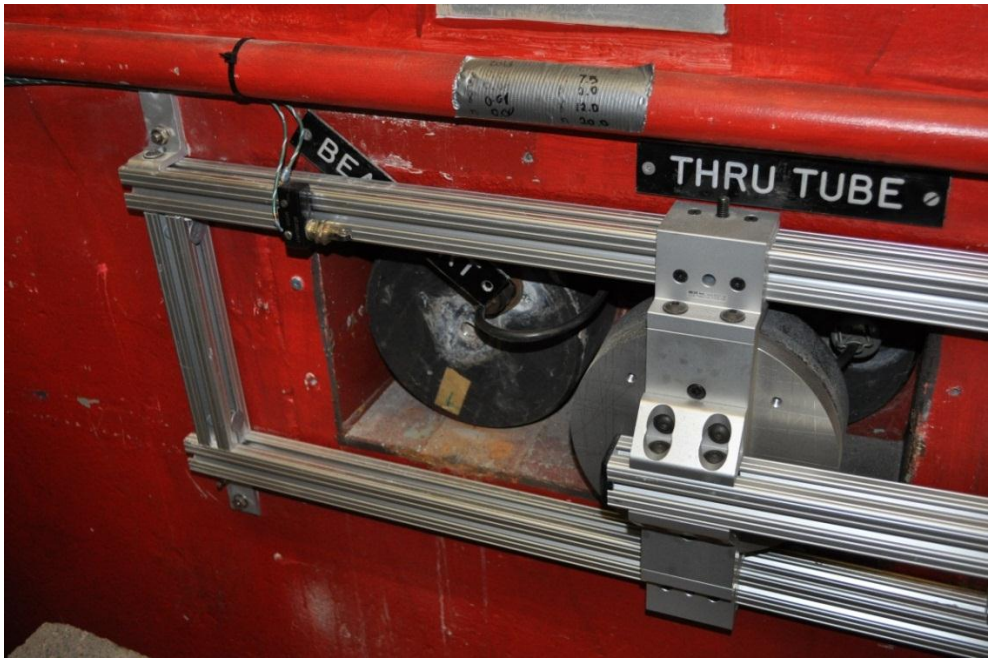

Figure 8-4: Close-up view of shutter system. This view shows how the shutter may be used for both the beam port and the through tube.

8.1.2 Walls

In addition to the shutter, concrete walls and borated polyethylene walls were constructed to reduce the radiation levels at the east wall of the reactor building. The tenth value for concrete is 12 inches. This is the thickness of concrete required to reduce the intensity of a gamma field to one tenth of its initial value [Lamarsh, 1983]. The concrete walls that were constructed are u-shaped, providing shielding on three sides. This allows for lower dose rates where personnel are working on the lower level of the reactor building. The walls are 24 inches thick. This provides two tenth thicknesses of the concrete and also allowed for enough room to move the modified plugs in and out of the core, should the need arise. The concrete walls are 7 feet high. They were not built higher because personnel in the adjoining lab have no work areas above 7 feet, therefore there is no need to provide extra shielding at this height.

Figure 8-5: U-shaped concrete walls built along east wall of reactor building. The walls are 24 inches thick and 7 feet high.

On the back of the concrete wall, a borated polyethylene wall was built. The wall is two bricks thick and was built two feet above the ground. The wall itself is 4 feet high by 4 feet wide. The borated polyethylene contains 5 percent boron by weight. The boron is added because it has a very high thermal neutron absorption cross-section (764 b) [Lamarsh, 1983]. The wall positioning was determined by the most likely areas of occupancy in the adjoining laboratory space.

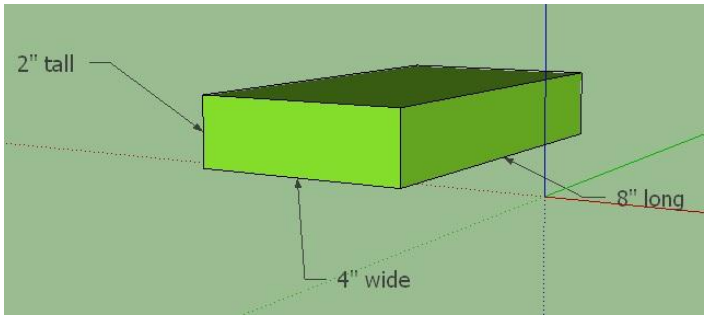

Figure 8-6: Drawing of borated polyethylene brick. The bricks are 2 inches by 4 inches by 8 inches.

8.1.3 Collar for the Face of the Reactor

In order to minimize streaming around the face of the reactor, a collar was constructed to fit flush against the reactor. The frame of the collar is constructed of aluminum and is 43 inches by 30 inches. The collar is 6 inches deep. The collar was filled with alternating layers of paraffin wax with boron carbide powder. The paraffin and the boron provide neutron shielding.

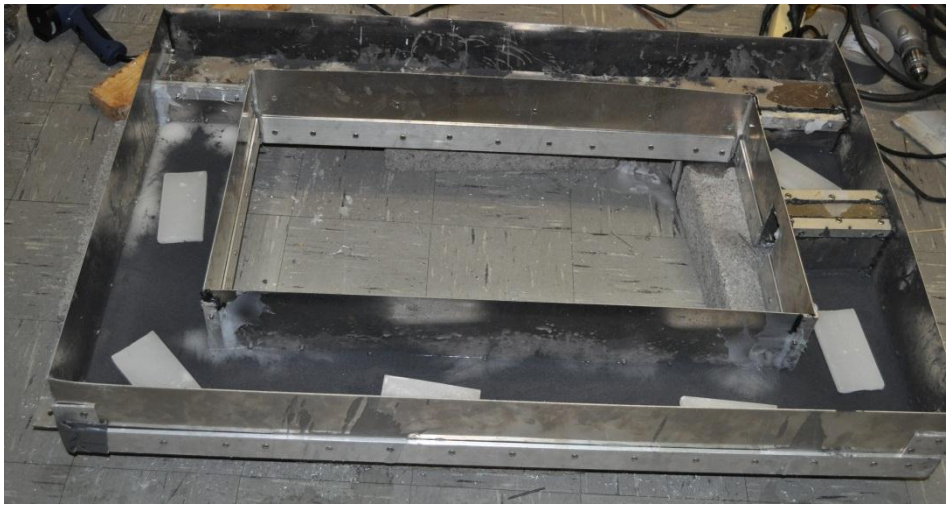

Figure 8-7: Filling of the collar. The collar was filled with paraffin wax and boron carbide powder.

Figure 8-8: Fitting of the collar onto the face of the reactor.

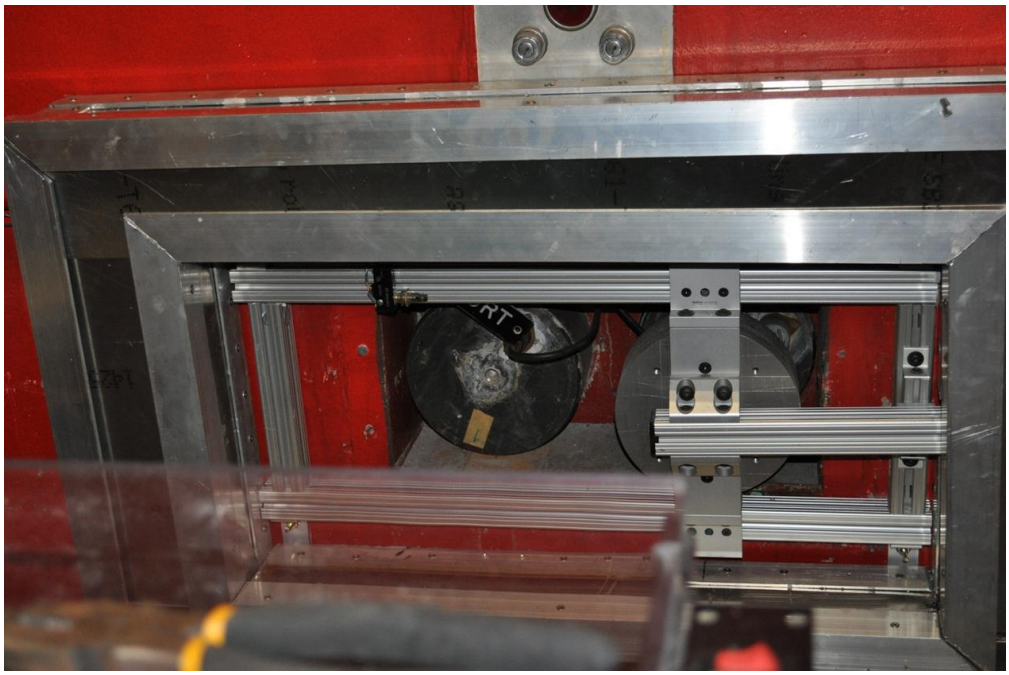

Figure 8-9: Image of the collar installed on the reactor face. Its design still allows for movement of the shutter.

8.1.4 Cave

The final shielding was a cave to enclose the sample holder. The shell of the cave was constructed from 0.25 inch Lexan to form a 25 inch by 25 inch by 25 inch hollow cave that is open on the front. A drawing of the box can be seen below. On one side of the cave, a system of nine fans provides 945 cubic feet per minute (cfm) air flow. The other side contains a vent with a filter over it. This allows the air to flow across the cave and and be filtered so no particulates could become activated during irradiation.

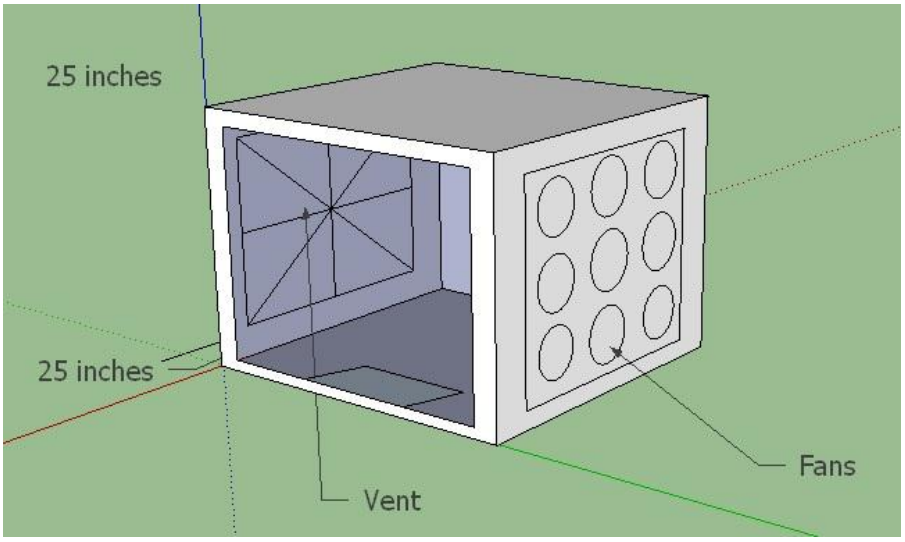

Figure 8-10: This figure shows the design of the cave. On one side are fans to draw air through the box to ensure adequate cooling and on the other side is a filter to ensure particulates are not activated in the flux from the reactor.

The cave is filled with a random array of borated polyethylene blocks shown in the figure below. This aids in reducing the dose rate near the opening while also allowing for adequate air flow through the box. The top and backside of the box are also lined with borated polyethylene blocks. The pattern for these blocks was designed so that there are no straight line paths for the neutrons to travel. Behind the borated polyethylene block on the backside of the cave is a layer of lead bricks. These bricks are 2 inches by 4 inches by 8 inches and provide additional gamma shielding. The tenth thickness for lead is 2 inches, so these bricks provide a tenth thickness of lead to reduce the gamma doses to one tenth of their values without the lead.

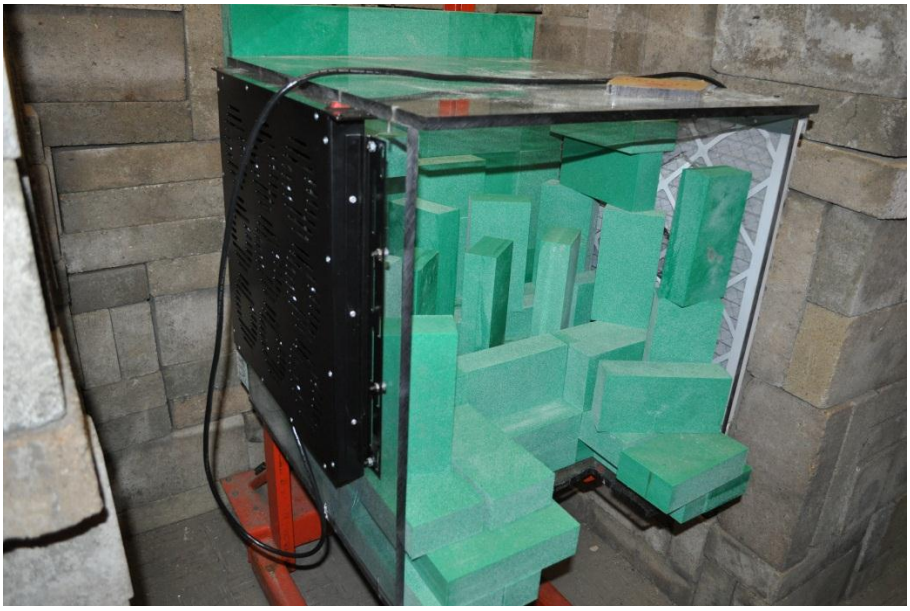

Figure 8-11: View of the interior of the cave. This photograph shows the random arrangement of the borated polyethylene blocks inside the cave, as well as the fans and filter on either side of the cave.

Figure 8-12: This image shows the south filtered side of the cave in place against the reactor face.

Figure 8-13: This image shows the north side of the cave installed against the reactor face.

8.1.5 Dose Mapping

Once the shielding was in place, the doses around the beam port and in the adjoining lab were mapped to ensure that the MUTR staff, as well as the students in the neighboring labs, were adequately protected during reactor operations. There are three categories of experiments at the MUTR:

1. Routine Experiments - experiments which have been previously performed in the course of the reactor program,
2. Modified Routine Experiments - those experiments which have not been performed previously but are similar to routine experiments in that the hazards are neither greater nor significantly different than those for the corresponding routine experiments, and
3. Special experiments - those experiments which are not routine or modified routine experiments.

While removing the beam port plug is not classified as a Special Experiment, operating the reactor with the modified "Beam Plugs" installed has not been performed in the past and is considered a "Special Experiment." Therefore a Special Experimental proposal was written for this operation and approved by the Reactor Safety Committee. A copy of the approved proposal can be found in Appendix A.

In general, the beam plugs were removed while the reactor was in a shutdown condition. While monitoring the radiation levels with neutron and gamma detectors, the modified beam plugs were installed. The reactor was then brought to low power critical. When the power level is first observed to be increasing (positive period) with no control rod withdrawal, or the Log Percent Power meter is stable or rises independently of control rod movement, the reactor is considered near critical. The power was raised incrementally while recording the gamma and neutron radiation levels. Approval was given by the senior reactor operator, after consultation with radiation safety personnel, for reactor power to be raised to the next increment. The locations and dose measurements at 250 kW are given in Figure 8-14 and Table 8-1.

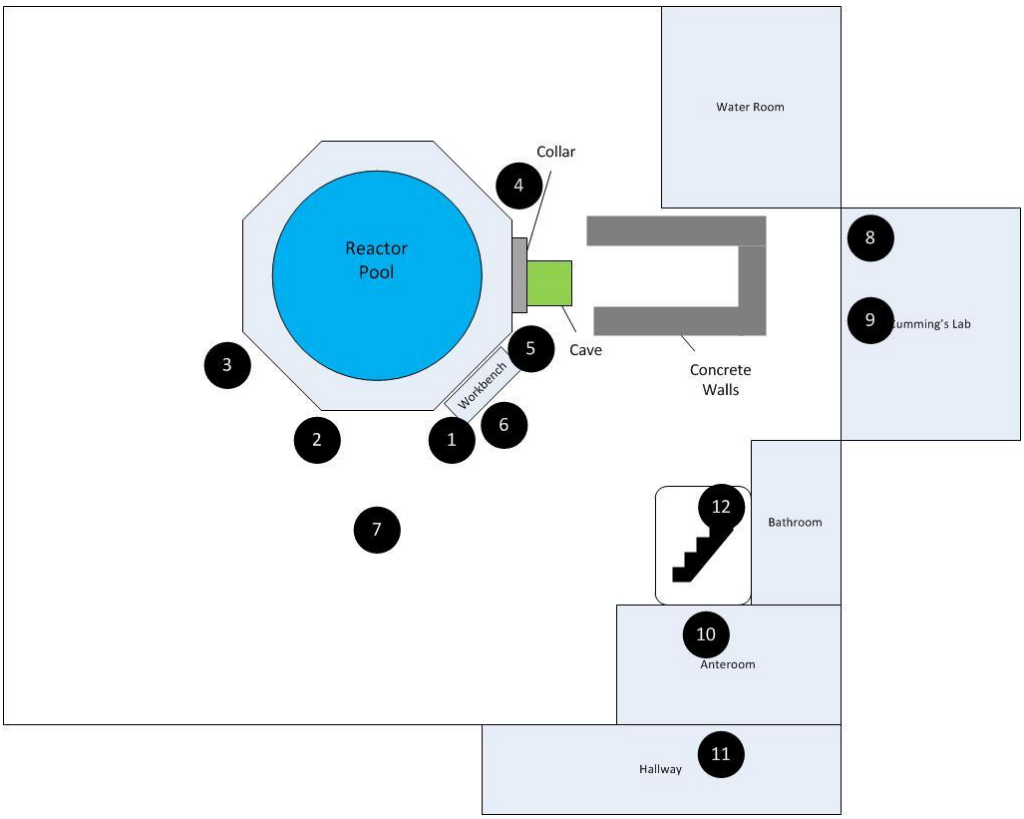

Figure 8-14: Locations of the dose measurements in Table 8-1.

Power Level	Position	Ion Chamber (mR/hr)	Neutron Detector (Rem Ball) (cpm)
250 kW	1	3.6	80
250 kW	2	3.2	BKGD
250 kW	3	2	BKGD
250 kW	4	10.5	1700
250 kW	5	12.5	1600
250 kW	6	3.2	220
250 kW	7	3	30
250 kW	8	0.07	BKGD
250 kW	9	0.12	BKGD
250 kW	10	0.55	40
250 kW	11	0.4	20
250 kW	12	2.1	280
250 kW	Upstairs Balcony	0.43	10
250 kW	Control Room	0.41	20

Table 8-1: Dose rate measurements taken in the vicinity of the east beam port with the beam shutter OPEN. The drawing above the table denotes the areas where measurements were taken. This table shows the gamma dose rate in mR/hr and the neutron dose rate in cpm at 250 kW.

The dose rates at the outside surface of the cave exceeded 100 mrem/hr. A high radiation area was established at the side concrete walls in accordance with 10 CFR 20.1601. The area was posted with high radiation signs that are applicable during reactor operations and the area is under video surveillance by the reactor operator.

8.2 East Beam Port Experimental Set-up

8.2.1 Sample Flow Path

For the experiments on the east beam port, research grade He was used. This gas first passed through a regulator (see Figure 8-15). A GC was used to analyze the composition of the gas phase flowing past the graphite surfaces. This gas phase consisted of He, which was bubbled through water (see Figure 8-16) in order to study the effects of a water-containing He environment on the degradation of graphite in radiation fields. Tygon tubing was used to transport the He to the sample and ¼" stainless steel piping was used to transport the He as the carrier gas to the GC.

Figure 8-15: This image shows the regulator system used to deliver the research grade He to the samples and to the GC, as the carrier gas.

Figure 8-16: Image of water bubbler used for east beam port experiments.

The He-water mixture then traveled to the humidity detector. An Omega Engineering, Inc. (Omega) HX86A humidity detector was used to measure the temperature and relative humidity of the gas entering the sample chamber. This detector was calibrated by Omega and has a temperature error of +/- 0.5 ºC and a relative humidity error of +/- 1.0 %. Both readings can be taken on the display of the detector (as seen in the Figure 8-17). An average of the temperatures and humidity levels over the runs was used for the samples. The probe is also capable of measuring the dew point.

Figure 8-17: Image of the HX86A used to measure the temperature and humidity of the gas entering the samples chamber.

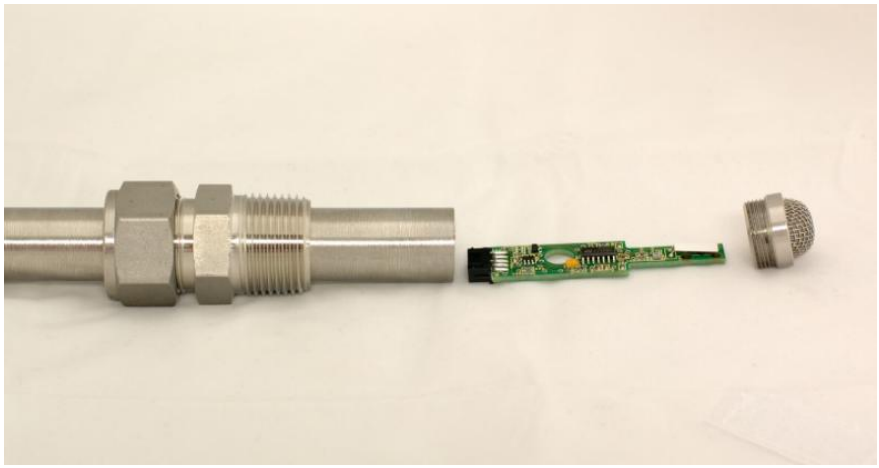

Figure 8-18: Close-up image of the HX86A probe, used to measure the temperature and humidity of the gas entering the sample chamber.

Once the gas passes the humidity probe, it is transported to the sample chamber. The sample chambers were made by Advanced Industrial Ceramics in California. The design of the chambers was based on the constraints of the heater used for the experiments. The

sample chamber was designed to fit inside the 1 inch inner diameter of the heater. The bottom of the sample chamber is 3.5 inches long and is tiered. The bottom tier is 2 inches long and has an outer diameter of 0.85 inches. The upper tier is 1.5 inches long with an outer diameter of 2 inches. A 2 inch wide and 1 inch long cap threads onto the bottom portion of the sample chamber. There are also two 12 inch extensions that thread into the cap and allow for the flow of the gas mixture through the chamber. The complete design can be seen below. The sample chamber is made from alumina (Al_2O_3). The properties of the alumina used are presented in the table below.

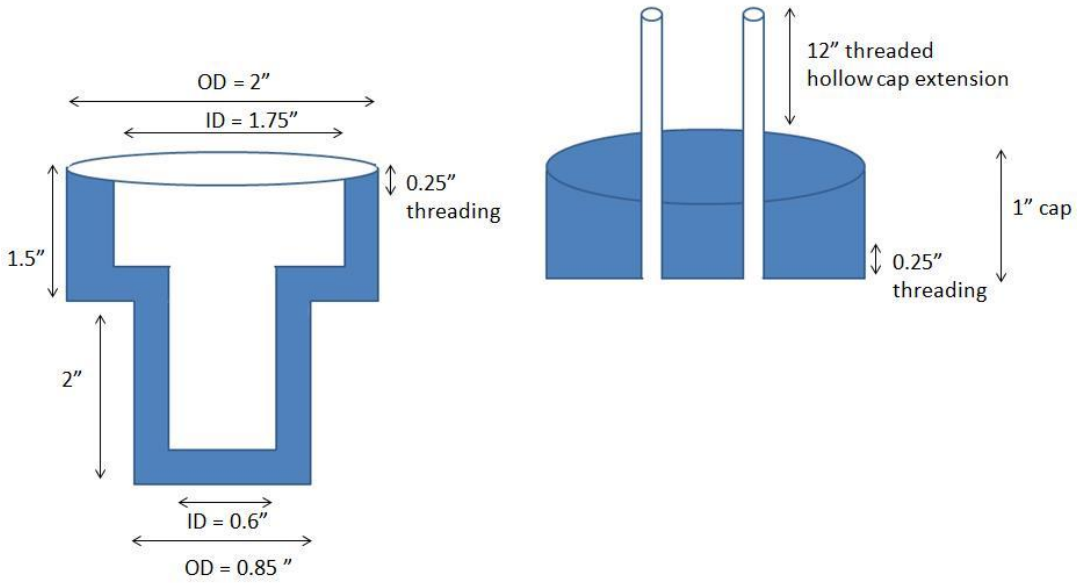

Figure 8-19: Design for the sample chamber.

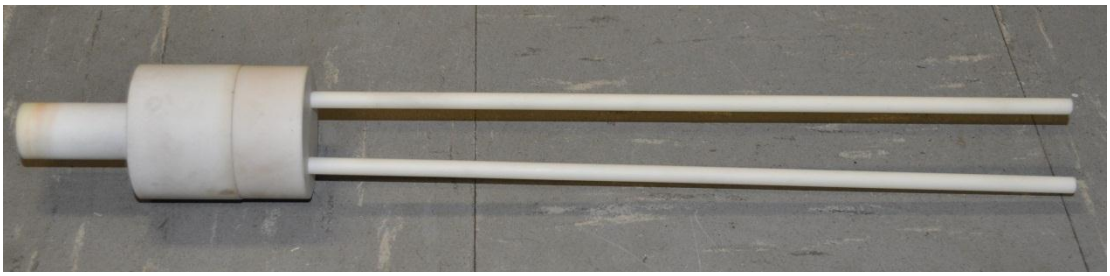

Figure 8-20: Photo of sample chamber used for east beam port experiments.

Property	Units	Value
Purity	%	99
Bulk Density	$kg/m^3 \times 10^{-3}$	3.9
Tensile Strength	MPa	262
Coefficient of Thermal Expansion	$\times 10^{-6}$/°C	8.2
Thermal Conductivity	W/m K	30
Specific Heat	J/kg K	800
Resistivity	Ω cm	$> 10^{14}$

Table 8-2: This table lists several properties of the Alumina used to make the sample chamber.

After leaving the sample chamber, the gas mixture is run through a small filter to remove the water vapor before entering the GC. The filter used is manufactured by Parker Hannifin Corporation and is a silica gel filter designed to remove only the water from the gas to protect the GC and also allow for analysis of the gas from the samples.

Figure 8-21: Parker Hannifin Corporation filter used to remove water vapor from the sample gas after leaving the sample chamber before it is injected into the GC.

8.2.2 GC

The filtered gas from the sample chamber goes to the GC. The GC that was used was a Gow-Mac 400 thermal conductivity gas chromatograph manufactured by Gow-Mac Instrument Co. (see Figure 8-22). This instrument was chosen because it is designed for high capability performance while withstanding rough or industrial use [Gow-Mac, 2010]. The flow system contains two columns, two injection ports and two needle valves for column flow control. The temperature of the injection ports, column oven and detector oven can be controlled individually. Two types of columns were used in the GC to detect and measure the different oxidation products that are formed from the oxidation of the graphite. The first was a Moleseive 13x. This column was used to measure the H_2, CO, and CH_4. The second was a Porapak Q for measuring the CO_2 and O_2. An image of the installed columns can be seen in Figure 8-23.

Figure 8-22: Gow-Mac 400 GC used for east beam port experiments.

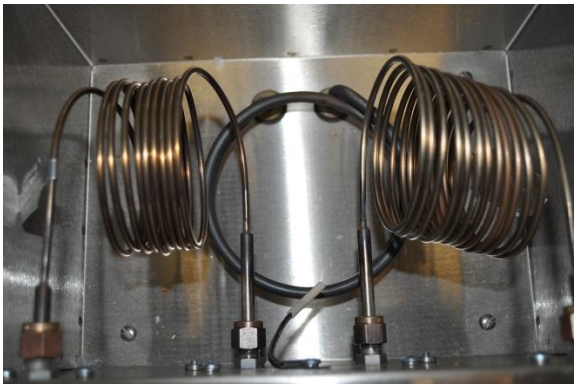

Figure 8-23: Installed columns in the Gow-Mac 400.

The GC has two pneumatically actuated sample valves. These are controlled by compressed air regulated to 30 – 50 pounds per square inch (psi). Building air was used to operate the valves in conjunction with a reducer set to 50 psi. The connections and reducer can be seen in Figure 8-24. Clarity Lite™ software was used to write a sampling program and to operate the valves. The system was connected to a binary timer that would activate the

circuit in accordance with the sampling program. A full description of the GC method is given in section 8.3.1.1 below.

Figure 8-24: Gas connections on the back of the GC. In the center is the carrier gas connection (He). The upper connections on the left and right are for operating the pneumatically actuated sample valves. Below those are the sample inlets.

8.2.3 Heater

The samples were heated to 1000 ºC using a Micropyretics Heaters International (MHI) high temperature robust radiator™. There were two important factors in choosing a heater for this application. The first was the operating temperatures. The HTGRs are expected to have outlet temperatures around 900 ºC, therefore the graphite in the core will experience temperatures near 1000 ºC. In the case of accidents these temperatures can reach 1700 ºC [Wickham, 1998]. The second was the material from which the heater was made. It was important that the heating element was nickel free, as nickel can absorb a neutron and produce Co-60 [IAEA, 2005]. The MHI robust radiator, model no. RHUL-MP1125-4, met all of the requirements. It is capable of temperatures of up to 1800 ºC. An image of the heater can be seen in Figure 8-25.

Figure 8-25: MHI robust radiator™ used for east beam port experiments.

The heater was controlled through the MHI data acquisition and control systems (DACS). This allowed the heater to be programmed to ramp up to 1000 ºC, maintain the temperature for the duration of the run and then ramp down to room temperature. The DACS system also provides a plot of the temperature of the heater over the duration of the run. Typically the irradiated runs were 8 hours in length (due to time constraints on the MUTR, two 8 hour runs were conducted instead of one 16 hour run) and the unirradiated runs were 16 hours in length. The entire control system for the heater can be seen in Figure 8-26.

Figure 8-26: MHI robust radiator™ connected to the control system with DACS software system open.

8.3 Analytical Techniques

Several analytical techniques were used to characterize the graphite prior to and after irradiation, with both the gamma and mixed field. These techniques can be divided into those that provide information on the oxidation of the graphite and those that provide information on the magnetic properties.

8.3.1 Graphite Oxidation Techniques

8.3.1.1 GC

Chromatography dates back to the early 1900s. Michael Tswett is credited as being the "father of chromatography." He was able to separate plant pigments using liquid chromatography and scientifically described the process [McNair and Miller, 2009].

The International Union of Pure and Applied Chemistry defines chromatography as a physical method of separation in which the components to be separated are distributed between two phases, one of which is stationary while the other moves in a definite direction. The various chromatographic processes are named according to the physical state of the

mobile phase. For gas chromatography (GC), the mobile phase is a gas. The first work on gas chromatography was published in 1952 by Martin and James. Gas chromatography has several advantages and disadvantages. It is relatively fast, providing results in a matter of minutes. It requires small sample sizes, typically microliters. It is also reliable, simple and relatively inexpensive. On the other hand, it is limited to volatile samples and is fairly difficult to use for large, preparative samples [McNair and Miller, 2009].

Figure 8-27 shows a typical GC. The carrier gas flows continually through the injection port, the column and the detector. The carrier gas used for these experiments was research grade He. Research grade He has a minimum purity of 99.9999 %. The guaranteed specifications are $N_2 < 1$ ppm, $H_2O < 0.2$ ppm and $O_2 < 1$ ppm. The flow rate of the carrier gas is controlled to ensure reproducible retention times and to minimize detector drift and noise. The flow rate used was 60 mL/min as recommended by Gow-Mac. The sample is injected into the heated injection port and travels through the column. The sample becomes partitioned between mobile and stationary phases and is separated into individual components based on relative solubility in the liquid phase. The carrier gas and sample then pass through a detector. The detector measures the quantity of the sample and generates an electrical signal. In this particular case the signal was sent to the Clarity Lite software which provided the chromatogram [DataApex, 2010].

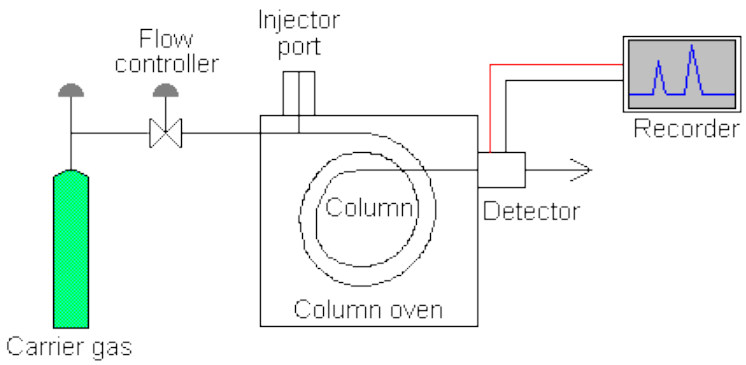

Figure 8-27: A typical GC. The carrier gas flows continually through the injection port, the column and the detector. The sample is injected into the heated injection port and travels through the column. It then enters the detector and the results are recorded [McNair and Miller, 2009].

8.3.1.2 Raman Spectroscopy

Raman spectroscopy is a spectroscopic technique based on inelastic scattering of monochromatic light, usually from a laser source [Ferraro and Nakamoto, 2003]. Photons from the laser light are absorbed by the sample and then reemitted. The frequency of the reemitted photons is shifted up or down in comparison with the original monochromatic frequency. This is known as the Raman shift. The Raman shift provides information about vibrational, rotational and other low frequency transitions in molecules [Ferraro and Nakamoto, 2003].

The Raman effect is based on molecular deformations in an electric field determined by the molecular polarizability, α. The laser beam can be considered an oscillating electromagnetic wave with an electrical vector E. When the laser beam interacts with the sample it induces an electric dipole moment, P, which deforms the molecules. This is given in the following equation [Ferraro and Nakamoto, 2003].

$$P = \alpha E$$

The excited molecules are transformed into oscillating dipoles and these dipoles emit light. Three frequencies are generated: Rayleigh, Stokes and Anti-Stokes. A molecule with no Raman-active modes absorbs a photon with the frequency υ_0. The excited molecule returns back to the same basic vibrational state and emits light with the same frequency, υ_0, as the excitation source. This is known as Raleigh scattering and accounts for approximately 99.99% of all of the scattered light. For the Stokes frequency, a photon is absorbed by Raman-active molecule which at the time of interaction is in the ground vibrational state. Part of the photon's energy is transferred to the Raman-active mode and the resulting frequency of scattered light is reduced. For the Anti-Stokes frequency, a photon is absorbed by a Raman-active molecule, which, at the time of interaction, is already an excited vibrational state. Excessive energy of excited Raman active mode is released, and the molecule returns to the basic vibrational state and the resulting frequency of scattered light goes up. The Stokes and Anti-stokes scattering account for about 0.001% of the scattered light [Sibilia, 1996]. The figure below shows the difference between the three frequencies generated.

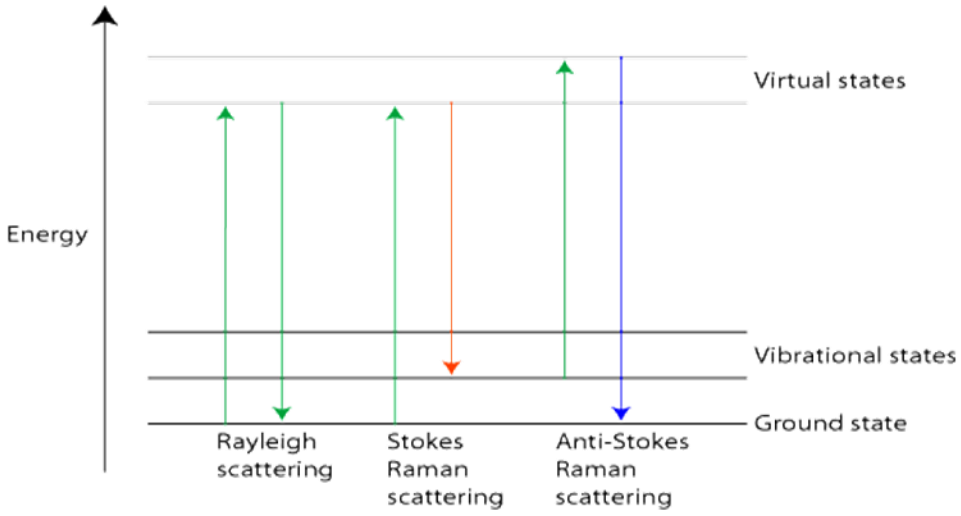

Figure 8-28: The three scattering frequencies generated by oscillating dipoles [Sibilia, 1996].

When performing Raman spectroscopy, a sample is normally illuminated with a laser beam in the ultraviolet (UV), visible (Vis) or near infrared (NIR) range. Scattered light is collected with a lens and is sent through an interference filter or spectrophotometer to obtain the Raman spectrum of a sample. Raman spectrum is measured by detecting the dispersed light with a high-sensitivity/low-noise multichannel detector. A schematic showing a typical Raman spectroscopy set-up is in Figure 8-29. Spontaneous Raman scattering is very weak and special measures must be taken to distinguish it from the predominant Rayleigh scattering. Notch filters, tunable filters, laser stop apertures, double and triple spectrometric systems are used to reduce Rayleigh scattering and obtain high-quality Raman spectra.

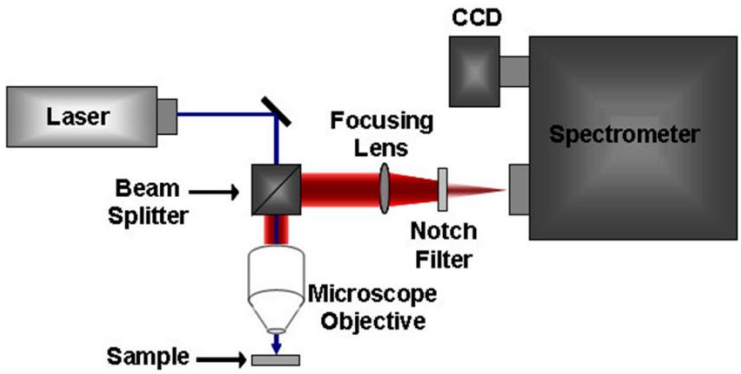

Figure 8-29: A typical Raman spectrometer. The laser is shined onto sample through a microscope. The returning light goes through a focusing lens and a notch filter (to remove the Rayleigh scattered light) before going to the spectrometer [Ferraro and Nakamoto, 2003].

In two-dimensional (2-D) graphite, electronic σ bands are responsible for the strong in-plane covalent bonds within the 2-D graphene sheets, while the π bands are responsible for weak van der Waals interactions between the sheets. The π bands are close to the Fermi level, therefore the electrons can be excited from the valence (π) to the conduction (π*) band optically. The optical transitions occur close to the corners of the 2-D hexagonal Brillouin zone (BZ), called the *K* points, where the valence and conduction bands touch each other.

The first BZ is the smallest volume entirely enclosed by the planes that are perpendicular bisectors of the reciprocal lattice vectors drawn from the origin. The energy dispersion around the *K* point is linear in *k* which is responsible for the unique solid-state properties of 2-D graphite [Dresselhaus et al., 2005]. This can be seen in the image below.

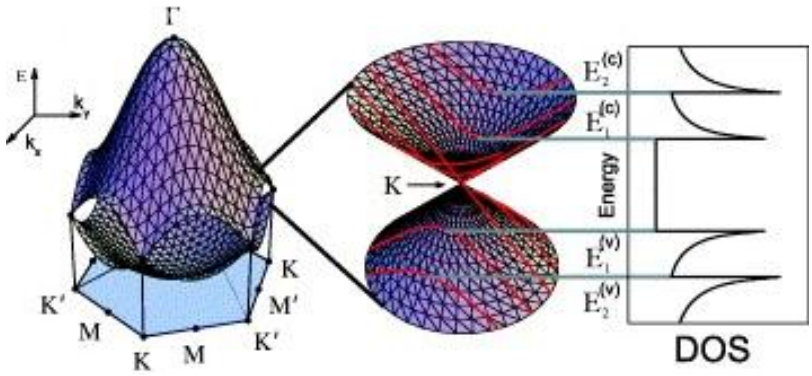

Figure 8-30: Constant energy surfaces for the two lowest conduction and two highest valence bands of 2-D graphite. On the right, shows an image of the constant energy contours of the cones near the K point in the BZ. The extreme left shows the density of electronic states versus the energy for the highest two valence bands and lowest two conduction bands [Dresselhaus, 2012].

It is necessary to understand the phonon dispersion in graphite in order to interpret the Raman spectra. The phonons are the quantized normal mode vibrations that strongly affect many properties in condensed matter systems, including thermal transport and mechanical properties. Three-dimensional (3-D) graphite is formed by stacking single graphene layers of 2-D graphite. In 2-D graphite, there are two carbon atoms per unit cell, which gives rise to six phonon dispersion relations. For a crystal that has at least two atoms in its unit cell, such as graphite, the dispersion relations exhibit two types of phonons, optical and acoustic. For graphite, three of the modes are acoustic (A) and the other three optic (O). Of the O modes, one is an out-of-plane (oT) modes and the other two are in plane modes, one is longitudinal (L) and the other is transverse (iTO) [Pimenta, et al., 2007]. The six phonon

dispersion curves are assigned to LO, iTO, oTO, LA, iTA, and oTA phonon modes and can be seen below.

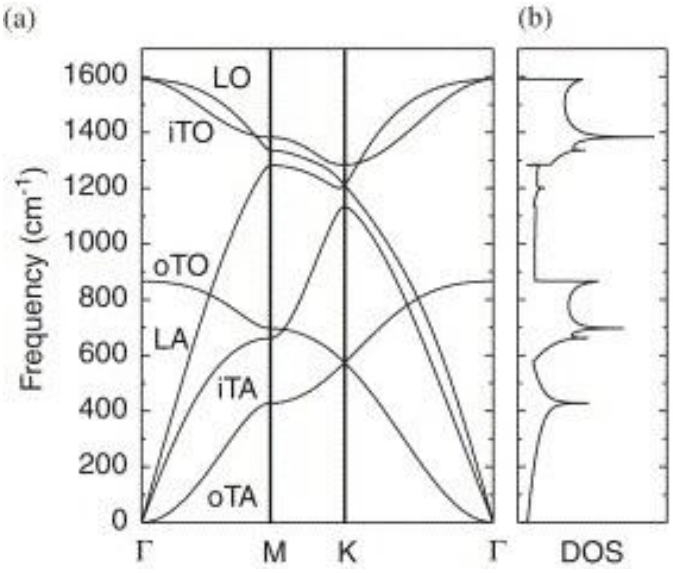

Figure 8-31: (a) This graph shows the calculated phonon dispersion relations of two dimensional graphite. (b) This graph shows phonon density of states for 2D graphite [Dresselhaus *et al.*, 2005].

Phonons play an important role as a carrier of thermal energy in thermal conduction processes and in thermodynamic properties, such as the heat capacity. They are also important in the scattering process for bringing electrons into equilibrium with the lattice in various electron transport phenomena, such as electrical conductivity and thermo-electricity. The vibrational spectra also determine the speed of sound, elastic properties of solids, and their mechanical properties. Phonons, through their interaction with electrons, can also mediate interactions and pairing between electrons, giving rise to superconductivity [Dresselhaus *et al.*, 2005].

The Raman spectra of graphite can provide information about properties of carbon materials, such as their phonon structure, electron structure and defects in the material. Raman spectroscopy is based on the inelastic scattering of light. During a scattering event an

electron is excited from the valence energy band to the conduction energy band by absorbing a photon. The excited electron is scattered by emitting or absorbing phonons and then relaxes to the valence band by emitting a photon. By measuring the intensity of the scattered light as a function of frequency downshift of the scattered light, an accurate measure of the phonon frequencies of the material is obtained. A model for the phonon dispersion relations can be determined by looking at the original geometrical structure of the crystal [Dresselhaus, *et al.*, 2005].

The most prominent features in the Raman spectra of graphitic materials are the G band appearing at 1582 cm^{-1} (graphite), the D band at about 1350 cm^{-1}, the D′ band at about 1620 cm^{-1} and the 2D band at about 2700 cm^{-1}. A typical Raman spectrum for graphite can be seen below with these peaks identified. The G band is a doubly degenerate (iTO and LO) phonon mode (E_{2g} symmetry) at the BZ center that is Raman active for sp^2 carbon networks. The G band in the Raman spectra indicates that the sample contains sp^2 carbon networks. The G mode is a bond stretching vibration of a pair of sp^2 sites and occurs whether the sp^2 sites are arranged as aromatic rings or not [Ferrari, 2007]. In contrast, sp^3 and sp carbon networks show characteristic Raman features at 1333 cm^{-1} and in the range 1850–2100 cm^{-1}, respectively. The D and D′ bands are defect-induced Raman features, and thus these bands cannot be seen for highly crystalline graphite. The D band is also associated with in-plane defects and heteroatoms. The D′ band is always present when the D band is present but its intensity decreases with increasing order in the sample [Beyssac *et al.*, 2003]. The integrated intensity ratio I_D/I_G for the D band and G band is widely used for characterizing the defect quantity in graphitic materials. An area ratio can also be used to estimate the degree of organization. This ratio is

$$\frac{Area\ D}{Area\ (G + D + D')}$$

Well-ordered samples will have an area ratio less than 0.5 [Beyssac et al., 2003].

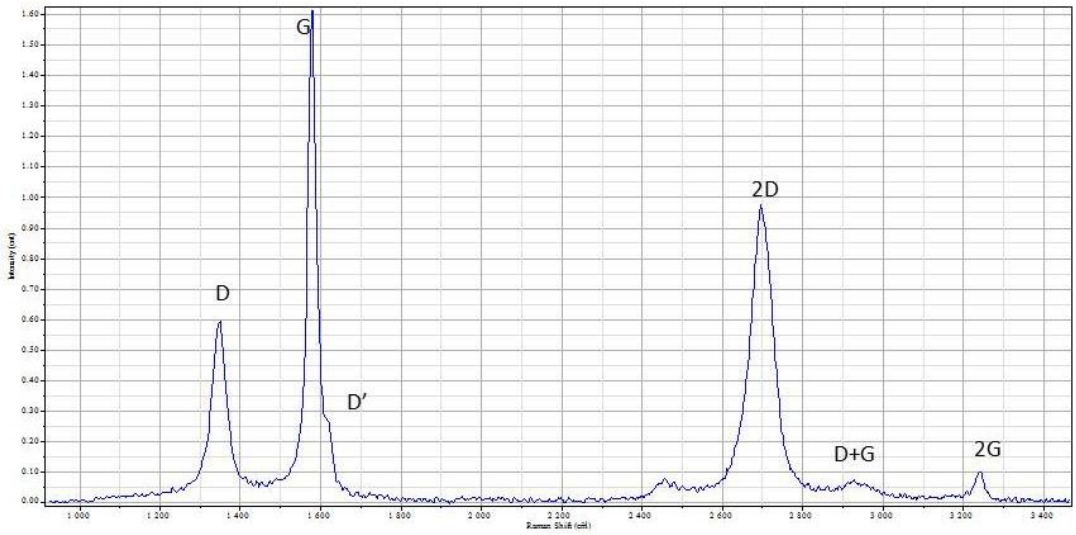

Figure 8-32: Raman spectra of PPEA AG control sample taken with a 532 nm laser. The labeled peaks correspond to the description in the text.

The Raman band appearing at 2500-2800 cm-, corresponds to the overtone of the D band and is labeled 2D. This band was originally called the G′ band because it is symmetry allowed and appears in the second-order Raman spectra of crystalline graphite not containing any disorder. The Raman feature around 2950 cm- is associated with a D+G combination mode and is associated with disorder as well [Pimenta, *et al.*, 2007].

In 1970, Tuinstra and Koenig performed Raman and x-ray diffraction studies of many graphitic samples with different in-plane crystallite sizes, L_a, and concluded that the ratio of the D and G band intensities (I_D/I_G) is inversely proportional to the in-plane crystallite sizes, L_a, which were obtained from the width of the x-ray diffraction peaks. The equation used to calculate the crystallite size, L_a, is

$$L_a\,(nm) = (2.4 \times 10^{-10})\,\lambda_{laser}^4 \left(\frac{I_D}{I_G}\right)^{-1} \quad .$$

The number of emitted phonons before relaxation of the lattice can be one, two, and so on, which are called, one-phonon, two-phonon and multi-phonon Raman processes, respectively. The order of a scattering event is defined as its number in the sequence of the total scattering events, including elastic scattering by an imperfection (such as a defect or edge) of the crystal. The lowest order process is the first-order Raman scattering process which gives Raman spectra involving one-phonon emission. A scattering event with only elastic scattering, i.e., change of photon direction but no frequency shift, corresponds to Rayleigh scattering of light. In order for an electron to recombine with a hole, the scattered **k** + **q** (bold indicated vectors) states should not differ from **k** by more than two times the photon wave vector [Dresselhaus *et al.*, 2005]. In 2-D graphite, the G band around 1582 cm^- is the only first-order Raman peak. In second-order double resonance Raman processes for sp^2 carbon materials, the electron (1) absorbs a photon at a **k** state, (2) scatters to **k + q** states, (3) scatters back to a **k** state, and (4) emits a photon by recombining with a hole at a **k** state [Pimenta *et al.*, 2007]. These relationships can be seen in Figure 8-35.

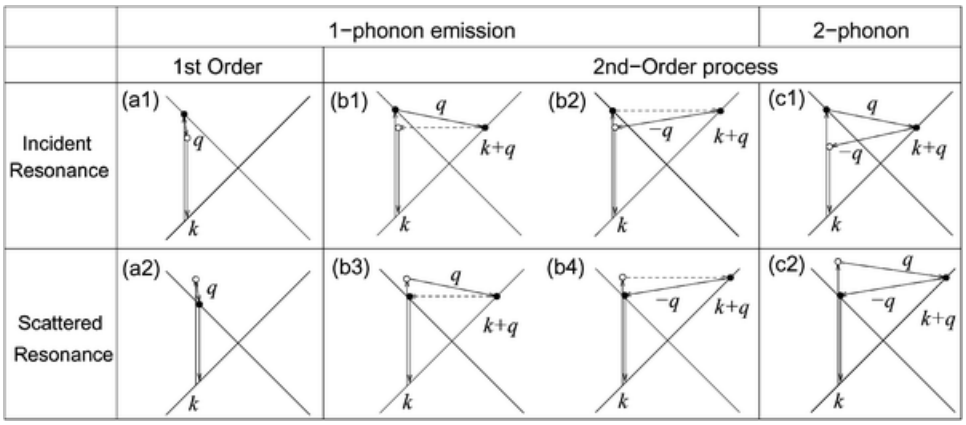

Figure 8-33: (a) First order Raman process. (b) One phonon second order processes. (c) Two-phonon second order Raman process. The top line represents incident photon resonance while the bottom line indicates scattered photon resonance conditions. For one phonon second order processes one of the scattering events is elastic and is represented by dashed lines. Resonance points are represented by solid circles [Dresselhaus *et al*., 2005].

In the case of the D-band and D′-band, the two scattering processes consist of one elastic scattering event by defects of the crystal and one inelastic scattering event by emitting or absorbing a phonon, shown in the one phonon second order image above. In the case of the 2D-band, both processes are inelastic scattering events involving two phonons [Pimenta et al., 2007].

8.3.1.3 XPS

X-ray photoelectron spectroscopy (XPS) is a surface sensitive tool that provides information about the chemical state and concentration of elements comprising the surface layers of a solid. It can effectively identify and quantify the outer 10 nm or less of any solid surface with all elements from lithium to uranium being detectable [Van der Heide, 2011]. The theoretical foundation was laid by Einstein in 1905 with the photoelectric equation:

$$h\nu = E_b + E_k + \varphi_s$$

where hν is the quantum energy, E_b is the binding energy of the electron, E_k is the kinetic energy of the ejected electron and φ_s is the work function of the equipment being used [Nefedov, 1988]. The work function represents the minimum energy required to remove an electron from the instrument assuming that a conductive sample in physical contact with the instrument is analyzed. The method of XPS can be summarized as the measurement of the kinetic energy of the inner or valence electron ejected by an incident photon with a known energy, hν. Knowing these, the binding energy can be calculated, which is a sensitive characteristic of chemical bonds in a compound and is the energy of ionization [Nefedov, 1988].

In XPS, the sample is placed in an ultrahigh vacuum environment and exposed to a low-energy, monochromatic x-ray source. The use of ultrahigh vacuum equipment maintains surface cleanliness. The incident x-rays cause the ejection of core-level electrons from sample atoms. The energy of a photoemitted core electron is its binding energy and is characteristic of the element from which it was emitted.

If the photon has sufficient energy, it is normally the most tightly bound electron (1s) that is ejected. These account for about 80 % of the interactions and the remaining 20 % are with L shell electrons. The ejection of a 1s electron is shown schematically in Figure 8-34. Electron binding energies are fully characteristic of the element from which the photoelectron originates [Chorkendorff and Niemantsverdriet, 2007]. When a core electron is ejected by the incident x-ray, an outer electron fills the core hole. The energy of this transition is balanced by the emission of an Auger electron or a characteristic x-ray. Analysis of Auger electrons can be used in XPS, in addition to emitted photoelectrons.

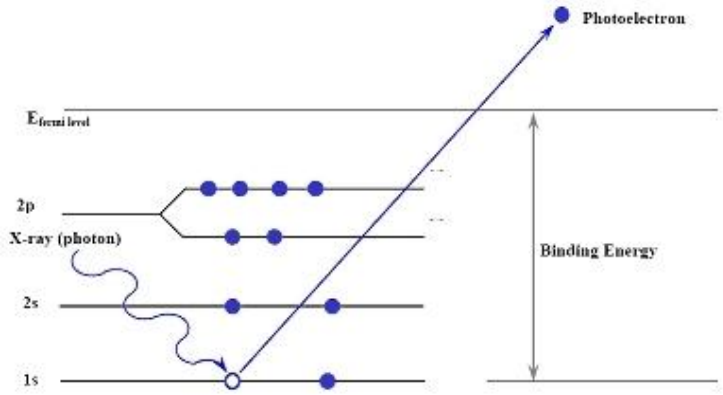

Figure 8-34: This image shows the photoelectric effect [Sibilia, 1996].

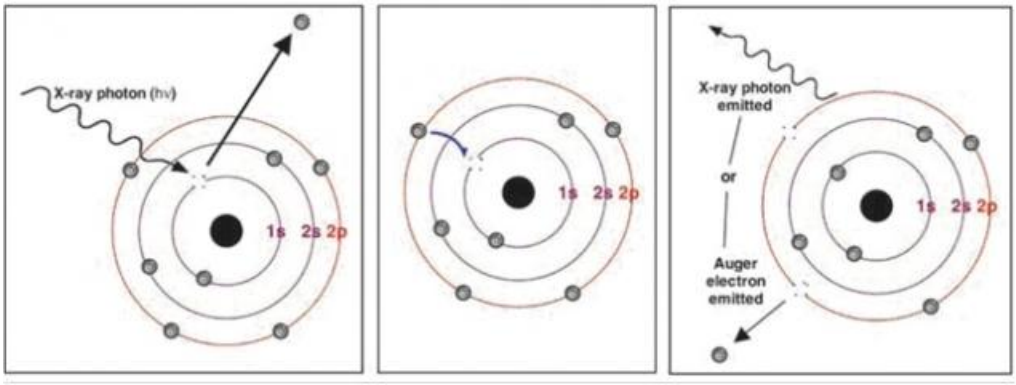

Figure 8-35: Photoelectric and Auger electron production [Chorkendorff and Niemantsverdriet, 2007].

The photoelectrons and Auger electrons emitted from the sample are detected by an electron energy analyzer. By counting the number of photoelectrons and Auger electrons as a function of their energy, a spectrum representing the surface composition is obtained. The energy corresponding to each peak is characteristic of an element present in the sampled volume. The area under a peak in the spectrum is a measure of the relative amount of the element represented by that peak. The peak shape and precise position indicates the chemical state for the element. Figure 8-36 shows a typical XPS set-up.

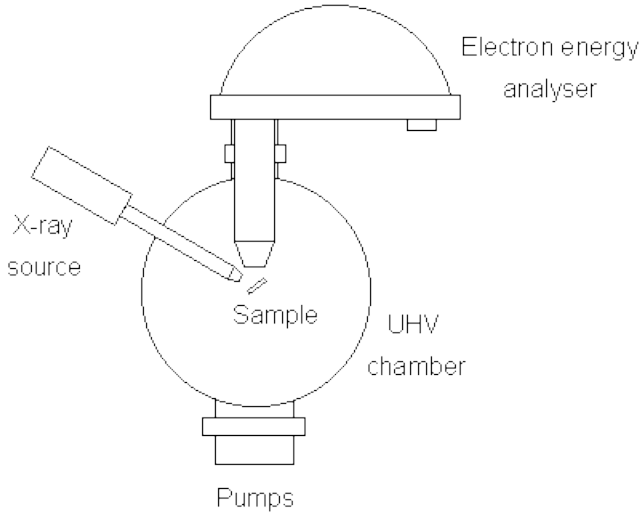

Figure 8-36: This image shows a typical set-up for XPS. The basic elements are: a source of fixed-energy radiation (an x-ray source), an electron energy analyzer (which can disperse the emitted electrons according to their kinetic energy, and thereby measure the flux of emitted electrons of a particular energy), and an ultra high vacuum environment to prevent surface contamination [Sibilia, 1996].

XPS is a surface sensitive technique because only those electrons generated near the surface escape and are detected. The photoelectrons of interest have relatively low kinetic energy. With a path length of one wavelength, approximately 63% of all electrons are scattered. The sampling depth is described as the depth at which 95% of all photoelectrons are scattered by the time they reach the surface. This is estimated as 3 wavelengths. The calculation for this can be seen below. For XPS, the sampling depth is approximately 3 to 10 nm due to inelastic collisions within the sample's atomic structure.

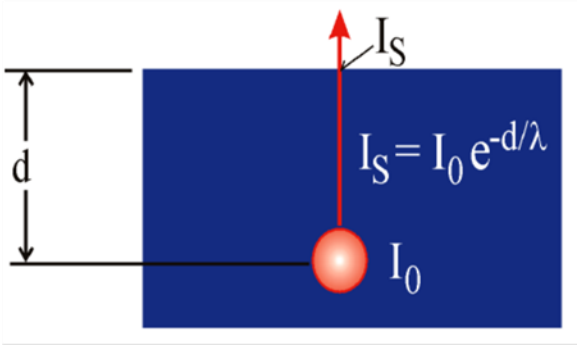

Figure 8-37: This image shows the method for calculating the sampling depth for XPS [Sibilia, 1996].

8.3.1.4 XRD

X-rays are produced in an x-ray tube consisting of two metal electrodes enclosed in a vacuum chamber. Electrons are produced by heating a tungsten filament cathode. The cathode is at a high negative potential and the electrons are accelerated toward the anode, which is at ground. The electrons collide with the water-cooled anode and the loss of energy is manifested as x-rays [Suryanarayana and Norton, 1998]. A typical x-ray tube can be seen below.

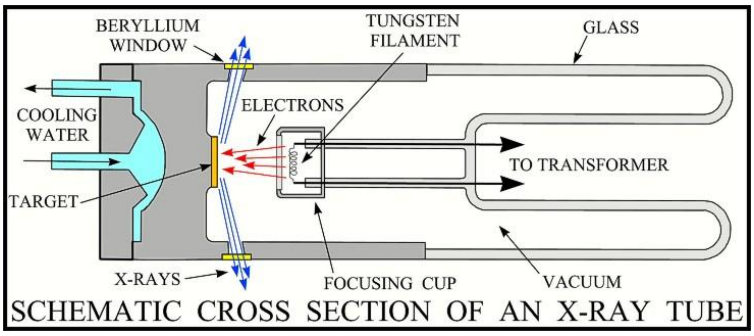

Figure 8-38: Cross-section of a typical x-ray tube [U.S. Geological Survey, 2001].

Diffraction can be defined as the modification of a wave by its interaction with an object. Three different processes are possible from this interaction. The first is coherent

scattering. This interaction produces beams with the same wavelength of the incident beam. The second is Compton scattering, in which the wavelength of the scattered beam increases due to a partial loss of photon energy in collisions with core electrons. The third interaction is absorption of the x-rays. In this interaction some photons may be dissipated in random directions due to scattering, some may lose their energy by ionizing an atom and some lose their energy through the photoelectric effect [Pecharsky and Zavalij, 2009]. Only coherent scattering results in the diffraction from periodic lattices.

Bragg's Law establishes relationships among the diffraction angle, wavelength and interplanar spacing. Diffraction occurs when the distance traveled by the x-rays reflected from successive planes differs by a complete number of wavelengths. By varying the angle, the Bragg's Law conditions are satisfied by different d-spacings in polycrystalline materials [Sibilia, 1996].

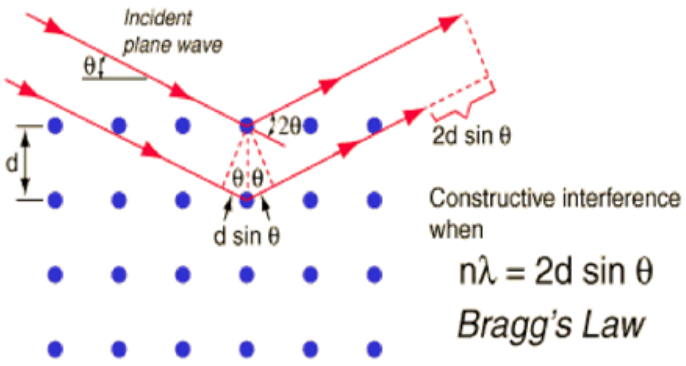

Figure 8-39: Illustration of Bragg's law [Suryanarayana and Norton, 1998].

Any material that is made up of an ordered array of atoms will yield a diffraction pattern. Determination of the three-dimensional structure of a compound is achieved by using single-crystal XRD. In this method the measurement of the diffraction pattern is generated from an oriented single-crystal sample. The diffraction pattern produced depends

on the atoms present, their locations and the thermal motion. A charge-coupled device (CCD) camera is used to capture the image. Fourier series analysis is used to refine the image and determine the chemical identity and molecular structure of the sample.

The powder XRD signal contains the same information as the single-crystal XRD signal but only in one-dimension. The diffraction pattern consists of rings of diffracted intensity with cone angles corresponding to the 2θ Bragg angles in each plane. This is a powerful technique for the identification and qualification of crystal phases within a known structure.

8.3.2 Magnetic Properties

8.3.2.1 EPR Spectroscopy

EPR is a technique for studying chemical species that have one or more unpaired electrons. These unpaired electrons may occur in unfilled conduction bands, electrons trapped in radiation damage sites, or free radicals, etc. Where more than one species exists in a sample, the spectral EPR lines arising from each can be simultaneously observed. Often definitive identification of the individual species is realized solely from the analysis of the EPR spectrum. Furthermore, EPR spectroscopy is capable of providing molecular structural details inaccessible by any other analytical tool [Eaton et al, 2010].

EPR spectroscopy is based on the magnetic properties associated with unpaired electrons. This effect is known as the Zeeman effect. The paramagnetic specimen is placed in a uniform magnetic field, which orients the unpaired electron with respect to the field. A paramagnetic material is one that is only attracted when in the presence of an externally applied field. The orientation is parallel or antiparallel and all free radicals orient to one of these two possible states, with a slightly energy difference between them. The two states are

designated by the projection of the electron spin, m_s, on the direction of the magnetic field. The difference between the energies of the two states is shown below:

$$\Delta E = g\mu_B B_0 \Delta m_s$$

where g is the g-factor, μ_B is the Bohr magneton (9.264×10^{-24} J/T), B_0 is the magnetic field and Δm_s is the change in spin state (+/- 1) [Eaton *et al.*, 2010]. This relationship can also be seen in the image below. The energy required to cause a transition between the two states is given in the following equation:

$$\Delta E = h\nu = g\mu_B B_0$$

where h is Planck's constant (6.626×10^{-34} Js), υ is the frequency of radiation, B_0 is the magnetic field, μ_B is the Bohr magneton (9.264×10^{-24} J/T), and g is the g-factor [Eaton *et al.*, 2010].

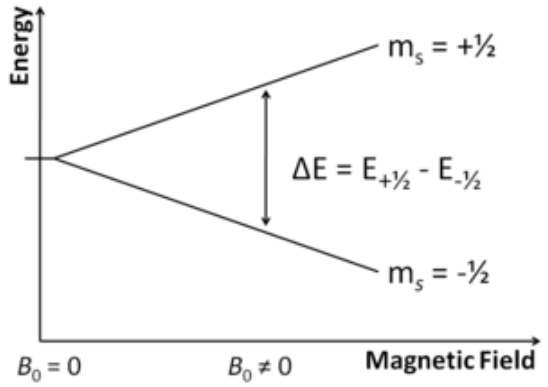

Figure 8-40: This image shows the energy splitting of electron spin states as a function of the magnetic field [Eaton *et al*, 2010].

The field for resonance is not unique for an individual compound because the spectra can be acquired at different microwave frequencies. The g-factor is independent of the

microwave frequency which makes it a better way to characterize signals. Carbon-centered radicals have a g-factor close to that of a free electron, which is 2.0023 [Eaton et al, 2010].

Additional information about the unpaired electron can be obtained from nuclear hyperfine interactions. The nuclei of atoms in a molecule have magnetic moments which produce a local magnetic field at the electron. This interaction between the nuclei and the electron is known as the hyperfine interaction [Weil and Bolton, 2007].

As there are more electrons in the lower-energy state, there is a net absorption of radiation energy, which can be observed as a spectroscopic absorption line which increases linearly with the magnetic field strength. In practice, the frequency is maintained at a constant value and the magnetic field strength is varied by means of small secondary coils so as to sweep across the value corresponding to maximum absorption. The size of the signal is defined as the integrated intensity or the area beneath the absorption curve, which is proportional of the concentration [Weil and Bolton, 2007].

The EPR spectrometer used was a Bruker EMX. The electromagnetic radiation source and detector are in a box called the microwave bridge. The sample is in a microwave cavity, which is a metal box that helps to amplify weak signals from the sample. There is a magnet to tune the electronic energy levels. In addition, there is a console, which contains signal processing and control electronics and a computer. The computer is used for analyzing data as well as coordinating all the units for acquiring a spectrum.

8.3.2.2 SQUID Magnetometer

SQUID stands for superconducting quantum interference device. The SQUID consists of two superconductors separated by thin insulating layers to form two parallel Josephson junctions. The Josephson junctions are based on the DC Josephson effect. The

Josephson effect is the phenomenon of supercurrent (i.e. a current that flows indefinitely long without any voltage applied) across two superconductors coupled by a weak link [McElfresh, 1994]. The weak link can consist of a thin insulating barrier (known as a superconductor–insulator–superconductor junction), a short section of non-superconducting metal, or a physical constriction that weakens the superconductivity at the point of contact.

The SQUID magnetometer used to analyze the graphite samples is manufactured by Quantum Design. It is a Magnetic Property Measurement System (MPMS) XL. The MPMS XL has five main systems. These are the temperature control system, magnet control system, the amplifier system, sample handling system and the computer operating system. The MPMS system also includes several superconducting components. These consist of a superconducting magnet to generate large magnetic fields, a superconducting detection coil which couples inductively to the sample, the SQUID connected to the detection coil and a superconducting magnetic shield which surrounds the SQUID.

Although the SQUID is what makes the MPMS so sensitive, it does not directly detect the magnetic field from the sample. The sample moves through a system of superconducting detection coils, which are connected to the SQUID with superconducting wires. This allows the current from the detection coils to inductively couple with the SQUID sensor. The SQUID electronics produce an output voltage that is proportional to the current flowing in the SQUID input coil. The thin-film SQUID device, located below the magnet but inside the superconducting shield, acts as a sensitive current-to-voltage converter. This can be seen in Figure 8-41.

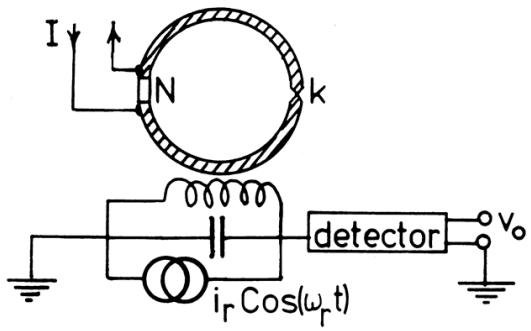

Figure 8-41: The image above depicts the thin-film SQUID device which acts as a sensitive current-to-voltage converter [McElfresh, 1994].

The sample is measured by moving it through the superconducting detection coils. As the sample moves through the coils, the magnetic moment of the sample induces an electric current in the detection coils. The detection coils, connecting wires and SQUID input coils form a closed superconducting loop. This means that any change in magnetic flux in the detection coils produces a change in the current in the detection circuit, which is proportional to the change in magnetic flux. The variations in current in the detection coils produce corresponding changes in SQUID output voltage which are proportional to the magnetic moment of the sample [McElfresh, 1994]. The system is calibrated using a small piece of material that has a known magnetic susceptibility and mass.

The SQUID is extremely sensitive to fluctuations in magnetic fields. This means that the SQUID must be shielded from fluctuations in the ambient magnetic field as well as from the large magnetic fields produced by the superconducting magnet. A superconducting shield is present in the design and performs two functions. It is used to shield the SQUID detector from the magnetic field generated by the superconducting magnet and it also traps and stabilizes the ambient magnetic field when the SQUID is first cooled to liquid He temperatures [McElfresh, 1994].

The set-up also includes a superconducting detection coil. This detection coil is made of a single piece of superconducting wire that is wound into a set of three coils to form a second-order gradiometer. The coils are placed at the center of the superconducting magnet outside the sample chamber. This placement ensures that the magnetic field from the sample, as the sample is moved, couples inductively with the coils. The gradiometer configuration is used to reduce noise in the detection circuit that is created by fluctuations in the magnetic field of the magnet [McElfresh, 1994].

The superconducting magnet in the system is wound in a solenoidal configuration. The magnet is connected in a closed loop and can be charged to a specific current and allowed to operate without needing an external power supply. In order to change the current flowing, the circuit must be opened. This is done by wrapping a small heater around a segment of the magnet's wire. By turning the heater on, that segment of the wire heats up and is no longer superconducting. This acts like an open circuit. By connecting a power source to each side of this open circuit it is possible to change the current in the magnet. Once the magnetic field is at the desired level, the heater is then turned off and the magnet returns to its superconducting state [McElfresh, 1994].

The sample space is made of a tube with a 9mm inner diameter. The space is maintained at low pressure with the use of He gas. At the top of the space is an airlock that can be evacuated and purged with the He gas. The airlock and sample space are separated by a ball valve which makes the airlock a part of the sample space when the valve is open. The lower portion of the space is lined with copper to provide a region with high thermal uniformity. There are two thermometers in the system. These are used for sample temperature and temperature control [McElfresh, 1994]. This technique is used to measure the diamagnetism of the graphite samples.

Chapter 9 Results and Discussion

9.1 Oxidation Results

9.1.1 Characterizing the oxidation of graphite using GC

The GC was used to analyze the gases coming from the sample chamber during the east beam port experiments. Clarity Lite software by DataApex was used for the analysis. A sequence method was created in the program to measure the samples. The sequence injected 10 µL of sample gas into one of the columns every 10 minutes. The columns were calibrated using He, CO, CO_2, argon (Ar) and methane (CH_4). The current was maintained at 150 °C and the columns were maintained at 250 °C. In order to ensure that the samples were injected at regular time intervals, a binary timer was used. Every 10 minutes and 8 seconds, the timer would inject the next sample into the GC.

The Boudouard reaction is discussed in detail in section 4.1.2 and can be seen below.

$$CO_2\ (gas) + C\ (solid) \rightarrow 2\ CO\ (gas) \quad [Marsh, 1989]$$

The Boudouard reaction is the redox reaction of a chemical equilibrium mixture of carbon monoxide and carbon dioxide at a given temperature. It is the disproportionation of carbon monoxide into carbon dioxide and graphite or its reverse.

$$2\ CO \leftrightarrow CO_2 + C$$

While the formation enthalpy of CO_2 is more negative than that of CO, the formation entropy of CO_2 is much lower. The Boudouard reaction implies that at lower temperatures the equilibrium is on the exothermic carbon dioxide side and on higher temperatures the endothermic formation of carbon monoxide is the dominant reaction. At 400 ºC, it lies almost completely on the side of carbon dioxide, while at 1000 ºC, it is entirely on the side of

carbon monoxide at 1 atm. Therefore, the experiments conducted at 1000 °C, should generate CO if there is oxidation occurring on the samples. The results indeed showed this. The graphs below compare the carbon dioxide calibration with the 1000 °C irradiated samples and the carbon monoxide calibrations with the 1000 °C irradiated samples. The PCIB samples showed a slightly greater amount of CO than the other graphite types.

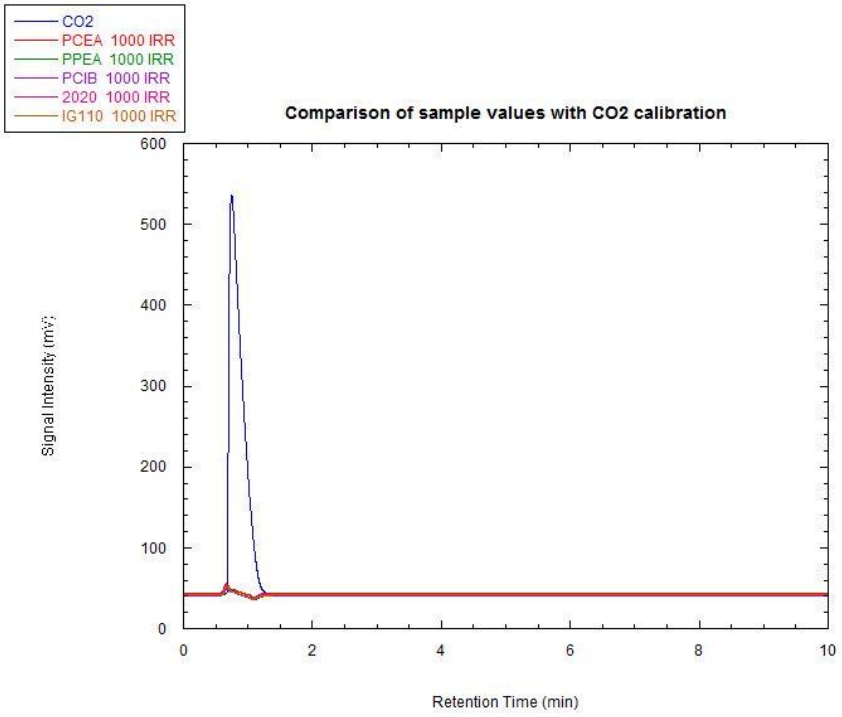

Figure 9-1: Comparison of 1000 °C irradiated samples with the carbon dioxide calibration data.

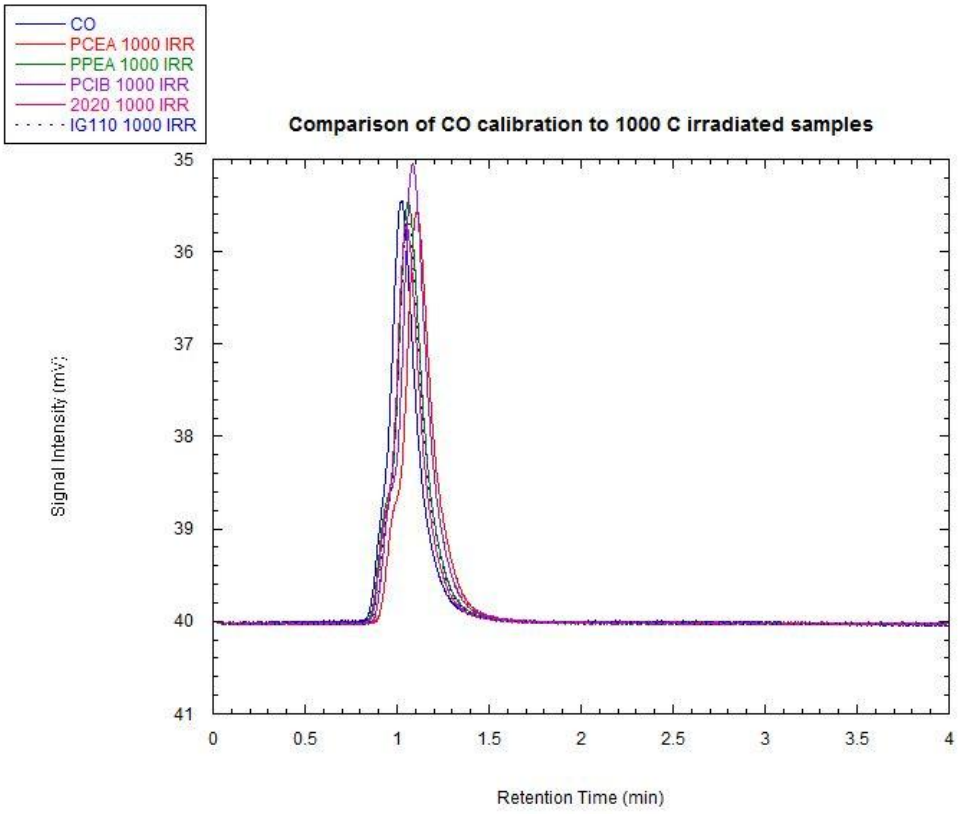

Figure 9-2: This graph shows the comparison between the carbon monoxide calibration data and the 1000 °C irradiated samples.

The room temperature experiments also showed some CO produced. The graph below shows typical results, PPEA in particular. The room temperature results are greatly reduced from the amount of CO produced at 1000 °C.

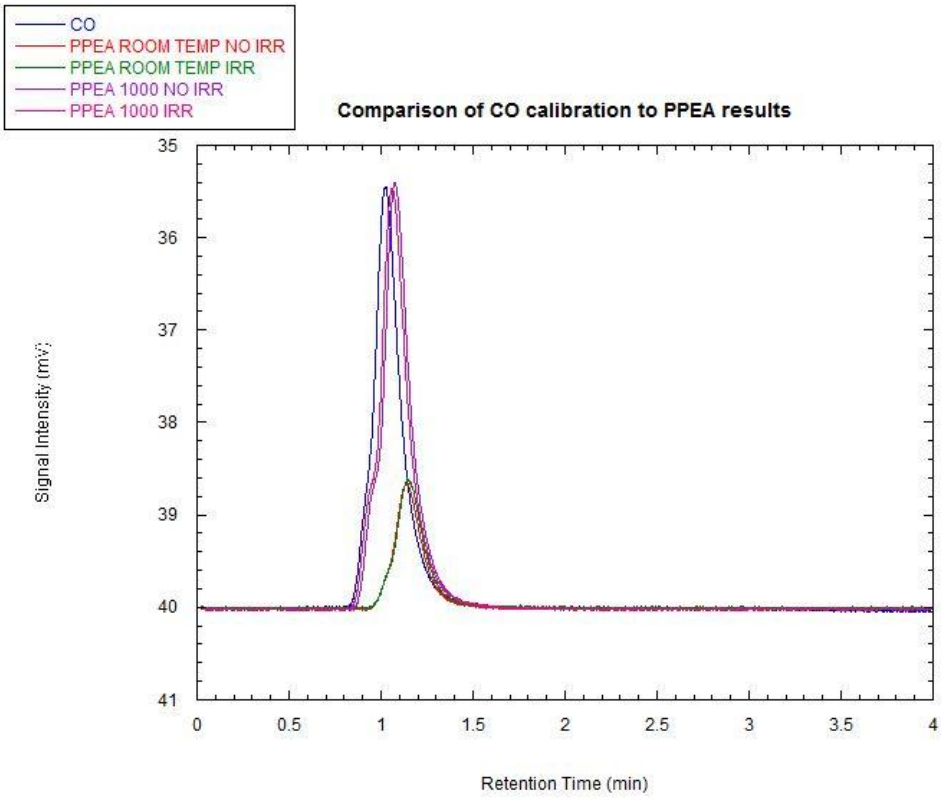

Figure 9-3: Comparison of PPEA samples in the room temperature and 1000 °C experiments to the CO calibration.

The information gathered from the GC results was used to calculate the G value for CO. The following equation was used:

$$G(product) = 9.648 \times 10^6 \times \frac{chemical\ yield}{absorbed\ dose \times \rho} \quad [Woods\ and\ Pikaev, 1994]$$

where G is in molecules/100 eV, chemical yield is mol/L, absorbed dose is Gy and ρ is in g/cm^3. The results can be seen in the following table. Values of 1.1E-03 to 1.3E-03 were calculated for the G-values, the higher value being for the experiments conducted at 1000 °C. The total absorbed gamma dose of the east beam port experiments was lower than what would be expected had the experiments been conducted within the beam port.

Graphite	Temperature	G(CO)	Constant	Chemical Yield	Absorbed Dose (Gy)	Density (g/cm^3)	Sample Volume (L)
PCEA	Room Temperature	1.1E-03	9.65E+06	9.9E-10	4.9	1.81	1.0E-05
	1000 °C	1.3E-03	9.65E+06	1.2E-09	4.9		1.0E-05
PPEA	Room Temperature	1.1E-03	9.65E+06	9.5E-10	4.9	1.7	1.0E-05
	1000 °C	1.4E-03	9.65E+06	1.2E-09	4.9		1.0E-05
PCIB	Room Temperature	1.1E-03	9.65E+06	9.1E-10	4.9	1.7	1.0E-05
	1000 °C	1.4E-03	9.65E+06	1.2E-09	4.9		1.0E-05
2020	Room Temperature	1.1E-03	9.65E+06	9.5E-10	4.9	1.78	1.0E-05
	1000 °C	1.3E-03	9.65E+06	1.2E-09	4.9		1.0E-05
IG-110	Room Temperature	1.1E-03	9.65E+06	9.9E-10	4.9	1.77	1.0E-05
	1000 °C	1.3E-03	9.65E+06	1.2E-09	4.9		1.0E-05

Table 9-1: G-value for carbon monoxide calculated from GC data.

9.1.2 Characterizing the irradiation induced changes in graphite using Raman spectroscopy

The Raman spectra were collected on a Horiba Yvon LabRam ARAMIS at the UMD Surface Analysis Center. The ARAMIS is equipped with two lasers (532 nm and 633 nm). The 532 nm laser was used for these samples.

Before collecting the spectrum the ARAMIS was first calibrated using a piece of silicon (Si). The light is focused on the sample using three objectives (x10, x50 and x100). The zero and the Si peak at 520 cm^{-1} are adjusted to calibrate the instrument.

The graphite spectra were collected using the 532 nm laser. No filters were used. The hole was set to 300 µm and the slit was set to 600 µm. The spectra were centered at 2300 cm^{-1} to ensure the entire spectrum could be seen. A three-second acquisition time was used. An image of each sample spot was collected. These images as well as all of the Raman spectra can be found in Appendix C.

The following table summarizes the Raman peak results for these experiments.

Graphite	Irradiation	D Peak (cm^{-1})	G Peak (cm^{-1})	2D Peak (cm^{-1})	D+G Peak (cm^{-1})	2G Peak (cm^{-1})
PCEA AG	Control	1346.6	1576.8	2715.3	2938.5	3244.9
	Gamma 15 MGy	1352.1	1582.2	2701.2	2947.6	3244.9
	Gamma 45 MGy	1349.7	1577.4	2707.6	2935.4	3235.2
	Gamma 87 MGy	1353.0	1571.4	2692.0	2899.5	3209.1
	AFRRI 1	1349.3	1582.2	2710.6	2936.3	3244.9
	AFRRI 2	1352.1	1576.8	2710.6	2931.7	3242.7
	Htr	1349.3	1582.2	2705.9	2938.5	3247.1
	Room Temp No Irr	1352.1	1579.5	2708.3	2938.6	3242.8
	Room Temp Irr	1341.1	1568.7	2682.6	2920.5	3218.9
	1000 C No Irr	1335.5	1560.6	2670.8	2913.6	3203.6
	1000 C Irr	1341.1	1560.6	2675.5	2900.0	3197.0
PCEA WG	Control	1352.3	1579.6	2717.7	2945.5	3245.0
	Gamma 15 MGy	1349.3	1582.2	2698.9	2952.1	3247.1
	Gamma 45 MGy	1352.1	1579.5	2703.6	2945.4	3240.6
	Gamma 87 MGy	1349.3	1576.8	2698.9	2936.3	3238.4
	AFRRI 1	1354.9	1579.5	2696.6	2934.0	3244.9
	AFRRI 2	1346.6	1571.4	2691.9	2936.3	3227.5
	Htr	1354.9	1579.5	2713.2	2938.5	3244.9
	Room Temp No Irr	1346.6	1571.4	2691.9	2930.3	3221.0
	Room Temp Irr	1354.9	1576.8	2701.3	2937.4	3238.5
	1000 C No Irr	1335.5	1555.2	2670.8	2902.1	3190.4
	1000 C Irr	1332.7	1557.9	2670.8	2903.9	3195.1
PPEA AG	Control	1349.5	1579.6	2696.7	2928.6	3242.9
	Gamma 15 MGy	1349.4	1585.0	2701.3	2938.6	3245.0
	Gamma 45 MGy	1343.8	1574.0	2687.2	2925.0	3231.9
	Gamma 87 MGy	1335.4	1557.8	2675.5	2895.0	3194.8
	AFRRI 1	1349.3	1574.1	2689.5	2929.5	3236.2
	AFRRI 2	1349.3	1579.5	2698.9	2943.1	3242.7

Graphite	Irradiation	D Peak (cm^{-1})	G Peak (cm^{-1})	2D Peak (cm^{-1})	D+G Peak (cm^{-1})	2G Peak (cm^{-1})
	Htr	1349.3	1579.5	2703.6	2947.9	3244.9
	Room Temp No Irr	1346.6	1576.8	2691.9	2929.5	3236.2
	Room Temp Irr	1354.9	1579.5	2717.7	2940.9	3245.0
	1000 C No Irr	1343.8	1568.7	2696.6	2916.2	3223.2
	1000 C Irr	1341.1	1568.7	2684.9	2927.3	3216.2
PPEA WG	Control	1346.7	1579.6	2694.3	2934.1	3242.9
	Gamma 15 MGy	1346.7	1579.6	2699.0	2952.2	3245.0
	Gamma 45 MGy	1343.8	1568.6	2684.9	2916.2	3219.7
	Gamma 87 MGy	1354.9	1579.5	2708.3	2938.6	3242.8
	AFRRI 1	1343.8	1574.1	2687.2	2924.9	3234.0
	AFRRI 2	1349.3	1579.5	2703.6	2947.9	3240.6
	Htr	1352.1	1582.2	2712.9	2937.3	3247.1
	Room Temp No Irr	1349.3	1579.5	2701.3	2930.3	3239.1
	Room Temp Irr	1343.8	1571.4	2692.0	2928.6	3228.6
	1000 C No Irr	1343.8	1574.1	2692.0	2922.7	3234.1
	1000 C Irr	1341.1	1560.6	2689.6	2912.7	3212.7
PCIB AG	Control	1352.2	1582.2	2701.3	2946.2	3242.8
	Gamma 15 MGy	1349.4	1579.5	2701.3	2938.6	3242.8
	Gamma 45 MGy	1346.5	1576.8	2696.6	2934.0	3238.4
	Gamma 87 MGy	1346.5	1574.0	2698.9	2933.8	3231.9
	AFRRI 1	1354.9	1582.2	2715.3	2949.7	3242.6
	AFRRI 2	1346.6	1576.8	2705.9	2937.3	3244.9
	Htr	1349.4	1579.5	2703.6	2945.4	3244.9
	Room Temp No Irr	1349.3	1579.5	2710.6	2922.7	3242.8
	Room Temp Irr	1349.4	1579.5	2703.7	2940.9	3242.8
	1000 C No Irr	1346.5	1571.3	2694.2	2940.8	3234.1
	1000 C Irr	1343.8	1574.0	2689.6	2927.2	3234.1
PCIB WG	Control	1357.7	1582.2	2710.6	2929.5	3247.1
	Gamma 15 MGy	1352.2	1579.6	2701.3	2938.6	3242.8
	Gamma 45 MGy	1346.5	1576.8	2691.9	2929.5	3234.1
	Gamma 87 MGy	1343.8	1574.0	2689.6	2919.7	3229.7
	AFRRI 1	1352.1	1582.2	2694.2	2945.3	3242.7
	AFRRI 2	1349.3	1576.8	2701.2	2943.1	3240.6
	Htr	1352.1	1579.5	2701.2	2936.3	3242.7
	Room Temp No Irr	1341.0	1568.7	2684.9	2907.4	3219.7
	Room Temp Irr	1346.6	1571.4	2689.6	2937.4	3238.5
	1000 C No Irr	1341.0	1565.9	2684.9	2913.6	3214.4
	1000 C Irr	1346.5	1574.0	2694.2	2931.8	3236.2
2020 AG	Control	1349.3	1582.2	2696.6	2947.6	3242.7

Graphite	Irradiation	D Peak (cm^{-1})	G Peak (cm^{-1})	2D Peak (cm^{-1})	D+G Peak (cm^{-1})	2G Peak (cm^{-1})
	Gamma 15 MGy	1349.4	1579.6	2701.3	2943.2	3242.8
	Gamma 45 MGy	1343.8	1571.3	2684.9	2925.0	3216.6
	Gamma 87 MGy	1343.8	1571.3	2689.6	2922.7	3231.9
	Room Temp No Irr	1343.8	1574.1	2696.6	2916.2	3221.5
	Room Temp Irr	1343.8	1566.0	2694.3	2929.5	3229.8
	1000 C No Irr	1341.0	1563.2	2677.8	2920.4	3210.1
	1000 C Irr	1341.0	1568.7	2682.5	2918.1	3221.5
2020 WG	Control	1346.6	1582.2	2698.9	2938.5	3247.1
	Gamma 15 MGy	1349.4	1579.6	2699.0	2959.0	3247.2
	Gamma 45 MGy	1341.0	1568.6	2680.2	2915.9	3223.2
	Gamma 87 MGy	1346.5	1574.0	2689.6	2938.6	3234.1
	Room Temp No Irr	1341.0	1571.4	2680.2	2906.8	3218.8
	Room Temp Irr	1341.0	1571.4	2680.2	2915.9	3218.8
	1000 C No Irr	1335.4	1557.8	2670.8	2897.6	3192.6
	1000 C Irr	1343.8	1574.1	2687.2	2932.1	3225.0
IG-110 AG	Control	1357.7	1582.2	2715.3	2945.3	3244.9
	Gamma 15 MGy	1346.6	1579.2	2706.0	2936.3	3242.8
	Gamma 45 MGy	1341.0	1563.2	2677.8	2909.0	3202.1
	Gamma 87 MGy	1349.3	1579.5	2696.6	2936.3	3238.4
	Room Temp No Irr	1343.8	1571.4	2684.9	2922.7	3221.0
	Room Temp Irr	1335.5	1560.6	2675.5	2911.4	3195.1
	1000 C No Irr	1341.0	1568.6	2680.2	2923.2	3212.7
	1000 C Irr	1343.8	1565.9	2682.5	2918.1	3221.0
IG-110 WG	Control	1346.6	1579.5	2696.6	2936.3	3247.1
	Gamma 15 MGy	1349.4	1576.8	2701.3	2947.6	3238.4
	Gamma 45 MGy	1354.9	1576.8	2703.6	2932.1	3238.4
	Gamma 87 MGy	1349.3	1574.0	2694.2	2933.8	3236.2
	Room Temp No Irr	1346.6	1576.8	2696.6	2935.6	3236.2
	Room Temp Irr	1352.2	1574.1	2694.3	2918.2	3234.1
	1000 C No Irr	1335.4	1560.5	2673.1	2903.8	3201.3
	1000 C Irr	1343.8	1568.7	2689.6	2917.9	3221.5

Table 9-2: Summary of Raman peaks (cm^{-}) for all experiments.

Ferrari and Robertson [2001] classified graphite as a three-stage model. The three stages of increasing amorphorisation are (1) graphite to nanocrystalline (nc-) graphite, (2) nc-graphite to sp^2 amorphous carbon (a-C), (3) sp^2 a-C to sp^3 ta-C. Highly sp^3 bonded a-C is

referred to as tetrahedral amorphous carbon (ta-C). The G position and ratio of D to G peak intensities, I_D/I_G, vary for the regions as shown below.

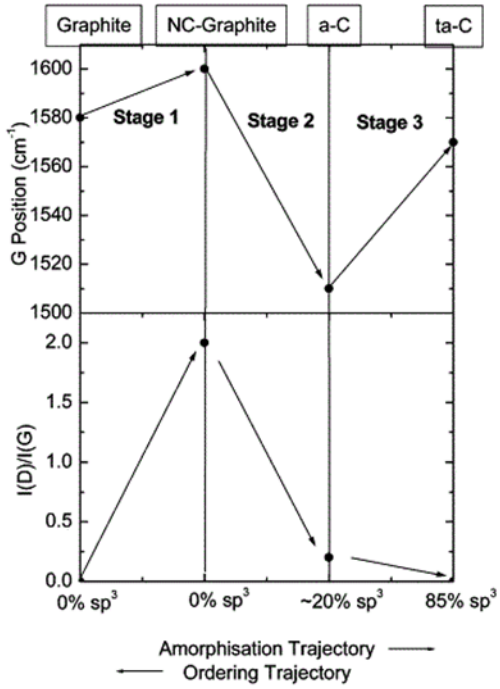

Figure 9-4: Three stage model of the variation of the Raman G position and the D to G intensity ratio, I_D/I_G, with increasing disorder [Ferrari and Robertson, 2001].

The results in the table above show that for these sets of experiments, the shift in peaks for a particular type of graphite was between 5 and 10 cm^-. The G peaks had an overall maximum of 1582 cm^- and a minimum of 1560 cm^-. The G peaks generally shifted to slightly lower numbers under the experimental conditions but when comparing to Ferrari and Robertson's [2001] chart above, these shifts are small and one cannot conclude that a G peak of 1560 cm^- shows an amorphous carbon. The lack of a definite shift in the G peak suggests that there is no observable chemical change taking place under these experimental conditions. A graph illustrating the shift in the G peak compared to the gamma irradiation dose is shown below.

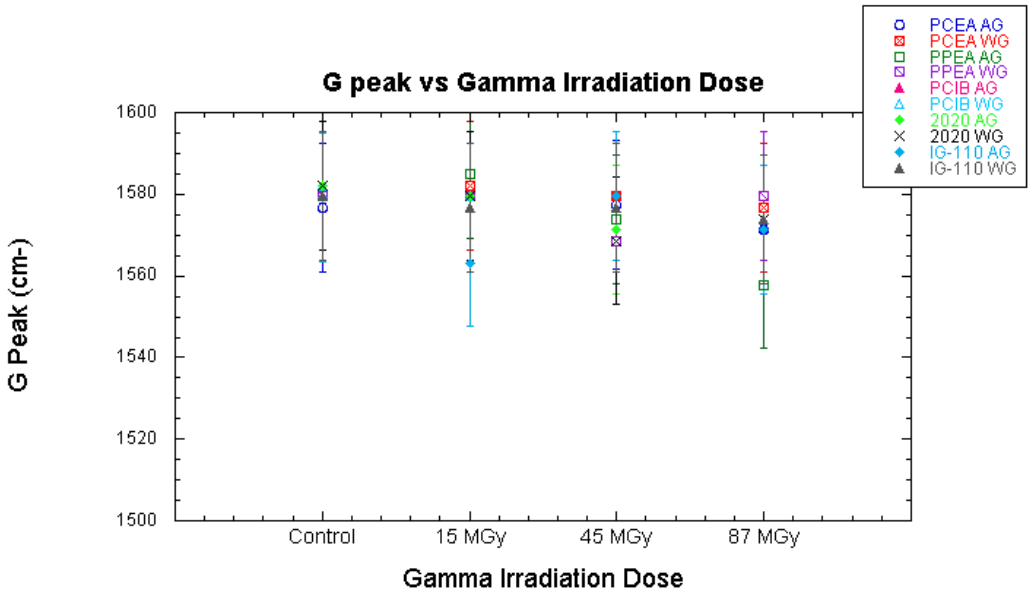

Figure 9-5: Comparison of the shift in the G peak compared to the gamma irradiation dose.

As stated previously, the intensity ratio I_D/I_G for the D band and G band is widely used for characterizing the defect quantity in graphitic materials. The table below shows the I_D/I_G for the various experiments conducted. Ten Raman spectra for each sample were used to calculate the I_D/I_G. The average value is listed as the I_D/I_G. From the 10 Raman spectra the sample standard deviation was calculated using the following equation:

$$s = \sqrt{\frac{\sum_{i=1}^{N}(x_i - \boldsymbol{x})^2}{N-1}} \quad [Skoog, et\ al., 1988]$$

where N is the number of samples, x is the individual sample and **x** is the sample mean. The standard deviation was then used to calculate the 95% confidence limit using the following equation.

$$95\ \%\ Confidence\ Limit = \boldsymbol{x} \pm \frac{zs}{\sqrt{N}} \quad [Skoog, et\ al., 1988]$$

where **x** is the sample mean, s is the sample standard deviation, N is the number of samples and z is 1.96 (from Skoog, et al. Table 2-5) [1988]. These values can be seen in the table below. Even though the samples were measured ten times, the 95 % confidence limit is still large compared to the ratio values. This is due to the topography of the samples. The graphites are rough and contain many divots. The variation in the surface of the graphite leads to variations in the intensities of the Raman spectra.

Graphite	Irradiation	I_D/I_G	95% Confidence Limit	L_a	I_{2D}/I_G	95% Confidence Limit
PCEA AG	Control	0.21	0.01	91.55	0.40	0.01
	Gamma 15 MGy	0.25	0.06	76.90	0.50	0.05
	Gamma 45 MGy	0.31	0.13	62.01	0.37	0.05
	Gamma 87 MGy	0.29	0.01	66.29	0.46	0.05
	AFRRI 1	0.31	0.02	62.01	0.53	0.01
	AFRRI 2	0.25	0.01	76.90	0.39	0.01
	Htr	0.35	0.05	54.93	0.46	0.08
	Room Temp No Irr	0.25	0.06	76.90	0.45	0.07
	Room Temp Irr	0.29	0.04	66.29	0.42	0.05
	1000 C No Irr	0.30	0.04	64.08	0.42	0.05
	1000 C Irr	0.22	0.05	87.38	0.35	0.05
PCEA WG	Control	0.34	0.04	56.54	0.43	0.02
	Gamma 15 MGy	0.23	0.03	83.59	0.50	0.04
	Gamma 45 MGy	0.25	0.04	76.90	0.52	0.06
	Gamma 87 MGy	0.32	0.01	60.08	0.51	0.03
	AFRRI 1	0.35	0.04	54.93	0.48	0.02
	AFRRI 2	0.37	0.04	51.96	0.53	0.05
	Htr	0.31	0.04	62.01	0.48	0.02
	Room Temp No Irr	0.33	0.10	58.26	0.50	0.06
	Room Temp Irr	0.32	0.10	60.08	0.47	0.05
	1000 C No Irr	0.28	0.11	68.66	0.38	0.13
	1000 C Irr	0.37	0.10	51.96	0.38	0.09
PPEA AG	Control	0.25	0.05	76.90	0.49	0.06
	Gamma 15 MGy	0.38	0.05	50.59	0.59	0.08
	Gamma 45 MGy	0.33	0.08	58.26	0.52	0.07
	Gamma 87 MGy	0.26	0.04	73.94	0.48	0.08
	AFRRI 1	0.31	0.06	62.01	0.47	0.04

Graphite	Irradiation	I_D/I_G	95% Confidence Limit	L_a	I_{2D}/I_G	95% Confidence Limit
	AFRRI 2	0.29	0.03	66.29	0.46	0.03
	Htr	0.29	0.04	66.29	0.44	0.04
	Room Temp No Irr	0.37	0.09	51.96	0.47	0.11
	Room Temp Irr	0.38	0.06	50.59	0.47	0.04
	1000 C No Irr	0.25	0.08	76.90	0.42	0.05
	1000 C Irr	0.34	0.08	56.54	0.47	0.06
PPEA WG	Control	0.36	0.04	53.40	0.43	0.03
	Gamma 15 MGy	0.28	0.04	68.66	0.49	0.04
	Gamma 45 MGy	0.26	0.07	73.94	0.46	0.11
	Gamma 87 MGy	0.29	0.05	66.29	0.55	0.03
	AFRRI 1	0.29	0.02	66.29	0.38	0.03
	AFRRI 2	0.32	0.03	60.08	0.46	0.03
	Htr	0.32	0.04	60.08	0.44	0.03
	Room Temp No Irr	0.36	0.06	53.40	0.43	0.05
	Room Temp Irr	0.39	0.10	49.29	0.40	0.06
	1000 C No Irr	0.34	0.03	56.54	0.45	0.08
	1000 C Irr	0.32	0.10	60.08	0.39	0.06
PCIB AG	Control	0.35	0.05	54.93	0.42	0.07
	Gamma 15 MGy	0.32	0.04	60.08	0.48	0.03
	Gamma 45 MGy	0.32	0.04	60.08	0.44	0.05
	Gamma 87 MGy	0.34	0.03	56.54	0.50	0.06
	AFRRI 1	0.34	0.02	56.54	0.38	0.03
	AFRRI 2	0.28	0.04	68.66	0.43	0.01
	Htr	0.32	0.06	60.08	0.47	0.03
	Room Temp No Irr	0.37	0.05	51.91	0.40	0.05
	Room Temp Irr	0.39	0.05	49.29	0.39	0.06
	1000 C No Irr	0.30	0.05	64.08	0.51	0.04
	1000 C Irr	0.35	0.10	54.93	0.47	0.04
PCIB WG	Control	0.30	0.01	64.08	0.49	0.07
	Gamma 15 MGy	0.32	0.08	60.08	0.49	0.07
	Gamma 45 MGy	0.34	0.10	56.54	0.44	0.06
	Gamma 87 MGy	0.35	0.08	54.93	0.44	0.04
	AFRRI 1	0.34	0.04	56.54	0.41	0.06
	AFRRI 2	0.36	0.06	53.40	0.38	0.04
	Htr	0.28	0.04	68.66	0.44	0.04
	Room Temp No Irr	0.30	0.08	64.08	0.39	0.05
	Room Temp Irr	0.39	0.05	49.29	0.42	0.04
	1000 C No Irr	0.29	0.10	65.78	0.43	0.05

Graphite	Irradiation	I_D/I_G	95% Confidence Limit	L_a	I_{2D}/I_G	95% Confidence Limit
	1000 C Irr	0.32	0.08	60.08	0.46	0.11
2020 AG	Control	0.25	0.04	76.90	0.48	0.08
	Gamma 15 MGy	0.30	0.05	64.08	0.47	0.04
	Gamma 45 MGy	0.27	0.04	71.20	0.48	0.03
	Gamma 87 MGy	0.37	0.04	51.96	0.51	0.02
	Room Temp No Irr	0.36	0.06	53.40	0.38	0.04
	Room Temp Irr	0.33	0.08	58.26	0.47	0.04
	1000 C No Irr	0.29	0.09	66.29	0.47	0.04
	1000 C Irr	0.39	0.05	49.29	0.43	0.04
2020 WG	Control	0.31	0.07	62.01	0.47	0.08
	Gamma 15 MGy	0.32	0.07	60.08	0.48	0.06
	Gamma 45 MGy	0.36	0.03	53.40	0.50	0.04
	Gamma 87 MGy	0.34	0.07	56.54	0.54	0.11
	Room Temp No Irr	0.31	0.03	62.01	0.51	0.07
	Room Temp Irr	0.33	0.06	58.26	0.43	0.07
	1000 C No Irr	0.33	0.08	58.26	0.46	0.04
	1000 C Irr	0.35	0.06	54.93	0.49	0.04
IG-110 AG	Control	0.25	0.06	76.90	0.49	0.05
	Gamma 15 MGy	0.31	0.01	62.86	0.40	0.02
	Gamma 45 MGy	0.32	0.10	60.08	0.39	0.06
	Gamma 87 MGy	0.38	0.06	50.59	0.55	0.03
	Room Temp No Irr	0.35	0.07	54.93	0.41	0.07
	Room Temp Irr	0.38	0.10	50.59	0.45	0.07
	1000 C No Irr	0.35	0.07	54.93	0.48	0.05
	1000 C Irr	0.36	0.11	53.40	0.44	0.04
IG-110 WG	Control	0.25	0.04	76.90	0.52	0.05
	Gamma 15 MGy	0.23	0.04	83.59	0.48	0.02
	Gamma 45 MGy	0.22	0.04	87.38	0.52	0.03
	Gamma 87 MGy	0.29	0.07	66.29	0.49	0.07
	Room Temp No Irr	0.28	0.10	68.66	0.42	0.06
	Room Temp Irr	0.30	0.08	64.08	0.50	0.04
	1000 C No Irr	0.26	0.09	73.94	0.42	0.04
	1000 C Irr	0.24	0.06	80.10	0.41	0.02

Table 9-3: I_D/I_G and I_{2D}/I_G including 95 % confidence levels for each experimental condition. Also shown are the calculated L_a values.

Another cause for the large 95 % confidence level values is due to the different types of graphite analyzed. The graphite pore sizes themselves vary widely between the samples, as seen in the table below. This also causes changes in the surface of the graphite samples. Images of all the graphite samples can be found in Appendix C. These images show the drastic differences in the surfaces of the graphite based on the particle size of the sample.

Graphite Type	Forming Method	Max Particle Size (μm)
PPEA	Extruded	760
PCEA	Extruded	800
PCIB	Isomolded	<1000
2020	Isomolded	15
IG-110	Isomolded	10 (mean)

Table 9-4: This table shows the 5 types of graphite used in the experiments. It lists their forming method and maximum particle size [NRC, 2010].

The changes between the control samples and the other conditions are small, approximately 0.1. Theodosiou *et al.* [2012] investigated ion-induced damage on graphite by using He^+ and Xe^+. Their results showed much larger changes in I_D/I_G, approximately 0.8 for 100 seconds of irradiation. The ion flux the samples were irradiated with produced an ion flux of approximately 5.0×10^{16} ions m^{-2} s^{-1}. As shown by that investigation, ions have a very pronounced damaging effect of the structure of the graphite. This is due to the Coulombic interaction between the ions and the carbon atoms. The flux for those experiments was much higher that the conditions at the east beam port of the reactor. The experiments conducted here have shown that gamma and neutron irradiations do not affect the structure of the graphite in the same way as ion irradiations.

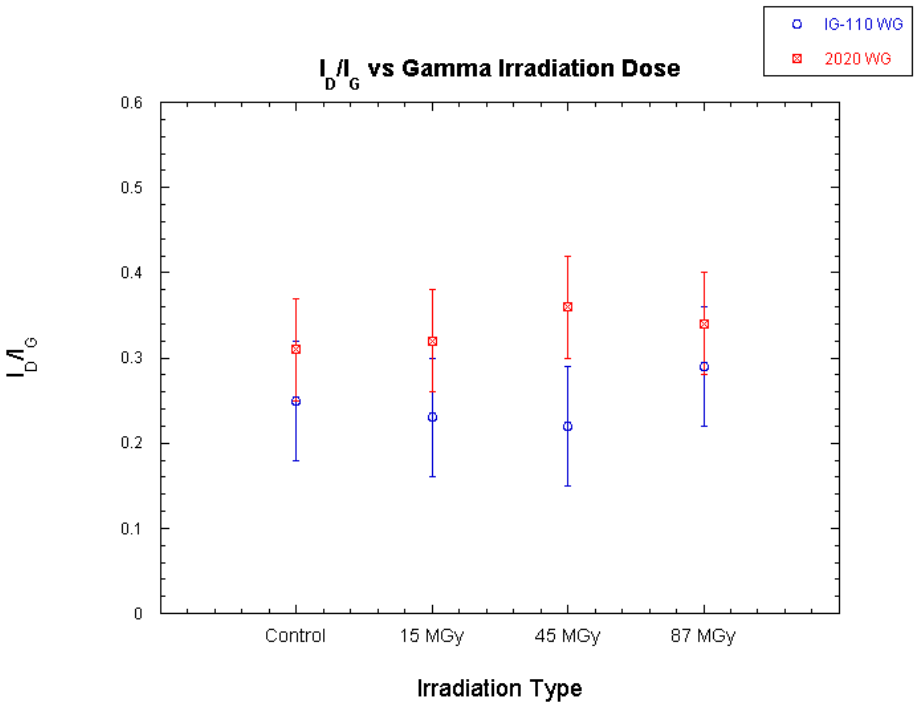

Figure 9-6: I_D/I_G ratio compared to the gamma irradiation dose of the samples. Error bars represent 95 % confidence levels.

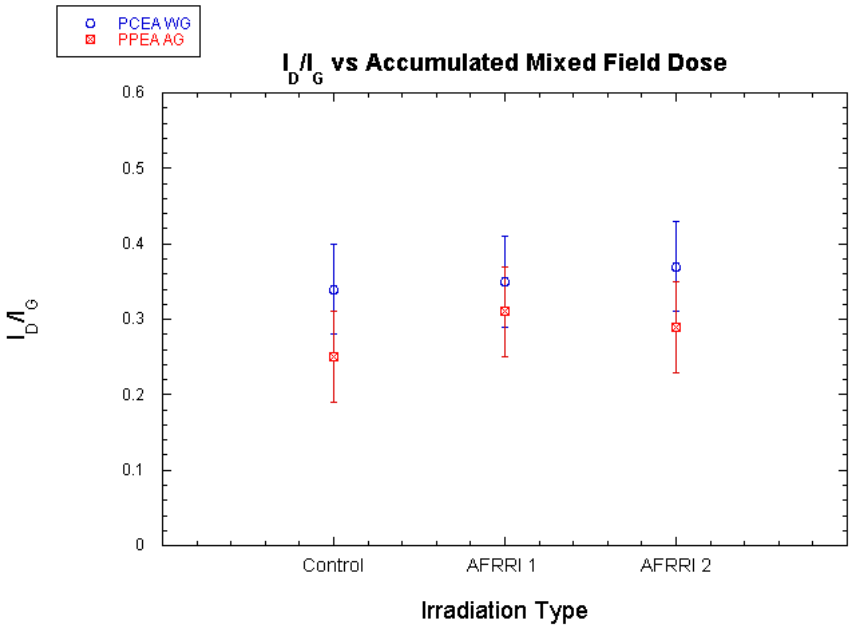

Figure 9-7: I_D/I_G ratio compared to the AFRRI mixed field irradiation doses. Error bars represent calculated 95 % confidence levels.

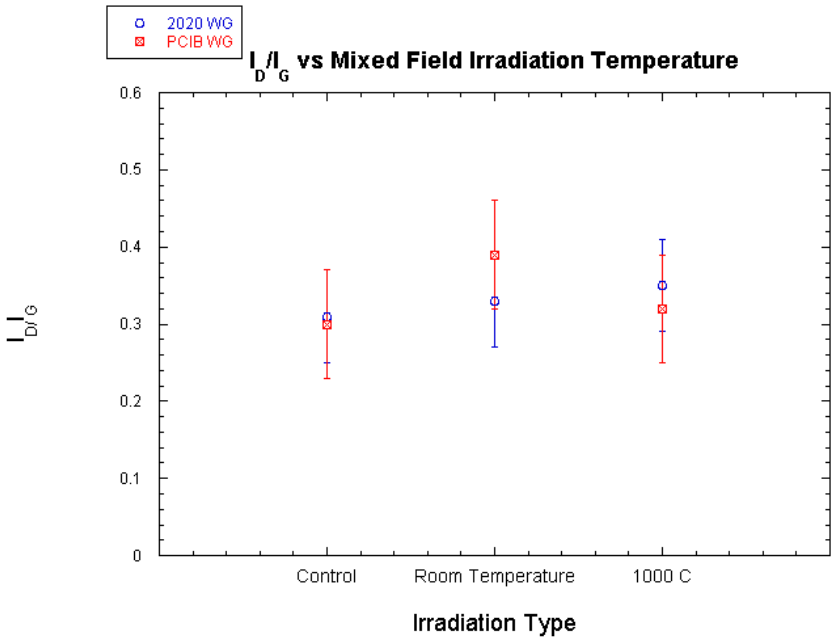

Figure 9-8: I_D/I_G ratio compared to the room temperature and 1000 °C mixed field irradiations conducted at the east beam port of the MUTR. Error bars represent 95 % confidence levels.

The neutron fluence limit placed on the graphite for use in HTGRs is 8 x 10^{25} n/cm^2 [NRC, 2010]. This number is based on degradation of the graphite due to stress and creep. The highest fluence received by the graphite samples was 5.4 x 10^{17} n/cm^2, received by the AFRRI 2 samples. The AFRRI 1 and rabbit heated samples each received a neutron fluence of 2.7 x 10^{17} n/cm^2. The east beam port experiments received a neutron fluence of 8.8 x 10^{11} n/cm^2. The average flux for a HTGR is approximately 1 x 10^{13} n cm^{-2} s^{-1} [NRC, 2010]. Due to the large flux of a full scale operating reactor, these experimental samples only received a small fraction of the fluence limit.

The Raman results suggest that neutron and gamma irradiation is not inducing an observable chemical change in the graphite. This can be explained by examining the effects of annealing on the graphite. Graphite annealing has long been studied. A summary of the

early graphite annealing experiments was written by Burton and Neubert in 1956. However, annealing studies are still ongoing due to the growth of interest in graphene and a lack in understanding of the chemical and dynamic properties of clusters of interstitials [Zerbetto, 1990].

The damaged caused by neutron irradiation can be divided into two categories, interstitials and vacancies. Interstitial atoms can be either sessile or mobile. As the groups of interstitial atoms become larger, their mobility decreases. Interstitial atoms have a migration energy of approximately 1 eV and are mobile at room temperature. Above 200 ºC, these interstitials can form into clusters of 2 to 4 atoms. As the temperature increases above 300 ºC, more interstitial atoms form together and begin to grow new basal planes. This new growth continues to temperatures up to 1400 ºC, where recombination with vacancies is more likely [Burchell, 2001]. As irradiation continues, the number of interstitial groups continues to increase. At a certain point, the likelihood of a newly formed interstitial combining with a mobile group will be less than the likelihood of combining with a sessile group. At this point the number of immobile groups continues to increase but the total number of interstitial groups remains the same.

The migration energy for a mono-vacancy is approximately 1.7 eV. Below 300º C, vacancies tend to be immobile but their mobility increases with increasing temperature. Between 300 ºC and 400 ºC, clusters of 2 to 4 vacancies diffuse through the basal plane. These vacancies begin to form loops above 650 ºC. The dislocation loops are formed by the additional of removal of a partial plane. As temperatures increase above 900 ºC, these vacancy loops give rise to collapsing vacancy lines [Burchell, 2001]. A more detailed discussion of interstitial and vacancies can be found in Chapter 3.

Because the fluence levels for these experiments were relatively low, it is assumed that an equilibrium was established between the neutron damage and the annealing effects. As stated above, at room temperature the interstitials formed are highly mobile and able to recombine with the sessile vacancies. In order to prove that this indeed was the case, irradiations at liquid nitrogen temperatures would need to be performed where the interstitials would be trapped in place. The Raman results would then be compared to show the differences between the equilibrium and non-equilibrium conditions.

Because these experiments were conducted on five very different types of graphite, these results could be used as an initial screening for future graphite types. For example, if a new type of graphite showed large Raman spectra changes under these conditions, additional experiments would need to be conducted to determine the causes and it could be deduced that the particular type of graphite would not be a good choice for a moderator in a nuclear reactor. These experimental results suggest that the use of these particular types of graphite could be chosen as a moderator in nuclear power plants because their structure allows them to withstand the gamma and neutron flux encountered in the reactor core.

9.1.3 Determining the oxygen content of graphite using XPS

The XPS data were collected on a Kratos Axis 165 (Manchester, U.K.) operating in hybrid mode using monochromatic Al Kα radiation (1486.6 eV) at 240 W at the UMD Nanocenter. The samples were mounted with double sided carbon tape, and the pressure of the instrument remained below 1×10^{-8} Torr throughout the data collection. Survey spectra were collected at a pass energy of 160 eV, while high resolution spectra were collected at a pass energy of 20 eV [Brozena, 2010]. All peaks were calibrated to the C1s peak at 284.8 eV.

The samples were cleaned with methanol prior to being analyzed. Upon first analysis, it was noted that some of the samples contained copper impurities. At first this was attributed to the sample cutting process, which used zinc coated copper wire. The contaminated samples were lightly sanded with SiC paper and rerun. After further investigation, it was determined that the copper impurities were coming from the methanol bottle in the laboratory. This bottle was removed and replaced and the samples were cleaned with the new bottle and rerun. No further copper impurities were noted.

9.1.3.1 Gamma irradiation effects

The table below summarizes all of the XPS gamma results. In general, the percent of oxygen increased with increasing gamma radiation. This is expected in the gamma radiation field since the gamma radiation induces oxidation in the graphite in air. The gamma radiation also raised the temperatures of the samples to approximately 100 °C during irradiation further increasing the oxidation of the graphite. A typical wide-range spectrum can also be seen below.

Graphite	C1s Peak	C1s Percent	O1s Peak	O1s Percent
PCEA AG				
Control	284.8	96.1 +/- 1.9	533.2	3.9 +/- 0.1
15 MGy Gamma	284.8	94.1 +/- 1.9	532.7	5.9 +/- 0.1
45 MGy Gamma	284.8	78.8 +/- 1.6	532.9	21.2 +/- 0.4
87 MGy Gamma	284.8	95.4 +/- 1.9	532.4	4.7 +/- 0.1
PCEA WG				
Control	284.8	94.7 +/- 1.9	533	5.3 +/- 0.1
15 MGy Gamma	284.8	93.3 +/- 1.9	532.7	6.7 +/- 0.1
45 MGy Gamma	284.8	87.3 +/- 1.7	532.3	12.7 +/- 0.3

Graphite	C1s Peak	C1s Percent	O1s Peak	O1s Percent
87 MGy Gamma	284.8	94.6 +/- 1.9	532.5	5.4 +/- 0.1
PPEA AG				
Control	284.8	96.2 +/- 1.9	532.5	3.8 +/- 0.1
15 MGy Gamma	284.8	96.4 +/- 1.9	532.5	3.6 +/- 0.1
45 MGy Gamma	284.8	91.8 +/- 1.8	532.8	8.3 +/- 0.2
87 MGy Gamma	284.8	95.6 +/- 1.9	532.5	4.4 +/- 0.1
PPEA WG				
Control	284.8	97.3 +/- 1.9	533.2	2.8 +/- 0.1
15 MGy Gamma	284.8	96.8 +/- 1.9	532.6	3.2 +/- 0.1
45 MGy Gamma	284.8	85.8 +/- 1.7	532.5	14.2 +/- 0.3
87 MGy Gamma	284.8	93.9 +/- 1.9	532.2	6.1 +/- 0.1
PCIB AG				
Control	284.8	93.1 +/- 1.9	533.9	6.8 +/- 0.1
15 MGy Gamma	284.8	96.2 +/- 1.9	532.6	3.8 +/- 0.1
45 MGy Gamma	284.8	87.1 +/- 1.7	532.1	12.9 +/- 0.3
87 MGy Gamma	284.8	92.7 +/- 1.9	531.8	7.3 +/- 0.1
PCIB WG				
Control	284.8	96.2 +/- 1.9	532.7	3.8 +/- 0.1
15 MGy Gamma	284.8	96.9 +/- 1.9	532.3	3.1 +/- 0.1
45 MGy Gamma	284.8	86.0 +/- 1.7	532.2	14.0 +/- 0.3
87 MGy Gamma	284.8	92.3 +/- 1.8	532.5	7.7 +/- 0.2
2020 AG				
Control	284.8	95.7 +/- 1.9	533	4.3 +/- 0.1
15 MGy Gamma	284.8	95.3 +/- 1.9	533	4.7 +/- 0.1
45 MGy Gamma	284.8	90.4 +/- 1.8	532.2	9.6 +/- 0.2
87 MGy Gamma	284.8	92.1 +/- 1.8	532.1	7.9 +/- 0.2
2020 WG				
Control	284.8	91.0 +/- 1.8	533.8	9.0 +/- 0.2
15 MGy Gamma	284.8	95.0 +/- 1.9	532.3	5.0 +/- 0.1

Graphite	C1s Peak	C1s Percent	O1s Peak	O1s Percent
45 MGy Gamma	284.8	84.1 +/- 1.7	531.9	15.9 +/- 0.3
87 MGy Gamma	284.8	94.9 +/- 1.9	532.2	5.2 +/- 0.1
IG-110 AG				
Control	284.8	96.2 +/- 1.9	532.5	3.8 +/- 0.1
15 MGy Gamma	284.8	96.1 +/- 1.9	532.9	3.9 +/- 0.1
45 MGy Gamma	284.8	92.3 +/- 1.8	532.1	7.6 +/- 0.2
87 MGy Gamma	284.8	91.4 +/- 1.8	531.8	8.6 +/- 0.2
IG-110 WG				
Control	284.8	95.1 +/- 1.9	532.5	4.9 +/- 0.1
15 MGy Gamma	284.8	93.9 +/- 1.9	533.1	6.1 +/- 0.1
45 MGy Gamma	284.8	87.3 +/- 1.7	532.3	12.8 +/- 0.3
87 MGy Gamma	284.8	87.7 +/- 1.8	532.6	12.3 +/- 0.2

Table 9-5: XPS results for the gamma irradiated graphite samples.

At high gamma doses, degassing was observed as the amount of oxygen decreased at 87 MGy. As the graphite is irradiated in air, it absorbs water and O_2. The oxygen will react with the carbon in the following equations:

$$2C\ (solid) + O_2\ (gas) \rightarrow 2CO\ (gas) \quad [Marsh, 1989]$$

$$C\ (solid) + O_2\ (gas) \rightarrow CO_2\ (gas) \quad [Marsh, 1989]$$

The reaction with oxygen and subsequent release of carbon dioxide and carbon monoxide from the carbon pores results in a decrease of oxygen on the surface of the graphite. The carbon reaction with water can be seen in the following reaction.

$$C\ (solid) + H_2O\ (gas) \rightarrow CO\ (gas) + H_2\ \ (gas) \quad [Marsh, 1989]$$

The hydrogen produced in this reaction reacts further with the graphite surface.

$$C\ (solid) + 2\ H_2\ (gas) \rightarrow CH_4\ (gas) \quad [Marsh, 1989]$$

These reactions are discussed in detail in Chapter 4. All four of these reaction result in the loss of carbon from the graphite sample in the form of CO and CO_2 and the release of gas.

The carbon dioxide that is produced will also react with the graphite surface through radiolysis. Gaseous carbon dioxide appears stable under radiolysis, except at very high dose rates. While the CO_2 appears stable, there is decomposition and recombination taking place. This process occurs when carbon dioxide is decomposed by the gamma radiation to form carbon monoxide and an oxygen free radical.

Gas Phase

$$CO_2 \rightarrow radiation \rightarrow CO + O^*$$

$$CO + O^* \rightarrow CO_2$$

Graphite Pore Surface

$$O^* + C \rightarrow CO$$

This reaction results in more carbon monoxide and carbon dioxide formation in the graphite leading to the reduction of oxygen on the surface on the graphite samples.

Another factor in the degasification of the graphite is the pore size of the graphite samples. Oxidation occurs primarily within the graphite pores, which initially makeup 20 % of the graphite volume [Linacre et. al., 1965]. Therefore, the smaller the pores in the graphite, the less oxidation is occurring in them. Li et al. studied to pore sizes of nuclear grade graphite and determined that the average pore sizes ranged from 5 to 35 μm. The

isostatically molded graphites have smaller pore sizes than those vibrationally molded or extruded. However, the IG-110 showed a much smaller pore size of 1.5 to 3 μm.

The IG-110 has the smallest pore size and the XPS results suggest that this results in further oxidation of the surface rather than degasification, as in the other graphite types. At 87 MGy, the IG-110 samples increase slightly in oxidation or remain the same. In the four other types of graphite, there is a large decrease in the percent of oxygen on the surface of the graphite with 87 MGy. In theory, the IG-110 retains a higher strength during gamma irradiation since carbon atoms are not lost through degasification. The XPS results for all of the gamma irradiated samples including IG-110 can be seen in the graphs below.

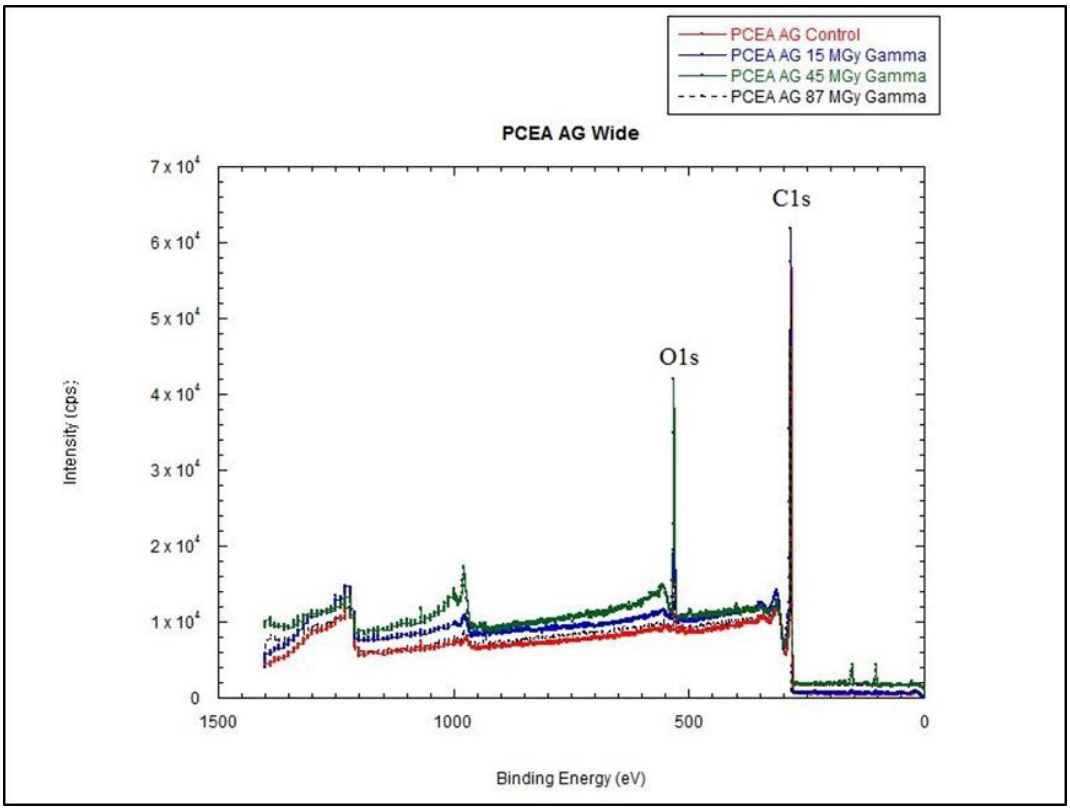

Figure 9-9: XPS wide-range spectrum for the gamma irradiated graphite samples of PCEA AG.

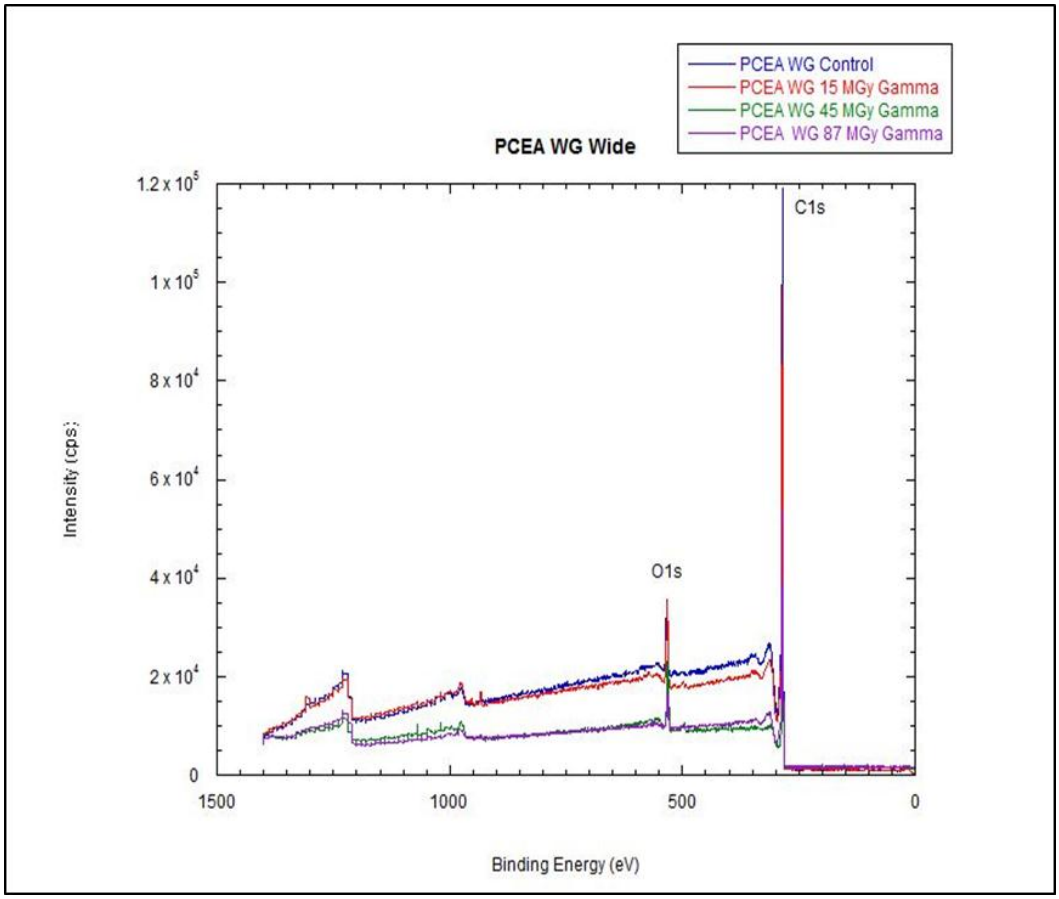

Figure 9-10: XPS wide-range spectrum for the gamma irradiated graphite samples of PCEA WG.

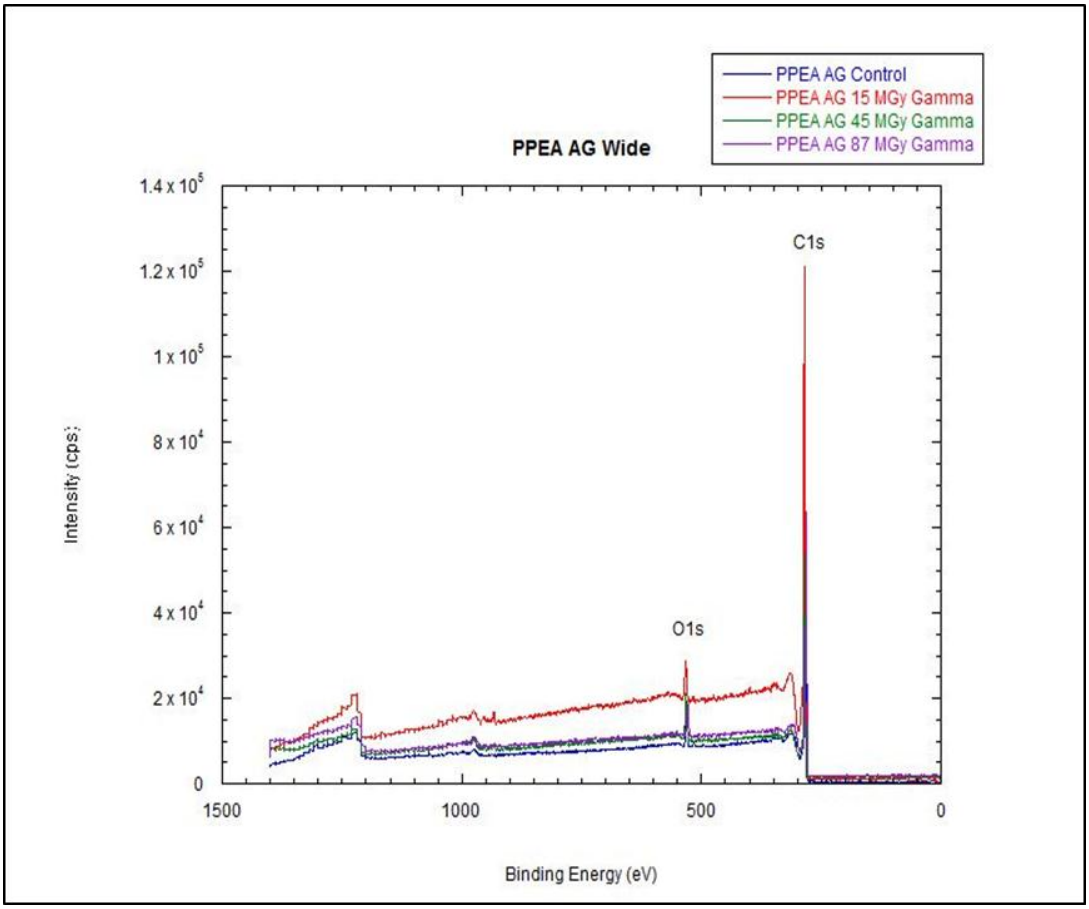

Figure 9-11: XPS wide-range spectrum for the gamma irradiated graphite samples of PPEA AG.

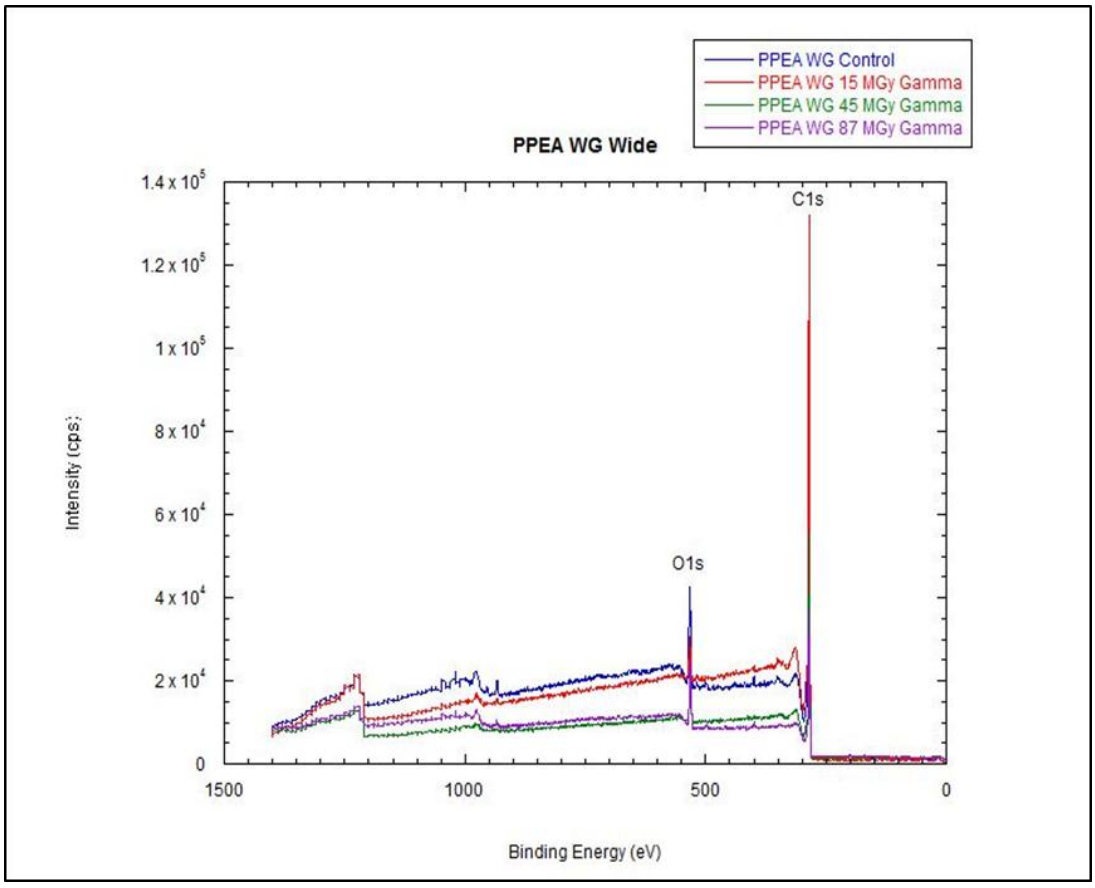

Figure 9-12: XPS wide-range spectrum for the gamma irradiated graphite samples of PPEA WG.

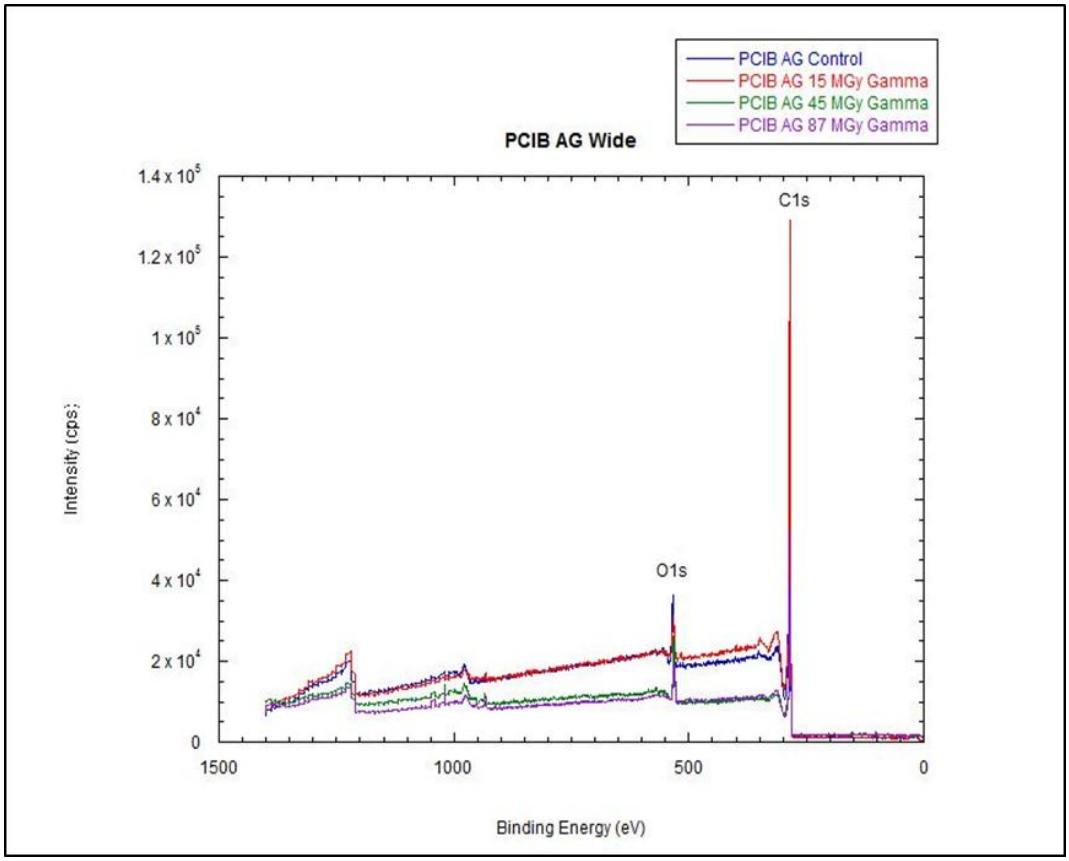

Figure 9-13: XPS wide-range spectrum for the gamma irradiated graphite samples of PCIB AG.

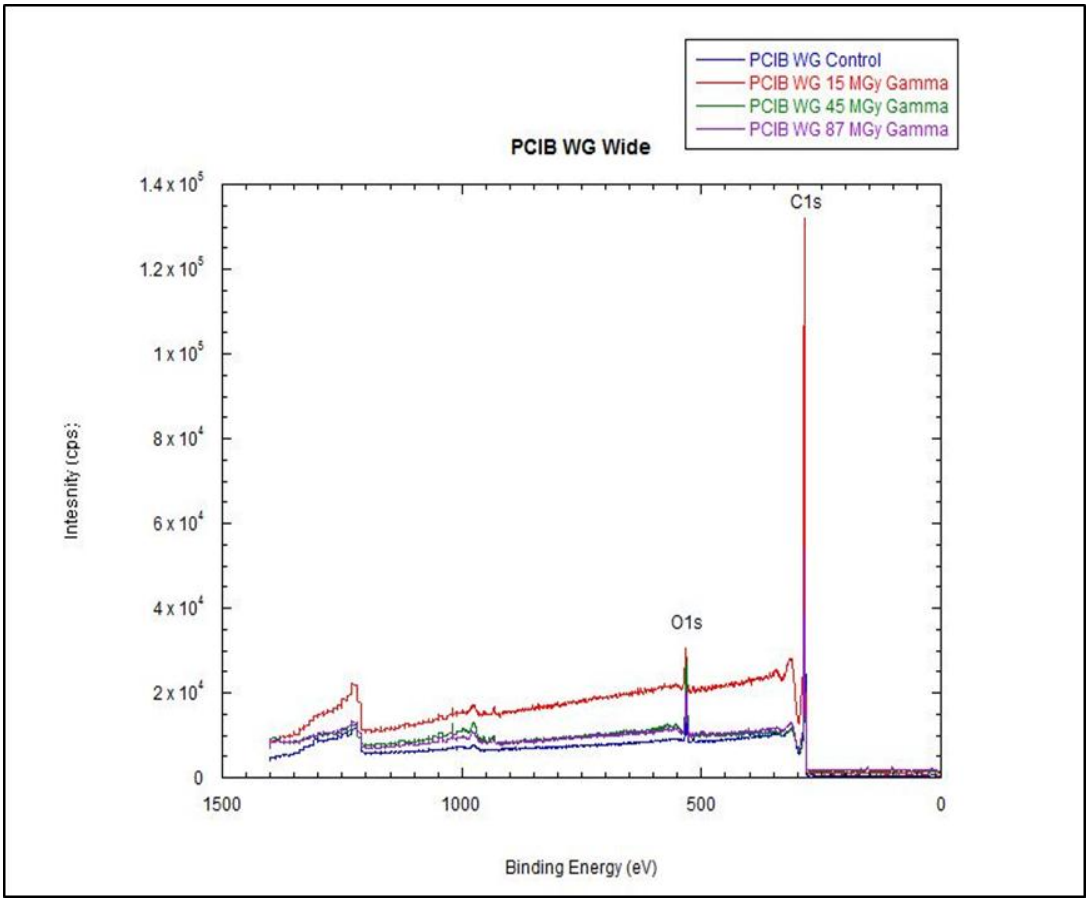

Figure 9-14: XPS wide-range spectrum for the gamma irradiated graphite samples of PCIB WG.

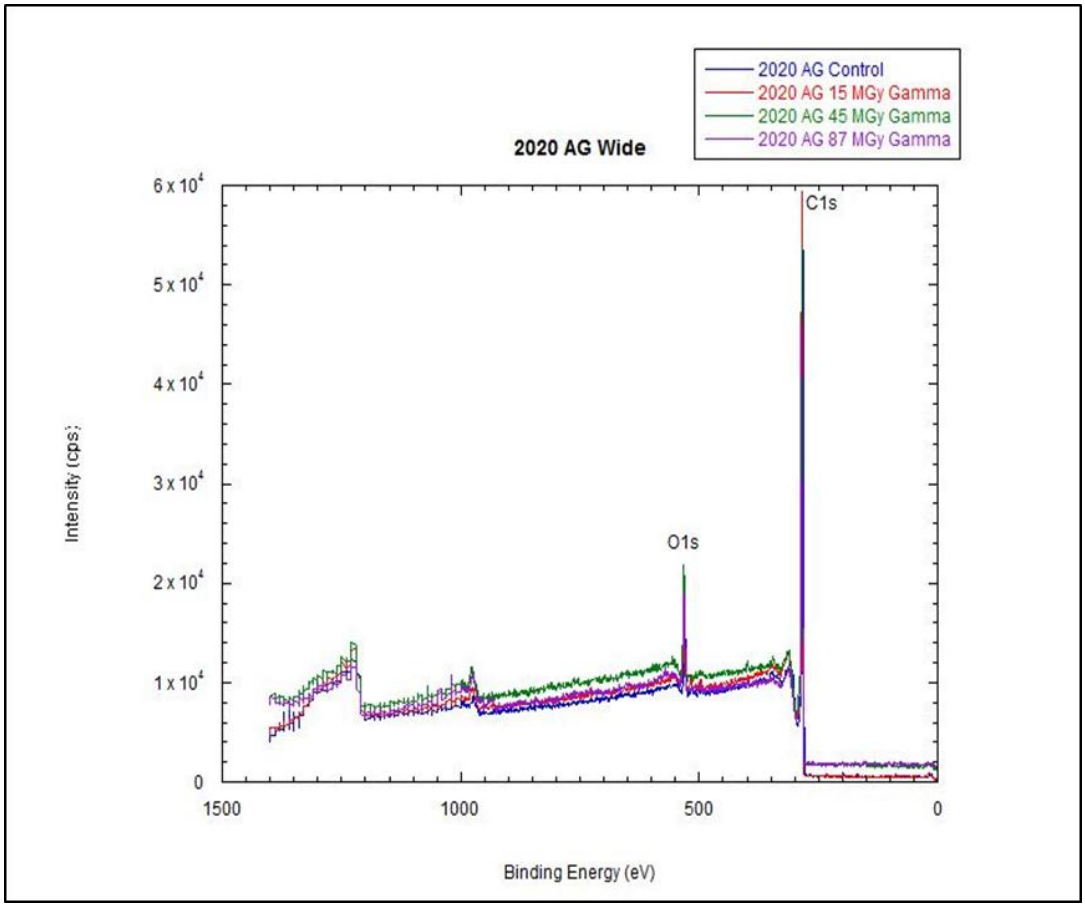

Figure 9-15: XPS wide-range spectrum for the gamma irradiated graphite samples of 2020 AG.

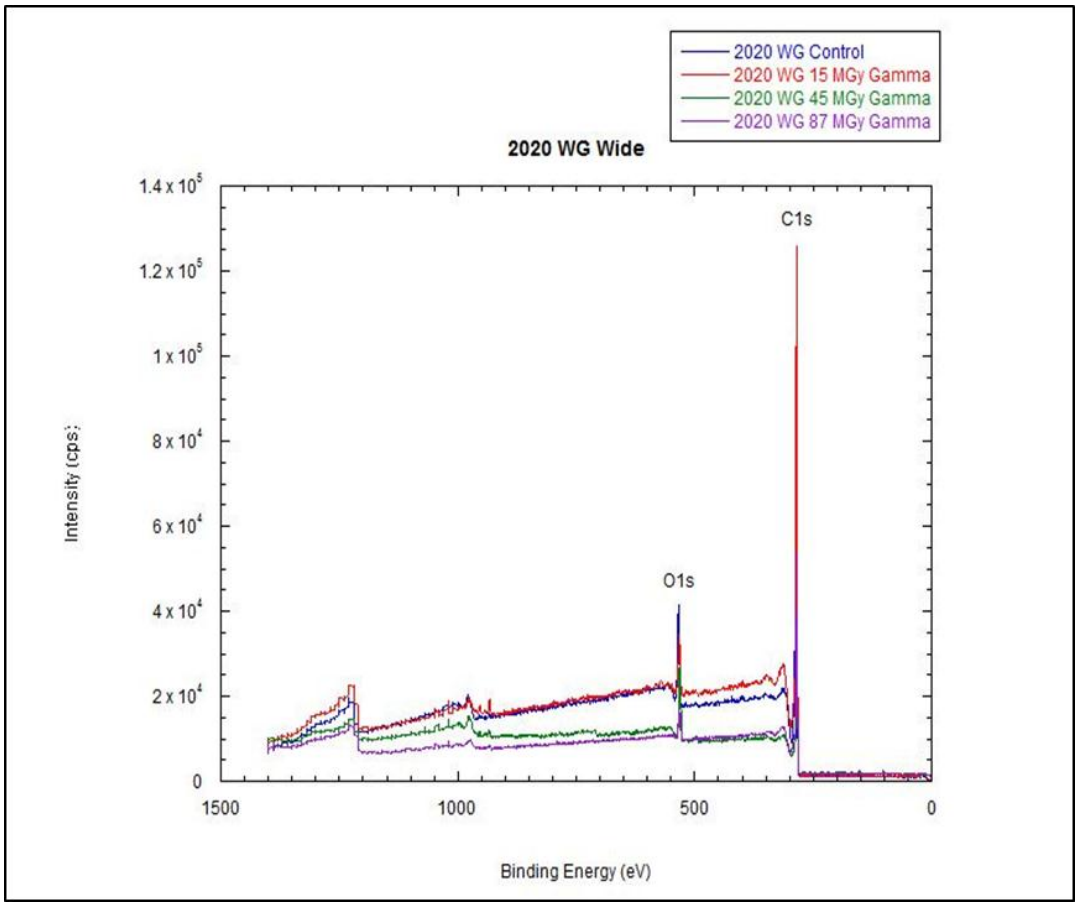

Figure 9-16: XPS wide-range spectrum for the gamma irradiated graphite samples of 2020 WG.

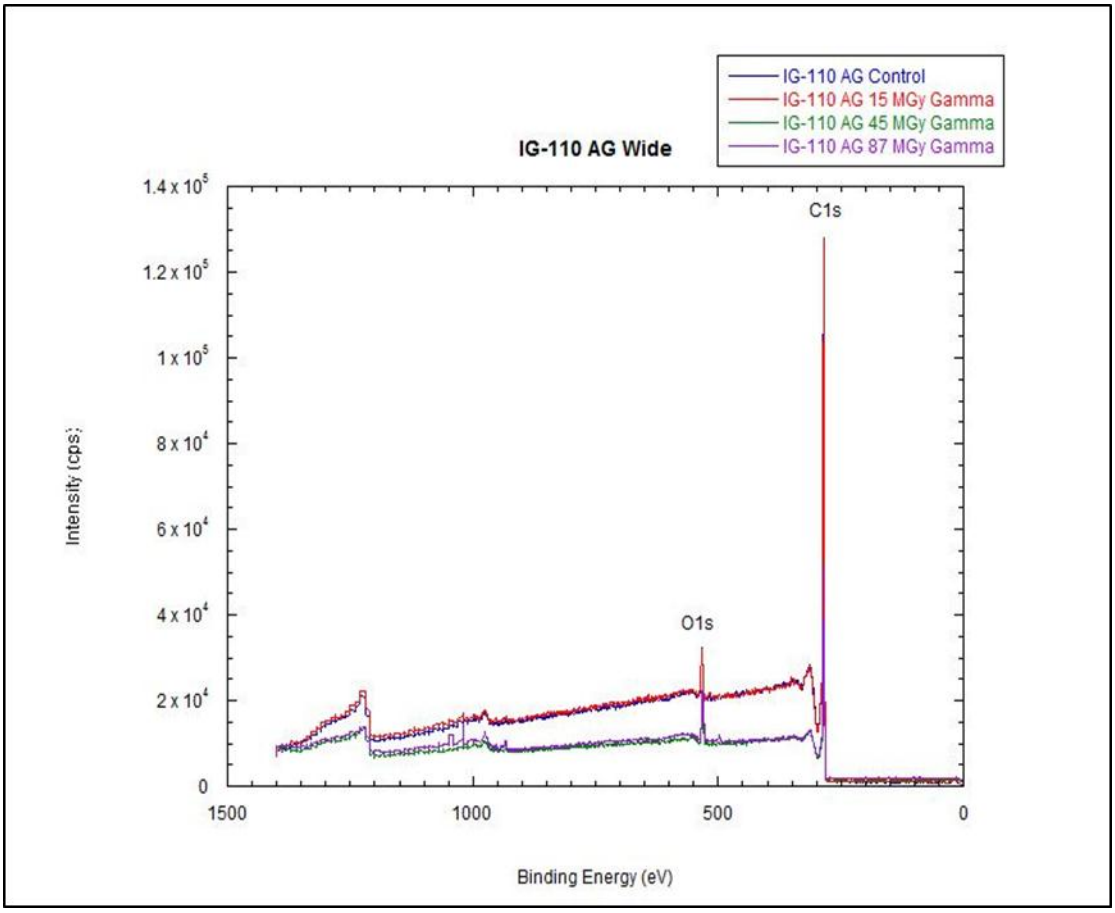

Figure 9-17: XPS wide-range spectrum for the gamma irradiated graphite samples of IG-110 AG.

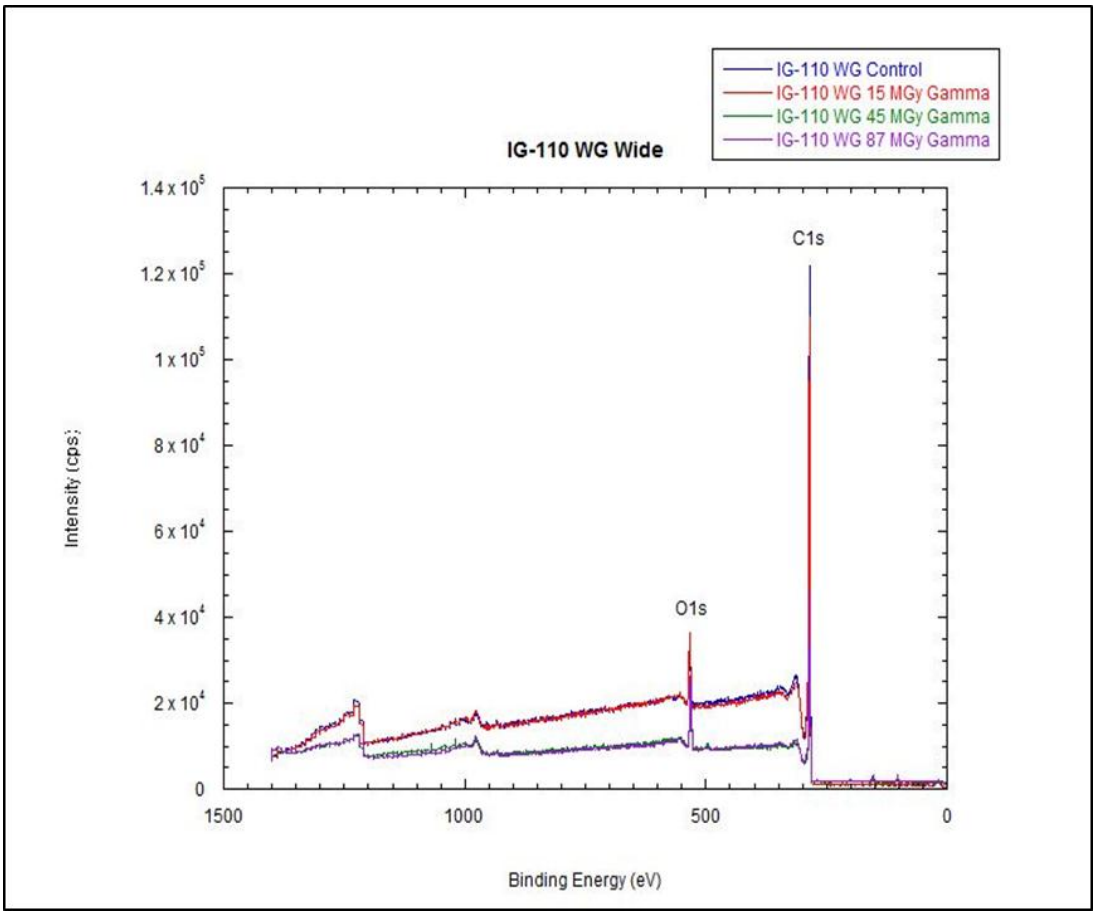

Figure 9-18: XPS wide-range spectrum for the gamma irradiated graphite samples of IG-110 WG.

9.1.3.2 Mixed field irradiation effects

The table below summarizes all of the mixed field irradiation XPS results. The first set of data if from the AFRRI and pneumatic system irradiations. PCEA, PPEA and PCIB samples were irradiation twice at AFRRI in air. The first AFRRI irradiation resulted in a total fluence of 2.7E17 n/cm^2. The second AFRRI irradiation doubled this dose to 5.4E17 n/cm^2. As seen in the table below, the results show that the oxygen present on the surface of the samples initially increased and then decreased with the second dose. This is consistent with the gamma irradiation data where the oxidation of the graphite increases until high doses

are reached that lead to degasification of the graphite through the formation of carbon monoxide and carbon dioxide.

Graphite	C1s Peak	C1s Percent	O1s Peak	O1s Percent
PCEA AG				
Control	284.8	96.7 +/- 1.9	533	3.3 +/- 0.1
AFRRI 1	284.8	93.0 +/- 1.9	533.1	7.0 +/- 0.1
AFRRI 2	284.8	97.2 +/- 1.9	533.2	2.8 +/- 0.1
RABBIT HTR	284.8	88.3 +/- 1.7	533.2	11.7 +/- 0.2
ROOM TEMP NO IRR	284.8	97.5 +/- 1.9	532.9	14.2 +/- 0.3
ROOM TEMP IRR	284.8	85.8 +/- 1.7	531.9	2.5 +/- 0.1
1000 C NO IRR	284.8	90.8 +/- 1.8	532	9.2 +/- 0.2
1000 C IRR	284.8	86.6 +/- 1.7	532.8	13.4 +/- 0.3
PCEA WG				
Control	284.8	97.7 +/- 2.0	533.2	2.3 +/- 0.1
AFRRI 1	284.8	95.9 +/- 1.9	533.2	4.1 +/- 0.1
AFRRI 2	284.8	97.4 +/- 1.9	532.6	2.6 +/- 0.1
RABBIT HTR	284.8	81.0 +/- 1.6	533.2	19.0 +/- 0.4
ROOM TEMP NO IRR	284.8	89.3 +/- 1.8	531.9	10.7 +/- 0.2
ROOM TEMP IRR	284.8	96.9 +/- 1.9	532.4	3.1 +/- 0.1
1000 C NO IRR	284.8	95.7 +/- 1.9	532.1	4.3 +/- 0.1
1000 C IRR	284.8	88.2 +/- 1.8	532.3	11.8 +/- 0.2
PPEA AG				
Control	284.6	96.1 +/- 1.9	532.8	3.9 +/- 0.1
AFRRI 1	284.8	93.9 +/- 1/9	533.2	6.1 +/- 0.1
AFRRI 2	284.8	96.8 +/- 1.9	533.4	3.2 +/- 0.1
RABBIT HTR	284.8	84.9 +/- 1.7	533.2	15.1 +/- 0.3
ROOM TEMP NO IRR	284.8	87.9 +/- 1.8	532.2	12.1 +/- 0.2
ROOM TEMP IRR	284.8	93.2 +/- 1.9	532.7	6.8 +/- 0.1

Graphite	C1s Peak	C1s Percent	O1s Peak	O1s Percent
1000 C NO IRR	284.8	92.0 +/- 1.8	532.2	8.0 +/- 0.2
1000 C IRR	284.8	88.3 +/- 1.8	532	11.7 +/- 0.2
PPEA WG				
Control	284.6	97.3 +/- 1.9	533.2	2.8 +/- 0.1
AFRRI 1	284.8	95.6 +/- 1.9	532.9	4.4 +/- 0.1
AFRRI 2	284.8	97.3 +/- 1.9	532.7	2.7 +/- 0.1
RABBIT HTR	284.8	64.2 +/- 1.3	533.4	35.8 +/- 0.7
ROOM TEMP NO IRR	284.8	86.3 +/- 1.7	532.3	13.7 +/- 0.3
ROOM TEMP IRR	284.8	94.8 +/- 1.9	532.7	5.2 +/- 0.1
1000 C NO IRR	284.8	95.2 +/- 1.9	532.2	4.8 +/- 0.1
1000 C IRR	284.8	91.0 +/- 1.8	531.9	9.0 +/- 0.2
PCIB AG				
Control	284.8	93.2 +/- 1.9	533.2	3.8 +/- 0.1
AFRRI 1	284.8	94.0 +/- 1.9	533.1	6.0 +/- 0.1
AFRRI 2	284.8	97.4 +/- 1.9	532.8	2.6 +/- 0.1
RABBIT HTR	284.8	88.8 +/- 1.8	533.3	11.2 +/- 0.2
ROOM TEMP NO IRR	284.8	87.3 +/- 1.7	532.4	12.7 +/- 0.3
ROOM TEMP IRR	284.8	96.6 +/- 1.9	532.9	3.5 +/- 0.1
1000 C NO IRR	284.8	94.4 +/- 1.9	531.1	5.6 +/- 0.1
1000 C IRR	284.8	92.2 +/- 1.8	532.3	7.8 +/- 0.2
PCIB WG				
Control	284.8	96.2 +/- 1.9	532.5	3.8 +/- 0.1
AFRRI 1	284.8	95.2 +/- 1.9	533	4.8 +/- 0.1
AFRRI 2	284.8	95.2 +/- 1.9	532.8	4.8 +/- 0.1
RABBIT HTR	284.8	82.7 +/- 1.7	533.1	17.3 +/- 0.3
ROOM TEMP NO IRR	284.8	97.4 +/- 1.9	532.3	11.0 +/- 0.2
ROOM TEMP IRR	284.8	89.0 +/- 1.8	532.6	2.7 +/- 0.1
1000 C NO IRR	284.8	94.5 +/- 1.9	532.8	5.5 +/- 0.1
1000 C IRR	284.8	93.3 +/- 1.9	531	6.7 +/- 0.1

Graphite	C1s Peak	C1s Percent	O1s Peak	O1s Percent
2020 AG				
ROOM TEMP NO IRR	284.8	89.2 +/- 1.8	532	10.8 +/- 0.2
ROOM TEMP IRR	284.8	93.7 +/- 1.9	532.4	6.3 +/- 0.1
1000 C NO IRR	284.8	92.3 +/- 1.8	532.3	7.7 +/- 0.2
1000 C IRR	284.8	90.1 +/- 1.8	531.6	9.9 +/- 0.2
2020 WG				
ROOM TEMP NO IRR	284.8	87.9 +/- 1.8	531.7	12.1 +/- 0.2
ROOM TEMP IRR	284.8	95.0 +/- 1.9	532.4	5.0 +/- 0.1
1000 C NO IRR	284.8	91.5 +/- 1.8	531	8.5 +/- 0.2
1000 C IRR	284.8	84.7 +/- 1.7	530.7	15.3 +/- 0.3
IG-110 AG				
ROOM TEMP NO IRR	284.8	96.8 +/- 1.9	532	3.2 +/- 0.1
ROOM TEMP IRR	284.8	93.5 +/- 1.9	532.2	6.5 +/- 0.1
1000 C NO IRR	284.8	92.5 +/- 1.8	531.8	6.4 +/- 0.1
1000 C IRR	284.8	93.6 +/- 1.9	532.3	7.6 +/- 0.2
IG-110 WG				
ROOM TEMP NO IRR	284.8	97.3 +/- 1.9	532.4	2.7 +/- 0.1
ROOM TEMP IRR	284.8	94.7 +/- 1.9	532	5.3 +/- 0.1
1000 C NO IRR	284.8	94.0 +/- 1.9	532.3	6.0 +/- 0.1
1000 C IRR	284.8	89.5 +/- 1.8	530.7	10.5 +/- 0.2

Table 9-6: XPS results for the mixed field irradiated graphite samples.

The samples that were irradiated in the pneumatic system received the same dose as the first AFRRI samples, 2.7E17 n/cm^2, but the samples were heated to 300 °C during the irradiation. The results show that the elevated temperature increased the oxidation of the graphite when compared to the same dose at room temperature. This temperature corresponds to region 1. Region 1 is control by kinetics and it corresponds to temperatures less than 700 ºC. The reactant gas concentration is uniform throughout the bulk of the carbon

sample and is equal to the concentration in the gas phase. This is also known as the "chemical" regime because the reaction rate is largely determined by the intrinsic reactivity of the graphite. The reaction rate with air only becomes significant as temperatures approach 400 ºC. At this temperature the rate of reaction is 3-8 x 10^{-10} kg/kg s. The XPS graphs showing the AFRRI and pneumatic system results for PCEA, PPEA and PCIB are shown below.

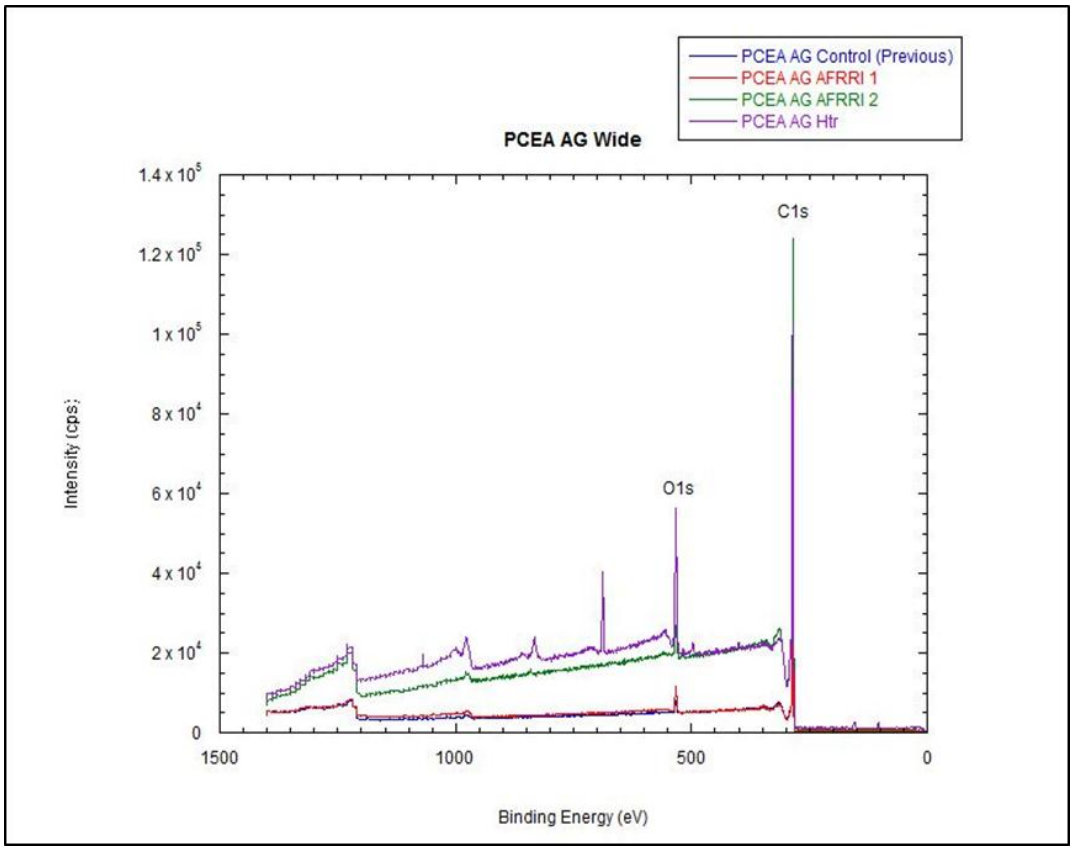

Figure 9-19: XPS spectra for PCEA AG control, AFRRI irradiated and 300 °C rabbit irradiated samples.

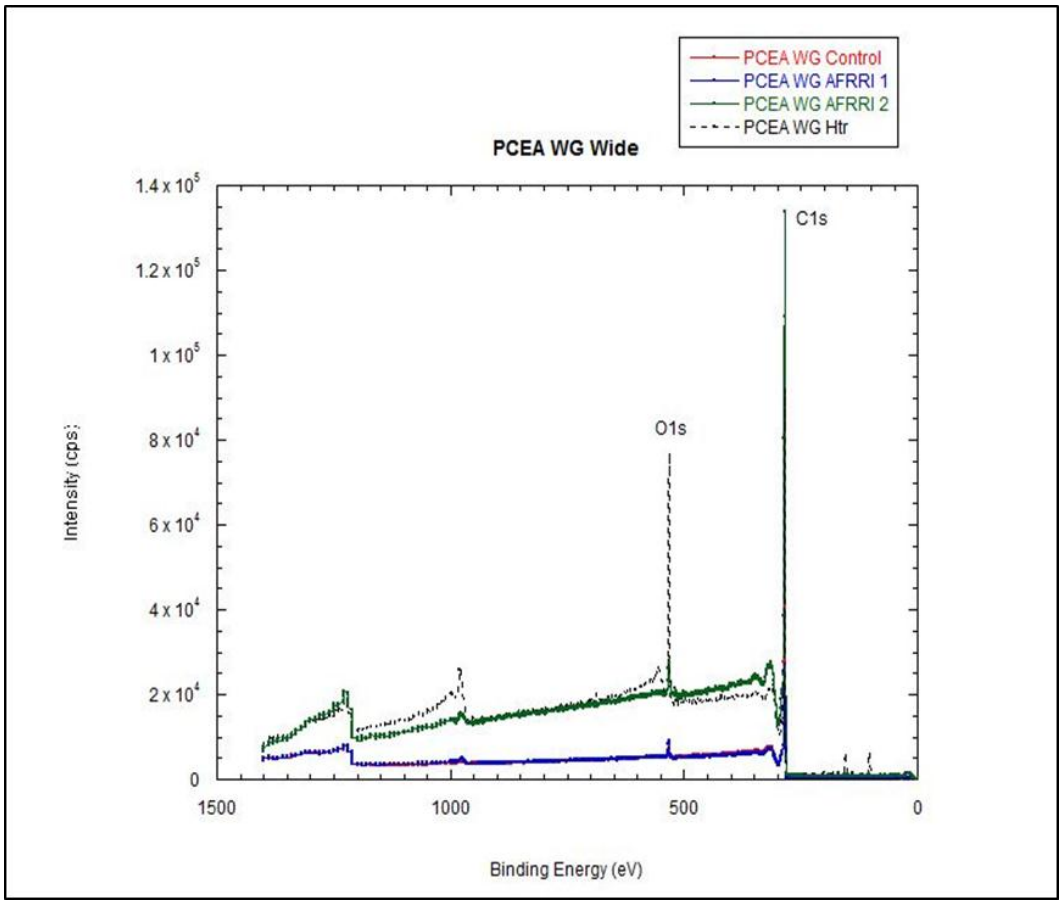

Figure 9-20: The graph above shows the results for the AFRRI irradiations and pneumatic system irradiation for PCEA WG.

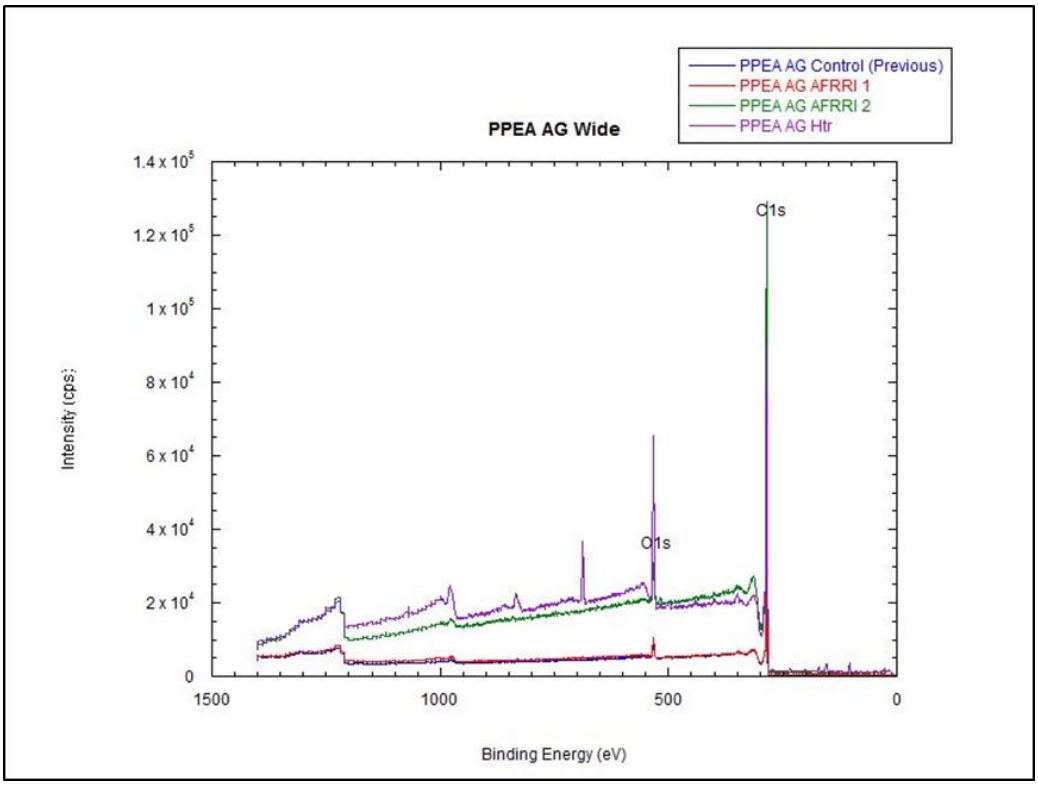

Figure 9-21: XPS spectra for PPEA AG control, AFRRI irradiated and 300 °C rabbit irradiated samples.

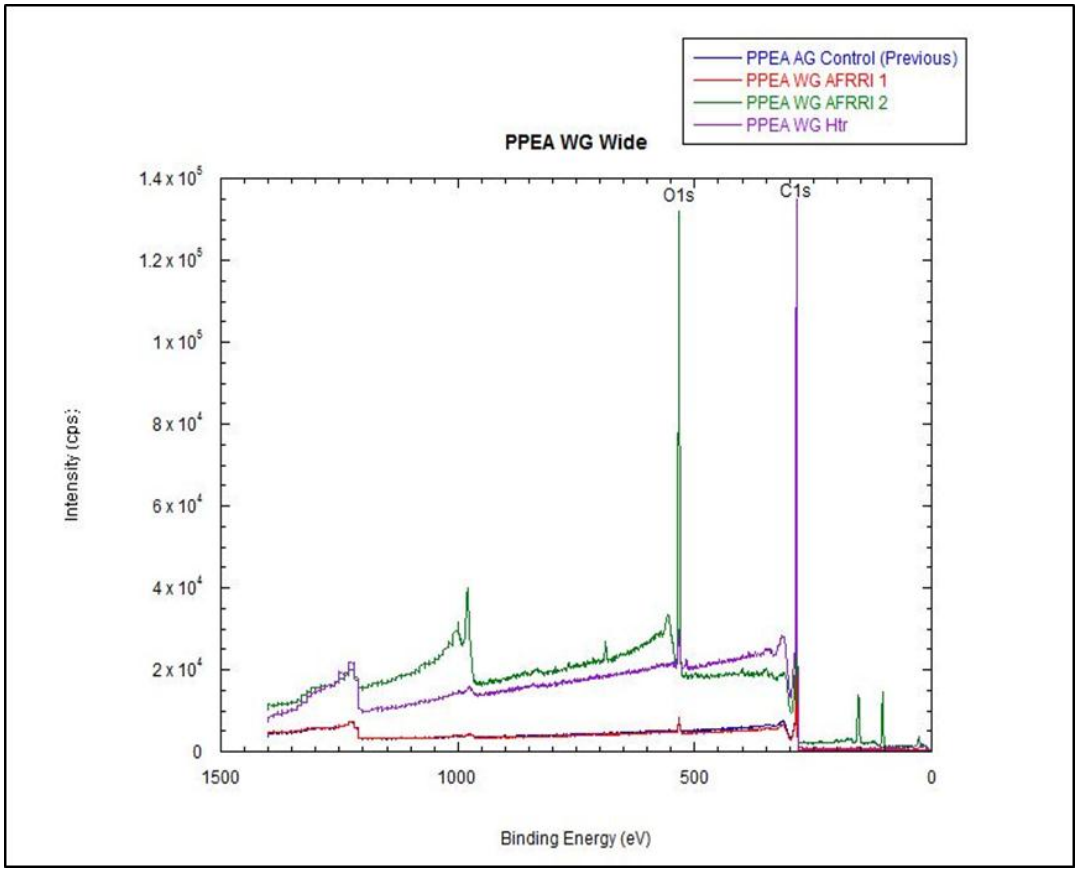

Figure 9-22: XPS spectra for PPEA WG control, AFRRI irradiated and 300 °C rabbit irradiated samples.

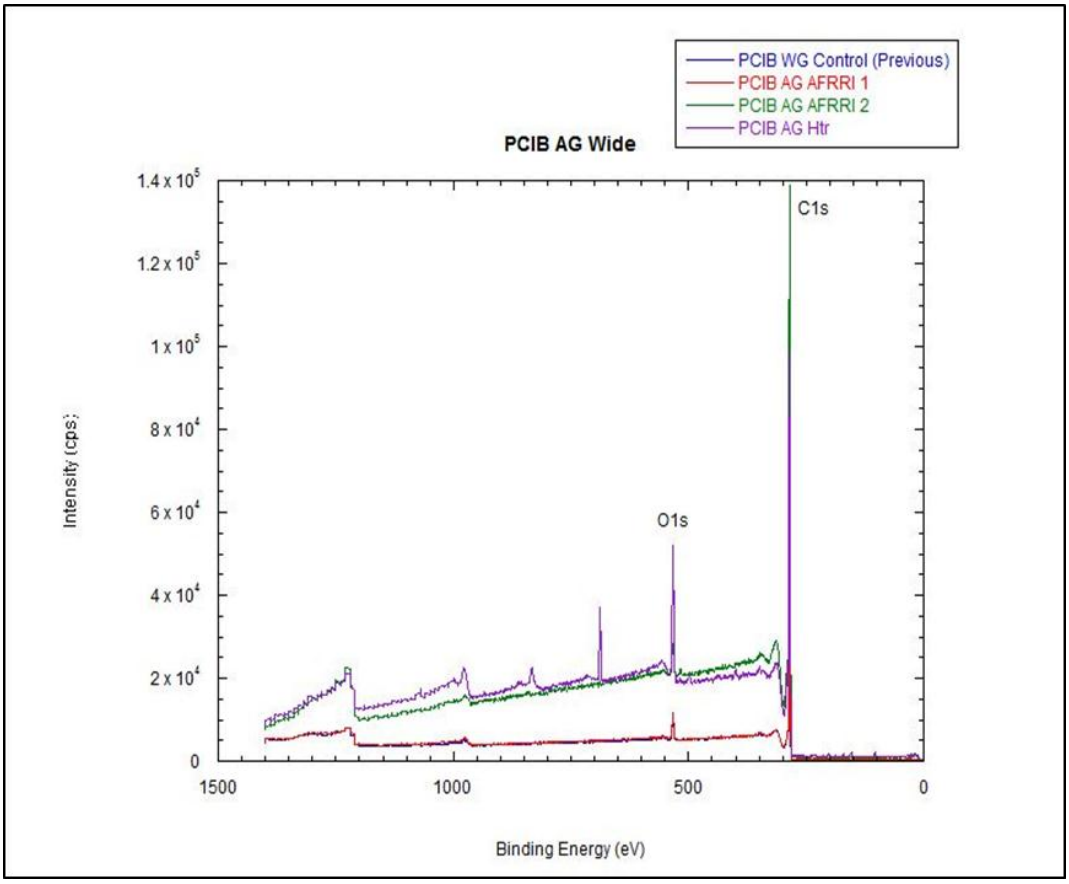

Figure 9-23: XPS spectra for PCIB AG control, AFRRI irradiated and 300 °C rabbit irradiated samples.

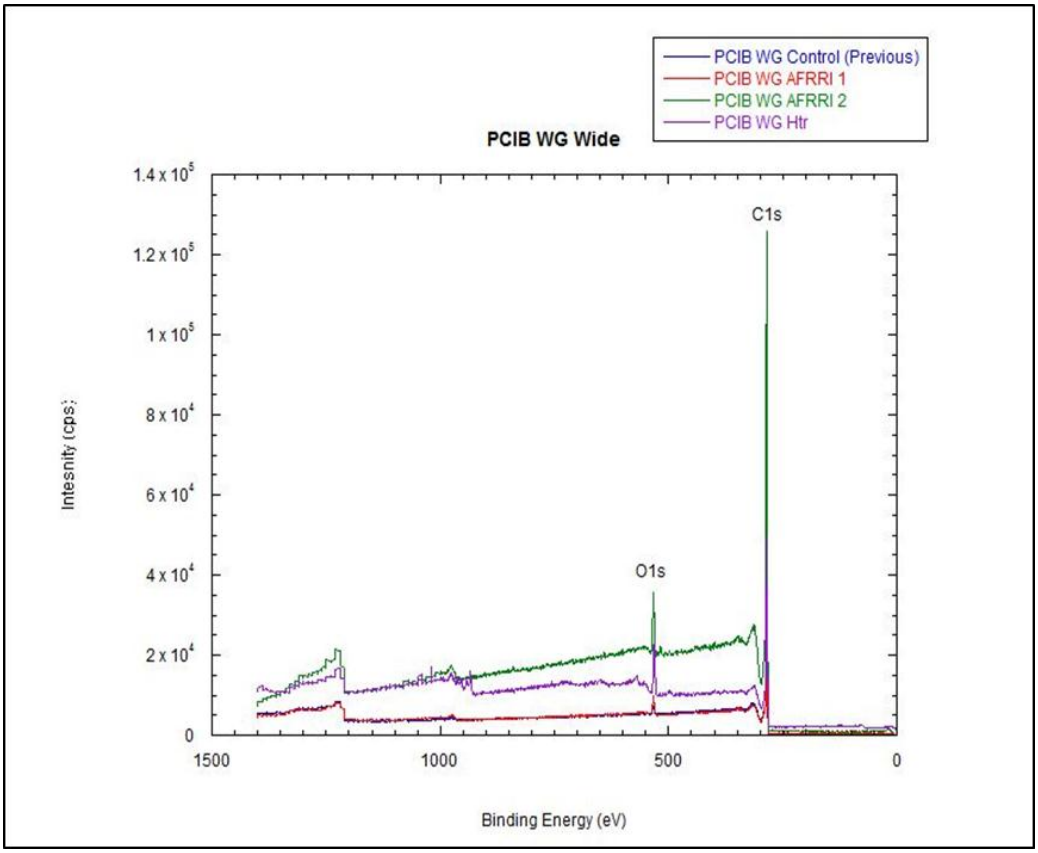

Figure 9-24: XPS spectra for PCIB AG control, AFRRI irradiated and 300 °C rabbit irradiated samples.

Two sets of experiments were run with all 5 types of graphite on the east beam port of the MUTR. The first set involved exposing the samples to the He-water mixture at room temperature. Half of the samples were irradiated and the other half were not. For the PCEA, PPEA, PCIB and 2020 graphites, the XPS results showed that the oxidation of the graphite without irradiation was higher than the percent of oxygen in the samples that were irradiated. This results show a degasification of the graphite under irradiation. This is consistent with the results seen in the AFRRI irradiation of the graphite. The XPS graphs illustrating this can be seen below.

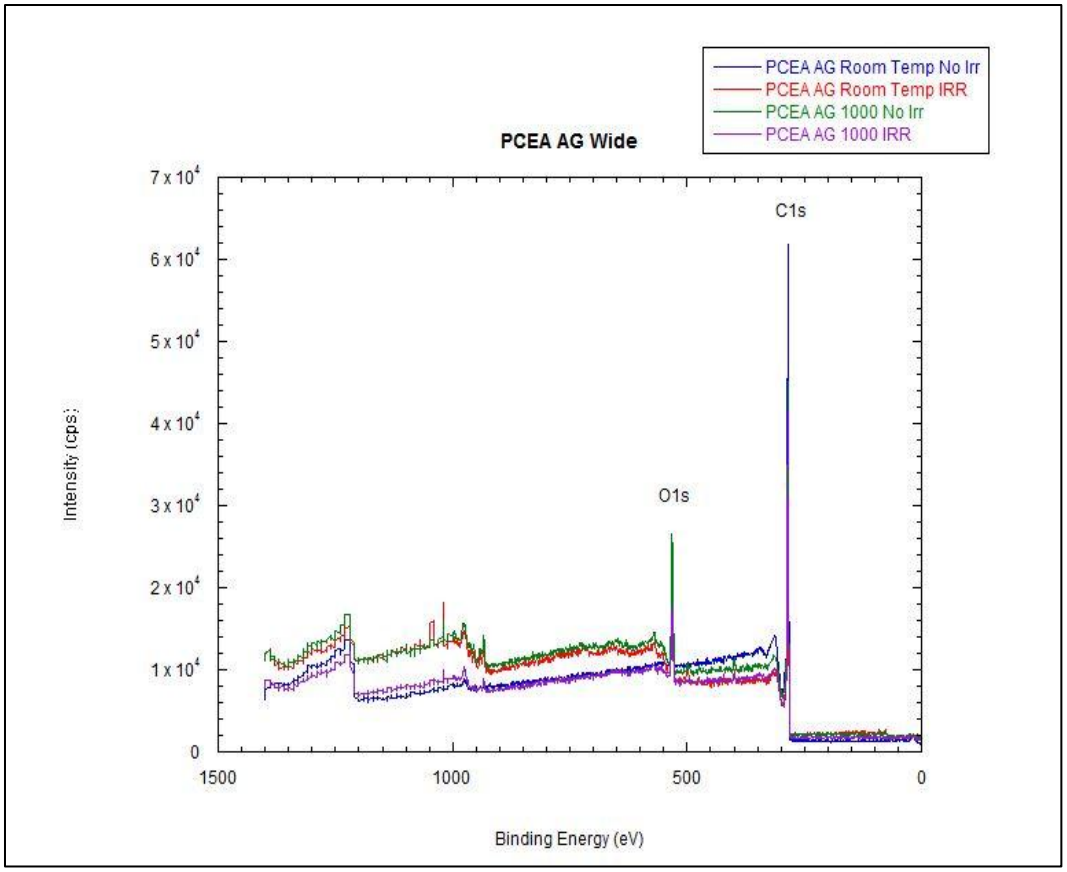

Figure 9-25: XPS spectra for PCEA AG east beam port experiments.

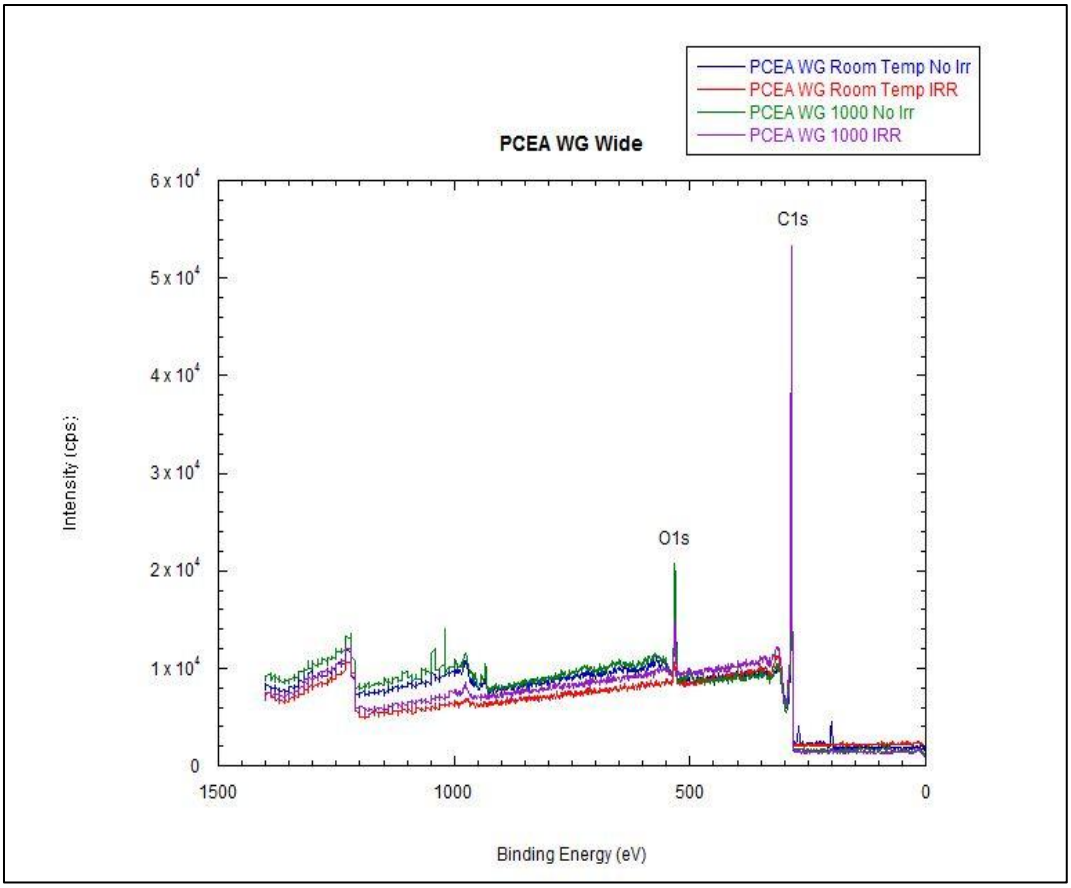

Figure 9-26: XPS spectra for PCEA WG east beam port experiments.

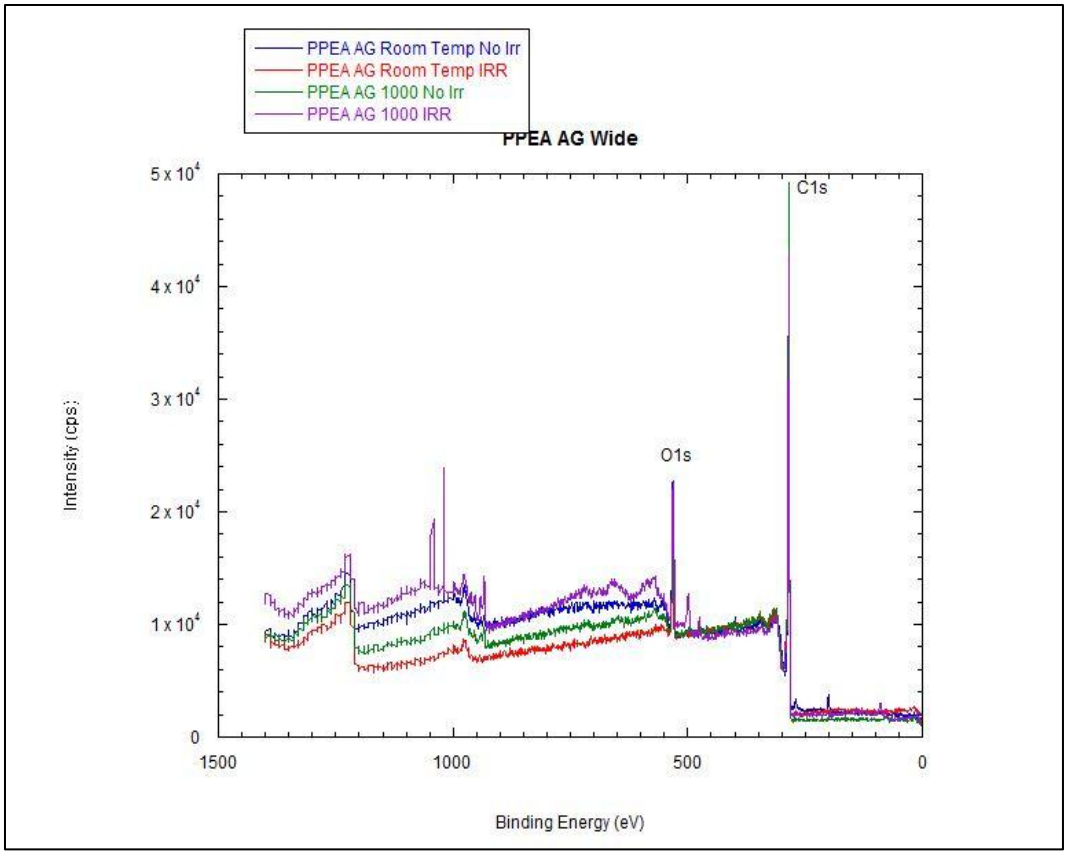

Figure 9-27: XPS spectra for PPEA AG east beam port experiments.

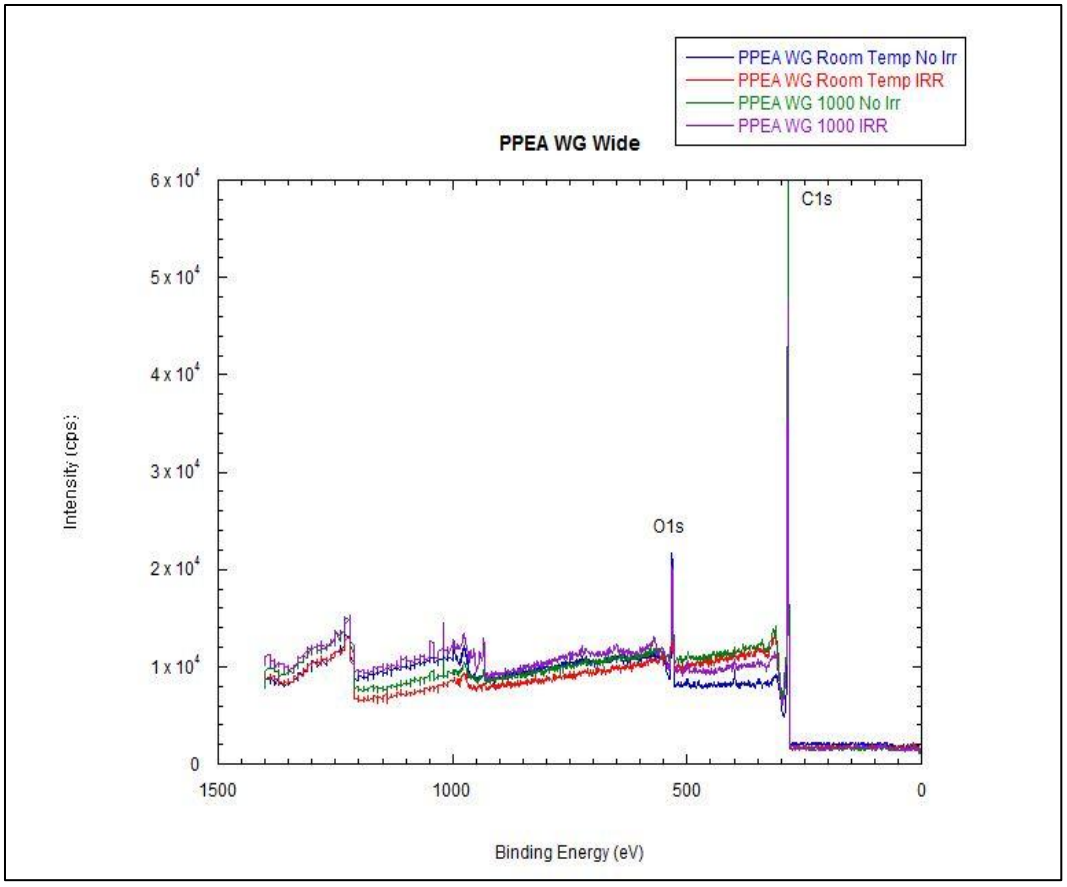

Figure 9-28: XPS spectra for PPEA WG east beam port experiments.

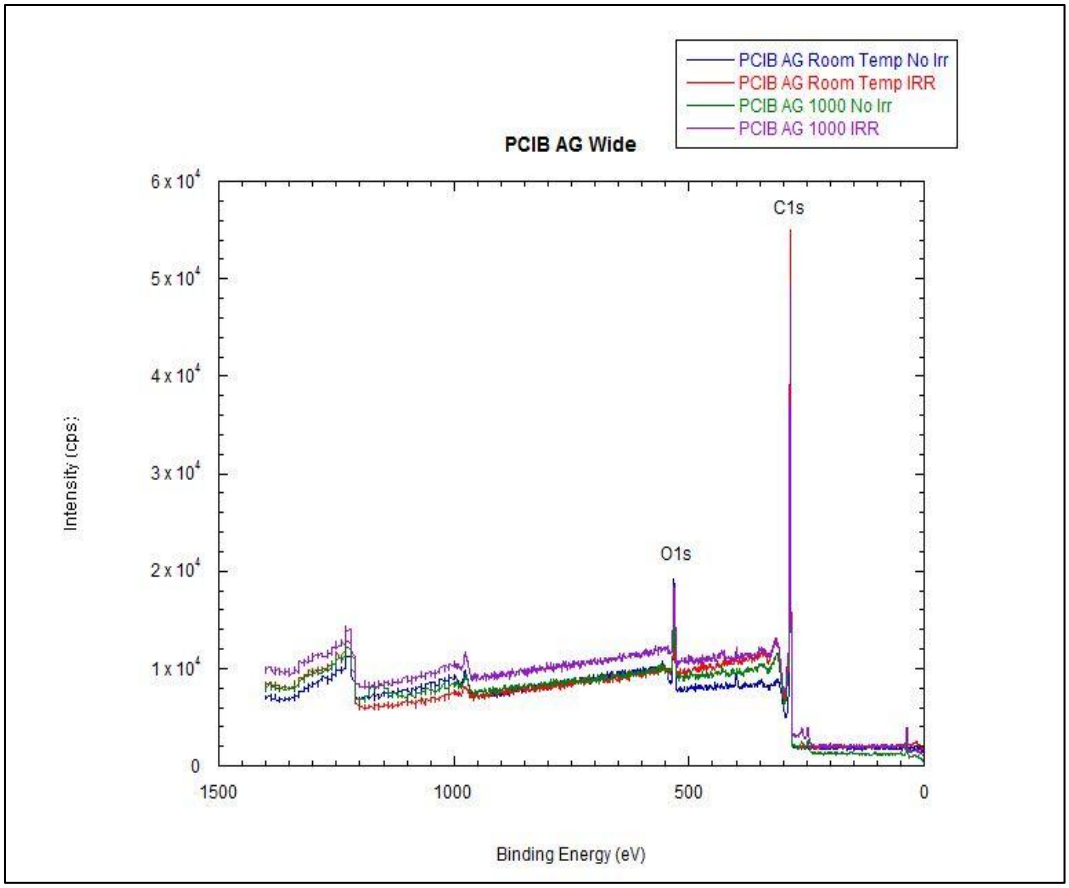

Figure 9-29: XPS spectra for PCIB AG east beam port experiments.

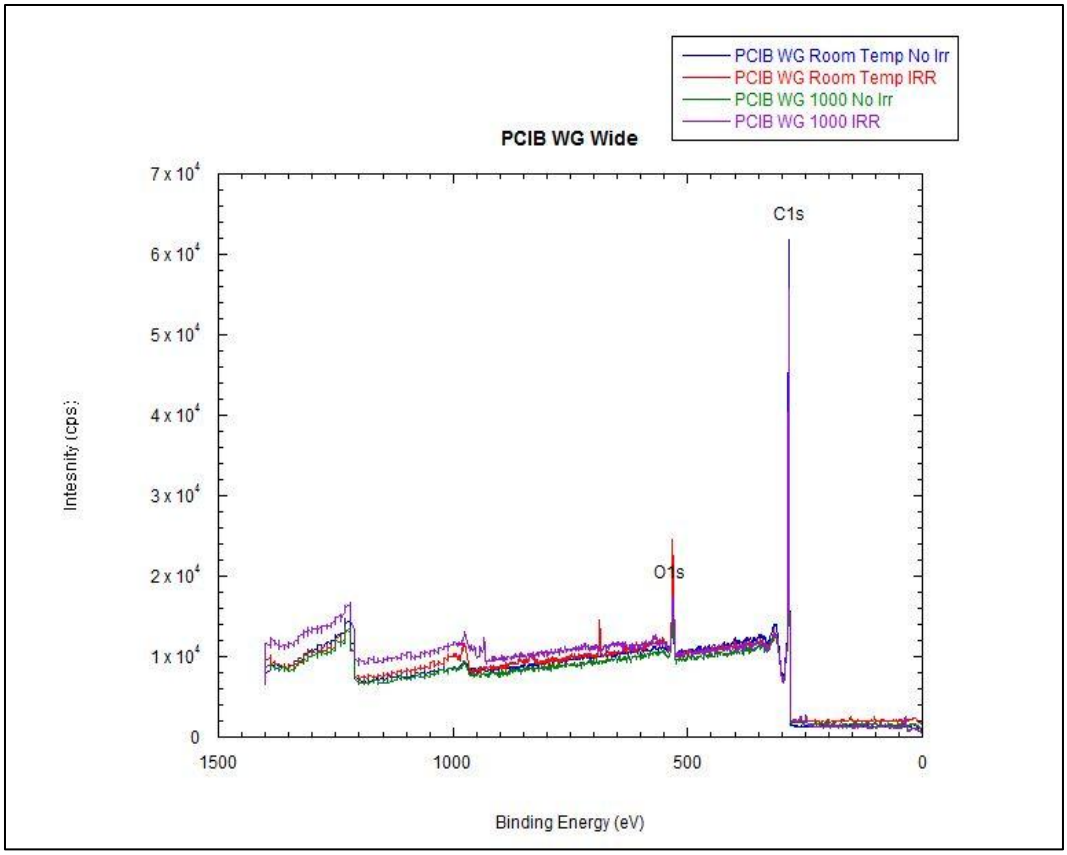

Figure 9-30: XPS spectra for PCIB WG east beam port experiments.

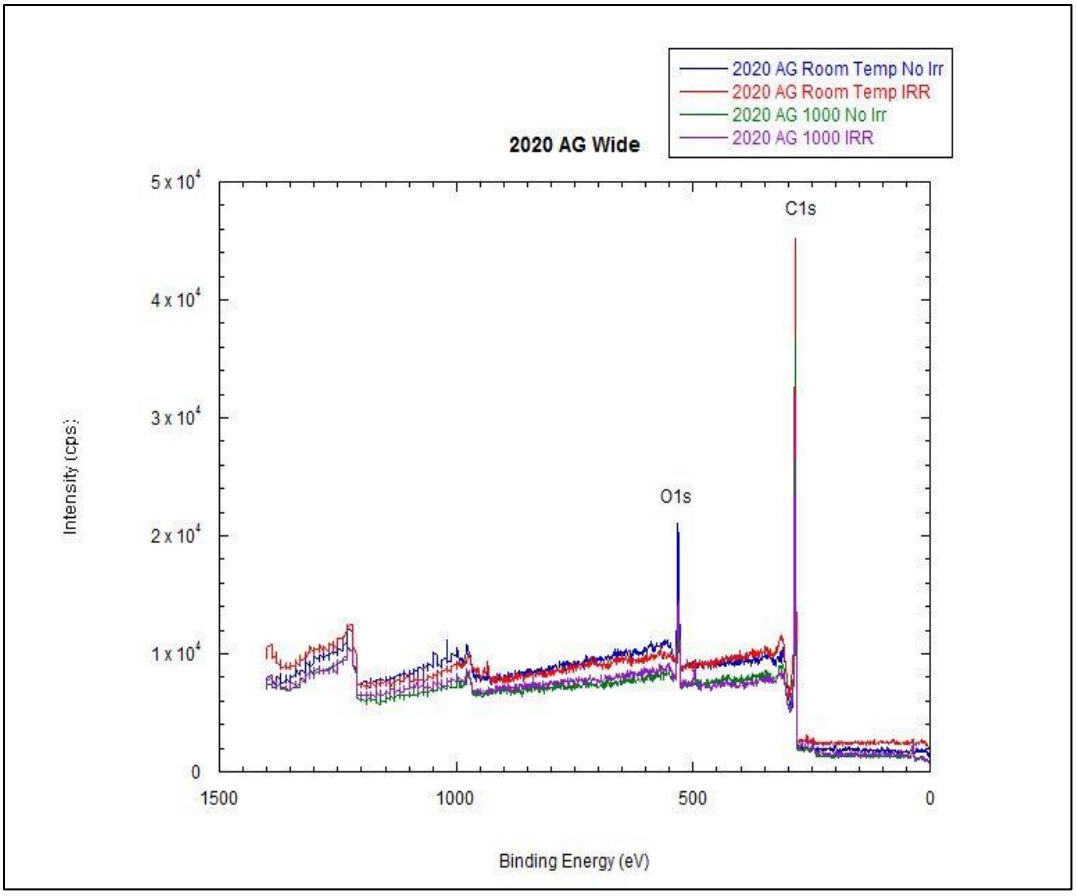

Figure 9-31: XPS spectra for 2020 AG east beam port experiments.

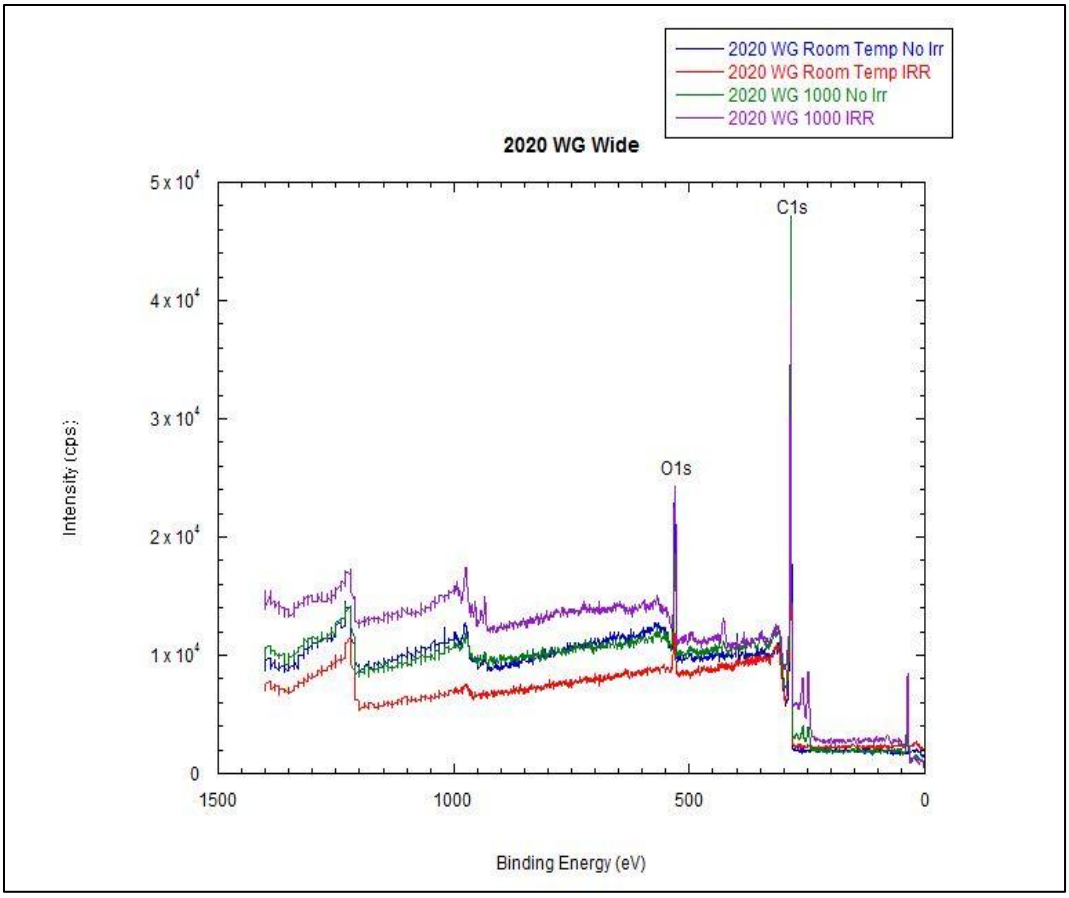

Figure 9-32: XPS spectra for 2020 WG east beam port experiments.

However, the IG-110 showed a smaller initial oxidation of the graphite and an increase in the oxidation when irradiated. This can be linked to the pore size discussion in the previous section. As previously stated, the IG-110 has the smallest pore size of the graphite grades analyzed and since most oxidation occurs in the pores, there is initially less oxidation occurring in the IG-110 graphite. The bombardment of the lattice by neutrons during irradiation leads to increasing oxidation.

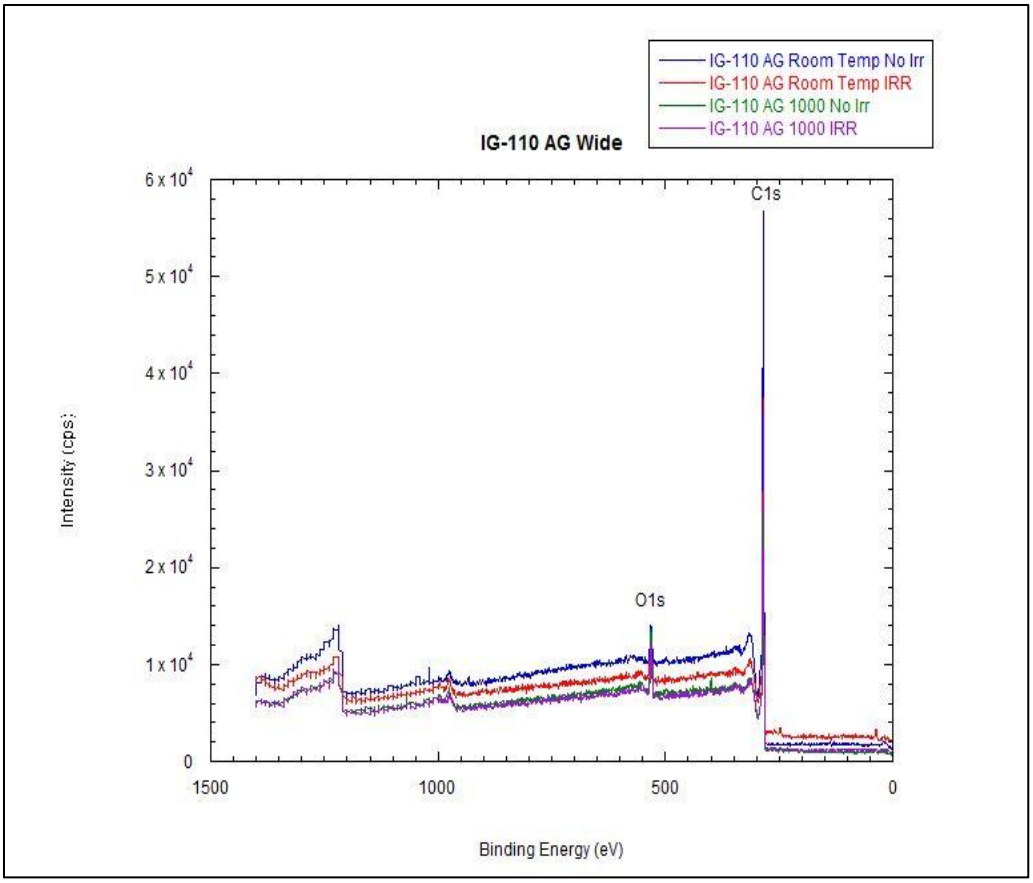

Figure 9-33: XPS spectra for IG-110 AG east beam port experiments.

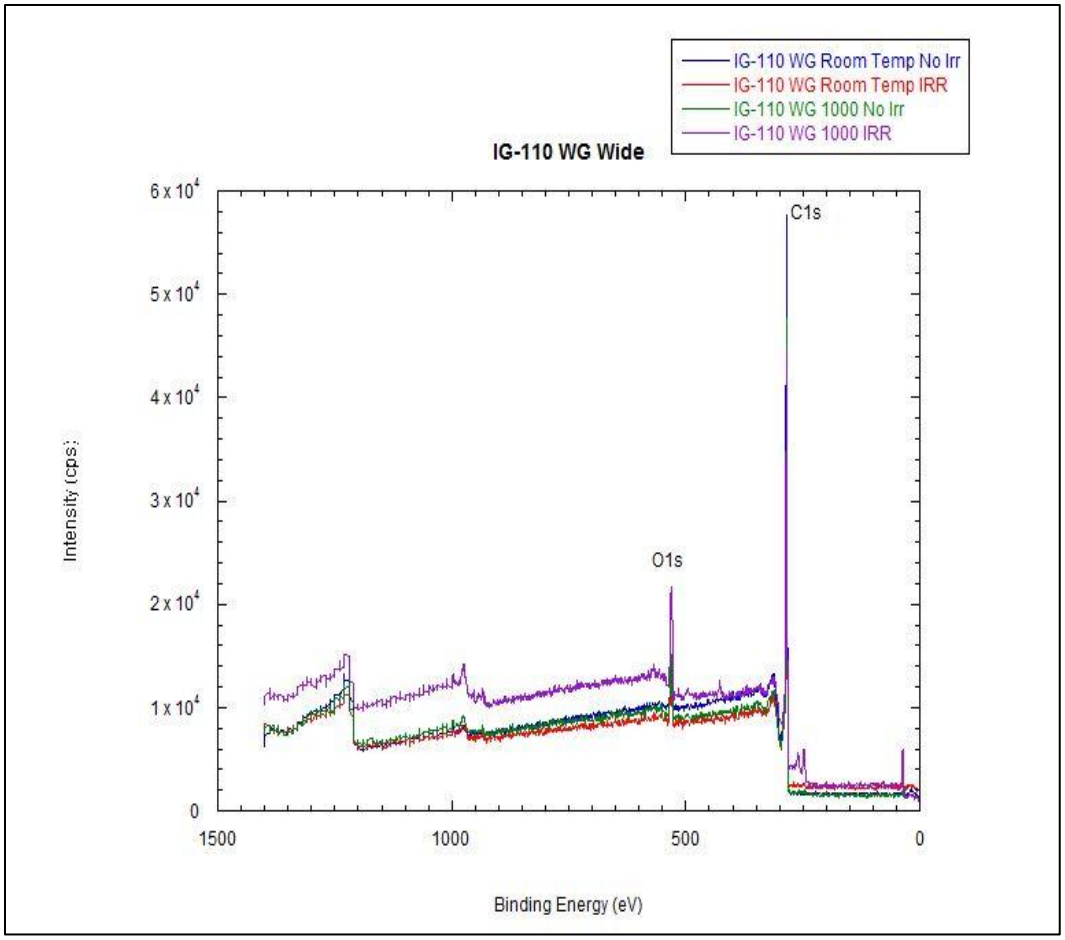

Figure 9-34: XPS spectra for IG-110 WG east beam port experiments.

The second set of experiments at the east beam port of the MUTR were carried out at 1000 °C. For all types of graphite there was an increase in the percent oxygen in the samples from the unirradiated to the irradiated samples. These temperatures correspond to region 2, when looking at the temperature regions of graphite oxidation. The reaction of graphite with water is important in this region because this region includes normal operating temperatures for HTGRs. Small in-leakage from the steam side can enter into the gas side where it can react with the hot graphite. The partial pressure of the water vapor is variable in the system. The rate equation can be presented in the following form:

$$r = AP^n$$

Where r is the reaction rate (kg/kg s), A is the rate constant (s^{-1} $(Nm^{-2})^{-1}$). Over the temperature range of 1000 – 1200 ºC, n is typically equal to 0.5 [Marsh, 1989]. These samples were also in a He-water environment. The water reaction with graphite can be seen below.

$$C\ (solid) + H_2O\ (gas) \rightarrow CO\ (gas) + H_2\ \ (gas) \quad [Marsh, 1989]$$

The XPS results from this experiment can be seen below.

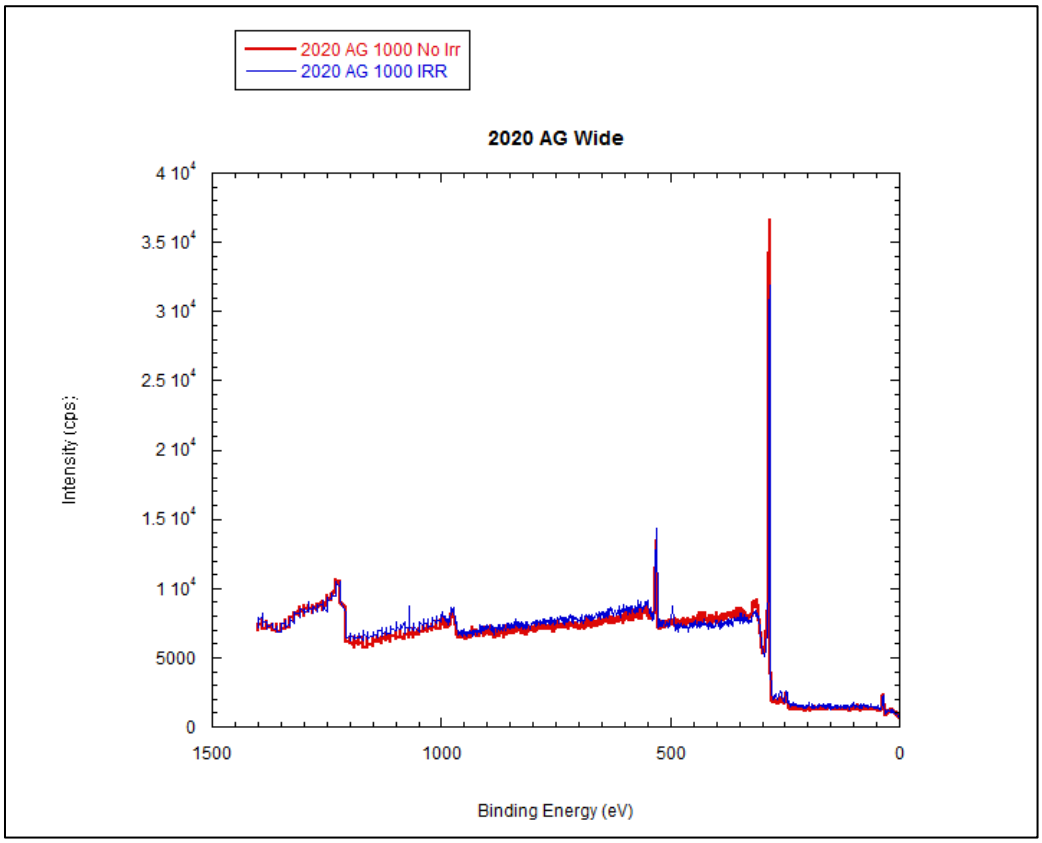

Figure 9-35: XPS results for 2020 AG. These results show the increase in oxygen between the 1000 °C unirradiated and irradiated samples.

9.1.4 Determining structural changes in graphite using XRD

The XRD data were collected on a Bruker C2 Discover using a Cu Kα sealed x-ray tube with a Göbbel mirror at the University of Maryland X-ray Crystallographic center. The C2 is also equipped with the GADDS software for data collection, display and data processing. Data were collected from 10 to 95 degrees.

A typical XRD graphite image showing the Debye rings associated with graphite can be seen below along with the corresponding diffraction pattern. The Miller indices corresponding to the Bragg peaks are labeled.

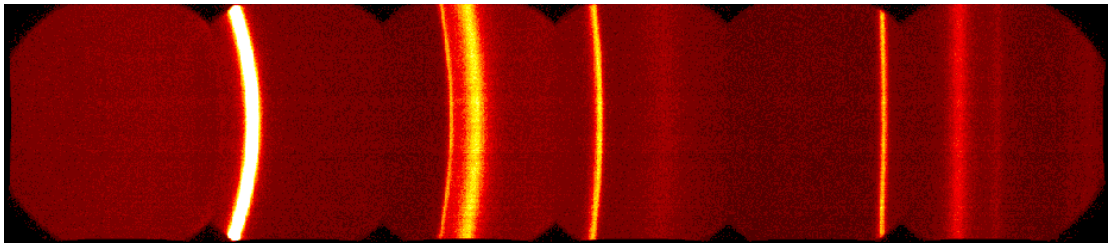

Figure 9-36: PPEA WG 1000 °C unirradiated east beam port sample.

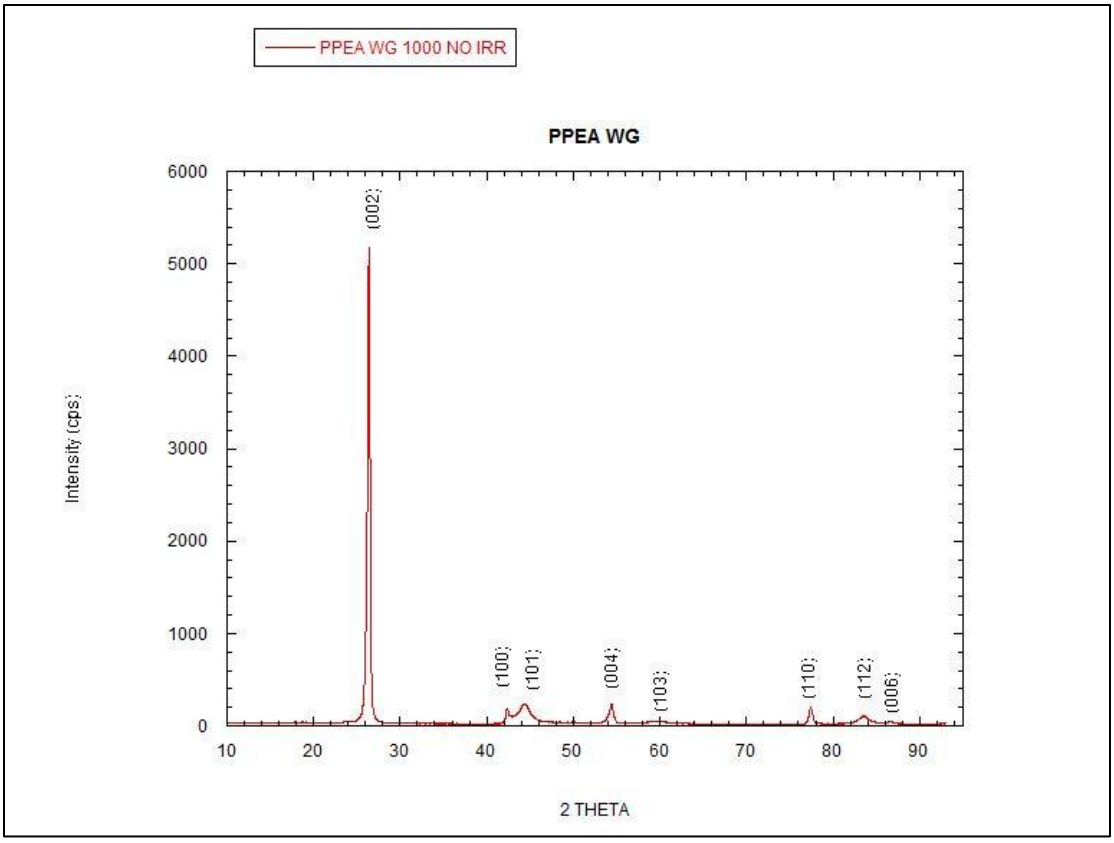

Figure 9-37: XRD spectrum of PPEA WG 1000 °C unirradiated east beam port sample. The Miller indices associated with each Bragg peak are labeled.

The positions of the Bragg peaks are established from the Bragg's law as a function of the wavelength and interplanar spacing (d-spacing). The d-spacing for a hexagonal system, such as graphite can be calculated using the equation below.

$$d_{hkl} = \left(\frac{h^2}{a^2} + \frac{k^2}{b^2} + \frac{l^2}{c^2}\right)^{-\frac{1}{2}}$$

Since h, k, and l are integers, both the resultant d-values and Bragg angles for arrays of discrete values for a given set of unit cell dimensions [Pecharsky and Zavalij, 2009].

A complete table showing all of the XRD results for each of the samples can be found in Appendix E. The results show that there are no significant changes in the crystal structure of the samples for any of the experiments conducted. The graphs for all of the samples analyzed showing the XRD results can be seen below.

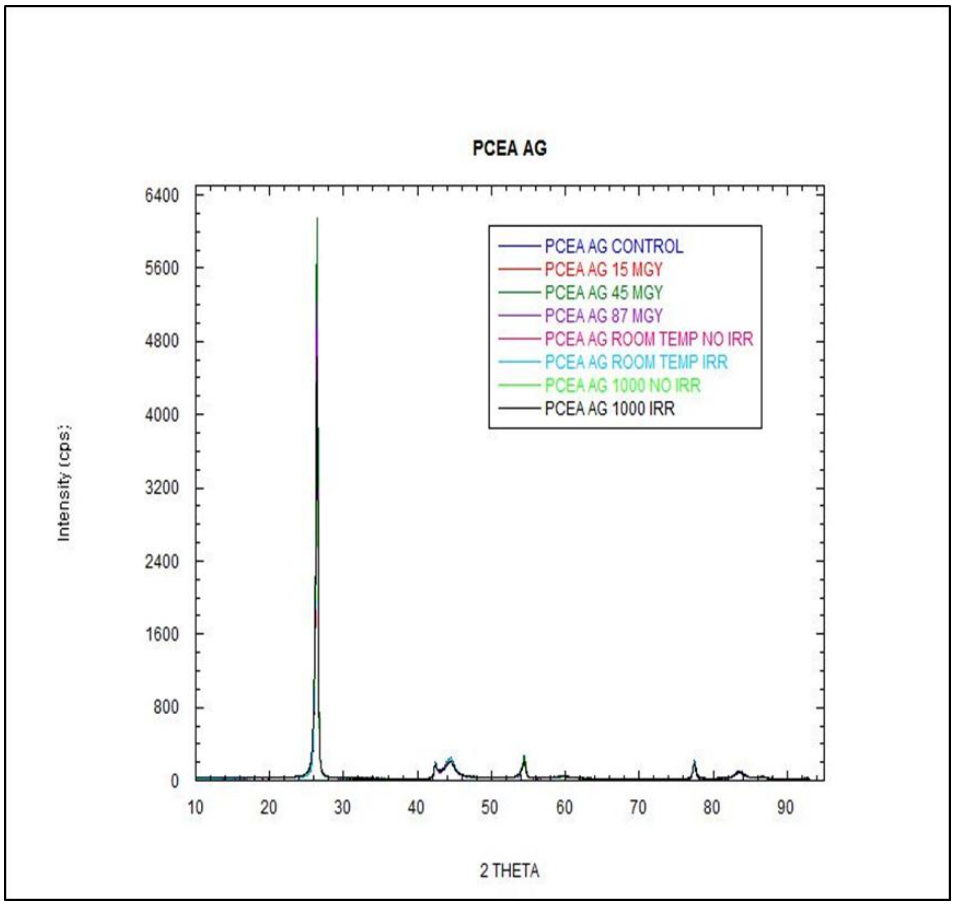

Figure 9-38: XRD results for PCEA AG. The graph shows the gamma irradiation results as well as the mixed field irradiation results.

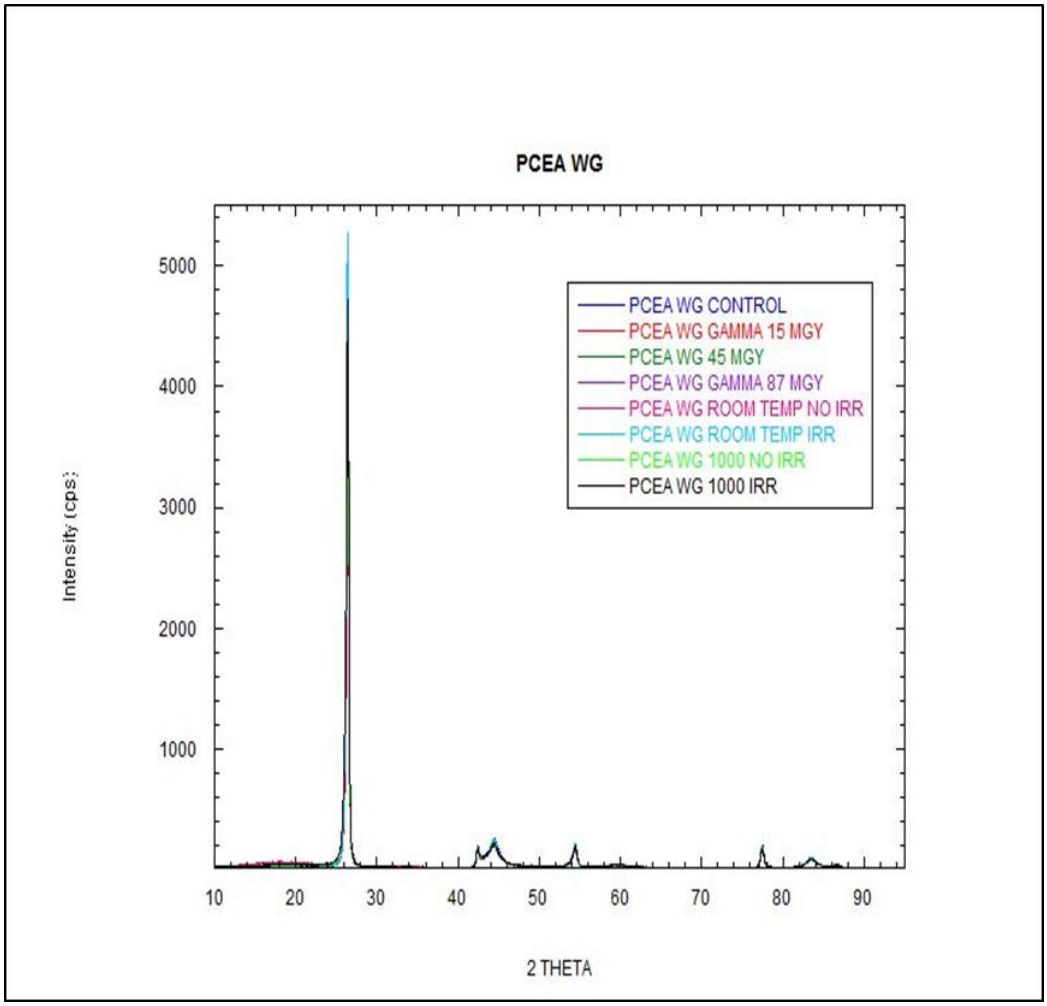

Figure 9-39: XRD results for PCEA WG. The graph shows the gamma irradiation results as well as the mixed field irradiation results.

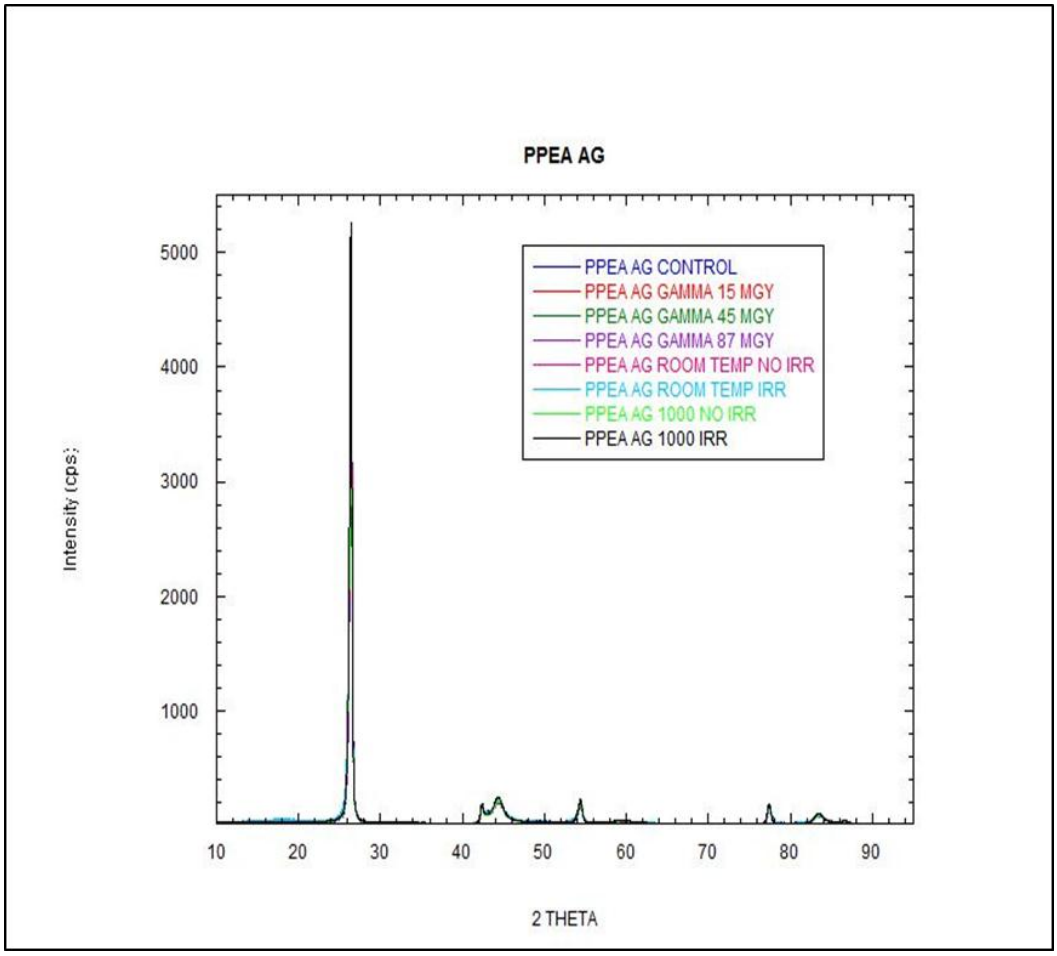

Figure 9-40: XRD results for PPEA AG. The graph shows the gamma irradiation results as well as the mixed field irradiation results.

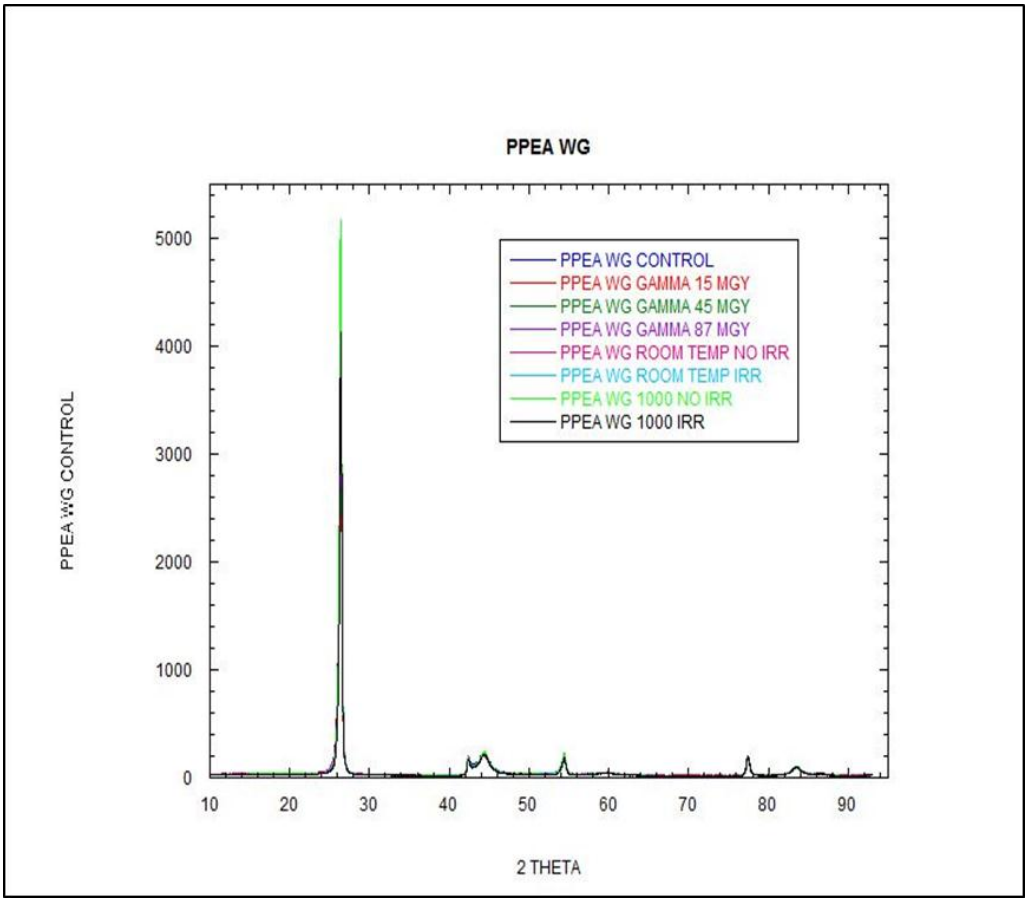

Figure 9-41: XRD results for PPEA WG. The graph shows the gamma irradiation results as well as the mixed field irradiation results.

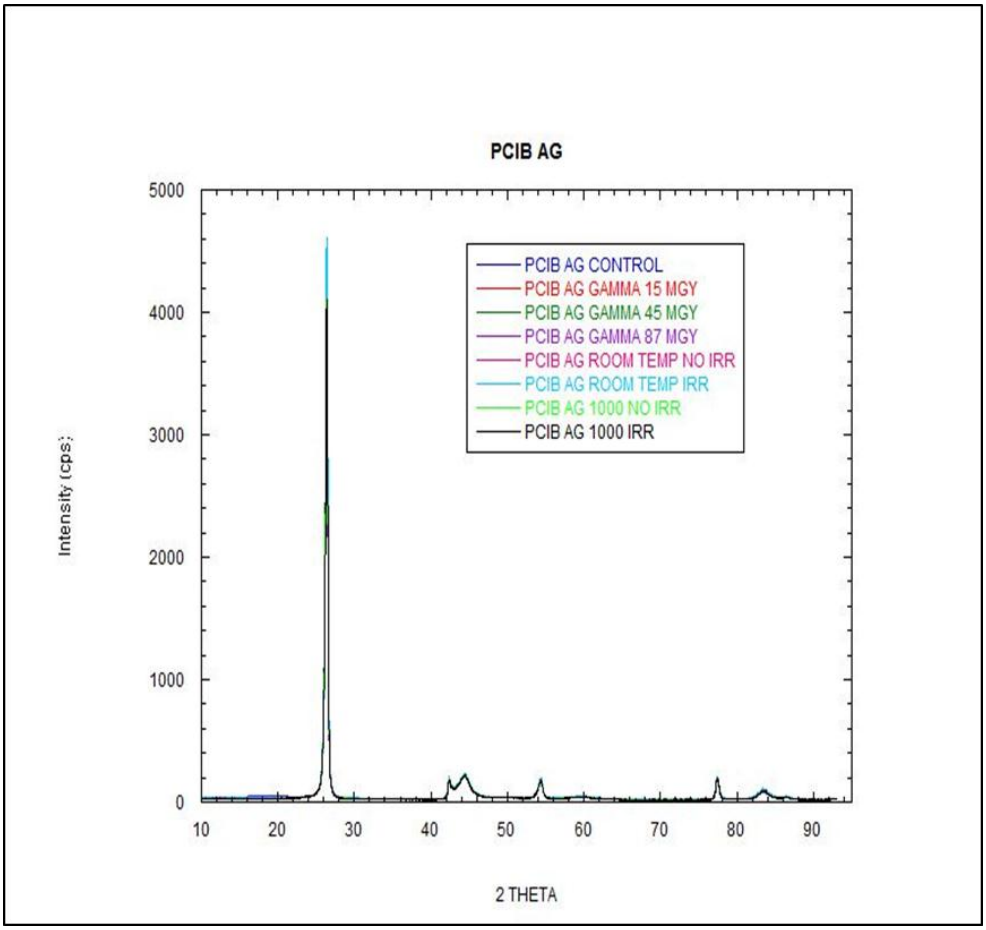

Figure 9-42: XRD results for PCIB AG. The graph shows the gamma irradiation results as well as the mixed field irradiation results.

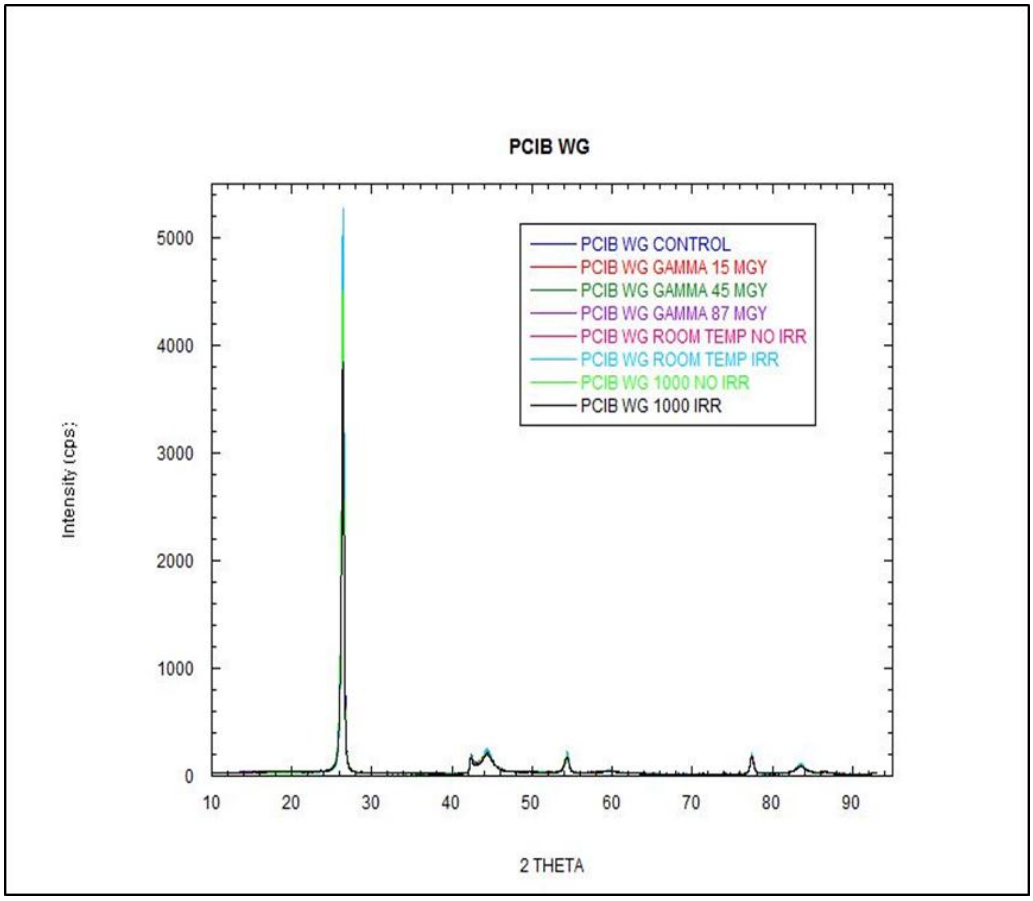

Figure 9-43: XRD results for PCIB WG. The graph shows the gamma irradiation results as well as the mixed field irradiation results.

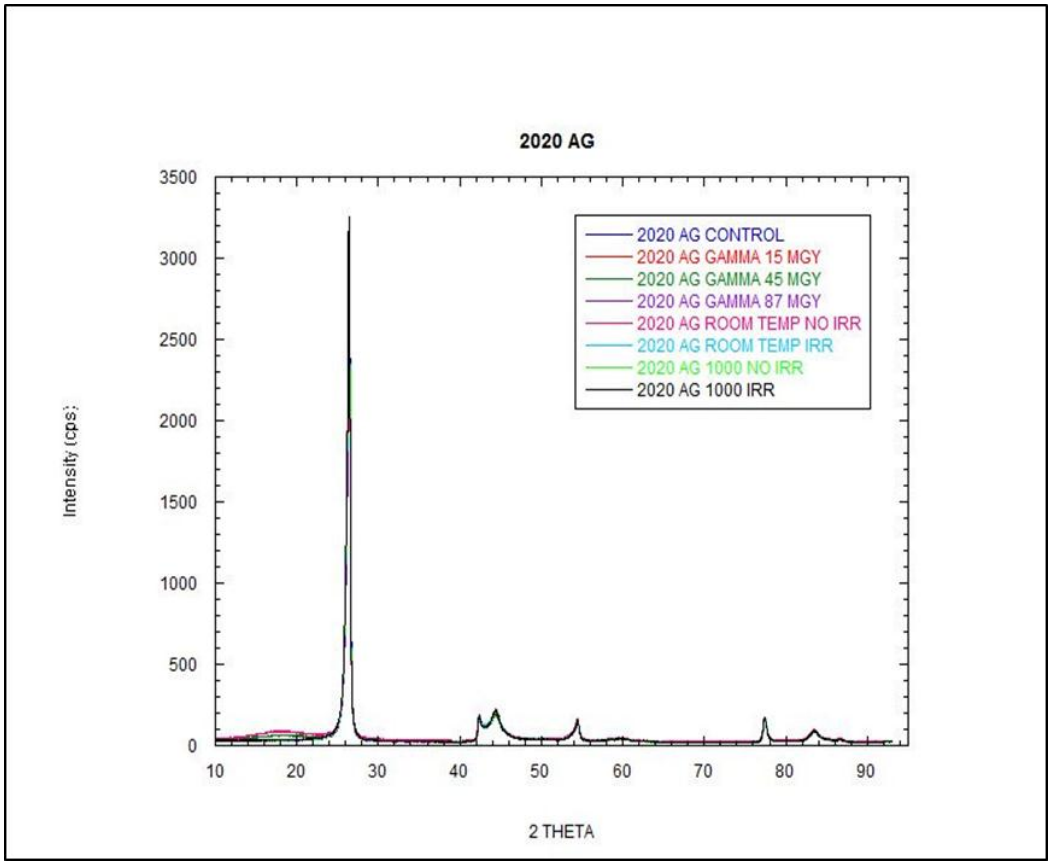

Figure 9-44: XRD results for 2020 AG. The graph shows the gamma irradiation results as well as the mixed field irradiation results.

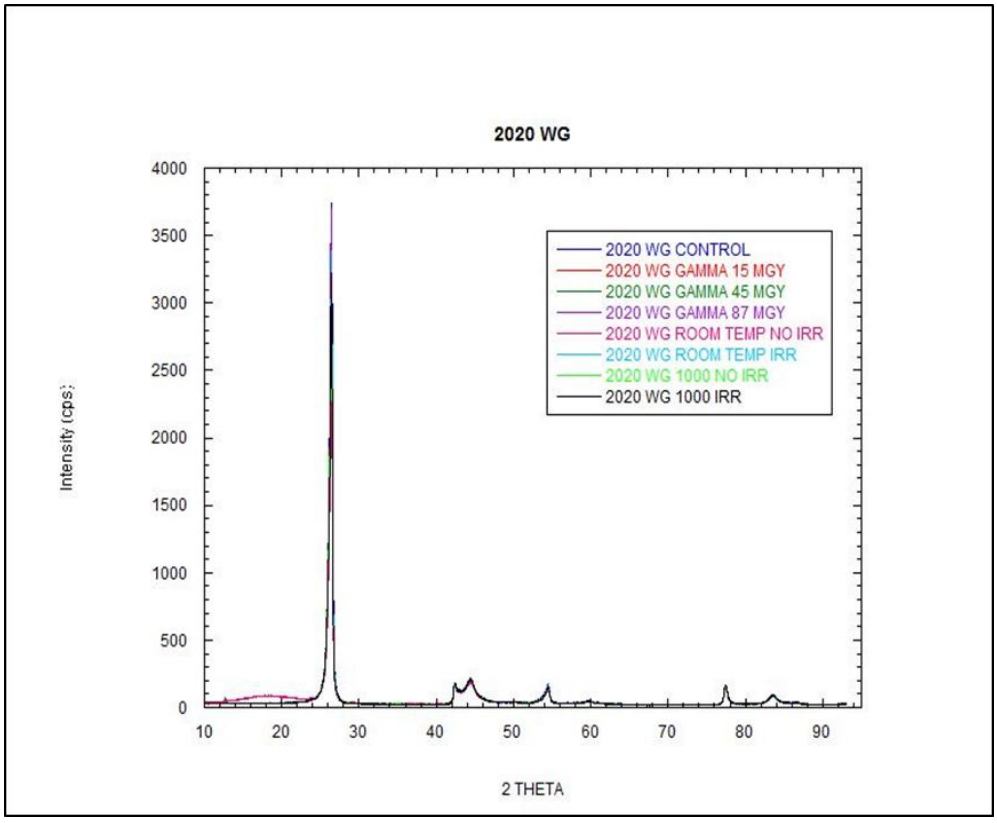

Figure 9-45: XRD results for 2020 WG. The graph shows the gamma irradiation results as well as the mixed field irradiation results.

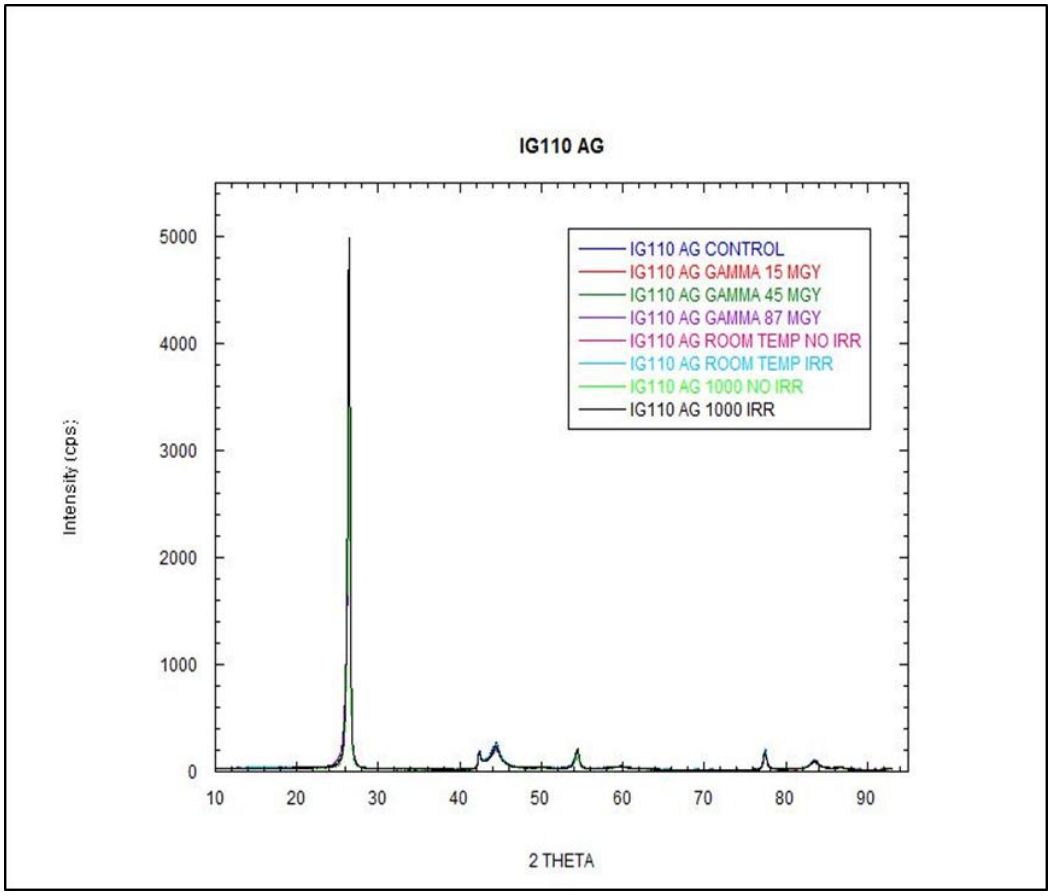

Figure 9-46: XRD results for IG-110 AG. The graph shows the gamma irradiation results as well as the mixed field irradiation results.

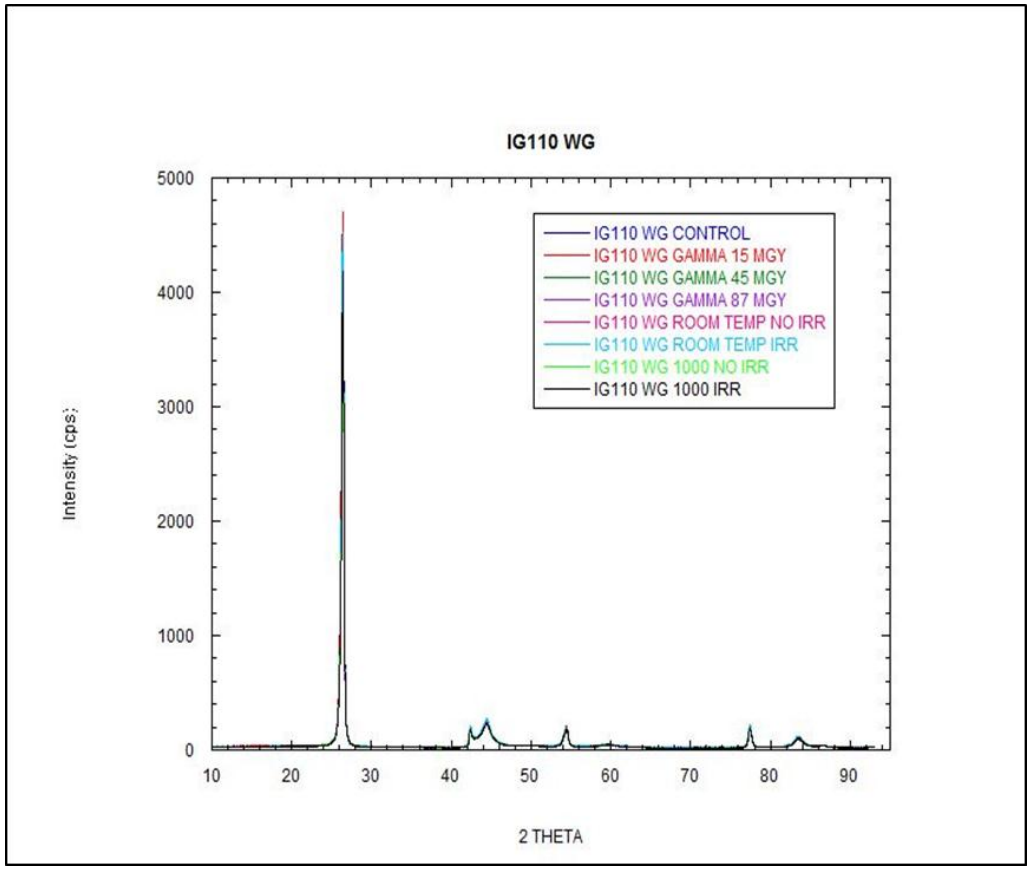

Figure 9-47: XRD results for IG-110 WG. The graph shows the gamma irradiation results as well as the mixed field irradiation results.

Several recent studies by the Laboratori Nationali di Legnaro (2009 and 2010) focused on radiation damage of certain graphites. Proton accelerators were used to deliver approximately 1.6×10^{18} protons to a 0.2 cm^2 area of the graphite. Even at these high doses, no change was observed in the XRD results for their samples. This coincides with the results obtained from the experiments conducted at UMD.

Several samples showed an amorphous peak below the (002) peak of the graphite. This area showed on several samples and appeared to be random. These graphs can be seen below. In order to determine whether this peak was due to an impurity on the samples, one sample that showed the peak was cleaned with a mixture of nitric acid and hydrochloric acid.

After it was cleaned, it was rinsed several times with deionized water. This cleaned sample as well as another uncleaned sample we rerun in the XRD. The graph below shows that the amorphous peak was not removed after cleaning of the sample indicating that the amorphous area is due to an impurity on the sample. The second uncleaned sample that was run does not show the amorphous region. This amorphous peak can be discounted when looking at the results. This impurity did not affect the results of the other peaks in the samples as those with and without the peak showed similar results.

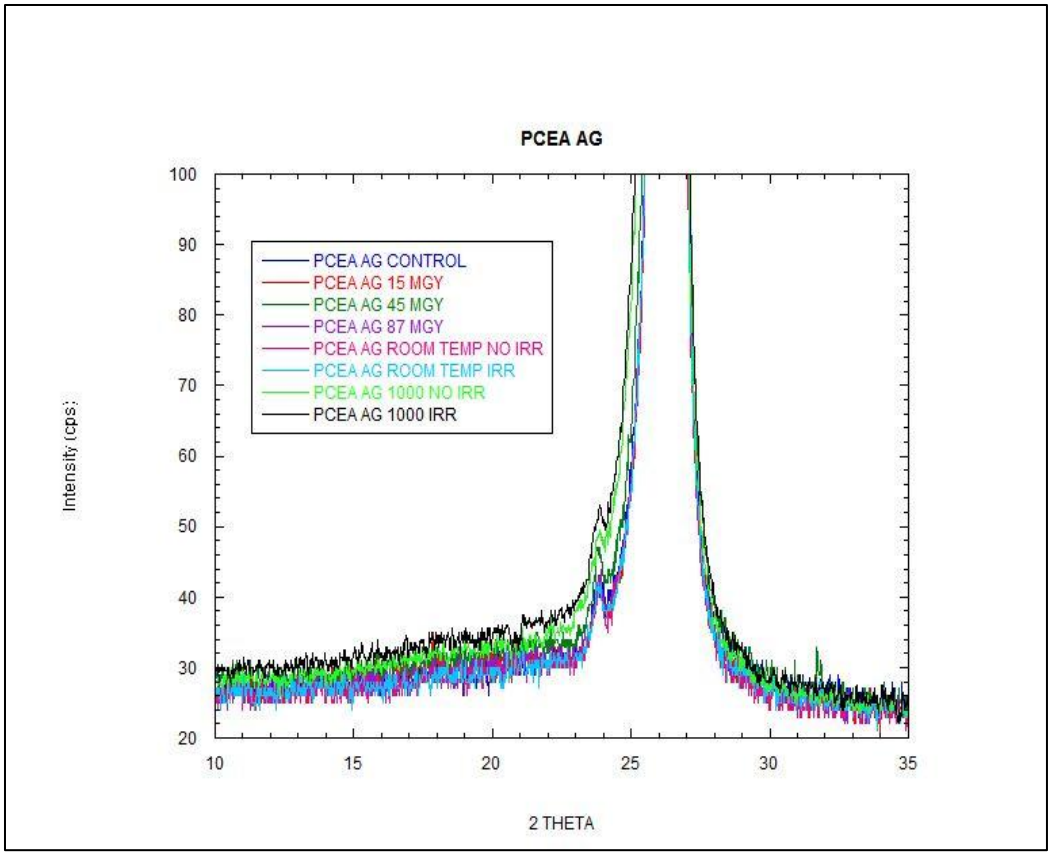

Figure 9-48: PCEA AG 002 peak.

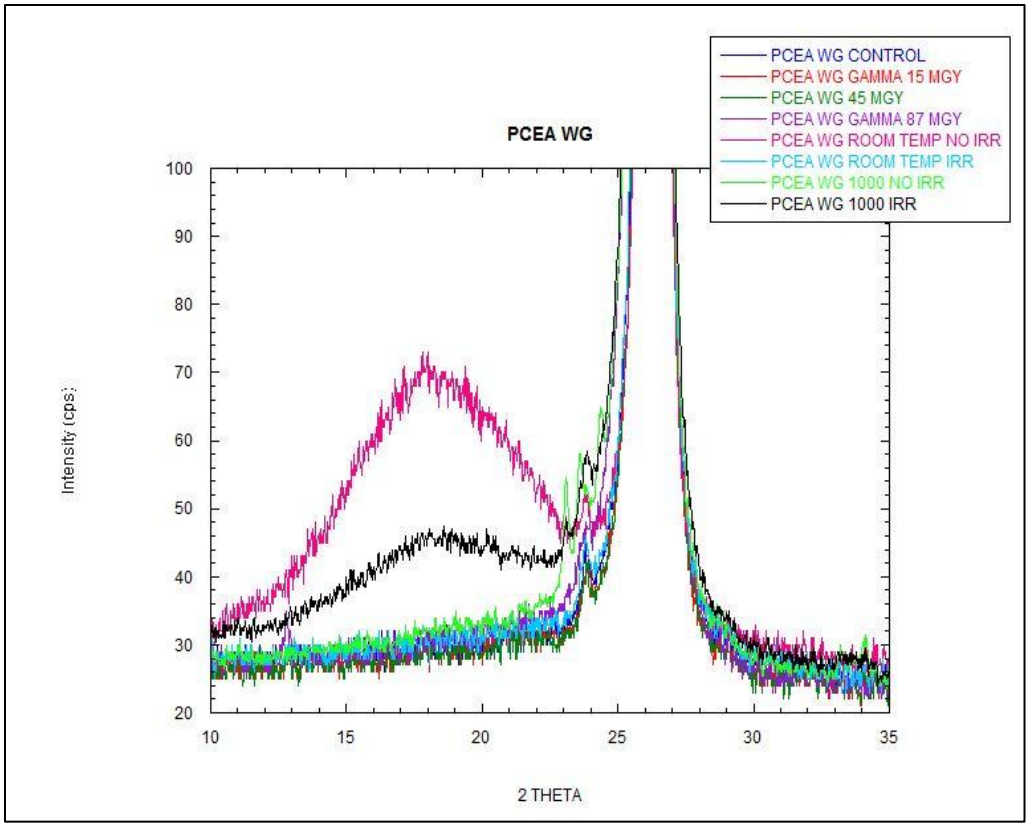

Figure 9-49: PCEA WG 002 peak. Broad peak between 10 and 20 indicates an amorphous area.

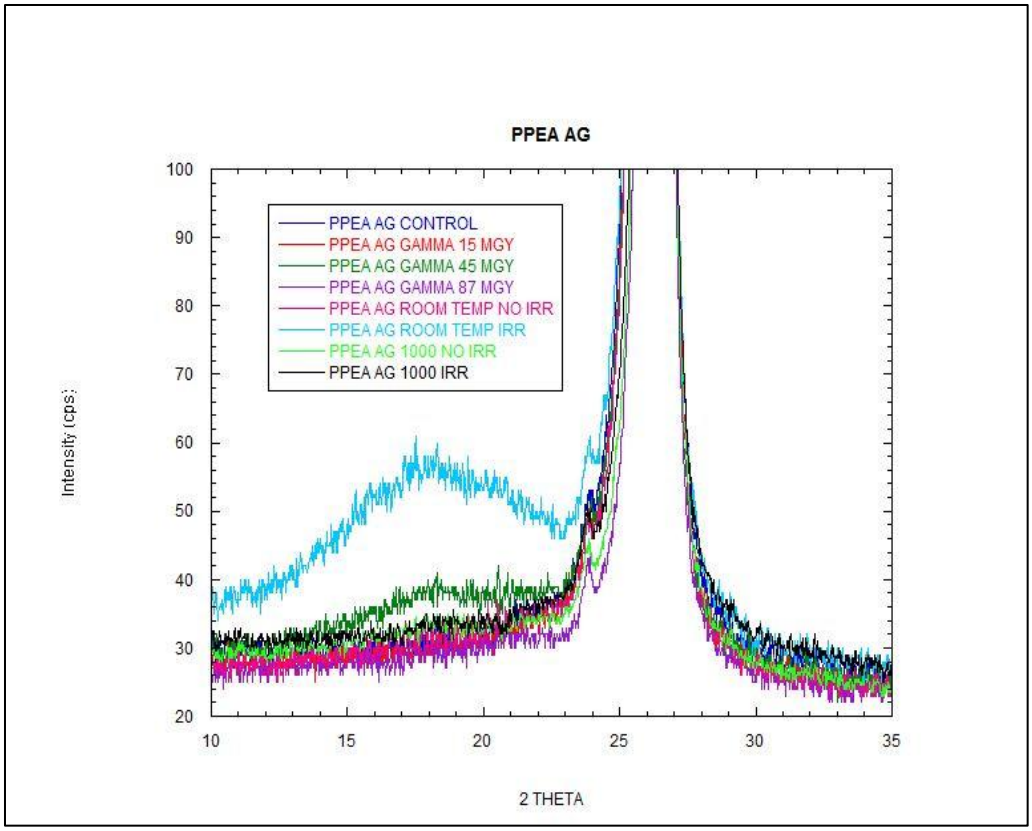

Figure 9-50: PPEA AG 002 peak. Broad peak between 10 and 20 indicates an amorphous area.

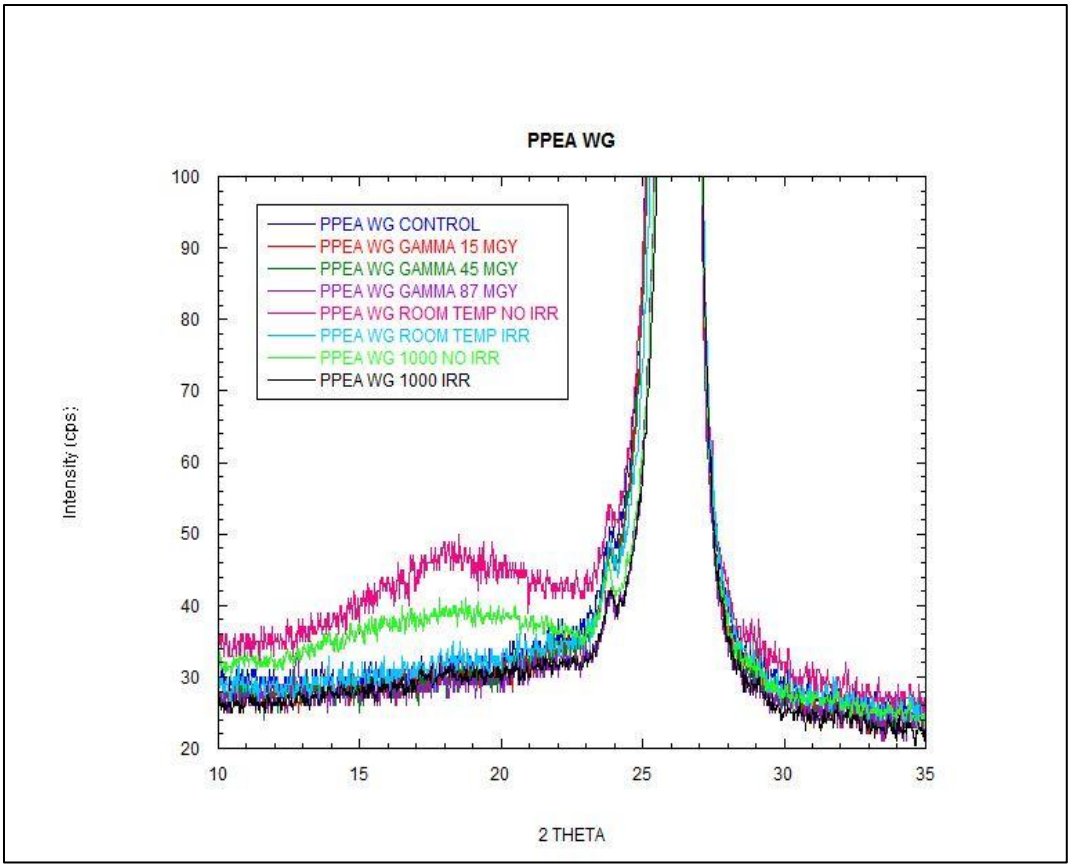

Figure 9-51: PPEA WG 002 peak. Broad peak between 10 and 20 indicates an amorphous area.

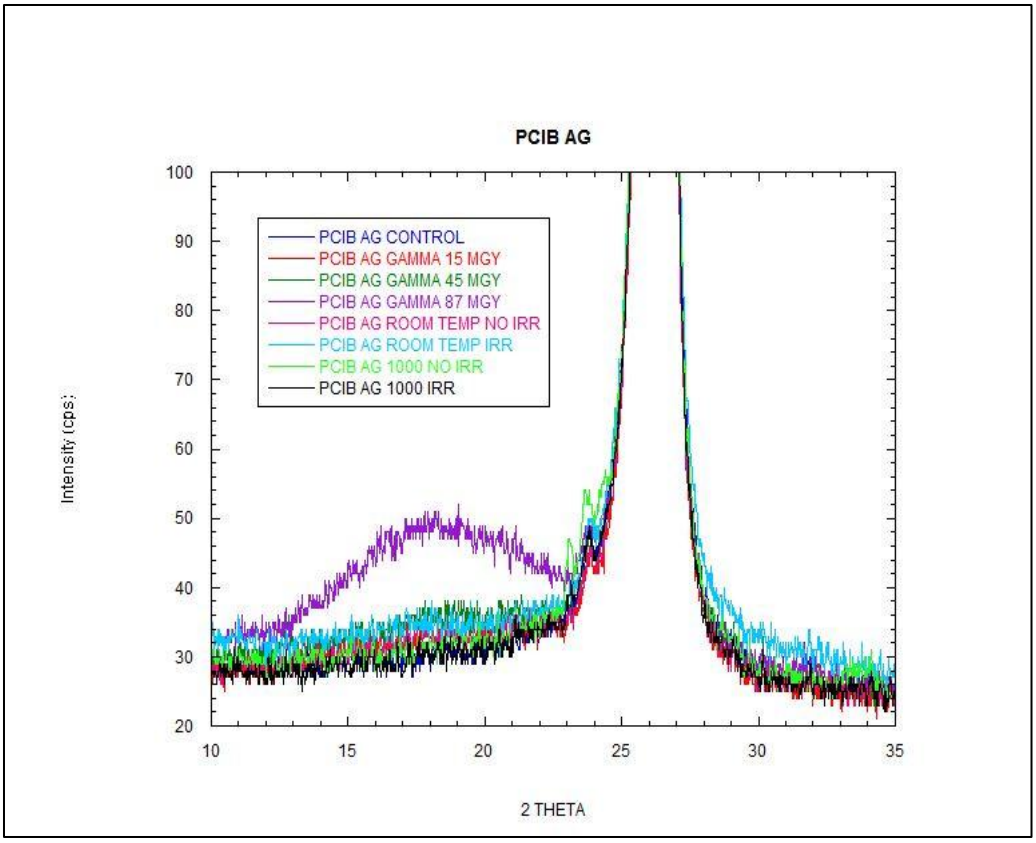

Figure 9-52: PCIB AG 002 peak. Broad peak between 10 and 20 indicates an amorphous area.

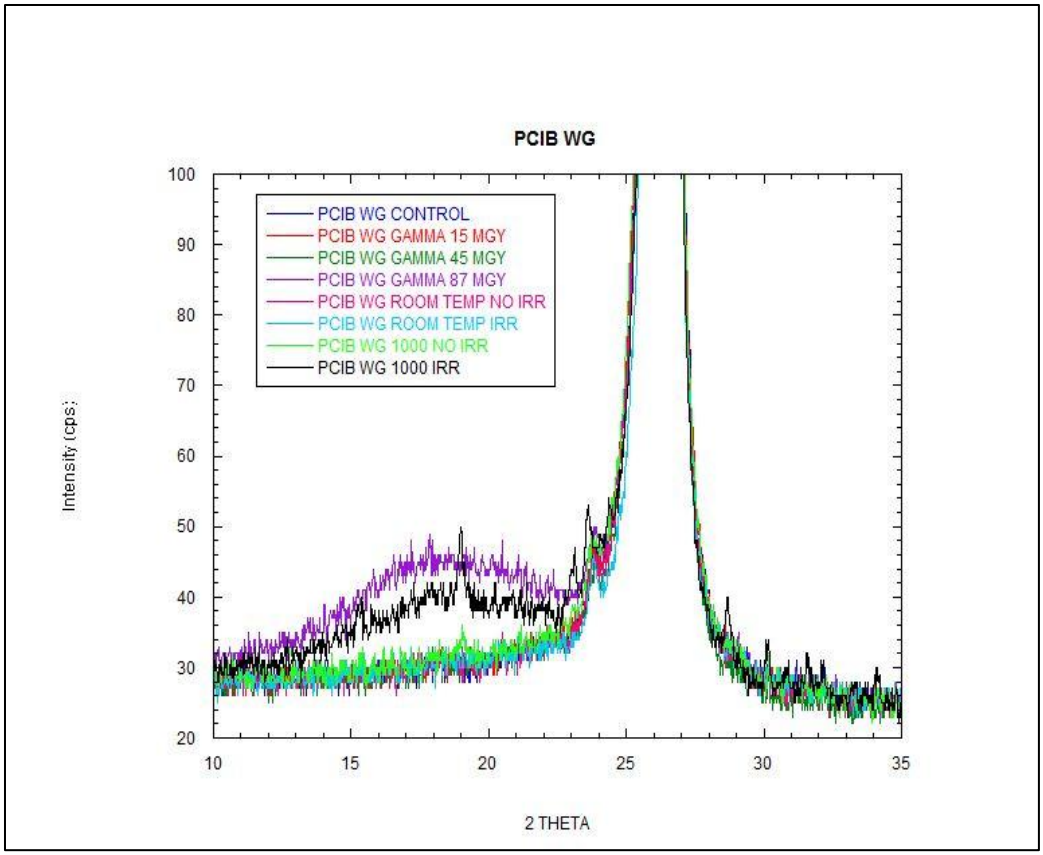

Figure 9-53: PCIB WG 002 peak. Broad peak between 10 and 20 indicates an amorphous area.

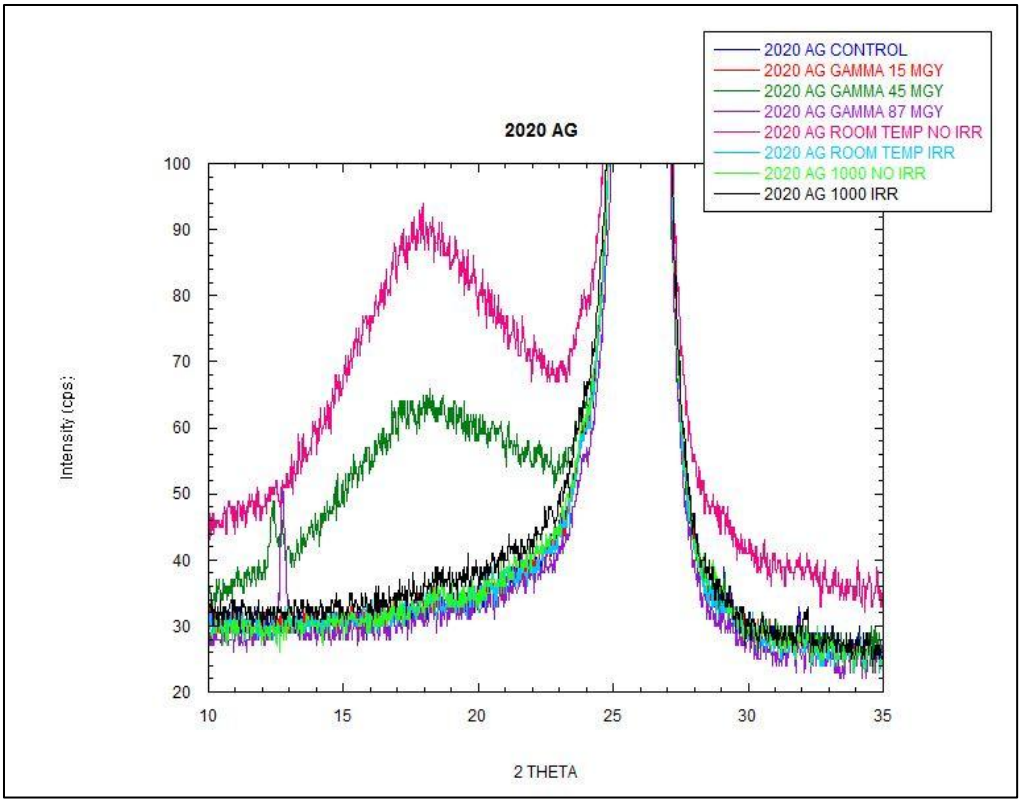

Figure 9-54: 2020 AG 002 peak. Broad peak between 10 and 20 indicates an amorphous area.

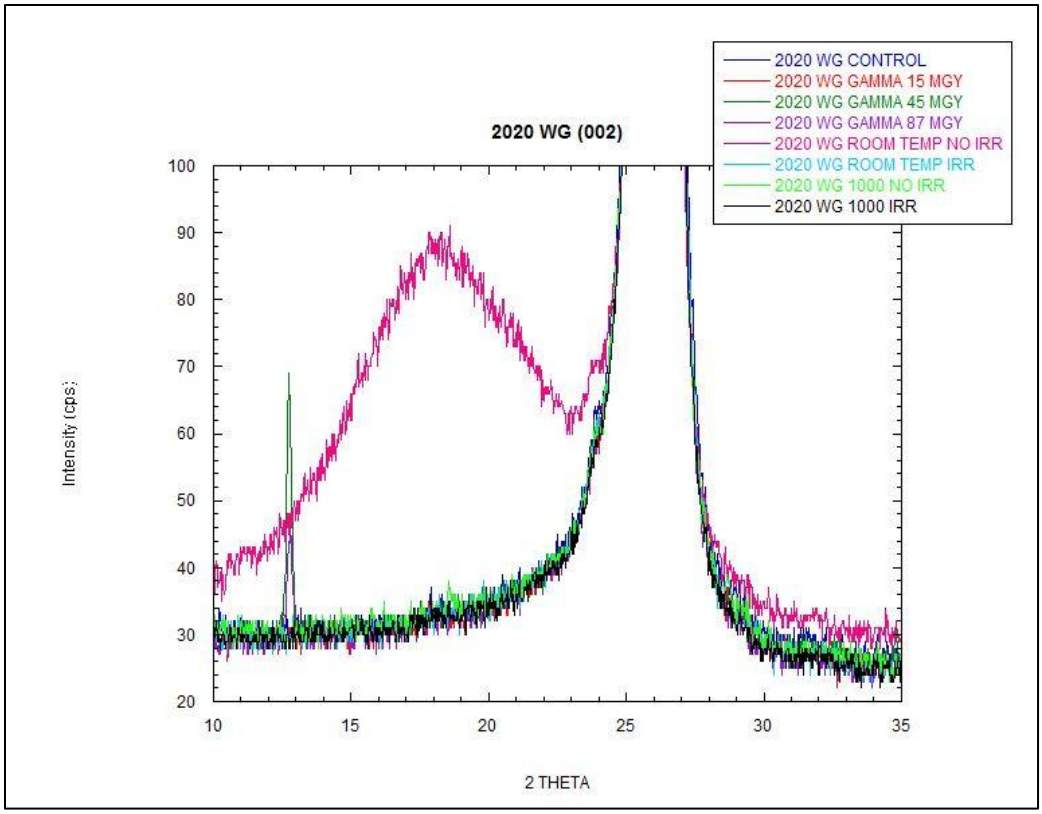

Figure 9-55: 2020 WG 002 peak. Broad peak between 10 and 20 indicates an amorphous area.

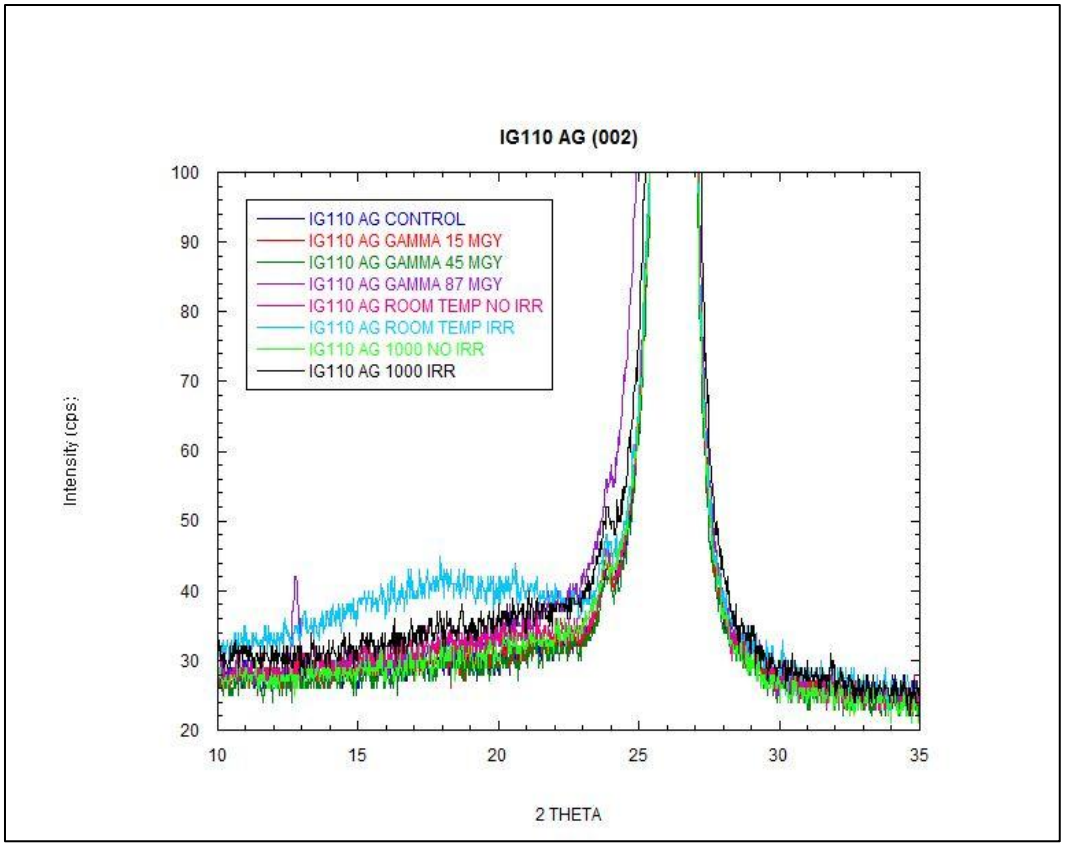

Figure 9-56: IG-110 AG 002 peak. Broad peak between 10 and 20 indicates an amorphous area.

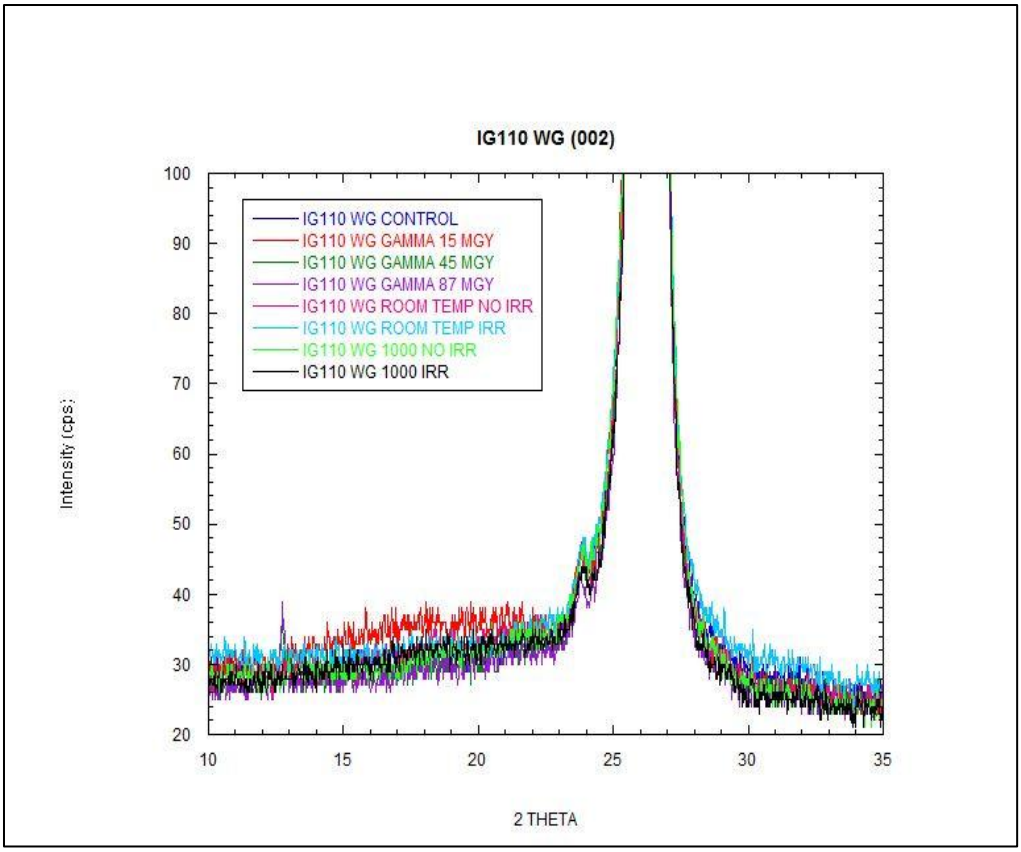

Figure 9-57: IG-110 WG 002 peak. Broad peak between 10 and 20 indicates an amorphous area.

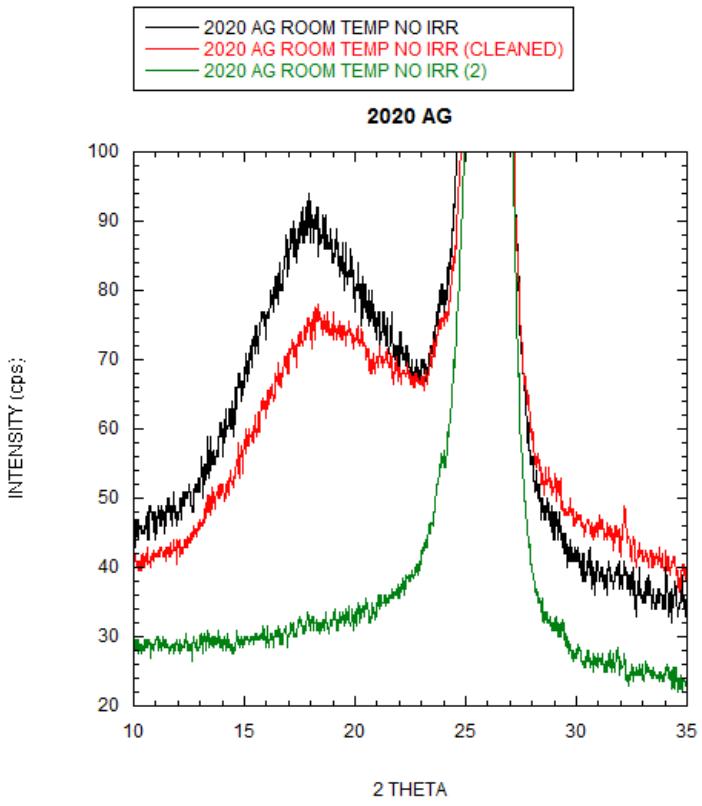

Figure 9-58: XRD results for the two uncleaned and one cleaned (nitric acid and hydrochloric acid) samples.

The (004) peak at 54 degrees was used to determine peak broadening, which would indicate an increase in interlayer spacing of the samples since this peak was not affected by the impurity at (002). A typical graph showing the (004) peak can be seen in Figure 9-59. The FWHM data for all samples can be found in the table in Appendix C. The graph below shows that there are no significant changes in the FWHM of the samples, indicating that there is no change in the interlayer spacing of the samples. This is confirmed by the data in Appendix C. For all samples, no significant increase in inter-layer spacing was noted for any of the experiments conducted.

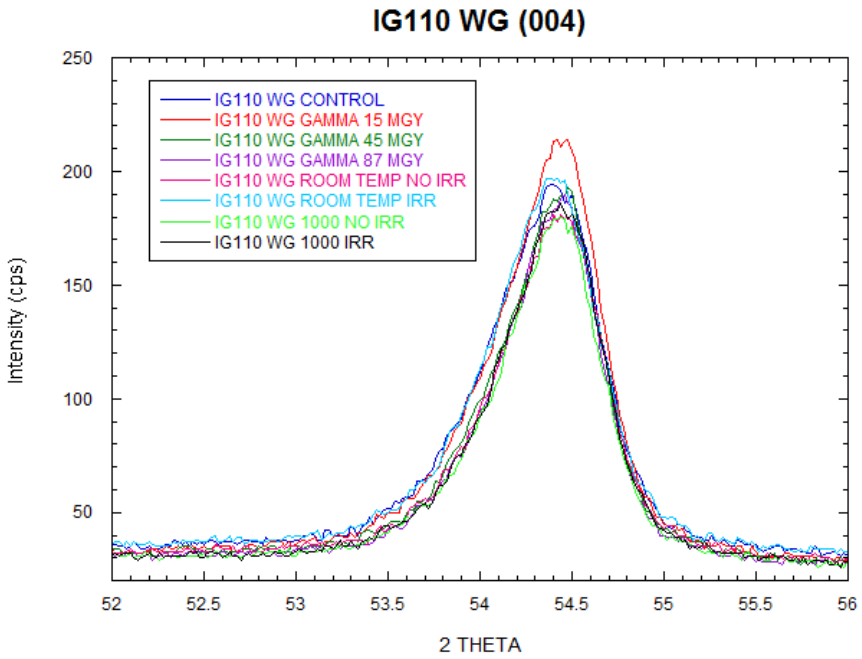

Figure 9-59: IG-110 WG (004) peak. No significant broadening is noted, indicating that there is little to no change in the interlayer spacing of the samples.

The results indicate that all five graphite types analyzed would be acceptable for use in nuclear reactors. The structure of the graphite, as analyzed by XRD, was unchanged by the high gamma irradiations and mixed field irradiation performed on the samples. Should significant changes occur, it would be necessary to determine whether that particular graphite was still acceptable for use within a nuclear reactor. Since certain graphite reflectors in the HTGR are expected to last for the life of the reactor, it is important that the structure of the graphite stay sound when exposed to high doses of radiation.

9.2 Magnetic Properties

9.2.1 Invesitgating the mechanism causing changes to the unpaired electrons in graphite using EPR spectroscopy

The EPR used to measure the samples in these experiments was a Bruker EMX. The following parameters were used in the data collection:

Center Field	3390 Gauss
Sweep Width	1000 Gauss
Power	20.02 mW
Attenuation	10 dB
Receiver Gain	2×10^3
Modulation Amplitude	3 Gauss
Time Constant	40.96 msec
Conversion Time	20.48 msec

Table 9-7: EPR data collection parameters.

From these parameters and the following equation, the g value can be calculated

$$hv = (g_e + \Delta g)\beta B$$

where h is Planck's constant, v is the microwave frequency, β is the Bohr magneton, B is the magnetic field and g_e is the g value for a free electron in a vacuum (2.00232) [Eaton, *et al.*, 2010]. The $\Delta g + g_e$ = g value of the sample. This value contains the chemical information that lies in the interaction between the electron and the electronic structure of the molecule. For organic radicals, the g value is very close to g_e with values ranging from 1.99-2.01. This equation can be simplified as

$$g = \frac{71.4484\ v\ (in\ GHz)}{B\ (in\ mT)}$$

where one tesla equals 10000 gauss [Reiger, 2007]. Using this equation the g value for graphite is calculated as 2.00.

The spins per gram for each sample can also be determined using the following equation:

$$[X] = \frac{[std]A_x R_x (scan_x)^2 G_{std} M_{std} (g_{std})^2 [s(s+1)]_{std}}{A_{std} R_{std} (scan_{std})^2 G_x M_x (g_x)^2 [s(s+1)]_x} \quad [Weil\ and\ Bolton, 2007]$$

where:

	Input (Standard, $MnSO_4$)	Input (Graphite Sample)
[ ] = spin concentration (spins/gram)	$3.1x10^{21}$	[X]
A = sample area under the absorption curve (DI/N)	1.7E8	A_x
$R = \frac{\sum_j d_j}{d_k}$ where d_k is the degeneracy of the most intense line and $\sum_j d_j$ is the sum of the degeneracies of all N lines in the spectrum	1	1
G = Gain of the signal amplifier	$8x10^2$	$2x10^3$
M = Modulation amplitude (Gauss)	10.62	3
Scan = Sweep width	2000	1000
g = g-value	2.3	2.00
s = spin	5/2	0

The spins per gram calculated for the graphite samples were on the order of 10^{16}. These are very small concentrations which can be difficult to measure with EPR. The free radicals being measured by EPR are very active. It is important to measure the samples as

soon as possible after irradiation. All graphite samples were measured on the day the irradiation was completed but even delays of an hour can affect the spin concentration, especially at such low numbers.

The DI/N measurements for each sample were determined three times. The average value was used to calculate spins per gram. From the three DI/N measurements the sample standard deviation was calculated using the following equation:

$$s = \sqrt{\frac{\sum_{i=1}^{N}(x_i - \boldsymbol{x})^2}{N-1}} \quad [Skoog, et\ al., 1988]$$

where N is the number of samples, x is the individual sample and **x** is the sample mean. The standard deviation was then used to calculate the 95% confidence limit using the following equation.

$$95\ \%\ Confidence\ Limit = \boldsymbol{x} \pm \frac{zs}{\sqrt{N}} \quad [Skoog, et\ al., 1988]$$

Where **x** is the sample mean, s is the sample standard deviation, N is the number of samples and z is 1.96 (from Skoog, et al. Table 2-5) [1988]. These values for PCEA AG can be seen in the table below.

Graphite	Irradiation Type	Total Dose (MGy)	Avg DI/N	Sample Standard Deviation	95% Confidence Limit
PCEA AG	Control	0	1.49E+02	0.38	1.30
	190.12	15.3	1.38E+02	0.24	0.82
	564.05	45.4	8.36E+01	0.02	0.08
	564.05	45.4	1.29E+02	0.08	0.26
	1081.4	87.1	1.81E+02	0.06	0.19
	RoomTemp No Irr		2.20E+02	0.14	0.48
	Room Temp Irr		2.64E+02	0.04	0.15
	1000 C No Irr		5.13E+01	0.09	0.31
	1000 C Irr		1.14E+02	0.29	0.97

Table 9-8: Standard sample deviation and 95% confidence limits for PCEA AG EPR samples.

The hyperfines of the various graphite types were alike. Below are typical hyperfines for each of the graphites. As calculated above there is one line for the graphite samples.

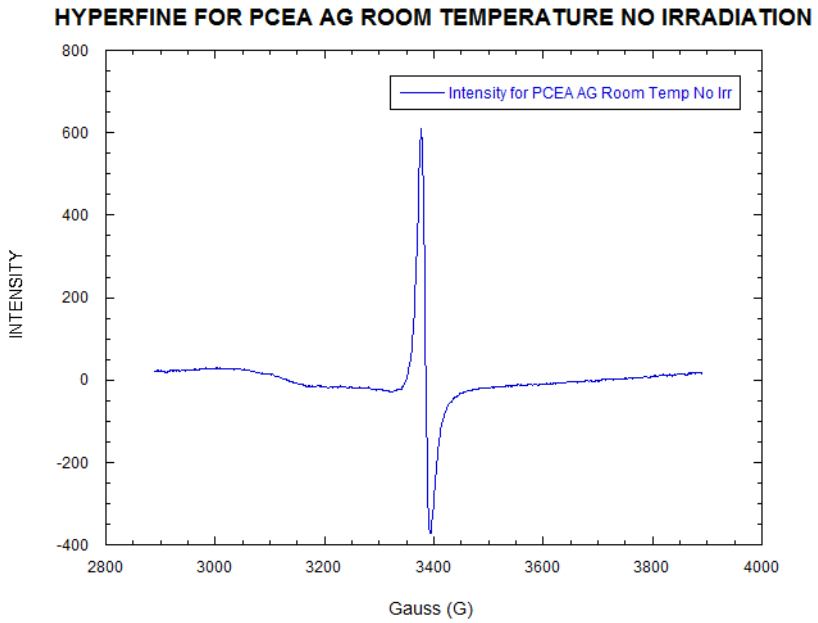

Figure 9-60: Typical hyperfine for PCEA AG.

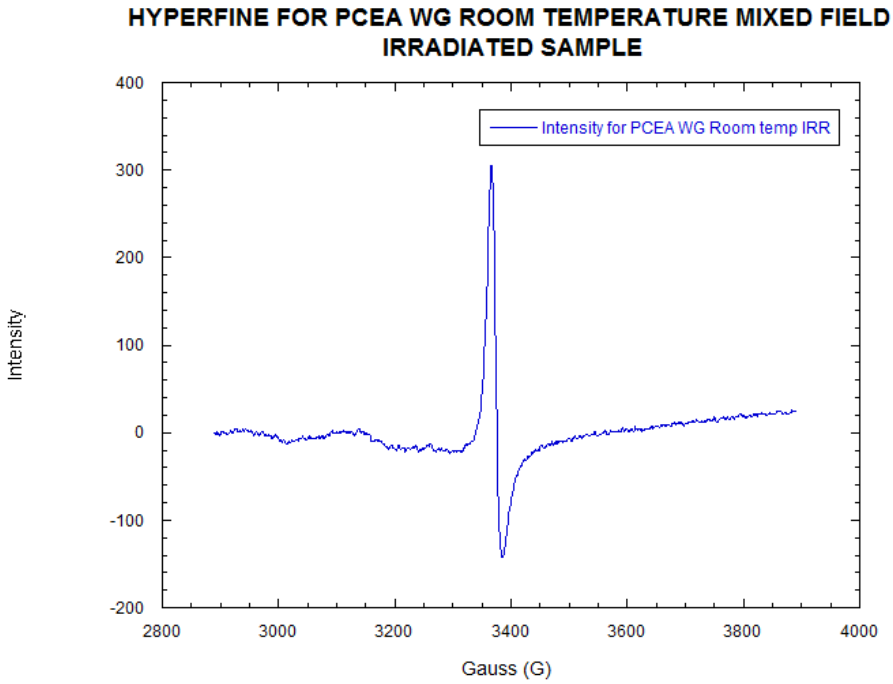

Figure 9-61: Typical hyperfine for PCEA WG.

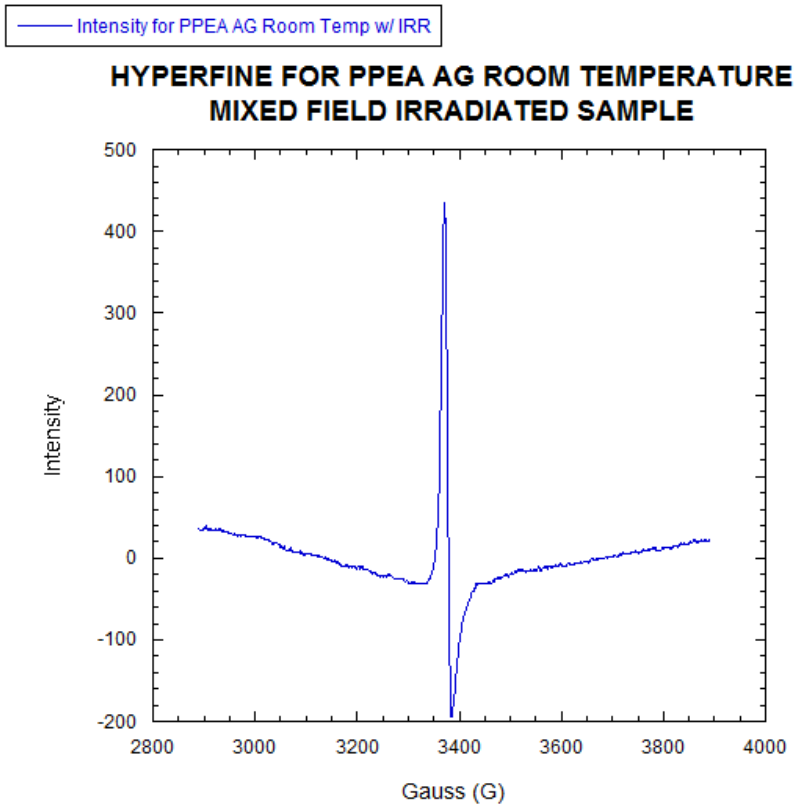

Figure 9-62: Typical hyperfine for PPEA AG.

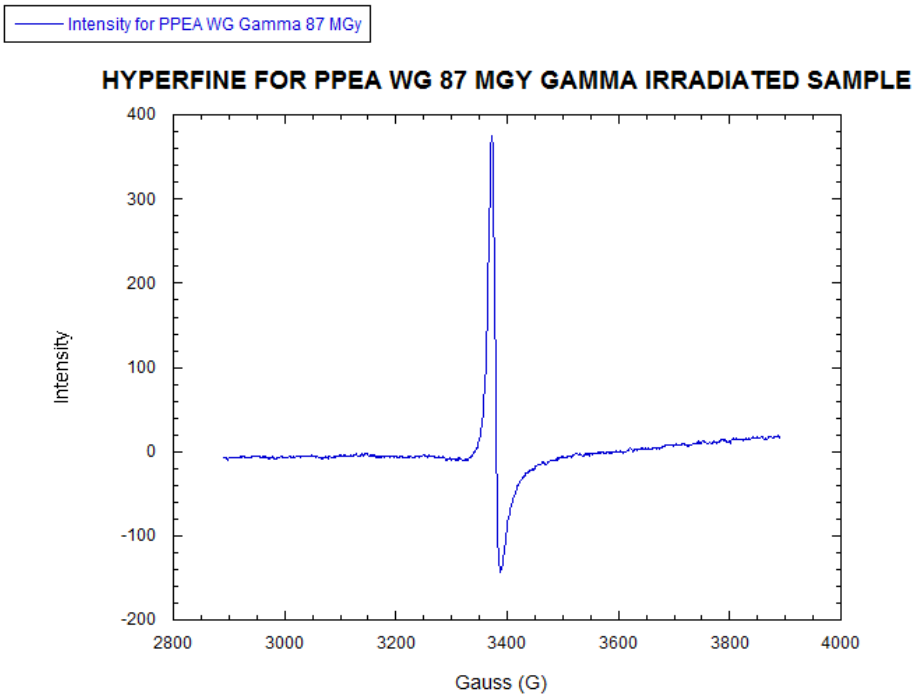

Figure 9-63: Typical hyperfine for PPEA WG.

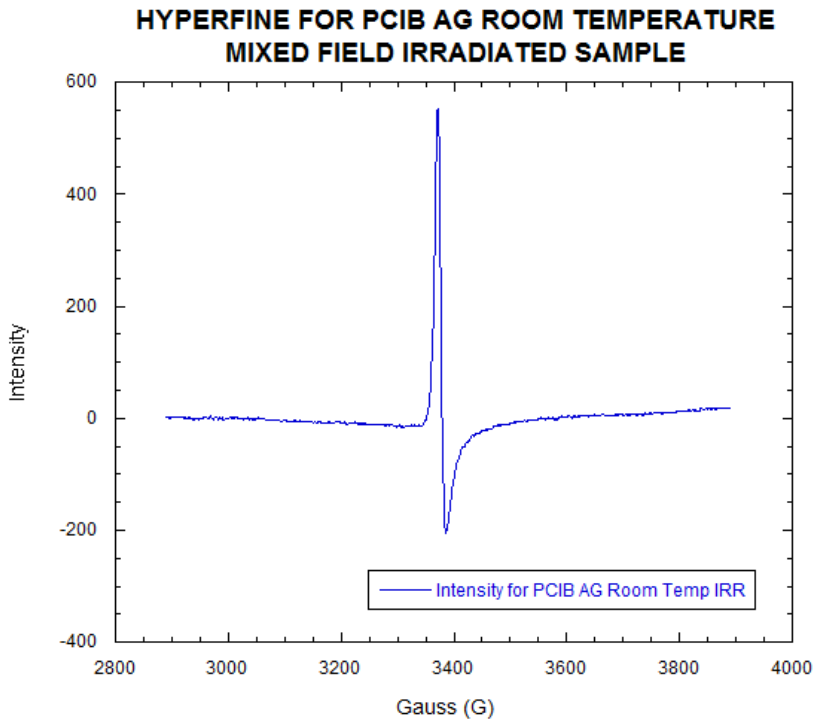

Figure 9-64: Typical hyperfine for PCIB AG.

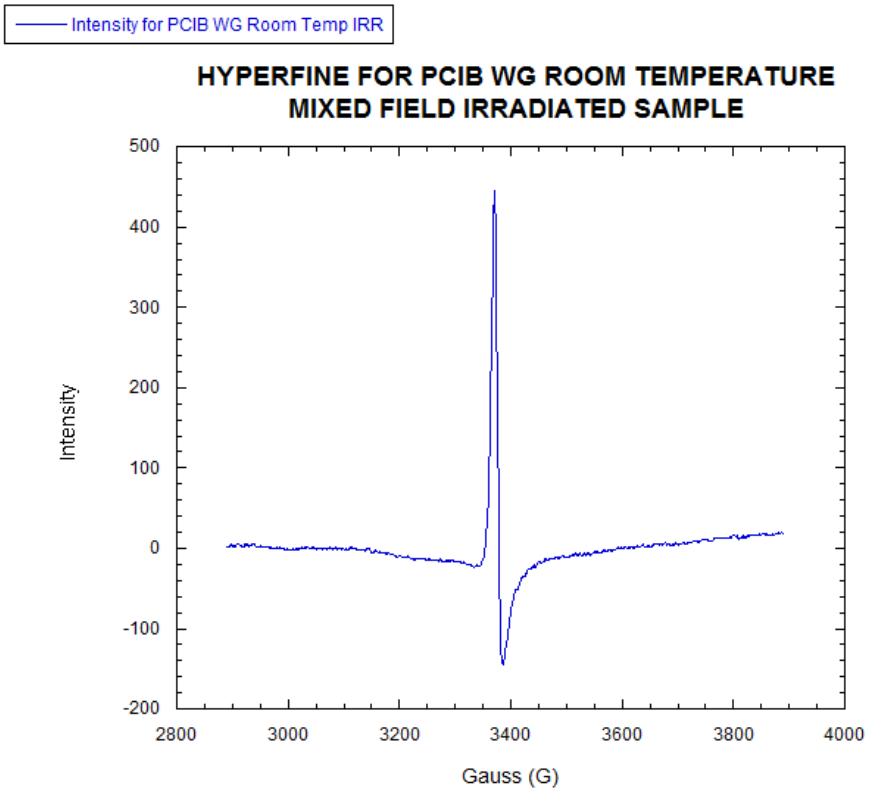

Figure 9-65: Typical hyperfine for PCIB WG.

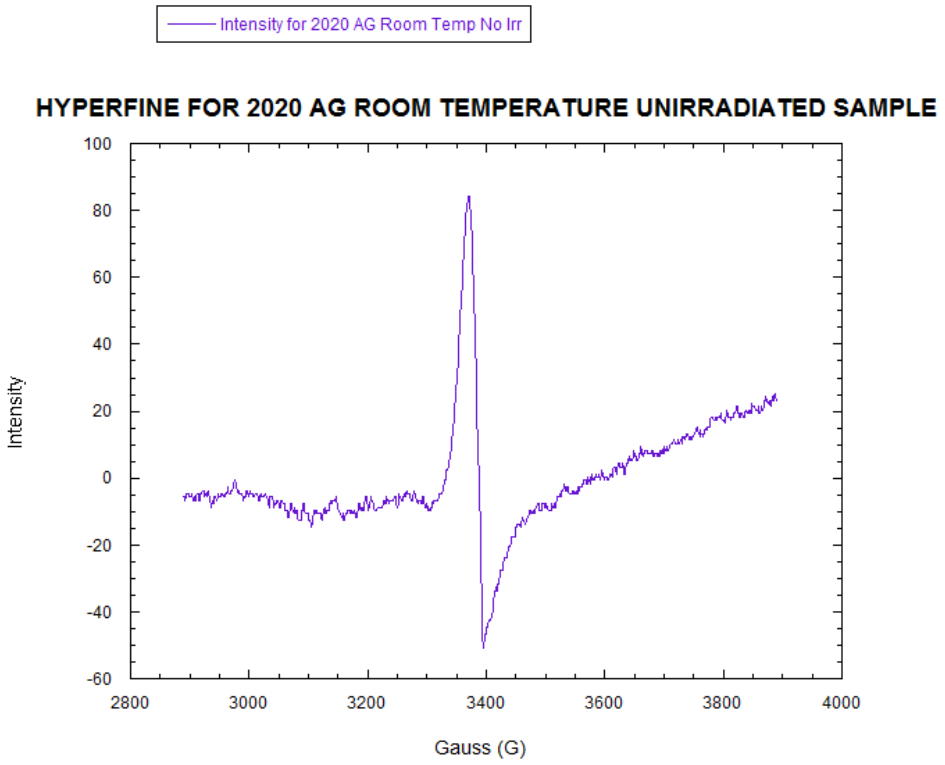

Figure 9-66: Typical hyperfine for 2020 AG.

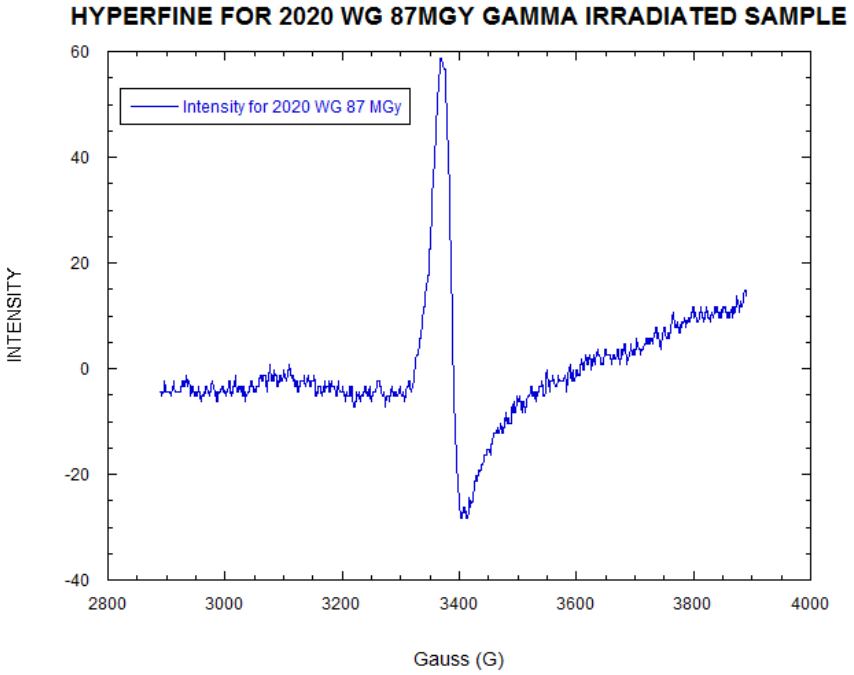

Figure 9-67: Typical hyperfine for 2020 WG.

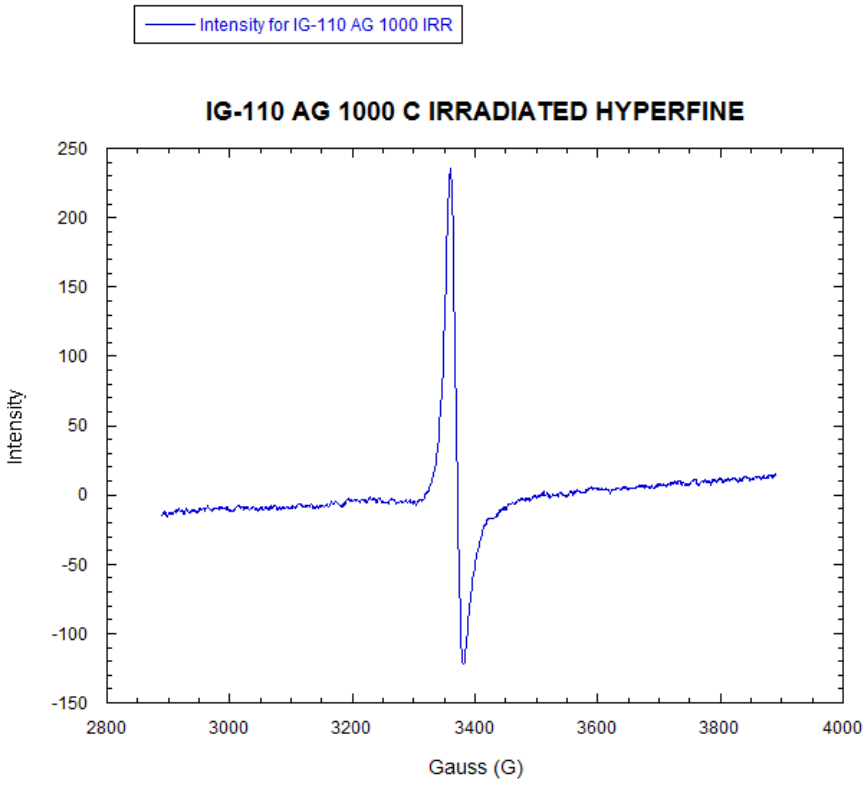

Figure 9-68: Typical hyperfine for IG-110 AG. This sample was irradiated with mixed field irradiation at 1000 °C.

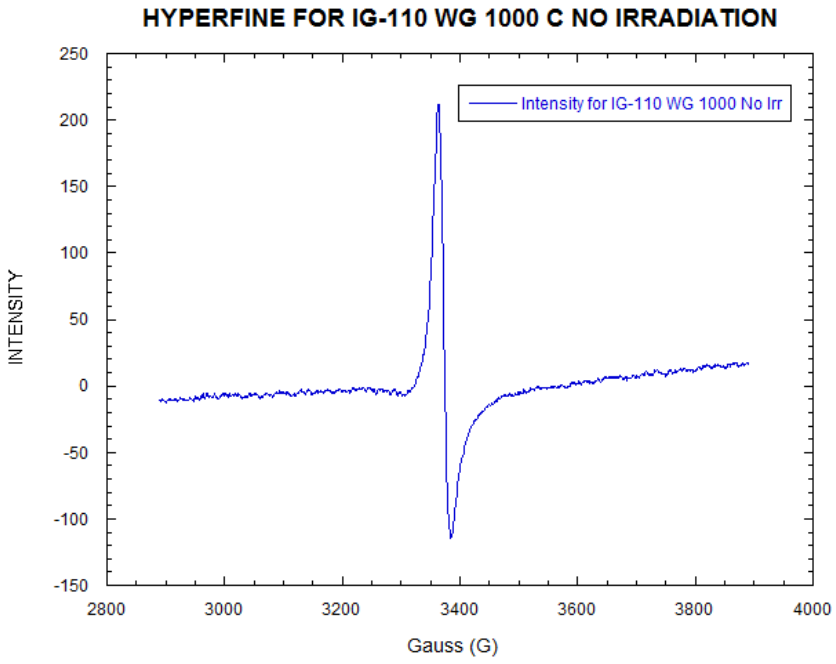

Figure 9-69: Typical hyperfine for IG-110 WG.

The gamma irradiation results are shown in the bar graphs below. In general the spins per gram are at first reduced and then increase significantly at the 87 MGy dose. It has long been known that gamma radiation can have an annealing effect on materials. Oak Ridge National Laboratory began publishing papers on this phenomenon as early as 1962 [Curtis and Crawford, 1962]. These results indicate that the gamma radiation is having an annealing effect on the graphite up to and including the 45 MGy doses. Most likely it is imperfections and dangling bonds from the cutting process that are filling vacancies in the graphite structure. As stated previously, interstitial atoms are mobile at room temperature while vacancies are sessile. This means that at the gamma irradiation temperatures, approximately

100 °C, that interstitial atoms can also move through the graphite structure to fill vacancies, reducing the number of unpaired electrons within the sample.

At very high gamma doses, 87 MGy, there is a significant increase in the number of spins per gram of the samples. This indicates that at high doses the displacements created are larger and more sp^3 hybridized bonds are breaking. The number of carbon atoms moving and refilling vacancies is less than the number of vacancies and interstitials being created resulting in an increase in the unpaired electrons of the sample.

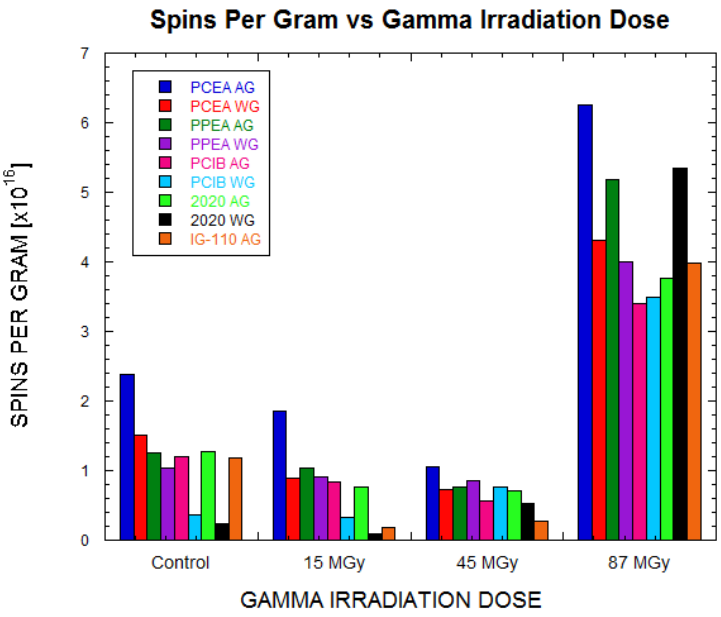

Figure 9-70: The graph above illustrates the change in spins per gram versus the gamma irradiation dose for all graphite grades. The three doses represented are 15 MGy, 45 MGy and 87 MGy.

The changes for the mixed field irradiations, both at room temperature and 1000 °C, are not significant. This results in little change in the spins per gram for the samples. As stated previously, the spins per gram for the graphite samples are very small and it is difficult

to get accurate measurements on the EPR at low concentrations. It is especially difficult to get consistent measurements when small changes in time can cause variations in the measurements. For the 1000 °C samples, this is especially difficult because it is necessary for the samples to cool before they may be handled and measured.

The neutron fluence limit placed on the graphite for use in HTGRs is 8 x 10^{25} n/cm^2 [NRC, 2010]. This number is based on degradation of the graphite due to stress and creep. The east beam port experiments received a neutron fluence of 8.8 x 10^{11} n/cm^2. The average flux for a HTGR is approximately 1 x 10^{13} n cm^{-2} s^{-1} [NRC, 2010]. Due to the large flux of a full scale operating reactor, these experimental samples only received a small fraction of the fluence limit as a result no significant changes were seen in the spins per gram for the mixed field irradiated samples. Bar graphs showing the room temperature and 1000 °C samples spins per gram can be seen below.

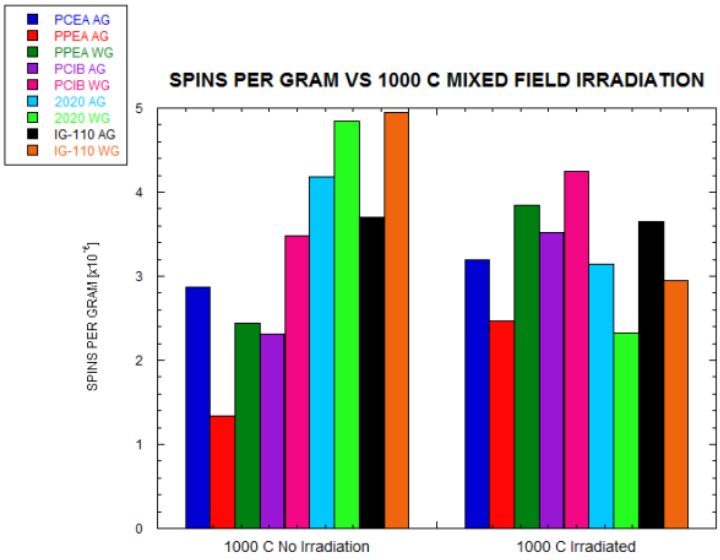

Figure 9-71: Bar graphs representing the 1000 °C irradiated and unirradiated samples.

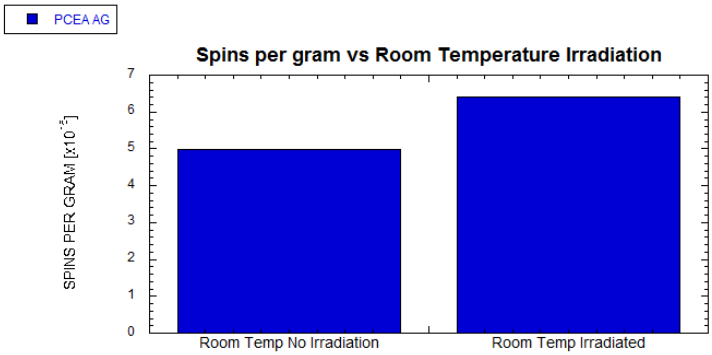
PCEA AG
Spins per gram vs Room Temperature Irradiation
SPINS PER GRAM [x10⁻⁵]
0
1
2
3
4
5
6
7
Room Temp No Irradiation
Room Temp Irradiated

a.

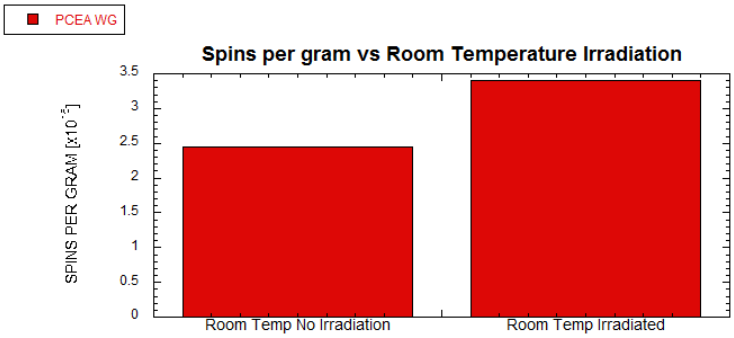
PCEA WG
Spins per gram vs Room Temperature Irradiation
SPINS PER GRAM [x10⁻⁵]
0
0.5
1
1.5
2
2.5
3
3.5
Room Temp No Irradiation
Room Temp Irradiated

b.

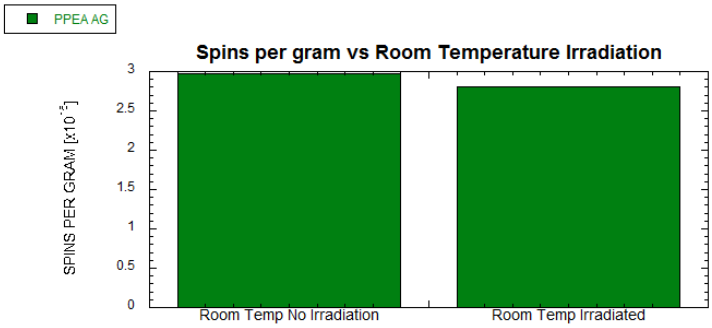
PPEA AG
Spins per gram vs Room Temperature Irradiation
SPINS PER GRAM [x10⁻⁵]
0
0.5
1
1.5
2
2.5
3
Room Temp No Irradiation
Room Temp Irradiated

c.

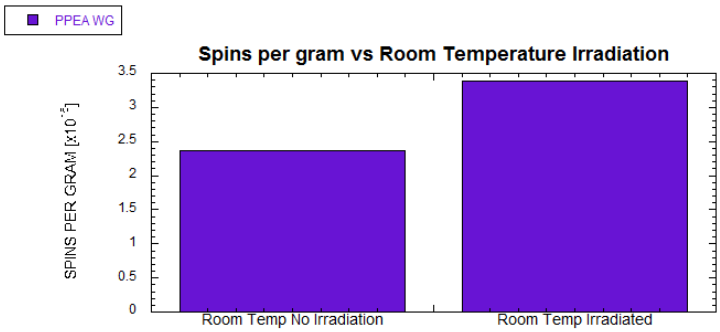
PPEA WG
Spins per gram vs Room Temperature Irradiation
SPINS PER GRAM [x10⁻⁵]
3.5
3
2.5
2
1.5
1
0.5
0
Room Temp No Irradiation
Room Temp Irradiated

d.

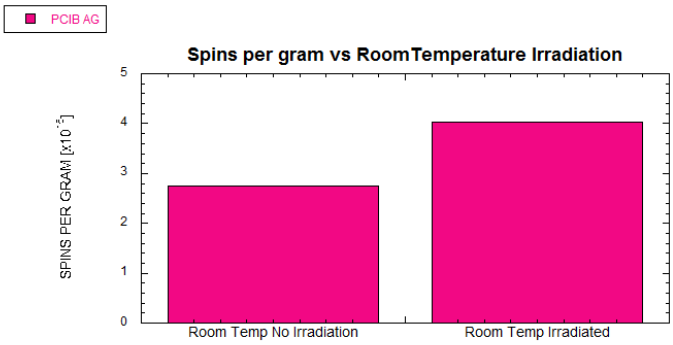
PCIB AG
Spins per gram vs RoomTemperature Irradiation
SPINS PER GRAM [x10⁻⁵]
5
4
3
2
1
0
Room Temp No Irradiation
Room Temp Irradiated

e.

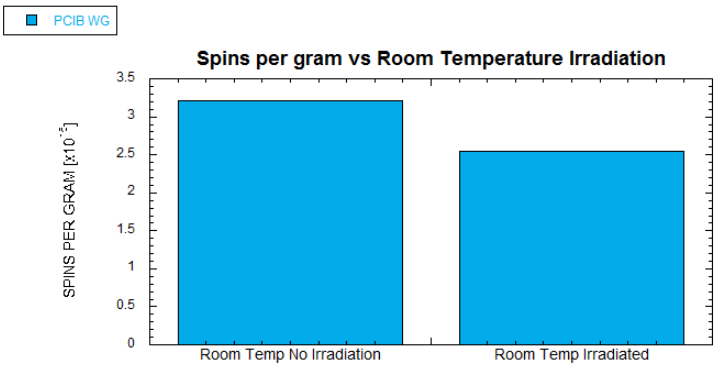
PCIB WG
Spins per gram vs Room Temperature Irradiation
SPINS PER GRAM [x10⁻⁵]
3.5
3
2.5
2
1.5
1
0.5
0
Room Temp No Irradiation
Room Temp Irradiated

f.

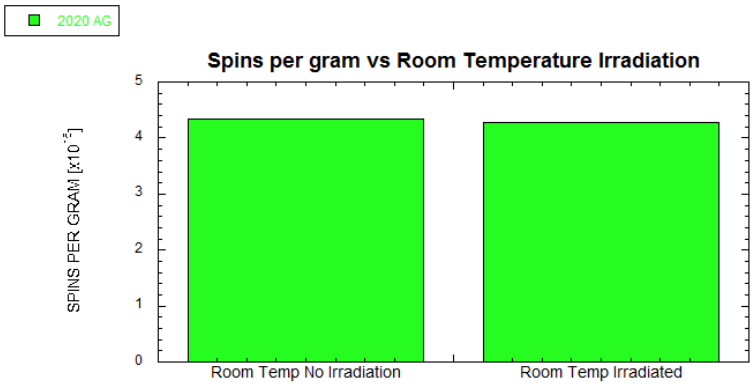

g.

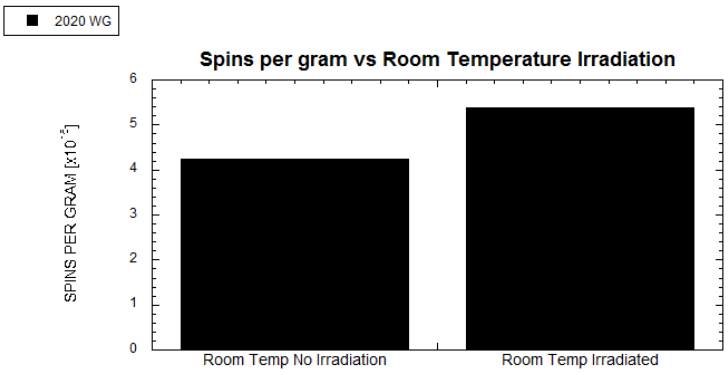

h.

Figure 9-72: Bar graphs representing the room temperature irradiated and unirradiated samples. Graph a. represents PCEA AG, b. PCEA WG, c. PPEA AG, d. PPEA WG, e. PCIB AG, f. PCIB WG, g. 2020 AG, and h. 2020 WG.

9.2.2 Investigation of the radiation-induced changes diamagnetic properties of PCEA using the SQUID magnetometer

The samples were measured using a Quantum Design MPMS XL at the University of Maryland in the Center for Nanophysics and Advanced Materials. The maximum sample size for the instrument is 9 mm and the instrument has a temperature range of 1.8 – 400 K. For AC susceptibility measurements from 0.1 Hz to 1 KHz, the instrument has a sensitivity of 2×10^{-8} emu at 0 T. The samples were run at 0.1 T. The error for the SQUID measurements is 10^{-6} emu, which corresponds to less than 1 percent for the measured samples.

Graphite has a large diamagnetic susceptibility [Delhaès, 2001]. The first measurements on the diamagnetic properties of graphite were performed by Ganguli and Krishnan [1941]. These data were taken between 90 K and 1000 K. Their data were later confirmed by Poquet *et al.* [1960], who measured the properties from 77 K to 2000 K. It was first thought that the large diamagnetic susceptibility (χ) was due to the π electron delocalization in the graphite layers. Since graphite is a narrow band overlap semimetal, the magnetic behavior results from the presence of charge carriers. The large diamagnetic susceptibility of graphite can be explained in terms of its energy band structure [Delhaès, 2001].

The explanation of the diamagnetism in graphite was given by McClure [1960]. His first calculations were based on a simplified two-dimensional band structure and gave the correct order of magnitude and temperature dependence at high temperatures ($T > 1000$ K). A full understanding of the magnetic behavior of graphite was obtained with a three-dimensional band model developed by Sharma, Johnson and McClure [1974]. Maaroufi *et al.* [1982] conducted experiments close to 0 K and calculated the maximum diamagnetism for HOPG at 32 K (see pristine sample in Figure 9-73). The temperature of the maximum diamagnetism varies for different graphites due to differences in the Fermi levels. For these experiments the maximum diamagnetism was observed at 15 K (see Figure 9-74 and 9-75).

Structure defects in the graphite structures may act as electron donors or acceptors and produce changes in the Fermi level position. This effect was examined by Maaroufi, *et al.* [1982] and showed that with neutron irradiation, resulting in doses of 10^{17} neutrons/cm^2, the diamagnetism becomes smaller due to the increase in the number of defects. They also showed that the presence of interstitial atoms produced by the neutron irradiation lowered the interplane interaction leading to a reduction of the diamagnetism of the samples. These

results can be seen in the image below. Kish graphite has been shown to have seven-atom rings and three-atom rings in its structure (see Figure 9-76). These defects cause a shift in the Fermi level in the conduction band and cause the maximum diamagnetism to shift to 45 K, higher than the 32 K observed for HOPG [Delhaès, 2001]. The results of my experiments can be seen in the graphs below. There was a slight decrease in the diamagnetism of the rabbit irradiated samples at 300 °C samples. This change is consistent with the changes seen by Maaroufi et al. [1982]. The changes were smaller since the amount of irradiation was smaller. It would be necessary to measure the same samples several times to determine whether the data are reproducible.

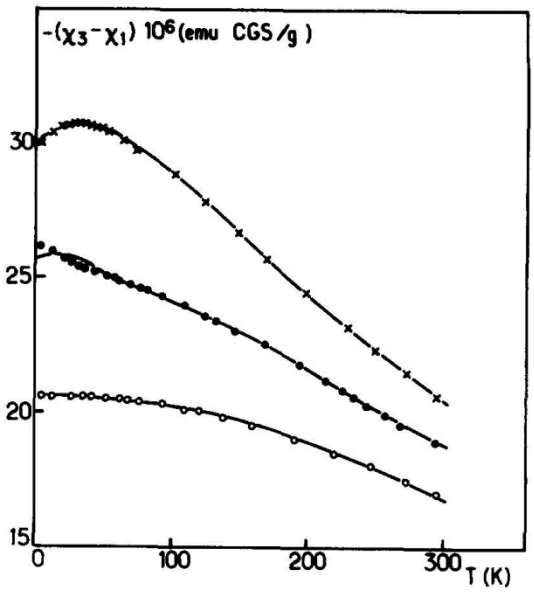

Figure 9-73: Diamagnetic anisotropy of PGCCL samples: X, pristine; •, neutron-irradiated (26C sample); 0, neutron irradiated (28C sample) [Maaroufi, et al., 1982].

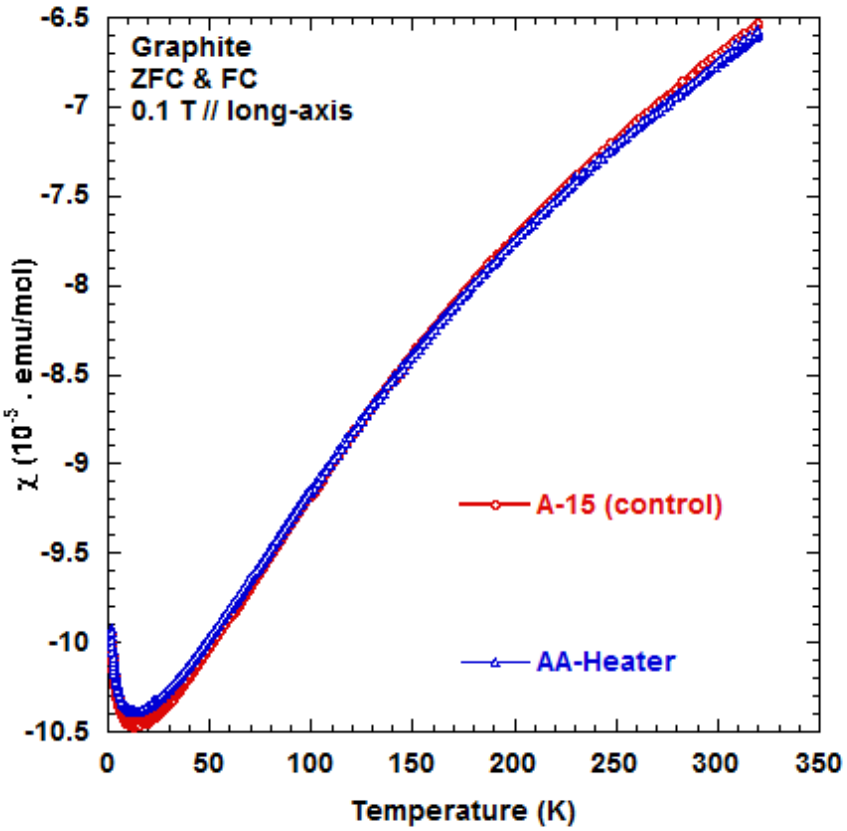

Figure 9-74: SQUID measurement for PCEA AG control and mixed field irradiated rabbit sample. These results show a slight decrease in the diamagnetism with mixed field irradiation.

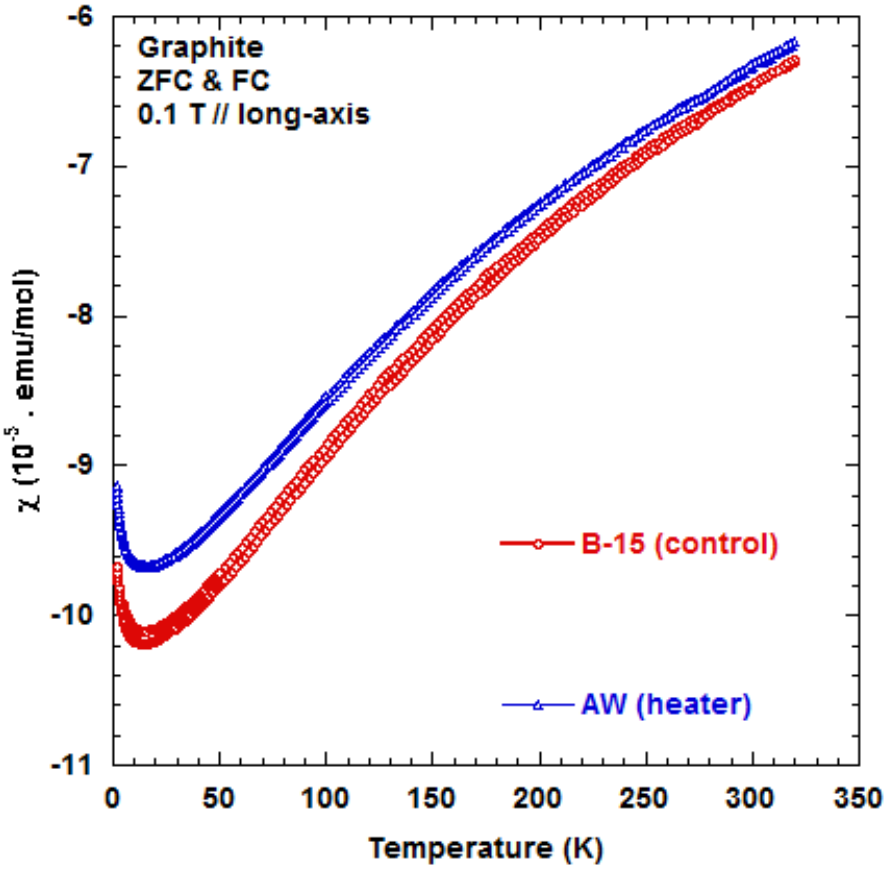

Figure 9-75: SQUID measurement for PCEA WG control and mixed field irradiated rabbit sample. These results show a decrease in the diamagnetism with mixed field irradiation.

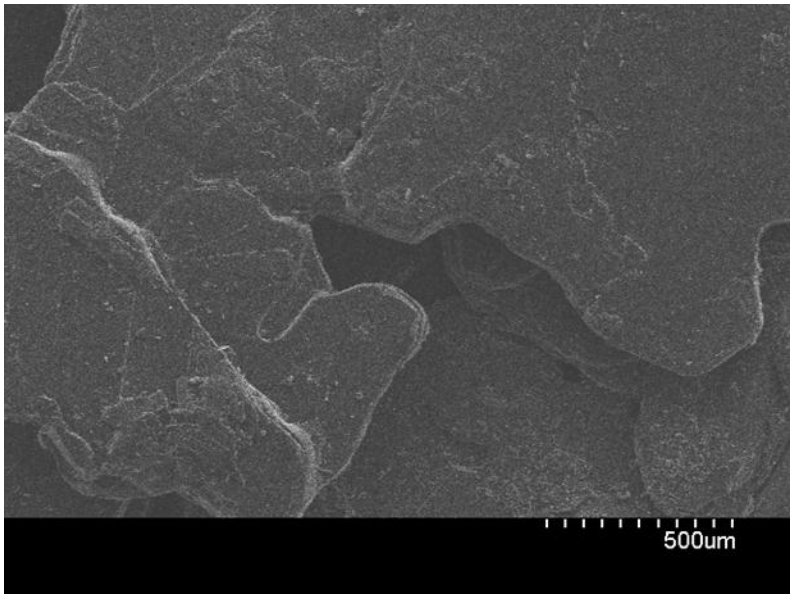

Figure 9-76: Image of natural Kish graphite [Delhaès, 2001].:

Figures 9-77 and 9-78 below show the results of the gamma irradiated sample SQUID measurements. Only a few samples were measured. The maximum diamagnetism for PCEA was determined to be at 15 K for all samples measured. For each of the graphite sample measured, there is an increase in the diamagnetism with 87 MGy of gamma irradiation. Little to no information can be found on the effect of gamma irradiation on graphite. From the observations from these results, it appears that the gamma radiation is causing breakage of the sp^3 hybridized bonds in the graphite. The destruction of these bonds leads to the production of free electrons. This suggests that there is an enhancement of the conduction band leading to an increase in the diamagnetism of the samples. As stated earlier, only one sample was measured for each type. It cannot be determined from these results whether or not the data is reproducible. SQUID analysis of the other grades of graphite needs to be completed before a definite conclusion can be determined.

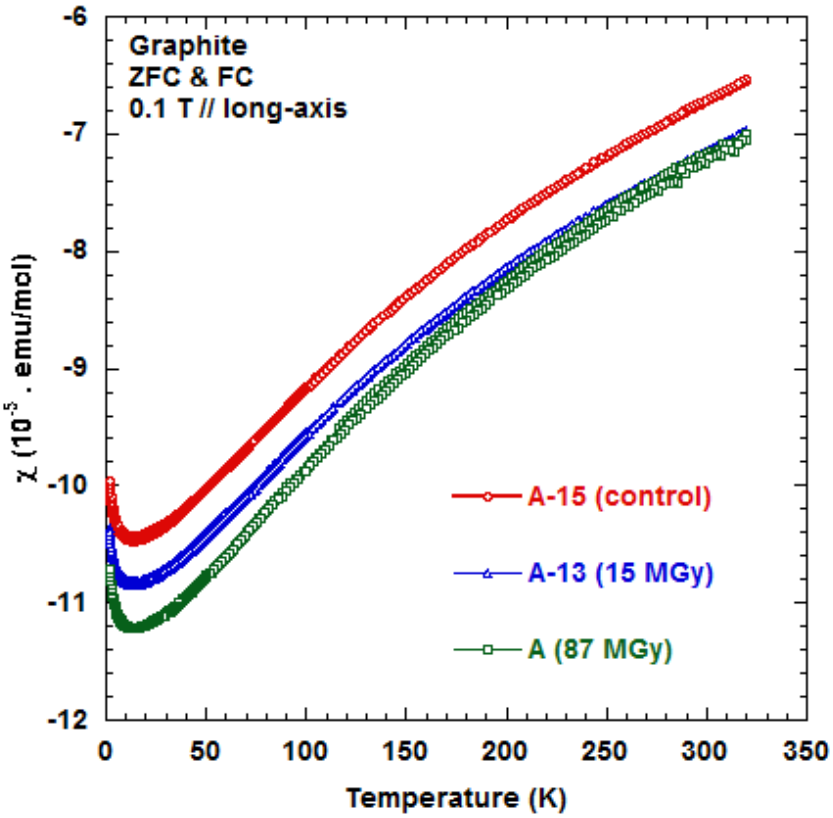

Figure 9-77: SQUID measurement for PCEA AG samples. These results show an increase in the diamagnetism with gamma irradiation.

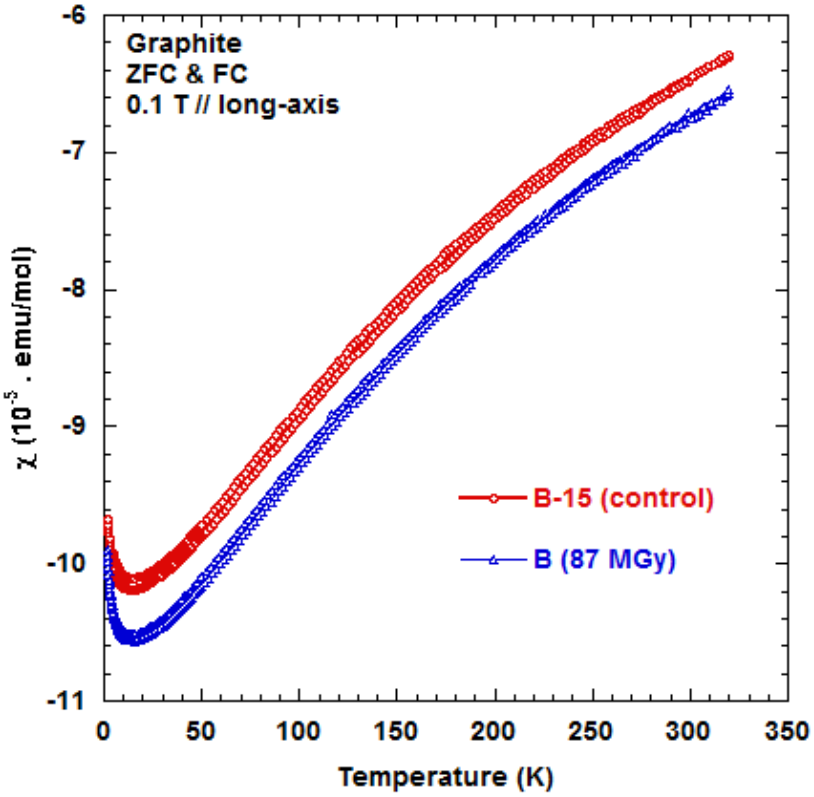

Figure 9-78: SQUID measurement for PCEA WG samples. These results show an increase in the diamagnetism with gamma irradiation.

Chapter 10 Conclusions and Future Work

10.1 Conclusions

Based on my strategy to elucidate the mechanism for gamma and neutron radiation degradations for nuclear grade graphite at elevated temperatures, I reached these conclusions through the examination of changes in the chemical and physical properties.

My results verified that at ambient temperatures the Boudouard equilibrium is on the exothermic carbon dioxide side and at higher temperatures (1000 °C) the endothermic formation of carbon monoxide is the dominant reaction. The appearance of carbon oxides is evidence for reactions of water vapor with the graphite surface as shown in the following equations.

$$C\ (solid) + H_2O\ (gas) \rightarrow CO\ (gas) + H_2\ (gas)$$

$$C\ (solid) + 2\ H_2O\ (gas) \rightarrow CO_2(gas) + 2\ H_2(gas)$$

From these results it is concluded that the nuclear grade graphite follows the Boudouard reaction seen below.

$$CO_2\ (gas) + C\ (solid) \rightarrow 2\ CO\ (gas)$$

It is also concluded that the pore size of nuclear grade graphite affects the oxidation. Investigation of the oxidation of the gamma irradiated sample using XPS showed that in general, the percentage of surface oxygen increased with increasing dose of gamma radiation. This is expected in the gamma radiation field since the gamma radiation induces oxidation in the graphite. At high gamma radiation doses, degassing was observed as the amount of oxygen decreased at 87 MGy. Under normal conditions, graphite contains water from the

humidity in the air and oxygen. The oxygen and water reside in the pores of the graphite. The oxygen will react with the carbon in the following equations:

$$2C\ (solid) + O_2\ (gas) \rightarrow 2CO\ (gas)$$

$$C\ (solid) + O_2\ (gas) \rightarrow CO_2\ (gas)$$

The reaction with oxygen and subsequent release of carbon dioxide and carbon monoxide from the carbon pores results in a decrease in the amount of oxygen on the surface of the graphite. The carbon reaction with water can be seen in the following equation:

$$C\ (solid) + H_2O\ (gas) \rightarrow CO\ (gas) + H_2\ \ (gas)$$

The hydrogen produced in this reaction reacts further with the graphite surface.

$$C\ (solid) + 2\ H_2\ (gas) \rightarrow CH_4\ (gas)$$

However, methane was not seen. The absence of methane may suggest that the concentration of hydrogen produced is very small or that the hydrogen leaves the surface of the graphite before the reaction occurs. The reaction between carbon and hydrogen is slow since carbon and hydrogen are both reducing species. All four of these reactions result in the loss of carbon from the graphite sample and the release of gas.

Oxidation occurs primarily within the graphite pores, which initially make up 20 % of the graphite volume. Therefore, smaller pore sizes result in less oxygen present in the pores, reducing the amount of oxidation. However, larger pore sizes result in a larger surface area increasing the oxidation of the sample. This was seen in the particular graphite grades analyzed. In general the nuclear grade graphite pore sized range from 5 to 35 μm. However, IG-110 has much smaller pore sizes, 1.5 to 3 μm. The smaller pore sizes resulted in less

surface oxidation of the graphite. It is concluded that smaller pore sizes in nuclear graphite will result in high resistance to radiation induced oxidation.

No observable changes were noted in the crystallinity of the graphite samples. This conclusion was the result of the analysis of the XRD spectra. Unlike the gamma doses for the samples, the neutron doses were much lower than those expected in HTGRs. It was concluded that under these irradiation conditions, all five grades of nuclear graphite showed resistance to structural damage induced by neutron irradiation. Should significant changes had occurred at these lower doses, it would have been necessary to determine whether that particular graphite was still acceptable for use within a nuclear reactor. Since certain graphite reflectors in the HTGR are expected to stay in place for the life of the reactor, it is important that the structure of the graphite stays sound under high doses of radiation.

Bond rupture between the graphene layers was induced by gamma irradiation equivalent to lifetime gamma dose for HTGR. This conclusion was achieved through the observation of the increase in both the paramagnetic and diamagnetic properties of the nuclear grade graphite upon gamma irradiation. Based on the EPR of the gamma-irradiated samples, the number of spins per gram is at first reduced and then increases significantly at the 87 MGy dose. These results suggest that the gamma radiation anneals the graphite at doses up to and including the 45 MGy. Most likely, this effect reduces the number of defects and dangling bonds from the cutting process. This results in the filling vacancies and electron traps in the graphite structure.

At very high gamma doses, such as 87 MGy, there is a significant increase in the number of spins per gram of the samples. This indicates that the electron traps have been filled and the unpaired electrons from the rupture of the sp^3 hybridized bonds are directly

contributing to the paramagnetism of the sample. This conclusion is further illustrated by the SQUID results. There are few results on the diamagnetism of gamma irradiated graphite. This research shows that diamagnetism also increases due to the rupture of the sp^3 hybridized bonds that donate free electrons.

The changes in the EPR spectra for the mixed field irradiations illustrate that the unpaired electrons are filling the electron traps but the neutrons are also creating more traps. This results in an unchanged paramagnetism of the samples. The SQUID results showed slight decreases in the diamagnetism of the mixed field irradiated samples. This is consistent with previous experiments conducted by Maaroufi.

These results show that all five of the nuclear graphite grades analyzed under these experimental conditions exhibit strong resistance to damage caused by gamma and neutron irradiation. In the future, if a grade of graphite shows significant oxidation and structural changes under the conditions used in the present tests, it should not be considered as a candidate for use in nuclear reactors. This knowledge base of nuclear graphite is crucial in determining appropriate grades of graphite for use in nuclear reactors.

These results lend themselves to being used as screening tests of new grades of nuclear graphite. If the graphites show significant degradation and structural changes at these levels of irradiation, they should not be considered for use in nuclear reactors. The samples in these experiments were only exposed to a fraction of the neutron doses expected in an operating reactor. To prove that they can withstand such an environment, they must first be able to withstand these lower doses. Thus the results of the present work provide valuable screening to identify grades of graphite that merit advanced testing at doses closer to those expected in actual reactor service.

10.2 Future Work

There is a need for future work on graphite as new proposed nuclear graphite grades are introduced. Since the graphite properties are a function of the starting materials (i.e., the feed stock), each nuclear graphite grade must be characterized fully before use in a nuclear reactor.

It is necessary to irradiate the samples in a mixed field to much higher doses in the helium and water environment. The east beam port experiments received neutron doses on the order of 10^{11} n/cm^2. However, the doses expected for graphite in HTGRs are of the order of 10^{25} n/cm^2. In order to examine the effect of high doses of mixed field irradiation, further experiments must be carried out at accumulated fluences near 10^{20} n/cm^2. This will allow more in-depth characterization of the oxidation effects on the graphite at high temperatures. An enclosed apparatus could be placed in the pool at the MUTR and receive doses for an entire year or more. The environment could have the helium and water vapor mixture and give results would be closer to the dose rates that would be expected to be received by the graphite moderator in an operating HTGR.

It would also be enlightening to gather some graphite samples from operating gas-cooled reactors. The United Kingdom has several Magnox reactors that are still in operation. Although those reactors are cooled using CO_2, the oxidation and neutron effects can be compared to the samples run in the MUTR.

Magnetic properties of the samples run in these experiments need to continue to be examined. Only one grade of graphite was examined in the SQUID. The other four graphite grades may show different changes in the diamagnetic strength of the samples. The different

types of graphite may also exhibit different maximum diamagnetism values. The data that were collected also needs to be rerun to ensure reproducibility of the data.

The samples from these experiments can also easily be prepared for further examination. For instance, if a clean highly ordered pyrolytic graphite sample can be run in the XPS, the changes in the sp^2-sp^3 hybridization of the samples can be characterized and modeled. This would lead to further insight into the mechanism leading to the oxidation of the graphite. Once the mechanism is fully understood, steps can be taken to lessen the oxidation effects on the graphite.

Accident scenario studies should also be done on graphite at different stages of irradiation. This information would lead to information on the maximum amount of oxidation the graphite samples would encounter in the HTGRs.

Correlations should be established between changes in the spectroscopic and magnetic properties and changes in the mechanical properties upon exposure to high doses of radiation. Idaho National Laboratory and Oak Ridge National Laboratory have done much research on the changes in the mechanical properties. By correlating the information, plant designers have a much broader picture of how the graphite will react in the reactor environment.

Since graphite properties are determined by the starting material, there will always be new types of nuclear graphite produced. This fact ensures that these characterizations will need to be carried out for each type of nuclear grade graphite before it can be approved for use in nuclear power plants.

10.3 Contribution to Science

My research contributed to the science and engineering of nuclear graphite as follows:

- My results were consistent with the Bourdourd equilibrium. At lower temperatures the equilibrium is on the exothermic carbon dioxide side and on higher temperatures the endothermic formation of carbon monoxide is the dominant reaction.
- A certain degree of bond rupture occurs between the graphene layers by gamma radiation. Gamma doses comparable to the lifetime doses for HTGRs were used. This conclusion was achieved through the observation of the increase in paramagnetic and diamagnetic properties of the graphite.
- Smaller pore sizes result in less oxygen present in the pores, reducing the amount of oxidation. Larger pore size results in a larger surface area increasing the oxidation. It is concluded that smaller pore sizes in nuclear graphite will result in higher resistance to radiation induced oxidation.
- There was no observable change in crystallinity of the nuclear grade graphites. Unlike, gamma doses the neutron doses were much less than expected in HTGRs.
- These results demonstrate that thermal annealing is occurring at elevated temperatures during mixed field irradiation. The mobility of the electron traps increases at elevated temperatures. That will increase the probability of unpaired electrons filling the electron traps.
- Results show that all five of the nuclear graphite grades analyzed under these experimental conditions exhibit strong resistance to damage caused by gamma and neutron irradiation as well as thermal effects. In the future, if a grade of graphite

shows significant oxidation and structural changes under the conditions used in the present tests, it should be reconsidered as a candidate for use in nuclear reactors

Appendix A. The Manufacturing of Graphite

In medieval times, a large amount of pure graphite was discovered in Borrowdale, Cumberland. It was originally used for marking sheep and it eventually gave rise to the pencil industry. These deposits have long since run out. Other large deposits of natural graphite have also been found in Madagascar, Korea and the United States. Today, most graphite is made synthetically. Figure 2-2 shows a typical manufacturing process for nuclear graphite. The process typically takes 6 to 9 months to perform. The final product is largely determined by the starting materials.

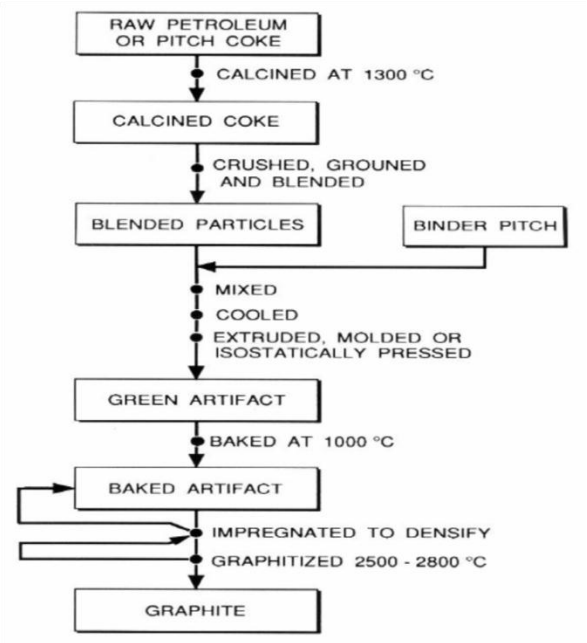

Figure A-1: Manufacturing process for nuclear graphite (Hassel and Mark, 1924). The entire process takes 6 to 9 months to complete.

Graphite is commonly made by the Acheson process [1895]. The filler material is normally petroleum coke but anthracite and lampback may be used. Petroleum coke is easily graphitized and achieves a higher degree of crystallinity that other filler materials, when

heated to a temperature range of 2800 ºC to 3000 ºC. Petroleum coke and coal-tar pitch are used in today's graphite process.

Petroleum coke is a by-product in the refining process of petroleum crude. It is produced in the cracking of heavy refinery oil. The cracking process decomposes the large hydrocarbon molecules into smaller ones. The cracking process can utilize thermal or catalytic cracking. In thermal cracking the oil is pressurized and fed through heated coils. The oil is heated to approximately 500 ºC. At this point the oil is fed into a reaction chamber where the pressure is raised to 500 psi. After the reaction chamber, the oil enters a flash chamber, where lighter fractions are vaporized. Most plants in the United States use the catalytic cracking method because it is capable of producing higher octane gasoline. The catalytic cracking process uses a catalyst, normally aluminum silicate, to increase the reactivity of the molecules in the gas-oil feed stock. Once the hot catalyst is added, the oil is vaporized and then goes to a reaction chamber. The cracked materials are fed to a fractionator and then separated by boiling. The heaviest components will be left on the bottom and these will then be coked.

Coking is essentially another more rigorous thermal cracking process. The main purpose of coking is to produce additional gasoline and gas oil from the residue of the initial cracking process. There are three different methods of coking: batch, fluid and delayed. Batch coking is performed in stills but this method has been superseded by the delayed coking process. Fluid coking uses a fluidized bed of hot coke particles. These particles are maintained at temperatures of 500 ºC and pressures of 20 to 40 psi. The coker feeds are heated and sprayed into the fluidized bed. The most commonly used process is the delayed coking process. In this process the heated feed stocks are fed into the bottom of a fractionator, where light fractions are flashed off. It is then pumped through the coking

heater where the temperature is raised to approximately 500 ºC [Hassel and Mark, 1924]. This induces further cracking. The heated stock is then passed into the coke drum. The heated stock remains in the drum for a period of time, normally 24 hours. This is a batch operation and normally involves two drums. While coking is taking place in one drum, the other drum is being emptied and preheated for the next run. The time to complete one cycle is about 48 hours. The coke is removed from the drums by high velocity water jets.

Calcination

After the raw coke is produced, it then goes through a calcination process. This is a heat-treatment process that utilizes temperatures of up to 1400 ºC. This process removes the volatile materials from the coke and also causes shrinkage of the material. Most of the impurities present in the coke at this point are hydrogen, sulfur, nitrogen and vanadium. Vanadium is normally the largest impurity, approximately 15 ppm [Hassel and Mark, 1924]. This process can be performed at either the refinery or the carbon plant.

One type of calciner utilizes a long, inclined steel tube lined with bricks. The tube is approximately 150 feet long and 8 feet in diameter. There is a fire at the low end of the tube which ignites the volatile gases. This is turn provides much of the thermal energy required to perform the calcining process. The tube is also rotated slowly and the coke moves slowly down to the low end of the tube. It takes approximately 2 hours for the coke to travel the length of the tube. This process can produce about 10 tons of coke per hour [Hassel and Mark, 1924].

Once the coke leaves the steel tube it is cooled to temperatures below 200 ºC. This can be done by either a controlled water spray or by passing the coke through water-cooled ducts. Approximately 25 % of the weight of the initial coke is lost during the calcining

process. This loss is due not only to the loss of volatile materials but also the loss of the water that was added during the removal of the coke from the coking drums. As these substances are removed from the coke, the carbon bonds are disrupted but they then reform. During the reformation further cross-linking and polymerization occur with the carbon bonds and these processes lead to increased mechanical strength and also a greater order of the carbon atoms.

The coke is then fed through a one-inch mesh screen. Material that does not fit through the mesh is sent to a crusher where it is reduced in size. The ground material is separated by particle size. Those pieces smaller than about 0.5 mm are sent to be crushed further in a mill into the "flour" component [Nightingale, 1962]. The final diameter size will range from 2 to 300 μm. Both the flour and the coke particles are placed in bins to await the mixing process.

The calcined cokes from different refineries will appear different. The properties of the coke itself are largely determined by the feed material. The difference in the shape of the particles comes from the difference in alignment of the crystals in the raw coke. This determines how the calcined material fractures. A high degree of crystal alignment leads to flakes or needle-shaped particles. Less ordered alignments result in cubical or spherical particles.

Binder

Coal-tar pitch is most commonly used as the binder material. It is a by-product of coke ovens. There are three important requirements for a binder. The first is that the material should be thermoplastic. A thermoplastic material is a material the shape of which can be changed at elevated temperatures. This allows thorough mixing of the filler and binder, aids

in forming the filler-binder mixture and allows storage of the final product at room temperature with no deformation.

Another requirement is that the binder needs to have high carbon content. This ensures that bonding can occur between the binder and the coke. Coal-tar pitch contains about 93 percent carbon. It also has a high specific gravity. The higher the specific gravity, the more carbon atoms can be deposited in and around the coke filler particles. Coal-tar pitch has a specific gravity of 1.30 g/cm^3 [Nightingale, 1962], which is above the density of the other binder materials, making coal-tar pitch a good choice for a binder.

Formation of the Green Artifact

In order to form the nuclear graphite blocks, the flour and particles are mixed together to form the filler. The filler is then mixed with the binder and prepared to form the graphite blocks. The percentage of filler to binder varies based on the method of forming. For extruded samples, the mixture is approximately 30 parts of binder by weight to 100 parts of filler. The main purpose of the mixing is to ensure a uniform distribution between the pitch and coke components.

At this point the graphite is extruded, molded or isostatically pressed into the desired shape. During the extrusion process, which normally occurs using a cylinder-die assembly, the particles tend to align themselves with their long dimension parallel to the direction of the extrusion. Those that are isostatically molded tend to give the least anisotropic graphite. This helps to ensure that swelling and contraction during temperature changes and irradiation does not occur in any one direction and makes isostatically molded graphite better for nuclear environments. At this point the graphite is referred to as a green artifact since it has not yet been graphitized.

Baking of the Green Artifact

The purpose of the baking process is to transform the pitch from a thermoplastic material to a rigid solid. This must be done while the shape of the artifact is preserved. The baking process is the most critical in the graphite formation process. The final baking temperature is between 800 ºC and 1000 ºC.

As the green artifact reaches 200 – 300 ºC, it must be supported by a permeable pack because the artifact loses its mechanical strength. It is also important for the support to be permeable so that the volatile gases are able to escape the body. Because we are trying to maintain the shape of the body and the volatile gases being evolved makeup about 10 percent of the weight of the article, the initial heating process must be very slow up to about 500 ºC. The temperature is then raised to the final baking temperature. Cross-linking occurs at this temperature, causing the carbon to become hard and brittle. Shrinkage in volume also occurs during the baking process, resulting in the loss of about 5 percent of the size.

The physical properties of the baked carbons vary. This variation is caused by differences in baking temperatures, the coke used and the binder to filler ratio. After baking, the carbon is brittle and hard to machine [Nightingale, 1962].

Once the baking process is completed, the artifact is impregnated to reduce the porosity and increase the bulk density. Coal-tar pitch is typically used as the impregnator as well. This process takes place in a large autoclave. The artifacts are heated to 200 ºC and then molten pitch is added. A pressure of 100 psi is maintained for several hours [Nightingale, 1962]. Afterwards, the artifacts are cooled with a water spray.

Graphitization

Prior to graphitization, the artifacts show no real crystal structure. This is mostly due to the residual hydrogen within the artifact. For this process the temperature of the carbon is raised to 3000 ºC. In industrial manufacture the process is carried out by stacking electrodes on top of one another in walls which are surrounded by a coke powder [Blackman, 1970]. By the time the temperature reaches 1500 ºC, most of the hydrogen has evolved and all that remains is the carbon and metallic impurities. From 1500 ºC to 2500 ºC crystal growth is occurring. Above 2500 ºC, some crystal growth continues but the dominant process is annealing of the graphite. The properties of the graphite continue to improve as the temperature is increased to 3000 ºC. At this point nuclear graphite is born. The following table shows typical nuclear graphite properties.

Property	Value	Standard Deviation
Bulk Density, g/cm^3	1.70	0.02
Electrical Resistivity, µohm-cm		
Parallel to grain	734	59
Perpendicular to grain	940	111
Thermal Conductivity, cal/sec cm ºC		
Parallel to grain	0.543	
Perpendicular to grain	0.330	
Tensile Strength, psi		
Parallel to grain	1440	254
Perpendicular to grain	1260	308
Young's Modulus, psi		
Parallel to grain	1.49 x 10^6	0.14 x 10^6
Perpendicular to grain	1.11 x 10^6	0.09 x 10^6

Table A-1: Typical Properties of Room-Temperature Graphite (Nightingale, 1962).

Once graphitization is complete the graphite is purified. There are three methods of purification: treatment with pure coke, thermal purification and gas purification. The first method is not used because of the restrictive choice of raw materials. Gas purification is most widely used for nuclear graphite.

Most non-nuclear graphites are produced using the thermal purification method. In this method, the graphite is heated. This temperature is tightly controlled between 2200 to 2800 ºC. It is held here for a period of time in order to allow the impurities to diffuse out.

The gas purification process uses gases to permeate the bulk graphite and graphite crystals. The gases react with the impurities, thereby removing them from the matrix. The

most widely used gas is chlorine. The gas is carried to the furnace through side heaters and the excess gas and reaction products are collected in the top of the furnace. Once the graphite enters the cooling portion of the cycle, the furnace is filled with nitrogen or other inert gas. This removes the residual chlorine from the pores of the graphite [Blackman, 1970].

Appendix B. Raman Spectroscopy Results

The results shown in this appendix are similar to the results in Section 9.1.2. The images illustrate the areas examined by Raman spectroscopy. Unfortunately, no conclusive results could be determined from the images.

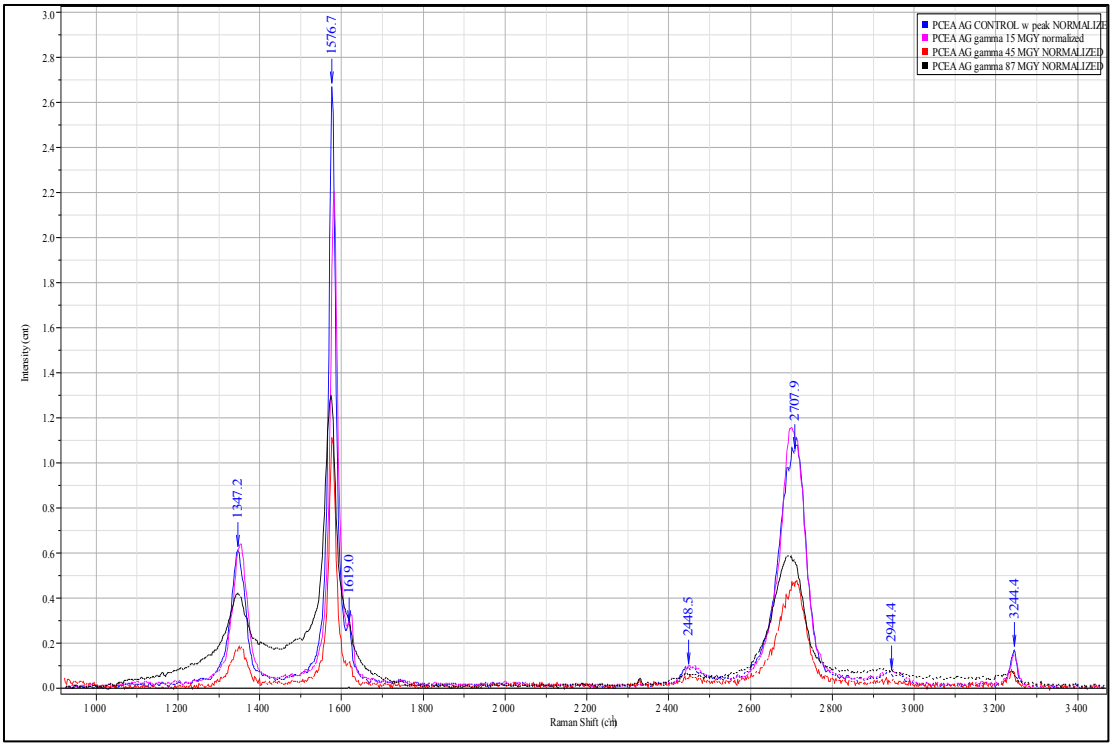

Figure B-1: PCEA AG control and gamma Raman spectra.

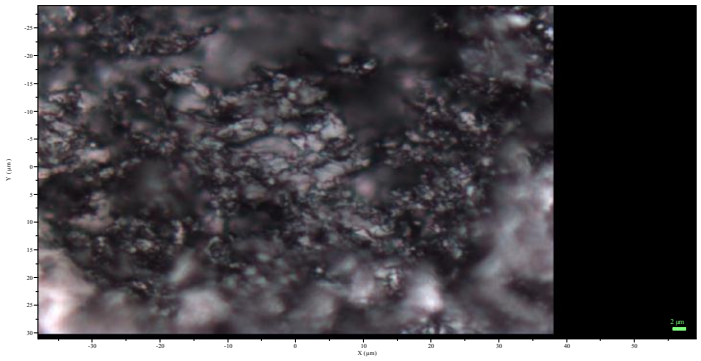

Figure B-2: Image of PCEA AG control sample prior to Raman spectra collection.

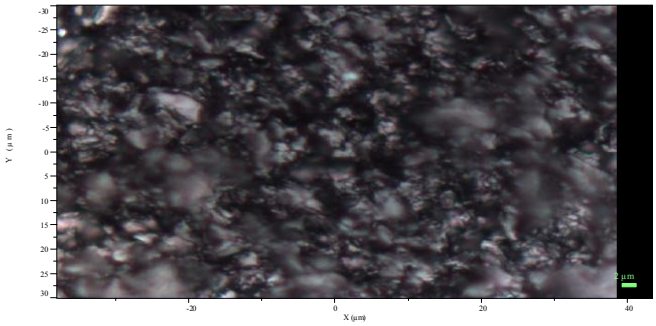

Figure B-3: Image of PCEA AG 15 MGy gamma irradiated sample prior to Raman spectra collection.

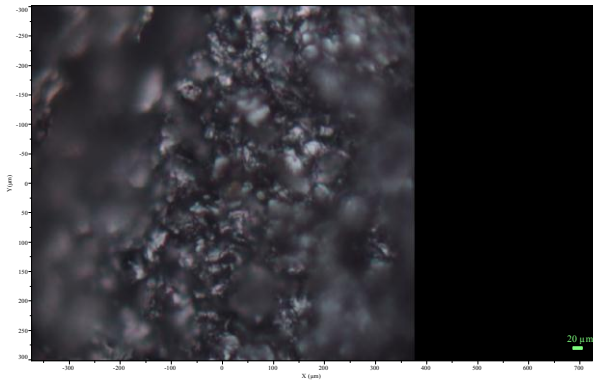

Figure B-4: Image of PCEA AG 45 MGy gamma irradiated sample prior to Raman spectra collection.

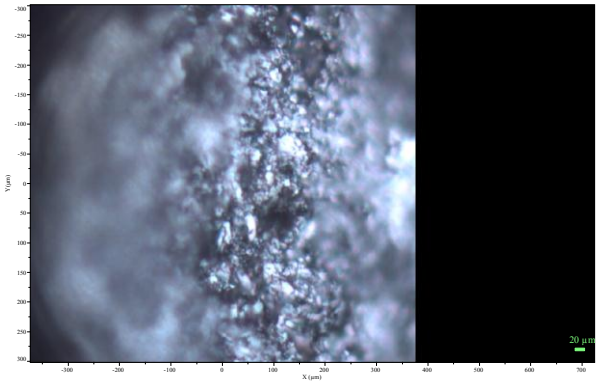

Figure B-5: Image of PCEA AG 87 MGy gamma irradiated sample prior to Raman spectra collection.

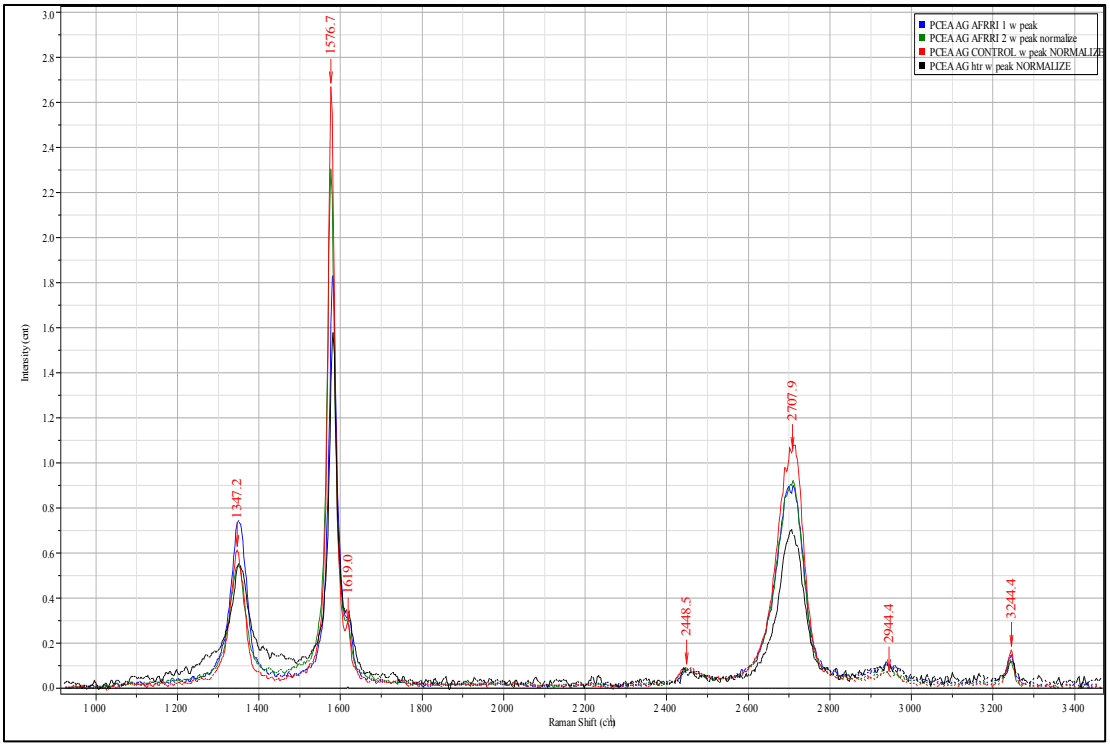

Figure B-6: PCEA AG control, AFRRI and rabbit heater (300 °C) samples Raman spectra.

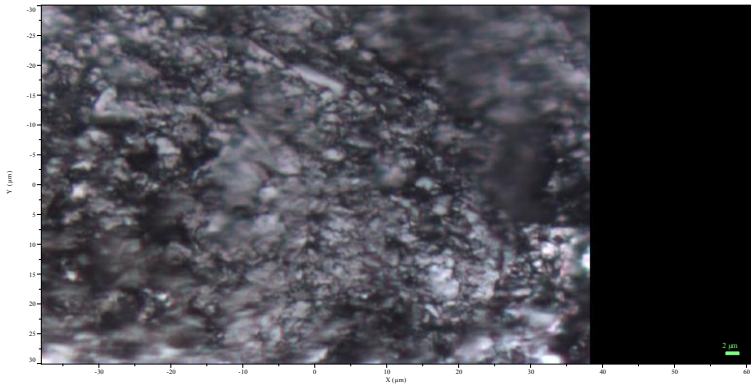

Figure B-7: Image of PCEA AG AFRRI 1 sample prior to Raman spectra collection.

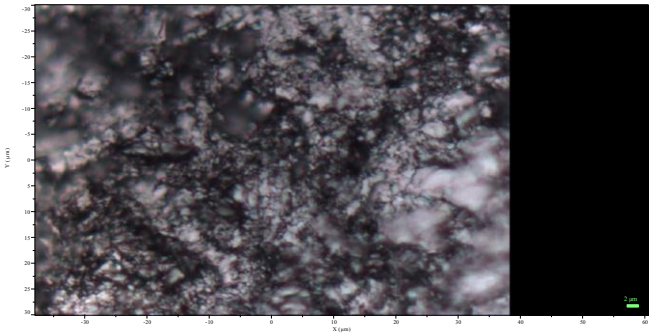

Figure B-8: Image of PCEA AG AFRRI 2 sample prior to Raman spectra collection.

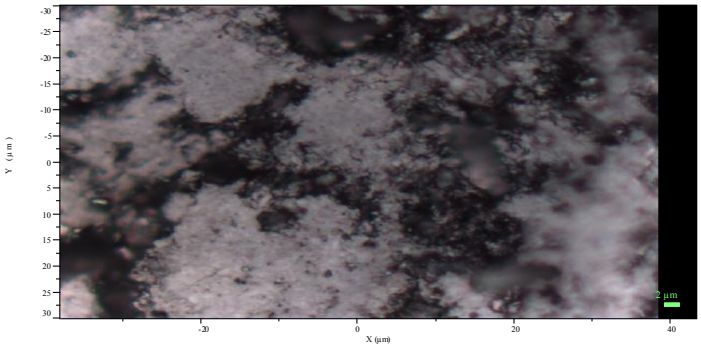

Figure B-9: Image of PCEA AG 300 °C rabbit irradiated sample prior to Raman spectra collection.

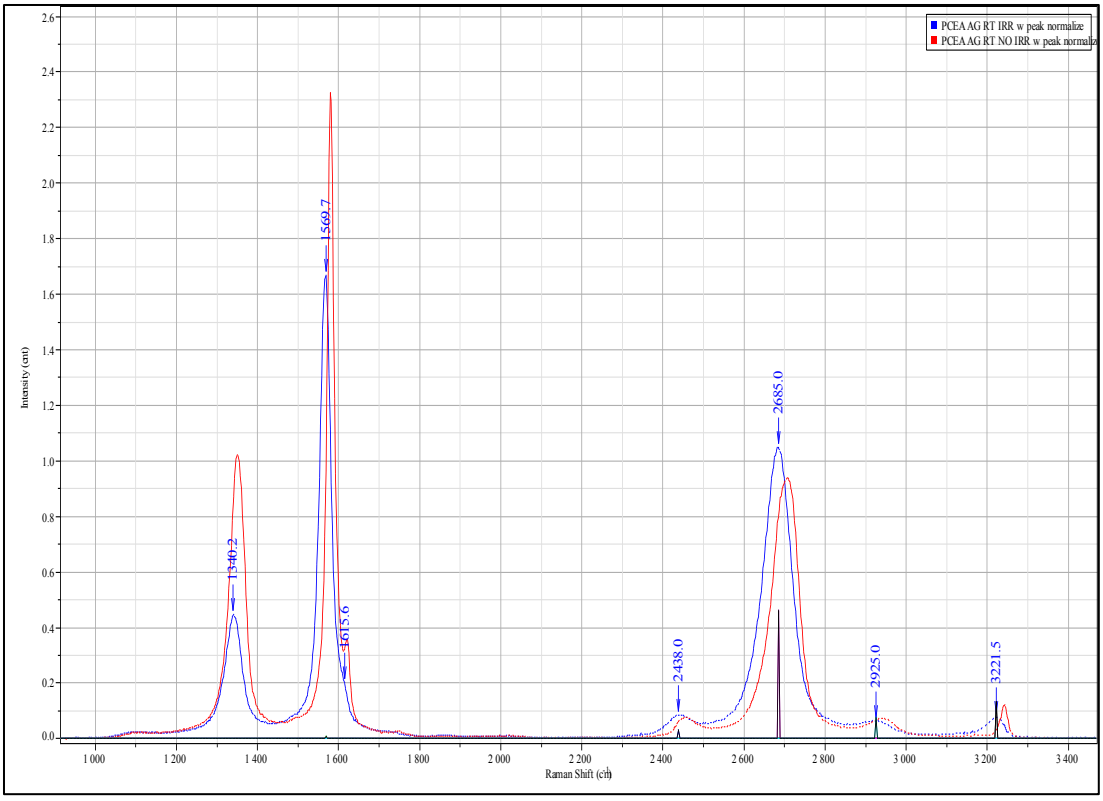

Figure B-10: Raman spectra of PCEA AG room temperature irradiated and unirradiated samples.

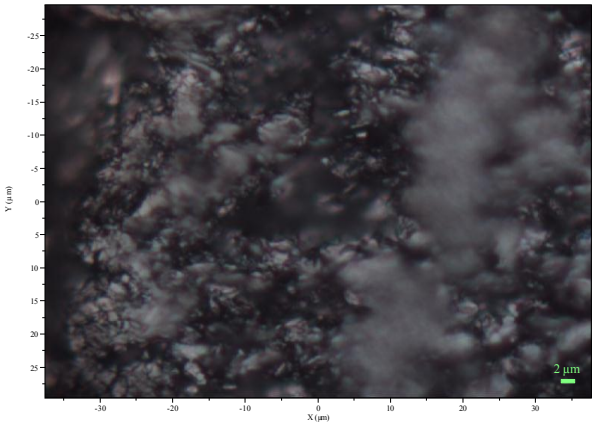

Figure B-11: Image of PCEA AG room temperature unirradiated sample prior to Raman spectra collection.

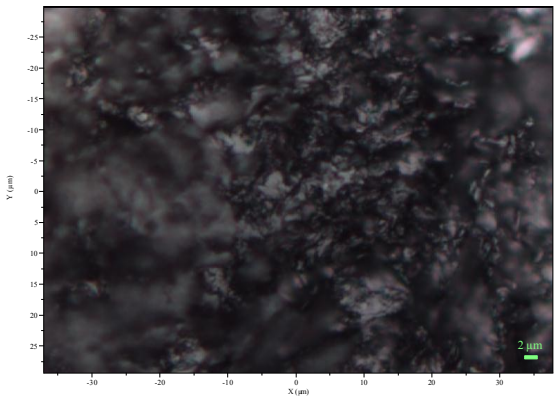

Figure B-12: Image of PCEA AG room temperature irradiated east beam port sample prior to Raman spectra collection.

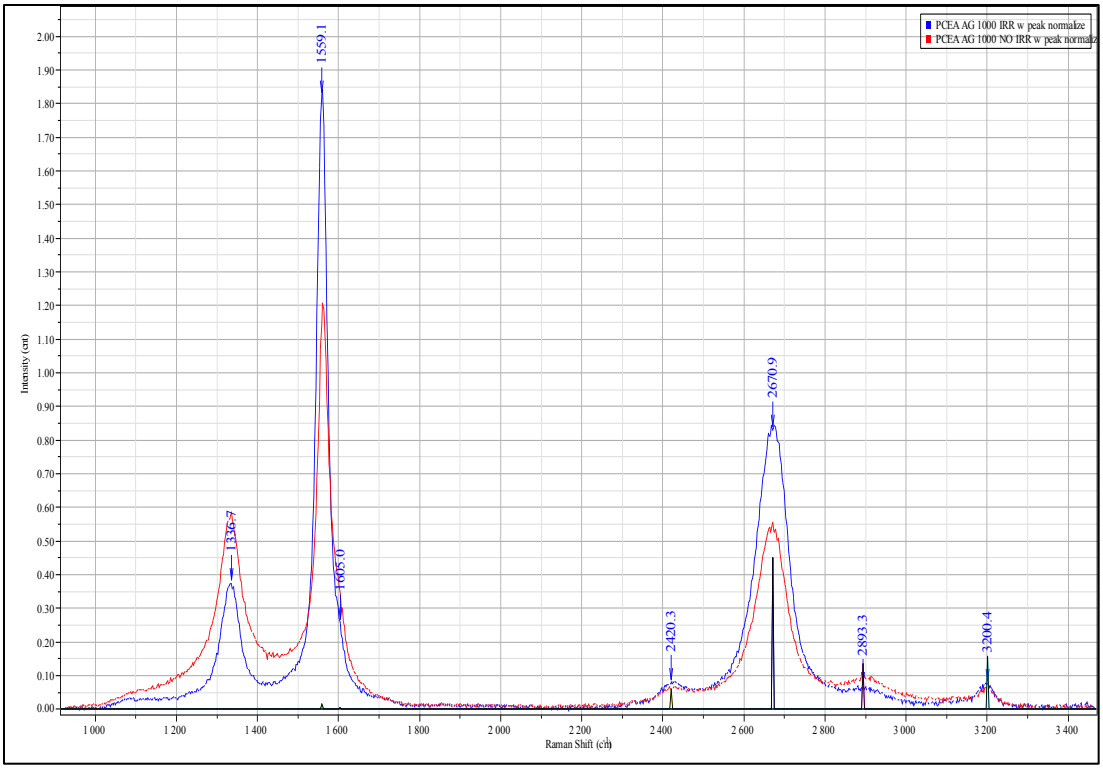

Figure B-13: Raman spectra of PCEA AG 1000 °C irradiated and unirradiated samples.

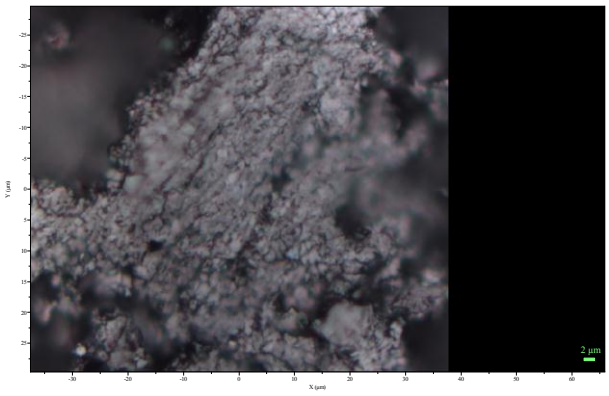

Figure B-14: Image of PCEA AG unirradiated 1000 °C sample prior to Raman spectra collection.

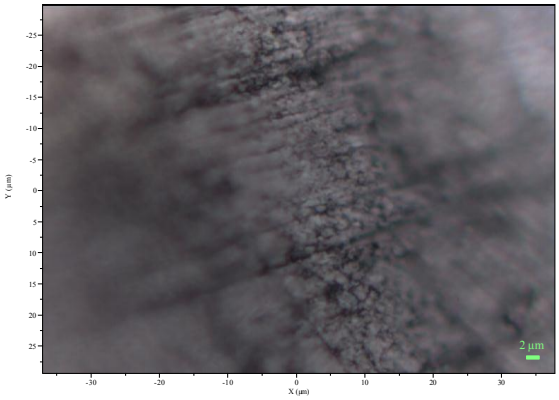

Figure B-15: Image of PCEA AG irradiated 1000 °C sample prior to Raman spectra collection.

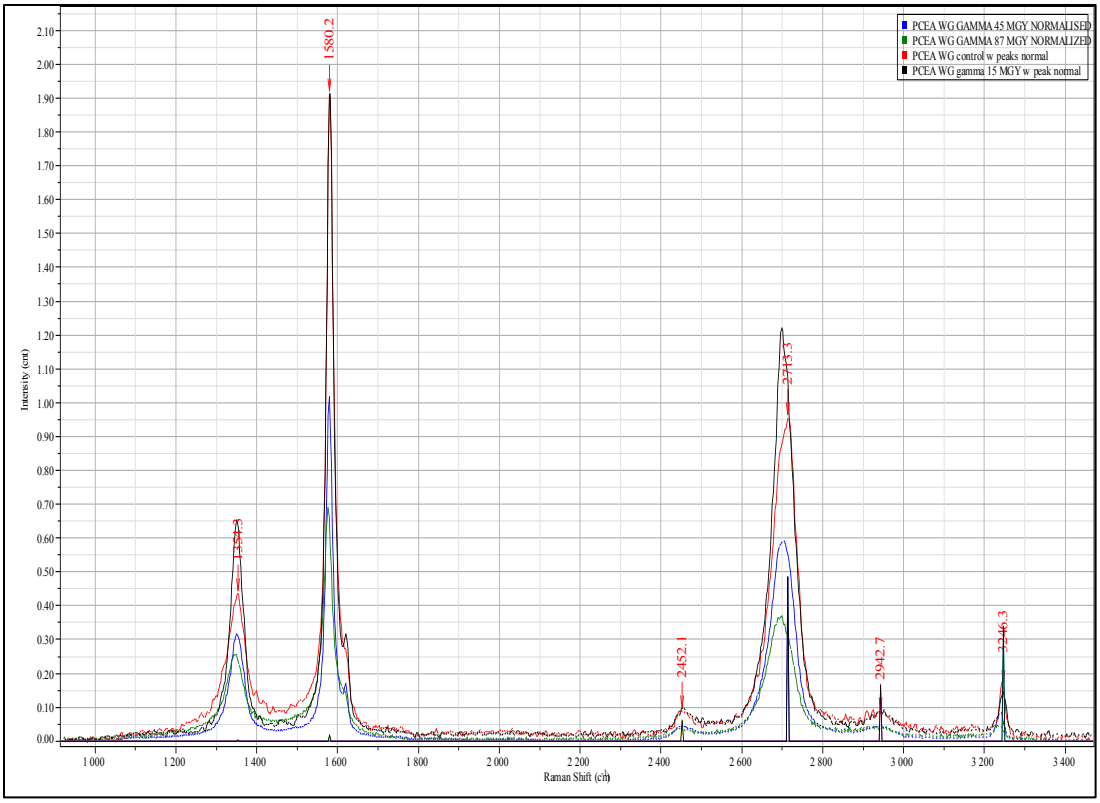

Figure B-16: Raman spectra of PCEA WG control and gamma irradiated samples.

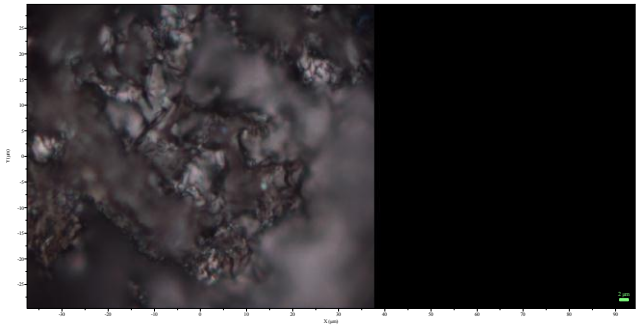

Figure B-17: Image of PCEA WG control sample prior to Raman spectra collection.

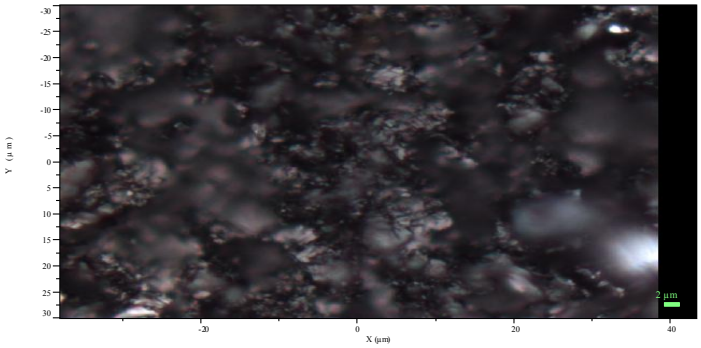

Figure B-18: Image of PCEA WG 15 MGy gamma irradiated sample prior to Raman spectra collection.

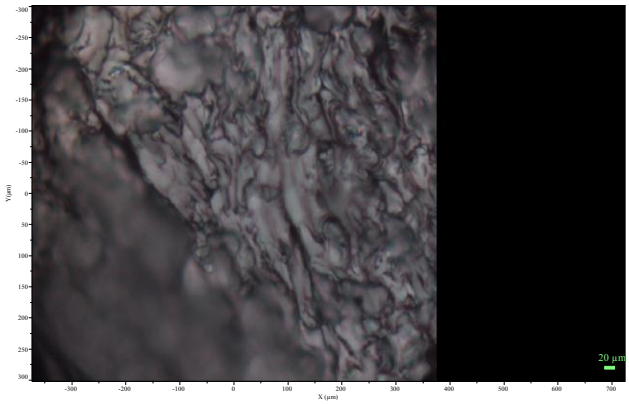

Figure B-19: Image of PCEA WG 45 MGy gamma irradiated sample prior to Raman spectra collection.

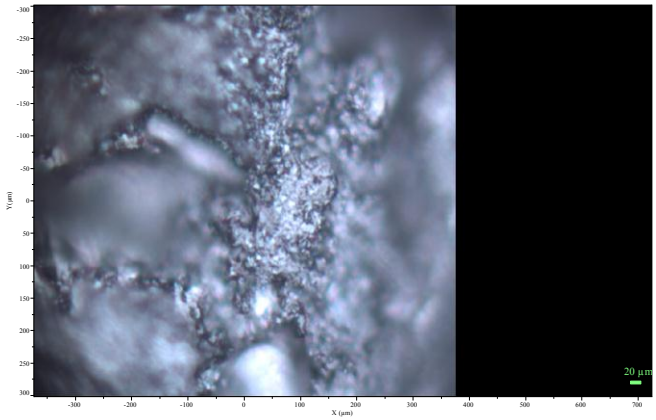

Figure B-20: Image of PCEA WG 87 MGy gamma irradiated sample prior to Raman spectra collection.

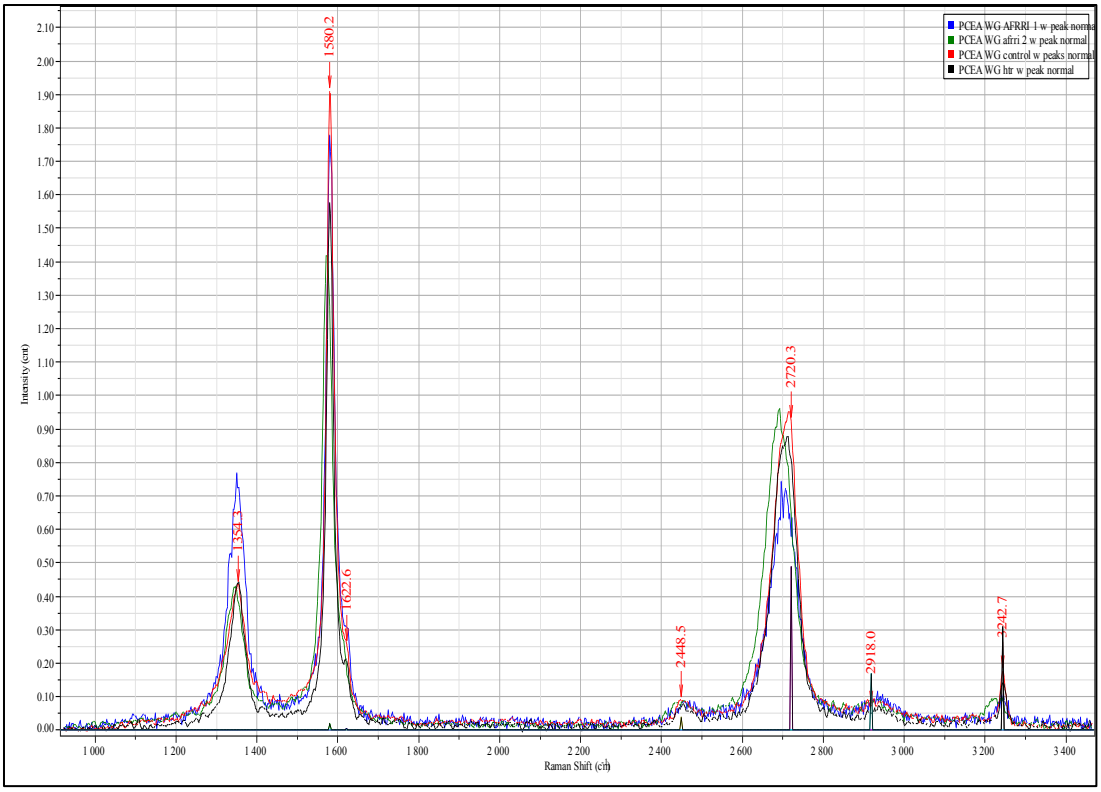

Figure B-21: Raman spectra of PCEA WG control, AFRRI irradiated and 300 °C rabbit irradiated samples.

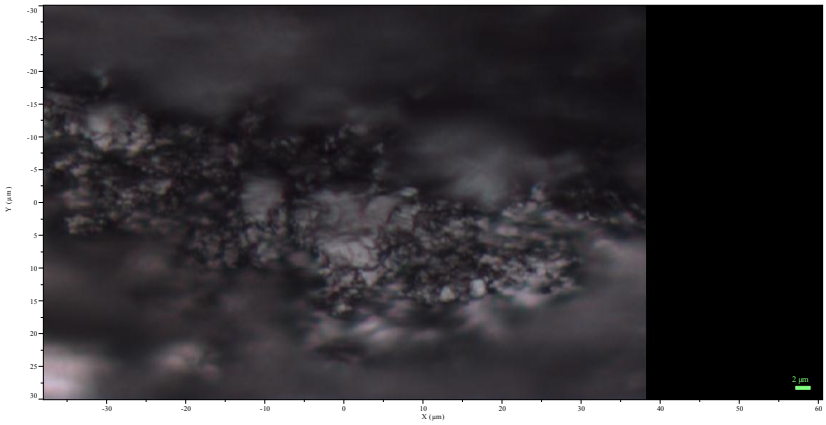

Figure B-22: Image of PCEA WG AFRRI 1 sample prior to Raman spectra collection.

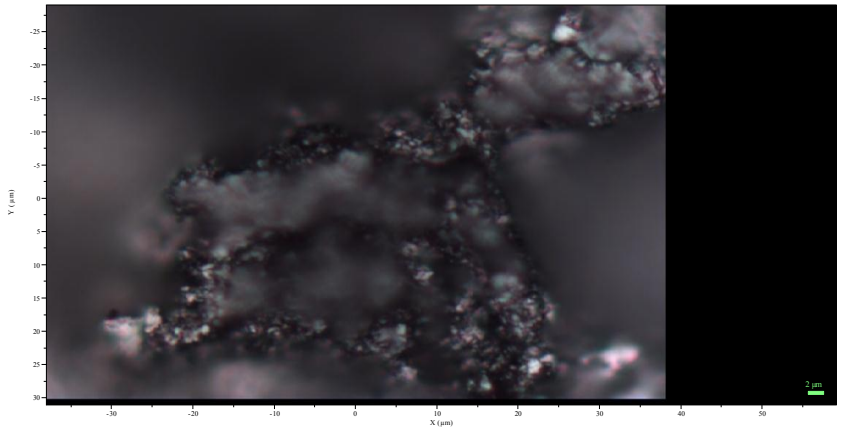

Figure B-23: Image of PCEA WG AFRRI 2 sample prior to Raman spectra collection.

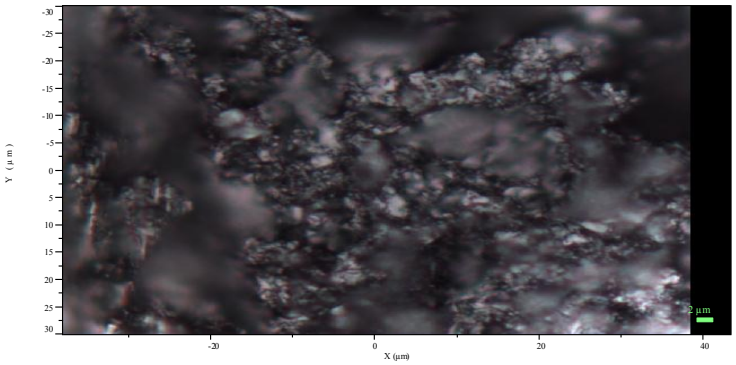

Figure B-24: Image of PCEA WG 300 °C rabbit irradiated sample prior to Raman spectra collection.

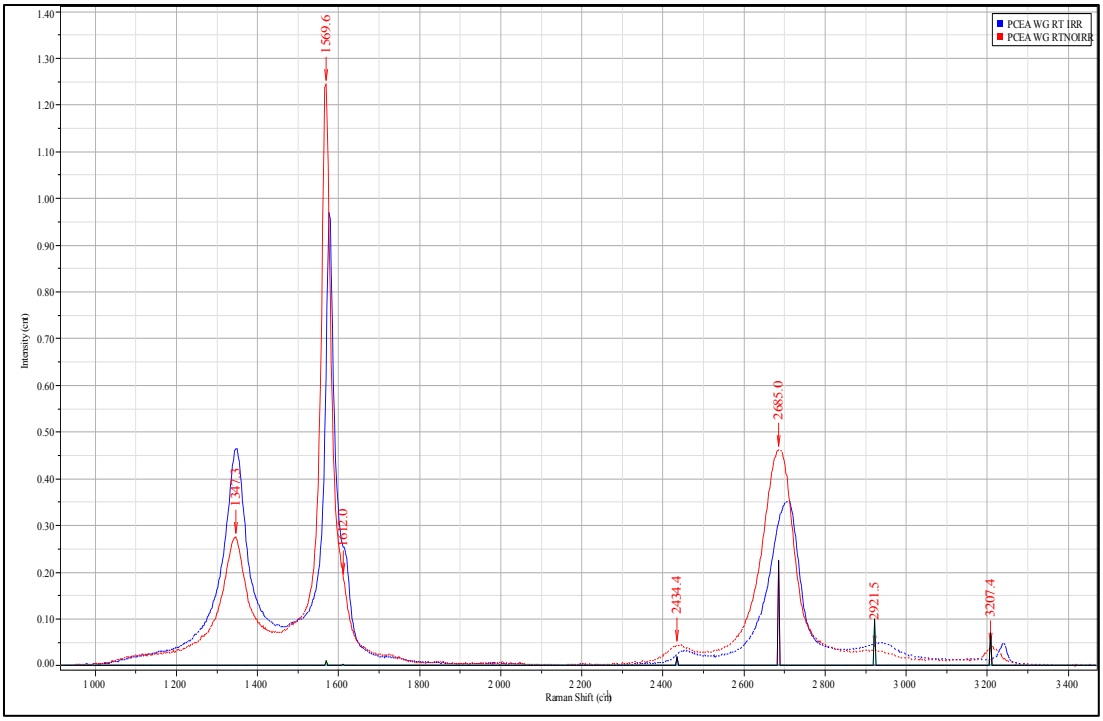

Figure B-25: Raman spectra of PCEA WG room temperature irradiated and unirradiated samples.

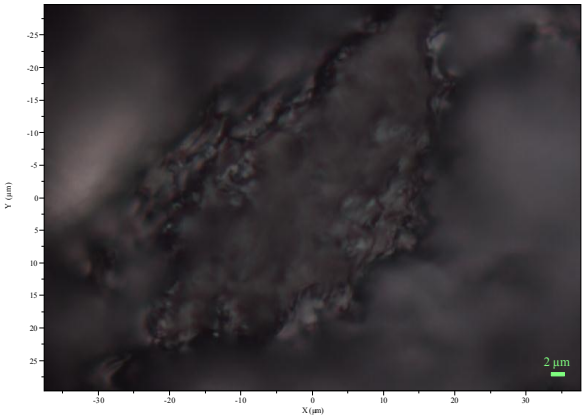

Figure B-26: Image of PCEA WG room temperature unirradiated sample prior to Raman spectra collection.

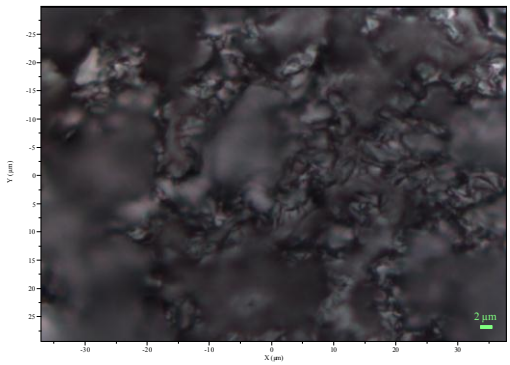

Figure B-27: Image of PCEA WG room temperature east beam port irradiated sample prior to Raman spectra collection.

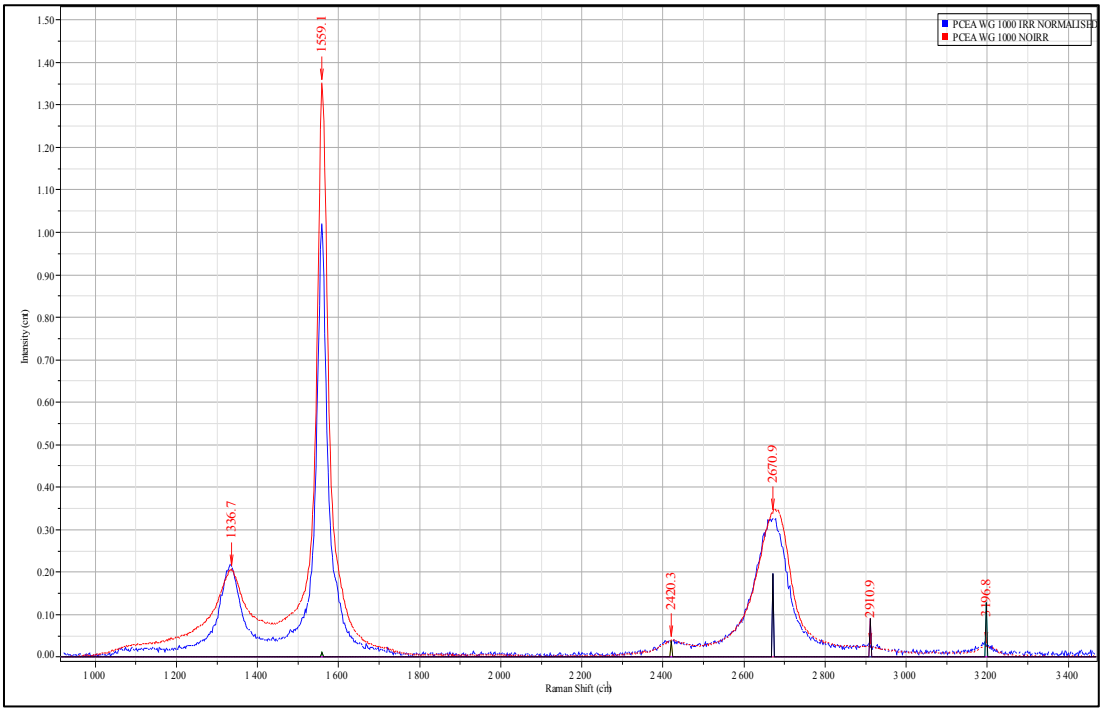

Figure C8: Raman spectra of PCEA WG 1000 °C irradiated and unirradiated samples.

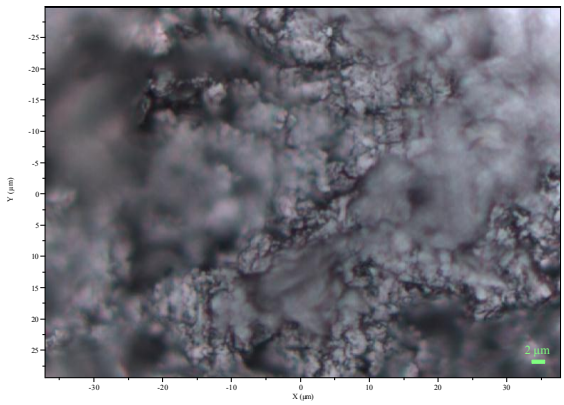

Figure B-28: Image of PCEA WG 1000 °C unirradiated sample prior to Raman spectra collection.

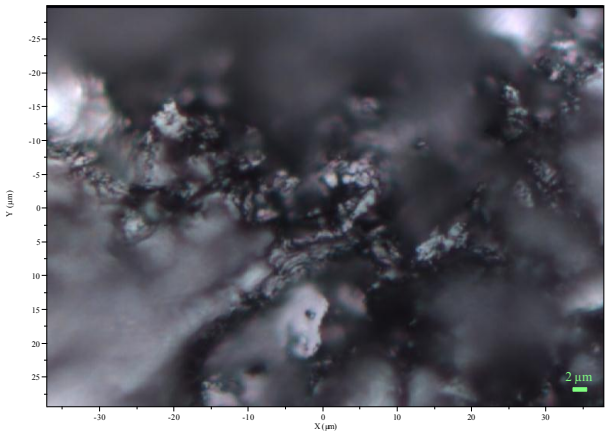

Figure B-29: Image of PCEA WG 1000 °C irradiated sample prior to Raman spectra collection.

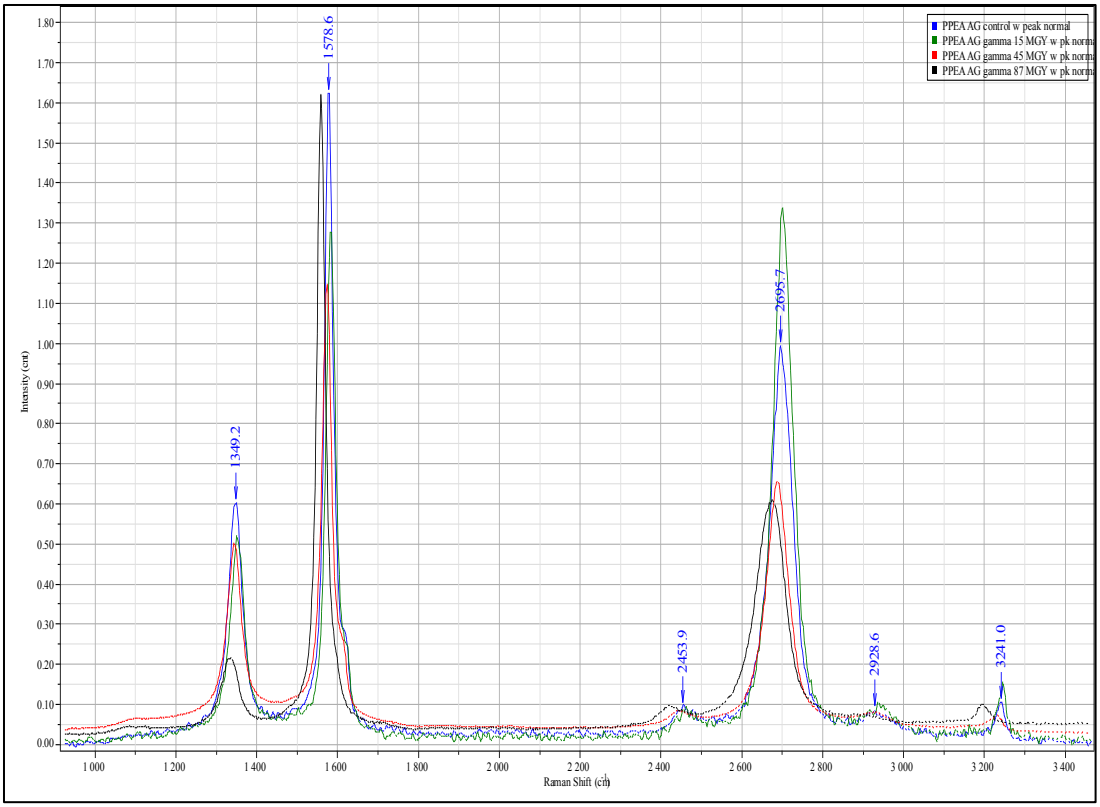

Figure B-30: Raman spectra of PPEA AG control and gamma irradiated samples.

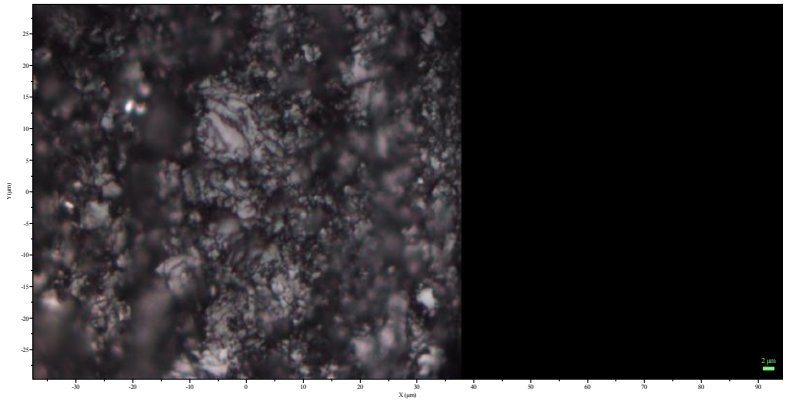

Figure B-31: Image of PPEA AG control sample prior to Raman spectra collection.

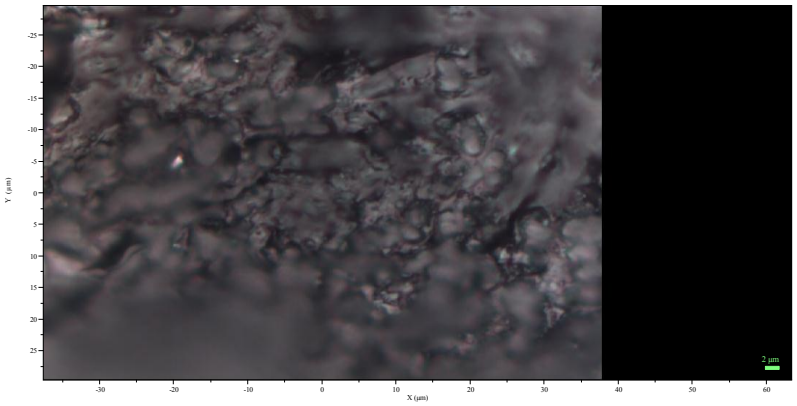

Figure B-32: Image of PPEA AG 15 MGy gamma irradiated sample prior to Raman spectra collection.

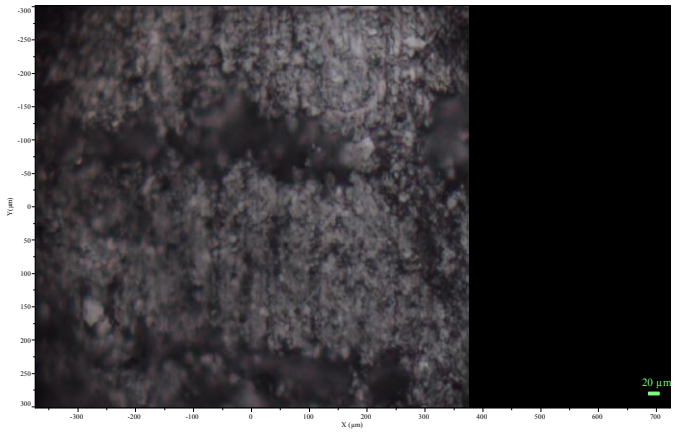

Figure B-33: Image of PPEA AG 45 MGy gamma irradiated sample prior to Raman spectra collection.

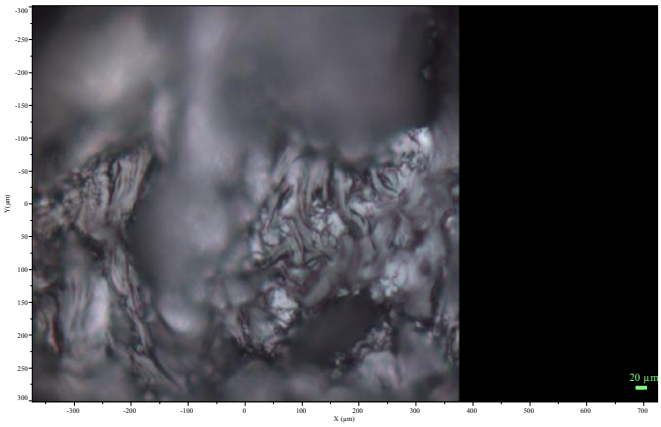

Figure B-34: Image of PPEA AG 87 MGy gamma irradiated sample prior to Raman spectra collection.

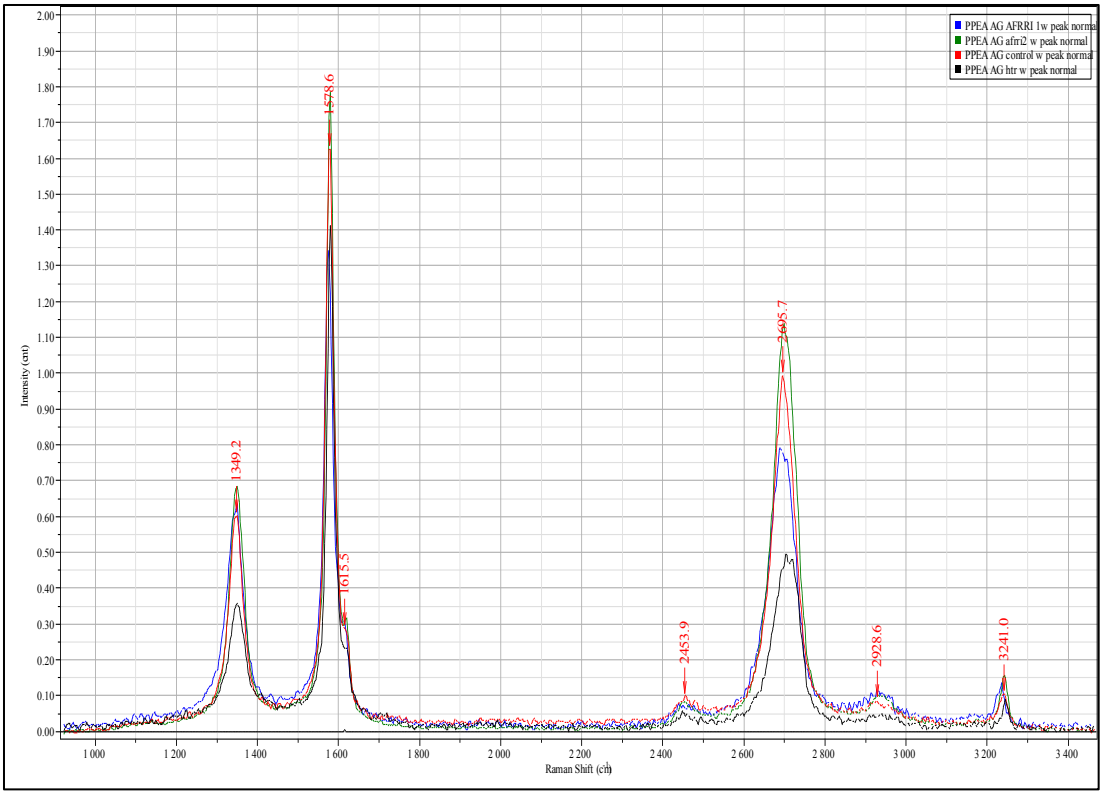

Figure B-35: Raman spectra of PPEA WG control, AFRRI irradiated and rabbit irradiated samples.

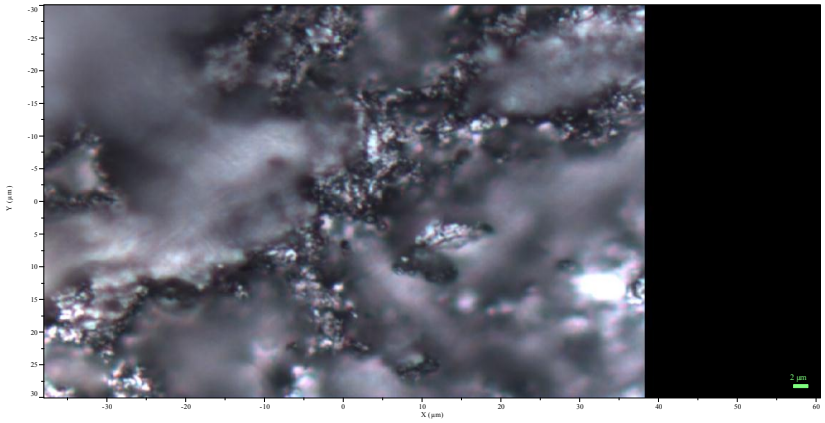

Figure B-36: Image of PPEA AG AFRRI 1 sample prior to Raman spectra collection.

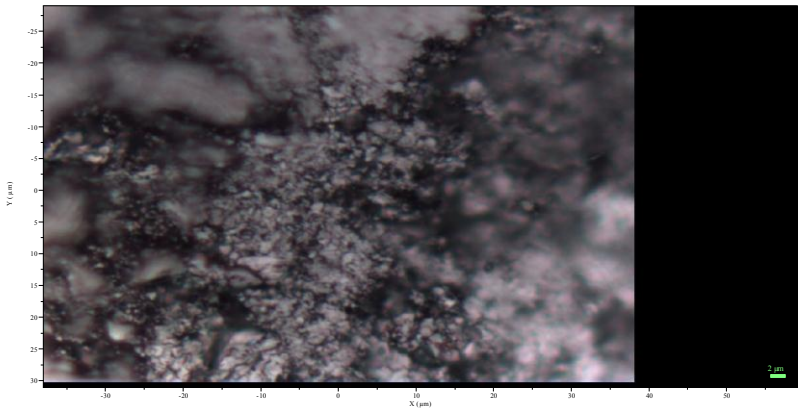

Figure B-37: Image of PPEA AG AFRRI 2 sample prior to Raman spectra collection.

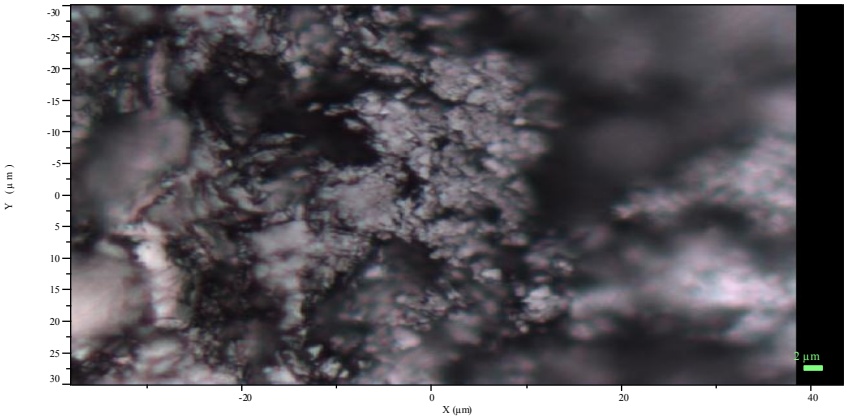

Figure B-38: Image of PPEA AG 300 °C rabbit irradiated sample prior to Raman spectra collection.

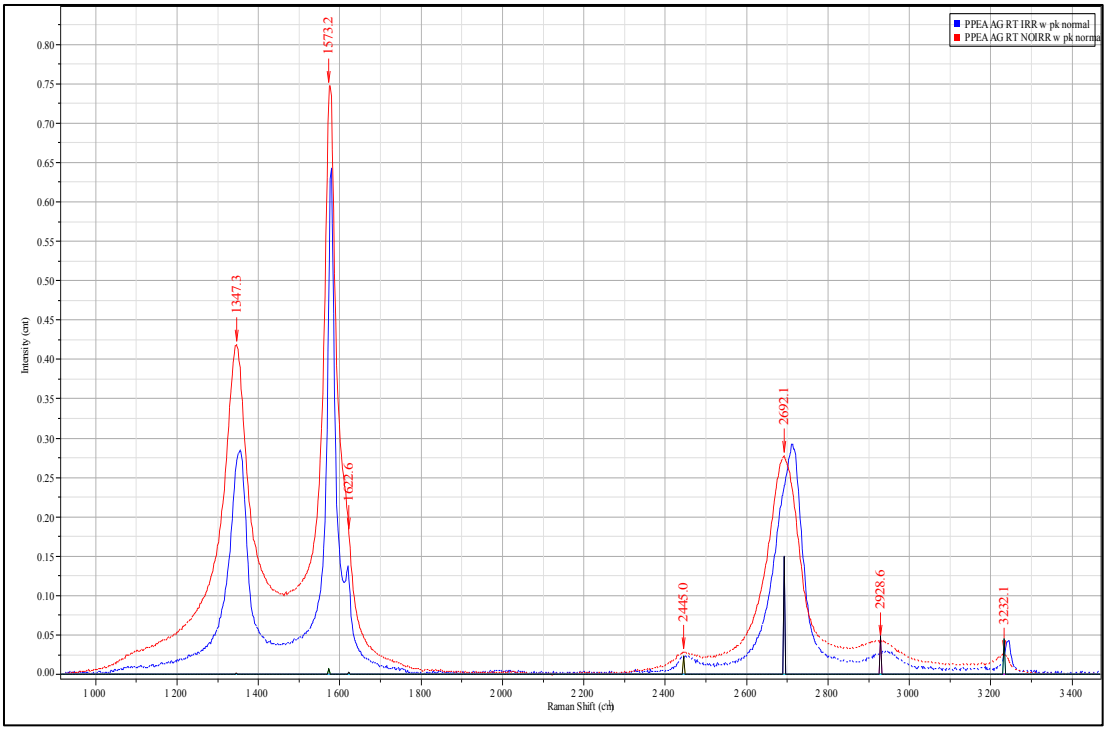

Figure B-39: Raman spectra of PPEA AG room temperature irradiated and unirradiated samples.

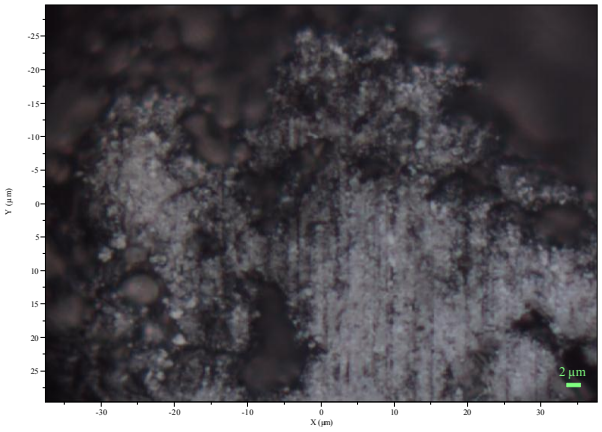

Figure B-40: Image of PPEA AG room temperature unirradiated sample prior to Raman spectra collection.

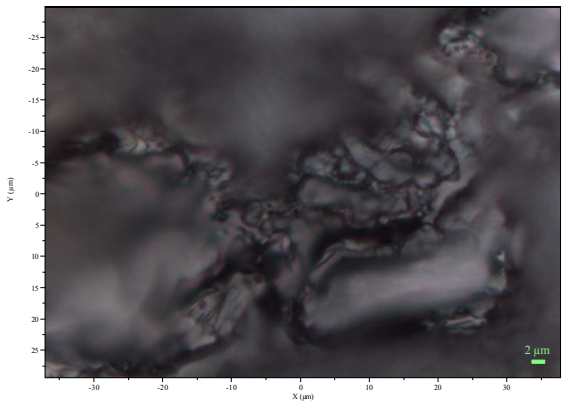

Figure B-41: Image of PPEA AG room temperature east beam port irradiated sample prior to Raman spectra collection.

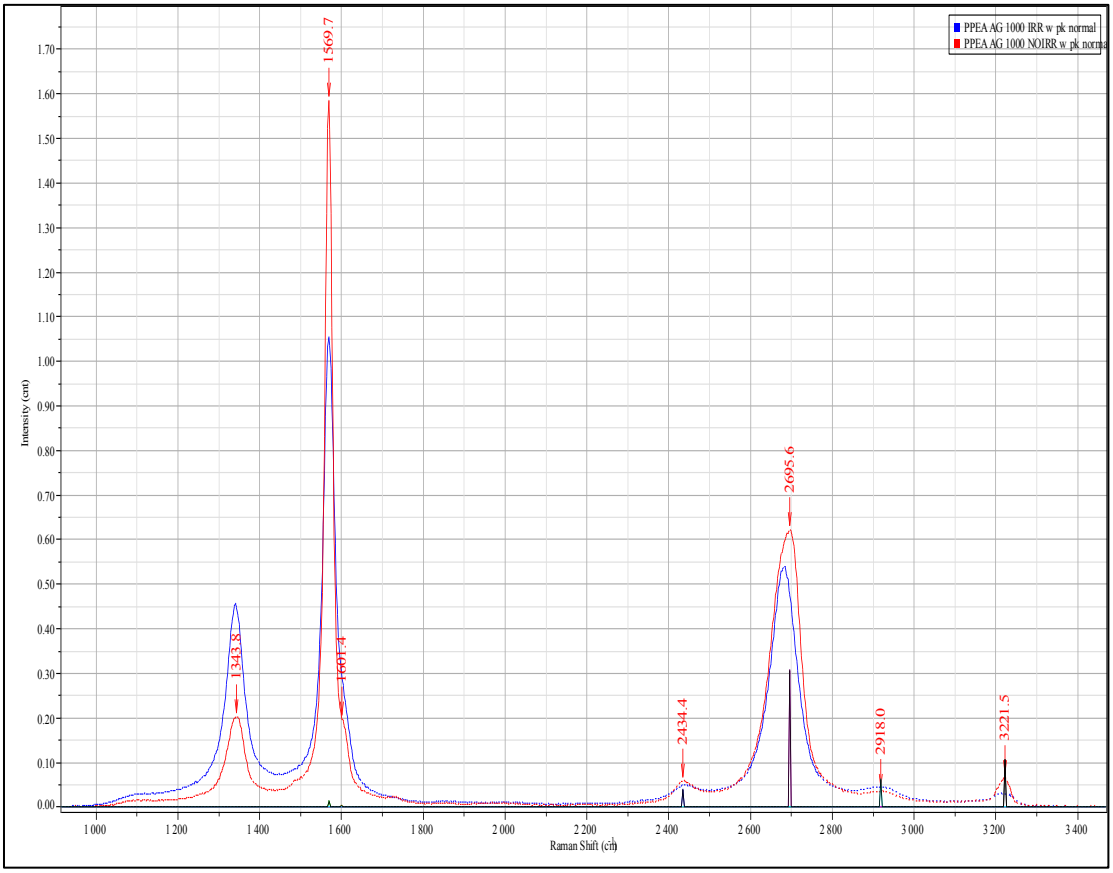

Figure B-42: Raman spectra of PPEA AG 1000 °C irradiated and unirradiated samples.

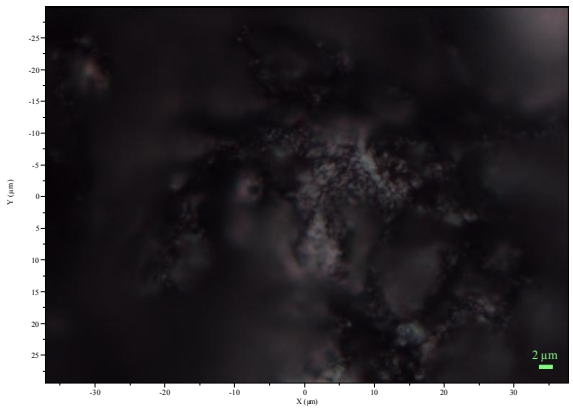

Figure B-43: Image of PPEA AG 1000 °C unirradiated east beam port sample prior to Raman spectra collection.

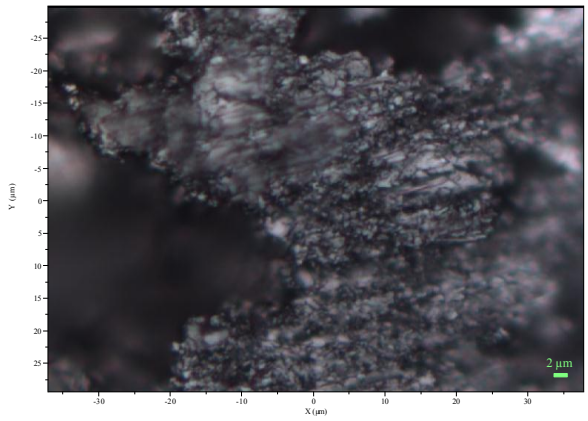

Figure B-44: Image of PPEA AG 1000 °C irradiated east beam port sample prior to Raman spectra collection.

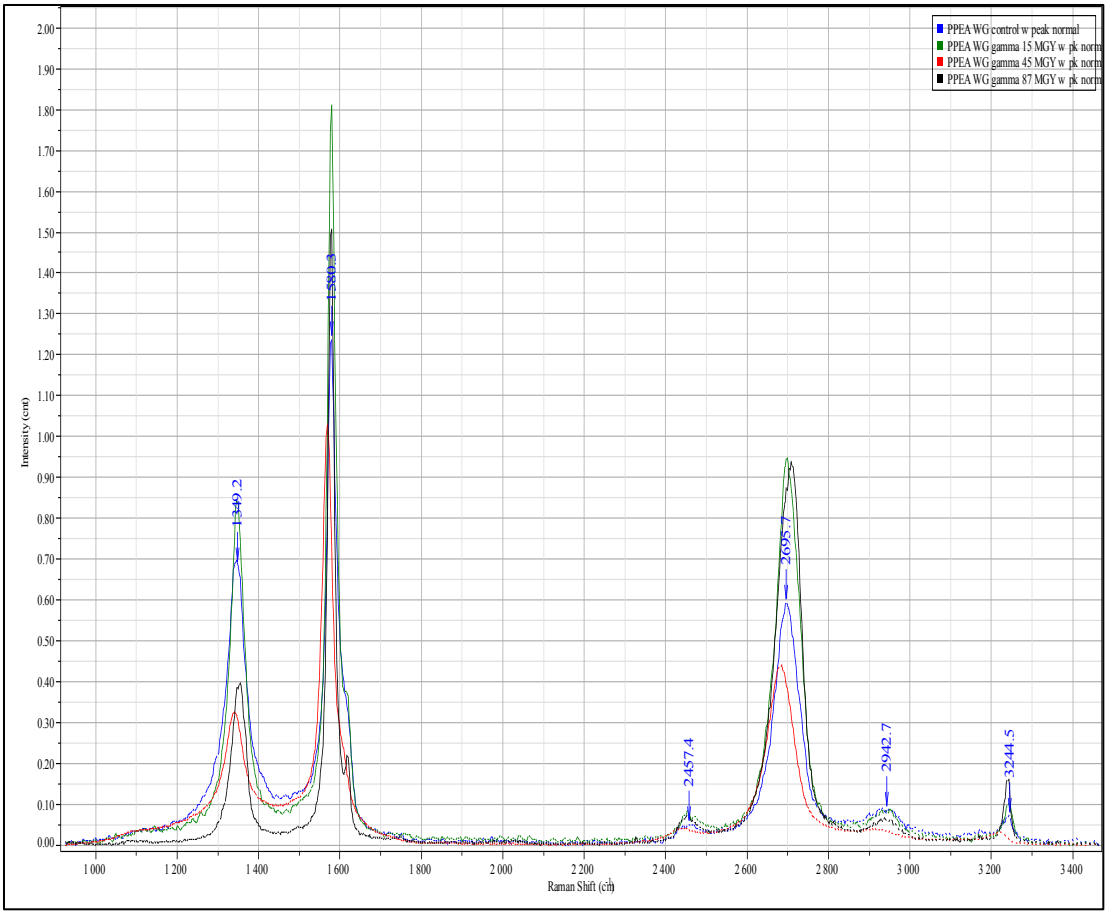

Figure B-45: Raman spectra of PPEA WG control and gamma irradiated samples.

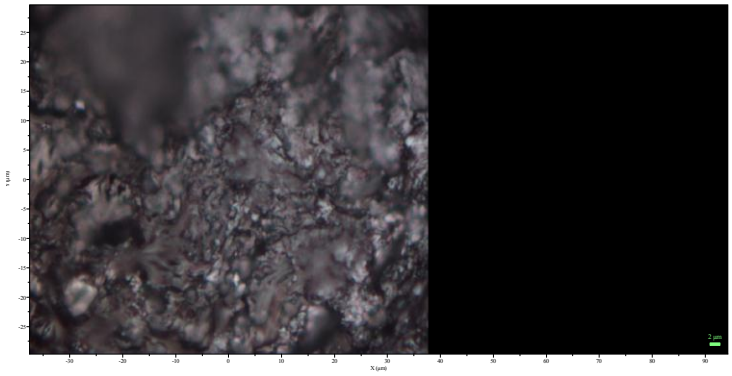

Figure B-46: Image of PPEA WG control sample prior to Raman spectra collection.

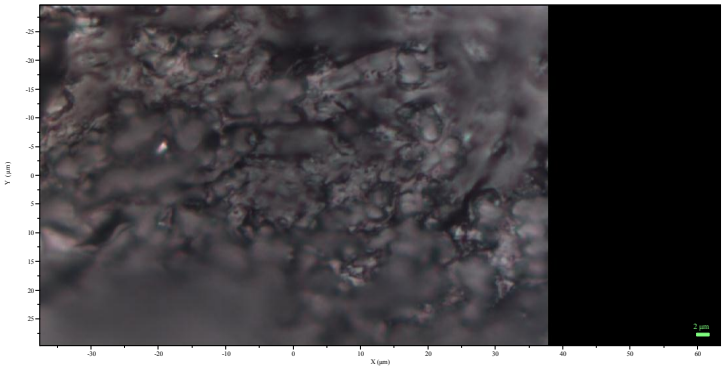

Figure B-47: Image of PPEA WG 15 MGy gamma irradiated sample prior to Raman spectra collection.

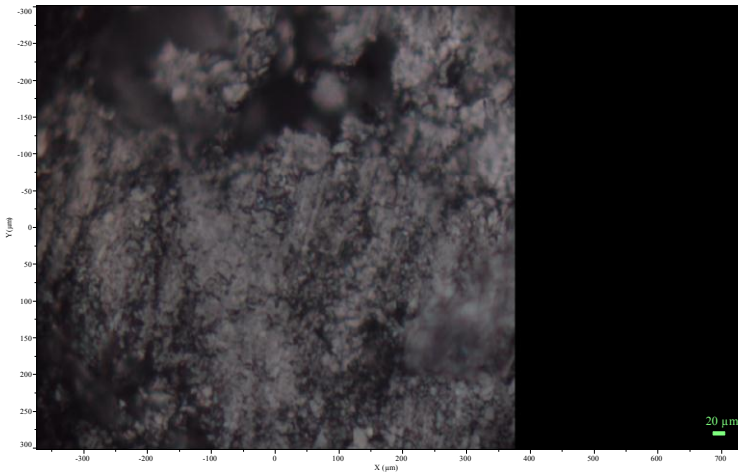

Figure B-48: Image of PPEA WG 45 MGy gamma irradiated sample prior to Raman spectra collection.

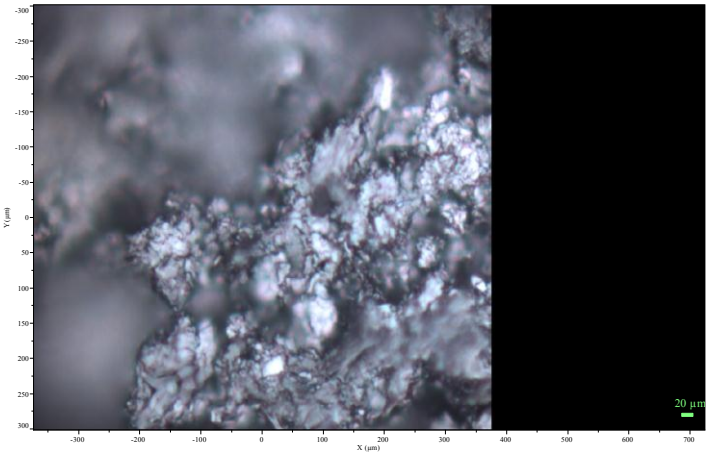

Figure B-49: Image of PPEA WG 87 MGy gamma irradiated sample prior to Raman spectra collection.

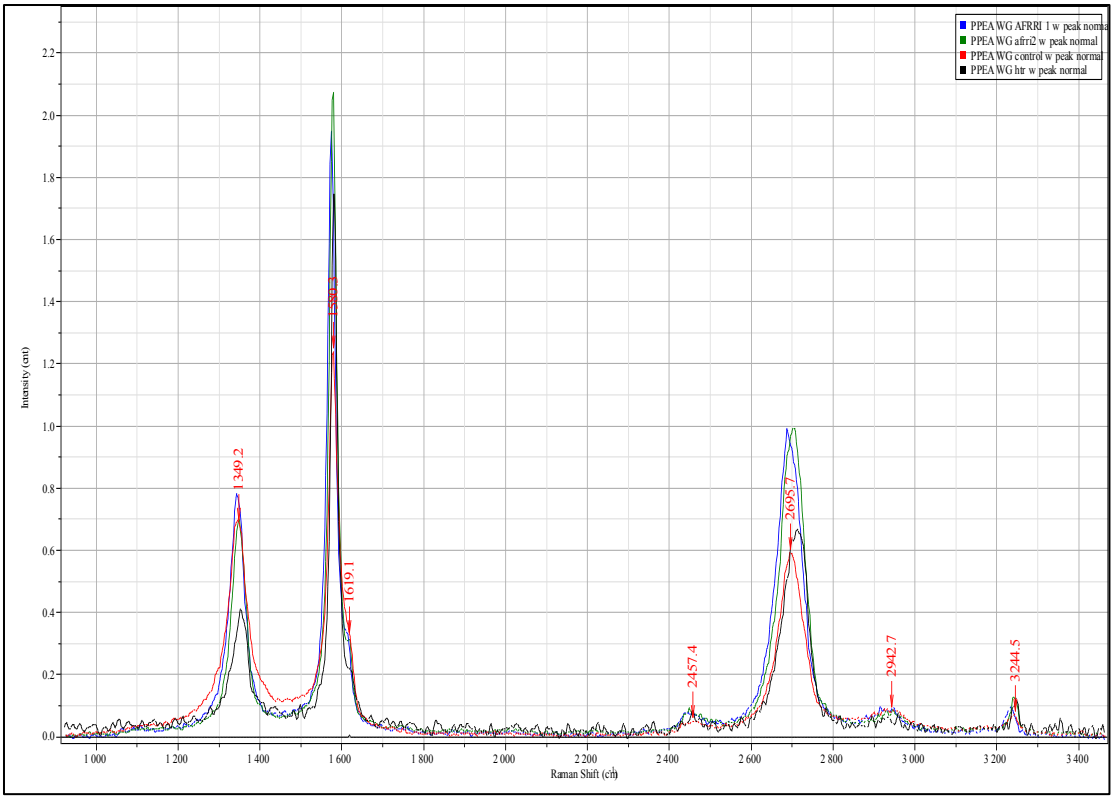

Figure B-50: Raman spectra of PPEA WG control, AFRRI irradiated and 300 °C rabbit irradiated samples.

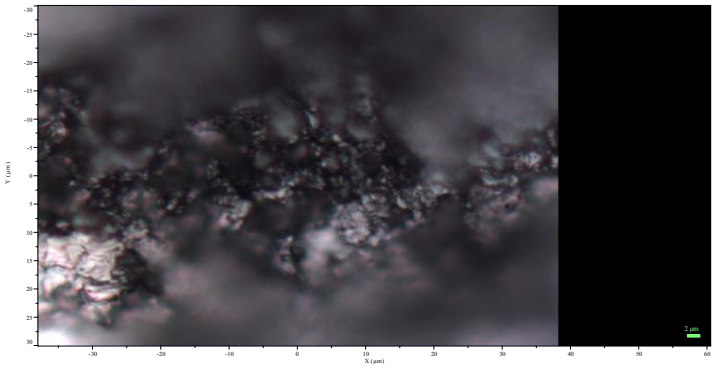

Figure B-51: Image of PPEA WG AFRRI 1 sample prior to Raman spectra collection.

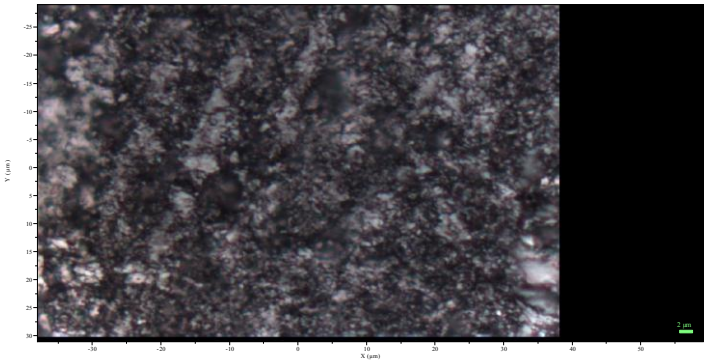

Figure B-52: Image of PPEA WG AFRRI 2 sample prior to Raman spectra collection.

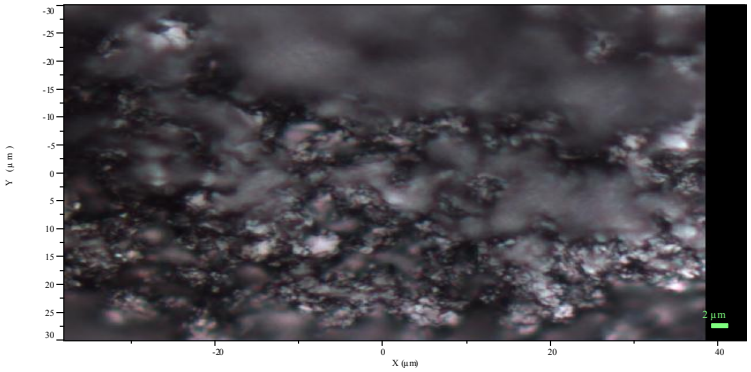

Figure B-53: Image of PPEA WG 300 °C rabbit irradiated sample prior to Raman spectra collection.

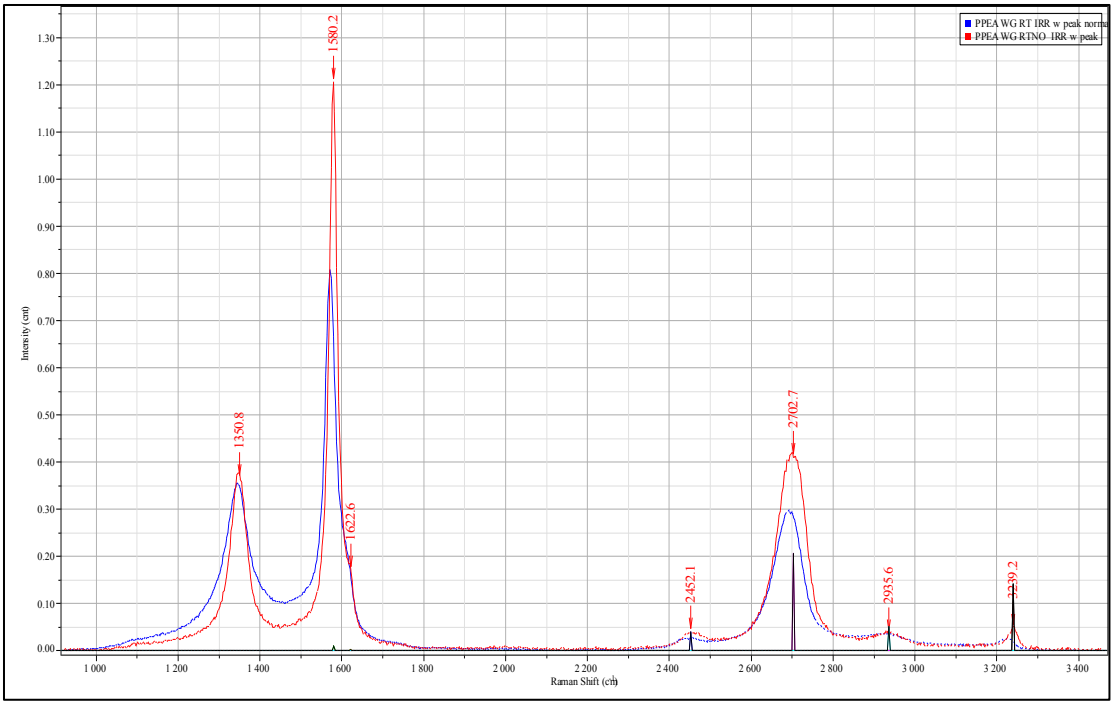

Figure B-54: Raman spectra of PPEA WG room temperature irradiated and unirradiated samples.

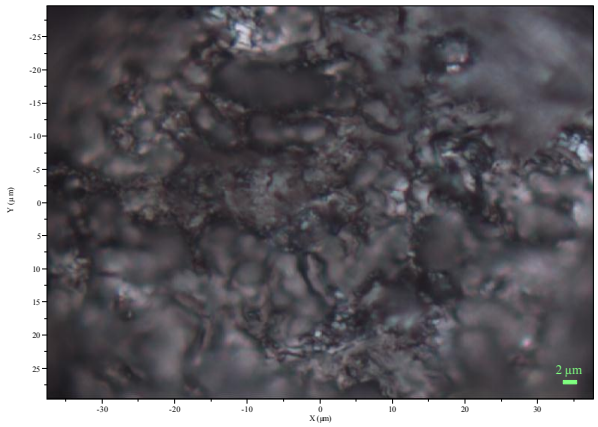

Figure B-55: Image of PPEA WG room temperature unirradiated east beam port sample prior to Raman spectra collection.

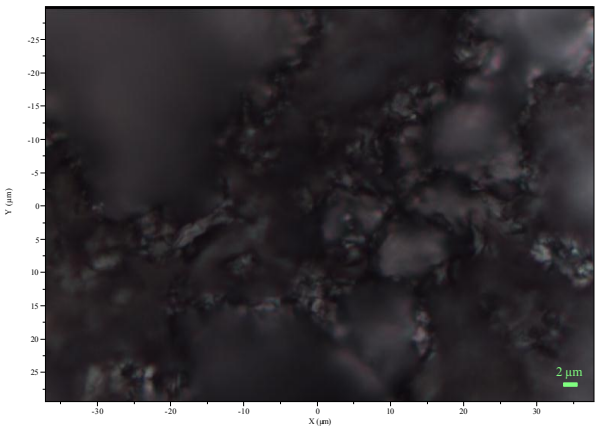

Figure B-56: Image of PPEA WG room temperature east beam port irradiated sample prior to Raman spectra collection.

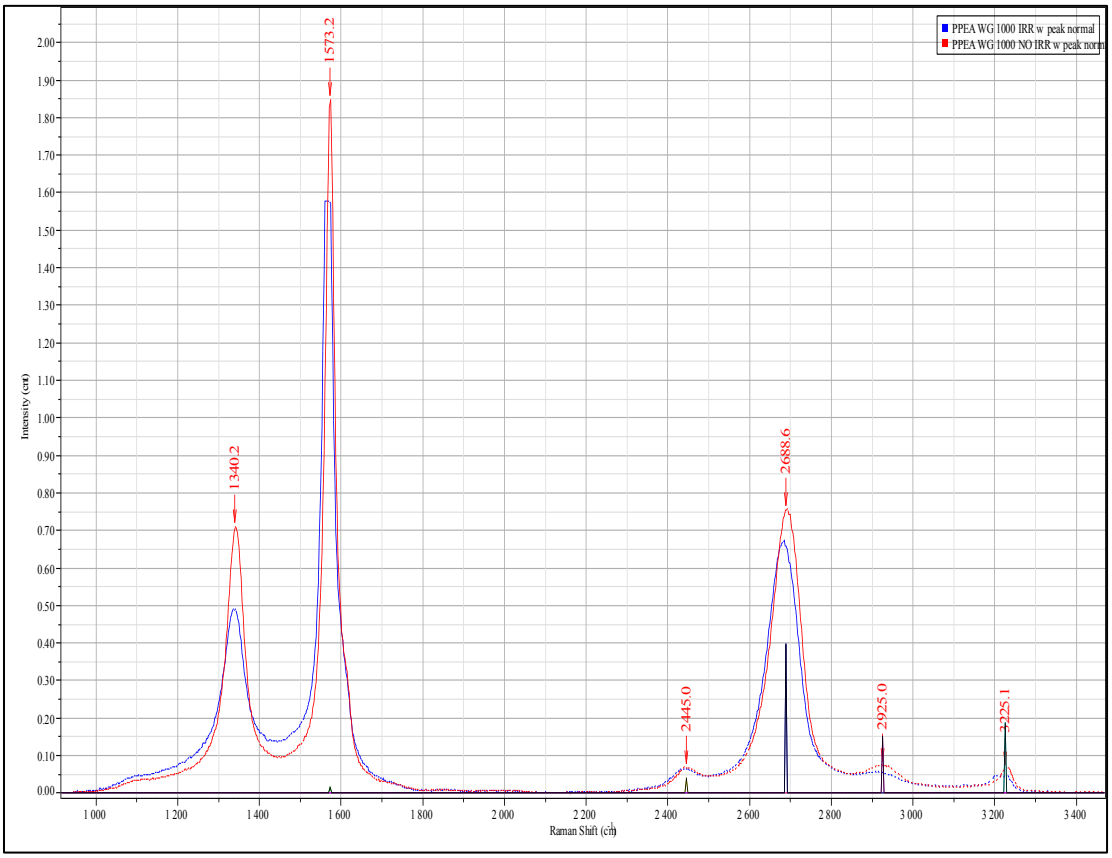

Figure B-57: Raman spectra of PPEA WG 1000 °C irradiated and unirradiated samples.

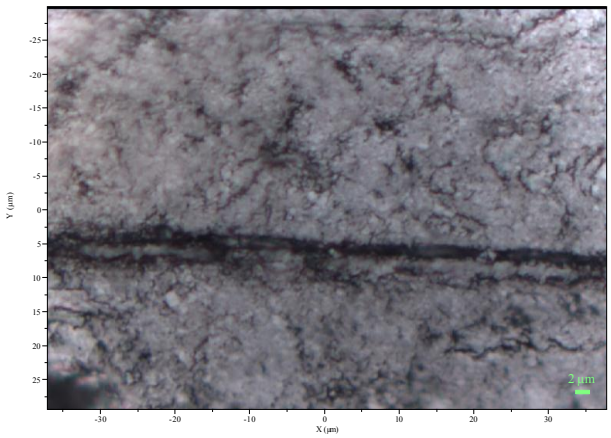

Figure B-58: Image of PPEA WG 1000 °C unirradiated east beam port sample prior to Raman spectra collection.

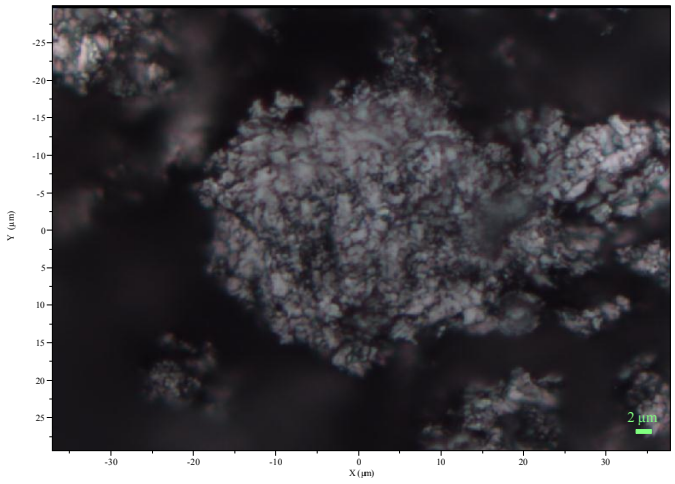

Figure B-59: Image of PPEA WG 1000 °C irradiated east beam port sample prior to Raman spectra collection.

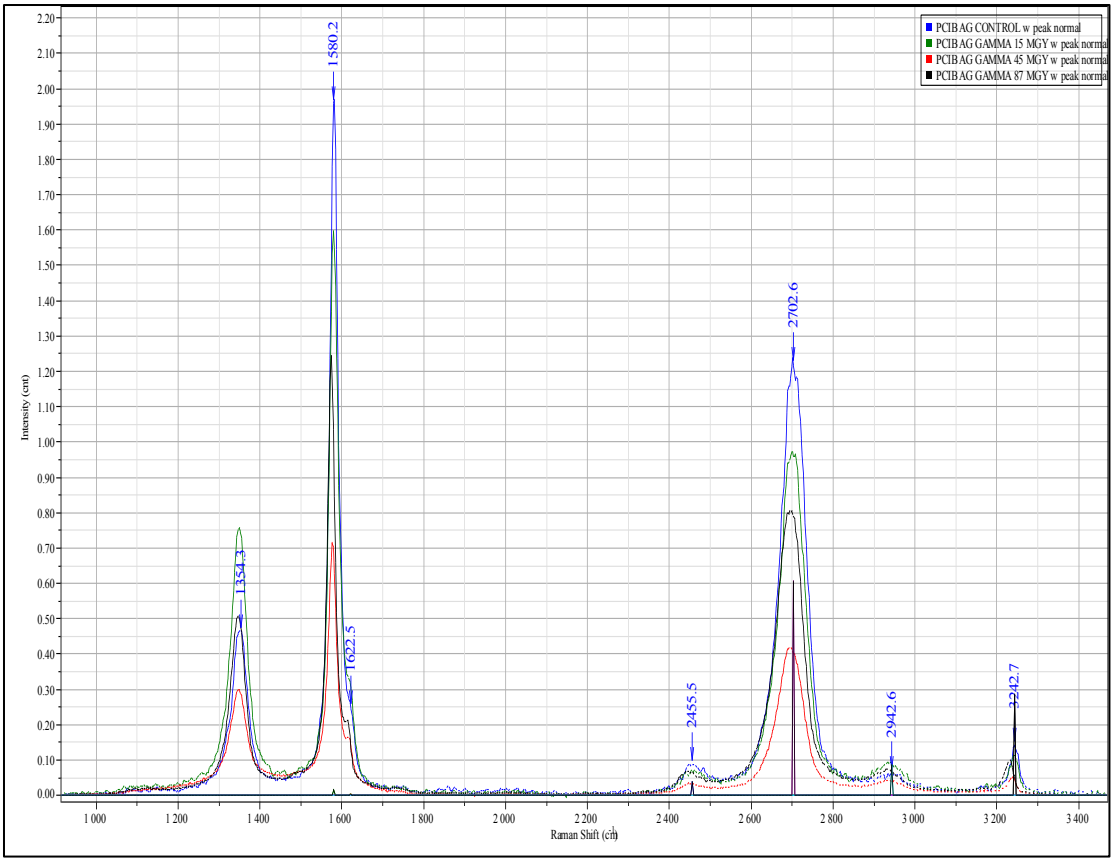

Figure B-60: Raman spectra for PCIB AG control and gamma irradiated samples.

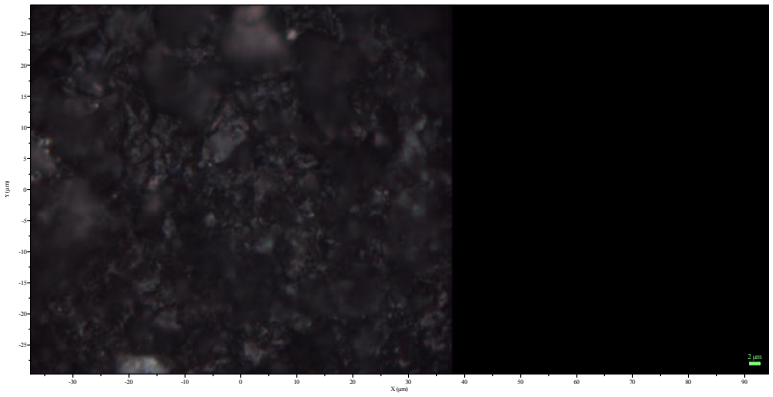

Figure B-61: Image of PCIB AG control sample prior to Raman spectra collection.

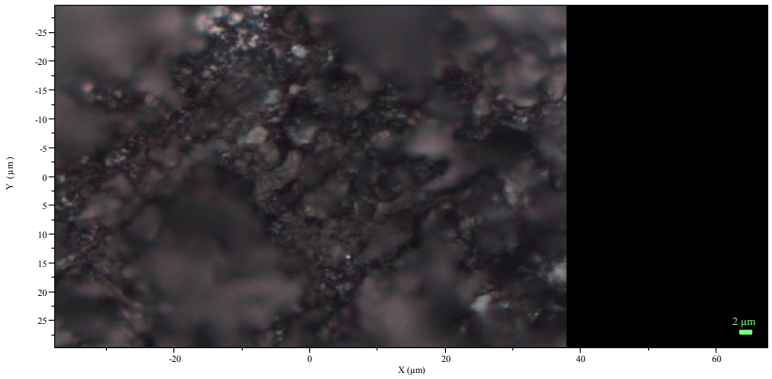

Figure B-62: Image of PCIB AG 15 MGy gamma irradiated sample prior to Raman spectra collection.

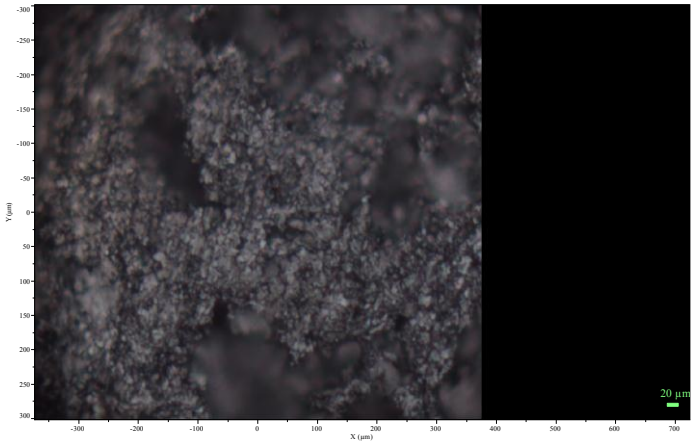

Figure B-63: Image of PCIB AG 45 MGy gamma irradiated sample prior to Raman spectra collection.

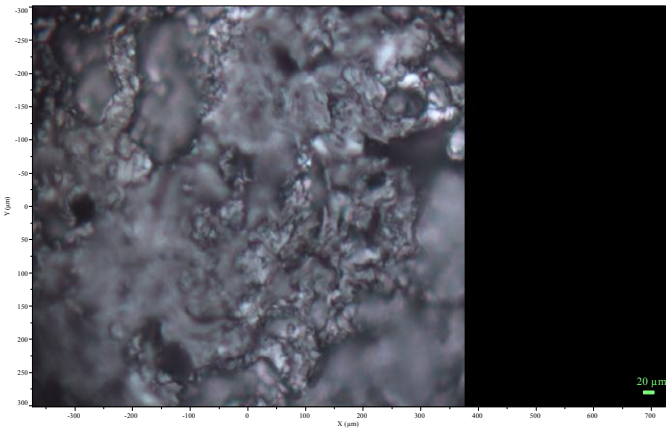

Figure B-64: Image of PCIB AG 87 MGy gamma irradiated sample prior to Raman spectra collection.

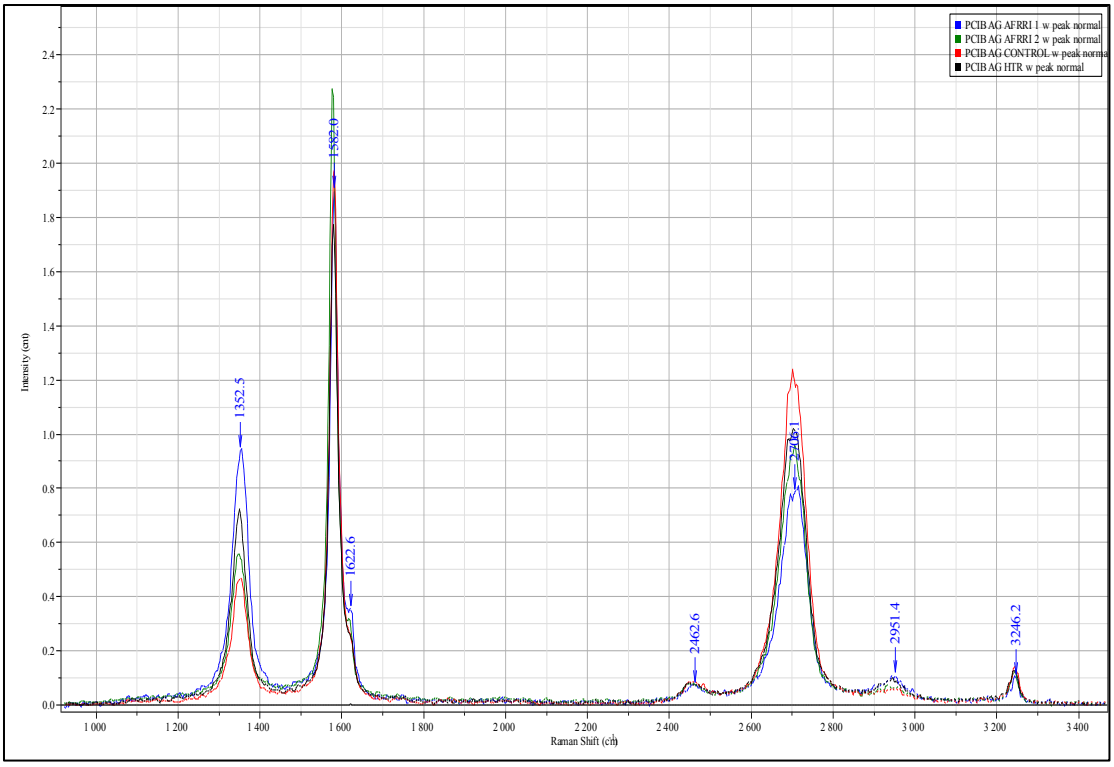

Figure B-65: Raman spectra for PCIB AG control, AFRRI irradiated and 300 °C rabbit irradiated samples.

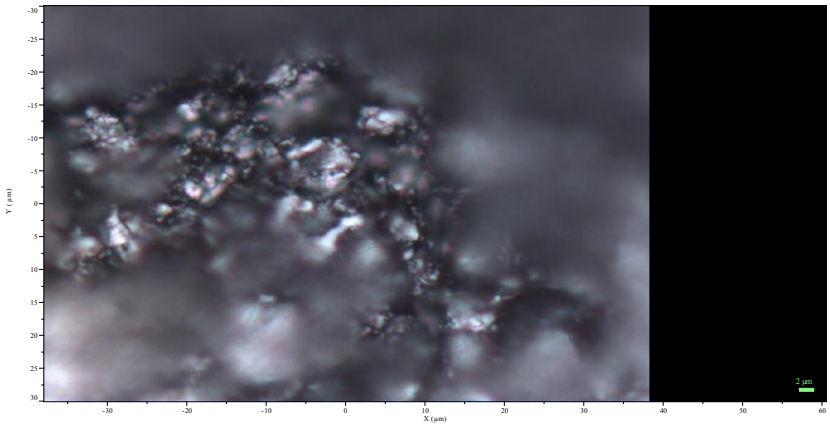

Figure B-66: Image of PCIB AG AFRRI 1 sample prior to Raman spectra collection.

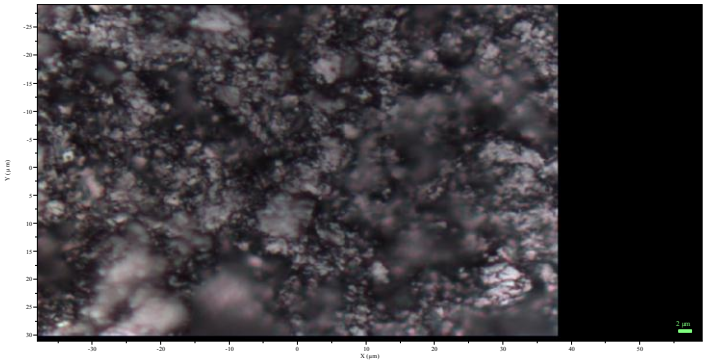

Figure B-67: Image of PCIB AG AFRRI 2 sample prior to Raman spectra collection.

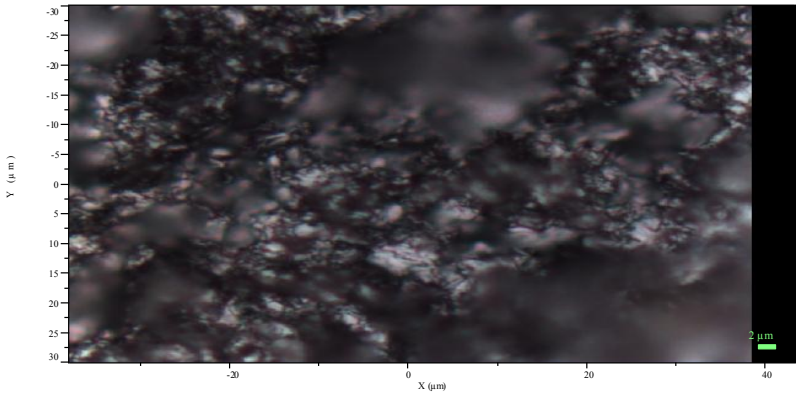

Figure B-68: Image of PCIB AG 300 °C rabbit irradiated sample prior to Raman spectra collection.

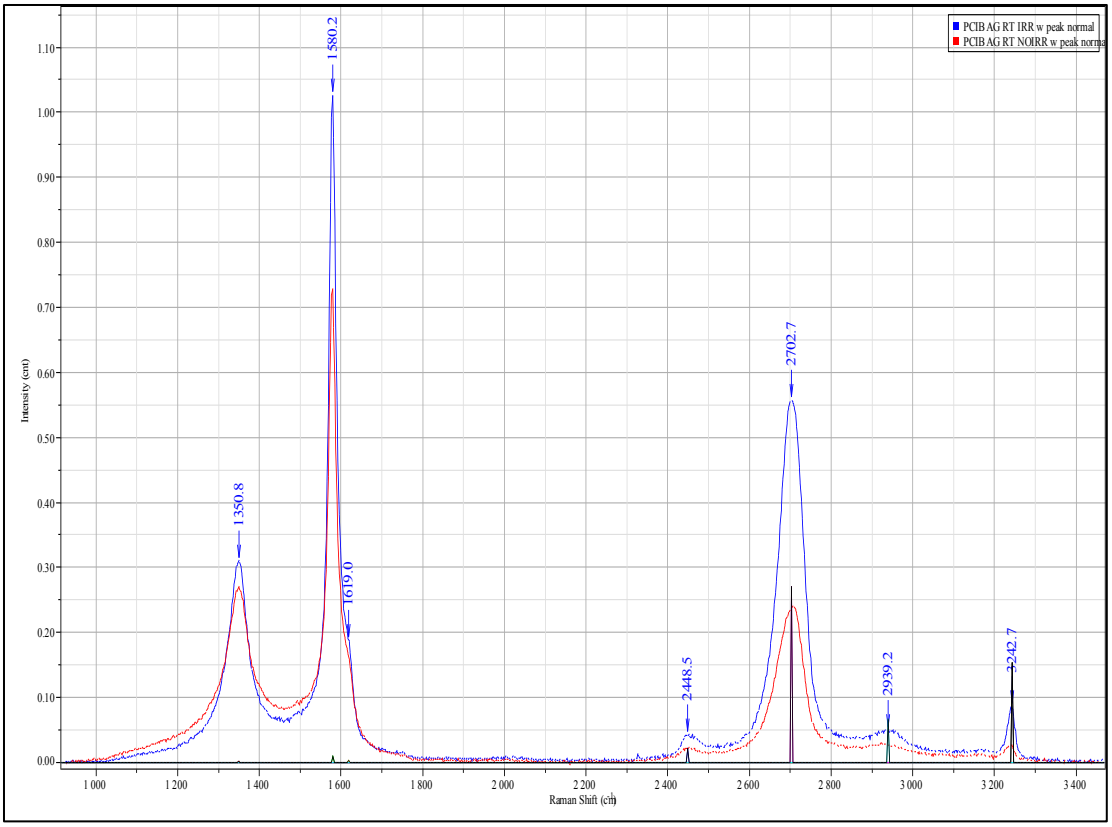

Figure B-69: Raman spectra for PCIB AG room temperature irradiated and unirradiated samples.

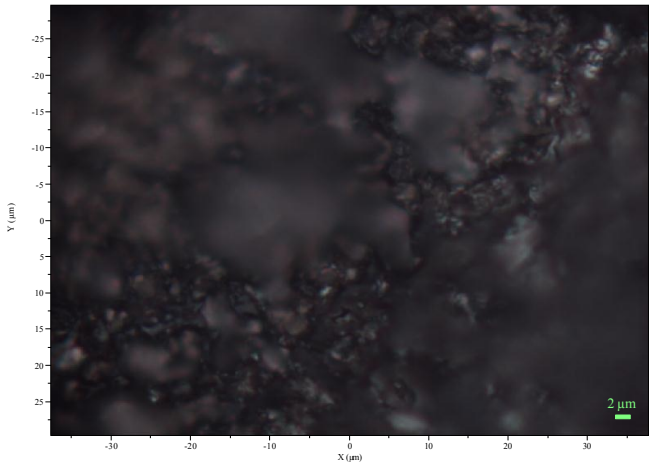

Figure B-70: Image of PCIB AG room temperature unirradiated east beam port sample prior to Raman spectra collection.

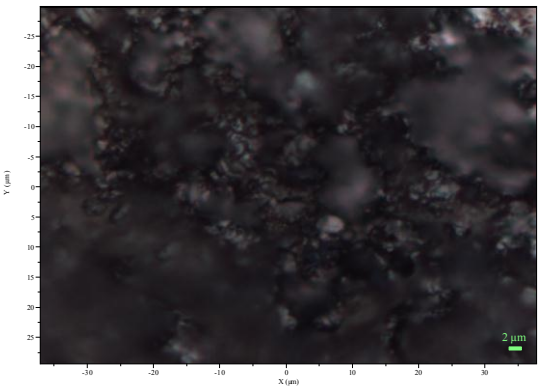

Figure B-71: Image of room temperature irradiated east beam port sample prior to Raman spectra collection.

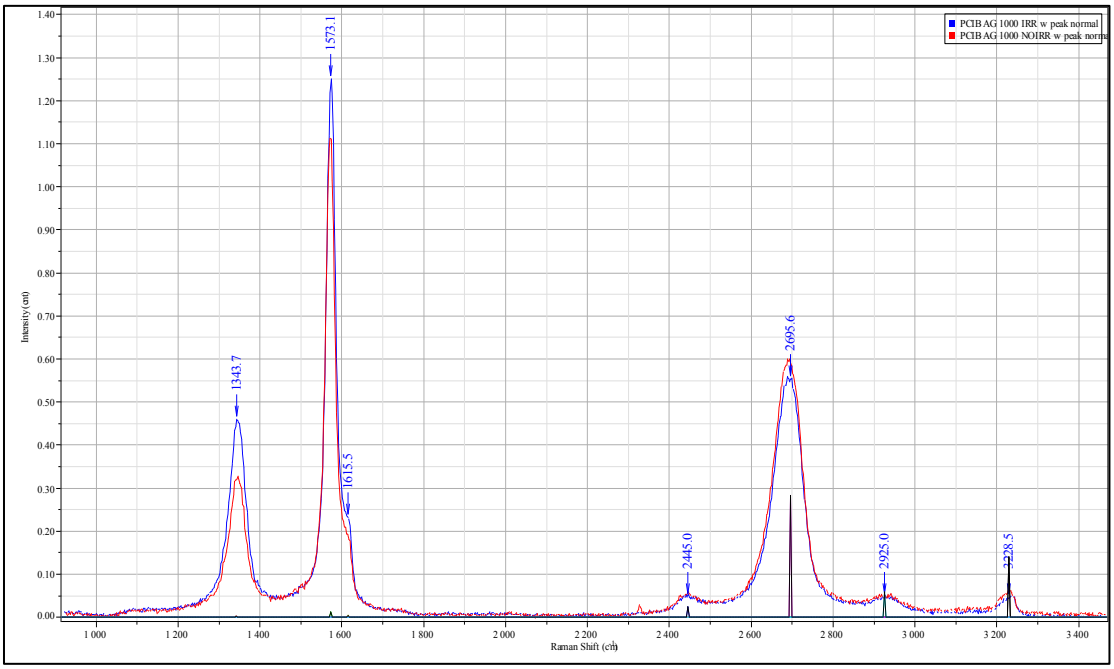

Figure B-72: Raman spectra for PCIB AG 1000 °C irradiated and unirradiated samples.

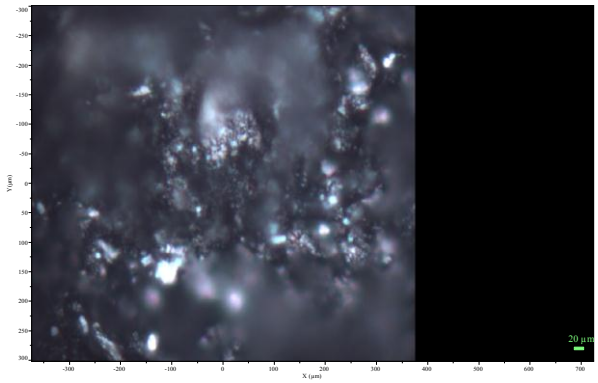

Figure B-73: Image of PCIB AG 1000 °C unirradiated east beam port sample prior to Raman spectra collection.

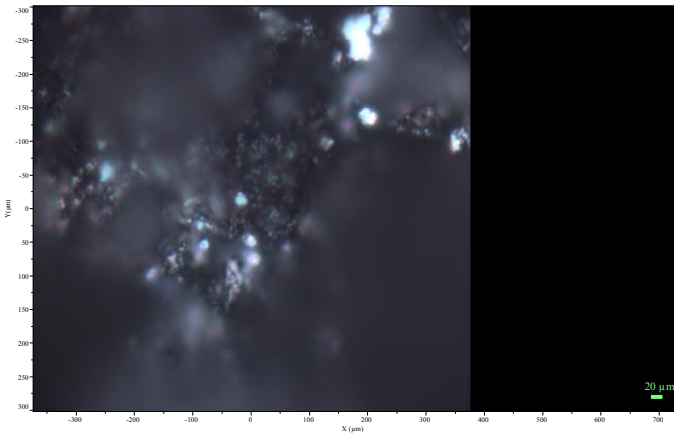

Figure B-74: Image of PCIB AG 1000 °C irradiated east beam port sample prior to Raman spectra collection.

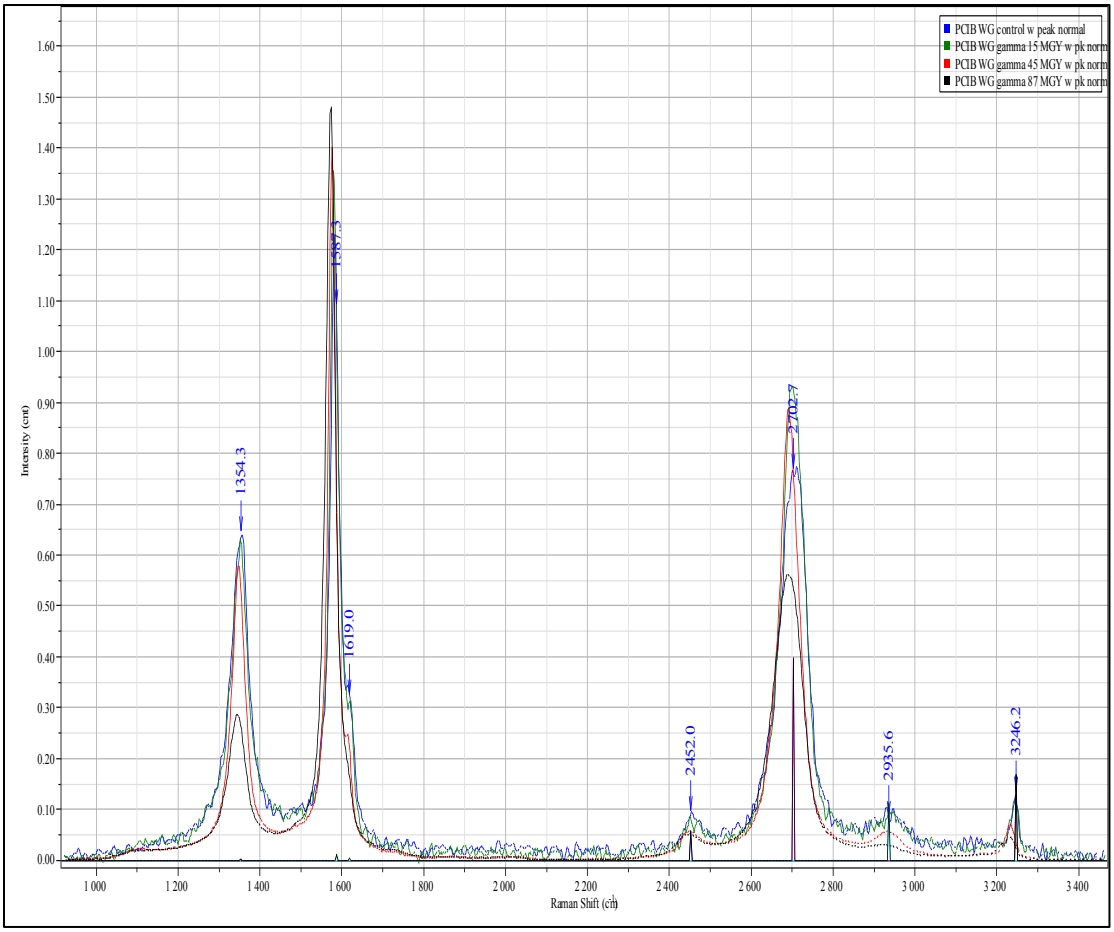

Figure B-75: Raman spectra for PCIB WG control and gamma irradiated samples.

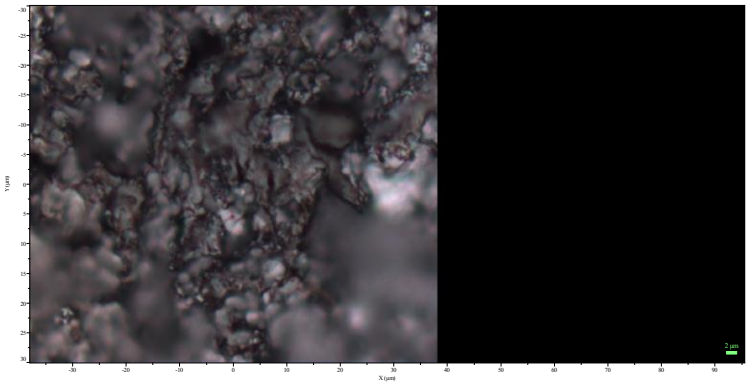

Figure B-76: Image of PCIB WG control sample prior to Raman spectra collection.

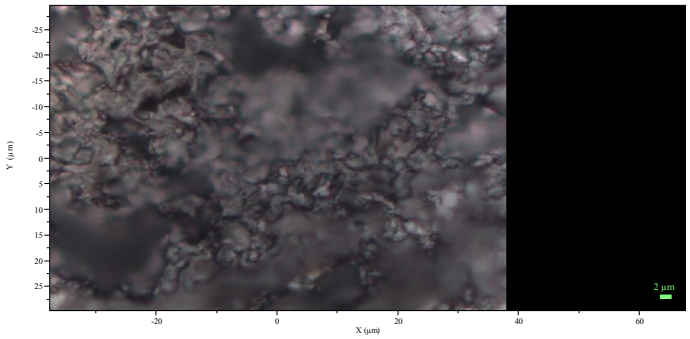

Figure B-77: Image of PCIB WG 15 MGy gamma irradiated sample prior to Raman spectra collection,

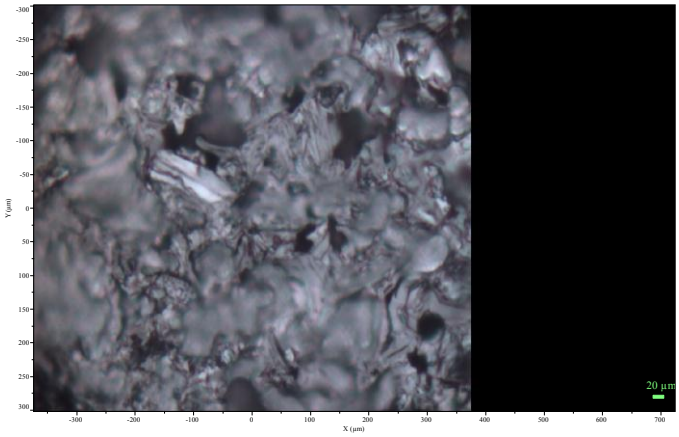

Figure B-78: Image of PCIB WG 45 MGy gamma irradiated sample prior to Raman spectra collection.

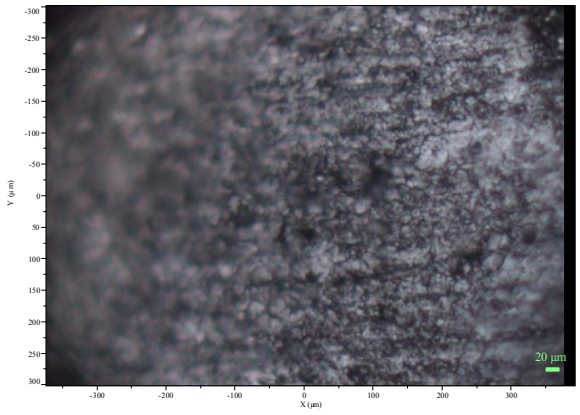

Figure B-79: Image of PCIB WG 87 MGy gamma irradiated sample prior to Raman spectra collection.

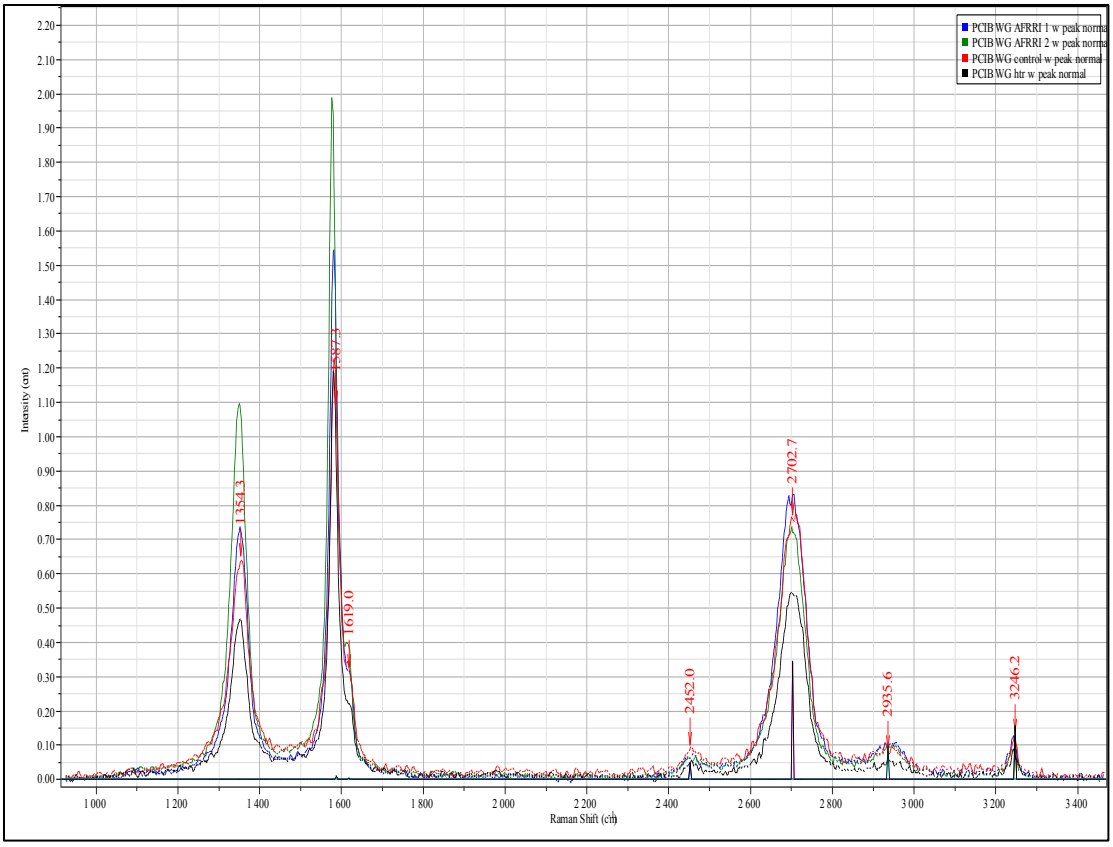

Figure B-80: Raman spectra for PCIB WG control, AFRRI irradiated and 300 °C rabbit irradiated samples.

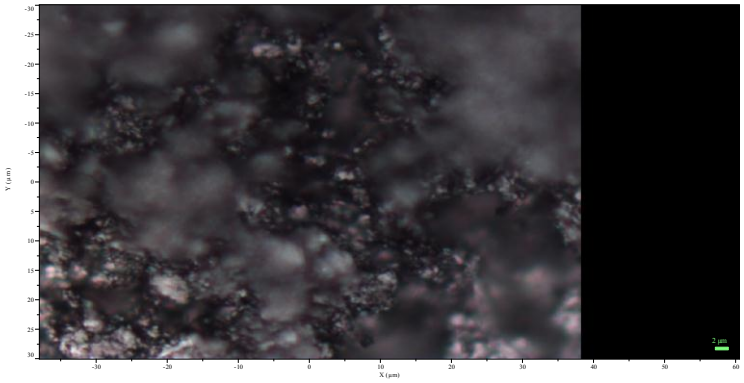

Figure B-81: Image of PCIB WG AFRRI 1 irradiated sample prior to Raman spectra collection.

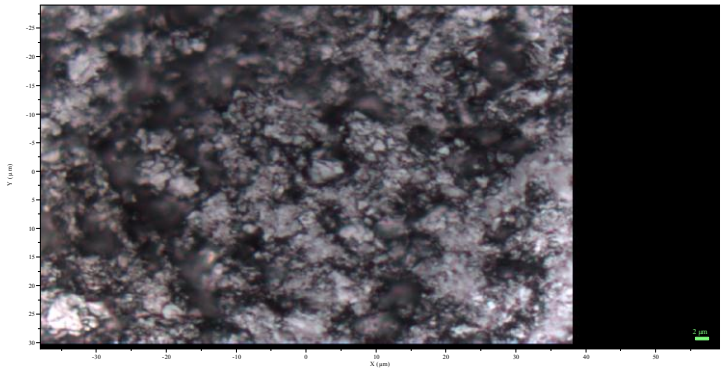

Figure B-82: Image of PCIB WG AFRRI 2 sample prior to Raman spectra collection.

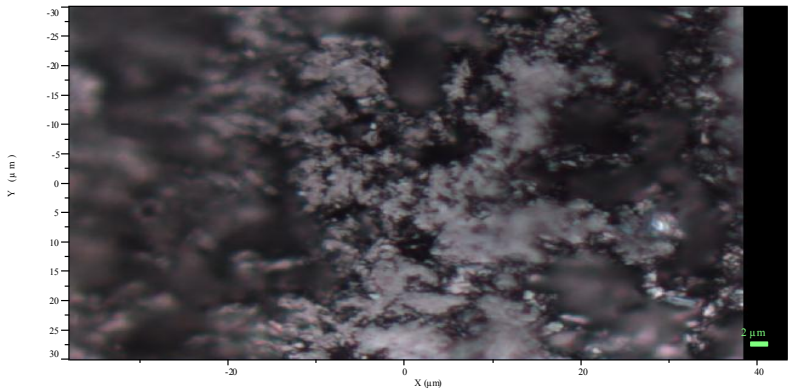

Figure B-83: Image of PCIB WG 300 °C rabbit irradiated sample prior to Raman spectra collection.

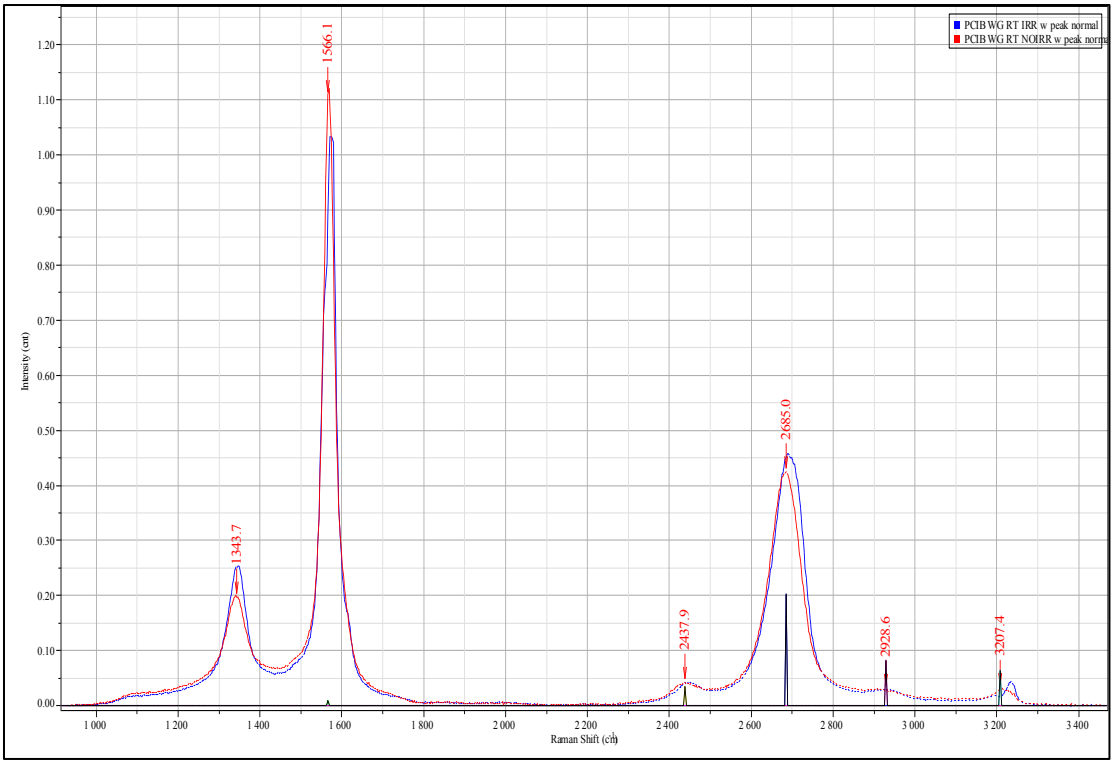

Figure B-84: Raman spectra for PCIB WG room temperature irradiated and unirradiated samples.

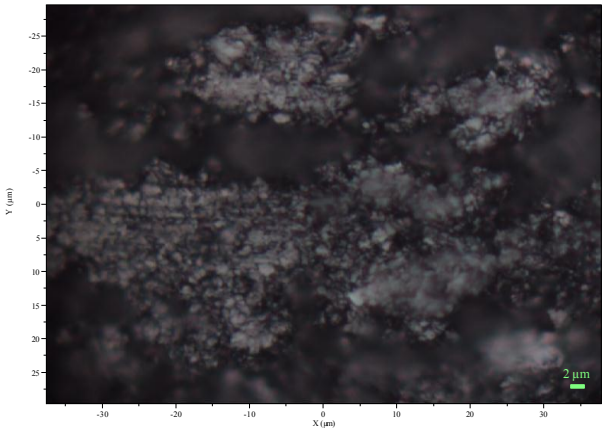

Figure B-85: Image of PCIB WG room temperature unirradiated east beam port sample prior to Raman spectra collection.

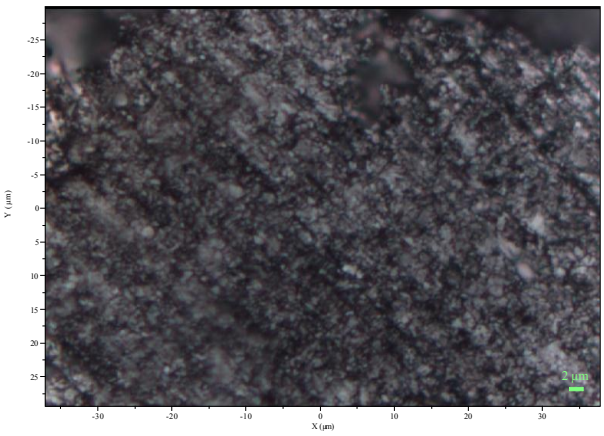

Figure B-86: Image of PCIB WG room temperature irradiated east beam port sample prior to Raman spectra collection.

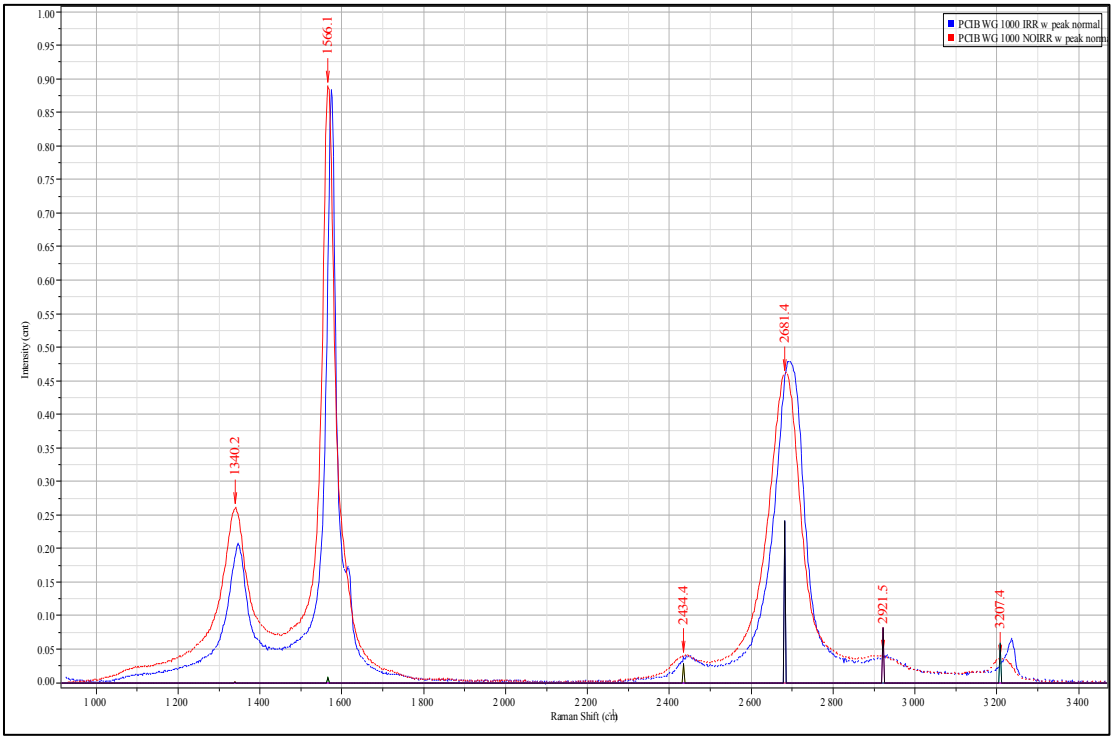

Figure B-87: Raman spectra for PCIB WG 1000 °C irradiated and unirradiated samples.

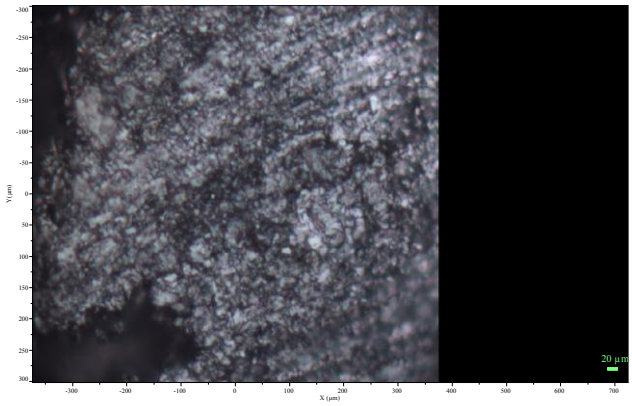

Figure B-88: Image of PCIB WG 1000 °C unirradiated east beam port sample prior to Raman spectra collection.

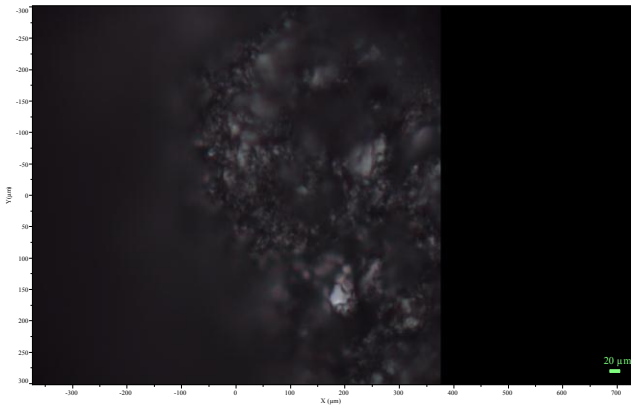

Figure B-89: Image of PCIB WG 1000 °C irradiated east beam port sample prior to Raman spectra collection.

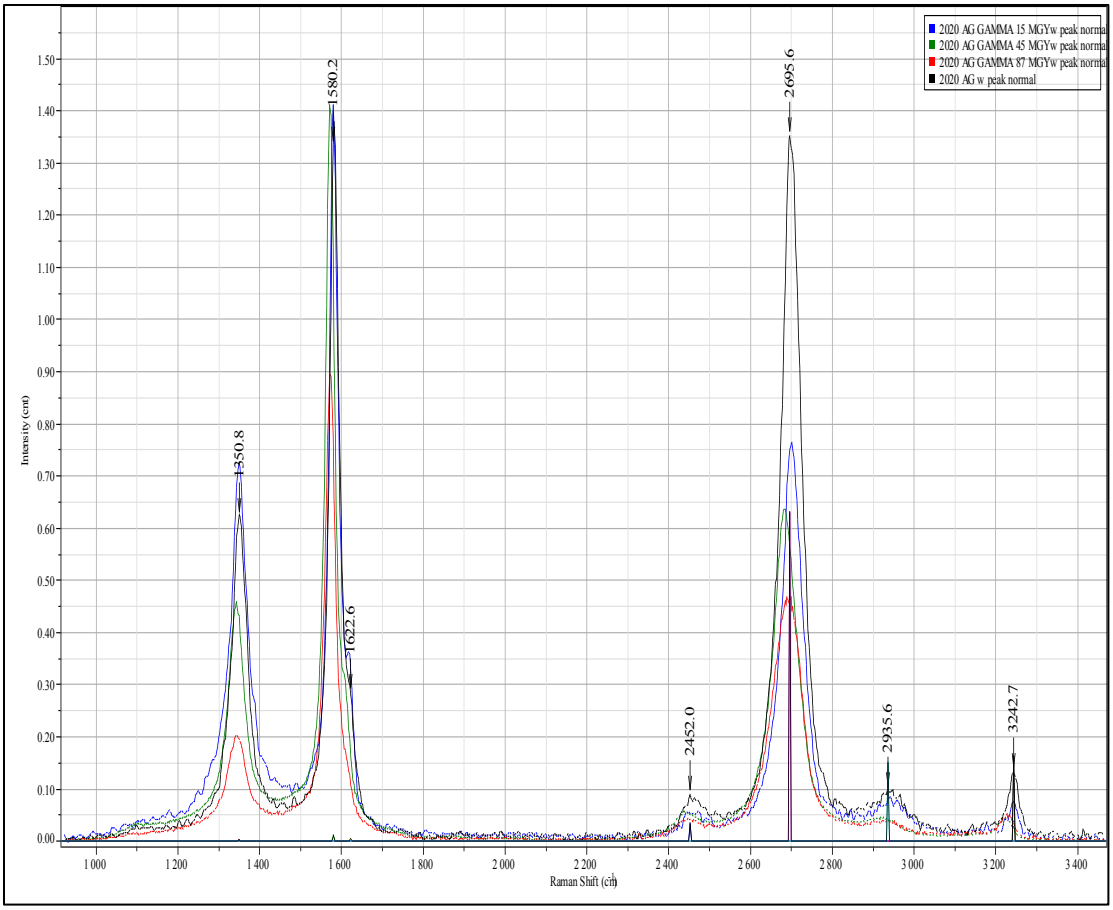

Figure B-90: Raman spectra for 2020 AG control and gamma irradiated samples.

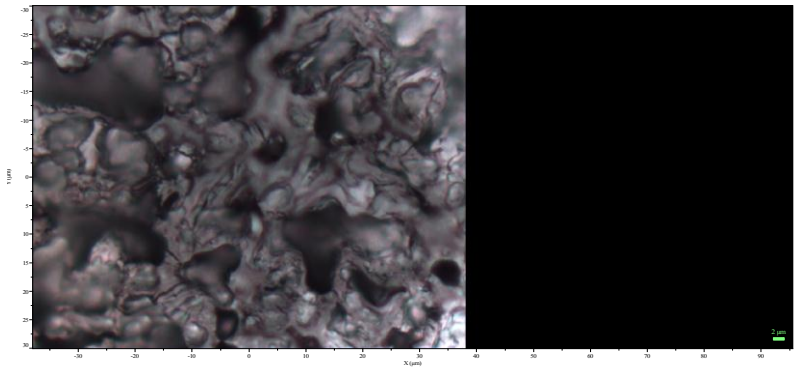

Figure B-91: Image of 202 AG control sample prior to Raman spectra collection.

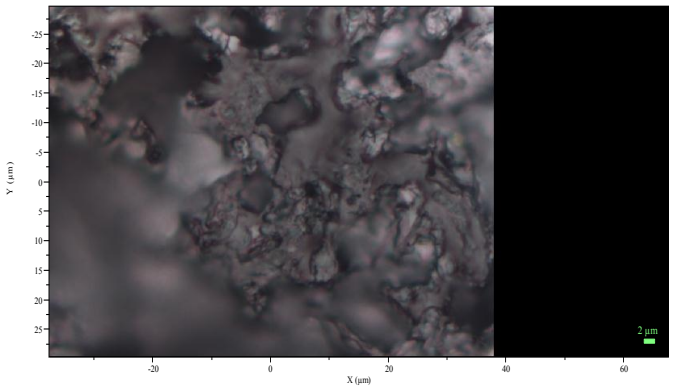

Figure B-92: Image of 2020 AG 15 MGy gamma irradiated sample prior to Raman spectra collection.

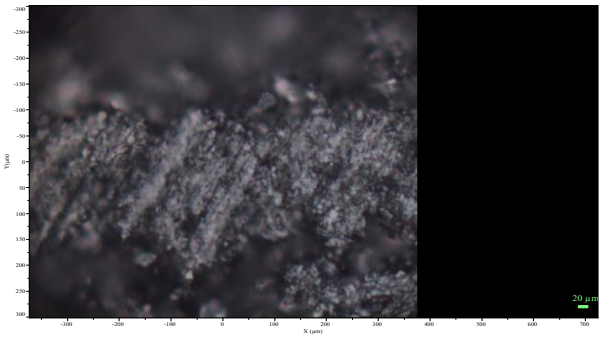

Figure B-93: Image of 2020 AG 45 MGy gamma irradiated sample prior to Raman spectra collection.

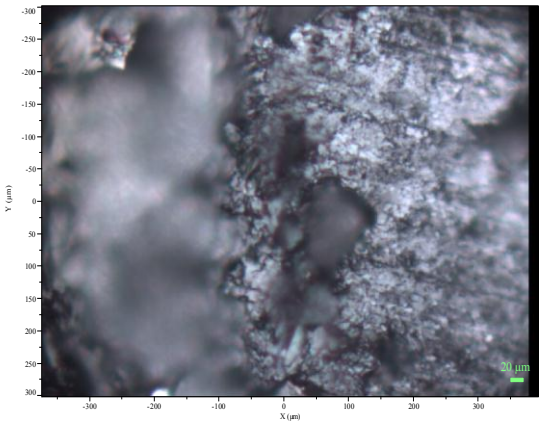

Figure B-94: Image of 2020 AG 87 MGy gamma irradiated sample prior to Raman spectra collection.

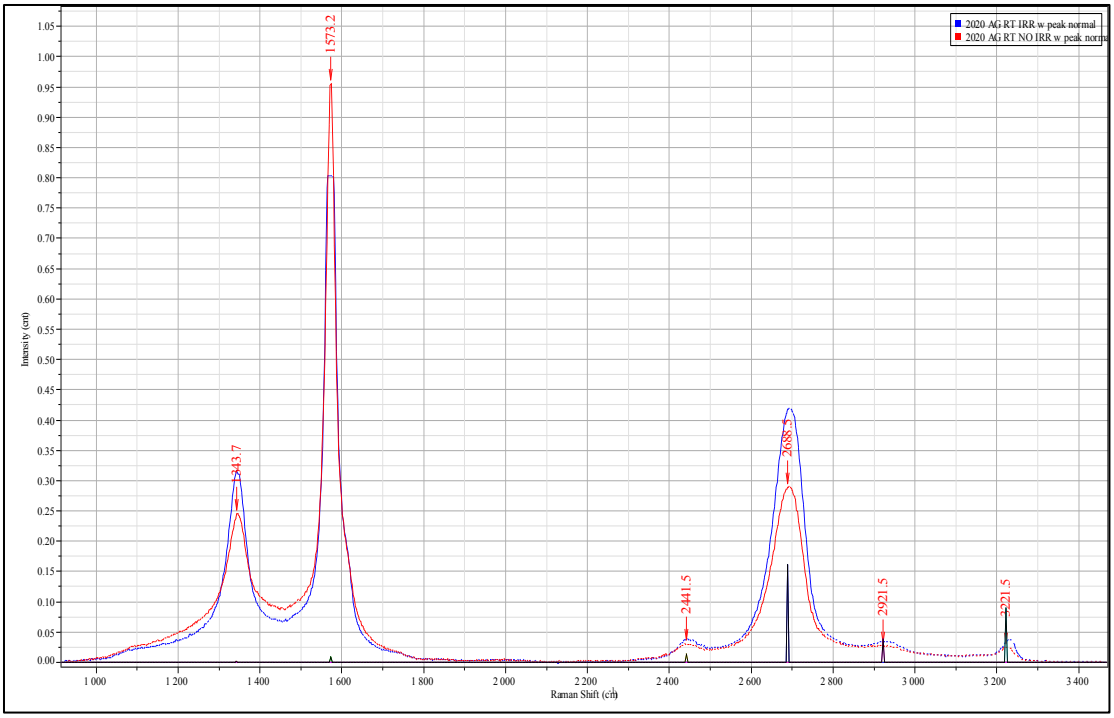

Figure B-95: Raman spectra for 2020 AG room temperature irradiated and unirradiated samples.

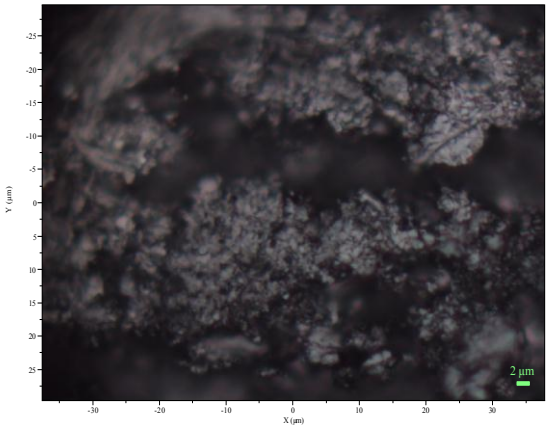

Figure B-96: Image of 2020 AG room temperature east beam port unirradiated sample prior to Raman spectra collection.

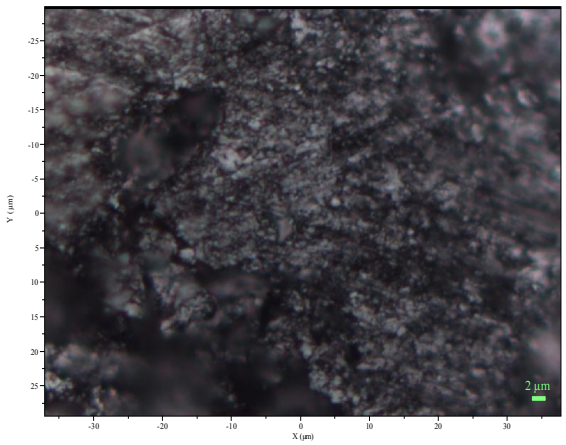

Figure B-97: Image of 2020 AG room temperature east beam port irradiated sample prior to Raman spectra collection.

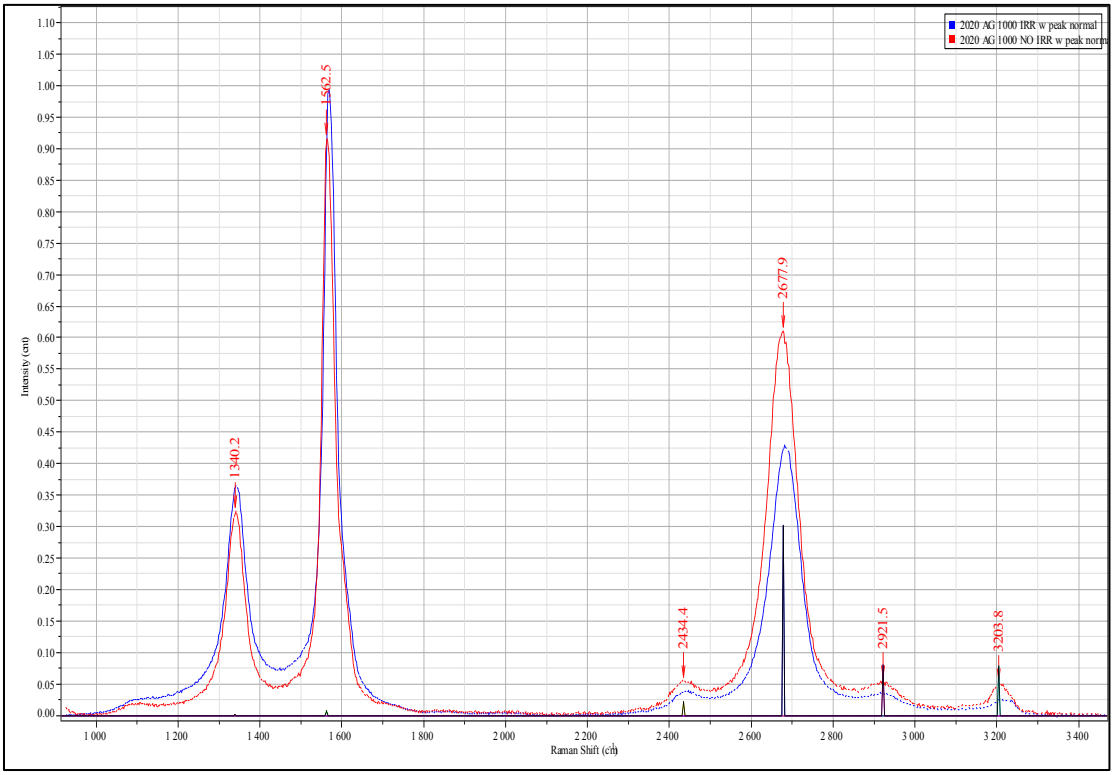

Figure B-98: Raman spectra for 2020 AG 1000 °C irradiated and unirradiated samples.

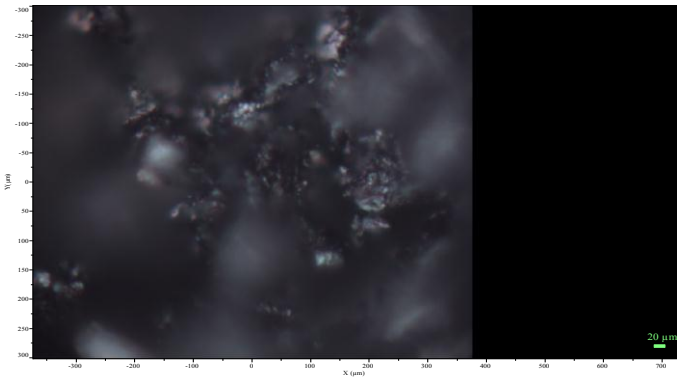

Figure B-99: Image of 2020 AG 1000 °C unirradiated east beam port sample prior to Raman spectra collection.

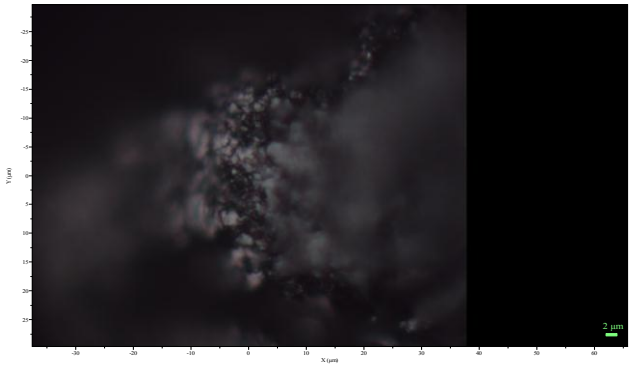

Figure B-100: Image of 2020 AG 1000 °C irradiated east beam port sample prior to Raman spectra collection.

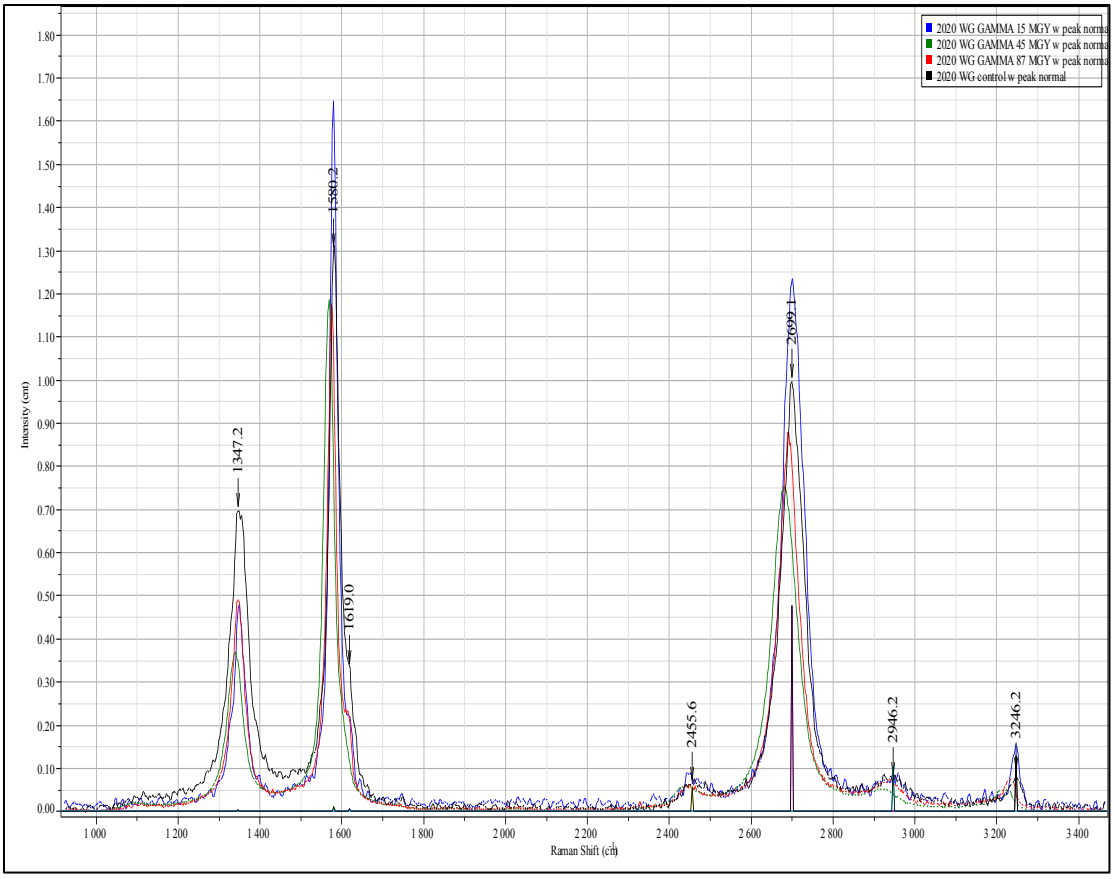

Figure B-101: Raman spectra for 2020 WG control and gamma irradiated samples.

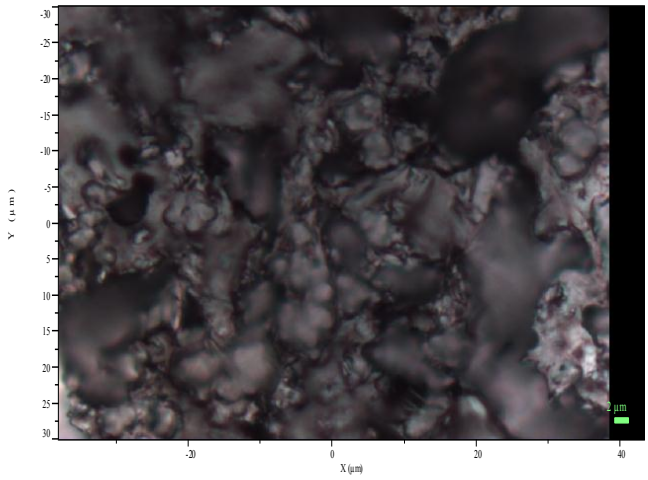

Figure B-102: Image of 2020 WG control sample prior to Raman sample collection.

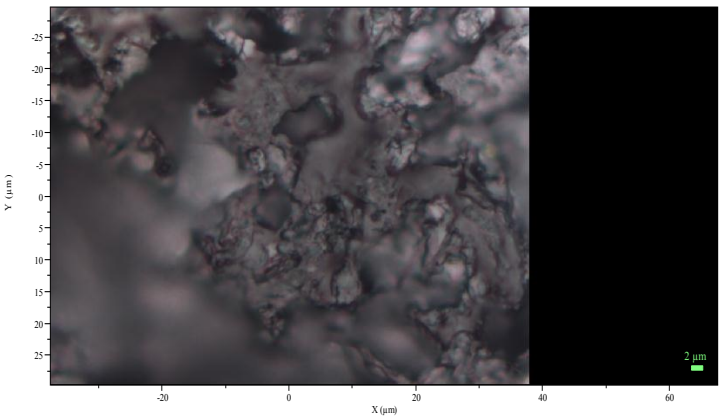

Figure B-103: Image of 2020 WG 15 MGy gamma irradiated sample prior to Raman spectra collection.

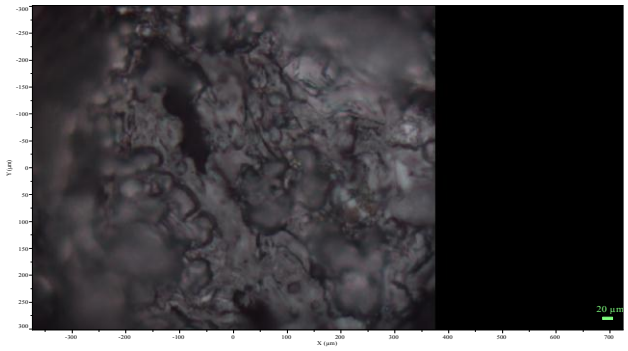

Figure B-104: Image of 2020 WG 45 MGy gamma irradiated sample prior to Raman spectra collection.

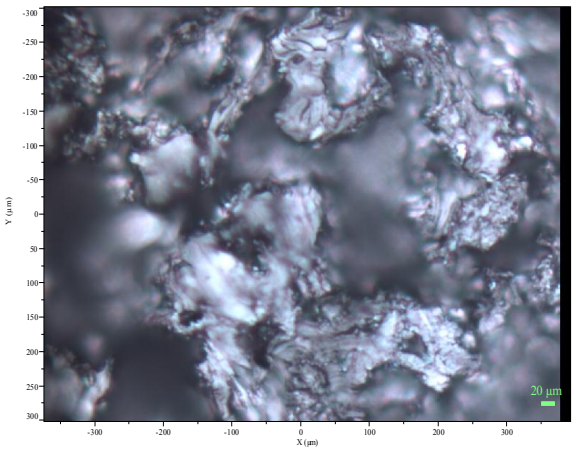

Figure B-105: Image of 2020 WG 87MGy gamma irradiated sample prior to Raman spectra collection.

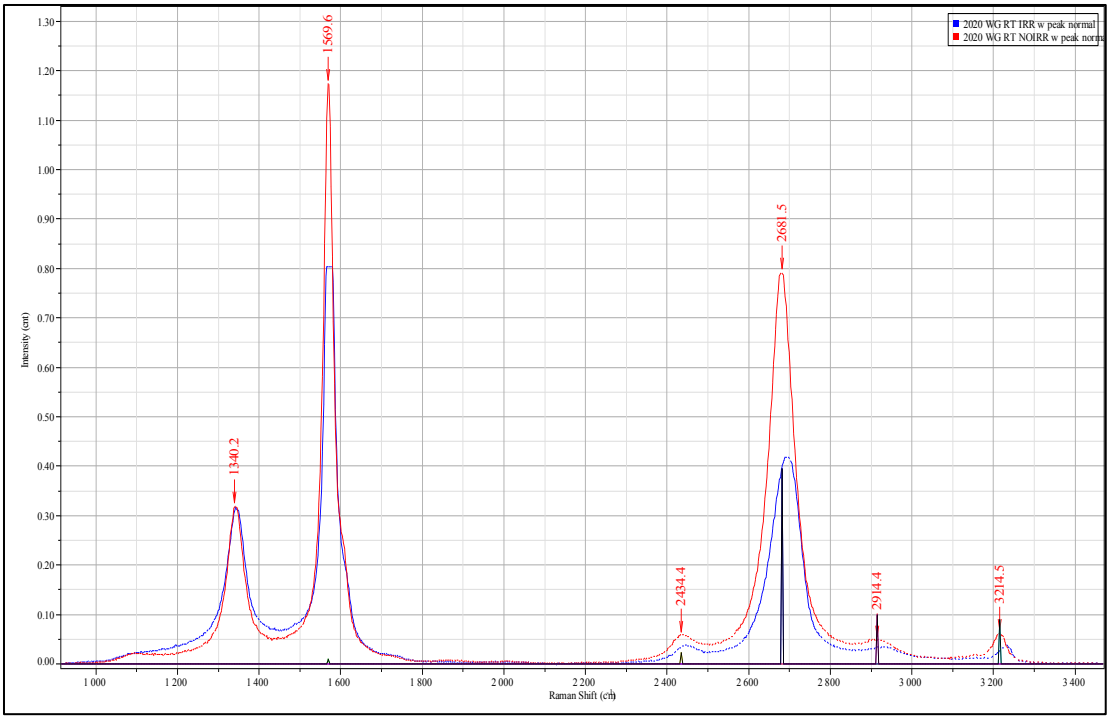

Figure B-106: Raman spectra for 2020 WG room temperature irradiated and unirradiated samples.

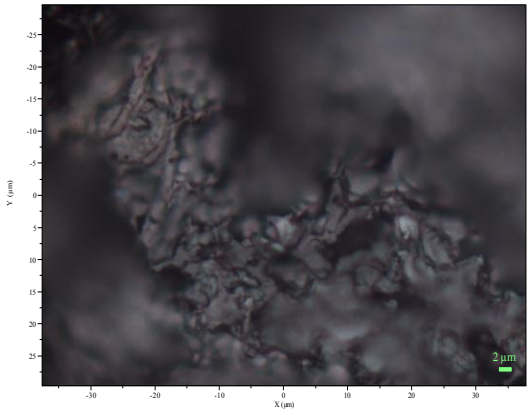

Figure B-107: Image of 2020 WG room temperature east beam port unirradiated sample prior to Raman spectra collection.

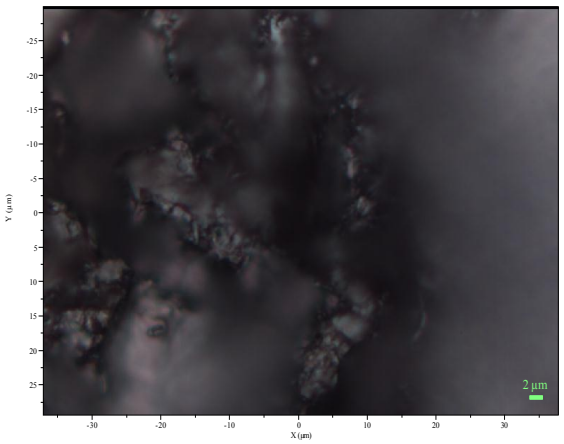

Figure B-108: Image of 2020 WG room temperature east beam port irradiated sample prior to Raman spectra correction.

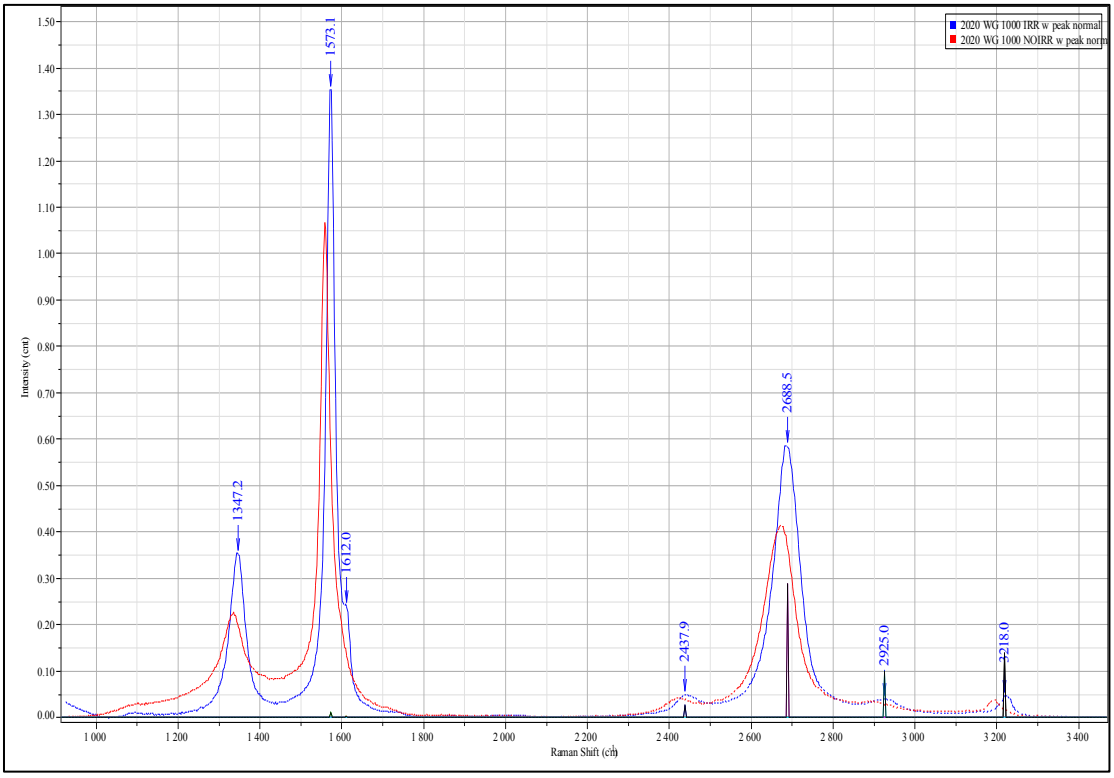

Figure B-109: Raman spectra for 2020 WG 1000 °C irradiated and unirradiated samples.

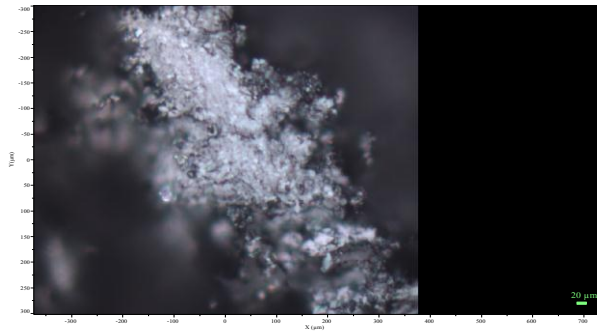

Figure B-110: Image of 2020 WG 1000 °C unirradiated east beam port sample prior to Raman spectra collection.

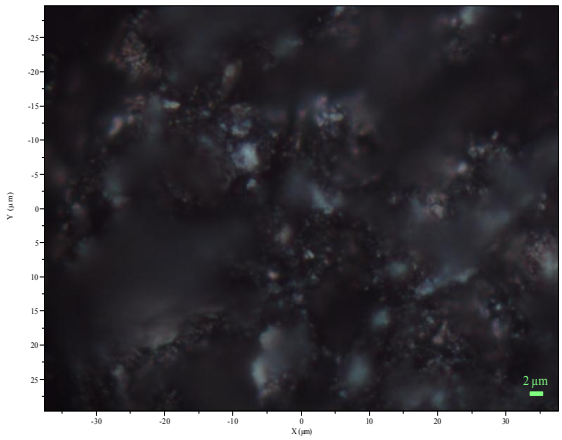

Figure B-111: Image of 2020 WG 1000 °C unirradiated east beam port sample prior to Raman spectra collection.

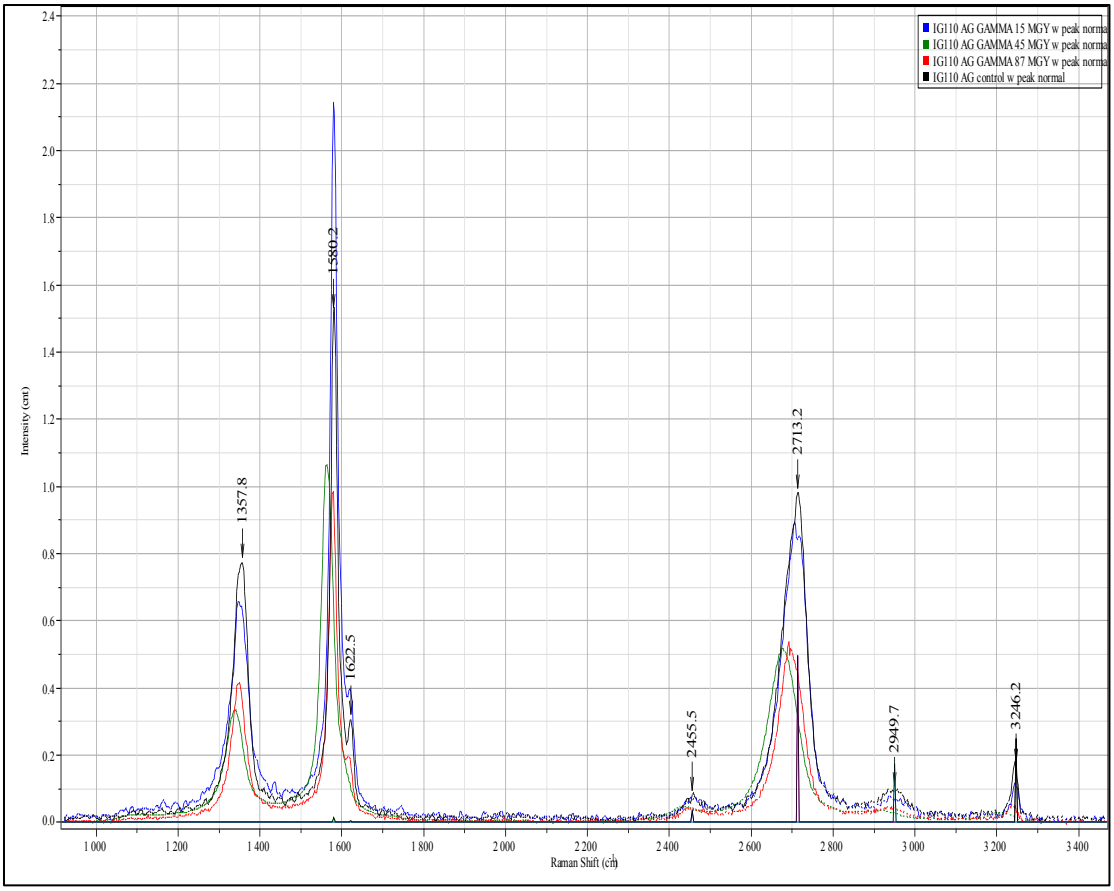

Figure B-112: Raman spectra for IG-110 AG control and gamma irradiated samples.

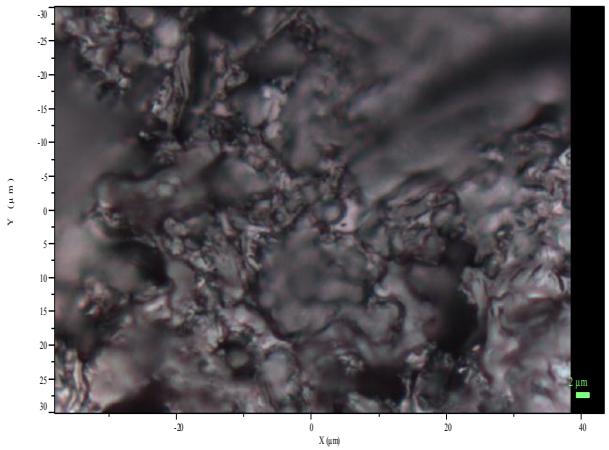

Figure B-113: Image of IG-110 AG control sample prior to Raman spectra collection.

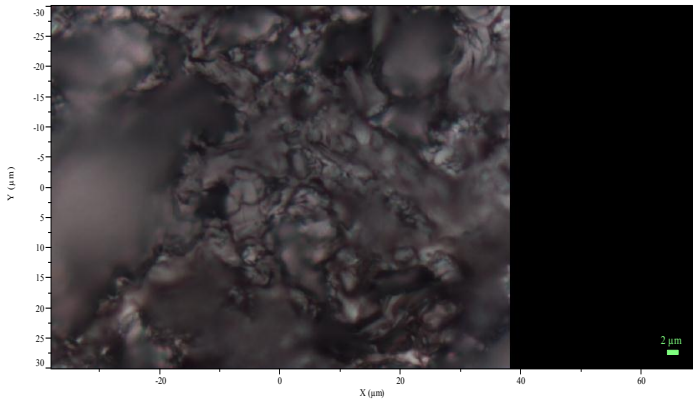

Figure B-114: Image of IG-110 AG 15 MGy gamma irradiated sample prior to Raman spectra collection.

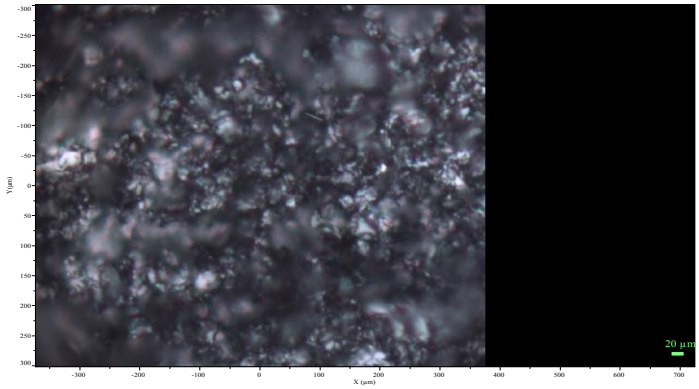

Figure B-115: Image of IG-110 AG 45 MGy gamma irradiated sample prior to Raman spectra collection.

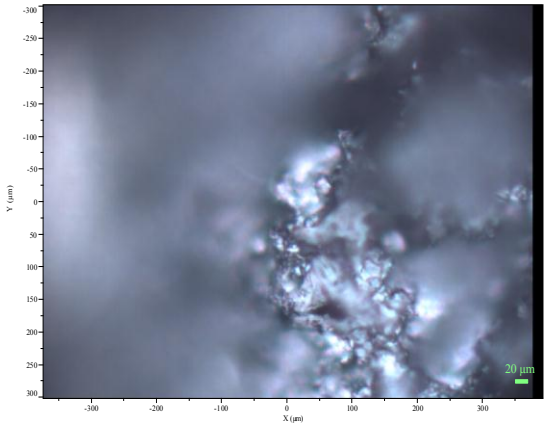

Figure B-116: Image of IG-110 AG 87 MGy gamma irradiated sample prior to Raman spectra collection.

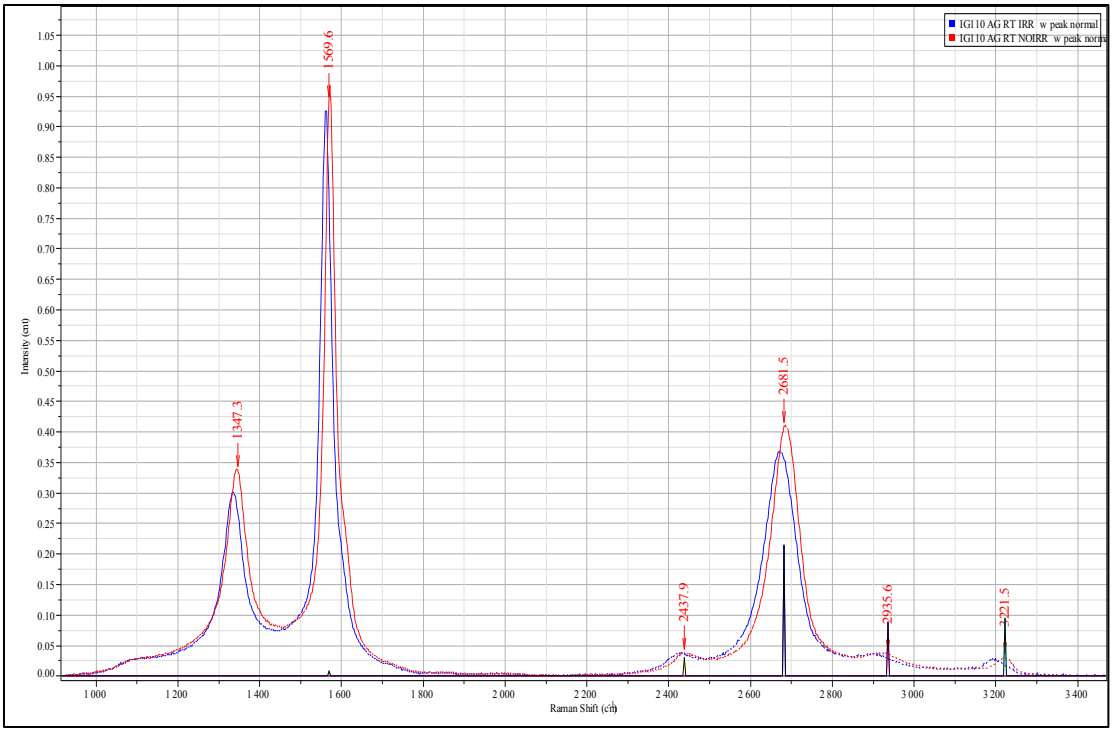

Figure B-117: Raman spectra for IG-110 AG room temperature irradiated and unirradiated samples.

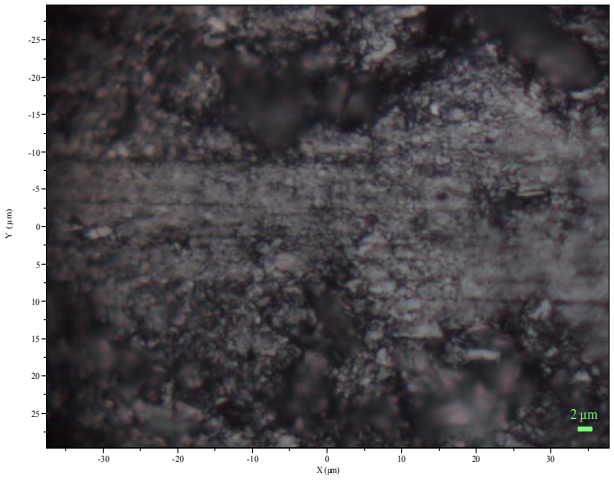

Figure B-118: Image of IG-110 AG room temperature east beam port unirradiated sample prior to Raman spectra collection.

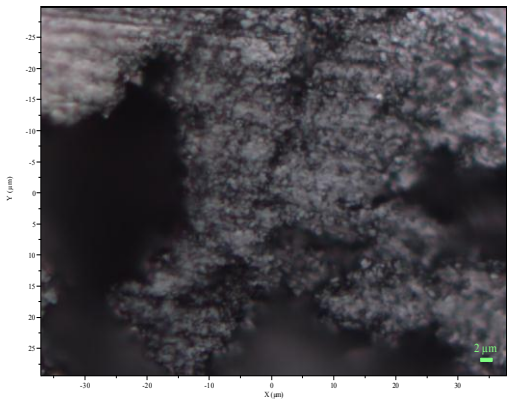

Figure B-119: Image of IG-110 AG room temperature east beam port irradiated sample prior to Raman spectra collection.

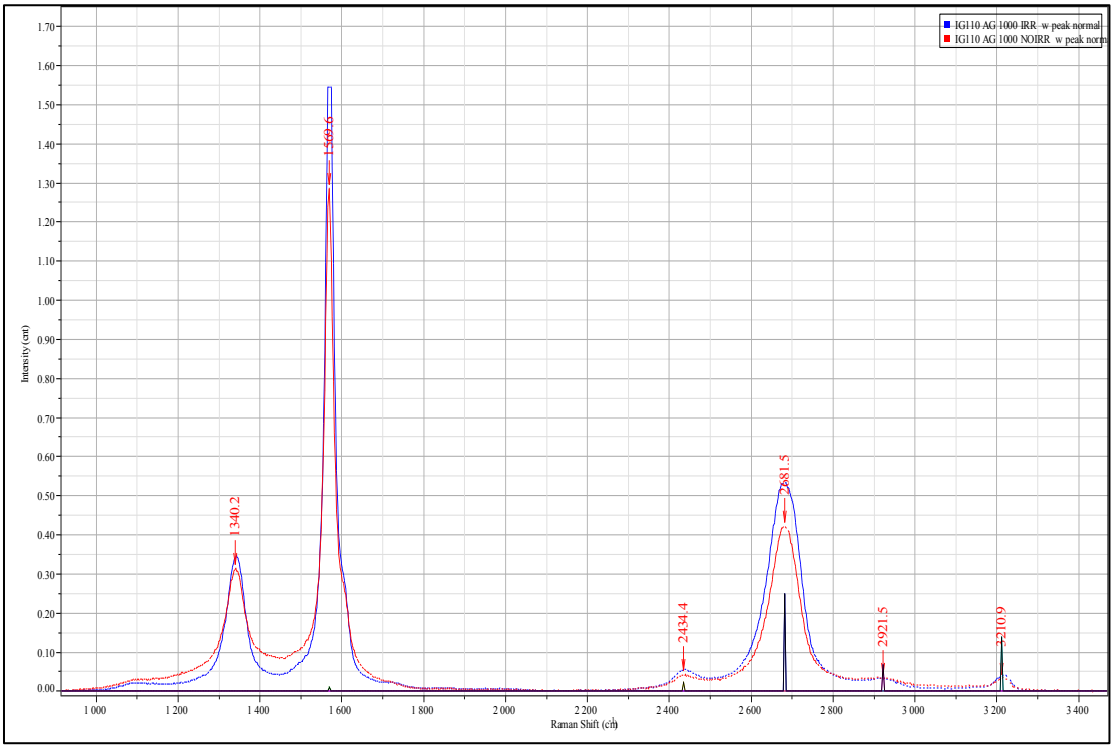

Figure B-120: Raman spectra for IG-110 AG 1000 °C irradiated and unirradiated samples.

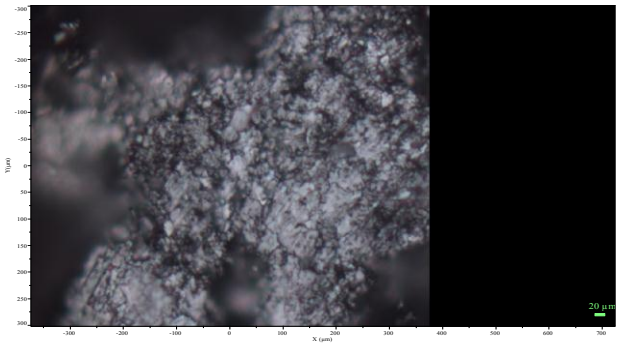

Figure B-121: Image of IG-110 AG 1000 °C unirradiated east beam port sample prior to Raman spectra collection.

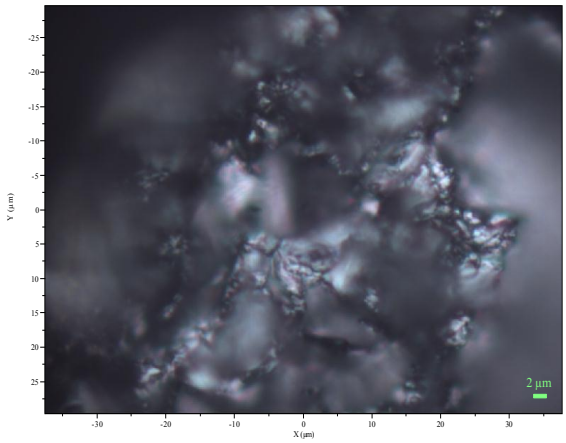

Figure B-122: Image of IG-110 AG 1000 °C irradiated east beam port sample prior to Raman spectra collection.

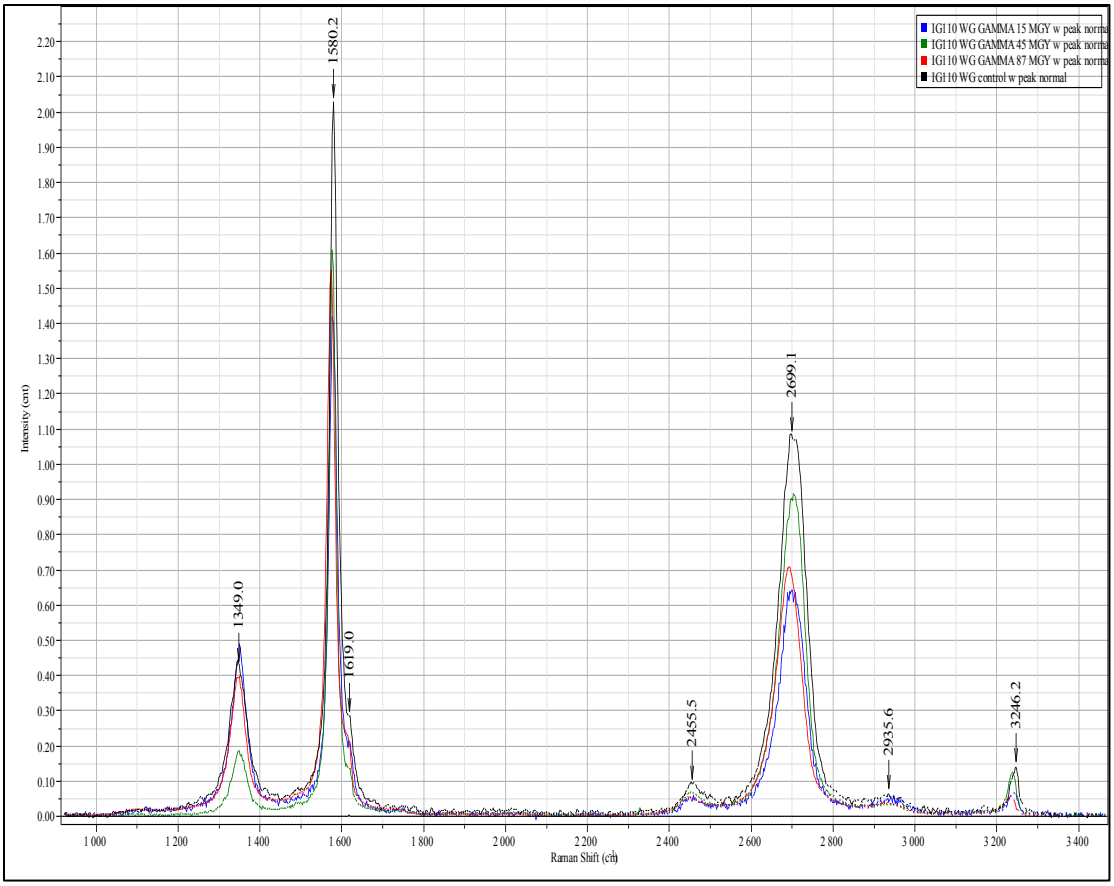

Figure B-123: Raman spectra for IG-110 WG control and gamma irradiated samples.

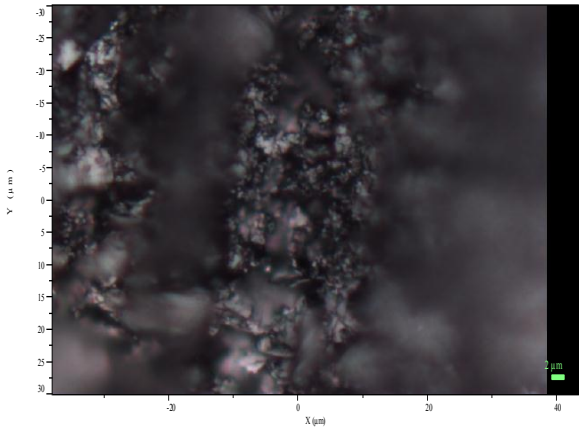

Figure B-124: Image of IG-110 WG control sample prior to Raman spectra collection.

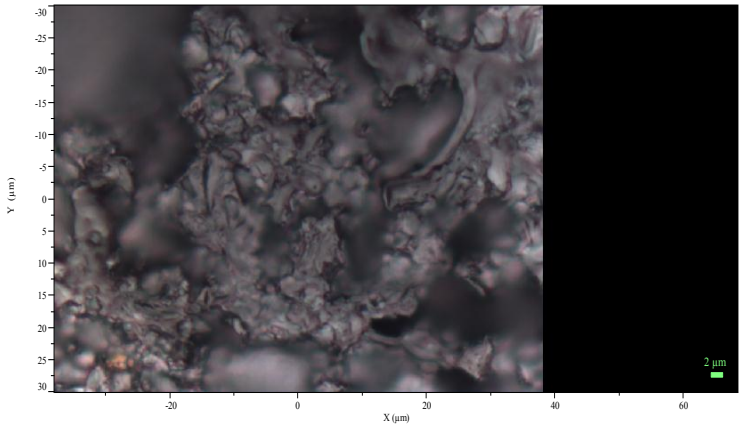

Figure B-125: Image of IG-110 WG 15 MGy gamma irradiated sample prior to Raman spectra collection.

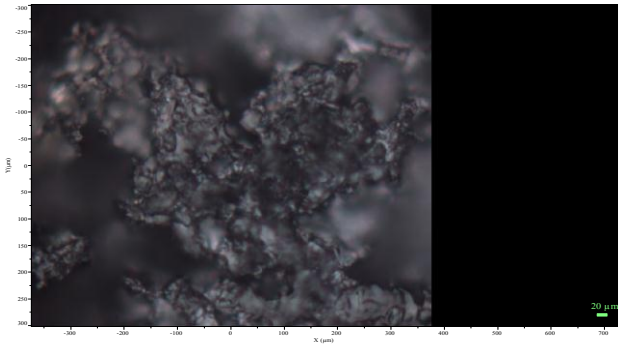

Figure B-126: Image of IG-110 WG 45 MGy gamma irradiated sample prior to Raman spectra collection.

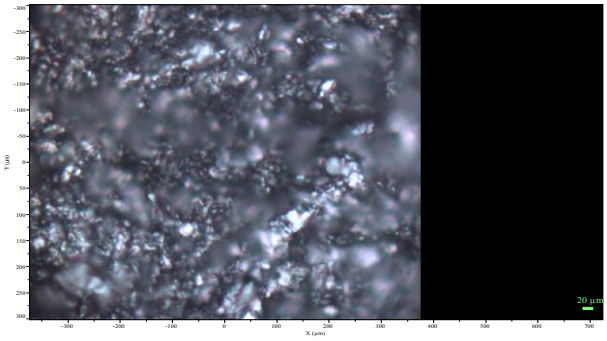

Figure B-127: Image of IG-110 WG 87 MGy gamma irradiated sample prior to Raman spectra collection.

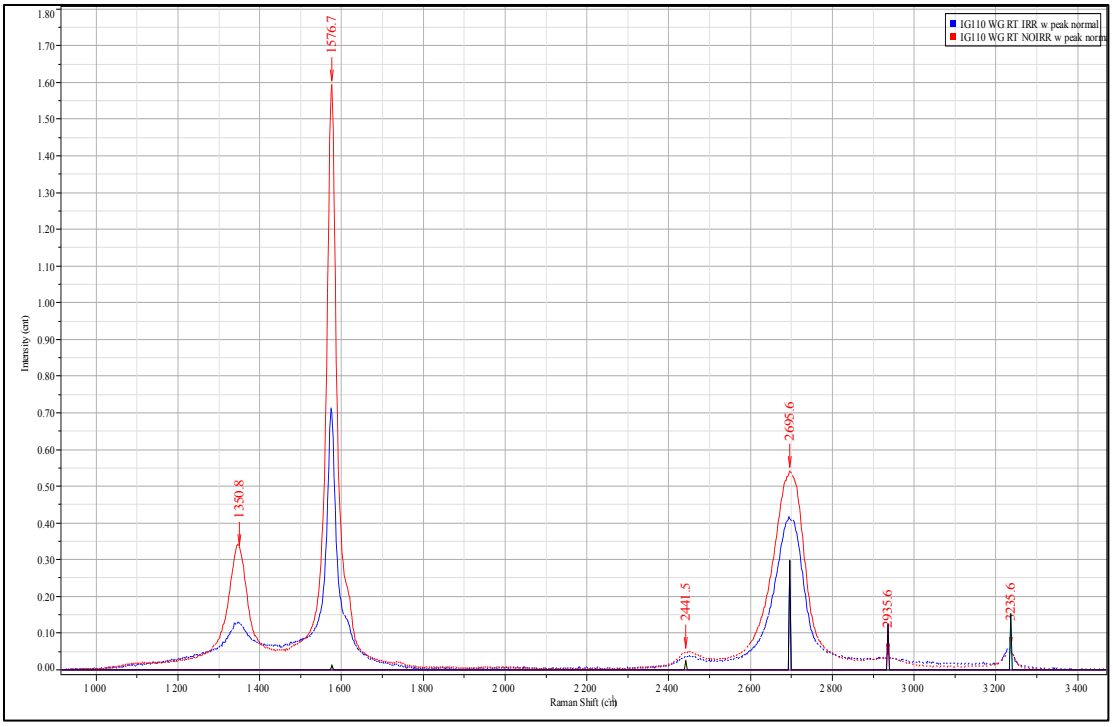

Figure B-128: Raman spectra for IG-110 WG room temperature irradiated and unirradiated samples.

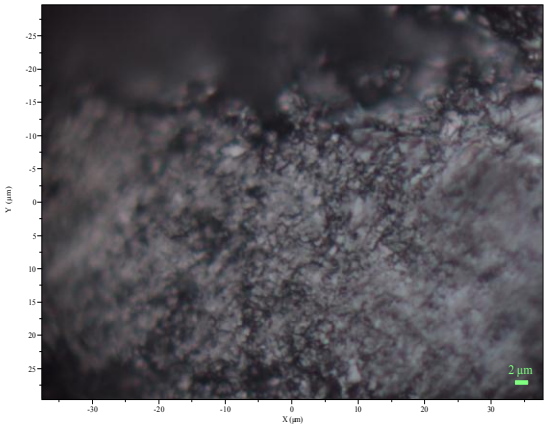

Figure B-129: Image of IG-110 WG room temperature east beam port unirradiated sample prior to Raman spectra collection.

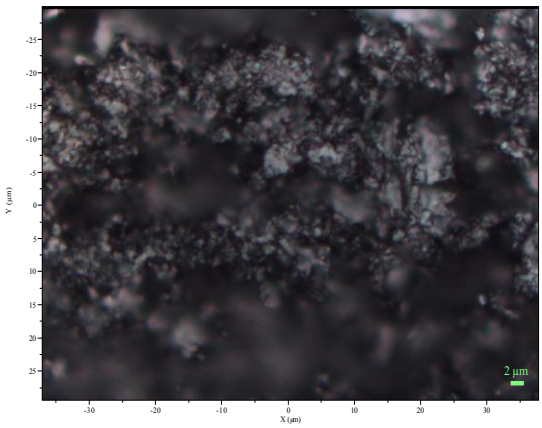

Figure B-130: Image of IG-110 WG room temperature east beam port irradiated sample prior to Raman spectra collection.

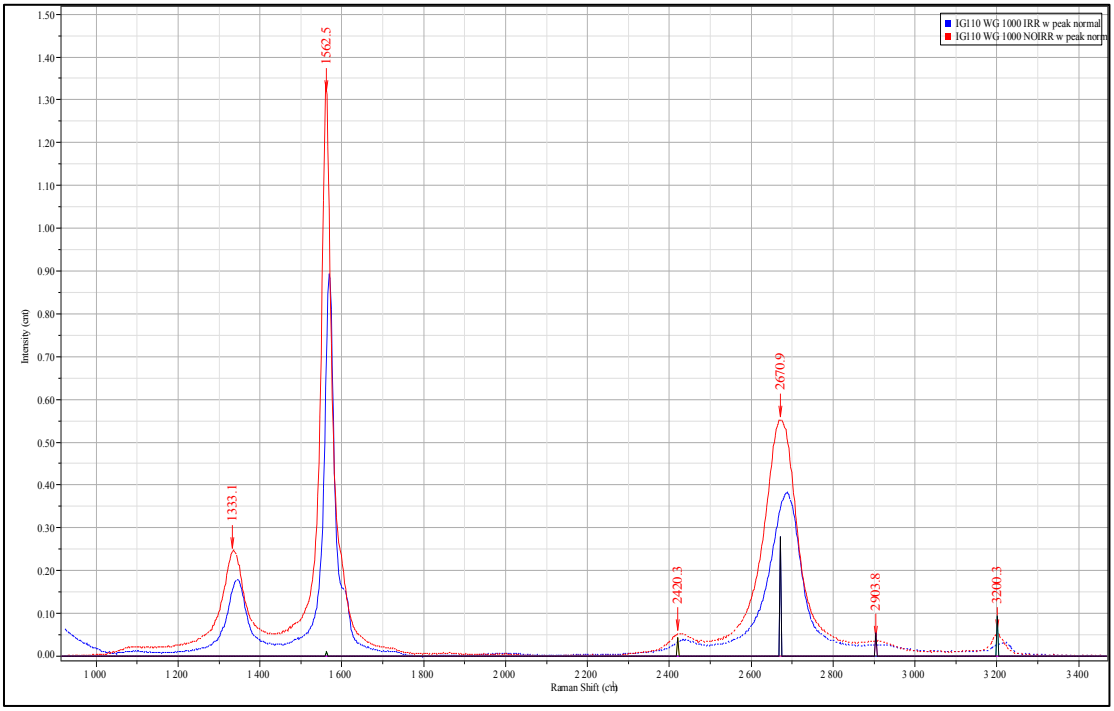

Figure B-131: Raman spectra for IG-110 WG 1000 °C irradiated and unirradiated samples.

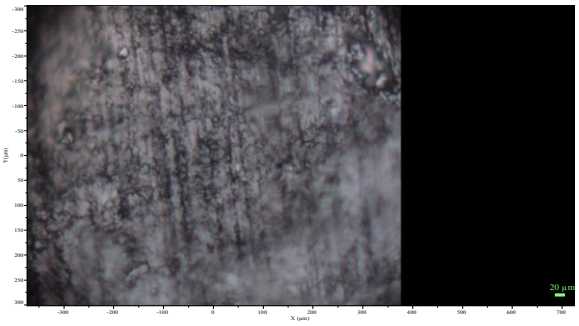

Figure B-132: Image of IG-110 WG 1000 °C unirradiated east beam port sample prior to Raman spectra collection.

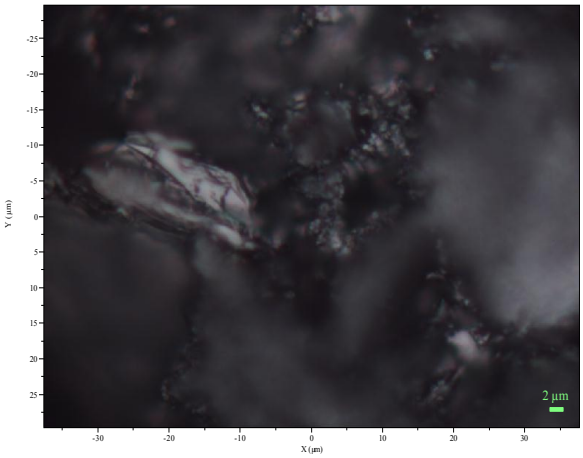

Figure B-133: Image of IG-110 WG 1000 °C irradiated east beam port sample prior to Raman spectra collection.

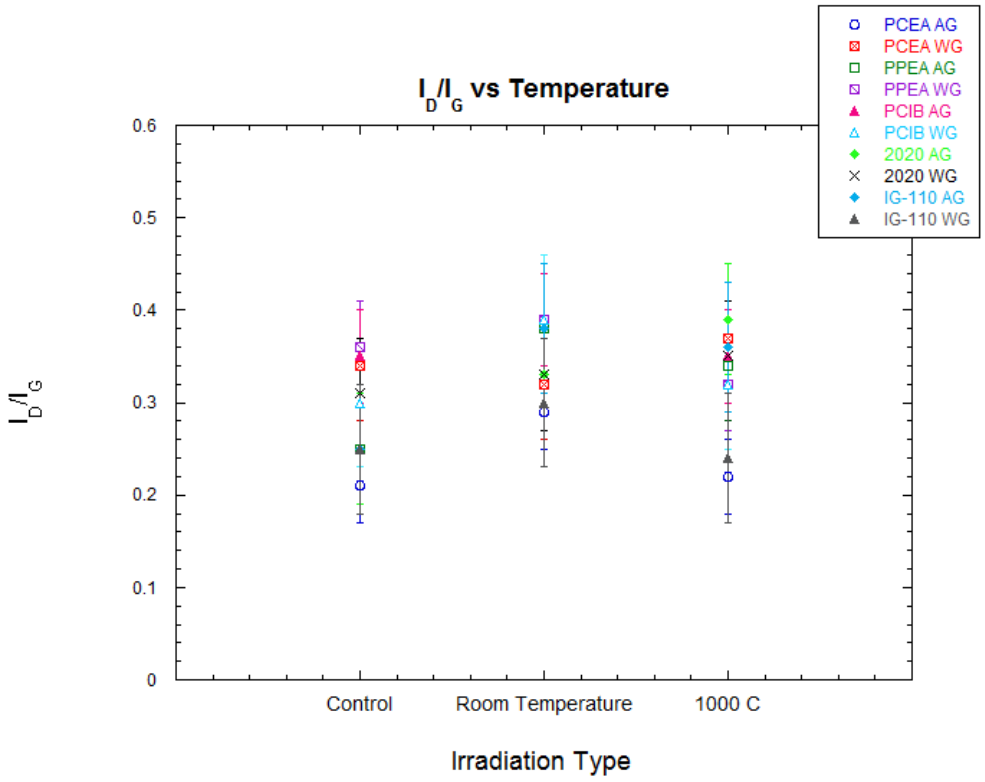

Figure B-134: I_D/I_G versus irradiation temperature for all graphite types. Error bars represent 95 % confidence limits.

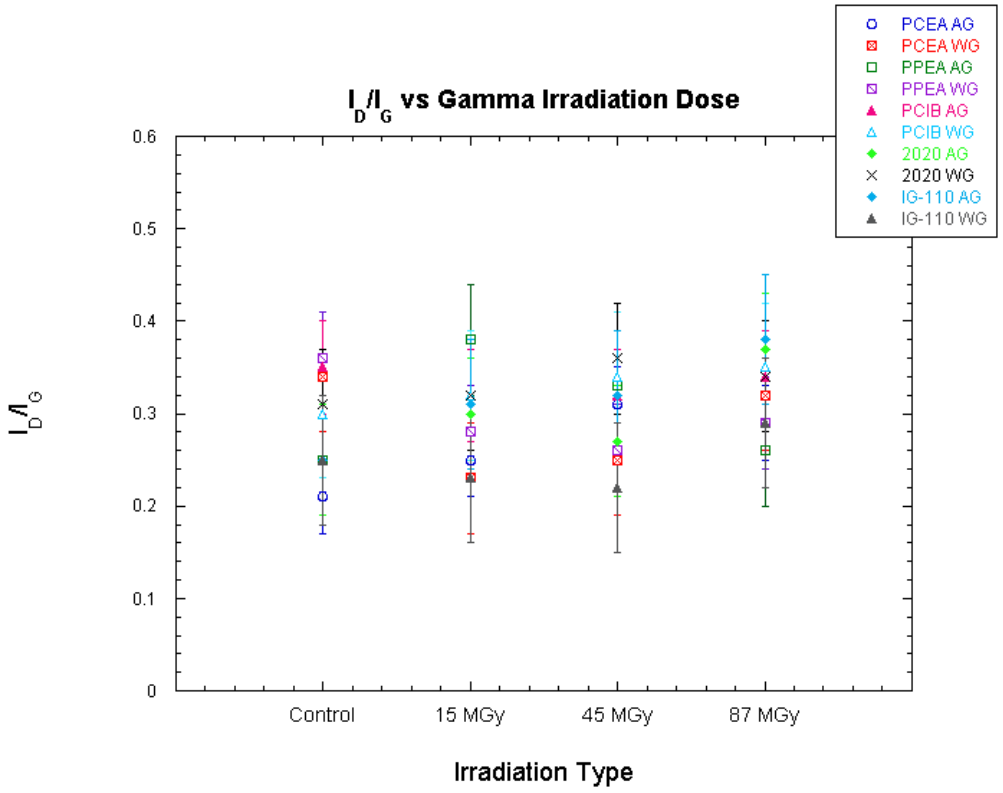

Figure B-135: I_D/I_G versus gamma irradiation dose for all graphite types. Error bars represent 95 % confidence limits.

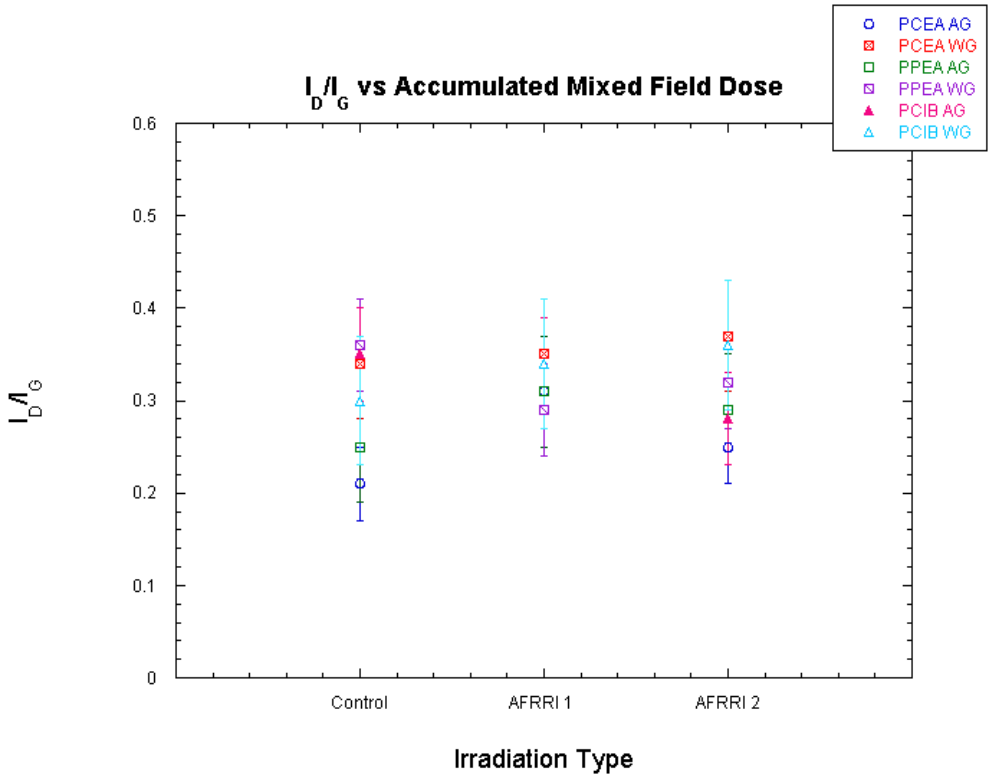

Figure B-136: I_D/I_G versus mixed field irradiation dose for the AFRRI irradiated graphite types. Error bars represent 95 % confidence limits.

Appendix C. XRD Results

This appendix contains the table below, which contains information on all of the XRD spectra collected in these experiments.

Graphite	Obs. Max (2θ)	d (Obs. Max) (A°)	Max Int. (cps)	Net Hght (cps)	FW HM (2θ)	Grav. C. (2θ)	d (GC) (A°)	Raw Area (cps* 2θ)	Net Area (cps*2θ)	Left Int. (cps)	Rt. Int. (cps)
PCEA AG											
Control	26.40	3.37	15.00	14.90	0.34	26.35	3.38	6.56	6.10	0.13	0.11
AFRRI 1	26.40	3.37	16.00	15.90	0.31	26.33	3.38	6.88	6.35		
AFRRI 2	26.40	3.37	17.10	17.00	0.31	26.34	3.38	7.22	6.69		
RABBIT HTR	26.39	3.37	21.00	20.90	0.32	26.33	3.38	8.99	8.38		
15 MGy GAMMA	26.42	3.37	16.00	15.80	0.31	26.37	3.38	6.65	6.22	0.12	0.11
45 MGy GAMMA	26.42	3.37	20.50	20.30	0.31	26.36	3.38	8.34	7.83	0.14	0.12
87 MGy GAMMA	26.43	3.37	16.10	16.00	0.30	26.39	3.38	6.50	6.05	0.13	0.11
ROOM TEMP NO IRR	26.41	3.37	14.50	14.40	0.33	26.35	3.38	6.30	5.87	0.11	0.11
ROOM TEMP IRR	26.41	3.37	15.00	14.90	0.33	26.36	3.38	6.52	6.08	0.13	0.11
1000 C NO IRR	26.40	3.37	13.50	13.40	0.36	26.31	3.38	6.64	6.11	0.08	0.06
1000 C IRR	26.41	3.37	15.40	15.20	0.35	26.32	3.38	7.44	6.86	0.08	0.06
PCEA WG											
Control	26.42	3.37	15.50	15.30	0.34	26.36	3.38	6.80	6.34	0.13	0.11
AFRRI 1	26.40	3.37	20.90	20.70	0.30	26.34	3.38	8.45	7.87		
AFRRI 2	26.38	3.38	14.60	14.40	0.37	26.28	3.39	7.40	6.81		
RABBIT HTR	26.41	3.37	14.40	14.30	0.30	26.35	3.38	6.04	5.56		
15 MGy GAMMA	26.42	3.37	14.20	14.10	0.33	26.36	3.38	6.18	5.75	0.13	0.11
45 MGy GAMMA	26.43	3.37	15.80	15.70	0.31	26.37	3.38	6.56	6.13	0.12	0.11
87 MGy GAMMA	26.41	3.37	13.20	13.10	0.34	26.31	3.38	6.40	5.87	0.16	0.11

Graphite	Obs. Max (2θ)	d (Obs. Max) (A°)	Max Int. (cps)	Net Hght (cps)	FW HM (2θ)	Grav. C. (2θ)	d (GC) (A°)	Raw Area (cps* 2θ)	Net Area (cps*2θ)	Left Int. (cps)	Rt. Int. (cps)
ROOM TEMP NO IRR	26.41	3.37	12.60	12.50	0.31	26.36	3.38	5.45	4.97	0.16	0.12
ROOM TEMP IRR	26.41	3.37	17.60	17.40	0.32	26.35	3.38	7.30	6.83	0.14	0.12
1000 C NO IRR	26.40	3.37	14.30	14.10	0.35	26.30	3.39	6.94	6.39	0.09	0.06
1000 C IRR	26.42	3.37	15.70	15.50	0.35	26.32	3.38	7.59	7.00	0.09	0.06
PPEA AG											
Control	26.41	3.37	14.40	14.20	0.39	26.32	3.38	7.45	6.86	0.17	0.12
AFRRI 1	26.37	3.38	20.20	20.10	0.34	26.28	3.39	9.55	8.88		
AFRRI 2	26.38	3.38	18.00	17.80	0.34	26.29	3.39	8.66	8.01		
RABBIT HTR	26.40	3.37	14.60	14.50	0.35	26.30	3.39	7.14	6.58		
15 MGy GAMMA	26.42	3.37	13.90	13.70	0.38	26.32	3.38	7.01	6.46	0.16	0.12
45 MGy GAMMA	26.40	3.37	12.50	12.40	0.39	26.30	3.39	6.46	5.91	0.16	0.12
87 MGy GAMMA	26.41	3.37	17.50	17.30	0.30	26.36	3.38	7.01	6.56	0.13	0.11
ROOM TEMP NO IRR	26.42	3.37	14.20	14.10	0.36	26.32	3.38	7.05	6.51	0.16	0.11
ROOM TEMP IRR	26.39	3.37	15.50	15.30	0.37	26.31	3.38	7.72	7.09	0.19	0.13
1000 C NO IRR	26.40	3.37	15.80	15.60	0.32	26.34	3.38	6.96	6.47	0.07	0.06
1000 C IRR	26.39	3.37	17.50	17.30	0.35	26.33	3.38	7.86	7.31	0.08	0.07
PPEA WG											
Control	26.41	3.37	12.90	12.80	0.39	26.31	3.38	6.76	6.19	0.16	0.12
AFRRI 1	26.41	3.37	16.00	15.80	0.32	26.31	3.39	7.45	6.88		
AFRRI 2	26.40	3.37	15.50	15.40	0.30	26.33	3.38	6.60	6.10		
RABBIT HTR	26.38	3.38	16.20	16.10	0.36	26.29	3.39	8.10	7.48		
15 MGy GAMMA	26.40	3.37	12.50	12.30	0.38	26.30	3.39	6.36	5.83	0.16	0.11
45 MGy GAMMA	26.40	3.37	12.50	12.30	0.39	26.30	3.39	6.44	5.90	0.16	0.11
87 MGy	26.41	3.37	13.50	13.30	0.34	26.34	3.38	6.12	5.66	0.13	0.10

Graphite	Obs. Max (2θ)	d (Obs. Max) (A°)	Max Int. (cps)	Net Hght (cps)	FW HM (2θ)	Grav. C. (2θ)	d (GC) (A°)	Raw Area (cps* 2θ)	Net Area (cps*2θ)	Left Int. (cps)	Rt. Int. (cps)
GAMMA											
ROOM TEMP NO IRR	26.40	3.37	15.10	15.00	0.35	26.32	3.38	7.23	6.65	0.17	0.13
ROOM TEMP IRR	26.39	3.37	12.00	11.80	0.39	26.30	3.39	6.28	5.74	0.16	0.11
1000 C NO IRR	26.42	3.37	13.70	13.60	0.31	26.36	3.38	5.90	5.43	0.07	0.06
1000 C IRR	26.40	3.37	17.20	17.00	0.33	26.33	3.38	7.42	6.94	0.07	0.05
PCIB AG											
Control	26.39	3.37	14.30	14.10	0.38	26.33	3.38	6.99	6.45	0.15	0.12
AFRRI 1	26.38	3.38	13.20	13.10	0.34	26.31	3.38	6.28	5.75		
AFRRI 2	26.37	3.38	15.70	15.50	0.35	26.30	3.39	7.47	6.90		
RABBIT HTR	26.38	3.38	15.60	15.50	0.34	26.31	3.38	7.31	6.76		
15 MGy GAMMA	26.39	3.37	12.90	12.80	0.37	26.32	3.38	6.30	5.82	0.14	0.11
45 MGy GAMMA	26.37	3.38	14.00	13.90	0.38	26.31	3.39	6.85	6.33	0.15	0.12
87 MGy GAMMA	26.38	3.38	12.80	12.60	0.36	26.32	3.38	6.19	5.67	0.16	0.11
ROOM TEMP NO IRR	26.39	3.37	13.20	13.00	0.37	26.32	3.38	6.42	5.92	0.15	0.11
ROOM TEMP IRR	26.39	3.37	15.30	15.10	0.35	26.34	3.38	7.07	6.50	0.16	0.14
1000 C NO IRR	26.39	3.37	13.70	13.50	0.35	26.33	3.38	6.48	5.97	0.17	0.12
1000 C IRR	26.37	3.38	13.70	13.50	0.38	26.31	3.38	6.76	6.22	0.15	0.11
PCIB WG											
Control	26.41	3.37	14.20	14.00	0.38	26.35	3.38	6.92	6.40	0.15	0.12
AFRRI 1	26.37	3.38	18.10	18.00	0.34	26.30	3.39	8.52	7.89		
AFRRI 2	26.37	3.38	16.10	15.90	0.36	26.30	3.39	7.75	7.14		
RABBIT HTR	26.39	3.37	14.80	14.70	0.34	26.32	3.38	6.98	6.44		
15 MGy GAMMA	26.39	3.37	15.50	15.30	0.37	26.33	3.38	7.39	6.86	0.15	0.12
45 MGy GAMMA	26.40	3.37	13.80	13.60	0.34	26.33	3.38	6.40	5.91	0.14	0.11

Graphite	Obs. Max (2θ)	d (Obs. Max) (A°)	Max Int. (cps)	Net Hght (cps)	FW HM (2θ)	Grav. C. (2θ)	d (GC) (A°)	Raw Area (cps* 2θ)	Net Area (cps*2θ)	Left Int. (cps)	Rt. Int. (cps)
87 MGy GAMMA	26.39	3.37	13.60	13.40	0.37	26.33	3.38	6.57	6.04	0.16	0.12
ROOM TEMP NO IRR	26.39	3.37	13.70	13.50	0.38	26.32	3.38	6.66	6.16	0.15	0.11
ROOM TEMP IRR	26.40	3.37	15.30	15.10	0.37	26.33	3.38	7.32	6.78	0.15	0.12
1000 C NO IRR	26.39	3.37	12.80	12.60	0.35	26.33	3.38	6.03	5.53	0.16	0.12
1000 C IRR	26.38	3.38	15.00	14.90	0.37	26.32	3.38	7.29	6.75	0.16	0.11
2020 AG											
Control	26.41	3.37	10.50	10.30	0.44	26.28	3.39	6.42	5.72	0.21	0.13
15 MGy GAMMA	26.40	3.37	10.70	10.50	0.43	26.27	3.39	6.51	5.81	0.21	0.13
45 MGy GAMMA	26.41	3.37	10.10	9.88	0.38	26.27	3.39	5.77	5.09	0.21	0.13
87 MGy GAMMA	26.42	3.37	9.98	9.78	0.39	26.28	3.39	5.76	5.12	0.19	0.12
ROOM TEMP NO IRR	26.39	3.37	10.60	10.30	0.40	26.26	3.39	6.21	5.39	0.27	0.17
ROOM TEMP IRR	26.42	3.37	10.30	10.10	0.44	26.27	3.39	6.31	5.62	0.20	0.13
1000 C NO IRR	26.41	3.37	10.80	10.50	0.43	26.27	3.39	6.46	5.75	0.21	0.13
1000 C IRR	26.39	3.37	10.80	10.60	0.42	26.25	3.39	6.46	5.72	0.23	0.13
2020 WG											
Control	26.43	3.37	12.40	12.20	0.42	26.29	3.39	7.28	6.54	0.21	0.14
15 MGy GAMMA	26.42	3.37	11.20	11.00	0.42	26.28	3.39	6.57	5.88	0.21	0.12
45 MGy GAMMA	26.41	3.37	11.60	11.40	0.41	26.27	3.39	6.77	6.07	0.21	0.13
87 MGy GAMMA	26.41	3.37	12.30	12.10	0.37	26.28	3.39	6.73	6.05	0.20	0.13
ROOM TEMP NO IRR	26.41	3.37	8.26	8.03	0.44	26.27	3.39	5.19	4.47	0.23	0.15
ROOM TEMP IRR	26.43	3.37	11.20	11.00	0.42	26.29	3.39	6.64	5.94	0.21	0.13
1000 C NO	26.41	3.37	10.50	10.30	0.44	26.26	3.39	6.38	5.69	0.21	0.13

Graphite	Obs. Max (2θ)	d (Obs. Max) (A°)	Max Int. (cps)	Net Hght (cps)	FW HM (2θ)	Grav. C. (2θ)	d (GC) (A°)	Raw Area (cps* 2θ)	Net Area (cps*2θ)	Left Int. (cps)	Rt. Int. (cps)
IRR											
1000 C IRR	26.42	3.37	10.70	10.50	0.40	26.28	3.39	6.25	5.57	0.20	0.13
IG-110 AG											
Control	26.42	3.37	13.00	12.80	0.37	26.35	3.38	6.30	5.82	0.14	0.12
15 MGy GAMMA	26.41	3.37	13.70	13.60	0.37	26.34	3.38	6.57	6.08	0.14	0.11
45 MGy GAMMA	26.41	3.37	13.20	13.10	0.37	26.34	3.38	6.31	5.85	0.13	0.11
87 MGy GAMMA	26.42	3.37	9.98	9.77	0.39	26.28	3.39	5.74	5.11	0.19	0.12
ROOM TEMP NO IRR	26.42	3.37	15.00	14.80	0.34	26.35	3.38	6.87	6.38	0.14	0.11
ROOM TEMP IRR	26.41	3.37	13.70	13.60	0.38	26.34	3.38	6.67	6.16	0.15	0.12
1000 C NO IRR	26.40	3.37	11.40	11.20	0.36	26.33	3.38	5.51	5.02	0.14	0.11
1000 C IRR	26.41	3.37	16.60	16.40	0.35	26.35	3.38	7.74	7.17	0.16	0.13
IG-110 WG											
Control	26.41	3.37	14.60	14.40	0.37	26.35	3.38	6.99	6.48	0.14	0.12
15 MGy GAMMA	26.40	3.37	15.70	15.50	0.36	26.33	3.38	7.30	6.79	0.14	0.12
45 MGy GAMMA	26.41	3.37	14.20	14.00	0.35	26.34	3.38	6.59	6.12	0.14	0.11
87 MGy GAMMA	26.42	3.37	14.10	14.00	0.33	26.35	3.38	6.32	5.86	0.13	0.11
ROOM TEMP NO IRR	26.42	3.37	13.80	13.70	0.37	26.35	3.38	6.65	6.15	0.14	0.12
ROOM TEMP IRR	26.41	3.37	15.10	14.90	0.36	26.35	3.38	7.02	6.48	0.15	0.13
1000 C NO IRR	26.42	3.37	13.10	12.90	0.35	26.34	3.38	6.29	5.77	0.15	0.12
1000 C IRR	26.42	3.37	13.90	13.80	0.34	26.36	3.38	6.33	5.87	0.14	0.11
PCEA AG											
Control	54.39	1.69	0.66	0.55	0.62	54.31	1.69	0.73	0.40	0.12	0.11
AFRRI 1	54.34	1.69	0.77	0.65	0.60	54.26	1.69	1.00	0.46		

Graphite	Obs. Max (2θ)	d (Obs. Max) (A°)	Max Int. (cps)	Net Hght (cps)	FW HM (2θ)	Grav. C. (2θ)	d (GC) (A°)	Raw Area (cps* 2θ)	Net Area (cps*2θ)	Left Int. (cps)	Rt. Int. (cps)
AFRRI 2	54.35	1.69	0.80	0.68	0.57	54.25	1.69	1.01	0.47		
RABBIT HTR	54.34	1.69	0.87	0.73	0.62	54.25	1.69	1.14	0.55		
15 MGy GAMMA	54.41	1.68	0.70	0.59	0.56	54.35	1.69	0.71	0.40	0.11	0.10
45 MGy GAMMA	54.43	1.68	0.89	0.77	0.56	54.34	1.69	0.87	0.52	0.12	0.11
87 MGy GAMMA	54.42	1.68	0.69	0.58	0.55	54.36	1.69	0.69	0.38	0.11	0.10
ROOM TEMP NO IRR	54.40	1.69	0.66	0.55	0.59	54.32	1.69	0.70	0.39	0.11	0.10
ROOM TEMP IRR	54.41	1.68	0.67	0.56	0.59	54.33	1.69	0.72	0.40	0.11	0.10
1000 C NO IRR	54.40	1.69	0.58	0.47	0.64	54.28	1.69	0.70	0.37	0.06	0.05
1000 C IRR	54.43	1.68	0.68	0.57	0.62	54.30	1.69	0.77	0.42	0.06	0.05
PCEA WG											
Control	54.41	1.68	0.69	0.58	0.60	54.33	1.69	0.75	0.41	0.12	0.10
AFRRI 1	54.40	1.69	0.89	0.76	0.60	54.26	1.69	1.10	0.55		
AFRRI 2	54.34	1.69	0.77	0.64	0.68	54.17	1.69	1.09	0.52		
RABBIT HTR	54.38	1.69	0.71	0.59	0.57	54.27	1.69	0.91	0.41		
15 MGy GAMMA	54.46	1.68	0.63	0.53	0.57	54.35	1.69	0.67	0.36	0.11	0.10
45 MGy GAMMA	54.43	1.68	0.72	0.62	0.55	54.36	1.69	0.71	0.40	0.11	0.10
87 MGy GAMMA	54.36	1.69	0.60	0.49	0.63	54.29	1.69	0.70	0.37	0.11	0.10
ROOM TEMP NO IRR	54.40	1.69	0.64	0.54	0.55	54.35	1.69	0.66	0.36	0.11	0.10
ROOM TEMP IRR	54.36	1.69	0.74	0.63	0.58	54.33	1.69	0.76	0.43	0.12	0.11
1000 C NO IRR	54.44	1.68	0.61	0.50	0.63	54.28	1.69	0.73	0.38	0.06	0.05
1000 C IRR	54.43	1.68	0.66	0.54	0.62	54.31	1.69	0.76	0.40	0.06	0.05
PPEA AG											
Control	54.44	1.68	0.63	0.50	0.72	54.27	1.69	0.81	0.42	0.13	0.12

Graphite	Obs. Max (2θ)	d (Obs. Max) (A°)	Max Int. (cps)	Net Hght (cps)	FW HM (2θ)	Grav. C. (2θ)	d (GC) (A°)	Raw Area (cps* 2θ)	Net Area (cps*2θ)	Left Int. (cps)	Rt. Int. (cps)
AFRRI 1	54.33	1.69	0.79	0.65	0.68	54.17	1.69	1.13	0.55		
AFRRI 2	54.34	1.69	0.80	0.67	0.68	54.18	1.69	1.14	0.55		
RABBIT HTR	54.37	1.69	0.74	0.61	0.67	54.20	1.69	1.05	0.51		
15 MGy GAMMA	54.41	1.68	0.62	0.50	0.66	54.28	1.69	0.76	0.40	0.12	0.11
45 MGy GAMMA	54.44	1.68	0.56	0.44	0.70	54.25	1.69	0.70	0.35	0.12	0.10
87 MGy GAMMA	54.42	1.68	0.68	0.58	0.55	54.36	1.69	0.67	0.37	0.11	0.09
ROOM TEMP NO IRR	54.41	1.68	0.59	0.48	0.68	54.29	1.69	0.72	0.38	0.12	0.10
ROOM TEMP IRR	54.38	1.69	0.63	0.50	0.70	54.26	1.69	0.79	0.41	0.13	0.11
1000 C NO IRR	54.43	1.68	0.79	0.70	0.53	54.36	1.69	0.75	0.45	0.05	0.05
1000 C IRR	54.39	1.69	0.76	0.65	0.57	54.32	1.69	0.77	0.44	0.06	0.05
PPEA WG											
Control	54.44	1.68	0.56	0.44	0.71	54.25	1.69	0.73	0.37	0.13	0.11
AFRRI 1	54.38	1.69	0.78	0.66	0.64	54.23	1.69	1.07	0.53		
AFRRI 2	54.36	1.69	0.84	0.72	0.58	54.26	1.69	1.03	0.51		
RABBIT HTR	54.35	1.69	0.74	0.61	0.71	54.19	1.69	1.10	0.52		
15 MGy GAMMA	54.40	1.69	0.58	0.47	0.65	54.28	1.69	0.69	0.36	0.11	0.10
45 MGy GAMMA	54.44	1.68	0.55	0.44	0.68	54.27	1.69	0.69	0.35	0.12	0.10
87 MGy GAMMA	54.42	1.68	0.61	0.51	0.61	54.34	1.69	0.67	0.36	0.11	0.10
ROOM TEMP NO IRR	54.48	1.68	0.65	0.53	0.66	54.29	1.69	0.79	0.41	0.13	0.11
ROOM TEMP IRR	54.39	1.69	0.56	0.45	0.68	54.26	1.69	0.70	0.35	0.12	0.10
1000 C NO IRR	54.42	1.68	0.77	0.66	0.57	54.34	1.69	0.76	0.44	0.06	0.05
1000 C IRR	54.42	1.68	0.61	0.51	0.55	54.36	1.69	0.64	0.34	0.05	0.05
PCIB AG											

Graphite	Obs. Max (2θ)	d (Obs. Max) (A°)	Max Int. (cps)	Net Hght (cps)	FW HM (2θ)	Grav. C. (2θ)	d (GC) (A°)	Raw Area (cps* 2θ)	Net Area (cps*2θ)	Left Int. (cps)	Rt. Int. (cps)
Control	54.40	1.69	0.63	0.51	0.71	54.27	1.69	0.77	0.41	0.12	0.11
AFRRI 1	54.31	1.69	0.69	0.57	0.66	54.22	1.69	0.97	0.45		
AFRRI 2	54.30	1.69	0.74	0.61	0.70	54.19	1.69	1.05	0.49		
RABBIT HTR	54.32	1.69	0.74	0.61	0.67	54.21	1.69	1.03	0.50		
15 MGy GAMMA	54.38	1.69	0.59	0.48	0.68	54.29	1.69	0.70	0.37	0.11	0.10
45 MGy GAMMA	54.42	1.68	0.59	0.48	0.70	54.26	1.69	0.74	0.39	0.12	0.11
87 MGy GAMMA	54.37	1.69	0.59	0.48	0.65	54.28	1.69	0.69	0.36	0.12	0.10
ROOM TEMP NO IRR	54.37	1.69	0.60	0.49	0.66	54.27	1.69	0.71	0.37	0.11	0.10
ROOM TEMP IRR	54.36	1.69	0.66	0.54	0.65	54.29	1.69	0.78	0.41	0.13	0.12
1000 C NO IRR	54.37	1.69	0.58	0.48	0.65	54.29	1.69	0.68	0.36	0.12	0.11
1000 C IRR	54.35	1.69	0.60	0.48	0.66	54.27	1.69	0.72	0.38	0.11	0.10
PCIB WG											
Control	54.37	1.69	0.62	0.50	0.70	54.28	1.69	0.76	0.41	0.12	0.11
AFRRI 1	54.30	1.69	0.78	0.64	0.67	54.20	1.69	1.10	0.52		
AFRRI 2	54.36	1.69	0.74	0.61	0.69	54.19	1.69	1.07	0.50		
RABBIT HTR	54.33	1.69	0.72	0.60	0.66	54.22	1.69	1.01	0.48		
15 MGy GAMMA	54.37	1.69	0.68	0.57	0.67	54.28	1.69	0.79	0.44	0.12	0.11
45 MGy GAMMA	54.42	1.68	0.58	0.48	0.64	54.30	1.69	0.68	0.36	0.11	0.10
87 MGy GAMMA	54.37	1.69	0.60	0.49	0.65	54.28	1.69	0.71	0.38	0.11	0.10
ROOM TEMP NO IRR	54.36	1.69	0.60	0.49	0.68	54.27	1.69	0.73	0.39	0.12	0.11
ROOM TEMP IRR	54.38	1.69	0.66	0.55	0.68	54.28	1.69	0.78	0.42	0.12	0.11
1000 C NO IRR	54.37	1.69	0.58	0.47	0.65	54.29	1.69	0.67	0.35	0.12	0.10
1000 C IRR	54.37	1.69	0.65	0.54	0.68	54.28	1.69	0.75	0.41	0.11	0.10

Graphite	Obs. Max (2θ)	d (Obs. Max) (A°)	Max Int. (cps)	Net Hght (cps)	FW HM (2θ)	Grav. C. (2θ)	d (GC) (A°)	Raw Area (cps* 2θ)	Net Area (cps*2θ)	Left Int. (cps)	Rt. Int. (cps)
2020 AG											
Control	54.50	1.68	0.49	0.36	0.76	54.23	1.69	0.73	0.33	0.13	0.11
15 MGy GAMMA	54.41	1.68	0.50	0.37	0.73	54.24	1.69	0.72	0.32	0.13	0.12
45 MGy GAMMA	54.43	1.68	0.50	0.38	0.59	54.26	1.69	0.64	0.30	0.12	0.10
87 MGy GAMMA	54.48	1.68	0.47	0.36	0.65	54.26	1.69	0.64	0.29	0.12	0.10
ROOM TEMP NO IRR	54.44	1.68	0.53	0.39	0.71	54.21	1.69	0.76	0.33	0.14	0.13
ROOM TEMP IRR	54.44	1.68	0.51	0.38	0.72	54.24	1.69	0.70	0.31	0.12	0.11
1000 C NO IRR	54.44	1.68	0.52	0.40	0.62	54.27	1.69	0.66	0.31	0.12	0.10
1000 C IRR	54.43	1.68	0.51	0.39	0.63	54.25	1.69	0.67	0.30	0.12	0.10
2020 WG											
Control	54.50	1.68	0.55	0.42	0.75	54.26	1.69	0.77	0.37	0.13	0.11
15 MGy GAMMA	54.44	1.68	0.52	0.40	0.71	54.27	1.69	0.70	0.32	0.12	0.11
45 MGy GAMMA	54.48	1.68	0.54	0.42	0.67	54.26	1.69	0.71	0.34	0.12	0.11
87 MGy GAMMA	54.45	1.68	0.59	0.48	0.61	54.27	1.69	0.72	0.36	0.12	0.10
ROOM TEMP NO IRR	54.43	1.68	0.44	0.32	0.65	54.23	1.69	0.63	0.26	0.12	0.10
ROOM TEMP IRR	54.50	1.68	0.53	0.41	0.68	54.26	1.69	0.72	0.34	0.13	0.11
1000 C NO IRR	54.43	1.68	0.48	0.36	0.69	54.24	1.69	0.67	0.30	0.12	0.10
1000 C IRR	54.50	1.68	0.51	0.39	0.64	54.27	1.69	0.68	0.31	0.12	0.10
IG-110 AG											
Control	54.46	1.68	0.57	0.45	0.72	54.31	1.69	0.70	0.36	0.12	0.10
15 MGy GAMMA	54.46	1.68	0.60	0.49	0.68	54.31	1.69	0.72	0.38	0.12	0.10
45 MGy GAMMA	54.41	1.68	0.62	0.52	0.62	54.32	1.69	0.70	0.38	0.11	0.10

Graphite	Obs. Max (2θ)	d (Obs. Max) (A°)	Max Int. (cps)	Net Hght (cps)	FW HM (2θ)	Grav. C. (2θ)	d (GC) (A°)	Raw Area (cps* 2θ)	Net Area (cps*2θ)	Left Int. (cps)	Rt. Int. (cps)
87 MGy GAMMA	54.44	1.68	0.48	0.36	0.64	54.25	1.69	0.64	0.29	0.12	0.10
ROOM TEMP NO IRR	54.46	1.68	0.63	0.53	0.64	54.33	1.69	0.71	0.39	0.11	0.10
ROOM TEMP IRR	54.40	1.69	0.60	0.49	0.71	54.30	1.69	0.74	0.39	0.12	0.11
1000 C NO IRR	54.40	1.69	0.53	0.43	0.63	54.32	1.69	0.61	0.32	0.10	0.09
1000 C IRR	54.42	1.68	0.69	0.58	0.62	54.34	1.69	0.76	0.43	0.12	0.10
IG-110 WG											
Control	54.41	1.69	0.64	0.53	0.68	54.31	1.69	0.77	0.42	0.12	0.11
15 MGy GAMMA	54.43	1.68	0.71	0.60	0.63	54.33	1.69	0.78	0.45	0.11	0.10
45 MGy GAMMA	54.48	1.68	0.63	0.52	0.64	54.34	1.69	0.71	0.39	0.11	0.10
87 MGy GAMMA	54.42	1.68	0.63	0.52	0.61	54.34	1.69	0.68	0.37	0.11	0.10
ROOM TEMP NO IRR	54.43	1.68	0.60	0.49	0.65	54.33	1.69	0.70	0.37	0.11	0.10
ROOM TEMP IRR	54.39	1.69	0.65	0.53	0.67	54.31	1.69	0.77	0.41	0.13	0.11
1000 C NO IRR	54.42	1.68	0.60	0.50	0.62	54.34	1.69	0.66	0.36	0.11	0.10
1000 C IRR	54.43	1.68	0.62	0.52	0.64	54.34	1.69	0.69	0.38	0.11	0.10
PCEA AG											
Control	59.14	1.56	0.16	0.05	2.71	59.69	1.55	0.66	0.15		
AFRRI 1	59.32	1.56	0.16	0.06	2.79	59.55	1.55	0.83	0.18		
AFRRI 2	59.60	1.55	0.17	0.07	2.69	59.57	1.55	0.84	0.20		
RABBIT HTR	59.86	1.54	0.19	0.07	2.63	59.62	1.55	0.93	0.20		
15 MGy GAMMA	59.86	1.54	0.15	0.06	2.33	59.73	1.55	0.61	0.14		
45 MGy GAMMA	59.86	1.54	0.17	0.07	2.19	59.71	1.55	0.68	0.16		
87 MGy GAMMA	59.88	1.54	0.16	0.06	2.17	59.69	1.55	0.62	0.14		
ROOM TEMP	59.88	1.54	0.15	0.06	2.26	59.74	1.55	0.63	0.15		

Graphite	Obs. Max (2θ)	d (Obs. Max) (A°)	Max Int. (cps)	Net Hght (cps)	FW HM (2θ)	Grav. C. (2θ)	d (GC) (A°)	Raw Area (cps* 2θ)	Net Area (cps*2θ)	Left Int. (cps)	Rt. Int. (cps)
NO IRR											
ROOM TEMP IRR	59.58	1.55	0.16	0.06	2.14	59.72	1.55	0.63	0.14		
1000 C NO IRR	59.88	1.54	0.15	0.05	2.30	59.77	1.55	0.61	0.12		
1000 C IRR	59.60	1.55	0.15	0.05	2.15	59.67	1.55	0.62	0.13		
PCEA WG											
Control	59.62	1.55	0.17	0.07	2.25	59.72	1.55	0.67	0.16		
AFRRI 1	59.84	1.54	0.18	0.07	2.77	59.61	1.55	0.89	0.21		
AFRRI 2	59.60	1.55	0.16	0.06	2.63	59.59	1.55	0.84	0.15		
RABBIT HTR	59.86	1.54	0.16	0.06	2.64	59.62	1.55	0.79	0.17		
15 MGy GAMMA	59.86	1.54	0.16	0.06	2.18	59.70	1.55	0.62	0.14		
45 MGy GAMMA	59.64	1.55	0.15	0.06	1.89	59.75	1.55	0.62	0.12		
87 MGy GAMMA	59.80	1.55	0.14	0.05	2.11	59.68	1.55	0.59	0.11		
ROOM TEMP NO IRR	59.58	1.55	0.15	0.06	2.18	59.68	1.55	0.61	0.13		
ROOM TEMP IRR	59.86	1.54	0.17	0.07	2.28	59.71	1.55	0.67	0.16		
1000 C NO IRR	59.88	1.54	0.15	0.05	2.17	59.68	1.55	0.61	0.12		
1000 C IRR	59.86	1.54	0.15	0.05	2.31	59.71	1.55	0.63	0.13		
PPEA AG											
Control	59.66	1.55	0.16	0.05	2.03	59.74	1.55	0.66	0.12		
AFRRI 1	59.60	1.55	0.17	0.06	2.55	59.58	1.55	0.88	0.16		
AFRRI 2	59.36	1.56	0.17	0.06	2.81	59.58	1.55	0.86	0.16		
RABBIT HTR	59.88	1.54	0.16	0.05	2.63	59.66	1.55	0.80	0.14		
15 MGy GAMMA	59.84	1.54	0.15	0.05	2.26	59.79	1.55	0.63	0.13		
45 MGy GAMMA	59.60	1.55	0.15	0.05	2.29	59.69	1.55	0.61	0.11		
87 MGy GAMMA	59.86	1.54	0.15	0.06	2.13	59.69	1.55	0.60	0.15		

Graphite	Obs. Max (2θ)	d (Obs. Max) (A°)	Max Int. (cps)	Net Hght (cps)	FW HM (2θ)	Grav. C. (2θ)	d (GC) (A°)	Raw Area (cps* 2θ)	Net Area (cps*2θ)	Left Int. (cps)	Rt. Int. (cps)
ROOM TEMP NO IRR	59.68	1.55	0.15	0.05	1.98	59.76	1.55	0.60	0.12		
ROOM TEMP IRR	59.58	1.55	0.16	0.05	2.34	59.68	1.55	0.66	0.13		
1000 C NO IRR	59.86	1.54	0.16	0.07	2.10	59.69	1.55	0.61	0.15		
1000 C IRR	59.65	1.55	0.17	0.07	2.26	59.66	1.55	0.67	0.16		
PPEA WG											
Control	59.86	1.54	0.15	0.05	2.14	59.73	1.55	0.65	0.12		
AFRRI 1	59.60	1.55	0.16	0.06	2.77	59.58	1.55	0.80	0.16		
AFRRI 2	59.88	1.54	0.17	0.07	2.61	59.62	1.55	0.84	0.19		
RABBIT HTR	60.02	1.54	0.16	0.05	2.82	59.60	1.55	0.84	0.15		
15 MGy GAMMA	59.86	1.54	0.14	0.05	2.15	59.71	1.55	0.59	0.11		
45 MGy GAMMA	59.66	1.55	0.15	0.05	2.20	59.63	1.55	0.61	0.12		
87 MGy GAMMA	59.58	1.55	0.16	0.07	2.05	59.73	1.55	0.60	0.15		
ROOM TEMP NO IRR	59.86	1.54	0.17	0.06	2.14	59.74	1.55	0.68	0.14		
ROOM TEMP IRR	59.74	1.55	0.15	0.05	2.23	59.66	1.55	0.61	0.11		
1000 C NO IRR	59.86	1.54	0.16	0.06	2.19	59.70	1.55	0.65	0.14		
1000 C IRR	59.74	1.55	0.15	0.06	2.19	59.71	1.55	0.59	0.14		
PCIB AG											
Control	59.86	1.54	0.16	0.06	2.39	59.73	1.55	0.66	0.14		
AFRRI 1	59.60	1.55	0.15	0.05	2.67	59.56	1.55	0.79	0.14		
AFRRI 2	59.60	1.55	0.17	0.06	2.65	59.50	1.55	0.84	0.17		
RABBIT HTR	59.66	1.55	0.16	0.06	2.96	59.56	1.55	0.83	0.16		
15 MGy GAMMA	59.90	1.54	0.15	0.05	2.01	59.68	1.55	0.60	0.11		
45 MGy GAMMA	59.58	1.55	0.15	0.05	2.39	59.74	1.55	0.64	0.13		
87 MGy	59.86	1.54	0.15	0.05	2.24	59.71	1.55	0.61	0.12		

Graphite	Obs. Max (2θ)	d (Obs. Max) (A°)	Max Int. (cps)	Net Hght (cps)	FW HM (2θ)	Grav. C. (2θ)	d (GC) (A°)	Raw Area (cps* 2θ)	Net Area (cps*2θ)	Left Int. (cps)	Rt. Int. (cps)
GAMMA											
ROOM TEMP NO IRR	59.78	1.55	0.15	0.05	2.15	59.73	1.55	0.62	0.11		
ROOM TEMP IRR	59.67	1.55	0.17	0.06	2.05	59.62	1.55	0.68	0.12		
1000 C NO IRR	59.86	1.54	0.14	0.05	2.09	59.73	1.55	0.60	0.11		
1000 C IRR	59.88	1.54	0.15	0.05	2.19	59.61	1.55	0.63	0.12		
PCIB WG											
Control	59.92	1.54	0.16	0.05	1.93	59.74	1.55	0.66	0.11		
AFRRI 1	59.78	1.55	0.17	0.06	2.58	59.45	1.55	0.88	0.17		
AFRRI 2	59.60	1.55	0.17	0.06	2.62	59.51	1.55	0.85	0.16		
RABBIT HTR	59.88	1.54	0.16	0.06	2.57	59.59	1.55	0.82	0.16		
15 MGy GAMMA	60.12	1.54	0.15	0.05	2.19	59.72	1.55	0.65	0.12		
45 MGy GAMMA	59.90	1.54	0.14	0.05	2.19	59.71	1.55	0.60	0.12		
87 MGy GAMMA	59.86	1.54	0.15	0.05	2.44	59.67	1.55	0.62	0.12		
ROOM TEMP NO IRR	60.14	1.54	0.15	0.05	2.51	59.67	1.55	0.64	0.12		
ROOM TEMP IRR	59.62	1.55	0.16	0.05	2.32	59.61	1.55	0.65	0.12		
1000 C NO IRR	59.59	1.55	0.14	0.05	2.23	59.76	1.55	0.59	0.11		
1000 C IRR	59.84	1.54	0.15	0.05	2.11	59.69	1.55	0.63	0.13		
2020 AG											
Control	59.88	1.54	0.16	0.05	1.91	59.68	1.55	0.64	0.11		
15 MGy GAMMA	59.86	1.54	0.15	0.05	1.91	59.69	1.55	0.63	0.10		
45 MGy GAMMA	59.60	1.55	0.14	0.05	1.79	59.81	1.55	0.57	0.09		
87 MGy GAMMA	59.86	1.54	0.14	0.05	2.00	59.72	1.55	0.57	0.10		
ROOM TEMP NO IRR	59.56	1.55	0.16	0.05	1.81	59.67	1.55	0.68	0.11		

Graphite	Obs. Max (2θ)	d (Obs. Max) (A°)	Max Int. (cps)	Net Hght (cps)	FW HM (2θ)	Grav. C. (2θ)	d (GC) (A°)	Raw Area (cps* 2θ)	Net Area (cps*2θ)	Left Int. (cps)	Rt. Int. (cps)
ROOM TEMP IRR	59.60	1.55	0.15	0.05	1.87	59.71	1.55	0.61	0.11		
1000 C NO IRR	59.86	1.54	0.14	0.05	1.89	59.70	1.55	0.58	0.11		
1000 C IRR	59.52	1.55	0.15	0.05	1.89	59.68	1.55	0.60	0.10		
2020 WG											
Control	59.86	1.54	0.16	0.05	2.12	59.75	1.55	0.64	0.11		
15 MGy GAMMA	59.67	1.55	0.15	0.05	1.91	59.70	1.55	0.60	0.09		
45 MGy GAMMA	59.86	1.54	0.14	0.05	2.10	59.64	1.55	0.60	0.11		
87 MGy GAMMA	59.90	1.54	0.14	0.05	1.92	59.69	1.55	0.58	0.10		
ROOM TEMP NO IRR	59.58	1.55	0.14	0.05	1.98	59.62	1.55	0.58	0.10		
ROOM TEMP IRR	59.71	1.55	0.15	0.05	1.90	59.70	1.55	0.60	0.12		
1000 C NO IRR	59.92	1.54	0.14	0.05	1.85	59.68	1.55	0.60	0.11		
1000 C IRR	59.86	1.54	0.14	0.05	1.79	59.69	1.55	0.58	0.09		
IG-110 AG											
Control	59.86	1.54	0.17	0.07	1.84	59.67	1.55	0.64	0.14		
15 MGy GAMMA	59.64	1.55	0.16	0.06	2.01	59.68	1.55	0.64	0.13		
45 MGy GAMMA	59.88	1.54	0.16	0.06	1.68	59.74	1.55	0.62	0.13		
87 MGy GAMMA	59.86	1.54	0.14	0.05	1.76	59.74	1.55	0.57	0.10		
ROOM TEMP NO IRR	59.70	1.55	0.16	0.07	1.77	59.74	1.55	0.62	0.14		
ROOM TEMP IRR	59.86	1.54	0.17	0.07	1.88	59.76	1.55	0.66	0.13		
1000 C NO IRR	59.86	1.54	0.15	0.06	1.64	59.74	1.55	0.57	0.12		
1000 C IRR	59.64	1.55	0.17	0.07	1.72	59.75	1.55	0.63	0.14		
IG-110 WG											

Graphite	Obs. Max (2θ)	d (Obs. Max) (A°)	Max Int. (cps)	Net Hght (cps)	FW HM (2θ)	Grav. C. (2θ)	d (GC) (A°)	Raw Area (cps* 2θ)	Net Area (cps*2θ)	Left Int. (cps)	Rt. Int. (cps)
Control	59.88	1.54	0.17	0.07	1.72	59.72	1.55	0.67	0.15		
15 MGy GAMMA	59.68	1.55	0.17	0.07	1.86	59.72	1.55	0.64	0.15		
45 MGy GAMMA	59.84	1.54	0.16	0.07	1.77	59.73	1.55	0.62	0.13		
87 MGy GAMMA	59.60	1.55	0.16	0.07	1.79	59.72	1.55	0.60	0.14		
ROOM TEMP NO IRR	59.64	1.55	0.16	0.06	1.76	59.73	1.55	0.62	0.13		
ROOM TEMP IRR	59.88	1.54	0.17	0.07	1.84	59.65	1.55	0.69	0.15		
1000 C NO IRR	59.73	1.55	0.16	0.06	1.79	59.66	1.55	0.59	0.13		
1000 C IRR	59.86	1.54	0.16	0.07	1.63	59.70	1.55	0.61	0.14		
PCEA AG											
Control	77.44	1.23	0.71	0.63	0.47	77.45	1.23	0.52	0.34	0.07	0.08
AFRRI 1	77.43	1.23	0.78	0.70	0.46	77.51	1.23	0.65	0.38		
AFRRI 2	77.43	1.23	0.77	0.69	0.46	77.50	1.23	0.64	0.37		
RABBIT HTR	77.42	1.23	0.82	0.74	0.48	77.50	1.23	0.70	0.41		
15 MGy GAMMA	77.44	1.23	0.65	0.57	0.47	77.47	1.23	0.46	0.30	0.06	0.08
45 MGy GAMMA	77.42	1.23	0.59	0.51	0.48	77.45	1.23	0.43	0.28	0.07	0.08
87 MGy GAMMA	77.44	1.23	0.70	0.62	0.45	77.47	1.23	0.48	0.32	0.07	0.08
ROOM TEMP NO IRR	77.40	1.23	0.64	0.56	0.47	77.48	1.23	0.46	0.30	0.07	0.08
ROOM TEMP IRR	77.43	1.23	0.68	0.60	0.46	77.46	1.23	0.47	0.31	0.07	0.08
1000 C NO IRR	77.44	1.23	0.62	0.54	0.48	77.49	1.23	0.46	0.29	0.03	0.04
1000 C IRR	77.43	1.23	0.61	0.53	0.48	77.48	1.23	0.45	0.29	0.03	0.04
PCEA WG											
Control	77.40	1.23	0.69	0.61	0.47	77.47	1.23	0.50	0.33	0.07	0.08
AFRRI 1	77.43	1.23	0.81	0.72	0.46	77.50	1.23	0.67	0.38		

Graphite	Obs. Max (2θ)	d (Obs. Max) (A°)	Max Int. (cps)	Net Hght (cps)	FW HM (2θ)	Grav. C. (2θ)	d (GC) (A°)	Raw Area (cps* 2θ)	Net Area (cps*2θ)	Left Int. (cps)	Rt. Int. (cps)
AFRRI 2	77.45	1.23	0.69	0.61	0.47	77.55	1.23	0.63	0.35		
RABBIT HTR	77.42	1.23	0.83	0.75	0.46	77.50	1.23	0.66	0.40		
15 MGy GAMMA	77.40	1.23	0.69	0.61	0.47	77.48	1.23	0.48	0.32	0.07	0.08
45 MGy GAMMA	77.40	1.23	0.65	0.57	0.48	77.48	1.23	0.45	0.30	0.06	0.08
87 MGy GAMMA	77.42	1.23	0.62	0.54	0.47	77.48	1.23	0.45	0.29	0.07	0.09
ROOM TEMP NO IRR	77.44	1.23	0.64	0.56	0.46	77.47	1.23	0.45	0.29	0.07	0.08
ROOM TEMP IRR	77.42	1.23	0.69	0.61	0.45	77.46	1.23	0.47	0.31	0.07	0.08
1000 C NO IRR	77.43	1.23	0.59	0.51	0.49	77.48	1.23	0.45	0.28	0.03	0.04
1000 C IRR	77.44	1.23	0.60	0.51	0.48	77.49	1.23	0.45	0.28	0.03	0.04
PPEA AG											
Control	77.45	1.23	0.62	0.53	0.49	77.48	1.23	0.49	0.30	0.07	0.10
AFRRI 1	77.41	1.23	0.76	0.67	0.48	77.51	1.23	0.68	0.38		
AFRRI 2	77.44	1.23	0.68	0.59	0.48	77.53	1.23	0.64	0.34		
RABBIT HTR	77.44	1.23	0.67	0.59	0.48	77.54	1.23	0.62	0.34		
15 MGy GAMMA	77.45	1.23	0.60	0.52	0.49	77.48	1.23	0.46	0.29	0.07	0.09
45 MGy GAMMA	77.44	1.23	0.63	0.55	0.48	77.48	1.23	0.47	0.30	0.07	0.09
87 MGy GAMMA	77.42	1.23	0.63	0.56	0.48	77.45	1.23	0.44	0.30	0.06	0.08
ROOM TEMP NO IRR	77.44	1.23	0.61	0.52	0.48	77.49	1.23	0.45	0.29	0.07	0.09
ROOM TEMP IRR	77.44	1.23	0.60	0.51	0.50	77.47	1.23	0.48	0.29	0.07	0.09
1000 C NO IRR	77.38	1.23	0.59	0.52	0.47	77.42	1.23	0.41	0.27	0.03	0.03
1000 C IRR	77.39	1.23	0.64	0.57	0.48	77.41	1.23	0.46	0.30	0.03	0.04
PPEA WG											
Control	77.44	1.23	0.67	0.58	0.48	77.47	1.23	0.50	0.32	0.07	0.09

Graphite	Obs. Max (2θ)	d (Obs. Max) (A°)	Max Int. (cps)	Net Hght (cps)	FW HM (2θ)	Grav. C. (2θ)	d (GC) (A°)	Raw Area (cps* 2θ)	Net Area (cps*2θ)	Left Int. (cps)	Rt. Int. (cps)
AFRRI 1	77.44	1.23	0.65	0.57	0.48	77.54	1.23	0.60	0.33		
AFRRI 2	77.44	1.23	0.72	0.64	0.45	77.51	1.23	0.61	0.34		
RABBIT HTR	77.43	1.23	0.71	0.62	0.48	77.53	1.23	0.65	0.36		
15 MGy GAMMA	77.44	1.23	0.60	0.52	0.47	77.48	1.23	0.45	0.28	0.06	0.08
45 MGy GAMMA	77.44	1.23	0.61	0.53	0.48	77.48	1.23	0.45	0.29	0.07	0.09
87 MGy GAMMA	77.42	1.23	0.65	0.58	0.47	77.46	1.23	0.46	0.31	0.06	0.08
ROOM TEMP NO IRR	77.43	1.23	0.65	0.56	0.48	77.47	1.23	0.49	0.30	0.08	0.09
ROOM TEMP IRR	77.44	1.23	0.63	0.55	0.47	77.48	1.23	0.47	0.30	0.06	0.09
1000 C NO IRR	77.41	1.23	0.67	0.59	0.46	77.45	1.23	0.47	0.31	0.03	0.04
1000 C IRR	77.42	1.23	0.65	0.57	0.47	77.45	1.23	0.45	0.30	0.03	0.04
PCIB AG											
Control	77.45	1.23	0.64	0.55	0.50	77.47	1.23	0.49	0.32	0.07	0.09
AFRRI 1	77.44	1.23	0.72	0.64	0.47	77.52	1.23	0.63	0.36		
AFRRI 2	77.45	1.23	0.73	0.65	0.48	77.53	1.23	0.65	0.37		
RABBIT HTR	77.43	1.23	0.74	0.66	0.47	77.52	1.23	0.65	0.37		
15 MGy GAMMA	77.40	1.23	0.63	0.55	0.49	77.49	1.23	0.47	0.30	0.06	0.08
45 MGy GAMMA	77.42	1.23	0.66	0.58	0.48	77.46	1.23	0.48	0.31	0.07	0.08
87 MGy GAMMA	77.43	1.23	0.63	0.55	0.47	77.47	1.23	0.46	0.30	0.06	0.08
ROOM TEMP NO IRR	77.43	1.23	0.64	0.56	0.48	77.47	1.23	0.47	0.30	0.07	0.08
ROOM TEMP IRR	77.40	1.23	0.70	0.60	0.50	77.48	1.23	0.53	0.34	0.08	0.10
1000 C NO IRR	77.43	1.23	0.65	0.57	0.48	77.48	1.23	0.47	0.31	0.07	0.08
1000 C IRR	77.43	1.23	0.64	0.56	0.48	77.46	1.23	0.47	0.31	0.07	0.08
PCIB WG											

Graphite	Obs. Max (2θ)	d (Obs. Max) (A°)	Max Int. (cps)	Net Hght (cps)	FW HM (2θ)	Grav. C. (2θ)	d (GC) (A°)	Raw Area (cps* 2θ)	Net Area (cps*2θ)	Left Int. (cps)	Rt. Int. (cps)
Control	77.46	1.23	0.66	0.57	0.49	77.48	1.23	0.49	0.32	0.07	0.09
AFRRI 1	77.44	1.23	0.77	0.69	0.48	77.52	1.23	0.68	0.38		
AFRRI 2	77.45	1.23	0.73	0.65	0.47	77.53	1.23	0.65	0.36		
RABBIT HTR	77.44	1.23	0.74	0.66	0.47	77.52	1.23	0.64	0.37		
15 MGy GAMMA	77.44	1.23	0.62	0.53	0.48	77.47	1.23	0.46	0.29	0.07	0.08
45 MGy GAMMA	77.44	1.23	0.66	0.58	0.48	77.47	1.23	0.48	0.31	0.06	0.08
87 MGy GAMMA	77.44	1.23	0.64	0.56	0.48	77.48	1.23	0.47	0.30	0.07	0.08
ROOM TEMP NO IRR	77.44	1.23	0.66	0.58	0.47	77.48	1.23	0.48	0.31	0.07	0.08
ROOM TEMP IRR	77.44	1.23	0.62	0.54	0.48	77.47	1.23	0.46	0.30	0.07	0.08
1000 C NO IRR	77.43	1.23	0.63	0.55	0.48	77.47	1.23	0.46	0.30	0.07	0.08
1000 C IRR	77.43	1.23	0.63	0.55	0.47	77.47	1.23	0.46	0.30	0.07	0.08
2020 AG											
Control	77.46	1.23	0.57	0.48	0.51	77.50	1.23	0.48	0.29	0.07	0.10
15 MGy GAMMA	77.40	1.23	0.56	0.47	0.52	77.48	1.23	0.47	0.28	0.07	0.10
45 MGy GAMMA	77.43	1.23	0.55	0.47	0.49	77.49	1.23	0.44	0.26	0.07	0.09
87 MGy GAMMA	77.44	1.23	0.56	0.48	0.50	77.50	1.23	0.45	0.27	0.07	0.09
ROOM TEMP NO IRR	77.41	1.23	0.58	0.47	0.52	77.46	1.23	0.50	0.29	0.08	0.11
ROOM TEMP IRR	77.44	1.23	0.57	0.48	0.49	77.50	1.23	0.46	0.27	0.07	0.10
1000 C NO IRR	77.40	1.23	0.54	0.46	0.50	77.50	1.23	0.44	0.26	0.06	0.09
1000 C IRR	77.41	1.23	0.56	0.47	0.50	77.48	1.23	0.45	0.27	0.07	0.10
2020 WG											
Control	77.47	1.23	0.55	0.45	0.52	77.50	1.23	0.46	0.27	0.07	0.10
15 MGy GAMMA	77.40	1.23	0.55	0.46	0.51	77.49	1.23	0.45	0.27	0.07	0.10

Graphite	Obs. Max (2θ)	d (Obs. Max) (A°)	Max Int. (cps)	Net Hght (cps)	FW HM (2θ)	Grav. C. (2θ)	d (GC) (A°)	Raw Area (cps* 2θ)	Net Area (cps*2θ)	Left Int. (cps)	Rt. Int. (cps)
45 MGy GAMMA	77.44	1.23	0.53	0.44	0.50	77.49	1.23	0.44	0.26	0.07	0.09
87 MGy GAMMA	77.42	1.23	0.52	0.44	0.50	77.48	1.23	0.43	0.25	0.07	0.09
ROOM TEMP NO IRR	77.40	1.23	0.53	0.44	0.51	77.50	1.23	0.44	0.26	0.07	0.09
ROOM TEMP IRR	77.45	1.23	0.55	0.46	0.51	77.50	1.23	0.45	0.26	0.07	0.10
1000 C NO IRR	77.44	1.23	0.56	0.47	0.50	77.49	1.23	0.45	0.27	0.07	0.10
1000 C IRR	77.44	1.23	0.56	0.47	0.50	77.49	1.23	0.46	0.27	0.07	0.09
IG-110 AG											
Control	77.45	1.23	0.70	0.61	0.48	77.48	1.23	0.49	0.33	0.07	0.08
15 MGy GAMMA	77.43	1.23	0.67	0.59	0.47	77.47	1.23	0.48	0.32	0.07	0.08
45 MGy GAMMA	77.43	1.23	0.65	0.57	0.46	77.47	1.23	0.46	0.30	0.06	0.08
87 MGy GAMMA	77.43	1.23	0.56	0.47	0.50	77.50	1.23	0.45	0.27	0.07	0.09
ROOM TEMP NO IRR	77.44	1.23	0.66	0.58	0.47	77.47	1.23	0.47	0.31	0.07	0.08
ROOM TEMP IRR	77.43	1.23	0.68	0.60	0.47	77.46	1.23	0.49	0.32	0.07	0.08
1000 C NO IRR	77.41	1.23	0.64	0.57	0.47	77.45	1.23	0.45	0.30	0.06	0.07
1000 C IRR	77.41	1.23	0.62	0.55	0.46	77.46	1.23	0.45	0.29	0.07	0.08
IG-110 WG											
Control	77.40	1.23	0.67	0.59	0.48	77.46	1.23	0.49	0.33	0.07	0.08
15 MGy GAMMA	77.43	1.23	0.63	0.55	0.46	77.46	1.23	0.45	0.29	0.07	0.08
45 MGy GAMMA	77.43	1.23	0.65	0.57	0.47	77.47	1.23	0.46	0.30	0.07	0.08
87 MGy GAMMA	77.43	1.23	0.65	0.57	0.47	77.47	1.23	0.46	0.30	0.06	0.08
ROOM TEMP NO IRR	77.40	1.23	0.66	0.58	0.47	77.49	1.23	0.47	0.31	0.06	0.08
ROOM TEMP	77.43	1.23	0.74	0.65	0.49	77.45	1.23	0.54	0.36	0.07	0.09

Graphite	Obs. Max (2θ)	d (Obs. Max) (A°)	Max Int. (cps)	Net Hght (cps)	FW HM (2θ)	Grav. C. (2θ)	d (GC) (A°)	Raw Area (cps* 2θ)	Net Area (cps*2θ)	Left Int. (cps)	Rt. Int. (cps)
IRR											
1000 C NO IRR	77.42	1.23	0.65	0.57	0.46	77.46	1.23	0.46	0.30	0.06	0.08
1000 C IRR	77.43	1.23	0.63	0.56	0.48	77.47	1.23	0.45	0.30	0.06	0.08
PCEA AG											
Control	83.40	1.16	0.36	0.25	1.28	83.53	1.16	0.74	0.35		
AFRRI 1	83.58	1.16	0.39	0.28	1.37	83.46	1.16	0.95	0.42		
AFRRI 2	83.56	1.16	0.39	0.28	1.34	83.47	1.16	0.94	0.44		
RABBIT HTR	83.40	1.16	0.43	0.31	1.34	83.47	1.16	1.03	0.47		
15 MGy GAMMA	83.44	1.16	0.32	0.23	1.26	83.53	1.16	0.68	0.32		
45 MGy GAMMA	83.42	1.16	0.32	0.21	1.26	83.52	1.16	0.68	0.30		
87 MGy GAMMA	83.40	1.16	0.34	0.24	1.26	83.54	1.16	0.71	0.34		
ROOM TEMP NO IRR	83.44	1.16	0.32	0.22	1.32	83.53	1.16	0.68	0.31		
ROOM TEMP IRR	83.40	1.16	0.33	0.23	1.26	83.54	1.16	0.69	0.32		
1000 C NO IRR	83.42	1.16	0.31	0.20	1.23	83.53	1.16	0.67	0.28		
1000 C IRR	83.44	1.16	0.31	0.20	1.22	83.53	1.16	0.67	0.28		
PCEA WG											
Control	83.46	1.16	0.35	0.25	1.27	83.53	1.16	0.71	0.35		
AFRRI 1	83.38	1.16	0.41	0.29	1.32	83.47	1.16	0.98	0.44		
AFRRI 2	83.53	1.16	0.35	0.23	1.34	83.46	1.16	0.92	0.36		
RABBIT HTR	83.56	1.16	0.42	0.31	1.19	83.46	1.16	0.96	0.46		
15 MGy GAMMA	83.48	1.16	0.36	0.26	1.16	83.54	1.16	0.70	0.34		
45 MGy GAMMA	83.60	1.16	0.34	0.24	1.20	83.54	1.16	0.69	0.33		
87 MGy GAMMA	83.40	1.16	0.30	0.19	1.27	83.52	1.16	0.66	0.27		
ROOM TEMP NO IRR	83.44	1.16	0.32	0.22	1.24	83.53	1.16	0.66	0.31		

Graphite	Obs. Max (2θ)	d (Obs. Max) (A°)	Max Int. (cps)	Net Hght (cps)	FW HM (2θ)	Grav. C. (2θ)	d (GC) (A°)	Raw Area (cps* 2θ)	Net Area (cps*2θ)	Left Int. (cps)	Rt. Int. (cps)
ROOM TEMP IRR	83.42	1.16	0.36	0.26	1.17	83.53	1.16	0.71	0.35		
1000 C NO IRR	83.53	1.16	0.30	0.19	1.25	83.52	1.16	0.66	0.26		
1000 C IRR	83.44	1.16	0.31	0.20	1.25	83.53	1.16	0.67	0.28		
PPEA AG											
Control	83.42	1.16	0.31	0.19	1.32	83.51	1.16	0.69	0.28		
AFRRI 1	83.56	1.16	0.38	0.26	1.29	83.45	1.16	0.97	0.39		
AFRRI 2	83.58	1.16	0.35	0.22	1.33	83.45	1.16	0.92	0.35		
RABBIT HTR	83.52	1.16	0.35	0.23	1.30	83.47	1.16	0.91	0.35		
15 MGy GAMMA	83.46	1.16	0.30	0.19	1.28	83.53	1.16	0.66	0.27		
45 MGy GAMMA	83.42	1.16	0.31	0.20	1.18	83.53	1.16	0.66	0.27		
87 MGy GAMMA	83.44	1.16	0.33	0.24	1.17	83.53	1.16	0.67	0.32		
ROOM TEMP NO IRR	83.44	1.16	0.29	0.19	1.25	83.54	1.16	0.65	0.27		
ROOM TEMP IRR	83.40	1.16	0.30	0.19	1.33	83.53	1.16	0.67	0.27		
1000 C NO IRR	83.42	1.16	0.34	0.25	1.08	83.51	1.16	0.64	0.31		
1000 C IRR	83.48	1.16	0.36	0.26	1.13	83.50	1.16	0.69	0.34		
PPEA WG											
Control	83.58	1.16	0.31	0.20	1.29	83.53	1.16	0.68	0.28		
AFRRI 1	83.53	1.16	0.34	0.22	1.34	83.46	1.16	0.88	0.34		
AFRRI 2	83.54	1.16	0.39	0.27	1.22	83.47	1.16	0.92	0.40		
RABBIT HTR	83.40	1.16	0.37	0.24	1.39	83.45	1.16	0.98	0.38		
15 MGy GAMMA	83.42	1.16	0.29	0.19	1.25	83.52	1.16	0.65	0.27		
45 MGy GAMMA	83.55	1.16	0.30	0.19	1.22	83.54	1.16	0.65	0.27		
87 MGy GAMMA	83.44	1.16	0.34	0.24	1.12	83.52	1.16	0.68	0.31		
ROOM TEMP	83.40	1.16	0.33	0.21	1.23	83.52	1.16	0.72	0.30		

Graphite	Obs. Max (2θ)	d (Obs. Max) (A°)	Max Int. (cps)	Net Hght (cps)	FW HM (2θ)	Grav. C. (2θ)	d (GC) (A°)	Raw Area (cps* 2θ)	Net Area (cps*2θ)	Left Int. (cps)	Rt. Int. (cps)
NO IRR											
ROOM TEMP IRR	83.42	1.16	0.30	0.19	1.25	83.52	1.16	0.66	0.27		
1000 C NO IRR	83.58	1.16	0.35	0.25	1.24	83.52	1.16	0.71	0.34		
1000 C IRR	83.44	1.16	0.33	0.23	1.24	83.52	1.16	0.67	0.32		
PCIB AG											
Control	83.56	1.16	0.32	0.21	1.31	83.52	1.16	0.70	0.30		
AFRRI 1	83.38	1.16	0.35	0.24	1.39	83.46	1.16	0.92	0.38		
AFRRI 2	83.40	1.16	0.36	0.24	1.41	83.46	1.16	0.95	0.40		
RABBIT HTR	83.52	1.16	0.37	0.25	1.35	83.44	1.16	0.95	0.40		
15 MGy GAMMA	83.58	1.16	0.31	0.20	1.33	83.52	1.16	0.67	0.28		
45 MGy GAMMA	83.44	1.16	0.31	0.21	1.28	83.50	1.16	0.68	0.29		
87 MGy GAMMA	83.58	1.16	0.31	0.20	1.35	83.52	1.16	0.66	0.29		
ROOM TEMP NO IRR	83.46	1.16	0.31	0.20	1.26	83.54	1.16	0.67	0.28		
ROOM TEMP IRR	83.44	1.16	0.37	0.24	1.35	83.50	1.16	0.80	0.35		
1000 C NO IRR	83.42	1.16	0.31	0.20	1.30	83.53	1.16	0.68	0.30		
1000 C IRR	83.46	1.16	0.32	0.21	1.25	83.51	1.16	0.68	0.29		
PCIB WG											
Control	83.60	1.16	0.32	0.21	1.28	83.53	1.16	0.69	0.29		
AFRRI 1	83.56	1.16	0.38	0.26	1.37	83.45	1.16	0.98	0.41		
AFRRI 2	83.58	1.16	0.36	0.24	1.39	83.45	1.16	0.94	0.39		
RABBIT HTR	83.56	1.16	0.37	0.25	1.35	83.45	1.16	0.94	0.40		
15 MGy GAMMA	83.46	1.16	0.31	0.20	1.24	83.52	1.16	0.67	0.29		
45 MGy GAMMA	83.42	1.16	0.32	0.21	1.32	83.51	1.16	0.69	0.31		
87 MGy GAMMA	83.46	1.16	0.31	0.20	1.28	83.52	1.16	0.67	0.29		

Graphite	Obs. Max (2θ)	d (Obs. Max) (A°)	Max Int. (cps)	Net Hght (cps)	FW HM (2θ)	Grav. C. (2θ)	d (GC) (A°)	Raw Area (cps* 2θ)	Net Area (cps*2θ)	Left Int. (cps)	Rt. Int. (cps)
ROOM TEMP NO IRR	83.58	1.16	0.32	0.21	1.27	83.53	1.16	0.68	0.30		
ROOM TEMP IRR	83.46	1.16	0.31	0.20	1.26	83.52	1.16	0.67	0.28		
1000 C NO IRR	83.60	1.16	0.31	0.20	1.32	83.51	1.16	0.67	0.29		
1000 C IRR	83.40	1.16	0.31	0.20	1.19	83.51	1.16	0.67	0.28		
2020 AG											
Control	83.55	1.16	0.31	0.20	1.08	83.52	1.16	0.66	0.25		
15 MGy GAMMA	83.60	1.16	0.30	0.19	1.10	83.54	1.16	0.65	0.25		
45 MGy GAMMA	83.58	1.16	0.30	0.19	1.07	83.54	1.16	0.62	0.24		
87 MGy GAMMA	83.55	1.16	0.30	0.19	1.08	83.55	1.16	0.63	0.24		
ROOM TEMP NO IRR	83.40	1.16	0.33	0.20	1.09	83.48	1.16	0.72	0.26		
ROOM TEMP IRR	83.68	1.15	0.30	0.19	1.13	83.53	1.16	0.64	0.25		
1000 C NO IRR	83.42	1.16	0.29	0.18	1.06	83.53	1.16	0.61	0.23		
1000 C IRR	83.56	1.16	0.30	0.20	1.05	83.52	1.16	0.63	0.24		
2020 WG											
Control	83.56	1.16	0.30	0.19	1.09	83.54	1.16	0.64	0.23		
15 MGy GAMMA	83.42	1.16	0.29	0.18	1.07	83.52	1.16	0.63	0.23		
45 MGy GAMMA	83.42	1.16	0.29	0.18	1.08	83.54	1.16	0.61	0.22		
87 MGy GAMMA	83.44	1.16	0.29	0.18	1.07	83.53	1.16	0.62	0.23		
ROOM TEMP NO IRR	83.40	1.16	0.28	0.17	1.12	83.54	1.16	0.61	0.23		
ROOM TEMP IRR	83.44	1.16	0.29	0.18	1.12	83.54	1.16	0.62	0.23		
1000 C NO IRR	83.42	1.16	0.30	0.19	1.05	83.53	1.16	0.63	0.23		
1000 C IRR	83.46	1.16	0.31	0.20	1.06	83.52	1.16	0.64	0.24		

Graphite	Obs. Max (2θ)	d (Obs. Max) (A°)	Max Int. (cps)	Net Hght (cps)	FW HM (2θ)	Grav. C. (2θ)	d (GC) (A°)	Raw Area (cps* 2θ)	Net Area (cps*2θ)	Left Int. (cps)	Rt. Int. (cps)
IG-110 AG											
Control	83.55	1.16	0.37	0.26	1.08	83.53	1.16	0.70	0.33		
15 MGy GAMMA	83.58	1.16	0.35	0.25	1.07	83.51	1.16	0.68	0.31		
45 MGy GAMMA	83.55	1.16	0.34	0.24	1.09	83.54	1.16	0.67	0.31		
87 MGy GAMMA	83.46	1.16	0.30	0.19	1.12	83.51	1.16	0.63	0.24		
ROOM TEMP NO IRR	83.46	1.16	0.35	0.25	1.11	83.53	1.16	0.69	0.32		
ROOM TEMP IRR	83.44	1.16	0.36	0.25	1.07	83.53	1.16	0.70	0.31		
1000 C NO IRR	83.46	1.16	0.34	0.24	1.04	83.53	1.16	0.66	0.31		
1000 C IRR	83.55	1.16	0.34	0.24	1.10	83.53	1.16	0.67	0.30		
IG-110 WG											
Control	83.44	1.16	0.36	0.25	1.09	83.53	1.16	0.71	0.32		
15 MGy GAMMA	83.46	1.16	0.34	0.23	1.07	83.55	1.16	0.67	0.29		
45 MGy GAMMA	83.60	1.16	0.35	0.24	1.04	83.54	1.16	0.68	0.31		
87 MGy GAMMA	83.46	1.16	0.34	0.24	1.08	83.53	1.16	0.68	0.31		
ROOM TEMP NO IRR	83.55	1.16	0.36	0.25	1.01	83.53	1.16	0.68	0.31		
ROOM TEMP IRR	83.56	1.16	0.40	0.28	1.14	83.50	1.16	0.80	0.36		
1000 C NO IRR	83.60	1.16	0.35	0.24	1.10	83.53	1.16	0.67	0.31		
1000 C IRR	83.44	1.16	0.34	0.24	1.12	83.53	1.16	0.68	0.31		

Table C-1: XRD data results for all samples.

Appendix D. Special Experimental Proposals Approved by the Reactor Safety Committee

MARYLAND UNIVERSITY TRAINING REACTOR

PROPOSAL TO DETERMINE THE GRAPHITE OXIDATION AND DAMAGE UNDER IRRADIATION IN AN IMPURE HELIUM ENVIRONMENT

Final version dated 11/18/2011

Experiment to be performed by Cameron Goodwin.

Approved _____, Director, Maryland University Training Reactor
Mohamad Al-Sheikhly

Approved _____, Chair, Reactor Safety Committee
Gary Pertmer

1.0 PURPOSE

While the effects of radiation on graphite have been studied in the past, the properties of graphite are largely dependent on the coke used in manufacturing the graphite. There are no longer any of the previously studied graphite types available for use in the HTGR. There are various types of graphite being considered for different uses in the HTGR and all of these graphite types need to be analyzed to determine how radiation will affect them. The purpose of this research is to study the mechanism of radiation effects on some of the new graphite types and try to establish a correlation between the type of graphite and the radiation effects. This will allow a better knowledge base for considering which graphite types are best suited for use in the HTGR.

This knowledge is especially important in determining which types of graphite are best suited for use in the HTGRs. Different types of graphite will be used for different purposes in the reactor. PCEA graphite is being discussed for use in the prismatic design as replaceable block and in the pebble-bed design as reflector and insulation blocks. IG-110 is being discussed for use as a replaceable reflector and as core support pedestals. Reactor core design parts such as replaceable reflector do not need to hold up as well to radiation effects because these items will be replaced approximately every 6 years or so during refueling. On the other hand, core support pedestals will not be replaced over the lifetime of the reactor. These parts must be able to withstand radiation effects over the lifetime of the core, approximately 40 years. By examining the mechanism of the irradiation effects on the different types of graphite, I can determine which grades are best suited for lifetime use in the HTGR.

High temperature oxidation experiments will be conducted using the MUTR. A high temperature heater (capable of temperatures up to 1700 C) will be used for the experiments. The modified access plugs used for the dose mapping of the East Beam Port will be inserted for this procedure. The graphite samples will be placed in front of the access port to the east beam port and they will be irradiated while exposing the samples to water enhanced helium through the sample space. The gases coming off of the samples will be analyzed by gas chromatography to determine the amounts of CO and CO2 present to determine the extent of oxidation. This research will allow for the analysis of radiation induced oxidation effects of the graphite samples. In order to characterize the effects of the oxidation on the graphite samples, the samples will be run in all three temperature regimes. Particular attention will be paid to the diffusion controlled regime (region 2, temperature range 700 C to 1200 C) since the HTGR is expected to operate within this range. These experiments will reflect everyday oxidation effects on the graphite present in the reactor core and will allow for determination of which types of graphite are best suited for the HTGR design. A photographs of the set-up can be seen in the appendix.

Any sample changes will be completed while the reactor is subcritical.

It is anticipated that these experiments will be completed before October 2012.

2.0 PRECAUTIONS AND REQUIREMENTS

2.1 Removing the beam port plug is not classified as a Special Experiment. However, operating the reactor with the East Beam Port with the modified "Beam Plugs" installed was approved as a "Special Experiment" in July 2011. Since this is the first time a heater will be placed outside of the east beam port it will be considered a "Special Experiment." Therefore this proposal requires the approval of the Reactor Safety Committee and the Reactor Director. This proposal must also comply with the guidelines set forth by 10 CFR 50.59.

2.2 The modified beam plugs will be installed prior to beginning the experiment and this will be documented in a "Note to File."

2.3 The modified beam plugs allow only a 2" diameter beam of unidirectional radiation to propagate through the beam port. A borated polyethylene bricks will serve as a shutter to open and close the beam passing through the beam port. This shutter is attached to a 6 foot arm and is operable from the northeast corner of the reactor, outside of the beamline. When the shutter is open, a warning light visible from the eastern half of the reactor building will illuminate, signifying that neutrons are passing through the experimental setup.

2.4 The Maryland University Training Reactor has previously been run at a number of power levels with the modified access plugs in place and with the beam shutter both open and closed. Dose rate measurements taken at these power levels, in a number of locations are listed, in Tables 1-3. Dose rates experienced by personnel during the proposed experiment are not expected to exceed those listed in Tables 1-3. If changes are made to the experimental configurations that are expected to increase dose rates to personnel, surveys should be completed before proceeding.

2.5 Some neutron dose rates listed in Tables 1-3, exceed 100 mrem/hr, however these measurements were taken with the Ludlum Model 15 neutron detector. The Radiation Safety Office determined that the Eperline Rem balls give more accurate dose measurements after consultation with many contacts. These measurements are about an order of magnitude less than the Model 15 and can be seen in Tables 1–3. Therefore, we do not expect the need to establish a high radiation area outside the beam. However, if at any time during the experiment, dose rates exceed 100 mrem/hr outside of the thermal-column neutron beam, the operation will be paused and a high radiation area will be established and marked, allowing control over individual access to the area in accordance with 10 CFR 20.1601. A high radiation area, if necessary, will be established under the approval of the Reactor Director. Posting and surveys of the area will be completed by RSO staff. Further investigation by the RSO staff is still being conducted and will be presented to the group at a date to be determined.

2.6 Video monitoring of the east beam port area and the east face of the reactor containment will be implemented. This video monitoring will be conducted from the reactor control room by the Reactor Operator.

2.7 Neutron detectors and gamma/beta detectors will be used to monitor the radiation levels during course of the entire procedure at random intervals.

2.8 In addition to whole body TLDs, personnel handling the access plugs or working with equipment in the beamline will wear ring and wrist badges.

2.9 Personnel shall not place any part of their body in the beamline when the beam shutter is open. Personnel will obey ALARA and time, distance, shielding principles at all times during the experiment.

2.10 After irradiation, components in this experiment must be surveyed by an available RSO staff member prior to removal from the MUTR facility. These surveys should indicate dose rates of any activated components and tag said components with this information.

3.0 REQUIRED MATERIALS AND EQUIPMENT

- 80/20 level, 80/20 track and borated polyethylene brick for shutter
- Installed shielding on reactor face: 43-in by 30-in Al-box was built to fit flush against reactor wall; 6-in deep; filled with paraffin mixed with boron carbide
- Cave: 24" x 24" Lexan box, filled with borated poly blocks in a random array to allow for air flow across heater
- Three 24" thick brick walls, 7 feet high
- Borated poly bricks (6" thick) on back side of concrete wall facing east wall of reactor building
- Heater
- Computer set-up
- Gas chromatographer (GC)

4.0 PROCEDURE

4.1 Ensure modified beam plugs are installed. If they are not, install in accordance with East Beam Port Characterization Proposal.
4.2 Position heater on heater stand.
4.3 Place samples into heater insert and place heater insert inside heater. The samples are 1 cm by 2 mm by 2mm. There are 10 sample types that need to be irradiated. The heater insert is 1 in OD and will fit snugly inside the heater.
4.4 Connect insert to research grade helium supply and GC using tubing.
4.5 Known amounts of water will be mixed with the helium to determine the oxidation effects of the impure helium.
4.6 Turn on fans to cool cave. These fans will not have an effect on the samples inside the heater but are used to ensure that the cave does not heat up. The melting point of polyethylene is 130 C. It is not anticipated that the cave will reach this temperature. The heat from the heater is localized and quickly dissipates.
4.7 Turn on heater to ramp up to desired temperatures. This is controlled via the computer. The heater is run by 208 V to the heater controller. This outlet is located on the reactor wall to the left of the east beam port and was installed by UMD electrical personnel. The power is transferred to the heater via two braided wires made especially for the heater.
4.8 Open shutter and ensure personnel are clear of any areas marked as High Radiation Area.
4.9 Bring reactor to 250 kW and irradiate samples. The goal is to have the samples receive an accumulated fluence similar to the fluence received to the AFRRI samples and the previous rabbit samples (5.4E+17 n/cm^2). This will require multiple runs to achieve these numbers. No run will exceed 8 hours.
4.10 Reactor will be shut down for sample changes.
4.11 After completing all measurements shut down the reactor.
4.12 When dose rates have decreased, close the shutter.

5.0 10CFR50.59 REVIEW

5.1 The removal of the beam port access plugs does not require a License Amendment Request (LAR) as allowed under 10CFR50.59 for the following reasons:

5.1.1 This removal of the plugs does not require a modification of the technical specifications. (10CFR50.59(c)(1)(i)

5.1.2 The proposed experiment has been evaluated and does not meet the criteria set forth in 10CFR50.59(c)(2)

FIGURES AND TABLES

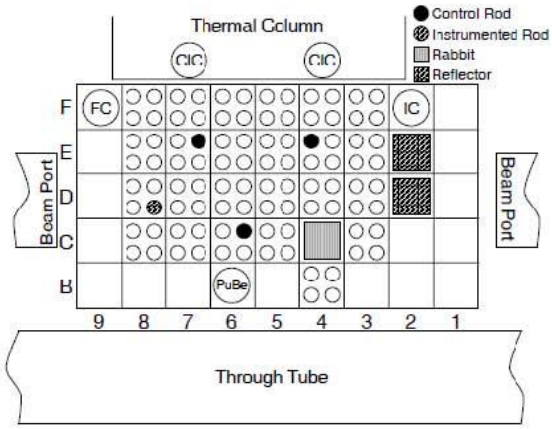

Figure 1. Plan view of MUTR core layout showing the orientation of the East Beam Port (south is at the top of the diagram).

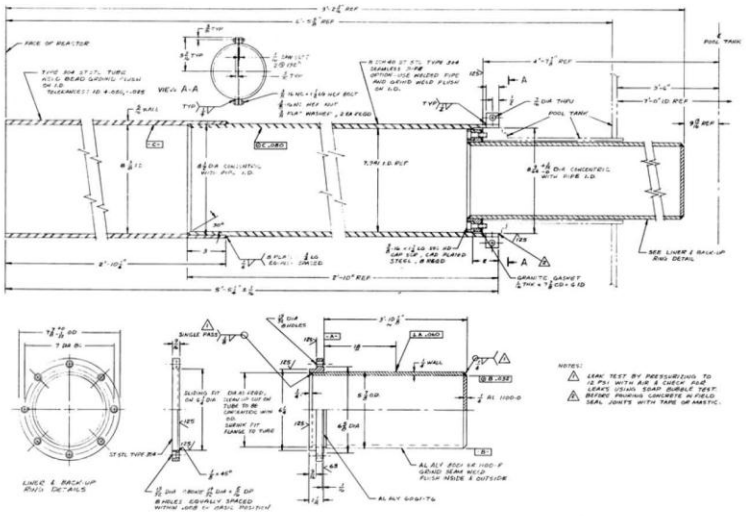

Figure 2. Blueprint of the MUTR East Beam Port from the Technical Specifications. Core begins at the right hand side of the diagram. Edge of concrete reactor containment appears at the left hand side of the diagram.

Figure 3. Head-on view and length-wise view of the modified beam plugs, which will be inserted into East Beam Port for experiments. There are two modified beam plugs, 31-in long Al-clad, concrete-filled plugs. They have a 2-in hole in the center to allow radiation out from the core.

Figure 4. Photo of heater being used in experiment. The heater is 4 inches wide with a 1 in opening. This heater contains no parts that will become Co-60 upon irradiation. Heater will be treated as RAM after experiments.

Figure 5. Handle controlling shutter for beam port.

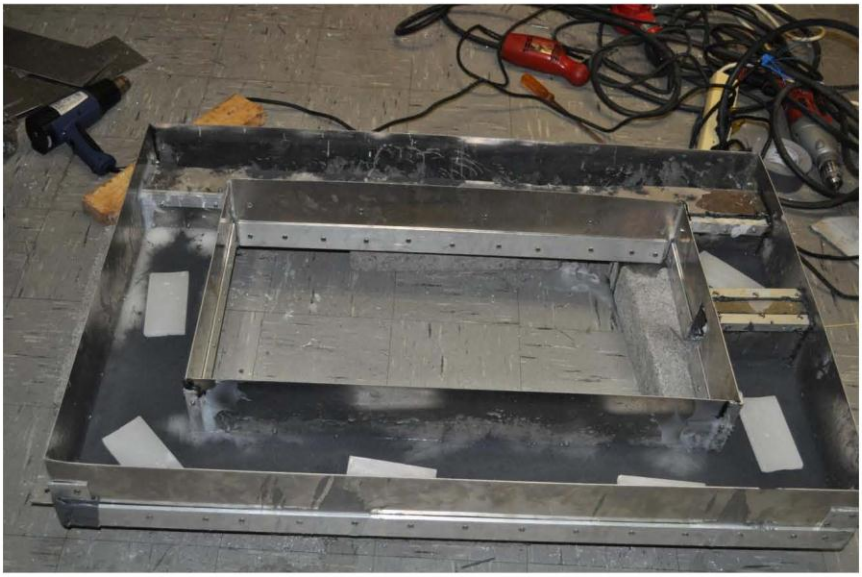

Figure 6. Photograph of the inside of the collar to be mounted on face of east reactor during filling with wax and boron carbide mixture

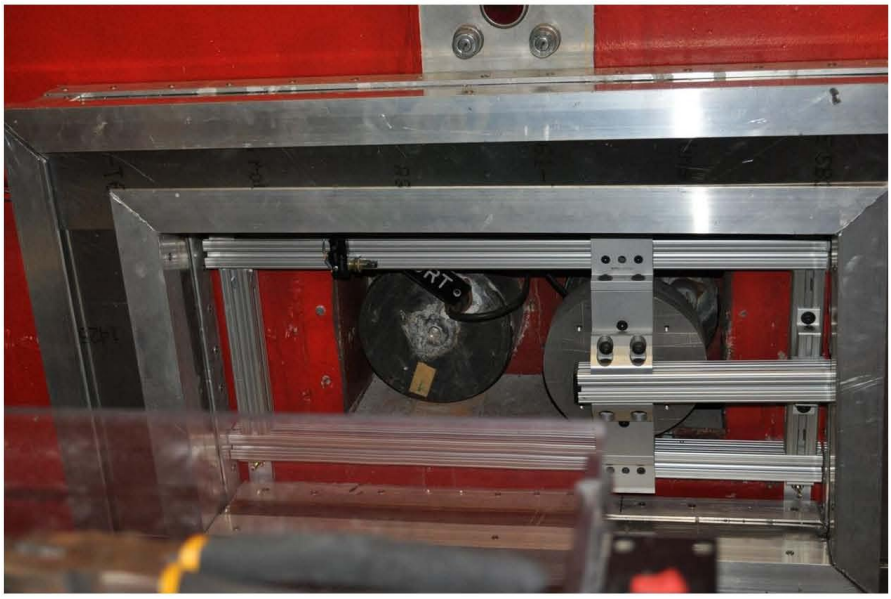

Figure 7. Photograph of the collar installed on face of east reactor.

Figure 8. Concrete walls built for shielding of east wall of reactor building.

Figure 9. Cave built for shielding of east reactor building wall and also for cooling of heater. This is a 24-in by 24-in Lexan box. Fans exhaust toward rear exit door and provide 945 cfm for cooling of the heater. Filled with 3 complete layers of borated poly bricks plus arrangement of bricks to ensure adequate air flow

Figure 10. Right side of box (filter side).

Figure 11: Left side of box (fan side).

Figure 12: Gow-Mac GC being used for experiment.

NOVEMBER 9, 2011 DOSE MAPPING ACTIVITIES

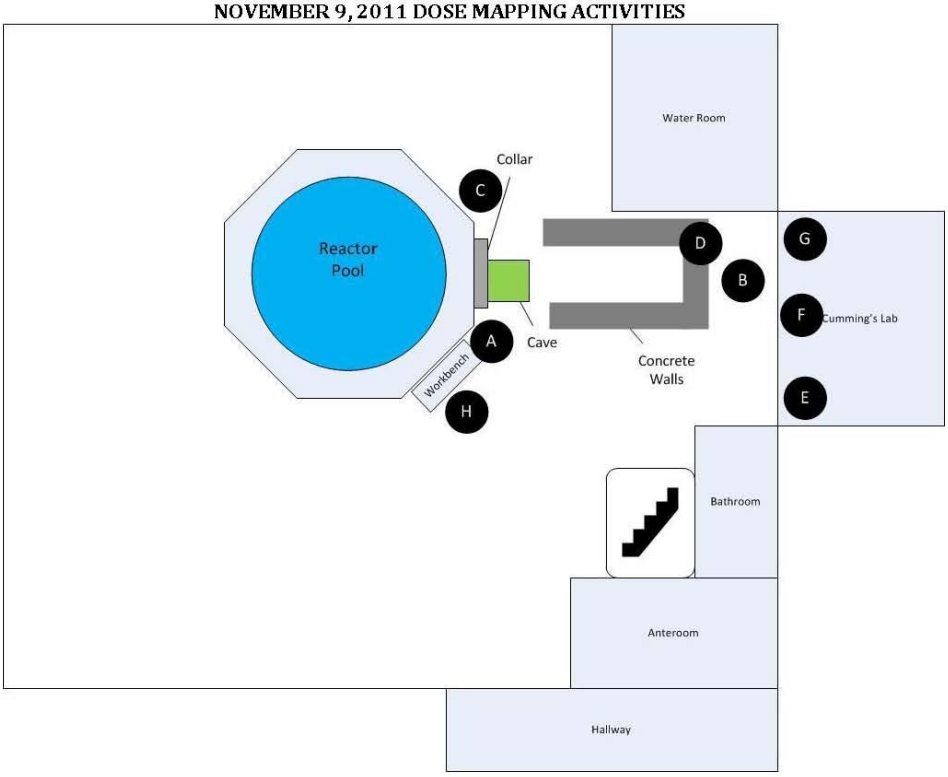

Time	Power Level	Position	Ion Chamber (mR/hr)	Neutron Detector (15) (cpm)	Neutron Detector (Rem Ball) (cpm)	GM (mr/hr)
1502	52 mW	A	0.01	0		
		B	0.013	0		
		C	0.01	0		
		D				0.05
1507	100 mW	A	0.01	0		
		B	0.01	0		
		C	0.01	0		
		D				0.05
1510	500 mW	A	0.01	0		
		B	0.01	0		

Time	Power Level	Position	Ion Chamber (mR/hr)	Neutron Detector (15) (cpm)	Neutron Detector (Rem Ball) (cpm)	GM (mr/hr)
		C	0.01	0		
		D				0.05
1514	1 W	A	0.01	0		
		B	0.01	0		
		C	0.01	0		
		D				0.05
1520	10 W	A	0.01	0		
		B	0.01	0		
		C	0.01	0		
		D				0.05
1524	100 W	A	0.01	0		
		B	0.01	0		
		C	0.01	0		
		D				0.05
1528	500 W	A	0.035	20		
		B	0.019	0		
		C	0.045	100		
		D				0.05
1535	1 kW	A	0.07	100		
		B	0.022	0		
		C	0.11	100		
		D				0.1
1541	5 kW	A	0.35	200		
		B	0.063	0		
		C	0.64	400		
		D				0.1
1552	10 kW	A	0.55	450		
		B	0.12	40		
		C	1.1	600		
		D				0.1
1600	15 kW	A	1	600		
		B	0.17	40		
		C	1	800		
		D				0.1
1607	20 kW	A	4	300		
		B	0.23	40		
		C	NT	NT		
		D				0.1
1613	25 kW	A	NT	NT		
		B	0.28	NT		
		C	NT	NT		

Time	Power Level	Position	Ion Chamber (mR/hr)	Neutron Detector (15) (cpm)	Neutron Detector (Rem Ball) (cpm)	GM (mr/hr)
		D				0.15
1617	50 kW	A	0.65	450		
		B	0.54	240		
		C	NT	NT		
		D				0.5
		E	0.028	10		
		F	0.028	10		
		G	0.028	10		
1625	100 kW	D			100-120	1
		E	0.045	20		
		F	0.028	20		
		G	0.035	20		
		H			30	2.5
1638	150 kW	D			150-200	1.6
		E	0.062	40		
		F	0.035	40		
		G	0.05	40		
		H			50	2.5
1643	200 kW	D			200-275	2.1
		E	0.051	60		
		F	0.044	60		
		G	0.064	60		
		H			60	3.5
1650	250 kW	D			300	2.5
		E	0.083	60		
		F	0.066	60		
		G	0.058	60		
		H			90	4.5

Table 1. November 9, 2011: Dose rate measurements as a function of power level, taken in the vicinity of the east beam port with the beam shutter OPEN. The drawing above the table denotes the areas where measurements were taken. NT signifies that measurements were not taken for this location and power level.

NOVEMBER 11, 2011 DOSE MAPPING ACTIVITIES

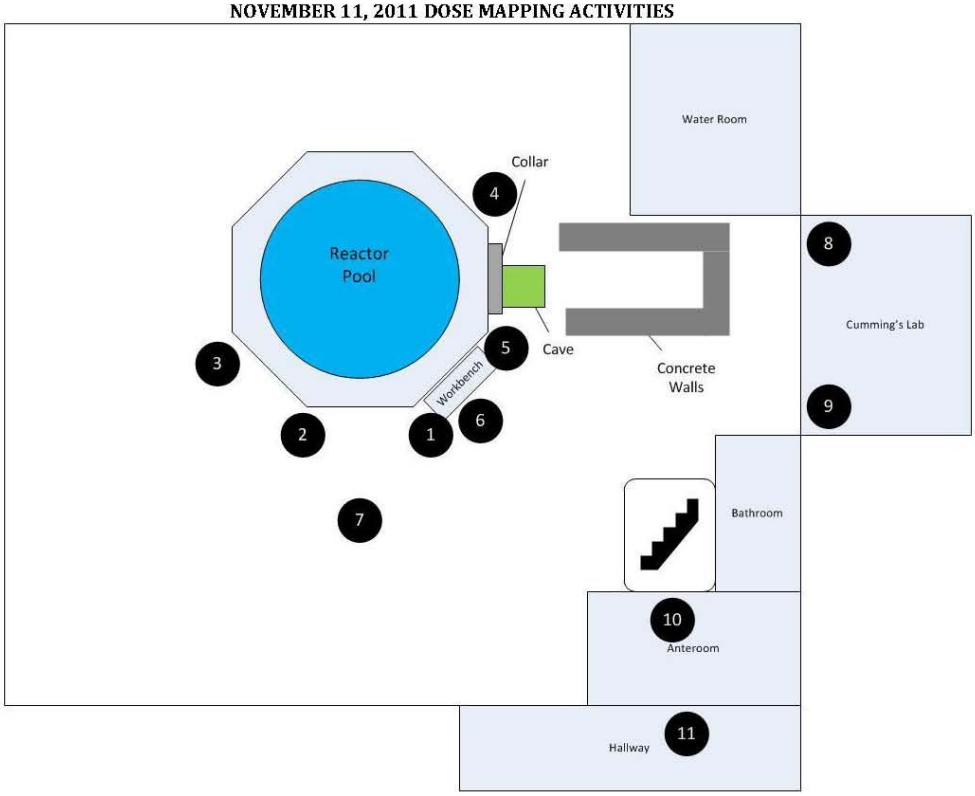

Power Level	Position	Ion Chamber (mR/hr)	Neutron Detector (15) (cpm)	Neutron Detector (Rem Ball) (cpm)
250 kW	1	2	600	
250 kW	2	1.7	95	
250 kW	3	1.2	40	
250 kW	4	5.6	4000	
250 kW	5	10.9	4000	
250 kW	6	2.9	2500	350
250 kW	7	1.8	240	
250 kW	8	0.06	100	10
250 kW	9	0.115	60	10
250 kW	10	0.4	500	60
250 kW	11	0.3	180	

Table 2. November 11, 2011: Dose rate measurements as a function of power level, taken in the vicinity of the east beam port with the beam shutter OPEN. The drawing above the table denotes the areas where measurements were taken. NT signifies that measurements were not taken for this location and power level.

NOVEMBER 17, 2011 DOSE MAPPING

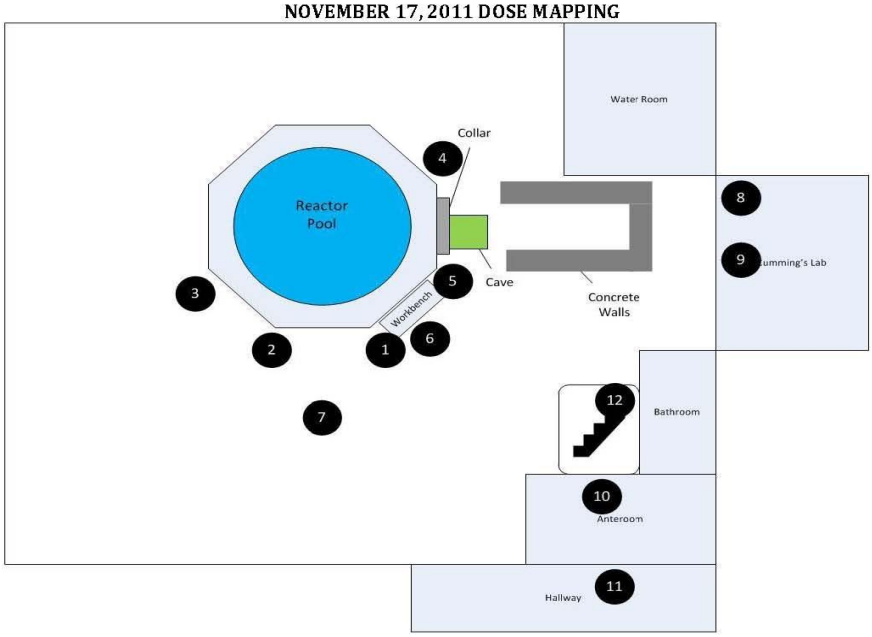

Power Level	Position	Ion Chamber (mR/hr)	Neutron Detector (Rem Ball) (cpm)
250 kW	1	3.6	80
250 kW	2	3.2	BKGD
250 kW	3	2	BKGD
250 kW	4	10.5	1700
250 kW	5	12.5	1600
250 kW	6	3.2	220
250 kW	7	3	30
250 kW	8	0.07	BKGD
250 kW	9	0.12	BKGD
250 kW	10	0.55	40
250 kW	11	0.4	20
250 kW	12	2.1	280
250 kW	Upstairs Balcony	0.43	10
250 kW	Control Room	0.41	20

Table 3. November 11, 2011: Dose rate measurements as a function of power level, taken in the vicinity of the east beam port with the beam shutter OPEN. The drawing above the table denotes the areas where measurements were taken. NT signifies that measurements were not taken for this location and power level.

§ 50.59 Changes, tests and experiments.

(a) Definitions for the purposes of this section:

(1) Change means a modification or addition to, or removal from, the facility or procedures that affects a design function, method of performing or controlling the function, or an evaluation that demonstrates that intended functions will be accomplished.

(2) Departure from a method of evaluation described in the FSAR (as updated) used in establishing the design bases or in the safety analyses means:

(i) Changing any of the elements of the method described in the FSAR (as updated) unless the results of the analysis are conservative or essentially the same; or

(ii) Changing from a method described in the FSAR to another method unless that method has been approved by NRC for the intended application.

(3) Facility as described in the final safety analysis report (as updated) means:

(i) The structures, systems, and components (SSC) that are described in the final safety analysis report (FSAR) (as updated),

(ii) The design and performance requirements for such SSCs described in the FSAR (as updated), and

(iii) The evaluations or methods of evaluation included in the FSAR (as updated) for such SSCs which demonstrate that their intended function(s) will be accomplished.

(4) Final Safety Analysis Report (as updated) means the Final Safety Analysis Report (or Final Hazards Summary Report) submitted in accordance with Sec. 50.34, as amended and supplemented, and as updated per the requirements of Sec. 50.71(e) or Sec. 50.71(f), as applicable.

(5) Procedures as described in the final safety analysis report (as updated) means those procedures that contain information described in the FSAR (as updated) such as how structures, systems, and components are operated and controlled (including assumed operator actions and response times).

(6) Tests or experiments not described in the final safety analysis report (as updated) means any activity where any structure, system, or component is utilized or controlled in a manner which is either:

(i) Outside the reference bounds of the design bases as described in the final safety analysis report (as updated) or

(ii) Inconsistent with the analyses or descriptions in the final safety analysis report (as updated).

(b) Applicability. This section applies to each holder of a license authorizing operation of a production or utilization facility, including the holder of a license authorizing operation of a nuclear power reactor that has submitted the certification of permanent cessation of operations required under Sec. 50.82(a)(1) or a reactor licensee whose license has been amended to allow possession of nuclear fuel but not operation of the facility.

(c)(1) A licensee may make changes in the facility as described in the final safety analysis report (as updated), make changes in the procedures as described in the final safety analysis report (as updated), and conduct tests or experiments not described in the final safety analysis report (as updated) without obtaining a license amendment pursuant to Sec. 50.90 only if:

(i) A change to the technical specifications incorporated in the license is not required, and

(ii) The change, test, or experiment does not meet any of the criteria in paragraph (c)(2) of this section.

(2) A licensee shall obtain a license amendment pursuant to Sec. 50.90 prior to implementing a proposed change, test, or experiment if the change, test, or experiment would:

(i) Result in more than a minimal increase in the frequency of occurrence of an accident previously evaluated in the final safety analysis report (as updated);

(ii) Result in more than a minimal increase in the likelihood of occurrence of a malfunction of a structure, system, or component (SSC) important to safety previously evaluated in the final safety analysis report (as updated);

(iii) Result in more than a minimal increase in the consequences of an accident previously evaluated in the final safety analysis report (as updated);

(iv) Result in more than a minimal increase in the consequences of a malfunction of an SSC important to safety previously evaluated in the final safety analysis report (as updated);

(v) Create a possibility for an accident of a different type than any previously evaluated in the final safety analysis report (as updated);

(vi) Create a possibility for a malfunction of an SSC important to safety with a different result than any previously evaluated in the final safety analysis report (as updated);

(vii) Result in a design basis limit for a fission product barrier as described in the FSAR (as updated) being exceeded or altered; or

(viii) Result in a departure from a method of evaluation described in the FSAR (as updated) used in establishing the design bases or in the safety analyses.

(3) In implementing this paragraph, the FSAR (as updated) is considered to include FSAR changes resulting from evaluations performed pursuant to this section and analyses performed

pursuant to Sec. 50.90 since submittal of the last update of the final safety analysis report pursuant to Sec. 50.71 of this part.

(4) The provisions in this section do not apply to changes to the facility or procedures when the applicable regulations establish more specific criteria for accomplishing such changes.

(d)(1) The licensee shall maintain records of changes in the facility, of changes in procedures, and of tests and experiments made pursuant to paragraph (c) of this section. These records must include a written evaluation which provides the bases for the determination that the change, test, or experiment does not require a license amendment pursuant to paragraph (c)(2) of this section.

(2) The licensee shall submit, as specified in Sec. 50.4, a report containing a brief description of any changes, tests, and experiments, including a summary of the evaluation of each. A report must be submitted at intervals not to exceed 24 months.

(3) The records of changes in the facility must be maintained until the termination of a license issued pursuant to this part or the termination of a license issued pursuant to 10 CFR part 54, whichever is later. Records of changes in procedures and records of tests and experiments must be maintained for a period of 5 years.

[64 FR 53613, Oct. 4, 1999, as amended at 66 FR 64738, Dec. 14, 2001]

10 CFR 20.1601

High Radiation Areas

2.1 Options for Access Control

Of the options for access control provided in 10 CFR 20.1601(a), the most widely used procedure at nuclear power plants is keeping high radiation areas locked. Although licensees have the option to control high radiation areas with the use of a control device to reduce radiation levels when an individual enters the area or the use of an alarm to alert the individual and the supervisor to an entry into a high radiation area, experience has shown that these options have limited practical application at nuclear power plants. In addition to the provisions of 10 CFR 20.160l(a), a nuclear power plant licensee may apply for Commission approval of alternative methods for control under 10 CFR 20.1601(c). See Regulatory Position 2.4 below.

2.2 Positive Access Control

Positive control over each individual entry is required by 10 CFR 20.1601(a)(3) when access is required to a high radiation area that is normally controlled by being locked. In a large facility such as a nuclear power plant, appropriate positive access controls can be instituted through the use of radiation work permits (RWPs) or an equivalent program. Such a system ensures appropriate supervision through specific procedures that establish requirements for control and delegate responsibility to qualified individuals. Procedures for establishing positive control over each entry should provide for:

1. Surveys that identify the radiation hazards in the area should be made and the results documented;
2. An appropriate level of supervision to determine that exposure of the individual to the hazards is warranted;
3. Communication of the nature and extent of the radiation hazards to each individual entering the area;
4. Protective measures (e.g., shielding, time limits, protective clothing, monitoring) to protect the individual from excessive or unnecessary radiation exposure; and
5. Permission for only authorized individuals to enter the high radiation area with all entries and exits documented.

2.3 Direct or Electronic Surveillance

Direct or electronic surveillance is identified in 10 CFR 20.1601(b) as a substitute for the controls required in 10 CFR 20.1601(a). The direct or electronic surveillance should have the following capabilities as a minimum.

1. Detect attempted unauthorized entry,
2. Warn individuals that their attempted entry is unauthorized, and

3. Alert the proper authority about an unauthorized entry so that action can be taken to correct the situation.

2.4 Alternative Methods for Access Control

The requirements in 10 CFR 20.1601(a) for access to high radiation areas may, in some instances, cause unnecessary restrictions on plant operations. According to 10 CFR 20.1601(c), licensees may apply to the Commission for approval to use alternative methods for control. The following method is acceptable to the NRC staff as an alternative to the requirements in 10 CFR 20.1601(a) for the control of access to high radiation areas.

Each high radiation area as defined in 10 CFR Part 20 should be barricaded[2] and conspicuously posted as a high radiation area, and entrance thereto should be controlled by requiring issuance of a radiation work permit (RWP) or equivalent. Individuals trained and qualified in radiation protection procedures (e.g., a health physics technician) or personnel continuously escorted by such individuals may be exempted from this RWP requirement while performing their assigned duties in high radiation areas where radiation doses could be received that are equal to or less than 0.01 Sv (1.0 rem) in 1 hour (measured at 30 centimeters from any source of radiation) provided they are otherwise following plant radiation protection procedures, or a general radiation protection RWP, for entry into such high radiation areas. Any individual or group of individuals permitted to enter such areas should be provided with or accompanied by one or more of the following:

- A radiation monitoring device that continuously indicates the radiation dose rate in the area,
- A radiation monitoring device that continuously integrates the radiation dose rate in the area and alarms when a preset integrated dose is received. Entry into such areas with this monitoring device may be made after the dose rates in the area have been determined and personnel have been made knowledgeable of them,
- An individual qualified in radiation protection procedures with a radiation dose rate monitoring device. This individual is responsible for providing positive radiation protection control over the activities within the area and should perform periodic radiation surveillance at the frequency specified in the radiation protection procedures or the applicable RWP.

In addition, areas that are accessible to personnel and that have radiation levels greater than 0.01 Sv (1.0 rem) (but less than 500 rads at 1 meter) in 1 hour at 30 cm from the radiation source, or from any surface penetrated by the radiation, should be provided with locked doors to prevent unauthorized entry, and the keys should be maintained under the administrative control of the shift supervisor on duty or health physics supervisor. Doors should remain locked except during periods of access by personnel under an approved RWP that specifies the dose rates in the immediate work areas and the maximum allowable stay time for individuals in that area. In lieu of a stay time specification on the RWP, direct or remote continuous surveillance (such as closed circuit TV cameras) may be made by personnel qualified in radiation protection procedures to provide positive exposure control over the activities being performed within the area.

Individual high radiation areas that are accessible to personnel, that could result in radiation doses greater than 0.01 Sv (1.0 rem) in 1 hour, and that are within large areas where no enclosure exists to enable locking and where no enclosure can be reasonably constructed around the individual area should be barricaded and conspicuously posted. A flashing light should be activated as a warning device whenever the dose rate in such an area exceeds or is expected to exceed 0.01 Sv (1.0 rem) in 1 hour at 30 cm from the radiation source or from any surface penetrated by the radiation.

2.5 Controls for High Radiation Areas (Control Points and Barriers)

Controls (e.g., locked doors, access control, and posting) for high radiation areas may be established at locations beyond the immediate boundaries of the high radiation areas to take advantage of natural or existing barriers. The use of one locked door, or one control point where positive control over personnel entry is exercised, to establish control over multiple high radiation areas is acceptable provided the following conditions are met:

1. The individual high radiation areas are barricaded and posted separately to identify the actual areas of concern,[3]
2. Control points are established sufficiently close to the high radiation areas that adequate supervision of access to the areas can be assured, and
3. The required protective measures and other requirements for entering the high radiation areas (e.g., dosimetry, monitoring) are enforced at the control point.[4]

2.6 Control of Keys

The shift supervisor or the radiation protection manager (or their respective designees) should administratively control the issuance of keys to personnel requiring access to high radiation areas and the return of the keys.

References

Acheson, E.G. (1895). U.S. Patent.

Advanced Industrial Ceramics. (2011). Address: 2449 Zanker Road, San Jose, CA 95131.

Armed Forces Radiobiology Research Institute. (2004). *Safety analysis report*. Bethesda, MD. Armed Forces Radiobiology Research Institute.

Bermudez, J., Udup, E., Tecchio, L.B., Maran, L. and Pranovi, L. (2009). Radiation damage analysis on CDG graphite for SPIRAL2 neutron converter: Preliminary results. *LNL Annual Report,* 136-137.

Bermudez, J., Acosta, G., Tecchio, L.B. and Udup, E. (2010). Progress in the study of the radiation damage on POCO graphite for SPIRAL2 neutron converter. *LNL Annual Report,* 278-29.

Beyssac, O., Goffé, B., Petitet, J., Froigneux, E., Moreau, M. and Rouzaud, J. (2003). On the characterization of disordered and heterogeneous carbonaceous materials by Raman spectroscopy. *Spectrochimica Acta Part A, 59,* 2267-2276.

Bioenergylist.org - Boudouard Reaction spreadsheet.

Blackman, L.C.F. (1970). *Modern aspects of graphite technology*. New York, NY. Academic Press, Inc.

Bonal, J.P. and Wu, C.H. (1996). Neutron irradiation effects on the thermal conductivity and the dimensional stability of carbon fiber composites. *Physica Scripta, 64,* 26-31.

Brown, L.M., Kelly, A. and Mayer R.M. (1969). The influence of boron on the clustering of radiation damage in graphite. *Philasophical Magazine, 19,* 721.

Brozena, A.H., Moskowitz, J., Shao, B., Deng, S., Liao, H., Gaskell, K.J. and Wand, Y. (2010). Outer wall selectively oxidized, water-soluble double-walled carbon nanotubes. *Journal of the American Chemical Society, 132,* 3932-3938.

Bruker Biospin. (2012). http://www.bruker-biospin.com/cwpractice.html.

Burchell, T. (2001). *Neutron irradiation damage in graphite and its effects on properties.* Oak Ridge, TN. Oak Ridge National Laboratory.

Burton, M. and Neubert, T.J. (1956). Effect of fast neutron bombardment on physical properties of graphite: A review of early work at the metallurgical laboratory. *Journal of Applied Physics, 27,* 557-567.

Canberra Industries, Inc. (2003). *Germanium detectors user's manual*. Meridian, CT. Canberra Industries, Inc.

Cataldo, F. (1999). A Raman study on radiation-damaged graphite by γ-rays. *Carbon, 38,* 623-641.

Chen, M., Zhou, H., Yang, H., Yu, F. and Sun, L. (2012). Layer-dependent fluorination and doping of graphene via plasma treatment. *Nanotechnology, 23,* 115706.

Chiang, Y., Birnie, D. III and Kingery, W.D. (1997). *Physical ceramics: Principles for ceramic science and engineering.* Hoboken, NJ. John Wiley & Sons, Inc.

Chorkendorff, I. and Neimantsverdriet, J.W. (2007). *Concepts of modern catalysis and kinetics.* Weinheim, Germany. Wiley-VCH.

Chunhe, T. and Jie, G. (2000). Improvement in oxidation resistance of the nuclear graphite by reaction-coated SiC coating. *Journal of Nuclear Materials, 224,* 103-108.

Contescu, C.I., Azad, S., Miller, D., Lance, M.J., Baker, F.S. and Burchell, T.D. (2008). Practical aspects for characterizing air oxidation of graphite. *Journal of Nuclear Materials, 381,* 15-24.

Cullity, B.D. (1956). *Elements of X-ray diffraction.* Reading, MA. Addison-Wesley Publishing Company, Inc.

Curtis, O.L. and Crawford, Jr., J.H. (1962). Radiation-induced recombination and trapping centers in germanium. *Physical Review, 126,* 1342-1349.

DataApex Ltd. (2010). *Clarity lite: Getting started*. Prague 13, The Czech Republic. DataApex Ltd.

Delhaès, P. (2001). *Graphite and precursors*. Amsterdam, The Netherlands. Gordon and Breach Science Publishers.

DelCul G.D., Spencer B.B., Forsberg C.W., Collins E.D. and Rickman W.S. (2002). *TRISO-coated fuel processing to support high-temperature gas-cooled reactors*. Oak Ridge, TN. Oak Ridge National Laboratory.

Dobrzhinetskaya, L.F., Faryad, S.W., Wallis, S. and Cuthbert, S. (2011). *Ultrahigh-pressure metamorphism: 25 years after the discovery of coesite and diamond.* Burlington, MA. Elsevier Inc.

Dresselhaus, M.S. (2012). Fifty years in studying carbon-based materials. *Physica Scripta, T146,* 014002.

Dresselhaus, M.S. and Dresselhaus, G. (2002). Intercalation compounds of graphite, *Advances in Physics, 51,* 1.

Dresselhaus, M.S., Dresselhaus, G., Saito, R. and Jorio, A. (2005). Raman spectroscopy of carbon nanotubes. *Physics Reports, 409,* 47-99.

Eaton, G.R., Eaton, S.S., Barr, D.P. and Weber, R.T. (2010). *Quantitative EPR.* New York, NY. SpringWeinNewYork.

Far West Technology (FWT), Inc. (2000). Address: 330-D South Kellog, Goleta, GA 93117.

Farahataziz and Rodgers, M.A. (1987). *Radiation chemistry, principles and applications*. New York, NY. VCH Publishers, Inc.

Ferrari, A.C. (2007). Raman spectroscopy of grapheme and graphite: Disorder, electron-phonon coupling, doping and nonadiabatic effects. *Solid State Communications, 143*, 47-57.

Ferrari, A.C. and Robertson, J. (2000). Resonant Raman spectroscopy of disordered, amorphous, and diamond like carbon. *Physics Review B, 61,* 14095-14100.

Ferraro, J.R. and Kazuo Nakamoto. (2003). *Introductory Raman spectroscopy.* San Diego, CA. Academic Press.

Ganguli, N. and Krishnan, K.S. (1941). The magnetic and other properties of the free electrons in graphite. *Proceedings of the Royal Society A, 177,* 168-182.

Gow-Mac Instrument Co. (2010). *Operating Manual*. Lehigh Valley, PA. Gow-Mac Instrument Co.

Gries, T., Vandenbulcke, L., Simon, P. and Canizares, A. (2007). Stresses in textured and polycrystalline cubic films by Raman spectroscopy: Application to diamond. *Journal of Applied Physics, 102,* 083519.

Guinier, A. (1994). *X-ray diffraction in crystals, imperfect crystals, and amorphous bodies.* Toronto, Ontario. General Publishing Company, Ltd.

Haerle, R., Riedo, E., Pasquaello, A. and Baldereschi, A. (2011). Sp^2/sp^3 hybridization ratio in amorphous carbon from C 1s core-level shifts: X-ray photoelectron spectroscopy and first-principles calculation. *Physical Review B, 65,* 045101.

Hassel, O. and Mark, H.Z. *Physica, 18,* 661.

Hennig, G.R. and Hove, J.E. (1956). Proceedings from the first international conference on the peaceful uses of atomic energy. *United Nations, 7,* 666.

Herzberg, G. (1945). *Molecular spectra and molecular structure: Infrared and Raman spectra of polyatomic molecules.* New York, NY. D. Van Nostran Company, Inc.

http://www.absoluteastronomy.com/topics/Crystallographic_defect.

Hull, A.W. (1917). A new method of x-ray crystal analysis. *Physics Review, 10,* 661.

Humphreys, J.C. and McLaughlin, W.L. (1981). Dye film dosimetry for radiation processing. *IEEE Transactions on Nuclear Science, NS-28,* 1797-1801.

Idaho National Laboratory. (2007). *Generation IV nuclear energy systems ten-year program plan - Fiscal year 2007.* Idaho National Laboratory.

International Atomic Energy Agency. (1996). *High temperature gas cooled reactor technology development: IAEA-TECDOC-988.* Vienna, Austria. IAEA.

International Atomic Energy Agency. (2000). *Irradiation damage in graphite due to fast neutrons in fission and fusion systems: IAEA-TECDOC-1154.* Vienna, Austria. IAEA.

International Atomic Energy Agency. (2005). *Effects of nickel on irradiation embrittlement of light water pressure vessel steels: IAEA-TECDOC-1441.* Vienna, Austria. IAEA.

International Union of Pure and Applied Chemistry. http://iupac.org.

James, A.T. and Martin, A.J.P. (1952). Gas-liquid partition chromatography: the separation and micro-estimation of volatile fatty acids from formic acid to dodecanoic acid. *Biochemistry Journal, 50,* 679.

Jaramillo, A., Spurlock, L.D., Young, V. and Brajter-Toth. (1999). XPS characterization of nanosized overoxidized polypyrrole films on graphite electrodes. *The Analyst, 124,* 1215-1221.

Johnson, G.R.A. (1973). *Radiation chemistry of nitrous oxide gas primary processes, elementary reactions, and yields.* Washington, DC. U.S. Government Printing Office.

Kelly, B. (1981). *Physics of graphite*. London, UK. Applied Science Publishers.

Kim, E., Oh, I., and Kwak, J. (2001). Atomic structure of highly ordered pyrolytic graphite doped with boron. *Electrochemistry Communications, 3,* 608-612.

Kim, E.S. and Cheon, H. (2006). *Journal of Nuclear Materials, 349,* 182-194.

Kudin, K.N., Ozbas, B., Schniepp, H.C., Prud'homme, R.K., Aksay, I.A. and Car, R. (2008). Raman spectra of graphite oxide and functionalized graphene sheets. *Nano Letters, 8,* 36-41.

Laine, N.R., Vastola, F.J. and Walker Jr., P.L. (1963). The importance of active surface area in the carbon-oxygen reaction. *Journal of Physical Chemistry, 67,* 2030.

Lamarsh, J.R. (1983) *Introduction to nuclear engineering, 2nd edition*. Reading, MA. Addison-Wesley Publishing Company, Inc.

Lee, Y. (2004). The second order Raman spectroscopy in carbon crystallinity. *Journal of Nuclear Materials, 325,* 174-179.

Li, Z.Q., Lu, C.J., Xia, Z.P., Zhou, Y. and Luo Z. (2007). X-ray diffraction patterns of graphite and turbostatic carbon. *Carbon, 45,* 1686-1695.

Linacre, J.K., Taylor, N.K. and Thomas, R.B. (1965). UKAEA Report AERE-R-4806.

Liu, J., Hou, M.D., Trautmann, C., Neumann, R., Müller, C., Wang, Z.G., Zhang, Q.X., Sun, Y.M., Jin, Y.F., Liu, H.W. and Gao, H.J. (2003). STM and Raman spectroscopic study of graphite irradiated by heavy ions. *Nuclear Instruments and Methods in Physics Research B, 212,* 303-307.

Lu, S., Blanco, C., Appleyard, S., Hammond, C. and Rand, B. (2002). Texture studies of carbon and graphite tapes by XRD texture goniometry. *Journal of Material Science, 37,* 5283-5290.

Maaroufi, A., Flandrois, S., Coulon, C. and Rouillon, J.C. (1982). Magnetic anisotropy of graphite and electronic energy band parameters. *Journal of Physics and Chemistry of Solids, 43,* 1103-1109.

Mao, W.L, Mao, H., Eng, P.J., Trainor, T.P., Newville, M., Kao, C., Heinz, D.L., Shu, J., Meng, Y. and Hemley, R.J. (2003). Bonding changes in compressed superhard graphite. *Science, 302,* 425-427.

Marsh, H. (1989). *Introduction to Carbon Science*. London, UK. Butterworths.

Maryland University Training Reactor. (2000). *Safety Analysis Report*. College Park, MD. University of Maryland.

Mathew, S., Joseph, B., Sekhar, B.R. and Dev, B.N. (2008). X-ray photoelectron and Raman spectroscopic studies of MeV proton irradiated graphite. *Nuclear Instruments and Methods in Physics Research B, 266,* 3241-3246.

Maultzsch, J., Reich, S., Thomsen, C., Requardt, H. and Ordejón. (2004). Phonon dispersion in graphite. *Physical Review Letters, 92,* 075501.

McElfresh, M. (1994). *Fundamentals of magnetism and magnetic measurements.* San Diego, CA. Quantum Design, Inc.

McClure, J.W. (1960). Theory of diamagnetism of graphite. *Physical Review, 119,* 606-613.

McLaughlin, W.L., Humpherys, J.C., Farahani, M. and Miller, A. (1985). Measurement of high doses near metal and ceramic interfaces. *High-Dose Dosimetry. Proceedings of a symposium.* IAEA, Vienna.

McNair, H.M. and Miller, J.M. (2009). *Basic gas chromatography*. Hoboken, NJ. John Wiley & Sons.

Miao, X., Tongay, S. and Hebard, A.F. (2012). Extinction of ferromagnetism in highly ordered pyrolytic graphite my annealing. *Carbon, 50,* 1614-1618.

Micropyretics Heaters International. (2011). *High Temperature Robust Radiation ™ Heating Element Manual*. Cincinnati, OH. Micropyretics Heaters International.

Miller, A. (1987). Commissioning of a radiation process. 6th Tihany Symposium of Radiation Chemistry, September 1986.

Miller, A. and Batsberg Pedersen, W. (1981). Dose distribution in electron irradiated plastic tubing. *Radiation Physics and Chemistry, 18,* 967-973.

Morar, J.F., Himpsel, F.J., Hollinger, G., Jordan, J.L., Hughes, G. and McFreely, F.R. (1986). C 1s excitation studies of diamond (111). *Physical Review B, 33,* 1340.

Nakamura, K. and Kitajima, M. (1992). Ion-irradiation effects on the phonon correlation length of graphite studied by Raman spectroscopy. *Physical Review B, 45,* 78-82.

Nefedov, V.I. (1988). *X-ray photoelectron spectroscopy of solid surfaces.* Utrecht, The Netherlands. VSP BV.

Nightingale, R.E. (1962). *Nuclear graphite*. New York, NY. Academic Press.

O'Donnell, J.H. and Sangster, D.F. (1970). *Principles of radiation chemistry.* New York, NY. American Elsevier Publishing Company, Inc.

Pabby, A.K., Rizvi, S.S.H. and Sastre, A.M. (2009). *Handbook of membrane separations: chemical, pharmaceutical, food and biotechnological applications.* Boca Raton, FL. Taylor & Francis Group, LLC.

Parker Hannifin Corporation. (2011). Address: 242 Neck Road, Haverhill, MA 01835.

Pecharsky, V.K. and Zavalij, P.Y. (2009). *Fundamentals of powder diffraction and structural characterization of materials*. New York, NY. Springer Science+Business Media, LLC.

Pierson, H.O. (1993). *Handbook of carbon, graphite, diamond and fullerenes*. New Jersey, Noyes Publications.

Pimenta, M.A., Dresselhaus, G., Dresselhaus, M.S., Cançado, L.G., Jorio, A. and Saito, R. (2007). Studying disorder in graphite-based systems by Raman spectroscopy. *Physical Chemistry Chemical Physics, 9,* 1276-1291.

Poquet, E., Lumbroso, N., Hoarau, J., Marchand, A., Pacault, A. and Soule, D.E. (1960). *Journal of Applied Physics, 80,* 1020-1028.

Primak, W. (1978). Annealing of radiation damage in graphite. *Journal of Applied Physics, 49,* 4761.

Reich, S. and Thomsen, C. (2004). Raman spectroscopy of graphite. *Philasophical Transactions of the Royal Society A, 362,* 2271-2288.

Reynolds, W.N. and Goggin P.R. (1960). The annealing of electron irradiation damage in graphite. *Philasophical Magazine, 5,* 1049.

Shengtao, Z., Anyan, G., Huanfang, G. and Xiangqian, C. (2011), Characterization of exfoliated graphite prepared with the method of secondary intervening. *International Journal of Industrial Chemistry, 2,* 123-130.

Sibilia, J.P. (1996). *A guide to materials characterization and chemical analysis*. New York, NY. Wiley-VCH.

Simmons, J.H.W. (1965). *Radiation damage in graphite*. London, UK. Pergamon Press.

Skoog, D.A., West, D.M. and Holler, F.J. (1988). *Fundamentals of analytical chemistry, 5th edition.* New York, NY. W.B. Saunders Company.

Snead, L. and Burchell, T. (2011). *Oxidation of high-quality graphite for IFE.* Oak Ridge, TN. Oak Ridge National Laboratory.

Spinks, J.W.T. and Woods, R.J. (1990). *An introduction to radiation chemistry*. New York, NY. John Wiley and Sons.

Stein, S.E. and Brown, R.L. (1985). Chemical theory of graphite-like molecules. *Carbon, 23,* 105.

Suryanarayana, C. and Norton, M.G. (1998). *X-ray diffraction: A practical approach.* New York, NY. Plenum Press.

Suthersan, S.S. (2002). *Natural and enhanced remediation systems*. Boca Raton, FL. CRC Press.

Swallow, A.J. (1973). *Radiation chemistry, an introduction*. New York, NY. John Wiley and Sons.

Sykes, M.L., Edwards, I.A.S. and Thomas, K.M. (1993). Metal carbonyl decomposition and carbon deposition in the advances gas-cooled nuclear reactor. *Carbon, 31,* 467-472.

Takamato, K. and Chance, M.R. (2006). Radiolytic protein footprinting with mass spectrometry to probe the structure of macromolecular complexes. *Annual Review of Biophysics and Biomolecular Structure, 35,* 251-276.

Tanabe, T. (1996). Radiation damage of graphite – Degradation of material parameters and defect structures. *Physica Scripta, 64,* 7-16.

Tanabe T. and Muto S. (1992). On the mechanism of dimensional change of neutron irradiated graphite. *Applied Physics Letters, 61,* 1638-1640.

Telling, R.H. and Heggie, M.I. (2007). Radiation defects in graphite. *Philosophical Magazine, 87,* 31.

Theodosiou, A., Carley, A.F. and Taylor, S.H. (2012). A Raman investigation into the effect of temperature on ion-induced damage of graphite. *Journal of Nuclear Materials, 426*, 26-30.

Tuinstra, F. and Koenig, J.L. (1970). Raman spectrum of graphite. *Journal of Chemical Physics, 53*, 1126-1130.

Turner, J.E. (1995). *Atoms, radiation, and radiation protection.* New York, NY. J. Wiley.

UCAR Carbon Company, Inc. (2002). Address: 12900 Snow Road, Parma, OH 44130.

U.S. Geological Survey. (2001). http://pubs.usgs.gov/of/2001/of01-041/htmldocs/xrpd.htm.

U.S. Nuclear Regulatory Commission. (2010). *HTGR Technology Course*. Rockville, MD. U.S. Nuclear Regulatory Commission.

U.S. Nuclear Regulatory Commission. (2012). *Title 10 of the Code of Federal Regulations*. Washington, DC. Office of the Federal Register.

Van der Heide, P. (2011). *X-ray photoelectron spectroscopy*. New York, NY. John Wiley & Sons.

Was, G.S. (2007). *Fundamentals of radiation materials science: Metals and alloys.* New York, NY. Springer.

Weil, J.A. and Bolton, J.R. (2007). *Electron paramagnetic resonance: Elementary theory and practical applications*. Hoboken, NJ. John Wiley & Sons, Inc.

Wickham, AJ. (1998). *Graphite moderator lifecycle behavior: IAEA-TECDOC-901*. Vienna, Austria. IAEA.

Wickam, A.J., Best, J.V. and Wood, C.J. (1977). Recent advances in the theories of carbon dioxide radiolysis and radiolytic graphite corrosion. *Radiation Physics and Chemistry, 10*, 107-117.

Willis, C., Boyd, A.W. and Binder, P.E. (1970). Carbon monoxide yields in the radiolysis of carbon dioxide at very high dose rates. *Canadian Journal of Chemistry, 48,* 1951-1954.

Woods, R.J. and Pikaev, A.K. (1994). *Applied radiation chemistry: Radiation processing*. New York, NY. John Wiley & Sons, Inc.

Xiaowei, L., Jean-Charles, R. and Suyuan, Y. (2004). Effect of temperature on graphite oxidation behavior. *Nuclear Engineering and Design, 227,* 273-280.

Yazyev, O.V., Tavernelli, I., Rothlisberger, U. and Helm, L. (2007). Early stages of radiation damage in graphite and carbon nanostructures; A first-principles molecular dynamics study. *Physical Review B, 75,* 115418.

Zerbetto, F. (1991). Annealing graphite-like structures. A Monte Carlo-quantum chemical study. *Chemical Physics, 150,* 39/45.

Zhao, Y.X. and Spain, I.L. (1989). X-ray diffraction data for graphite to 20 GPa. *Physical Review B, 40,* 993-997.

Li, Z., Chen, D., Fu, X., Miao, W., and Zhang, Z. The influence of pores on irradiation property of selected nuclear graphites. *Advances in Material Science and Engineering, 2012,* 640462.

Zumdahl, S.S. and Zumdahl, S.A. (2010). *Chemistry, 8th edition*. Belmont, CA. Centage Learning.